

Bharat Bhushan

Biomimetics

Bioinspired Hierarchical-Structured
Surfaces for Green Science
and Technology

**BIOLOGICAL AND MEDICAL PHYSICS,
BIOMEDICAL ENGINEERING**

For further volumes:
<http://www.springer.com/series/3740>

BIOLOGICAL AND MEDICAL PHYSICS, BIOMEDICAL ENGINEERING

The fields of biological and medical physics and biomedical engineering are broad, multidisciplinary and dynamic. They lie at the crossroads of frontier research in physics, biology, chemistry, and medicine. The Biological and Medical Physics, Biomedical Engineering Series is intended to be comprehensive, covering a broad range of topics important to the study of the physical, chemical and biological sciences. Its goal is to provide scientists and engineers with textbooks, monographs, and reference works to address the growing need for information.

Books in the series emphasize established and emergent areas of science including molecular, membrane, and mathematical biophysics; photosynthetic energy harvesting and conversion; information processing; physical principles of genetics; sensory communications; automata networks, neural networks, and cellular automata. Equally important will be coverage of applied aspects of biological and medical physics and biomedical engineering such as molecular electronic components and devices, biosensors, medicine, imaging, physical principles of renewable energy production, advanced prostheses, and environmental control and engineering.

Editor-in-Chief:

Elias Greenbaum, Oak Ridge National Laboratory, Oak Ridge, Tennessee, USA

Editorial Board:

Masuo Aizawa, Department of Bioengineering, Tokyo Institute of Technology, Yokohama, Japan

Olaf S. Andersen, Department of Physiology, Biophysics & Molecular Medicine, Cornell University, New York, USA

Robert H. Austin, Department of Physics, Princeton University, Princeton, New Jersey, USA

James Barber, Department of Biochemistry, Imperial College of Science, Technology and Medicine, London, England

Howard C. Berg, Department of Molecular and Cellular Biology, Harvard University, Cambridge, Massachusetts, USA

Victor Bloomfield, Department of Biochemistry, University of Minnesota, St. Paul, Minnesota, USA

Robert Callender, Department of Biochemistry, Albert Einstein College of Medicine, Bronx, New York, USA

Steven Chu, Lawrence Berkeley National Laboratory, Berkeley, California, USA

Louis J. DeFelice, Department of Pharmacology, Vanderbilt University, Nashville, Tennessee, USA

Johann Deisenhofer, Howard Hughes Medical Institute, The University of Texas, Dallas, Texas, USA

George Feher, Department of Physics, University of California, San Diego, La Jolla, California, USA

Hans Frauenfelder, Los Alamos National Laboratory, Los Alamos, New Mexico, USA

Ivar Giaever, Rensselaer Polytechnic Institute, Troy, New York, USA

Sol M. Gruner, Cornell University, Ithaca, New York, USA

Judith Herzfeld, Department of Chemistry, Brandeis University, Waltham, Massachusetts, USA

Mark S. Humayun, Doheny Eye Institute, Los Angeles, California, USA

Pierre Joliot, Institute de Biologie Physico-Chimique, Fondation Edmond de Rothschild, Paris, France

Lajos Keszthelyi, Institute of Biophysics, Hungarian Academy of Sciences, Szeged, Hungary

Robert S. Knox, Department of Physics and Astronomy, University of Rochester, Rochester, New York, USA

Aaron Lewis, Department of Applied Physics, Hebrew University, Jerusalem, Israel

Stuart M. Lindsay, Department of Physics and Astronomy, Arizona State University, Tempe, Arizona, USA

David Mauzerall, Rockefeller University, New York, New York, USA

Eugenie V. Mielczarek, Department of Physics and Astronomy, George Mason University, Fairfax, Virginia, USA

Markolf Niemz, Medical Faculty Mannheim, University of Heidelberg, Mannheim, Germany

V. Adrian Parsegian, Physical Science Laboratory, National Institutes of Health, Bethesda, Maryland, USA

Linda S. Powers, University of Arizona, Tucson, Arizona, USA

Earl W. Prohofsky, Department of Physics, Purdue University, West Lafayette, Indiana, USA

Andrew Rubin, Department of Biophysics, Moscow State University, Moscow, Russia

Michael Seibert, National Renewable Energy Laboratory, Golden, Colorado, USA

David Thomas, Department of Biochemistry, University of Minnesota Medical School, Minneapolis, Minnesota, USA

Bharat Bhushan

Biomimetics

Bioinspired
Hierarchical-Structured Surfaces
for Green Science and Technology

With 170 Figures



Springer

Professor Bharat Bhushan
Ohio State University
Nanoprobe Laboratory for Bio- and Nanotechnology and Biomimetics
201 West 19th Avenue
Columbus, OH 43210-1142, USA
E-mail: bhushan.2@osu.edu

Biological and Medical Physics, Biomedical Engineering ISSN 1618-7210
ISBN 978-3-642-25407-9 ISBN 978-3-642-25408-6 (eBook)
DOI 10.1007/978-3-642-25408-6
Springer Heidelberg New York Dordrecht London

Library of Congress Control Number: 2012940336

© Springer-Verlag Berlin Heidelberg 2012

This work is subject to copyright. All rights are reserved by the Publisher, whether the whole or part of the material is concerned, specifically the rights of translation, reprinting, reuse of illustrations, recitation, broadcasting, reproduction on microfilms or in any other physical way, and transmission or information storage and retrieval, electronic adaptation, computer software, or by similar or dissimilar methodology now known or hereafter developed. Exempted from this legal reservation are brief excerpts in connection with reviews or scholarly analysis or material supplied specifically for the purpose of being entered and executed on a computer system, for exclusive use by the purchaser of the work. Duplication of this publication or parts thereof is permitted only under the provisions of the Copyright Law of the Publisher's location, in its current version, and permission for use must always be obtained from Springer. Permissions for use may be obtained through RightsLink at the Copyright Clearance Center. Violations are liable to prosecution under the respective Copyright Law.

The use of general descriptive names, registered names, trademarks, service marks, etc. in this publication does not imply, even in the absence of a specific statement, that such names are exempt from the relevant protective laws and regulations and therefore free for general use.

While the advice and information in this book are believed to be true and accurate at the date of publication, neither the authors nor the editors nor the publisher can accept any legal responsibility for any errors or omissions that may be made. The publisher makes no warranty, express or implied, with respect to the material contained herein.

Printed on acid-free paper

Springer is part of Springer Science+Business Media (www.springer.com)

To my granddaughter Sahana Agarwal

Preface

Nature has developed materials, objects, and processes that function from the macroscale to the nanoscale. The emerging field of biomimetics allows one to mimic biology or nature to develop nanomaterials, nanodevices, and processes which provide desirable properties. Hierarchical structures with dimensions of features ranging from the macroscale to the nanoscale are extremely common in nature to provide properties of interest. The biologically inspired materials and structured surfaces are eco-friendly or green with minimum human impact on the environment and are being explored for various commercial applications. This recognition has led to “Green Science and Technology,” the term used for the first time in this book.

There are a large number of objects including bacteria, plants, land and aquatic animals, and seashells with properties of commercial interest. This book presents an overview of the general field of biomimetics and biomimetics-inspired surfaces. It deals with various examples of biomimetics, which include surfaces with roughness-induced superomniphobicity, self-cleaning, antifouling, and controlled adhesion. It primarily focuses on the *Lotus* effect which exhibits superhydrophobicity, self-cleaning, antifouling, low adhesion, and drag reduction. This book also includes the floating water fern which floats over water, rose petal effect which can provide either low adhesion or high adhesion, oleophobic/oleophilic surfaces inspired from aquatic animals, sharkskin which exhibits low drag and antifouling, and gecko feet which exhibits reversible adhesion.

This book provides theoretical background, characterization of natural objects and relevant mechanisms, and inspired structured surface of commercial interest. We hope this book would serve as a catalyst for further innovations as well as serve as a useful reference in the emerging field of biomimetics. This book should also serve as an excellent text for a one-semester graduate course in biomimetics or as a companion text for a general course in nanotechnology. Given the interdisciplinary nature of the discipline, the appeal of this book is expected to be broad.

The work reported in this book is largely based on the pioneering contributions made by former and present students, postdoctoral fellows, and visiting scholars. Special mention is deserved by Dr. Yong Chae Jung, a former Ph.D. student working in fabrication and characterization; Prof. Michael Nosonovsky, a former visiting

scholar and an ongoing collaborator in theoretical modeling; and Prof. Kerstin Koch of Nees-Institute for Biodiversity of Plants at University of Bonn, Germany, who spent a sabbatical year in the author's lab. All of them contributed immensely to the research on the *Lotus Effect*. Dr. Tae-Wan Kim, a visiting scholar, contributed immensely on theoretical modeling of Gecko Adhesion. Brian Dean, a graduate student, contributed to the understanding of the mechanisms of the sharks skin effect. Other postdoctoral fellows and students who have contributed include Dr. Andrei G. Peressadko (Gecko Adhesion), Zack Burton (*Lotus Effect*), Eun Kyu Her (Rose Petal Effect), Robert Sayer (Gecko Adhesion), James Hunt (*Salvinia Effect*), Daniel Ebert (*Lotus Effect*), and Dr. Hyungoo Lee (Gecko Adhesion). Finally, the author would like to thank Caterina Runyon-Spears for administrative support.

My special thanks goes to my wife Sudha, who has been forbearing of my 24/7 commitment to science.

Columbus, Ohio

Bharat Bhushan

Contents

1	Introduction	1
1.1	Lessons from Nature	2
1.2	Industrial Significance	6
1.3	Research Objective and Approach.....	6
1.4	Organization of the Book	7
	References	7
2	Roughness-Induced Superomniphobic Surfaces: Lessons from Nature	11
2.1	Definitions and Applications	11
2.2	Natural Superhydrophobic, Self-Cleaning, Low Adhesion/Drag Reduction Surfaces with Antifouling	13
2.3	Natural Superoleophobic, Self-Cleaning, and Low-Drag Surfaces with Antifouling	15
2.4	Natural Superhydrophobic and High-Adhesion Surfaces	15
2.5	Summary	16
	References	16
3	Modeling of Contact Angle for a Liquid in Contact with a Rough Surface	19
3.1	Contact Angle Definition	19
3.2	Homogenous and Heterogeneous Interfaces and the Wenzel and Cassie–Baxter Equations	20
3.2.1	Limitations of the Wenzel and Cassie Equations	26
3.2.2	Range of Applicability of the Wenzel and Cassie Equations	28
3.3	Contact Angle Hysteresis	32
3.4	Stability of a Composite Interface and Role of Hierarchical Structure	34
3.5	The Cassie–Baxter and Wenzel Wetting Regime Transition	38
3.6	Summary	42
	References	43

Part I Lotus Effect

4 Lotus Effect Surfaces in Nature	49
4.1 Plant Leaves	49
4.2 Characterization of Superhydrophobic and Hydrophilic Leaf Surfaces	51
4.2.1 Experimental Techniques	51
4.2.2 SEM Micrographs	52
4.2.3 Contact Angle Measurements	53
4.2.4 Surface Characterization Using an Optical Profiler	54
4.2.5 Surface Characterization, Adhesion, and Friction Using an AFM	57
4.2.6 Role of the Hierarchical Roughness	62
4.3 Summary	64
References	64
5 Fabrication Techniques Used for Structures with Superhydrophobicity, Self-Cleaning, Low Adhesion/Low Drag with Antifouling Properties	67
5.1 Roughening to Create One-Level Structure	67
5.2 Coating to Create One-Level Hydrophobic Structures	72
5.3 Methods to Create Two-Level (Hierarchical) Structures	73
References	75
6 Fabrication and Characterization of Micro-, Nano-, and Hierarchical Structured Surfaces	79
6.1 Introduction	79
6.2 Experimental Techniques	81
6.2.1 Contact Angle, Surface Roughness, and Adhesion	81
6.2.2 Droplet Evaporation Studies	82
6.2.3 Bouncing Droplet Studies	82
6.2.4 Vibrating Droplet Studies	82
6.2.5 Microdroplet Condensation and Evaporation Studies Using ESEM	83
6.2.6 Generation of Submicron Droplets	83
6.2.7 Waterfall/Jet Tests	86
6.2.8 Wear and Friction Tests	87
6.3 Micro- and Nanopatterned Polymers	88
6.3.1 Contact Angle	89
6.3.2 Effect of Submicron Droplet on Contact Angle	91
6.3.3 Adhesive Force	91
6.3.4 Summary	92
6.4 Micropatterned Si Surfaces	93
6.4.1 Cassie–Baxter and Wenzel Transition Criteria	96
6.4.2 Effect of Pitch Value on the Transition	98

6.4.3	Observation of Transition During the Droplet Evaporation	100
6.4.4	Another Cassie–Baxter and Wenzel Transition for Different Series	104
6.4.5	Contact Angle Hysteresis and Wetting–Dewetting Asymmetry	106
6.4.6	Contact Angle Measurements During Condensation and Evaporation of Microdroplets on Micropatterned Surfaces	110
6.4.7	Observation of Transition During the Bouncing Droplet	113
6.4.8	Summary	118
6.5	Ideal Surfaces with Hierarchical Structure	119
6.6	Hierarchical Structured Surfaces with Wax Platelets and Tubules Using Nature’s Route	120
6.6.1	Effect of Nanostructures with Various Wax Platelet Crystal Densities on Superhydrophobicity	125
6.6.2	Effect of Hierarchical Structure with Wax Platelets on the Superhydrophobicity	129
6.6.3	Effect of Hierarchical Structure with Wax Tubules on Superhydrophobicity	133
6.6.4	Self-Cleaning Efficiency of Hierarchical Structured Surfaces	140
6.6.5	Observation of Transition During the Bouncing Droplet	142
6.6.6	Observation of Transition During the Vibrating Droplet	146
6.6.7	Measurement of Fluid Drag Reduction	152
6.6.8	Summary	152
6.7	Mechanically Durable Hierarchical Structured Surfaces	153
6.7.1	CNT Composites	154
6.7.2	Nanoparticle Composites	163
6.8	Summary	169
	References	171

Part II Salvinia Effect

7	Fabrication and Characterization of Micropatterned Structures Inspired	179
7.1	Introduction	179
7.2	Characterization of Leaves and Fabrication of Inspired Structural Surfaces	181

7.3	Measurement of Contact Angle and Adhesion.....	182
7.3.1	Observation of Pinning and Contact Angle	182
7.3.2	Adhesion	184
7.4	Summary.....	184
	References.....	186

Part III Rose Petal Effect

8	Characterization of Rose Petals and Fabrication and Characterization of Superhydrophobic Surfaces with High and Low Adhesion	189
8.1	Introduction.....	189
8.2	Characterization of Two Kinds of Rose Petals and Their Underlying Mechanisms	190
8.3	Fabrication of Surfaces with High and Low Adhesion	196
8.4	Summary.....	205
	References.....	206

Part IV Oleophobic/Oleophilic Surfaces

9	Modeling, Fabrication, and Characterization of Oleophobic/Oleophilic Surfaces.....	209
9.1	Introduction.....	209
9.2	Modeling of Contact Angle for Various Surfaces.....	210
9.3	Experimental Techniques	211
9.4	Fabrication and Characterization of Oleophobic Surfaces	213
9.4.1	Wetting Behavior on Flat and Micropatterned Surfaces	214
9.4.2	Wetting Behavior on Flat and Micropatterned Surfaces with $C_{20}F_{42}$	218
9.4.3	Wetting Behavior on Nano- and Hierarchical Structures and Sharkskin Replica	220
9.5	Summary.....	222
	References.....	223

Part V Shark skin Effect

10	Shark skin Surface for Fluid-Drag Reduction in Turbulent Flow	227
10.1	Introduction	227
10.2	Mechanisms of Fluid Drag	229
10.3	Role of Riblets in Drag Reduction	232
10.4	Studies with Various Riblet Geometries.....	234
10.4.1	Studies with 2D Riblets	239
10.4.2	Studies with 3D Riblets	242
10.4.3	Riblet Trends in Pipe Flow	246

10.5	Riblet Fabrication and Applications	246
10.5.1	Riblet Dimension Selection	248
10.5.2	Application of Riblets for Drag Reduction and Antifouling	248
10.5.3	Riblet Fabrication Methods for Study and Applications	251
10.6	Effect of Fluid Slip and Polymer Additives on Fluid Drag	252
10.6.1	The Effect of Fluid Slip on Drag Reduction	253
10.6.2	Effect of Fish Mucus and Polymers on Fluid Drag	256
10.7	Summary	258
	References	262

Part VI Gecko Adhesion

11	Gecko Adhesion	269
11.1	Introduction	269
11.2	Hairy Attachment Systems	270
11.3	Tokay Gecko	272
11.3.1	Construction of Tokay Gecko	272
11.3.2	Adhesion Enhancement by Division of Contacts and Multilevel Hierarchical Structure	274
11.3.3	Peeling	277
11.3.4	Self-Cleaning	280
11.4	Attachment Mechanisms	283
11.4.1	van der Waals Forces	285
11.4.2	Capillary Forces	286
11.5	Adhesion Measurements and Data	287
11.5.1	Adhesion Under Ambient Conditions	288
11.5.2	Effects of Temperature	290
11.5.3	Effects of Humidity	291
11.5.4	Effects of Hydrophobicity	292
11.6	Adhesion Modeling of Fibrillar Structures	292
11.6.1	Single Spring Contact Analysis	294
11.6.2	The Multilevel Hierarchical Spring Analysis	295
11.6.3	Adhesion Results of the Multilevel Hierarchical Spring Model	298
11.6.4	Capillary Effects	305
11.7	Adhesion Database of Fibrillar Structures	310
11.7.1	Fiber Model	310
11.7.2	Single Fiber Contact Analysis	310
11.7.3	Constraints	311
11.7.4	Numerical Simulation	316
11.7.5	Results and Discussion	316

11.8	Fabrication of Gecko Skin-Inspired Structures	321
11.8.1	Single-Level Roughness Structures	321
11.8.2	Multilevel Hierarchical Structures	328
11.9	Summary	331
	References	333
12	Outlook	339
Index		341
Biography		349

Chapter 1

Introduction

*Nature always tends to act in the simplest way—Bernoulli
(In nature,) nothing is lacking and nothing is superfluous—Leonardo da Vinci*

Look deep into nature and you will understand everything—Albert Einstein

Biomimetics means mimicking biology or nature. Biomimetics allows biologically inspired design, adaptation, or derivation from nature. The word biomimetics was coined by polymath Otto Schmitt in 1957, who, in his doctoral research, developed a physical device that mimicked the electrical action of a nerve. Biomimetics is derived from the Greek word biomimesis. Other words used include bionics (coined in 1960 by Jack Steele of Wright-Patterson Air Force Base in Dayton, OH), biomimicry, and biognosis. The word biomimetics first appeared in Webster's dictionary in 1974 and is defined as "the study of the formation, structure or function of biologically produced substances and materials (as enzymes or silk) and biological mechanisms and processes (as protein synthesis or photosynthesis) especially for the purpose of synthesizing similar products by artificial mechanisms which mimic natural ones." The field of biomimetics is highly interdisciplinary. It involves the understanding of biological functions, structures, and principles of various objects found in nature by biologists, physicists, chemists, and material scientists and the biologically inspired design and fabrication of various materials and devices of commercial interest by engineers, material scientists, chemists, biologists, and others (Bhushan, 2009).

Nature has gone through evolution over the 3.8 billion years since life is estimated to have appeared on the Earth (Gordon, 1976). Biological materials are highly organized from the molecular to the nano-, micro-, and macroscales, often in a hierarchical manner with intricate nanoarchitecture that ultimately makes up a myriad of different functional elements (Alberts et al., 2008). Nature uses commonly found materials. Properties of materials and surfaces result from a complex interplay between surface structure and morphology and physical and

chemical properties. Many materials, surfaces, and objects in general provide multifunctionality.

Biomimetics-inspired materials and surfaces are eco-friendly or green which have generated significant interest and are helping to shape green science and technology.

1.1 Lessons from Nature

The understanding of the functions provided by objects and processes found in nature can guide us to design and produce nanomaterials, nanodevices, and processes (Bhushan, 2009). There are a large number of objects, including bacteria, plants, land and aquatic animals, and seashells, with properties of commercial interest. Figure 1.1 provides an overview of various objects from nature and their selected functions (Bhushan, 2009). These include bacteria (Jones and Aizawa, 1991), plants (Koch et al., 2008, 2009), insects/spiders/lizards/frogs (Autumn et al., 2000; Gorb, 2001; Bhushan, 2007, 2010), aquatic animals (Bechert et al., 1997, 2000; Dean and Bhushan, 2010), birds (Jakab, 1990; Bechert et al., 2000), seashells/bones/teeth (Lowenstam and Weiner, 1989; Sarikaya and Aksay, 1995; Mann, 2001; Alexander and Diskin, 2004; Meyers et al., 2008), spiderweb (Jin and Kaplan, 2003; Bar-Cohen, 2011), moth-eye effect (Genzer and Efimenko, 2006; Mueller, 2008) and structure coloration (Parker, 2009), the fur and skin of polar bears (Stegmaier et al., 2009), and biological systems with self-healing capacity (Fratzl and Weinkamer, 2007; Nosonovsky and Bhushan, 2009) and sensory-aid devices (Barth et al., 2003; Bar-Cohen, 2011).

Figure 1.2 shows a montage of some examples from nature (Bhushan, 2009). Some leaves of water-repellent plants, such as *Nelumbo nucifera* (Lotus), are known to be superhydrophobic, self-cleaning, and antifouling due to hierarchical roughness (microbumps superimposed with a nanostructure) and the presence of a hydrophobic wax coating (Neinhuis and Barthlott, 1997; Barthlott and Neinhuis, 1997; Wagner et al., 2003; Burton and Bhushan, 2006; Bhushan and Jung, 2006, 2011; Bhushan, 2009, 2011; Koch et al., 2008, 2009). Water droplets on these surfaces readily sit on the apex of nanostructures because air bubbles fill in the valleys of the structure under the droplet. Therefore, these leaves exhibit considerable superhydrophobicity (Fig. 1.2a). Two strategies used for catching insects by plants for digestion are having sticky surfaces or sliding structures. As an example, for catching insects using sticky surfaces, the glands of the carnivorous plants of the genus *Pinguicula* (butterworts) and *Drosera* (sundew), shown in Fig. 1.2b, secrete adhesives and enzymes to trap and digest small insects, such as mosquitoes and fruit flies (Koch et al., 2009). Water striders (*Gerris remigis*) have the ability to stand and walk upon a water surface without getting wet (Fig. 1.2c). Even the impact of rain droplets with a size greater than the water strider's size does not immerse it in the water. Gao and Jiang (2004) showed that the special hierarchical structure of the water strider's legs, which are covered by large numbers of oriented tiny hairs (microsetae) with fine nanogrooves and covered with cuticle wax, makes the

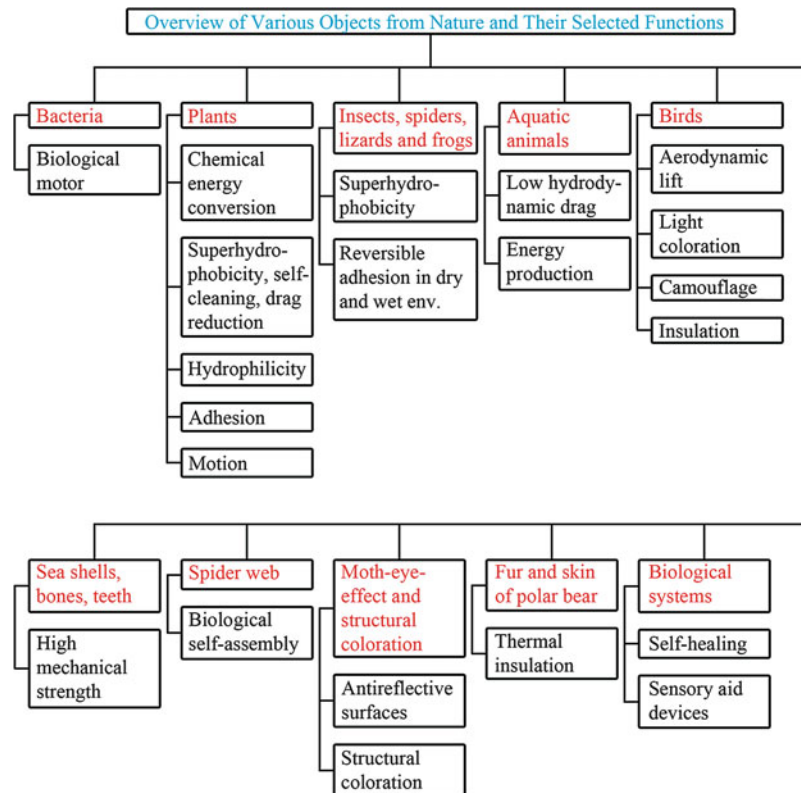


Fig. 1.1 An overview of various objects from nature and their selected function (Bhushan, 2009)

leg surfaces superhydrophobic, is responsible for the water resistance, and enables them to stand and walk quickly on the water surface.

A gecko is the largest animal that can produce high (dry) adhesion to support its weight with a high factor of safety. Gecko skin is comprised of a complex hierarchical structure of lamellae, setae, branches, and spatula (Autumn et al., 2000; Gao et al., 2005; Bhushan, 2007). The attachment pads on two feet of the Tokay gecko have an area of approximately 220 mm^2 (Fig. 1.2d). Approximately 3×10^6 setae on their toes that branch off into about three billion spatula on two feet can produce a clinging ability of approximately 20 N (vertical force required to pull a lizard down a nearly vertical (85°) surface) and allow them to climb vertical surfaces at speeds of over 1 m/s, with the capability to attach or detach their toes in milliseconds (Bhushan, 2007).

Shark skin, which is a model from nature for a low drag surface, is covered by very small individual tooth-like scales called dermal denticles (little skin teeth), ribbed with longitudinal grooves (aligned parallel to the local flow direction of the water). These grooved scales lift vortices to the tips of the scales, resulting

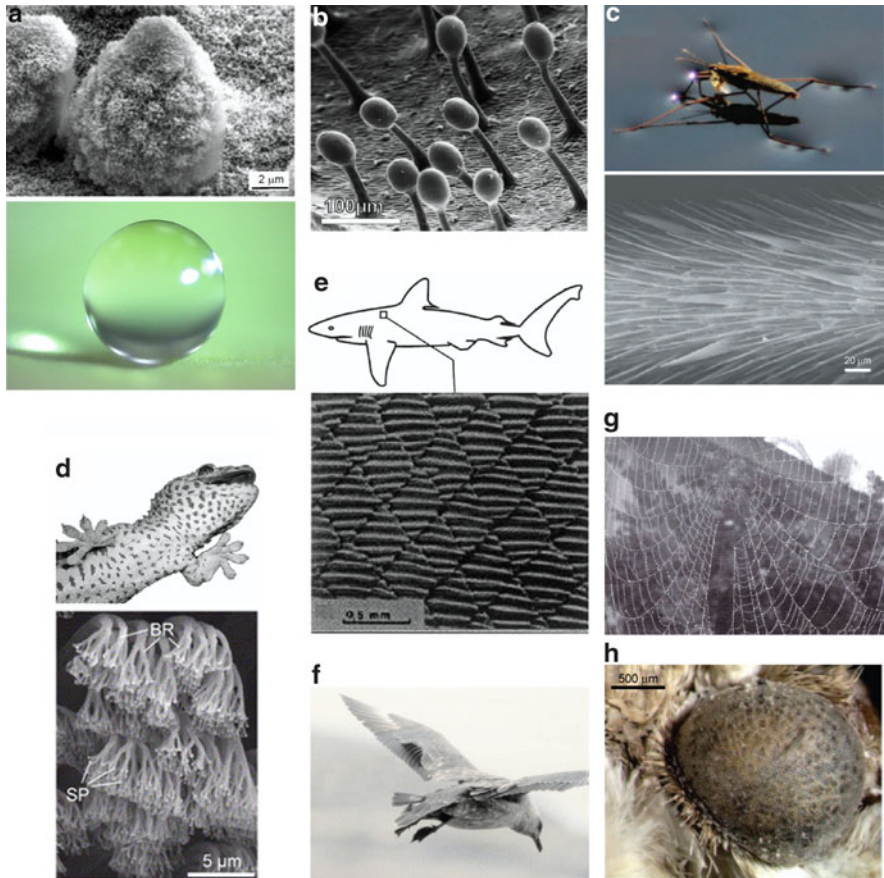


Fig. 1.2 Montage of some examples from nature (a) Lotus effect (Bhushan et al., 2009), (b) glands of carnivorous plant secrete adhesive to trap insects (Koch et al., 2009), (c) water strider walking on water (Gao and Jiang, 2004), (d) gecko foot exhibiting reversible adhesion (Gao et al., 2005), (e) scale structure of shark reducing drag (Jung and Bhushan, 2010), (f) wings of a bird in landing approach, (g) spiderweb made of silk material (Bar-Cohen, 2011), and (h) antireflective moth's eye (Genzer and Efimenco, 2006)

in water moving efficiently over their surface (Bechert et al., 2000; Dean and Bhushan, 2010). The spacing between these dermal denticles is such that microscopic aquatic organisms have difficulty adhering to the surface, making the skin surface antifouling (Carman et al., 2006; Genzer and Efimenco, 2006; Kesel and Liedert, 2007; Ralston and Swain, 2009; Bixler and Bhushan, 2012). An example of scale structure on the right front of a Galapagos shark (*Carcharhinus galapagensis*) is shown in Fig. 1.2e (Jung and Bhushan, 2010).

Birds consist of several consecutive rows of covering feathers on their wings, which are flexible (Fig. 1.2f). These movable flaps develop the lift. When a bird



Fig. 1.3 Biomimetics-inspired antique jewelry pieces crafted by Van Cleef and Arpels in early 1900s

lands, a few feathers are deployed in front of the leading edges of the wings, which help to reduce the drag on the wings.

The spider generates silk fiber and has a sufficient supply of raw material for its silk to span great distances (Jin and Kaplan, 2003; Bar-Cohen, 2011). Spiderweb is a structure built of a one-dimensional fiber (Fig. 1.2g). The fiber is very strong and continuous and is insoluble in water. The web can hold a significant amount of water droplets, and it is resistant to rain, wind, and sunlight (Sarikaya and Aksay, 1995; Bar-Cohen, 2011).

The eyes of moths are antireflective to visible light and consist of hundreds of hexagonally organized nanoscopic pillars, each approximately 200 nm in diameter and height, which result in a very low reflectance for visible light (Fig. 1.2h) (Genzer and Efimenko, 2006; Mueller, 2008). These nanostructures' optical surfaces make the eye surface nearly antireflective in any direction.

Scientists and engineers take inspiration from nature for the purpose of functionality and commercial applications. Artists take inspiration from nature for the purpose of beauty and design. Figure 1.3 shows four examples of bioinspired antique jewelry pieces crafted by Van Cleef and Arpels in the early 1900s.

1.2 Industrial Significance

The word biomimetics is relatively new; however, our ancestors looked to nature for inspiration and development of various materials and devices many centuries ago (Ball, 2002; Bar-Cohen, 2011; Vincent et al., 2006; Anonymous, 2007; Meyers et al., 2008). For example, the Chinese tried to make artificial silk some 3,000 years ago. Leonardo da Vinci, a genius of his time, studied how birds fly and proposed designs of flying machines. In the twentieth century, various products, including the design of aircraft, have been inspired by nature. Since the 1980s, the artificial intelligence and neural networks in information technology have been inspired by the desire to mimic the human brain. The existence of biocells and deoxyribonucleic acid (DNA) serves as a source of inspiration for nanotechnologists who hope to one day build self-assembled molecular-scale devices. In molecular biomimetics, proteins are being utilized in controlling materials formation in practical engineering toward self-assembled, hybrid, and functional materials structure (Grunwald et al., 2009; Tamerler and Sarikaya, 2009). Since the mid-1990s, the so-called Lotus effect has been used to develop a variety of surfaces for superhydrophobicity, self-cleaning, low adhesion, and drag reduction in fluid flow, as well as antifouling (Bhushan et al., 2009; Bhushan, 2011; Bhushan and Jung 2011). Replication of the dynamic climbing and peeling ability of geckos has been carried out to develop treads of wall-climbing robots (Cutkosky and Kim, 2009). Replication of shark skin has been used to develop moving objects with low drag, e.g., whole-body swimsuits (Dean and Bhushan, 2010). Nanoscale architecture used in nature for optical reflection and antireflection has been used to develop reflecting and antireflecting surfaces. In the field of biomimetic materials, there is an area of bioinspired ceramics based on sea shells and other biomimetic materials. Inspired by the fur of the polar bear, artificial furs and textiles have been developed. Self-healing of biological systems found in nature is of interest for self-repair. Biomimetics is also guiding in the development of sensory-aid devices.

Various features found in nature objects are on the nanoscale. The major emphasis on nanoscience and nanotechnology since early 1990s has provided a significant impetus in mimicking nature using nanofabrication techniques for commercial applications (Bhushan, 2010). Biomimetics has spurred interest across many disciplines. It is estimated that the 100 largest biomimetic products had generated US \$1.5 billion over 2005–2008. The annual sales are expected to continue to increase dramatically.

1.3 Research Objective and Approach

The objective of biomimetics research is to develop biologically inspired materials and surfaces of commercial interest. The approach is threefold:

- (1) Objects are selected from nature which provide functionality of commercial interest.

- (2) The objects are characterized to understand how a natural object provides functionality. Then, it is modeled and structures are generally fabricated in the lab using nature's route to verify one's understanding. Modeling is used to develop optimum structures.
- (3) Nature has a limited toolbox and uses rather basic materials and routine fabrication methods; it capitalizes on hierarchical structures. Once one understands how nature does it, one can then fabricate optimum structures using smart materials and fabrication techniques to provide functionality of interest.

1.4 Organization of the Book

This book primarily focuses on the Lotus Effect which exhibits superhydrophobicity, self-cleaning, and low adhesion/drag reduction, as well as antifouling. The book also includes the floating water fern which floats over water, rose petal effect which can provide either low adhesion or high adhesion, oleophobic/oleophilic surfaces inspired from aquatic animals, shark skin which exhibits low drag and antifouling, and gecko feet which exhibit reversible adhesion. We start with an introduction to roughness-induced superomniphobic surfaces and modeling of contact angle for a liquid in contact with a rough surface followed by the five topics just mentioned.

References

- Alberts B, Johnson A, Lewis J, Raff M, Roberts K, Walter P (eds) (2008) Molecular biology of the cell. Garland Science, New York
- Alexander RM, Diskin A (2004) Human bones: a scientific and pictorial investigation. Pi Press, New York
- Anonymous (2007) Biomimetics: strategies for product design inspired by nature. Department of Trade and Industry, London
- Autumn K, Liang YA, Hsieh ST, Zesch W, Chan WP, Kenny TW, Fearing R, Full RJ (2000) Adhesive force of a single gecko foot-hair. *Nature* 405:681–685
- Ball P (2002) Natural strategies for the molecular engineer. *Nanotechnology* 13:R15–R28
- Bar-Cohen Y (2011) Biomimetics: nature-based innovation. CRC, Boca Raton, FL
- Barth FG, Humphrey JAC, Secomb TW (2003) Sensors and sensing in biology and engineering. Springer, New York
- Barthlott W, Neinhuis C (1997) Purity of the sacred lotus, or escape from contamination in biological surfaces. *Planta* 202:1–8
- Bechert DW, Bruse M, Hage W, Van Der Hoeven JGT, Hoppe G (1997) Experiments on drag-reducing surfaces and their optimization with an adjustable geometry. *J Fluid Mech* 338:59–87
- Bechert DW, Bruse M, Hage W (2000) Experiments with three-dimensional ripples as an idealized model of shark skin. *Exp Fluids* 28:403–412
- Bhushan B (2007) Adhesion of multi-level hierarchical attachment systems in gecko feet. *J Adhes Sci Technol* 21:1213–1258
- Bhushan B (2009) Biomimetics: lessons from nature—an overview. *Philos Trans R Soc A* 367:1445–1486
- Bhushan B (2010) Springer handbook of nanotechnology, 3rd edn. Springer, Heidelberg

- Bhushan B (2011) Biomimetics inspired surfaces for drag reduction and oleophobicity/phobicity. *Beilstein J Nanotechnol* 2:66–84
- Bhushan B, Jung YC (2006) Micro and nanoscale characterization of hydrophobic and hydrophilic leaf surface. *Nanotechnology* 17:2758–2772
- Bhushan B, Jung YC (2011) Natural and biomimetic artificial surfaces for superhydrophobicity, self-cleaning, low adhesion, and drag reduction. *Prog Mater Sci* 56:1–108
- Bhushan B, Jung YC, Koch K (2009) Micro-, nano- and hierarchical structures for superhydrophobicity, self-cleaning and low adhesion. *Philos Trans R Soc A* 367:1631–1672
- Bixler GD, Bhushan B (2012) Biofouling: lessons from nature. *Philos Trans R Soc A* 370:2381–2417
- Burton Z, Bhushan B (2006) Surface characterization and adhesion and friction properties of hydrophobic leaf surfaces. *Ultramicroscopy* 106:709–719
- Carman ML, Estes TG, Feinburg AW, Schumacher JF, Wilkerson W, Wilson LH, Callow ME, Callow JA, Brennan AB (2006) Engineered antifouling microtopographies—correlating wettability with cell attachment. *Biofouling* 22:11–21
- Cutkosky MR, Kim S (2009) Design and fabrication of multi-materials structures for bio-inspired robots. *Philos Trans R Soc A* 367:1799–1813
- Dean B, Bhushan B (2010) Shark-skin surfaces for fluid-drag reduction in turbulent flow: a review. *Philos Trans R Soc A* 368:4775–4806; 368:5737
- Fratzl P, Weinkamer R (2007) Nature's hierarchical materials. *Prog Mater Sci* 52:1263–1334
- Gao XF, Jiang L (2004) Biophysics: water-repellent legs of water striders. *Nature* 432:36
- Gao H, Wang X, Yao H, Gorb S, Arzt E (2005) Mechanics of hierarchical adhesion structures of geckos. *Mech Mater* 37:275–285
- Genzer J, Efimenko K (2006) Recent developments in superhydrophobic surfaces and their relevance to marine fouling: a review. *Biofouling* 22:339–360
- Gorb S (2001) Attachment devices of insect cuticle. Kluwer Academic, Dordrecht
- Gordon JE (1976) The new science of strong materials, or why you don't fall through the floor, 2nd edn. Pelican-Penguin, London
- Grunwald I, Rischka K, Kast SM, Scheibel T, Bargel H (2009) Mimicking biopolymers on a molecular scale: nano(bio)technology based on engineering proteins. *Philos Trans R Soc A* 367:1727–1726
- Jakab PL (1990) Vision of a flying machine. Smithsonian Institution Press, Washington DC
- Jin H-J, Kaplan DL (2003) Mechanism of silk processing in insects and spiders. *Nature* 424: 1057–1061
- Jones CJ, Aizawa S (1991) The bacterial flagellum and flagellar motor: structure, assembly, and functions. *Adv Microb Physiol* 32:109–172
- Jung YC, Bhushan B (2010) Biomimetic structures for fluid drag reduction in laminar and turbulent flows. *J Phys Condens Matter* 22:035104
- Kesel A, Liedert R (2007) Learning from nature: non-toxic biofouling control by shark skin effect. *Comp Biochem Physiol A* 146:S130
- Koch K, Bhushan B, Barthlott W (2008) Diversity of structure, morphology, and wetting of plant surfaces (invited). *Soft Matter* 4:1943–1963
- Koch K, Bhushan B, Barthlott W (2009) Multifunctional surface structures of plants: an inspiration for biomimetics (invited). *Prog Mater Sci* 54:137–178
- Lowenstam HA, Weiner S (1989) On biomineralization. Oxford University Press, Oxford
- Mann S (2001) Biomineralization. Oxford University Press, Oxford
- Meyers MA, Chen PY, Lin AYM, Seki Y (2008) Biological materials: structure and mechanical properties. *Prog Mater Sci* 53:1–206
- Mueller T (2008) Biomimetics design by natures. National Geographic April 2008, 68–90
- Neinhuis C, Barthlott W (1997) Characterization and distribution of water-repellent, self-cleaning plant surfaces. *Ann Bot* 79:667–677
- Nosonovsky M, Bhushan B (2009) Thermodynamics of surface degradation, self-organization, and self-healing for biomimetic surfaces. *Philos Trans R Soc A* 367:1607–1627
- Parker AR (2009) Natural photonics for industrial applications. *Philos Trans R Soc A* 367: 1759–1782

- Ralston E, Swain G (2009) Bioinspiration—the solution for biofouling control? *Bioinsp Biomim* 4:1–9
- Sarikaya M, Aksay IA (1995) Biomimetic design and processing of materials. American Institute of Physics, Woodbury
- Stegmaier T, Linke M, Planck H (2009) Bionics in textiles: flexible and translucent thermal insulations for solar thermal applications. *Philos Trans R Soc A* 367:1749–1758
- Tamerler C, Sarikaya M (2009) Molecular biomimetics: nanotechnology and molecular medicine utilizing genetically engineered peptides. *Philos Trans R Soc A* 367:1705–1726
- Vincent JFV, Bogatyрева OA, Bogatyrev NR, Bowyer A, Pahl AK (2006) Biomimetics: its practice and theory. *J Roy Soc Interf* 3:471–482
- Wagner P, Furstner R, Barthlott W, Neinhuis C (2003) Quantitative assessment to the structural basis of water repellency in natural and technical surfaces. *J Exp Bot* 54:1295–1303

Chapter 2

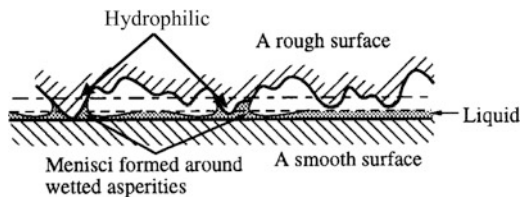
Roughness-Induced Superomniphobic Surfaces: Lessons from Nature

2.1 Definitions and Applications

The primary parameter that characterizes wetting is the static contact angle, which is defined as the angle that a liquid makes with a solid. The contact angle depends on several factors, such as surface energy, surface roughness, and its cleanliness (Adamson, 1990; Israelachvili, 1992; Bhushan, 1999, 2002, 2011a; Nosonovsky and Bhushan, 2008a). If the water wets the surface, referred to as wetting liquid or hydrophilic surface, the value of the static contact angle is $0 \leq \theta \leq 90^\circ$, whereas if the liquid does not wet the surface, referred to as a non-wetting liquid or hydrophobic surface, the value of the contact angle is $90^\circ < \theta \leq 180^\circ$. Surfaces with high energy, formed by polar molecules, tend to be hydrophilic, whereas those with low energy and built of nonpolar molecules tend to be hydrophobic. The term hydrophobic/hydrophilic, which was originally applied only to water (“hydro-” means “water” in Greek), is often used to describe the contact of a solid surface with any liquid. The term “oleophobic/oleophilic” is used with regard to wetting by oil and organic liquids. The terms “omniphobic” and “omniphilic” are used for surfaces which either repel or attract (or are wetted with) a wide range of liquids, including water, oils, solvents, and other low surface energy liquids, respectively.

Surfaces with a contact angle of less than 10° are called superhydrophilic, while surfaces with a contact angle between 150° and 180° are called superhydrophobic. In fluid flow, in order to have low drag and for applications requiring the self-cleaning feature, in addition to the high contact angle, superhydrophobic surfaces should also have very low water contact angle hysteresis. The contact angle at the front of the droplet (advancing contact angle) is greater than that at the back of the droplet (receding contact angle), resulting in contact angle hysteresis (CAH), which is the difference between the advancing and receding contact angles, representing two stable values. It occurs due to surface roughness and surface heterogeneity. Contact angle hysteresis reflects the irreversibility of the wetting/dewetting cycle. It is a measure of energy dissipation during the flow of a droplet along a solid surface. At a low value of CAH, the droplets may roll in addition to slide and

Fig. 2.1 A schematic diagram of condensed water vapor from the environment, forming meniscus bridges at asperity contacts which lead to an intrinsic attractive force



take contaminants with them, providing a self-cleaning ability known as the “Lotus Effect.” Surfaces with low contact angle hysteresis have a low water roll-off (tilt) angle, which denotes the angle to which a surface must be tilted for roll-off of water drops (Exstrand, 2002; Kijlstra et al., 2002; Bhushan and Jung, 2008; Nosonovsky and Bhushan, 2007, 2008a, b, c; Bhushan, 2009). The tangent of the tilt angle is equal to the coefficient of friction of a droplet sliding/rolling on a surface. Surfaces with CAH or a low tilting angle of $<10^\circ$ are self-cleaning surfaces and with low adhesion/drag and antifouling called the Lotus Effect.

Self-cleaning surfaces are of interest in various applications, including self-cleaning windows, windshields, exterior paints for buildings and navigation ships, utensils, roof tiles, textiles, and solar panels. Low adhesion and drag reduction in fluid flow is of interest in many applications including micro-/nanofluidics-based biosensor applications (Bhushan, 2010). To reduce pressure drop and volume loss in micro-/nanochannels, it is desirable to minimize the drag force in the solid–liquid interface. Low adhesion/drag also exhibits antifouling of interest in various applications including membranes used in desalination and water purification (Bixler and Bhushan, 2012).

Superhydrophobic surfaces can also be used for energy conservation and conversion (Nosonovsky and Bhushan, 2008a, d, 2009a, b, 2010). Recent advances in superhydrophobic surfaces make such applications possible. Several concepts can be used. First, the hydrophobic/hydrophilic properties of a surface significantly affect the capillary adhesion force that, in turn, affects friction and energy dissipation during the sliding contact of solid surfaces. Selection of a proper superhydrophobic surface allows the reduction of energy dissipation. Second, superhydrophobic and superoleophobic surfaces can be used for fuel economy. Third, the recently discovered effect of reversible superhydrophobicity provides potential for new ways of energy conversion such as the microscale capillary engine.

Wetting may lead to the formation of concave-shaped menisci at the interface between hydrophilic solid bodies during static or sliding contact. These menisci develop a negative pressure leading to an intrinsic attractive force which increases adhesion and friction (Fig. 2.1). In some cases, the wet friction force can be greater than the dry friction force, which is usually undesirable (Bhushan, 1996, 1999, 2002, 2003, 2010, 2011a). On the other hand, high adhesion is desirable in some applications, such as adhesive tapes and adhesion of cells to biomaterial surfaces; therefore, enhanced wetting would be desirable in these applications. Numerous applications, such as magnetic storage devices and micro-/nanoelectromechanical systems (MEMS/NEMS), require surfaces with low adhesion and stiction (Bhushan et al.,

1995; Bhushan, 1996, 1998, 2001, 2003, 2010, 2011a). As the size of these devices decreases, surface forces tend to dominate over the volume forces, and adhesion and stiction constitute a challenging problem for proper operation of these devices. This makes the development of superhydrophobic surfaces with nonadhesive characteristics crucial for many of these emerging applications.

A related problem is icing, which may occur due to sticking of supercooled water droplets onto a solid surface, also known as freezing rain or atmospheric icing. It is undesirable as it leads to glazing roadways, breaking tree limbs and power lines, and stalling airfoils of aircraft. Icophobicity is defined as a surface's ability to prevent ice formation or to have very low adhesion to form ice. A class of superhydrophobic surfaces may be icophobic as well (Cao et al., 2009).

Traditionally, hydrophobic surfaces can be achieved by selecting low surface energy materials/coatings. By using natures' route, both hydrophobic and superhydrophobic surfaces can be fabricated by introducing roughness which allows eco-friendly or green designs.

2.2 Natural Superhydrophobic, Self-Cleaning, Low Adhesion/Drag Reduction Surfaces with Antifouling

In the 1990s, biologists and materials scientists started to study natural superhydrophobic surfaces. Among them are the leaves of water-repellent plants, such as *Nelumbo nucifera* (Lotus), which have high contact angles with water (Fig. 2.2) (Neinhuis and Barthlott, 1997; Barthlott and Neinhuis, 1997; Wagner et al., 2003; Burton and Bhushan, 2006; Bhushan and Jung, 2006, 2011a; Bhushan, 2009; Koch et al., 2008, 2009a). The leaf surface is very rough due to so-called papillose epidermal cells, which form papillae or microasperities. In addition to the microscale roughness, the surface of the papillae is also rough, with nanoscale asperities composed of three-dimensional epicuticular waxes which are long chain hydrocarbons and hydrophobic. The wax on the Lotus leaf exists as tubules, but on other leaves, waxes exist also in the form of platelets or other morphologies (Koch et al., 2008, 2009a). The hierarchical structure of these leaves has been studied by Burton and Bhushan (2006) and Bhushan and Jung (2006). The water droplets on these surfaces readily sit on the apex of the nanostructures because air bubbles fill in the valleys of the structure under the droplet. Therefore, these leaves exhibit considerable superhydrophobicity and extremely low contact angle hysteresis. Static contact angle and contact angle hysteresis of a Lotus leaf are about 164° and 3°, respectively (Bhushan et al., 2009b; Koch et al., 2009b). Simply, wax makes the surface hydrophobic, and hierarchical structure makes it superhydrophobic with low contact angle hysteresis. Because of the latter, the water droplets on the leaves remove any contaminant particles from their surfaces when they roll off, leading to self-cleaning (Neinhuis and Barthlott, 1997).

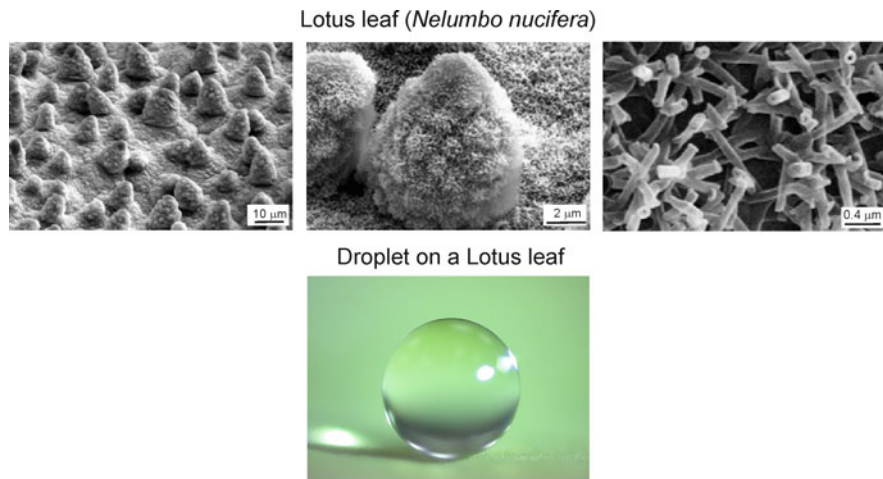


Fig. 2.2 SEM micrographs (shown at three magnifications) of Lotus (*Nelumbo nucifera*) leaf surface which consists of microstructure formed by papillose epidermal cells covered with 3D epicuticular wax tubules on surface, which create nanostructure, and image of water droplet sitting on the Lotus leaf (Bhushan et al., 2009b)

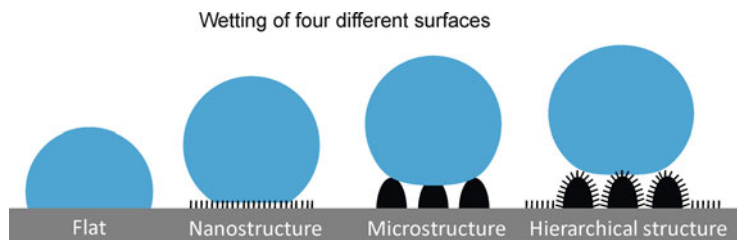


Fig. 2.3 Schematic and wetting of the four different surfaces. The largest contact area between the droplet and the surface is given in flat and microstructured surfaces, but is reduced in nanostructured surfaces and is minimized in hierarchical structured surfaces

It has been reported that all superhydrophobic and self-cleaning leaves consist of an intrinsic hierarchical structure (Koch et al., 2008, 2009a). Hierarchical structure provides air pocket formation, leading to the lowest contact area of an applied water droplet (Fig. 2.3), resulting in the reduction of contact angle hysteresis, tilt angle, and adhesive force responsible for self-cleaning, low adhesion, and antifouling (Bhushan and Jung, 2008, 2011; Nosonovsky and Bhushan, 2008a; Bhushan et al., 2009b; Bixler and Bhushan, 2012).

Other examples of biological objects include water striders (*Gerris remigis*) (Gao and Jiang, 2004) and mosquito (*Culex pipiens*) eyes (Gao et al., 2007). Their hierarchical structures are responsible for superhydrophobicity. Duck feathers and butterfly wings also provide superhydrophobicity (Bhushan, 2009). Their corrugated surfaces provide air pockets that prevent water from completely touching the surface.

2.3 Natural Superoleophobic, Self-Cleaning, and Low-Drag Surfaces with Antifouling

A model surface for superoleophobicity and self-cleaning is provided by sea animals such as fish and sharks, which are known to be well protected from contamination by oil pollution although they are wetted by water (Nosonovsky and Bhushan, 2009a; Jung and Bhushan, 2009). Fish scales have a hierarchical structure consisting of sector-like scales with diameters of 4–5mm covered by papillae 100–300 μm in length and 30–40 μm in width (Liu et al., 2009). Shark skin, which is a model from nature for a low-drag surface, is covered by very small individual tooth-like scales called dermal denticles (little skin teeth), shaped like small riblets with longitudinal grooves (aligned parallel to the local flow direction of the water). These riblets lift the vortices to the tips of the grooves and constrain them, resulting in water moving efficiently over their surface (Bechert et al., 2000; Bhushan, 2009, 2011b; Jung and Bhushan, 2009, 2010). The space between these dermal denticles is such that microscopic aquatic organisms have difficulty adhering to and colonizing the surface (Carman et al., 2006; Genzer and Efimenko, 2006; Kesel and Liedert, 2007; Ralston and Swain, 2009). If oil is present on the surfaces of sea animals in air or water, it repels oil and is oleophobic. Superoleophobic surfaces can also reduce significant losses of residual fuel in fuel tanks and pipes (Nosonovsky and Bhushan, 2008d).

2.4 Natural Superhydrophobic and High-Adhesion Surfaces

Unlike the Lotus leaf, some rose petals (*rosea Rehd*), scallions, and garlic exhibit superhydrophobicity with high contact angle hysteresis (Feng et al., 2008; Chang et al., 2009; Bhushan, 2010). While a water droplet can easily roll off the surface of a Lotus leaf, it stays pinned to the surface of these leaves. The different behavior of wetting between the Lotus leaf and the rose petal can be explained by different designs in the surface hierarchical micro- and nanostructure. Since the rose petal's microstructures have a larger pitch value than the Lotus leaf, the liquid is allowed to impregnate between the microstructure but partially penetrates into the nanostructure. This is referred to as the Cassie-impregnating wetting regime, in which the wetted surface area is less than that in the Wenzel regime but greater than that in the Cassie–Baxter regime, to be described later. Such an explanation implies that the extent of contact angle hysteresis increases with increasing wetted surface area, which is governed by surface micro- and nanostructure. These surfaces exhibit high adhesion.

2.5 Summary

The term omniphobic/omniphilic is used with regard to wetting by all liquids. A surface is superhydrophobic if it has a water contact angle above 150°. These surfaces are water repellent. These surfaces with low contact angle hysteresis (less than 10°) also have a self-cleaning effect, called the “Lotus Effect.” Water droplets roll off the surface and take contaminants with them. Self-cleaning surfaces with low adhesion/drag are of interest in various applications, e.g., self-cleaning windows, windshields, exterior paints for buildings, navigation ships and utensils, roof tiles, textiles, and solar panels. Low adhesion and drag reduction in fluid flow is of interest in many applications including micro-/nanofluidic-based biosensor applications. Also, superhydrophobic surfaces can be used for energy conservation and energy conversion. Low adhesion/drag also exhibits antifouling properties, e.g., membranes used in desalination and water purification.

Superhydrophobic surfaces are also desirable in the ambient environment to minimize stiction. When two hydrophilic surfaces come into contact, condensation of water vapor from the environment forms meniscus bridges at asperity contacts which lead to an intrinsic attractive force. This may lead to high adhesion and stiction.

Unlike Lotus leaves, some rose petals, scallions, and garlic exhibit superhydrophobicity with high contact angle hysteresis. These surfaces exhibit high adhesion.

Oleophobic/oleophilic is the term used with regard to wetting by oil and organic liquids. A model surface for superoleophobicity and self-cleaning is provided by many sea animals including fish and sharks, which are known to be well protected from contaminants from oil pollution although they are wetted by water. Structured surfaces of sea animals also exhibit antifouling.

References

- Adamson AV (1990) Physical chemistry of surfaces. Wiley, New York
Barthlott W, Neinhuis C (1997) Purity of the sacred lotus, or escape from contamination in biological surfaces. *Planta* 202:1–8
Bechert DW, Bruse M, Hage W (2000) Experiments with three-dimensional ripples as an idealized model of shark skin. *Exp Fluids* 28:403–412
Bhushan B (1996) Tribology and mechanics of magnetic storage systems, 2nd edn. Springer, New York
Bhushan B (1998) Tribology issues and opportunities in MEMS. Kluwer Academic, dordrecht
Bhushan B (1999) Principles and applications of tribology. Wiley, New York
Bhushan B (2001) Modern tribology handbook, vol 1–Principles of tribology; vol 2–Materials, coatings, and industrial applications. CRC, Boca Raton, FL
Bhushan B (2002) Introduction to tribology. Wiley, New York
Bhushan B (2003) Adhesion and stiction: mechanisms, measurement techniques and methods for reduction. *J Vac Sci Technol B* 21:2262–2296

- Bhushan B (2009) Biomimetics: lessons from nature—an overview. *Philos Trans R Soc A* 367: 1445–1486
- Bhushan B (2010) Springer handbook of nanotechnology, 3rd edn. Springer, Heidelberg
- Bhushan B (2011a) Nanotribology and Nanomechanics I—Measurement techniques, II—Nanotribology, biomimetics, and industrial applications, 3rd edn. Springer, Heidelberg
- Bhushan B (2011b) Biomimetics inspired surfaces for drag reduction and oleophobicity/phobicity. *Beilstein J Nanotechnol* 2:66–84
- Bhushan B, Her EK (2010) Fabrication of superhydrophobic surfaces with high and low adhesion inspired from rose petal. *Langmuir* 26:8207–8217
- Bhushan B, Jung YC (2006) Micro and nanoscale characterization of hydrophobic and hydrophilic leaf surface. *Nanotechnology* 17:2758–2772
- Bhushan B, Jung YC (2008) Wetting, adhesion and friction of superhydrophobic and hydrophilic leaves and fabricated micro/nanopatterned surfaces. *J Phys Condens Matter* 20:225010
- Bhushan B, Jung YC (2011) Natural and biomimetic artificial surfaces for superhydrophobicity, self-cleaning, low adhesion, and drag reduction. *Prog Mater Sci* 56:1–108
- Bhushan B, Israelachvili JN, Landman U (1995) Nanotribology: friction, wear and lubrication at the atomic scale. *Nature* 374:607–616
- Bhushan B, Jung YC, Koch K (2009a) Self-cleaning efficiency of artificial superhydrophobic surfaces. *Langmuir* 25:3240–3248
- Bhushan B, Jung YC, Koch K (2009b) Micro-, nano- and hierarchical structures for superhydrophobicity, self-cleaning and low adhesion. *Philos Trans R Soc A* 367:1631–1672
- Bixler GD, Bhushan B (2012) Biofouling: lessons from nature. *Philos Trans R Soc A* 370:2381–2417
- Burton Z, Bhushan B (2006) Surface characterization and adhesion and friction properties of hydrophobic leaf surfaces. *Ultramicroscopy* 106:709–719
- Cao L, Jones AK, Sikka VK, Wu J, Gao D (2009) Anti-icing superhydrophobic surfaces. *Langmuir* 25:12444–12448
- Carman ML, Estes TG, Feinburg AW, Schumacher JF, Wilkerson W, Wilson LH, Callow ME, Callow JA, Brennan AB (2006) Engineered antifouling microtopographies—correlating wettability with cell attachment. *Biofouling* 22:11–21
- Chang FM, Hong SJ, Sheng YJ, Tsao HK (2009) High contact angle hysteresis of superhydrophobic surfaces: hydrophobic defects. *Appl Phys Lett* 95:064102
- Exstrand CW (2002) Model for contact angle and hysteresis on rough and ultraphobic surfaces. *Langmuir* 18:7991–7999
- Feng L, Zhang Y, Xi J, Zhu Y, Wang N, Xia F, Jiang L (2008) Petal effect: a superhydrophobic state with high adhesive force. *Langmuir* 24:4114–4114
- Gao XF, Jiang L (2004) Biophysics: water-repellent legs of water striders. *Nature* 432:36
- Gao X, Yan X, Yao X, Xu L, Zhang K, Zhang J, Yang B, Jiang L (2007) The dry-style antifogging properties of mosquito compound eyes and artificial analogues prepared by soft lithography. *Adv Mater* 19:2213–2217
- Genzer J, Efimenko K (2006) Recent developments in superhydrophobic surfaces and their relevance to marine fouling: a review. *Biofouling* 22:339–360
- Israelachvili JN (1992) Intermolecular and surface forces, 2nd edn. Academic, London
- Jung YC, Bhushan B (2009) Wetting behavior of water and oil droplets in three phase interfaces for hydrophobicity/phobicity and oleophobicity/phobicity. *Langmuir* 25:14165–14173
- Jung YC, Bhushan B (2010) Biomimetic structures for fluid drag reduction in laminar and turbulent flows. *J Phys Condens Matter* 22:035104
- Kesel A, Liedert R (2007) Learning from nature: non-toxic biofouling control by shark skin effect. *Comp Biochem Physiol A* 146:S130
- Kijlstra J, Reihs K, Klami A (2002) Roughness and topology of ultra-hydrophobic surfaces. *Colloid Surf A Physicochem Eng Asp* 206:521–529
- Koch K, Bhushan B, Barthlott W (2008) Diversity of structure, morphology, and wetting of plant surfaces (invited). *Soft Matter* 4:1943–1963

- Koch K, Bhushan B, Barthlott W (2009a) Multifunctional surface structures of plants: an inspiration for biomimetics (invited). *Prog Mater Sci* 54:137–178
- Koch K, Bhushan B, Jung YC, Barthlott W (2009b) Fabrication of artificial lotus leaves and significance of hierarchical structure for superhydrophobicity and low adhesion. *Soft Matter* 5:1386–1393
- Liu M, Wang S, Wei Z, Song Y, Jiang L (2009) Bioinspired design of a superoleophobic and low adhesive water/solid interface. *Adv Mater* 21:665–669
- Neinhuis C, Barthlott W (1997) Characterization and distribution of water-repellent, self-cleaning plant surfaces. *Ann Bot (Lond)* 79:667–677
- Nosonovsky M, Bhushan B (2007a) Multiscale friction mechanisms and hierarchical surfaces in nano- and bio-tribology. *Mater Sci Eng R* 58:162–193
- Nosonovsky M, Bhushan B (2008a) Multiscale dissipative mechanisms and hierarchical surfaces: friction, superhydrophobicity, and biomimetics. Springer, Heidelberg
- Nosonovsky M, Bhushan B (2008b) Roughness-induced superhydrophobicity: a way to design non-adhesive surfaces. *J Phys Condens Matter* 20:225009
- Nosonovsky M, Bhushan B (2008c) Biologically-inspired surfaces: broadening the scope of roughness. *Adv Funct Mater* 18:843–855
- Nosonovsky M, Bhushan B (2008d) Superhydrophobicity for energy conversion and conservation applications. *J Adhes Sci Technol* 22:2105–2115
- Nosonovsky M, Bhushan B (2009a) Multiscale effects and capillary interactions in functional biomimetic surfaces for energy conversion and green engineering. *Philos Trans R Soc A* 367: 1511–1539
- Nosonovsky M, Bhushan B (2009b) Superhydrophobic surfaces and emerging applications: non-adhesion, energy, green engineering. *Curr Opin Colloid Interface Sci* 14:270–280
- Nosonovsky M, Bhushan B (2010) Green tribology: principles, research areas and challenges. *Philos Trans R Soc A* 368:4677–4694
- Ralston E, Swain G (2009) Bioinspiration—the solution for biofouling control? *Bioinspir Biomim* 4:1–9
- Wagner P, Furstner R, Barthlott W, Neinhuis C (2003) Quantitative assessment to the structural basis of water repellency in natural and technical surfaces. *J Exp Bot* 54:1295–1303

Chapter 3

Modeling of Contact Angle for a Liquid in Contact with a Rough Surface

In this chapter, the modeling of wetting of rough surfaces is presented.

3.1 Contact Angle Definition

The surface atoms or molecules of liquids or solids have fewer bonds with neighboring atoms, and therefore, they have higher energy than similar atoms and molecules in the interior. This additional energy is characterized quantitatively by the surface tension or free surface energy γ , which is equal to the work that is required to create a unit area of the surface at a constant pressure and temperature. The unit of γ is J/m² or N/m, and it can be interpreted either as energy per unit surface area or as tension force per unit length of a line at the surface. When a solid is in contact with liquid, the molecular attraction will reduce the energy of the system below that for the two separated surfaces. This is expressed by the Dupré equation

$$W_{SL} = \gamma_{SA} + \gamma_{LA} - \gamma_{SL} \quad (3.1)$$

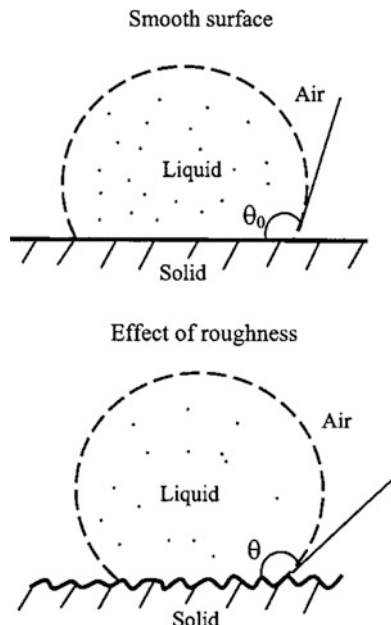
where W_{SL} is the work of adhesion per unit area, γ_{SA} and γ_{SL} are the surface energies of the solid against air and liquid, and γ_{LA} is the surface energy of liquid against air.

If a liquid droplet is placed on a smooth solid surface, the liquid and solid surfaces come together under equilibrium at a characteristic angle called the static contact angle θ_0 (Fig. 3.1). This contact angle can be determined by minimizing the net surface free energy of the system (Adamson, 1990; Israelachvili, 1992; Bhushan, 1999, 2002; Nosonovsky and Bhushan, 2008a). The total energy E_{tot} is given by

$$E_{tot} = \gamma_{LA}(A_{LA} + A_{SL}) - W_{SL}A_{SL} \quad (3.2)$$

where A_{SL} and A_{LA} are the contact areas of the liquid with the solid and air, respectively. It is assumed that the droplet of density ρ is smaller than the capillary length, $(\gamma_{LA}/\rho g)^{1/2}$, so that the gravitational potential energy can be neglected. It is

Fig. 3.1 Schematic of a liquid droplet in contact with a smooth solid surface (contact angle, θ_0) and with a rough solid surface (contact angle, θ)



also assumed that the volume and pressure are constant, so that the volumetric energy does not change. At the equilibrium $dE_{\text{tot}} = 0$, which yields

$$\gamma_{\text{LA}}(dA_{\text{LA}} + dA_{\text{SL}}) - W_{\text{SL}}dA_{\text{SL}} = 0. \quad (3.3)$$

For a droplet of constant volume, it is easy to show using geometrical considerations that

$$dA_{\text{LA}}/dA_{\text{SL}} = \cos \theta_0. \quad (3.4)$$

Combining (3.1), (3.3), and (3.4), the well-known Young equation for the contact angle is obtained:

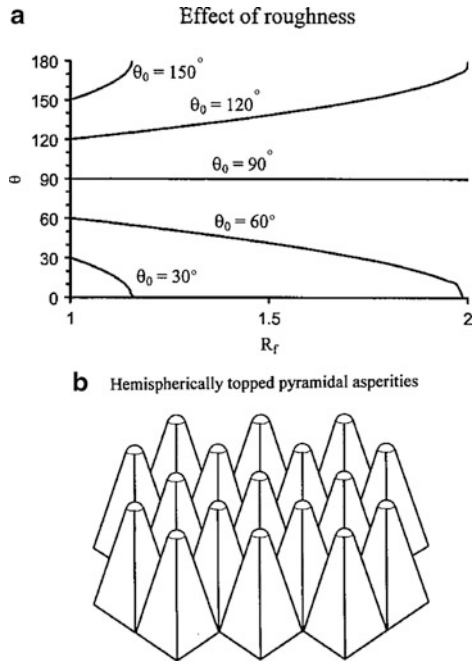
$$\cos \theta_0 = \frac{\gamma_{\text{SA}} - \gamma_{\text{SL}}}{\gamma_{\text{LA}}}. \quad (3.5)$$

Equation (3.5) provides an expression for the static contact angle for given surface energies. Note that although the term “air” is used, the analysis does not change in the case of another gas, such as water vapor.

3.2 Homogenous and Heterogeneous Interfaces and the Wenzel and Cassie–Baxter Equations

In this section, the equations that govern the contact angle of liquid with a rough surface and both homogenous and heterogeneous interfaces are introduced and discussed.

Fig. 3.2 (a) Contact angle for a rough surface (θ) as a function of the roughness factor (R_f) for various contact angles of the smooth surface (θ_0), and (b) schematic of square-based hemispherically topped pyramidal asperities with complete packing (Nosonovsky and Bhushan, 2005)



First, consider a water droplet on a rough surface with a homogeneous interface. The interface area increases with respect to that for a smooth surface. Using the surface force balance and empirical considerations, the contact angle of a water droplet upon a rough solid surface, θ , is related to that upon a smooth surface, θ_0 , for a homogeneous interface (Fig. 3.1), through the non-dimensional surface roughness factor, $R_f > 1$, equal to the ratio of the rough surface area, A_{SL} , to its flat projected area, A_F (Wenzel, 1936):

$$\cos \theta = \frac{dA_{LA}}{dA_F} = \frac{A_{SL}}{A_F} \frac{dA_{LA}}{dA_{SL}} = R_f \cos \theta_0 \quad (3.6)$$

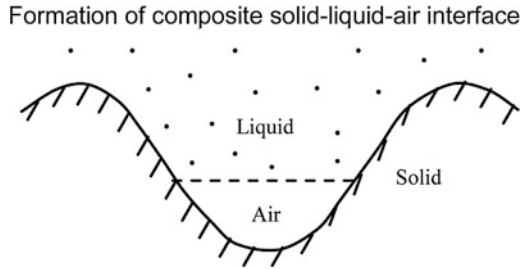
where,

$$R_f = \frac{A_{SL}}{A_F}. \quad (3.7)$$

This is called the Wenzel equation.

The dependence of the contact angle on the roughness factor is presented in Fig. 3.2a for different values of θ_0 . The Wenzel model predicts that a hydrophobic surface ($\theta_0 > 90^\circ$) becomes more hydrophobic with an increase in R_f , while a hydrophilic surface ($\theta_0 < 90^\circ$) becomes more hydrophilic with an increase in R_f (Nosonovsky and Bhushan, 2005; Jung and Bhushan, 2006). As an example, Fig. 3.2b shows a geometry with square-based hemispherically topped pyramidal asperities with a rounded top, which has complete packing. The size and shape of the asperities can be optimized for a desired roughness factor.

Fig. 3.3 Schematic of the formation of a composite solid–liquid–air interface for a rough surface



For a heterogeneous interface composed of two fractions, one with the fractional area f_1 and the contact angle θ_1 and the other with f_2 and θ_2 , respectively (so that $f_1 + f_2 = 1$), the contact angle is given by the Cassie equation ([Cassie, 1948](#)):

$$\cos \theta = f_1 \cos \theta_1 + f_2 \cos \theta_2. \quad (3.8)$$

In some cases, the gaseous phase including water vapor, commonly referred to as “air” in the literature, may be trapped in the cavities of a rough surface, resulting in a composite solid–liquid–air interface as opposed to the homogeneous solid–liquid interface. A composite interface (Fig. 3.3) consists of a fractional geometrical area of the solid–liquid interface under the droplet ($f_1 = f_{\text{SL}}$, $\theta_1 = \theta$) and of the liquid–air interface ($f_2 = f_{\text{LA}} = 1 - f_{\text{SL}}$, $\cos \theta_2 = -1$). For this case, combining (3.7) and (3.8) yields the so-called Cassie–Baxter equation ([Cassie and Baxter, 1944](#)):

$$\begin{aligned} \cos \theta &= R_f f_{\text{SL}} \cos \theta_0 - 1 + f_{\text{SL}}, \\ \text{or} \\ \cos \theta &= R_f \cos \theta_0 - f_{\text{LA}}(R_f \cos \theta_0 + 1). \end{aligned} \quad (3.9)$$

There is one more interface in which liquid film impregnates some of the cavities ahead of the droplet as well ([Cassie, 1948](#)). It consists of two fractions—solid–liquid homogeneous interface (Wenzel interface) and some of the neighboring cavities filled with liquid. The energy of such a rough surface with filled cavities is different from the energy of the surface with empty cavities. Filled cavities correspond to the water–water interface with $\cos \theta_2 = 1$ ($\theta_2 = 0^\circ$). Using (3.8) and (3.6) for this case, one gets

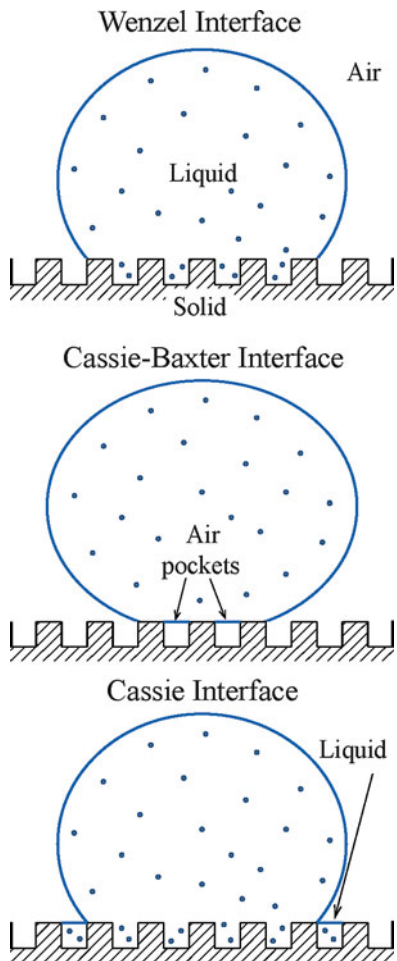
$$\cos \theta = 1 + f_{\text{SL}}(R_f \cos \theta_0 - 1). \quad (3.10)$$

A liquid film filling the cavities ahead of the droplet is possible when $\theta_0 < \theta_c$, where θ_c is the critical contact angle given by ([de Gennes et al., 2003](#))

$$\cos \theta_c = \frac{1 - f_{\text{SL}}}{R_f - f_{\text{SL}}}. \quad (3.11)$$

This wetting interface is referred to as the Cassie interface or the Cassie impregnating interface. Equation (3.10) is used sometimes for the homogeneous interface

Fig. 3.4 Schematics of configurations showing the Wenzel interface [homogeneous interface (3.6)], Cassie–Baxter interface [composite interface with air pockets (3.9)], and the Cassie interface [homogeneous interface and some of the neighboring cavities filled with liquid, also referred to as the Cassie impregnating interface (3.10)]



instead of (3.6), if the rough surface is covered by some of the cavities filled with liquid (de Gennes et al., 2003).

For easy comparison, Fig. 3.4 schematically shows liquid sitting on rough surfaces showing the Wenzel, Cassie–Baxter, and Cassie interfaces. An extension of these three regimes to nine regimes has been presented by Bhushan and Nosonovsky (2010).

Equation (3.9) for the composite interface was derived using (3.6) and (3.8), and it could also be obtained independently. For this purpose, two sets of interfaces are considered: a liquid-air interface with the ambient and a flat composite interface under the droplet, which itself involves solid–liquid, liquid–air, and solid–air interfaces. For fractional flat geometrical areas of the solid–liquid and liquid–air interfaces under the droplet, f_{SL} and f_{LA} ($f_{SL} = 1 - f_{LA}$), the flat area of the composite interface is (Nosonovsky and Bhushan, 2008a)

$$A_F = f_{SL} A_F + f_{LA} A_F = R_f A_{SL} + f_{LA} A_F. \quad (3.12)$$

In order to calculate the contact angle in a manner similar to the derivation of (3.6), the differential area of the liquid–air interface under the droplet, $f_{LA} dA_F$, should be subtracted from the differential of the total liquid–air area dA_{LA} , which yields the Cassie–Baxter equation (3.9):

$$\begin{aligned} \cos \theta &= \frac{dA_{LA} - f_{LA} dA_F}{dA_F} = \frac{A_{SL}}{A_F} \frac{dA_{LA}}{dA_{SL}} - f_{LA} \\ &= R_f f_{SL} \cos \theta_0 - f_{LA} \\ &= R_f \cos \theta_0 - f_{LA}(R_f \cos \theta_0 + 1). \end{aligned}$$

The dependence of the contact angle on the roughness factor and fractional liquid–air area for hydrophilic and hydrophobic surfaces with a composite interface is presented in Fig. 3.5a. According to (3.9), even for a hydrophilic surface, the contact angle increases with an increase of f_{LA} . At a high value of f_{LA} , a surface can become hydrophobic; however, the value required may be unachievable, or the formation of air pockets may become unstable. Using the Cassie–Baxter equation, the value of f_{LA} at which a hydrophilic surface could turn into a hydrophobic one is given as (Jung and Bhushan, 2006)

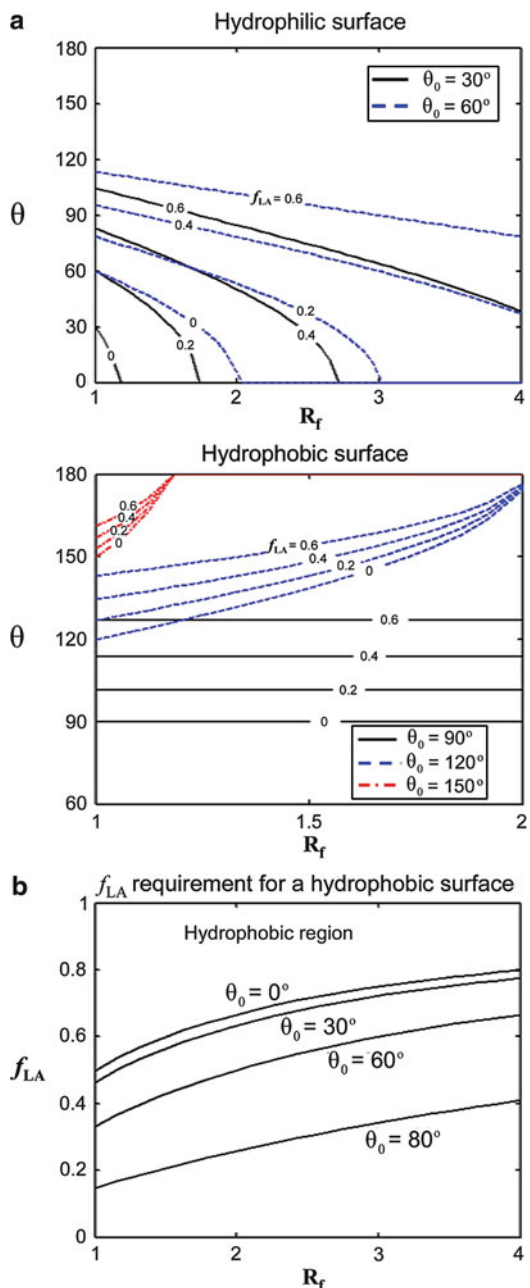
$$f_{LA} \geq \frac{R_f \cos \theta_0}{R_f \cos \theta_0 + 1} \quad \text{for } \theta_0 < 90^\circ. \quad (3.13)$$

Figure 3.5b shows the value of f_{LA} requirement as a function of R_f for four surfaces with different contact angles, θ_0 . Hydrophobic surfaces can be achieved above a certain f_{LA} value as predicted by (3.13). The upper part of each contact angle line is the hydrophobic region. For the hydrophobic surface, contact angle increases with an increase in f_{LA} both for smooth and rough surfaces.

For high f_{LA} , a nanopattern is desirable because whether a liquid–air interface is generated depends upon the ratio of distance between two adjacent asperities and droplet radius. Furthermore, asperities can pin liquid droplets and thus prevent liquid from filling the valleys between asperities. High R_f can be achieved by both micropatterns and nanopatterns.

Based on Nosonovsky and Bhushan (2008a, 2009), spreading of a liquid over a rough solid surface continues until simultaneously (3.5) (the Young equation) is satisfied locally at the triple line and the surface area is minimum over the entire liquid–air interface. The minimal surface area condition states that the sum of the inverse of the principal radii of curvature, R_1 and R_2 of the liquid surface, along the two mutually orthogonal planes (mean curvature), is constant at any point, which governs the shape of the liquid–air interface. The same condition is also the consequence of the Laplace equation, which relates pressure change through an interface, ΔP , with its mean curvature:

Fig. 3.5 (a) Contact angle for a rough surface (θ) as a function of the roughness factor (R_f) for various f_{LA} values on the hydrophilic surface and the hydrophobic surface, and (b) f_{LA} requirement for a hydrophilic surface to be hydrophobic as a function of the roughness factor (R_f) and θ_0 (Jung and Bhushan, 2006)



$$\frac{1}{R_1} + \frac{1}{R_2} = \frac{\Delta P}{\gamma_{LA}}. \quad (3.14)$$

Note that at the thermodynamic equilibrium (when condensation and evaporation occurs at the same speed), ΔP is dependent on the partial vapor pressure. For contact with saturated vapor, the mean curvature of the liquid–air interface is zero at equilibrium. A convex interface ($1/R_1 + 1/R_2 > 0$) results in evaporation prevailing over condensation; this is why small droplets tend to evaporate. However, a concave interface ($1/R_1 + 1/R_2 < 0$) results in condensation of saturated vapor prevailing over evaporation. Since the condensation prevails, a concave interface may be in thermodynamic equilibrium with undersaturated vapor. This is why concave menisci tend to condense even when the relative humidity is less than 100% (Nosonovsky and Bhushan, 2008a, 2009).

3.2.1 Limitations of the Wenzel and Cassie Equations

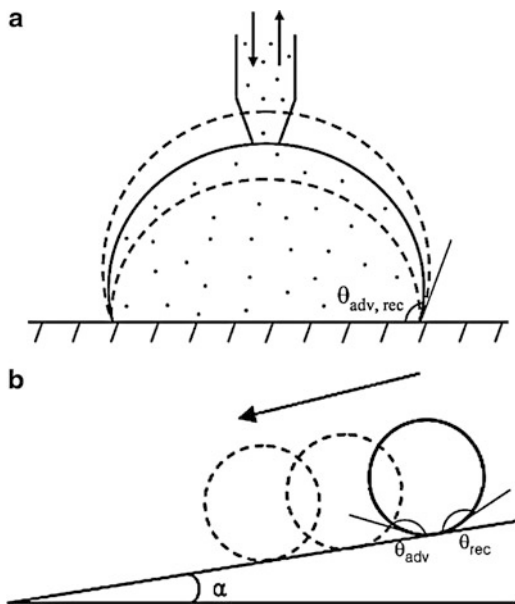
Based on Nosonovsky and Bhushan (2008a, d), the Cassie equation (3.8) is based on the assumption that the heterogeneous surface is composed of well-separated distinct patches of different material, so that the free surface energy can be averaged. It has been argued also that when the size of the chemical heterogeneities is very small (of atomic or molecular dimensions), the quantity that should be averaged is not the energy but the dipole moment of a macromolecule (Israelachvili and Gee, 1989), and (3.8) should be replaced by (Nosonovsky and Bhushan, 2008d)

$$(1 + \cos \theta)^2 = f_1(1 + \cos \theta_1)^2 + f_2(1 + \cos \theta_2)^2. \quad (3.15)$$

Experimental studies of polymers with different functional groups showed a good agreement with (3.15) (Tretinnikov, 2000).

Based on Nosonovsky and Bhushan (2008a, d), later investigations put the Wenzel and Cassie equations into a thermodynamic framework; however, they also showed that there is no one single value of the contact angle for a rough or heterogeneous surface (Johnson and Dettre, 1964; Marmur, 2003; Li and Amirfazli, 2006). The contact angle can be in a range of values between the receding contact angle, θ_{rec} , and the advancing contact angle, θ_{adv} . The system tends to achieve the receding contact angle when liquid is removed (e.g., at the rear end of a moving droplet), whereas the advancing contact angle is achieved when the liquid is added (e.g., at the front end of a moving droplet) (Fig. 3.6a). When the liquid is neither added nor removed, the system tends to have a static or “most stable” contact angle, which is given approximately by (3.5), (3.6), (3.8), and (3.10). Another way to define θ_{adv} and θ_{rec} is to consider a moving liquid droplet over a tilted surface as shown in Fig. 3.6b. The liquid is pumped at the leading edge, and the contact angle at this edge corresponds to the advancing contact angle. The liquid is pumped away from the trailing edge, and the angle at the trailing edge corresponds to the receding contact angle.

Fig. 3.6 (a) Liquid droplet in contact with a rough surface with liquid is added or removed (advancing and receding contact angles are θ_{adv} and θ_{rec} , respectively) and (b) tilted surface profile (tilt angle, α with a moving liquid droplet)



The contact angle provided by (3.5), (3.6), (3.8), and (3.10) is a macroscale parameter, so it is sometimes called “the apparent contact angle.” Based on Nosonovsky and Bhushan (2008a, c), the actual angle under which the liquid–air interface comes in contact with the solid surface at the micro- and nanoscale can be different. There are several reasons for that. First, water molecules tend to form a thin layer upon the surfaces of many materials. This is because of a long-distance van der Waals adhesion force that creates the so-called disjoining pressure (Derjaguin and Churaev, 1974). This pressure is dependent upon the liquid layer thickness and may lead to the formation of stable thin films. In this case, the shape of the droplet near the triple line (line of contact of the solid, liquid, and air, to be shown later in Fig. 3.8) transforms gradually from the spherical surface into a precursor layer, and thus, the nanoscale contact angle is much smaller than the apparent contact angle. In addition, adsorbed water monolayers and multilayers are common for many materials. Second, even carefully prepared atomically smooth surfaces exhibit a certain roughness and chemical heterogeneity. Water tends first to cover the hydrophilic spots with high surface energy and low contact angle (Checco et al., 2003). The tilt angle due to roughness can also contribute to the apparent contact angle. Third, the very concept of the static contact angle is not well defined. For practical purposes, the contact angle, which is formed after a droplet is gently placed upon a surface and stops propagating, is considered the static contact angle. However, depositing the droplet involves adding liquid while leaving it involves evaporation, so it is difficult to avoid dynamic effects. Fourth, for small droplets and curved triple lines, the effect of the contact line tension may be significant. Molecules at the surface of a liquid or solid phase have higher energy because

Table 3.1 Wetting of a superhydrophobic surface as a multiscale process ([Nosonovsky and Bhushan, 2007c, 2008c](#))

Scale level	Characteristic length	Parameters	Phenomena	Interface
Macroscale	Droplet radius (mm)	Contact angle, droplet radius	Contact angle hysteresis	2D
Microscale	Roughness detail (μm)	Shape of the droplet, position of the liquid–air interface (h)	Kinetic effects	3D solid surface, 2D liquid surface
Nanoscale	Molecular heterogeneity (nm)	Molecular description	Thermodynamic and dynamic effects	3D

they are bonded to fewer molecules than those in the bulk. This leads to surface tension and surface energy. In a similar manner, molecules at the concave surface and, especially, at the edge have fewer bonds than those at the surface, which leads to line tension and curvature dependence of the surface energy. This effect becomes important when the radius of curvature is comparable with the so-called Tolman's length, normally of the molecular size ([Anisimov, 2007](#)). However, the triple line at the nanoscale can be curved so that the line tension effects become important ([Pompe et al., 2000](#)).

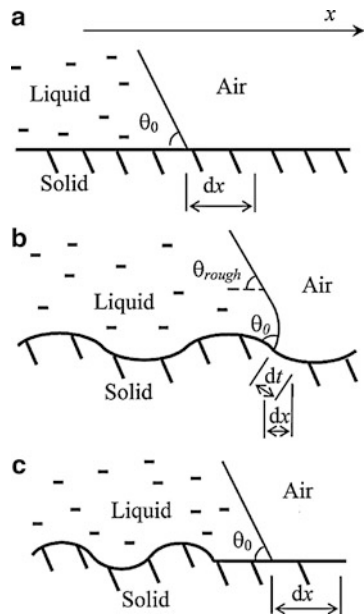
The contact angle, taking into account for the contact line effect, for a droplet with radius R is given by $\cos \theta = \cos \theta_0 + 2\tau/(R\gamma_{LA})$, where τ is the contact line tension and θ_0 is the value given by the Young equation ([Boruvka and Neumann, 1977](#)). Thus, while the contact angle is a convenient macroscale parameter, wetting is governed by interactions at the micro- and nanoscale, which determine the contact angle hysteresis and other wetting properties. Table 3.1 shows various scale levels which affect wetting of a superhydrophobic surface.

3.2.2 Range of Applicability of the Wenzel and Cassie Equations

[Gao and McCarthy \(2007\)](#) showed experimentally that the contact angle of a droplet is defined by the triple line and does not depend upon the roughness under the bulk of the droplet. A similar result for chemically heterogeneous surfaces was obtained by [Extrand \(2003\)](#). [Gao and McCarthy \(2007\)](#) concluded that the Wenzel and Cassie–Baxter equations “should be used with the knowledge of their fault.” The question remains, however, under what circumstances the Wenzel and Cassie–Baxter equations can be safely used and under what circumstances they become irrelevant.

Based on [Nosonovsky \(2007c\)](#), for a liquid front propagating along a rough two-dimensional profile (Fig. 3.7a, b), the derivative of the free surface energy

Fig. 3.7 Liquid front in contact with a (a) smooth solid surface and (b) rough solid surface, propagation for a distance dt along the curved surface corresponds to the distance dx along the horizontal surface. (c) Surface roughness under the bulk of the droplet does not affect the contact angle (Nosonovsky, 2007c)



(per liquid front length), W , by the profile length, t , yields the surface tension force $\sigma = dW/dt = \gamma_{SL} - \gamma_{SA}$. The quantity of practical interest is the component of the tension force that corresponds to the advancing of the liquid front in the horizontal direction for dx . This component is given by $dW/dx = (dW/dt)(dt/dx) = (\gamma_{SL} - \gamma_{SA})dt/dx$. It is noted that the derivative dt/dx is equal to Wenzel's roughness factor (R_f) in the case when the roughness factor is constant throughout the surface. Therefore, the Young equation (3.5), which relates the contact angle with solid, liquid, and air interface tensions, is modified as (Nosonovsky, 2007c)

$$\gamma_{LA} \cos \theta = R_f(\gamma_{SA} - \gamma_{SL}). \quad (3.16)$$

The empirical Wenzel equation (3.6) is a consequence of (3.16) combined with the Young equation.

Nosonovsky (2007c) showed that for a more complicated case of a nonuniform roughness, given by the profile $z(x)$, the local value of derivative, $r(x) = dt/dx = (1 + (dz/dx)^2)^{1/2}$, matters. In the cases that were studied experimentally by Gao and McCarthy (2007) and Extrand (2003), the roughness was present ($r > 1$) under the bulk of the droplet, but there was no roughness ($r = 0$) at the triple line, and the contact angle was given by (3.6) (Fig. 3.7c). In the general case of a 3D rough surface $z(x, y)$, the roughness factor can be defined as a function of the coordinates $r(x, y) = (1 + (dz/dx)^2 + (dz/dy)^2)^{1/2}$.

Equation (3.6) is valid for uniformly rough surfaces, that is, surfaces with $r = \text{constant}$, and for nonuniformly rough surfaces, the generalized Wenzel equation is formulated to determine the local contact angle (a function of x and y)

Table 3.2 Summary of experimental results for uniform and nonuniform rough and chemically heterogeneous surfaces

Experiment	Roughness/ hydrophobicity at the triple line and at the rest of the surface	Roughness at the bulk (under the droplet)	Experimental contact angle (compared with that at the rest of the surface)	Theoretical contact angle, Wenzel/Cassie equations	Theoretical contact angle, Wenzel– Cassie (3.17–3.18)
Gao and McCarthy (2007)	Hydrophobic	Hydrophilic	Not changed	Decreased	Not changed
	Rough Smooth	Smooth Rough	Not changed Not changed	Decreased Increased	Not changed Not changed
Exstrand (2003)	Hydrophilic	Hydrophobic	Not changed	Increased	Not changed
Bhushan et al. (2007)	Hydrophobic	Hydrophilic	Not changed	Decreased	Not changed
	Rough	Rough	Increased	Increased	Increased
Barbieri et al. (2007)	Rough	Rough	Increased	Increased	Increased

For nonuniform surfaces, the results are shown for droplets larger than the islands of nonuniformity. Detailed quantitative values of the contact angle in various sets of experiments can be found in the referred sources ([Nosonovsky, 2007c](#))

with rough surfaces at the triple line ([Nosonovsky, 2007c](#); [Nosonovsky and Bhushan, 2008a, b](#)):

$$\cos \theta = r(x, y) \cos \theta_0. \quad (3.17)$$

The difference between the Wenzel equation (3.6) and the Nosonovsky–Bhushan equation (3.17) is that the latter is valid for a nonuniform roughness with the roughness factor as the function of the coordinates. Equation (3.17) is consistent with the experimental results of the researchers who showed that roughness beneath the droplet does not affect the contact angle, since it predicts that only roughness at the triple line matters. It is also consistent with the results of the researchers who confirmed the Wenzel equation (for the case of the uniform roughness) and of those who reported that only the triple line matters (for nonuniform roughness). A summary of experimental results for uniform and nonuniform rough and chemically heterogeneous surfaces is shown in Table 3.2.

The Cassie equation for the composite surface can be generalized in a similar manner introducing the spatial dependence of the local densities, f_1 and f_2 of the solid–liquid interface with the contact angle, as a function of x and y , given by ([Nosonovsky, 2007c](#))

$$\cos \theta_{\text{composite}} = f_1(x, y) \cos \theta_1 + f_2(x, y) \cos \theta_2 \quad (3.18)$$

where $f_1 + f_2 = 1$, θ_1 and θ_2 are contact angles of the two components.

According to [Nosonovsky \(2007c\)](#), the important question remains, what should be the typical size of roughness/heterogeneity details in order for the generalized Wenzel and Cassie equations (3.17)–(3.18) to be valid? Some scholars have suggested that roughness/heterogeneity details should be comparable with the thickness of the liquid–air interface and thus “the roughness would have to be of molecular dimensions to alter the equilibrium conditions” ([Bartell and Shepard, 1953](#)), whereas others have claimed that roughness/heterogeneity details should be small compared with the linear size of the droplet ([Johnson and Dettre, 1964](#); [Li and Amirkazli, 2006](#); [Bhushan and Jung, 2007, 2008](#); [Jung and Bhushan, 2006, 2007, 2008a, b](#); [Bhushan et al., 2007](#); [Barbieri et al., 2007](#)). The interface in the analysis proposed earlier is an idealized 2D object, which has no thickness. In reality, the triple line zone has two characteristic dimensions: the thickness (of the order of molecular dimensions) and the length (of the order of the droplet size).

According to [Nosonovsky and Bhushan \(2008a, b\)](#), the apparent contact angle, given by (3.17)–(3.18), may be viewed as the result of averaging of the local contact angle at the triple line over its length, and thus, the size of the roughness/heterogeneity details should be small compared to the length (and not the thickness) of the triple line ([Nosonovsky and Bhushan, 2008b](#)). A rigorous definition of the generalized equation requires the consideration of several length scales. The length dx needed for averaging of the energy gives the length over which the averaging is performed to obtain $r(x, y)$. This length should be larger than roughness details. However, it is still smaller than the droplet size and the length scale at which the apparent contact angle is observed (at which local variations of the contact angle level out). Since of these lengths (the roughness size, dx , the droplet size) the first and the last are of practical importance, it is concluded that the roughness details should be smaller than the droplet size. When the liquid–air interface is studied at the length scale of roughness/heterogeneity details, the local contact angle, θ_0 , is given by (3.6)–(3.10). The liquid–air interface at that scale has perturbations caused by the roughness/heterogeneity, and the scale of the perturbations is the same as the scale of the roughness/heterogeneity details. However, when the same interface is studied at a larger scale, the effect of the perturbation vanishes, and apparent contact angle is given by (3.17)–(3.18) (Fig. 3.7c). This apparent contact angle is defined at the length scale for which the small perturbations of the liquid–air interface vanish, and the interface can be treated as a smooth surface. The values of $r(x, y)$, $f_1(x, y)$, $f_2(x, y)$ in (3.17)–(3.18) are average values over an area (x, y) with a size larger than a typical roughness/heterogeneity detail size. Therefore, the generalized Wenzel and Cassie equations can be used at the scale at which the effect of the interface perturbations vanish or, in other words, when the size of the solid surface roughness/heterogeneity details is small compared with the size of the liquid–air interface, which is of the same order as the size of the droplet ([Nosonovsky and Bhushan, 2008b](#)).

[Nosonovsky and Bhushan \(2008a, d\)](#) used the surface energy approach to find the domain of validity of the Wenzel and Cassie equations (uniformly rough surfaces) and generalized it for a more complicated case of nonuniform surfaces.

The generalized equations explain a wide range of existing experimental data, which could not be explained by the original Wenzel and Cassie equations.

3.3 Contact Angle Hysteresis

Contact angle hysteresis is another important characteristic of a solid–liquid interface. Contact angle hysteresis occurs due to surface roughness and heterogeneity. Although for surfaces with roughness carefully controlled on the molecular scale it is possible to achieve contact angle hysteresis as low as $< 1^\circ$ (Gupta et al., 2005), hysteresis cannot be eliminated completely, since even atomically smooth surfaces have a certain roughness and heterogeneity. Contact angle hysteresis is a measure of energy dissipation during the flow of a droplet along a solid surface. Low contact angle hysteresis results in a very low water roll-off angle, which denotes the angle to which a surface may be tilted for roll-off of water drops (i.e., very low drag) (Extrand, 2002; Kijlstra et al., 2002; Bhushan and Jung, 2007, 2008, 2011; Jung and Bhushan, 2007, 2008a) (Fig. 3.6b). Low water roll-off angle is important in liquid flow applications such as in micro-/nanochannels and surfaces with self-cleaning ability.

Certain conclusions about the relationship of contact angle hysteresis to roughness can be made. It is known that the energy gained for surfaces during contact is greater than the work of adhesion for separating the surfaces, due to so-called adhesion hysteresis. Factors that affect contact angle hysteresis include adhesion hysteresis, surface roughness, and inhomogeneity. Bhushan et al. (2007) and Nosonovsky (2007b) assumed that contact angle hysteresis is equal to the adhesion hysteresis term and the term corresponding to the effect of roughness, H_r . They further noted that adhesion hysteresis can be assumed to be proportional to the fractional solid–liquid area ($1 - f_{LA}$). Using (3.9), the difference of cosines of the advancing and receding angles is related to the difference of those for a nominally smooth surface, θ_{adv0} and θ_{rec0} , as

$$\cos \theta_{adv} - \cos \theta_{rec} = R_f(1 - f_{LA})(\cos \theta_{adv0} - \cos \theta_{rec0}) + H_r. \quad (3.19)$$

The first term in the right-hand part of the equation, which corresponds to the inherent contact angle hysteresis of a smooth surface, is proportional to the fraction of the solid-liquid contact area, $1 - f_{LA}$. The second term, H_r , is the effect of surface roughness, which is equal to the total perimeter of the asperity per unit area or, in other words, to the length density of the triple line (Bhushan et al., 2007). Thus, (3.19) involves both the term proportional to the solid–liquid interface area and to the triple line length. It is observed from (3.9) and (3.19) that increasing $f_{LA} \rightarrow 1$ results in increasing the contact angle ($\cos \theta \rightarrow -1$, $\theta \rightarrow \pi$) and decreasing the contact angle hysteresis ($\cos \theta_{adv} - \cos \theta_{rec} \rightarrow 0$). In the limiting case of very small solid-liquid fractional contact area under the droplet, when the contact angle

is large ($\cos \theta \approx -1 + (\pi - \theta)^2/2$, $\sin \theta \approx \theta - \pi$) and where the contact angle hysteresis is small ($\theta_{\text{adv}} \approx \theta \approx \theta_{\text{rec}}$), based on (3.9) and (3.19) (Nosonovsky and Bhushan, 2007b),

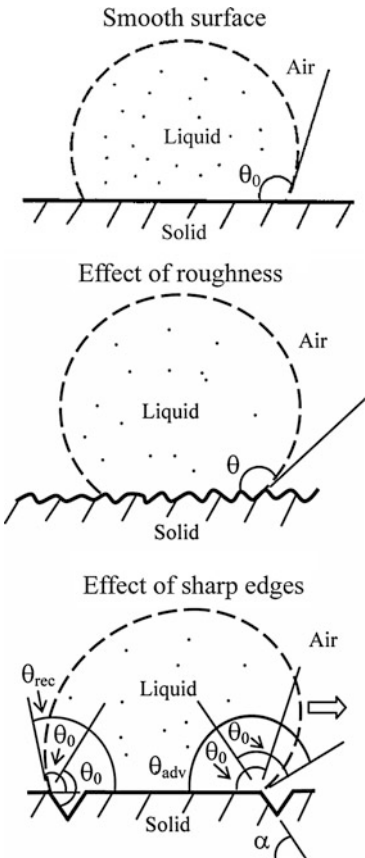
$$\pi - \theta = \sqrt{2(1 - f_{\text{LA}})(R_f \cos \theta_0 + 1)}, \quad (3.20)$$

$$\theta_{\text{adv}} - \theta_{\text{rec}} = (1 - f_{\text{LA}})R_f \frac{\cos \theta_{\text{a0}} - \cos \theta_{\text{r0}}}{-\sin \theta} = (\sqrt{1 - f_{\text{LA}}})R_f \frac{\cos \theta_{\text{r0}} - \cos \theta_{\text{a0}}}{\sqrt{2(R_f \cos \theta_0 + 1)}}. \quad (3.21)$$

For the homogeneous interface, $f_{\text{LA}} = 0$, whereas for the composite interface, f_{LA} is a nonzero number. It is observed from (3.20)–(3.21) that for a homogeneous interface, increasing roughness (high R_f) leads to increasing the contact angle hysteresis (high values of $\theta_{\text{adv}} - \theta_{\text{rec}}$), while for the composite interface, an approach to unity of f_{LA} provides both high contact angle and small contact angle hysteresis (Jung and Bhushan, 2006; Bhushan et al., 2007; Nosonovsky and Bhushan, 2007b, d). Therefore, the composite interface is desirable for low contact angle hysteresis.

A sharp edge can pin the line of contact of the solid, liquid, and air (also known as the “triple line”) at a position far from stable equilibrium, that is, at contact angles different from θ_0 (Eustathopoulos et al., 1999). This effect is illustrated in the bottom sketch of Fig. 3.8, which shows a droplet propagating along a solid surface with grooves. Based on Nosonovsky and Bhushan (2005, 2008a), at the edge point, the contact angle is not defined and can have any value between the values corresponding to contact with the horizontal and inclined surfaces. For a droplet moving from left to right, the triple line will be pinned at the edge point until it will be able to proceed to the inclined plane. As it is observed from Fig. 3.8, the change of the surface slope (α) at the edge is the cause of the pinning. Because of the pinning, the value of the contact angle at the front of the droplet (dynamic maximum advancing contact angle or $\theta_{\text{adv}} = \theta_0 + \alpha$) is greater than θ_0 , whereas the value of the contact angle at the back of the droplet (dynamic minimum receding contact angle or $\theta_{\text{rec}} = \theta_0 - \alpha$) is smaller than θ_0 . A hysteresis domain of the dynamic contact angle is thus defined by the difference $\theta_{\text{adv}} - \theta_{\text{rec}}$. The liquid can travel easily along the surface if the contact angle hysteresis is small. It is noted that the static contact angle lies within the hysteresis domain; therefore, increasing the static contact angle up to the values of a superhydrophobic surface (approaching 180°) will also result in a reduction of the contact angle hysteresis. In a similar manner, contact angle hysteresis can also exist even if the surface slope changes smoothly, without sharp edges. There is an analogy between the two mechanisms leading to contact angle hysteresis (energy dissipation at the solid–liquid interface and pinning of the triple line) and dissipation mechanisms of dry friction (adhesion and deformation) (Nosonovsky, 2007b).

Fig. 3.8 A liquid droplet in contact with a solid surface-smooth surface, contact angle θ_0 ; rough surface, contact angle θ ; and a surface with sharp edges. For a droplet moving from left to right on a sharp edge (shown by arrow), the contact angle at a sharp edge may take any value between the contact angle with the horizontal and inclined planes. This effect results in the difference between advancing ($\theta_{adv} = \theta_0 + \alpha$) and receding ($\theta_{rec} = \theta_0 - \alpha$) contact angles (Nosonovsky and Bhushan, 2005)



3.4 Stability of a Composite Interface and Role of Hierarchical Structure

Stability of the composite interface is an important issue. Even though it may be geometrically possible for the system to become composite, it may be energetically profitable for the liquid to penetrate into the valleys between asperities and form a homogeneous interface. Marmur (2003) formulated geometrical conditions for a surface under which the energy of the system has a local minimum and the composite interface may exist. Patankar (2004) pointed out that whether the homogeneous or composite interface exists depends on the system's history, that is, on whether the droplet was formed at the surface or deposited.

Based on Nosonovsky (2007b, 2008a), formation of a composite interface is a multiscale phenomenon which depends upon the relative sizes of the liquid droplet and roughness details. The composite interface is fragile and can be irreversibly transformed into the homogeneous interface, thus damaging superhydrophobicity.

In order to form a stable composite interface with air pockets between solid and liquid, the destabilizing factors such as capillary waves, nanodroplet condensation, surface inhomogeneity, and liquid pressure should be avoided, whose description follows:

- First, the capillary waves at the liquid–air interface may destabilize the composite interface. Due to an external perturbation, a standing capillary wave can form at the liquid-air interface. If the amplitude of the capillary wave is greater than the height of the asperity, the liquid can touch the valley between the asperities, and if the angle under which the liquid comes in contact with the solid is greater than θ_0 , it is energetically profitable for the liquid to fill the valley ([Nosonovsky and Bhushan, 2005, 2006a](#)). When the composite interface is destroyed and space between the asperities is filled with water, it is highly unlikely that the composite interface will be formed again because the transition from the non-composite solid–liquid interface to a composite interface would require a large activation energy. Such a transition has never been observed. The effect of capillary waves is more pronounced for small asperities with height comparable with wave amplitude.
- Second, nanodroplets may condensate and accumulate in the valleys between asperities and eventually destroy the composite interface. [Cheng et al. \(2005\)](#) observed condensation of submicron-sized droplets on a Lotus leaf surface and found that droplets tend to condense at areas adjacent to bumps (i.e., in the valleys) and have a contact angle of less than 90°, whereas larger droplets have higher contact angles, thus demonstrating that the contact angle is scale dependent. The scale effect is observed for small droplets or at small distances near the triple line. Scale dependence of the contact angle has been reported by [Nosonovsky and Bhushan \(2007b, 2008a\)](#). At nanoscale distances from the triple line, the liquid touches the solid under a much lower contact angle.
- Third, even hydrophobic surfaces are usually not chemically homogeneous and can have hydrophilic spots. It is known from experiments that for droplets of submicron size, the value of the contact angle is usually smaller than for droplets at the macroscale ([Lafuma and Quéré, 2003](#)). [Checco et al. \(2003\)](#) suggested that surface inhomogeneity is responsible for this scale effect, since nanodroplets tend to sit at the highest free surface energy (most hydrophilic) spots and thus have lower contact angles. Their phenomenological numerical simulations showed good agreement with experimental data.

[Nosonovsky and Bhushan \(2007a, b, c, d, 2008a, b, c, e\)](#) have demonstrated that a combination of microroughness and nanoroughness (multiscale roughness) with convex surfaces can help resist the destabilization by pinning the interface. It also helps in preventing the gaps between the asperities from filling with liquid, even in the case of a hydrophilic material. The effect of roughness on wetting is scale dependent, and the mechanisms that lead to destabilization of a composite interface are also scale dependent. To effectively resist these scale-dependent mechanisms, it is expected that a multiscale roughness is optimum for superhydrophobicity.

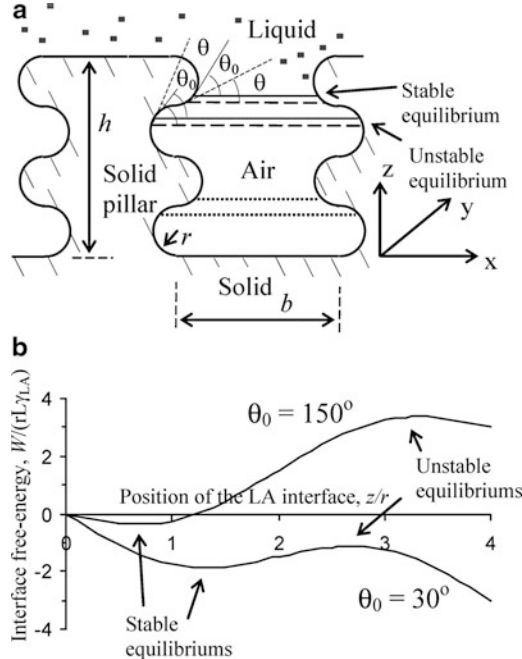


Fig. 3.9 Two-dimensional pillars with semicircular bumps/grooves. (a) Schematics of the structure. The bumps may pin the triple line because an advance of the LA interface results in a decrease of the contact angle ($\theta < \theta_0$), making equilibrium stable. Grooves provide with equilibrium positions, which satisfy the Young equation; however, the equilibrium is unstable, because an advance of the LA interface results in an increase of the contact angle ($\theta > \theta_0$). (b) Energy profiles for configurations in (a) with bumps and grooves for hydrophilic ($\theta_0 = 30^\circ$) and hydrophobic ($\theta_0 = 150^\circ$) materials. Energy (normalized by $L\gamma_{LA}$) is shown as a function of vertical position of the interface z (normalized by the radius of bumps/grooves r). Bumps result in stable equilibria (energy minima), whereas grooves result in unstable equilibria (energy maxima) (Nosonovsky, 2007a)

Nosonovsky (2007a) considered a two-dimensional structure with rectangular pillars of height h and width a separated by distance b , covered with small semicircular bumps (convex) and grooves (concave) of radius r (Fig. 3.9a). If the distance between the pillars is small in comparison with the capillary length, the effect of gravity is negligible, it can be assumed that the liquid-air interface is a horizontal plane, and its position is characterized by the vertical coordinate z . The free energy is given by (Nosonovsky, 2007a)

$$W = A_{SL}\gamma_{SL} + A_{SA}\gamma_{SA} + A_{LA}\gamma_{LA} = rL\gamma_{LA} (\sin \alpha - \alpha \cos \theta_0), \quad 0 < z < h \quad (3.22)$$

where $\alpha = a \cos((r-z)/r) + 2\pi N$ is the angle corresponding to vertical position of the interface z , N is the number of ridges or grooves, and L is length of the grooves in the y -direction, which is required based on the dimensional considerations.

The dependence is presented in Fig. 3.9b, for the cases of hydrophobic ($\theta_0 = 150^\circ$) and hydrophilic ($\theta_0 = 30^\circ$) materials for both the convex surface (with bumps) and concave surface (with grooves). It is seen that for the convex surface, there are many states of stable equilibrium (shown in Fig. 3.9a with dotted lines), separated by energy barriers which correspond to every ridge, whereas for the concave surface, equilibrium states are unstable. Therefore, the ridges can pin the triple line and thus lead to a composite interface. In the case of a hydrophilic surface, each lower position of the equilibrium state corresponds to a lower value of W ; therefore, when the liquid advances from one equilibrium state to the next, the total energy decreases, and thus, liquid's advance is energetically profitable. When the liquid reaches the bottom of the valley and completely fills the space between the pillars forming a homogeneous interface, the total energy decreases dramatically by the value of (Nosonovsky, 2007a)

$$\Delta W = bL(\gamma_{SA} + \gamma_{LA} - \gamma_{SL}) = bL\gamma_{LA}(1 + \cos\theta_0). \quad (3.23)$$

The opposite transition from a homogeneous interface to a composite interface requires high activation energy ΔW and is thus unlikely, making the transition from composite interface to homogeneous interface irreversible. If the distance between the pillars b is much greater than r , the energy barriers which separate the equilibrium states, $2\pi r L \gamma_{LA} \cos\theta_0$, will be relatively small compared to ΔW , and low activation energy will be required for the liquid to spread and propagate from one equilibrium state to the other (Nosonovsky and Bhushan, 2007b, d).

For the interface to be stable, the value of the contact angle should decrease when the liquid-air interface advances, whereas for receding liquid, the contact angle should increase. For a two-dimensional surface, the change of angle is equal to the change of the slope of the surface, and whether the configuration is stable or not depends on the sign of curvature of the surface. As indicated earlier, the convex surface (with bumps) leads to a stable interface, whereas a concave surface (with grooves) leads to an unstable interface. This approach was suggested for creating superoleophobic surfaces, since the surface tension of oil and organic liquids is much lower than that of water, and it is difficult to create a surface not wetted by oil (Tuteja et al., 2007). Since oleophilic surfaces in air (solid-oil-air system) can become superoleophobic when immersed in water (solid-oil-water system), underwater superoleophobility has potential for self-cleaning antifouling surfaces for ships.

An experiment suggesting that the sign of curvature is indeed important for hydrophobicity was conducted by Sun et al. (2005). They produced both a positive and a negative replica of a Lotus leaf surface by nanocasting using poly(dimethylsiloxane), which has a contact angle with water of about 105° . This value is close to the contact angle of the wax which covers Lotus leaves [about 103° as reported by Kamusewitz et al. (1999)]. The positive and negative replicas have the same roughness factor and thus should produce the same contact angle in the case of a homogeneous interface, according to (3.6); however, the values of surface curvature are opposite. The value of contact angle for the positive replica was found

to be 160° (same as for Lotus leaf), while for the negative replica, it was only 110° . This result suggests that the high contact angle for Lotus leaf is due to the composite rather than homogeneous interface, and that the sign of surface curvature indeed plays a critical role in the formation of the composite interface.

3.5 The Cassie–Baxter and Wenzel Wetting Regime Transition

Since superhydrophobicity requires a stable composite interface, it is important to understand the destabilization mechanisms for the Cassie–Baxter and Wenzel wetting transition. Based on [Nosonovsky and Bhushan \(2008a, d\)](#), it is known from experimental observations that the transition from the Cassie–Baxter to the Wenzel regime can be an irreversible event. Whereas such a transition can be induced, for example, by applying pressure or force to the droplet ([Jung and Bhushan, 2008b](#); [Nosonovsky and Bhushan, 2008f](#)), electric voltage ([Krupenkin et al., 2004](#); [Bahadur and Garimella, 2007](#)), light for a photocatalytic texture ([Feng et al., 2004](#)), and vibration ([Bormashenko et al., 2007](#)), the opposite transition is never observed.

Several approaches have been proposed for investigation of the transition between the metastable Cassie–Baxter and Wenzel regimes, referred to as “the Cassie–Wenzel transition.” It has been suggested that the transition takes place when the net surface energy of the Wenzel regime becomes equal to that of the Cassie–Baxter regime or, in other words, when the contact angle predicted by the Cassie–Baxter equation is equal to that predicted by the Wenzel equation. [Lafuma and Quéré \(2003\)](#) noticed that in certain cases, the transition does not occur even when it is energetically profitable and considered such a Cassie–Baxter state metastable. [Extrand \(2003\)](#) suggested that the weight of the droplet is responsible for the transition and proposed the contact line density model, according to which the transition takes place when the weight exceeds the surface tension force at the triple line. [Patankar \(2004\)](#) proposed a transition criterion based on energy balance. There is an energy barrier in going from a higher energy Cassie–Baxter droplet to a lower energy Wenzel droplet. The most probable mechanism is that the decrease in the gravitational potential energy during the transition helps in overcoming the energy barrier. This energy barrier was estimated by considering an intermediate state in which the water fills the grooves below the contact area of a Cassie–Baxter droplet, but the liquid–solid contact is yet to be formed at the bottom of the valleys. [Quéré \(2005\)](#) also suggested that the droplet curvature (which depends upon the pressure difference between the inside and the outside of the droplet) governs the transition. [Nosonovsky and Bhushan \(2005, 2006a, b\)](#) proposed a probabilistic model for wetting of rough surfaces with a certain probability associated with every equilibrium state. According to their model, the overall contact angle with a two-dimensional rough profile is calculated by assuming that the overall configuration of a droplet occurs as a result of superposition of numerous metastable states.

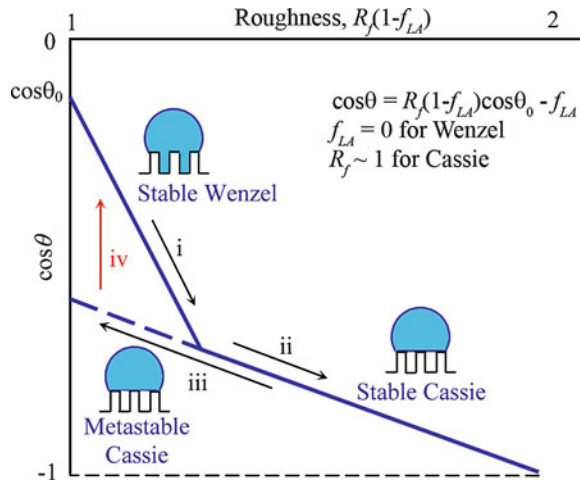


Fig. 3.10 Wetting hysteresis for a superhydrophobic surface. Contact angle as a function of roughness. The stable Wenzel state (i) can transform into the stable Cassie state with increasing roughness (ii). The metastable Cassie state (iii) can abruptly transform (iv) into the stable Wenzel state. The transition i–ii corresponds to equal Wenzel and Cassie states free energies, whereas the transition iv corresponds to a significant energy dissipation, and thus, it is irreversible (Nosonovsky and Bhushan, 2008d)

Numerous experimental results support many of these approaches; however, it is not clear which particular mechanism prevails.

Based on Nosonovsky and Bhushan (2008a, d), there is an asymmetry between the wetting and dewetting processes, since less energy is released during wetting than the amount required for dewetting due to adhesion hysteresis. Adhesion hysteresis is one of the reasons that leads to contact angle hysteresis, and it also results in the hysteresis of the Wenzel and Cassie–Baxter state transition. Figure 3.10 shows the contact angle of a rough surface as a function of surface roughness parameter, given by (3.9). Here it is assumed that $R_f \sim 1$ for a Cassie–Baxter regime with a stable composite interface, and the liquid droplet sits flat over the surface. It is noted that at a certain point, the contact angles given by the Wenzel and Cassie–Baxter equations are the same, and $R_f = (1 - f_{LA}) - f_{LA}/\cos \theta_0$. At this point, the lines corresponding to the Wenzel and Cassie–Baxter regimes intersect. This point corresponds to an equal net energy of the Cassie–Baxter and Wenzel regimes. For a lower roughness (e.g., larger pitch between the asperities), the Wenzel state is more energetically profitable, whereas for a higher roughness, the Cassie–Baxter regime is more energetically profitable.

It is observed from Fig. 3.10 that an increase of roughness may lead to the transition between the Wenzel and Cassie–Baxter regimes at the intersection point. With decreasing roughness, the system is expected to transit to the Wenzel state. However, experiments (Bhushan and Jung, 2007, 2008; Jung and Bhushan, 2007, 2008a, b; Bhushan et al., 2007; Barbieri et al., 2007) show that despite the energy

in the Wenzel regime being lower than that in the Cassie–Baxter regime, the transition does not necessarily occur and the droplet may remain in the metastable Cassie–Baxter regime. This is because there are energy barriers associated with the transition, which occurs due to destabilization by dynamic effects (such as waves and vibration) ([Nosonovsky and Bhushan, 2008a, d](#)).

In order to understand contact angle hysteresis and the transition between the Cassie–Baxter and Wenzel regimes, [Nosonovsky and Bhushan \(2008a, d\)](#) analyzed the shape of the free surface energy profile. The free surface energy of a droplet upon a smooth surface as a function of the contact angle has a distinct minimum which corresponds to the most stable contact angle. As shown in Fig. 3.11a, the macroscale profile of the net surface energy allows us to find the contact angle (corresponding to energy minimums); however, it fails to predict contact angle hysteresis and the Cassie–Baxter and Wenzel transition, which are governed by micro- and nanoscale effects. As soon as microscale substrate roughness is introduced, the droplet shape cannot be considered as an ideal truncated sphere anymore, and energy profiles have multiple energy minimums, corresponding to the location of the asperities (Fig. 3.11b). The microscale energy profile (solid line) has numerous energy maxima and minima due to surface asperities. While exact calculation of the energy profile for a 3D droplet is complicated, a qualitative shape may be obtained by assuming a periodic sinusoidal dependence ([Johnson and Dettre, 1964](#)), superimposed upon the macroscale profile, as shown in Fig. 3.11b ([Nosonovsky and Bhushan, 2008a, d](#)). Thus, the advancing and receding contact angles can be identified as the maximum and minimum possible contact angles corresponding to energy minimum points. However, the transition between the Wenzel and Cassie–Baxter branches still cannot be explained. Note also that Fig. 3.11b explains qualitatively the hysteresis due to the kinetic effect of the asperities but not the inherited adhesion hysteresis, which is characterized by the molecular length scale and cannot be captured by the microscale model.

Based on [Nosonovsky and Bhushan \(2008a, d\)](#), the energy profile as a function of the contact angle does not provide information on how the transition between the Cassie–Baxter and Wenzel regimes occurs, because their two states correspond to completely isolated branches of the energy profile in Fig. 3.11a, b. However, the energy may depend not only upon the contact angle but also upon micro-/nanoscale parameters, such as the vertical position of the liquid-air interface under the droplet, h (assuming that the interface is a horizontal plane), or similar geometrical parameters (assuming a more complicated shape of the interface). In order to investigate the Wenzel and Cassie–Baxter transition, [Nosonovsky and Bhushan \(2008a, d\)](#) studied the dependence of the energy upon these parameters. They assume that the liquid-air interface under the droplet is a flat horizontal plane. When such air layer thickness or the vertical position of the liquid–air interface, h , is introduced, the energy can be studied as a function of the droplet's shape, the contact angle, and h (Fig. 3.11c). For an ideal situation, the energy profile has an abrupt minimum at the point corresponding to the Wenzel state, which corresponds to the sudden net energy change due to the destruction of the solid-air and liquid-air interfaces ($\gamma_{SL} - \gamma_{SA} - \gamma_{LA} = -\gamma_{LA}(\cos \theta + 1)$ times the interface area)

Fig. 3.11 Schematics of net free energy profiles.

(a) Macroscale description; energy minimums correspond to the Wenzel and Cassie states. (b) Microscale description with multiple energy minimums due to surface texture. Largest and smallest values of the energy minimum correspond to the advancing and receding contact angles. (c) Origin of the two branches (Wenzel and Cassie) is found when a dependence of energy upon h (air layer thickness or vertical position of the liquid–air interface) is considered for the microscale description (*solid line*) and nanoscale imperfectionness (*dashed line*) (Nosonovsky and Bhushan, 2008d). When the nanoscale imperfectness is introduced, it is observed that the Wenzel state corresponds to an energy minimum and the energy barrier for the Wenzel–Cassie transition is much smaller than for the opposite transition

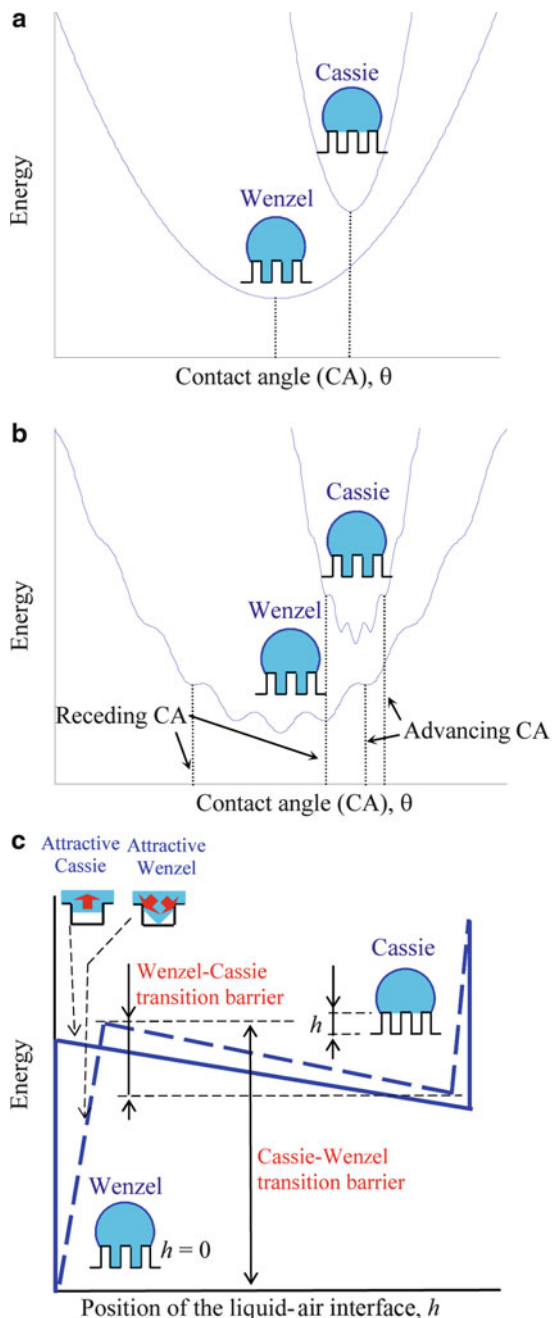


(Fig. 3.11c). In a more realistic case, the liquid–air interface cannot be considered horizontal due to nanoscale imperfection or dynamic effects such as the capillary waves (Nosonovsky and Bhushan, 2006a). A typical size of the imperfection is much smaller than the size of details of the surface texture and thus belongs to the molecular scale level. The height of the interface, h , can now be treated as an average height. The energy dependence upon h is now not as abrupt as in the idealized case. For example, for the “triangular” shape as shown in Fig. 3.11c, the Wenzel state may become the second attractor for the system. It is seen that there are two equilibriums which correspond to the Wenzel and Cassie–Baxter regimes, with the Wenzel state corresponding to a much lower energy level. The energy dependence upon h governs the transition between the two states, and it is observed that a much larger energy barrier exists for the transition from Wenzel to Cassie–Baxter regime than for the opposite transition. This is why the first transition has never been observed experimentally (Nosonovsky and Bhushan, 2007c).

3.6 Summary

The modeling of wetting of rough surfaces is presented. There are two primary wetting regimes—Wenzel and Cassie–Baxter regimes. In the Wenzel regime, a water droplet completely wets the rough surface with a homogenous interface. The contact angle of a rough surface is altered by the roughness details—roughness factor R_f —which is a ratio of the surface area to its flat projected area. The Wenzel equation predicts that a hydrophobic surface becomes more hydrophobic while a hydrophilic surface becomes more hydrophilic with an increase in roughness. In the Cassie–Baxter regime, a heterogeneous or composite interface with air pockets trapped between the roughness asperities is formed. The contact angle is altered by the roughness details and fractional liquid–air area (f_{LA}). The Cassie–Baxter equation predicts that even for a hydrophilic surface, the surface can become hydrophobic with an increase of f_{LA} ; however, the f_{LA} value required may be very high or the formation of air pockets may become unstable. Whether a liquid–air interface is generated depends upon the ratio of distance between two adjacent asperities and droplet radius.

Another property of interest in fluid flow is contact angle hysteresis, which is the difference between the advancing and receding contact angles. It occurs due to surface roughness and heterogeneity. Hysteresis cannot be eliminated completely, since even atomically smooth surfaces have a certain roughness and heterogeneity. Contact angle hysteresis is a measure of energy dissipation during the flow of a droplet along a solid surface. Low contact angle hysteresis results in a very low water roll-off angle, implying low drag and self-cleaning ability. It turns out that it is efficient to increase both contact angle and reduce contact angle hysteresis by having a moderate roughness and large fractional liquid–air area.

A composite interface is metastable, and its stability is an important issue. The formation of a composite interface is a multiscale phenomenon that depends on the

relative sizes of the liquid droplet and the roughness details. Destabilizing factors include capillary wave, condensation and accumulation of nanodroplets, and surface inhomogeneity (with hydrophilic spots). A microstructure resists capillary waves present at the liquid-air interface. A nanostructure prevents nanodroplets from filling the valleys between asperities and pin the droplet. A combination of microstructure and nanostructure with convex surfaces can help resist the destabilization by pinning the interface. Based on the modeling and observation of natural objects (present in the next chapter), it is widely understood that a hierarchical surface structure is needed to develop a composite interface with high stability.

References

- Adamson AV (1990) Physical chemistry of surfaces. Wiley, New York
- Anisimov MA (2007) Divergence of Tolman's length for a droplet near the critical point. *Phys Rev Lett* 98:035702
- Bahadur V, Garimella SV (2007) Electrowetting-based control of static droplet states on rough surfaces. *Langmuir* 23:4918–4924
- Barbieri L, Wagner E, Hoffmann P (2007) Water wetting transition parameters of perfluorinated substrates with periodically distributed flat-top microscale obstacles. *Langmuir* 23:1723–1734
- Bartell FE, Shepard JW (1953) Surface roughness as related to hysteresis of contact angles. *J Phys Chem* 57:455–458
- Bhushan B (1999) Principles and applications of tribology. Wiley, New York
- Bhushan B (2002) Introduction to tribology. Wiley, New York
- Bhushan B, Jung YC (2007) Wetting study of patterned surfaces for superhydrophobicity. *Ultramicroscopy* 107:1033–1041
- Bhushan B, Jung YC (2008) Wetting, adhesion and friction of superhydrophobic and hydrophilic leaves and fabricated micro/nanopatterned surfaces. *J Phys Condens Matter* 20:225010
- Bhushan B, Jung YC (2011) Natural and biomimetic artificial surfaces for superhydrophobicity, self-cleaning, low adhesion, and drag reduction. *Prog Mater Sci* 56:1–108
- Bhushan B, Nosonovsky M (2010) The rose petal effect and the modes of superhydrophobicity. *Philos Trans R Soc A* 368:4713–4728
- Bhushan B, Nosonovsky M, Jung YC (2007) Towards optimization of patterned superhydrophobic surfaces. *J R Soc Interface* 4:643–648
- Bormashenko E, Pogreb R, Whyman G, Erlich M (2007) Cassie-Wenzel wetting transition in vibrated drops deposited on the rough surfaces: is dynamic Cassie-Wenzel transition 2D or 1D affair? *Langmuir* 23:6501–6503
- Boruvka L, Neumann AW (1977) Generalization of the classical theory of capillarity. *J Chem Phys* 66:5464–5476
- Cassie ABD (1948) Contact angles. *Discuss Faraday Soc* 3:11–16
- Cassie ABD, Baxter S (1944) Wettability of porous surfaces. *Trans Faraday Soc* 40:546–551
- Checco A, Guenoun P, Daillant J (2003) Nonlinear dependence of the contact angle of nanodroplets on contact line curvatures. *Phys Rev Lett* 91:186101
- Cheng YT, Rodak DE, Angelopoulos A, Gacek T (2005) Microscopic observations of condensation of water on lotus leaves. *Appl Phys Lett* 87:194112
- de Gennes PG, Brochard-Wyart F, Quérè D (2003) Capillarity and wetting phenomena. Springer, Berlin
- Derjaguin BV, Churaev NV (1974) Structural component of disjoining pressure. *J Colloid Interface Sci* 49:249–255
- Eustathopoulos N, Nicholas MG, Drevet B (1999) Wettability at high temperatures. Pergamon, Amsterdam

- Exstrand CW (2002) Model for contact angle and hysteresis on rough and ultraphobic surfaces. *Langmuir* 18:7991–7999
- Exstrand CW (2003) Contact angle hysteresis on surfaces with chemically heterogeneous islands. *Langmuir* 19:3793–3796
- Feng XJ, Feng L, Jin MH, Zhai J, Jiang L, Zhu DB (2004) Reversible super-hydrophobicity to super-hydrophilicity transition of aligned ZnO nanorod films. *J Am Chem Soc* 126:62–63
- Gao L, McCarthy TJ (2007) How Wenzel and Cassie were wrong. *Langmuir* 23:3762–3765
- Gupta P, Ulman A, Fanfan F, Korniakov A, Loos K (2005) Mixed self-assembled monolayer of alkanethiolates on ultrasmooth gold do not exhibit contact angle hysteresis. *J Am Chem Soc* 127:4–5
- Israelachvili JN (1992) Intermolecular and surface forces, 2nd edn. Academic, London
- Israelachvili JN, Gee ML (1989) Contact angles on chemically heterogeneous surfaces. *Langmuir* 5:288–289
- Johnson RE, Dettre RH (1964) Contact angle hysteresis. In: Fowkes FM (ed) Contact angle, wettability, and adhesion. Advances in chemistry series, vol 43. American Chemical Society, Washington, DC, pp 112–135
- Jung YC, Bhushan B (2006) Contact angle, adhesion, and friction properties of micro- and nanopatterned polymers for superhydrophobicity. *Nanotechnology* 17, 4970–4980
- Jung YC, Bhushan B (2007) Wetting transition of water droplets on superhydrophobic patterned surfaces. *Scripta Mater* 57:1057–1060
- Jung YC, Bhushan B (2008a) Wetting behavior during evaporation and condensation of water microdroplets on superhydrophobic patterned surfaces. *J Microsc* 229:127–140
- Jung YC, Bhushan B (2008b) Dynamic effects of bouncing water droplets on superhydrophobic surfaces. *Langmuir* 24:6262–6269
- Kamusewitz H, Possart W, Paul D (1999) The relation between Young's equilibrium contact angle and the hysteresis on rough paraffin wax surfaces. *Colloid Surf A Physicochem Eng Asp* 156:271–279
- Kijlstra J, Reihs K, Klami A (2002) Roughness and topology of ultra-hydrophobic surfaces. *Colloid Surf A Physicochem Eng Asp* 206:521–529
- Krupenkin TN, Taylor JA, Schneider TM, Yang S (2004) From rolling ball to complete wetting: the dynamic tuning of liquids on nanostructured surfaces. *Langmuir* 20:3824–3827
- Lafuma A, Quéré D (2003) Superhydrophobic states. *Nat Mater* 2:457–460
- Li W, Amirfazli A (2006) A thermodynamic approach for determining the contact angle hysteresis for superhydrophobic surfaces. *J Colloid Interface Sci* 292:195–201
- Marmur A, (2003) Wetting on hydrophobic rough surfaces: to be heterogeneous or not to be? *Langmuir* 19:8343–8348
- Nosonovsky M (2007a) Multiscale roughness and stability of superhydrophobic biomimetic interfaces. *Langmuir* 23:3157–3161
- Nosonovsky M (2007b) Model for solid-liquid and solid-solid friction for rough surfaces with adhesion hysteresis. *J Chem Phys* 126:224701
- Nosonovsky M (2007c) On the range of applicability of the Wenzel and Cassie equations. *Langmuir* 23:9919–9920
- Nosonovsky M, Bhushan B (2005) Roughness optimization for biomimetic superhydrophobic surfaces. *Microsyst Technol* 11:535–549
- Nosonovsky M, Bhushan B (2006a) Stochastic model for metastable wetting of roughness-induced superhydrophobic surfaces. *Microsyst Technol* 12:231–237
- Nosonovsky M, Bhushan B (2006b) Wetting of rough three-dimensional superhydrophobic surfaces. *Microsyst Technol* 12:273–281
- Nosonovsky M, Bhushan B (2007a) Multiscale friction mechanisms and hierarchical surfaces in nano- and bio-tribology. *Mater Sci Eng R* 58:162–193
- Nosonovsky M, Bhushan B (2007b) Hierarchical roughness makes superhydrophobic surfaces stable. *Microelectron Eng* 84:382–386
- Nosonovsky M, Bhushan B (2007c) Biomimetic superhydrophobic surfaces: multiscale approach. *Nano Lett* 7:2633–2637

- Nosonovsky M, Bhushan B (2007d) Hierarchical roughness optimization for biomimetic superhydrophobic surfaces. *Ultramicroscopy* 107:969–979
- Nosonovsky M, Bhushan B (2008a) Multiscale dissipative mechanisms and hierarchical surfaces: friction, superhydrophobicity, and biomimetics. Springer, Heidelberg
- Nosonovsky M, Bhushan B (2008b) Roughness-induced superhydrophobicity: a way to design non-adhesive surfaces. *J Phys Condens Matter* 20:225009
- Nosonovsky M, Bhushan B (2008c) Biologically-inspired surfaces: broadening the scope of roughness. *Adv Funct Mater* 18:843–855
- Nosonovsky M, Bhushan B (2008d) Patterned non-adhesive surfaces: superhydrophobicity and wetting regime transitions. *Langmuir* 24:1525–1533
- Nosonovsky M, Bhushan B (2008e) Do hierarchical mechanisms of superhydrophobicity lead to self-organized criticality? *Scripta Mater* 59:941–944
- Nosonovsky M, Bhushan B (2008f) Energy transitions in superhydrophobicity: low adhesion, easy flow and bouncing. *J Phys Condens Matter* 20:395005
- Nosonovsky M, Bhushan B (2009) Superhydrophobic surfaces and emerging applications: non-adhesion, energy, green engineering. *Curr Opin Colloid Interface Sci* 14:270–280
- Patankar NA (2004) Transition between superhydrophobic states on rough surfaces. *Langmuir* 20:7097–7102
- Pompe T, Fery A, Herminghaus S (2000) Measurement of contact line tension by analysis of the three-phase boundary with nanometer resolution. In: Drellich J, Laskowski JS, Mittal KL (eds) Apparent and microscopic contact angles. VSP, Utrecht, pp 3–12
- Quéré D (2005) Non-sticking drops. *Rep Prog Phys* 68:2495–2535
- Sun M, Luo C, Xu L, Ji H, Ouyang Q, Yu D, Chen Y (2005) Artificial lotus leaf by nanocasting. *Langmuir* 21:8978–8981
- Tretinnikov ON (2000) Wettability and microstructure of polymer surfaces: stereochemical and conformational aspects. In: Drellich J, Laskowski JS, Mittal KL (eds) Apparent and microscopic contact angles. VSP, Utrecht, pp 111–128
- Tuteja A, Choi W, Ma M, Mabry JM, Mazzella SA, Rutledge GC, McKinley GH, Cohen RE (2007) Designing superoleophobic surfaces. *Science* 318:1618–1622
- Wenzel RN (1936) Resistance of Solid surfaces to wetting by water. *Ind. Eng Chem* 28:988–994

Part I

Lotus Effect

*brahmaṇy adhaya karmani
sangam tyaktva karoti yah
lipyate na sa papena
padma-patram ivambhasa*

Translation—One who performs his duty without attachment, surrendering the results unto the Supreme God, is not affected by sinful action, as the lotus leaf is untouched by water—Bhagwat Gita, Chap. 5, Text 10.

Chapter 4

Lotus Effect Surfaces in Nature

Many biological surfaces are known to be superhydrophobic and self-cleaning with low adhesion/low drag. They also exhibit antifouling properties. In this chapter, various plant leaves, their roughness, and wax coatings in relation to their hydrophobic/hydrophilic and self-cleaning properties ([Bhushan and Jung, 2011](#)) will be discussed. Surface characterization of hydrophobic and hydrophilic leaves on the micro- and nanoscale is presented to understand the role of microbumps and nanobumps. In addition, the contact angle and adhesion and friction properties of these leaves are considered. The knowledge gained by examining these properties of the leaves and by quantitatively analyzing the surface structure will help in the design of superhydrophobic and self-cleaning surfaces.

4.1 Plant Leaves

Hydrophobic and water-repellent abilities of many plant leaves have been known for a long time. Scanning electron microscope (SEM) studies since the 1970s have revealed that the hydrophobicity of the leaf surface is related to its microstructure. The outer cells covering a plant, especially the leaf, are called epidermis cells. The epidermis in all plant surfaces is covered by a thin extracellular membrane, called a cuticle. The plant cuticle is a composite material mainly built up of a cutin network and hydrophobic waxes ([Barthlott and Neinhuis, 1997](#); [Koch et al., 2008, 2009a](#)). The chemical structure of the epicuticular waxes has been studied extensively by plant scientists and lipid chemists in recent decades ([Baker, 1982](#); [Jetter et al., 2006](#)). The epicuticular waxes can be either thin with a 2D structure or thick with a 3D structure or a combination thereof. It is believed that waxes diffuse through the cuticle via a lipidic pathway ([Koch et al., 2009c](#)). After diffusion of the wax, the tubular or platelet type wax morphologies grow by crystallization or self-assembly. The plants are able to repair the wax layer by self-assembly.

The hydrophobicity of the leaves is related to another important effect, the ability to remain clean after being immersed in dirty water, known as self-cleaning.

This ability is best known for the Lotus (*Nelumbo nucifera*) leaf that is considered by some Asian cultures as “sacred” due to its purity. Not surprisingly, the ability of Lotus-like surfaces for self-cleaning and water repellency was dubbed the “Lotus Effect.” As far as the biological implications of the Lotus Effect, self-cleaning plays an important role in the defense against pathogens binding to the leaf surface. Many spores and conidia of pathogenic organisms—most fungi—require water for germination and can infect leaves only in the presence of water. This provides antifouling leaf surfaces.

[Neinhuis and Barthlott \(1997\)](#) systematically studied the surfaces and wetting properties of about 200 water-repellent plants; for a comprehensive review, see [Koch et al. \(2008, 2009a\)](#). Among the epidermal relief features are the papillose epidermal cells either with every epidermal cell forming a single papilla or cells being divided into papillae. The scale of the epidermal relief ranged from 5 μm in multipapillate cells to 100 μm in large epidermal cells. Some cells also are convex (rather than having real papillae) and/or had hairs (trichomes). [Neinhuis and Barthlott \(1997\)](#) also found various types and shapes of wax crystals at the surface. Also see [Koch et al. \(2008, 2009a\)](#). Interestingly, the hairy surfaces with a thin film of wax exhibited water repellency for short periods (minutes), after which water penetrated between the hairs, whereas hairs with a thick film led to strong water repellency. The wax crystal creates nanoroughness, in addition to the microroughness created by the papillae. Apparently, roughness plays the dominant role in the Lotus Effect.

The SEM study reveals that the Lotus leaf surface is covered by “bumps,” more exactly called papillae (papillose epidermal cells), which, in turn, are covered by an additional layer of epicuticular waxes ([Barthlott and Neinhuis, 1997](#)). The wax is present in crystalline tubules, composed of a mixture of long-chain aliphatic compounds, principally nonacosanol and nonacosanediols ([Koch et al., 2006, 2008, 2009a](#)). The wax is hydrophobic with a water contact angle of about 95–110°, and the hierarchical structure present results in a high contact angle making the surface superhydrophobic, based on the Wenzel and Cassie–Baxter models discussed in the preceding chapter. The experimental value of the static water contact angle with the Lotus leaf was reported to be about 164° ([Bhushan et al., 2009a; Koch et al., 2009b](#)). Indeed, taking the papillae density of 3,400 per square millimeter, the average radius of the hemispherical asperities $r = 10 \mu\text{m}$ and the aspect ratio $h/r = 1$ provides, based on (3.6), the value of the roughness factor $R_f \approx 4$ ([Nosonovsky and Bhushan, 2005](#)). Taking the value of the contact angle for wax, $\theta_0 = 104^\circ$ ([Kamusewitz et al., 1999](#)), the calculation with the Wenzel equation yields $\theta = 165^\circ$, which is close to the experimentally observed values ([Nosonovsky and Bhushan, 2005](#)). However, the simple Wenzel model may not be sufficient to explain the Lotus effect, as the roughness structure forms a composite interface. Moreover, its structure has hierarchical roughness. So, a number of more sophisticated models have been developed to study the role of hierarchical roughness on contact angle ([Nosonovsky and Bhushan, 2008](#)). A qualitative explanation for self-cleaning is that on a smooth surface contamination particles are mainly redistributed by a water droplet; on a rough surface, they adhere to the droplet and are removed from the leaves when the droplet rolls off.

4.2 Characterization of Superhydrophobic and Hydrophilic Leaf Surfaces

In order to understand the mechanisms of hydrophobicity in plant leaves, a comprehensive comparative study of superhydrophobic and hydrophilic leaf surfaces and their properties was carried out by [Bhushan and Jung \(2006\)](#) and [Burton and Bhushan \(2006\)](#). Below is a discussion of the findings of the study.

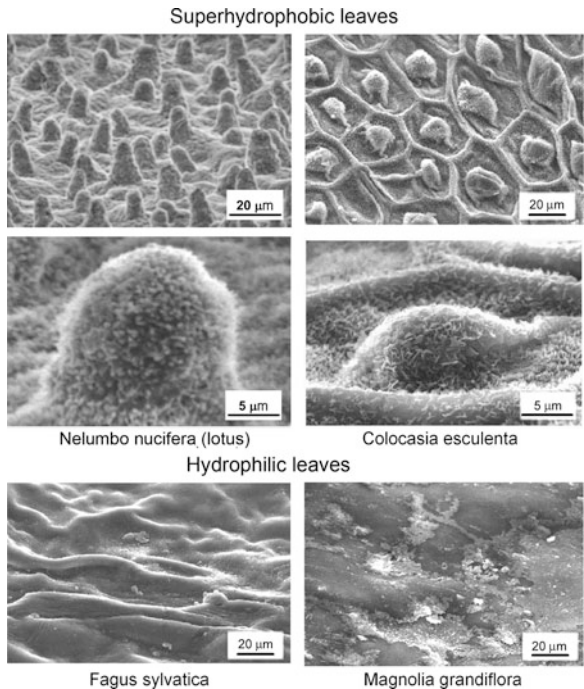
4.2.1 Experimental Techniques

The static contact angles were measured using a Rame-Hart model 100 contact angle goniometer with droplets of deionized (DI) water ([Burton and Bhushan, 2006](#); [Bhushan and Jung, 2006](#)). Droplets of about 5 μL in volume (with diameter of a spherical droplet about 2.1mm) were gently deposited on the substrate using a microsyringe for the static contact angle. All measurements were made by five different points for each sample at $22 \pm 1^\circ\text{C}$ and $50 \pm 5\%$ RH. The measurement results were reproducible within $\pm 3^\circ$.

An optical profiler was used to measure surface roughness for different surface structures ([Burton and Bhushan, 2006](#); [Bhushan and Jung, 2006](#)). A greater Z-range of the optical profiler of 2mm is a distinct advantage over the surface roughness measurements with an atomic force microscope (AFM) which has a Z-range on the order of 7 μm , but it has only a maximum lateral resolution of approximately 0.6 μm ([Bhushan, 1999, 2002](#)). A commercial AFM was used for additional surface roughness measurements with a high lateral resolution (sub nm) and for adhesion and friction measurements ([Burton and Bhushan, 2005](#); [Bhushan and Jung, 2006](#)). The measurements for surface roughness were performed with a square pyramidal Si(100) tip with a native oxide layer which had a nominal radius of 20 nm on a rectangular Si(100) cantilever with a spring constant of 3 N m^{-1} in the tapping mode.

Adhesion and friction force at various relative humidities (RH) were measured using a 15 μm -radius borosilicate ball ([Bhushan, 1999, 2002, 2011](#)). A large tip radius was used to measure contributions from several microbumps and a large number of nanobumps. Friction force was measured under a normal load ranging from 20 to 250 nN using a 90° scan angle at the velocity of 100 $\mu\text{m/s}$ in 50 μm and at a velocity of 4 $\mu\text{m/s}$ in 2 μm scans. The quantitative measurement of friction force was calibrated by the method described by [Bhushan \(2011\)](#). The normal load was varied (20–250 nN), and a friction force measurement was taken at each increment. By plotting the friction force as a function of normal load, an average coefficient of friction was obtained from the slope of the fit line of the data. The adhesive force was measured using the force distance curve approach. In this technique, the AFM tip is brought into contact with the sample by extending the piezo vertically, then retracting the piezo and calculating the force required to separate the tip from the sample. The adhesive force is obtained by multiplying the cantilever spring

Fig. 4.1 Scanning electron micrographs of the relatively rough, water-repellent leaf surfaces of *Nelumbo nucifera* (Lotus) and *Colocasia esculenta* and the relatively smooth, wettable leaf surfaces of *Fagus sylvatica* and *Magnolia grandiflora* (Bhushan and Jung, 2006)



constant with the cantilever deflection during the retraction between zero value and the maximum negative value. The method is described in detail by Bhushan (1999, 2002, 2011).

4.2.2 SEM Micrographs

Figure 4.1 shows the SEM micrographs of two superhydrophobic leaves—Lotus (*N. nucifera*) and elephant ear or taro plant (*Colocasia esculenta*), referred to as Lotus and Colocasia, respectively—and two hydrophilic leaves, beech (*Fagus sylvatica*) and Magnolia (*Magnolia grandiflora*), referred to as Fagus and Magnolia, respectively (Bhushan and Jung, 2006). Lotus and Colocasia are characterized by papillose epidermal cells responsible for the creation of papillae or microbumps on the surfaces and an additional layer of 3D epicuticular waxes which are a mixture of very long-chain fatty acids molecules (compounds with chains >20 carbon atoms) and create nanostructure on the entire surface. Fagus and Magnolia are characterized by rather flat tabular cells with a thin wax film with a 2D structure (Barthlott and Neinhuis, 1997). The leaves are not self-cleaning, and contaminant particles from ambient are accumulated, which make them hydrophilic.

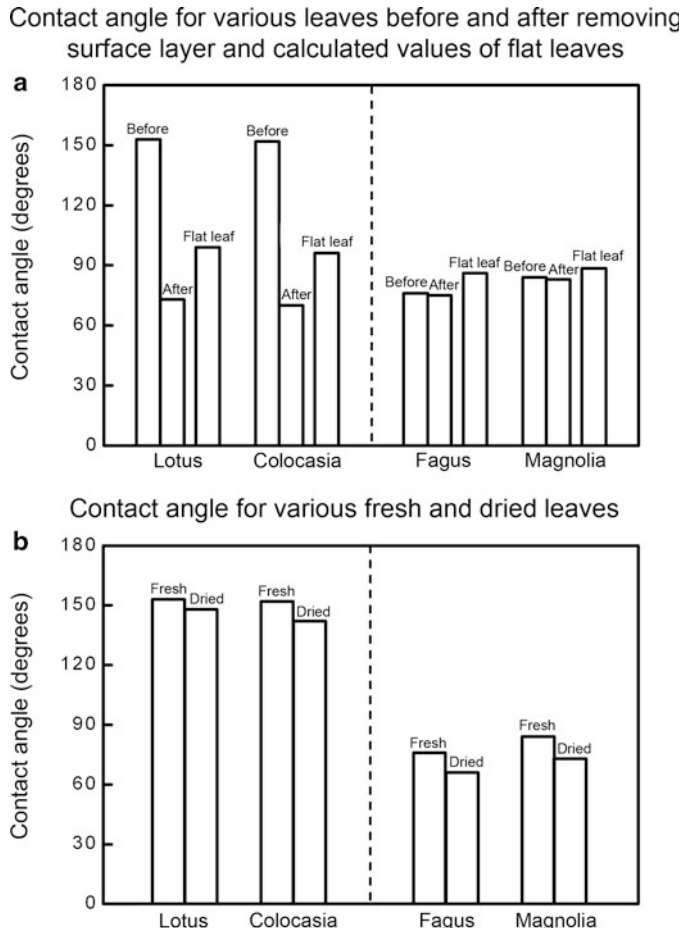


Fig. 4.2 Contact angle measurements and calculations for the leaf surfaces, (a) before and after removing the surface layer as well as calculated values, and (b) fresh and dried leaves. The contact angle on a smooth surface for the four leaves was obtained using the roughness factor calculated ([Bhushan and Jung, 2006](#))

4.2.3 Contact Angle Measurements

Figure 4.2a shows the contact angles for the superhydrophobic and hydrophilic leaves before and after applying acetone. The acetone was applied in order to remove any wax present on the surface. As a result, for the superhydrophobic leaves, the contact angle dramatically reduced, whereas for the hydrophilic leaves, the contact angle was almost unchanged. It is known that there is a very thin 2D wax layer on the hydrophilic leaves, which introduces little roughness. In contrast, superhydrophobic leaves are known to have a thin 3D wax layer on their surface

consisting of nanoscale roughness over microroughness created by the papillae, which results in a hierarchical roughness. The combination of this wax and the roughness of the leaf create a superhydrophobic surface.

[Bhushan and Jung \(2006\)](#) calculated the contact angles for leaves with smooth surfaces using the Wenzel equation and the calculated R_f and the contact angle of the four leaves. The results are presented in Fig. 4.2a. The approximate values of R_f for Lotus and Colocasia are 5.6 and 8.4 and for Fagus and Magnolia are 3.4 and 3.8, respectively. Based on the calculations, the contact angles on smooth surfaces were approximately 99° for Lotus and 96° for Colocasia. For both Fagus and Magnolia, the contact angles for the smooth surfaces were found to be approximately 86° and 88°. A further discussion on the effect of R_f on the contact angle will be presented later.

Figure 4.2b shows the contact angles for both fresh and dried states for the four leaves. There is a decrease in the contact angle for all four leaves when they are dried. For Lotus and Colocasia, this decrease is present because it is found that a fresh leaf has taller bumps than a dried leaf (data to be presented later), which will give a larger contact angle, according to the Wenzel equation. When the surface area is at a maximum compared to the footprint area, as with a fresh leaf, the roughness factor will be at a maximum and will only reduce when shrinking has occurred after drying. To understand the reason for the decrease of contact angle after drying of hydrophilic leaves, dried Magnolia leaves were also measured using an AFM. It is found that the dried leaf (peak–valley (P–V) height = 7 μm, mid-width = 15 μm, and peak radius = 18 μm) has taller bumps than a fresh leaf (P–V height = 3 μm, mid-width = 12 μm, and peak radius = 15 μm), which increases the roughness, and the contact angle decreases, leading to a more hydrophilic surface. The mid-width is defined as the width of the bump at a height equal to half of peak to mean line value.

4.2.4 Surface Characterization Using an Optical Profiler

The use of an optical profiler allows measurements to be made on fresh leaves which have a large P–V distance. Three different surface height maps for superhydrophobic and hydrophilic leaves are shown in Figs. 4.3 and 4.4 ([Bhushan and Jung, 2006](#)). In each figure, a 3D map and a flat map along with a 2D profile in a given location of the flat 3D map are shown. A scan size of 60 μm × 50 μm was used to obtain a sufficient amount of bumps to characterize the surface but also to maintain enough resolution to get an accurate measurement.

The structures found with the optical profiler correlate well with the SEM images shown in Fig. 4.1. The bumps on the Lotus leaf are distributed on the entire surface, but the Colocasia leaf shows a very different structure to that of the Lotus. The surface structure for Colocasia not only has bumps similar to Lotus but also surrounding each bump is a ridge that keeps the bumps separated. With these ridges, the bumps have a hexagonal (honeycomb) packing geometry that allows for the

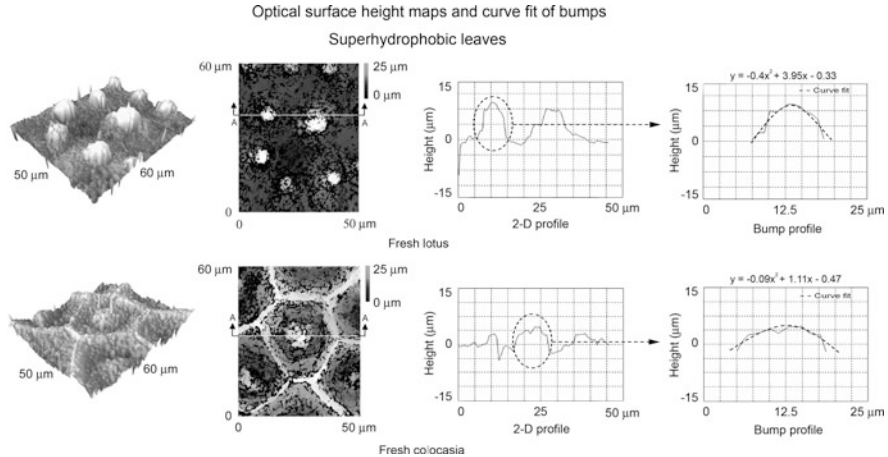


Fig. 4.3 Surface height maps and 2D profiles of superhydrophobic leaves using an optical profiler. For Lotus leaf, a microbump is defined as a single, independent microstructure protruding from the surface. For Colocasia leaf, a microbump is defined as the single, independent protrusion from the leaf surface, whereas a ridge is defined as the structure that surrounds each bump and is completely interconnected on the leaf. A curve has been fitted to each profile to show exactly how the bump shape behaves. The radius of curvature is calculated from the parabolic curve fit of the bump (Bhushan and Jung, 2006)

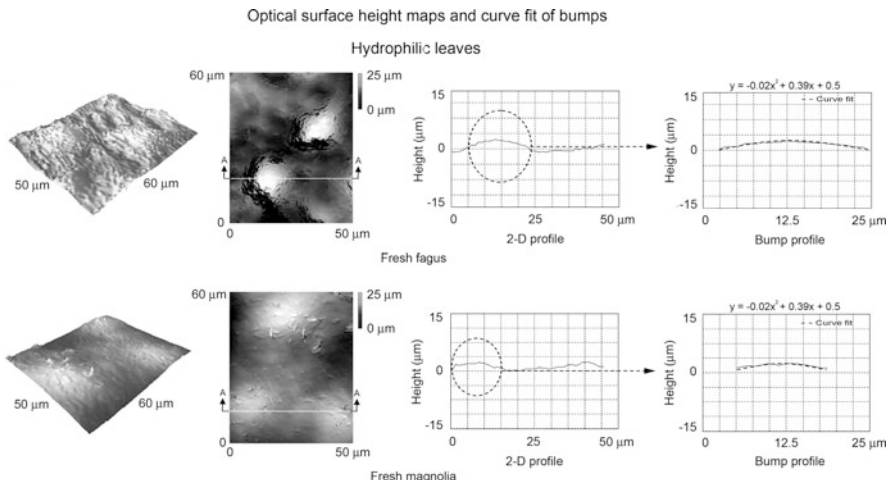


Fig. 4.4 Surface height maps and 2D profiles of hydrophilic leaves using an optical profiler. For Fagus and Magnolia leaves, a microbump is defined as a single, independent microstructure protruding from the surface. A curve has been fitted to each profile to show exactly how the bump shape behaves. The radius of curvature is calculated from the parabolic curve fit of the bump (Bhushan and Jung, 2006)

Table 4.1 Microbump and nanobump map statistics for superhydrophobic and hydrophilic leaves, measured both fresh and dried using an optical profiler and AFM ([Bhushan and Jung, 2006](#))

Leaf	Microbump Scan size (50 × 50 μm)			Nanobump Scan size (2 × 2 μm)		
	P–V height (μm)	Mid-width (μm)	Peak radius (μm)	P–V height (μm)	Mid-width (μm)	Peak radius (μm)
<i>Lotus</i>						
Fresh	13 ^a	10 ^a	3 ^a	0.78 ^b	0.40 ^b	0.15 ^b
Dried	9 ^b	10 ^b	4 ^b	0.67 ^b	0.25 ^b	0.10 ^b
<i>Colocasia</i>						
Fresh Bump	9 ^a	15 ^a	5 ^a	0.53 ^b	0.25 ^b	0.07 ^b
Ridge	8 ^a	7 ^a	4 ^a	0.68 ^b	0.30 ^b	0.12 ^b
Dried Bump	5 ^b	15 ^b	7 ^b	0.48 ^b	0.20 ^b	0.06 ^b
Ridge	4 ^b	8 ^b	4 ^b	0.57 ^b	0.25 ^b	0.11 ^b
<i>Fagus</i>						
Fresh	5 ^a 4 ^b	10 ^a 5 ^b	15 ^a 10 ^b	0.18 ^b	0.04 ^b	0.01 ^b
<i>Magnolia</i>						
Fresh	4 ^a 3 ^b	13 ^a 12 ^b	17 ^a 15 ^b	0.07 ^b	0.05 ^b	0.04 ^b

^aData measured using optical profiler^bData measured using AFM

maximum number of bumps in a given area. The bumps of Lotus and both bumps and ridges of Colocasia contribute to the superhydrophobic nature since they both increase the R_f factor and result in air pockets between the droplet of water and the surface. In Fagus and Magnolia height maps, short bumps can be seen on the surface. This means that with decreased bump height, the probability of air pocket formation decreases, and bumps have a less beneficial effect on the contact angle.

As shown in 2D profiles of superhydrophobic and hydrophilic leaves in Figs. 4.3 and 4.4, a curve has been fitted to each profile to show exactly how the bump shape behaves. For each leaf, a second-order curve fit has been given to the profiles to show how closely the profile is followed. By using the second-order curve fitting of the profiles, the radius of curvature can be found ([Bhushan and Jung, 2006](#); [Burton and Bhushan, 2006](#)).

Using these optical surface height maps, different statistical parameters of bumps and ridges can be found to characterize the surface: P–V height, mid-width, and peak radius ([Bhushan, 1999, 2002](#)). Table 4.1 shows these quantities found in the optical height maps for the four leaves. Comparing the superhydrophobic and hydrophilic leaves, it can be seen that the P–V height for bumps of Lotus and Colocasia is much taller than that for the bumps of Fagus and Magnolia. The peak radius for the bumps of Lotus and Colocasia is also smaller than that for the bumps of Fagus and Magnolia. However, the values of mid-width for the bumps of the four leaves are similar.

4.2.5 Surface Characterization, Adhesion, and Friction Using an AFM

4.2.5.1 Comparison of Two AFM Measurement Techniques

To measure topographic images of the leaf surfaces, both the contact and tapping modes were first used (Bhushan and Jung, 2006). Figure 4.5 shows surface height maps of dried Lotus obtained using the two techniques. In the contact mode, local height variation for Lotus leaf was observed in $50\text{ }\mu\text{m}$ scan size. However, little height variation was obtained in a $2\text{ }\mu\text{m}$ scan even at loads as low as 2nN . This could be due to the substantial frictional force generated as the probe scanned over the sample. The frictional force can damage the sample. The tapping mode technique allows high-resolution topographic imaging of sample surfaces that are easily damaged, loosely held to their substrate, or difficult to image by other AFM techniques (Bhushan, 1999, 2002). As shown in Fig. 4.5, with the tapping mode technique, the soft and fragile leaves can be imaged successfully. Therefore, the tapping mode technique was used to examine the surface roughness of the superhydrophobic and hydrophilic leaves using an AFM.

4.2.5.2 Surface Characterization

The AFM has a Z -range on the order of $7\text{ }\mu\text{m}$ and cannot be used for measurements in a conventional way because of the high P–V distances of a Lotus leaf. Burton and Bhushan (2006) developed a new method to fully determine the bump profiles. In order to compensate for the large P–V distance, two scans were made for each height: one measurement that scans the tops of the bumps and another measurement that scans the bottom or valleys of the bumps. The total height of the bumps is embedded within the two scans. Figure 4.6 shows the $50\text{ }\mu\text{m}$ surface height maps obtained using this method (Bhushan and Jung, 2006). The 2D profiles in the right column take the profiles from the top scan and the bottom scan for each scan size and splice them together to get the total profile of the leaf. The $2\text{ }\mu\text{m}$ surface height maps for both fresh and dried Lotus can also be seen in Fig. 4.6. This scan area was selected on the top of a microbump obtained in the $50\text{ }\mu\text{m}$ surface height map. It can be seen that nanobumps are randomly and densely distributed on the entire surface of the Lotus leaf.

Bhushan and Jung (2006) also measured the surface height maps for hydrophilic leaves in both $50\text{ }\mu\text{m}$ and $2\text{ }\mu\text{m}$ scan sizes as shown in Fig. 4.7. For Fagus and Magnolia, microbumps were found on the surface, and the P–V distance of these leaves is lower than that of Lotus and Colocasia. It can be seen in the $2\text{ }\mu\text{m}$ surface height maps that nanobumps selected on the peak of the microbump have an extremely low P–V distance.

AFM surface height maps of dried lotus by two techniques

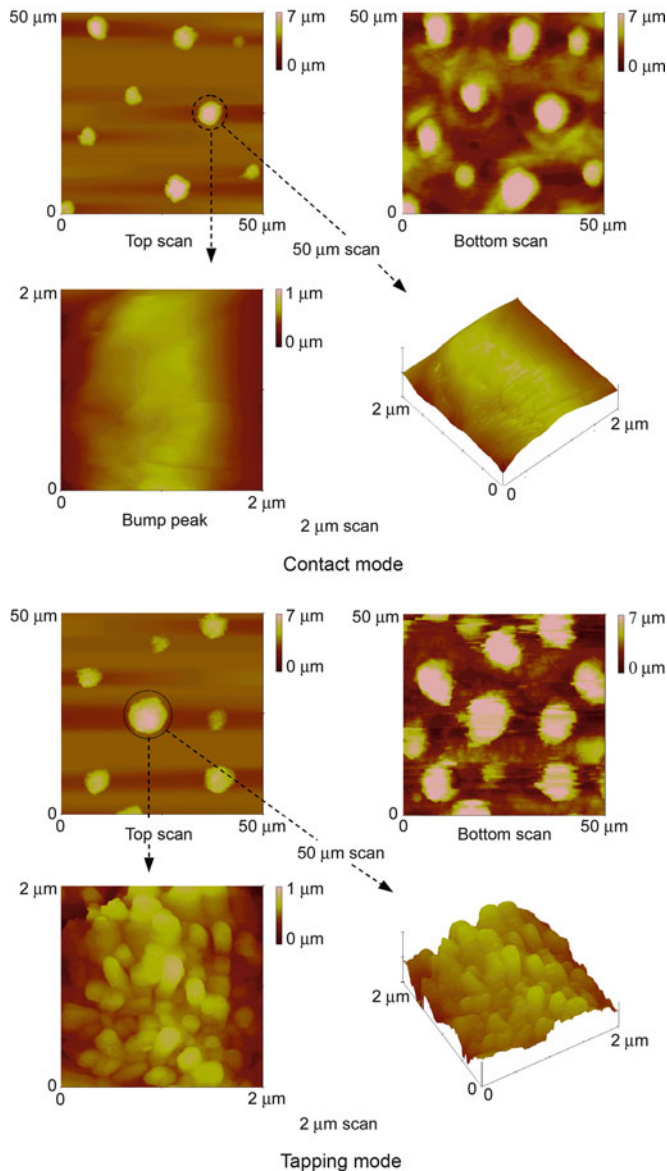


Fig. 4.5 Surface height maps showing the *top scan* and *bottom scan* in a 50 μm scan size and the bump peak scan selected in a 2 μm scan size for a Lotus leaf using an AFM in contact mode and tapping mode. Two methods were used to determine a suitable method to obtain high resolution of nanotopography for a Lotus leaf (Bhushan and Jung, 2006)

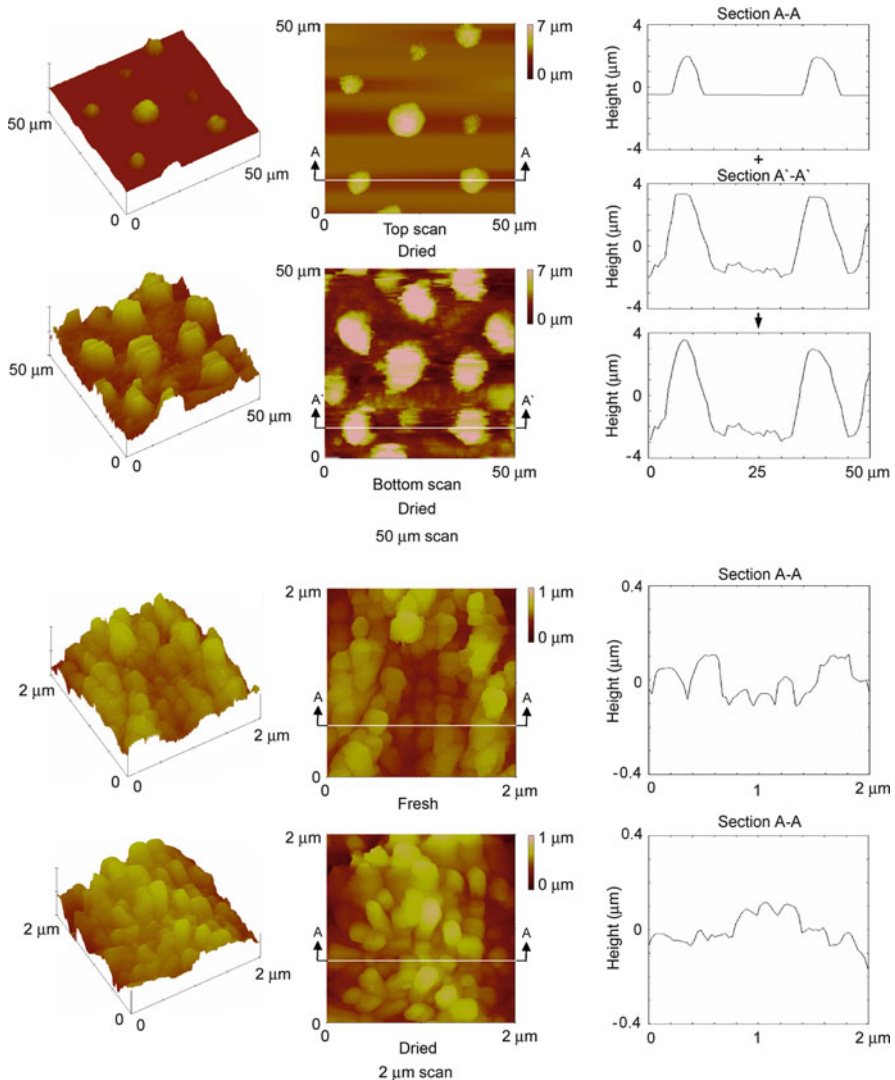
AFM surface height maps of fresh and dried lotus with 50 μm and 2 μm scans

Fig. 4.6 Surface height maps and 2D profiles showing the top scan and bottom scan of a dried Lotus leaf in 50 μm scan (because the P-V distance of a dried Lotus leaf is greater than the Z-range of an AFM), and the *top scan* of both fresh and dried Lotus in a 2 μm scan (Bhushan and Jung, 2006). A splicing technique was used to determine the bump profiles. In order to compensate for the large P-V distance, the total height of the bumps is embedded within the *top scan* and *bottom scan*

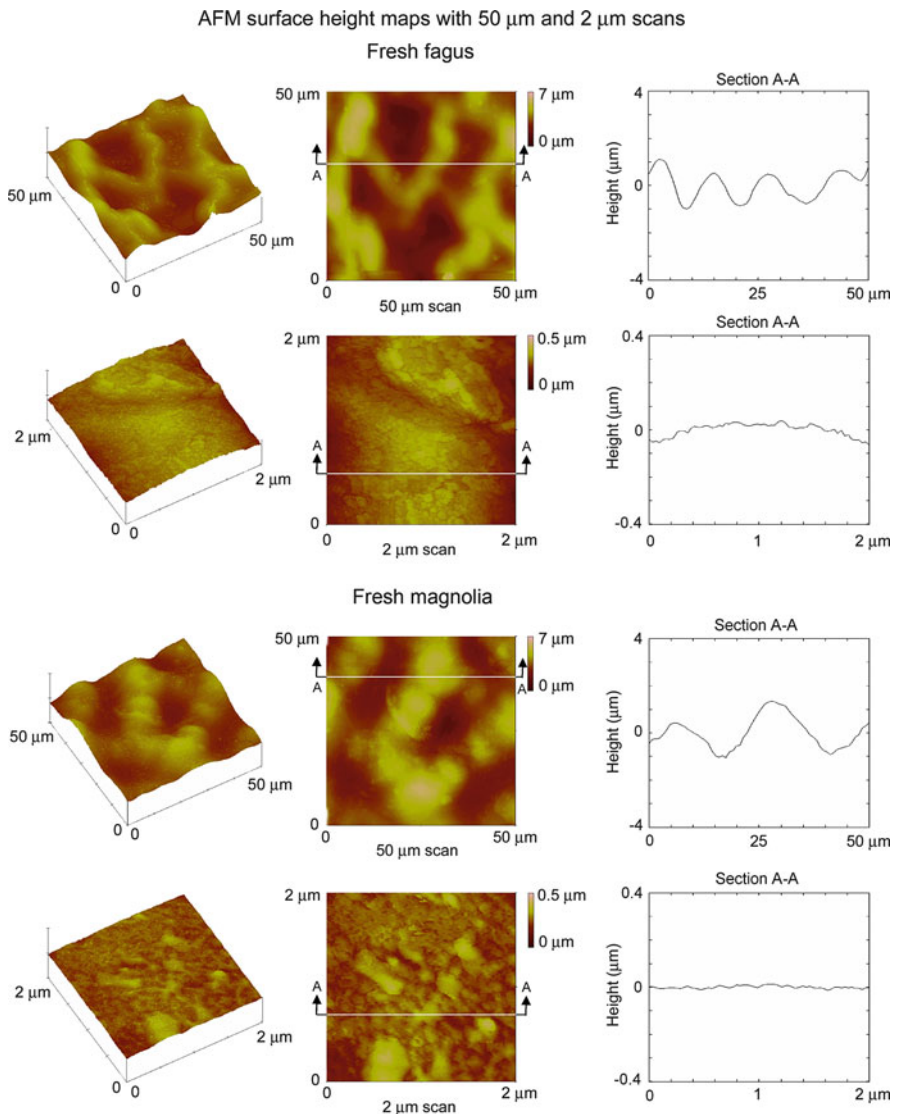
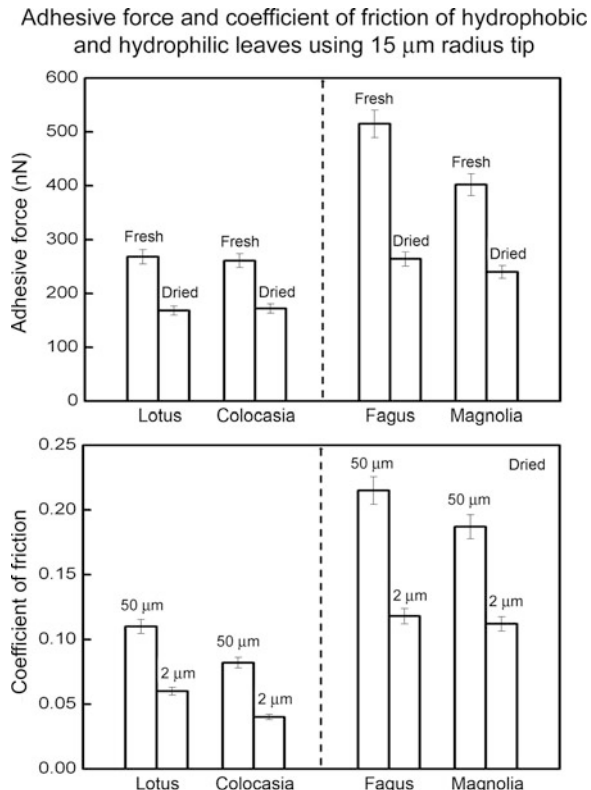


Fig. 4.7 Surface height maps and 2D profiles of Fagus and Magnolia using an AFM in both 50 μm and 2 μm scans ([Bhushan and Jung, 2006](#))

Using the AFM surface height maps, different statistical parameters of bumps and ridges can be obtained: P-V height, mid-width, and peak radius. These quantities for the four leaves are listed in Table 4.1. It can be seen that the values correlate well with the values obtained from optical profiler scans except for the bump height, which decreases by more than half because of leaf shrinkage.

Fig. 4.8 Adhesive force for fresh and dried leaves, and the coefficient of friction for dried leaves for 50 μm and 2 μm scan sizes for hydrophobic and hydrophilic leaves. All measurements were made using an AFM with 15 μm -radius borosilicate tip.

Reproducibility for both adhesive force and coefficient of friction is $\pm 5\%$ for all measurements (Bhushan and Jung, 2006)



4.2.5.3 Adhesive Force and Friction

Adhesive force and coefficient of friction of superhydrophobic and hydrophilic leaves using AFM are presented in Fig. 4.8 (Bhushan and Jung, 2006). For each type of leaf, adhesive force measurements were made for both fresh and dried leaves using a 15 μm -radius tip. It is found that the dried leaves had a lower adhesive force than the fresh leaves. Adhesive force arises from several sources in changing the presence of a thin liquid film, such as an adsorbed water layer that causes meniscus bridges to build up around the contacting and near-contacting bumps as a result of surface energy effects (Bhushan, 1999, 2002). When the leaves are fresh, there is moisture within the plant material that causes the leaf to be soft, and when the tip comes into contact with the leaf sample, the sample will deform, and a larger real area of contact between the tip and sample will occur, and the adhesive force will increase. After the leaf has dried, the moisture that was in the plant material is gone, and there is not as much deformation of the leaf when the tip comes into contact with the leaf sample. Hence, the adhesive force is decreased because the real area of contact has decreased.

Table 4.2 Roughness factor and contact angle ($\Delta\theta = \theta - \theta_0$) calculated using R_f on the smooth surface for hydrophobic and hydrophilic leaves measured using an AFM, both microscale and nanoscale (Bhushan and Jung, 2006)

Leaf (contact angle)	Scan size	State	R_f	$\Delta\theta$ (deg)
Lotus (153°)	50 μm	Dried	5.6	54 ^a
	2 μm	Fresh	20	61 ^b
		Dried	16	60 ^b
Colocasia (152°)	50 μm	Dried	8.4	56 ^a
	2 μm bump	Fresh	18	60 ^b
		Dried	14	59 ^b
	2 μm ridge	Fresh	18	60 ^b
		Dried	15	59 ^b
Fagus (76°)	50 μm	Fresh	3.4	-10 ^a
	2 μm	Fresh	5.3	2 ^b
Magnolia (84°)	50 μm	Fresh	3.8	-4 ^a
	2 μm	Fresh	3.6	14 ^b

^aCalculations made using Wenzel equation

^bCalculations made using Cassie–Baxter equation. It is assumed that the contact area between the droplet and air is the half of the whole area of the rough surface

The adhesive force of Fagus and Magnolia is higher than that of Lotus and Colocasia. The reason is that the real area of contact between the tip and leaf surface is expected to be higher in hydrophilic leaves than in superhydrophobic leaves. In addition, the Fagus and Magnolia are hydrophilic and have a high affinity to water. The combination of high real area of contact and affinity to water are responsible for higher meniscus forces (Bhushan, 1999, 2002). The coefficient of friction was only measured on a dried plant surface with the same sliding velocity (10 $\mu\text{m/s}$) in different scan sizes rather than including the fresh surface because the P–V was too large to scan back and forth with the AFM to obtain friction force. As expected, the coefficient of friction for superhydrophobic leaves is lower than that for hydrophilic leaves due to the real area of contact between the tip and leaf sample, similar to the adhesive force results. When the scan size from microscale to nanoscale decreases, the coefficient of friction also decreases in each leaf. The reason for such dependence is the scale-dependent nature of the roughness of the leaf surface. Figures 4.6 and 4.7 show AFM topography images and 2D profiles of the surfaces for different scan sizes. The scan size dependence of the coefficient of friction has been reported previously (Poon and Bhushan, 1995; Koinkar and Bhushan, 1997; Tambe and Bhushan, 2004).

4.2.6 Role of the Hierarchical Roughness

The approximation of the roughness factor for the leaves on the micro- and nanoscale was made using AFM scan data (Bhushan and Jung, 2006). Roughness factors for various leaves are presented in Table 4.2. As mentioned earlier, the

open space between asperities on a surface has the potential to collect air, and its probability appears to be higher in nanobumps as the distance between bumps in the nanoscale is smaller than those in the microscale. Using roughness factor values, along with the contact angles (θ) from both superhydrophobic and hydrophilic surfaces, 153° and 152° in Lotus and Colocasia, and 76° and 84° in Fagus and Magnolia, respectively, the contact angles (θ_0) for the smooth surfaces can be calculated using the Wenzel equation (3.6) for microbumps and the Cassie–Baxter equation (3.9) for nanobumps. The contact angle ($\Delta\theta$) calculated using R_f on the smooth surface can be found in Table 4.2. It can be seen that the roughness factors and the differences ($\Delta\theta$) between θ and θ_0 on the nanoscale are higher than those in the microscale. This means that nanobumps on the top of a microbump increase contact angle more effectively than microbumps. In the case of hydrophilic leaves, the values of R_f and $\Delta\theta$ change very little on both scales.

Based on the data in Fig. 4.8, the coefficient of friction values on the nanoscale are much lower than those on the microscale. It is clearly observed that friction values are scale dependent. The height of a bump and the distance between bumps on the microscale is much larger than those on the nanoscale, which may be responsible for larger values of friction force on the microscale.

One difference between microbumps and nanobumps for surface enhancement of water repellency is the effect on contact angle hysteresis, in other words, the ease with which a droplet of water can roll on the surface. It has been stated earlier that contact angle hysteresis decreases and contact angle increases due to the decreased contact with the solid surface caused by the air pockets beneath the droplet. The surface with nanobumps has a high roughness factor compared with that of microbumps. With large distances between microbumps, the probability of air pocket formation decreases and is responsible for high contact angle hysteresis. Therefore, on the surface with nanobumps, the contact angle is high and contact angle hysteresis is low and drops rebound easily and can set into a rolling motion with a small tilt angle (Bhushan and Jung, 2006).

Natural water-repellent and self-cleaning surfaces such as the Lotus leaf (Koch et al., 2008, 2009a) or water strider leg (Gao and Jiang, 2004) have a hierarchical structure. However, the functionality of this hierarchical roughness remains a subject of discussion, and several explanations have been suggested. Nosonovsky and Bhushan (2008) showed that the mechanisms involved in superhydrophobicity are scale dependent, and thus, the roughness must be hierarchical in order to respond to these mechanisms. The surface must be able to repel both macroscopic and microscopic droplets. Fürstner et al. (2005) pointed out that artificial surfaces with one level of roughness can well repel large “artificial rain” droplets; however, they cannot repel small “artificial fog” droplets trapped in the valleys between the bumps, so the hierarchy may have to do with the ability to repel droplets of various size ranges. According to Gao and McCarthy (2006), the large bumps allow to maintain the composite interface while the small ones enhance the contact angle in accordance to the Wenzel model. Jung and Bhushan (2008) showed that a droplet with a radius of about 100–400 μm on micropatterned surfaces goes through transition from the composite interface to the solid–liquid interface as the pitch

increases, and Bhushan et al. (2008, 2009b, c) showed that the hierarchical structure can prevent the gaps between the pillars from filling with liquid until the droplet evaporated completely.

4.3 Summary

Various leaf surfaces on the micro- and nanoscale have been characterized, and attempts are made to separate out the effect of micro- and nanobumps and the wax on the hydrophobicity. For the superhydrophobic Lotus and Colocasia leaves, the leaf surface consists of microbumps formed by convex papilla epidermal cells covered with a 3D epicuticular wax (crystalline tubules composed of a mixture of secondary alcohol nonacosan-10-01 and nonacosanedoils) on the surface which self-assemble as nanotubules. Hierarchical surface and the presence of wax create a superhydrophobic and self-cleaning surface with low adhesion as well as with antifouling. Hydrophilic Fagus and Magnolia have rather flat tabular cells with a 2D thin wax film (not continuous) on the surface.

The next logical step in realizing superhydrophobic surfaces is to design surfaces based on an understanding of the leaves.

References

- Baker EA (1982) Chemistry and morphology of plant epicuticular waxes. In: Cutler DF, Alvin KL, Price CE (eds) *The plant cuticle*. Academic, London, pp 139–165
- Barthlott W, Neinhuis C (1997) Purity of the sacred lotus, or escape from contamination in biological surfaces. *Planta* 202:1–8
- Bhushan B (1999) *Principles and applications of tribology*. Wiley, New York
- Bhushan B (2002) *Introduction to tribology*. Wiley, New York
- Bhushan B (2011) Nanotribology and nanomechanics I—Measurement techniques, II—Nanotribology, biomimetics, and industrial applications, 3rd edn. Springer, Heidelberg
- Bhushan B, Jung YC (2006) Micro and nanoscale characterization of hydrophobic and hydrophilic leaf surface. *Nanotechnology* 17:2758–2772
- Bhushan B, Jung YC (2011) Natural and biomimetic artificial surfaces for superhydrophobicity, self-cleaning, low adhesion, and drag reduction. *Prog Mater Sci* 56:1–108
- Bhushan B, Koch K, Jung YC (2008) Nanostructures for superhydrophobicity and low adhesion. *Soft Matter* 4:1799–1804
- Bhushan B, Jung YC, Koch K (2009a) Micro-, nano- and hierarchical structures for superhydrophobicity, self-cleaning and low adhesion. *Philos Trans R Soc A* 367:1631–1672
- Bhushan B, Jung YC, Niemietz A, Koch K (2009b) Lotus-like biomimetic hierarchical structures developed by the self-assembly of tubular plant waxes. *Langmuir* 25:1659–1666
- Bhushan B, Koch K, Jung YC (2009c) Fabrication and characterization of the hierarchical structure for superhydrophobicity. *Ultramicroscopy* 109:1029–1034
- Burton Z, Bhushan B (2005) Hydrophobicity, adhesion, and friction properties of nanopatterned polymers and scale dependence for micro- and nanoelectromechanical systems. *Nano Lett* 5:1607–1613

- Burton Z, Bhushan B (2006) Surface characterization and adhesion and friction properties of hydrophobic leaf surfaces. *Ultramicroscopy* 106:709–719
- Fürstner R, Barthlott W, Neinhuis C, Walzel P (2005) Wetting and self-cleaning properties of artificial superhydrophobic surfaces. *Langmuir* 21:956–961
- Gao XF, Jiang L (2004) Biophysics: water-repellent legs of water striders. *Nature* 432:36
- Gao L, McCarthy TJ (2006) The lotus effect explained: two reasons why two length scales of topography are important. *Langmuir* 22:2966–2967
- Jetter R, Kunst L, Samuels AL (2006) Composition of plant cuticular waxes. In: Riederer M, Müller C (eds) *Biology of the plant cuticle*. Blackwell, Oxford, pp 145–181
- Jung YC, Bhushan B (2008) Wetting behavior during evaporation and condensation of water microdroplets on superhydrophobic patterned surfaces. *J Microsc* 229:127–140
- Kamusewitz H, Possart W, Paul D (1999) The relation between young's equilibrium contact angle and the hysteresis on rough paraffin wax surfaces *Colloid Surf A Physicochem Eng Asp* 156:271–279
- Koch K, Dommissse A, Barthlott W (2006) Chemistry and crystal growth of plant wax tubules of lotus (*Nelumbo nucifera*) and nasturtium (*Tropaeolum majus*) leaves on technical substrates. *Crystall Growth Des* 6:2571–2578
- Koch K, Bhushan B, Barthlott W (2008) Diversity of structure, morphology, and wetting of plant surfaces (invited). *Soft Matter* 4:1943–1963
- Koch K, Bhushan B, Barthlott W (2009a) Multifunctional surface structures of plants: an inspiration for biomimetics (invited). *Prog Mater Sci* 54:137–178
- Koch K, Bhushan B, Jung YC, Barthlott W (2009b) Fabrication of artificial lotus leaves and significance of hierarchical structure for superhydrophobicity and low adhesion. *Soft Matter* 5:1386–1393
- Koch K, Bhushan B, Eniskat H-J, Barthlott W (2009c) Self-healing of voids in the wax coating on plant surfaces. *Philos Trans R Soc A* 367:1673–1688
- Koinkar VN, Bhushan B (1997) Effect of scan size and surface roughness on microscale friction measurements. *J Appl Phys* 81:2472–2479
- Neinhuis C, Barthlott W (1997) Characterization and distribution of water-repellent, self-cleaning plant surfaces. *Ann Bot* 79:667–677
- Nosonovsky M, Bhushan B (2005) Roughness optimization for biomimetic superhydrophobic surfaces. *Microsyst Technol* 11:535–549
- Nosonovsky M, Bhushan B (2008) Multiscale dissipative mechanisms and hierarchical surfaces: friction, superhydrophobicity, and biomimetics. Springer, Heidelberg
- Poon CY, Bhushan B (1995) Comparison of surface roughness measurements by stylus profiler, AFM and non-contact optical profiler. *Wear* 190:76–88
- Tambe NS, Bhushan B (2004) Scale dependence of micro/nano-friction and adhesion of MEMS/NEMS materials, coatings and lubricants. *Nanotechnology* 15:1561–1570

Chapter 5

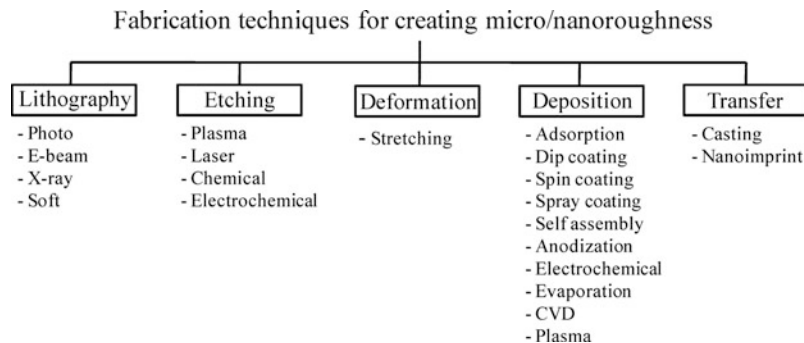
Fabrication Techniques Used for Structures with Superhydrophobicity, Self-Cleaning, Low Adhesion/Low Drag with Antifouling Properties

Fabrication of superhydrophobic surfaces has been an area of active research since the mid-1990s. In general, the same techniques that are used for micro- and nanostructure fabrication, such as lithography, etching, deposition, and self-assembly, have been utilized for producing superhydrophobic surfaces (Fig. 5.1; Table 5.1). The pros and cons of these techniques are summarized in Table 5.2. Among especially interesting developments is the creation of switchable surfaces that can be turned from hydrophobic to hydrophilic by surface energy modification through electrowetting, light and X-ray irradiation, dynamic effects, optical effects (e.g., the transparency, reflectivity or non-reflectivity) combined with the Lotus effect, hydrophobic interactions, and so on (Feng et al., 2004; Xu et al., 2005; Shirtcliffe et al., 2005; Wang et al., 2007; Krupenkin et al., 2007). An important requirement for potential applications for optics and self-cleaning glasses is the creation of transparent superhydrophobic surfaces. In order for the surface to be transparent, roughness details should be smaller than the wavelength of visible light (about 400–700 nm) (Nakajima et al., 1999).

Two main requirements for a superhydrophobic surface are that the surface should be rough and that it should be hydrophobic (low surface energy). These two requirements lead to two methods of producing a superhydrophobic surface: first, it is possible to make a rough surface from an initially hydrophobic material and, second, to modify a rough hydrophilic surface by modifying surface chemistry or applying a hydrophobic material upon it. Note that roughness is usually a more critical property than the low surface energy, since both moderately hydrophobic and very hydrophobic materials can exhibit similar wetting behavior when roughened.

5.1 Roughening to Create One-Level Structure

Lithography is a well-established technique, applied for creating a large area of periodic micro-/nanopatterns. It includes photo, E-beam, X-ray, and soft lithography. Bhushan and Jung (2007) produced micropatterned Si using photolithography. To

**Fig. 5.1** Typical methods to fabricate micro-/nanoroughened surfaces**Table 5.1** Typical materials and corresponding techniques to produce micro-/nanoroughness

Material	Technique	Contact angle (deg)	Notes	Source
Teflon	Plasma	168		Zhang et al. (2004a), Shiu et al. (2004)
Fluorinated block polymer solution	Casting under humid environment	160	Transparent	Yabu and Shimomura (2005)
PFOS	Electro- and chemical polymerization	152	Reversible (electric potential)	Xu et al. (2005)
PDMS	Laser treatment	166		Khorasani et al. (2005)
PS-PDMS block copolymer	Electrospinning	>150		Ma et al. (2005)
PS, PC, PMMA	Evaporation	>150		Bormashenko et al. (2006)
PS nanofiber	Nanoimprint	156		Lee et al. (2004)
Polyaniline nanofiber	Chemical polymerization	175		Chiou et al. (2007)
Polypropylene nanofibers	Porous nanomembrane patterning technique	173	Hierarchical	Lee and Bhushan (2012)
PET	Oxygen plasma etching	>150		Teshima et al. (2005)
Organotriethoxysilanes	Sol-gel	155	Reversible (temperature)	Shirtcliffe et al. (2005)
Al	Chemical etching	>150		Qian and Shen (2005)
Copper	Electrodeposition	160	Hierarchical	Shirtcliffe et al. (2004)
Si	Photolithography	170		Bhushan and Jung (2007)

(continued)

Table 5.1 (continued)

Material	Technique	Contact angle (deg)	Notes	Source
Si	E-beam lithography	164		Martines et al. (2005)
Si	X-ray lithography	>166		Fürstner et al. (2005)
PS, PMMA	AFM nanolithography			Martin et al. (2005), Cappella and Bonaccorso (2007)
Si	Casting	158	Plant leaf replica	Sun et al. (2005), Fürstner et al. (2005)
Si (black Si)	Plasma etching	>150	For liquid flow	Jansen et al. (1995)
Silica	Sol-gel	150		Hikita et al. (2005); Shang et al. (2005)
Silica	Layer-by-layer assembly	160	Hierarchical	Zhao et al. (2008)
Silica	Replication and spray coating	168	Hierarchical	Ebert and Bhushan (2012)
Polyelectrolyte multilayer surface overcoated with silica nanoparticles	Self-assembly	168		Zhai et al. (2004)
Epoxy resin with synthetic and plant waxes	Replication and self-assembly	173	Hierarchical	Bhushan et al. (2008a, b; 2009a, b); Koch et al. (2009b)
Nano-silica spheres	Dip coating	105		Klein et al. (2003)
Silica colloidal particles in PDMS	Spin coating	165	Hierarchical	Ming et al. (2005)
Au clusters	Electrochemical deposition	>150		Zhang et al. (2004b)
Carbon nanotubes	Chemical-vapor deposition	>165		Lau et al. (2003)
Carbon nanotubes	Chemical-vapor deposition	159	Hierarchical	Huang et al. (2005)
Carbon nanotubes	Replication and spray coating	170	Hierarchical	Jung and Bhushan (2009c)
ZnO, TiO ₂ nanorods	Sol-gel	>150	Reversible (UV irradiation)	Feng et al. (2004)

Table 5.2 Pros and cons of various fabrication techniques

Techniques	Pros	Cons
Lithography	Accuracy, large area	Slow process, high cost
Etching	Fast	Chemical contamination, less control
Deposition	Flexibility, cheap	Can be high temperature, less control
Self-assembly	Flexibility, cheap	Require suitable precursor

obtain a sample that is hydrophobic, a self-assembled monolayer (SAM) of 1,1,2,2,-tetrahydroperfluorodecyltrichlorosilane (PF_3) was deposited on the sample surfaces using a vapor-phase deposition technique. They obtained a superhydrophobic surface with a contact angle up to 170° . [Martines et al. \(2005\)](#) fabricated ordered arrays of nanopits and nanopillars by using electron beam lithography. They obtained a superhydrophobic surface with a static contact angle of 164° and contact angle hysteresis of 1° for a surface consisting of tall pillars with cusped tops after hydrophobization with octadecyltrichlorosilane (OTS). [Fürstner et al. \(2005\)](#) created silicon wafers with regular patterns of spikes by X-ray lithography. The wafer was hydrophobized by sputtering a layer of gold and subsequent immersion in a hexadecanethiol solution. AFM can be used in nanolithography to produce a nanostructure with the aid of solvent ([Cappella and Bonaccruso, 2007](#)) or electro field ([Martin et al., 2005](#)) on polystyrene (PS) and polymethylmethacrylate (PMMA), respectively. [Jung and Bhushan \(2006\)](#) created low-aspect-ratio asperities (LAR, 1:1 height-to-diameter ratio), high-aspect-ratio asperities (HAR, 3:1 height-to-diameter ratio), and a Lotus pattern (replica from the Lotus leaf), all on a PMMA surface using soft lithography. A self-assembled monolayer (SAM) of perfluorodecyltrioxysilane (PFDTES) was deposited on the patterned surfaces using a vapor-phase deposition technique.

One well-known and effective way to make rough surfaces is etching using either plasma, laser, chemical, or electrochemical techniques ([Ma and Hill, 2006](#)). [Jansen et al. \(1995\)](#) etched a silicon wafer using a fluorine-based plasma by utilizing the black silicon method to obtain isotropic, positively and negatively tapered, as well as vertical walls with smooth surfaces. [Coulson et al. \(2000\)](#) described an approach in plasma chemical roughening of poly(tetrafluoroethylene) (PTFE) substrates followed by the deposition of low surface energy plasma polymer layers, which give rise to high repellency towards polar and nonpolar probe liquids. A different approach was taken by [Shiu et al. \(2004\)](#), who treated a Teflon film with oxygen plasma and obtained a superhydrophobic surface with a contact angle of 168° . Fluorinated materials have a limited solubility, which makes it difficult to roughen them. However, they may be linked or blended with other materials, which are often easier to roughen, in order to make superhydrophobic surfaces. [Teshima et al. \(2005\)](#) obtained a transparent superhydrophobic surface from a poly(ethylene terephthalate) (PET) substrate via selective oxygen plasma etching followed by plasma-enhanced chemical-vapor deposition using tetramethylsilane (TMS) as the precursor. [Khorasani et al. \(2005\)](#) produced porous polydimethylsiloxane (PDMS) surfaces with the contact angle of 175° using CO_2 -pulsed laser

etching method as an excitation source for surface. [Qian and Shen \(2005\)](#) described a simple surface roughening method by dislocation-selective chemical etching on polycrystalline metals such as aluminum. After treatment with fluoroalkylsilane, the etched metallic surfaces exhibited superhydrophobicity. [Xu et al. \(2005\)](#) fabricated a reversible superhydrophobic surface with a double-roughened perfluorooctanesulfonate (PFOS) doped conducting polypyrrole (PPy) film by a combination of electropolymerization and chemical polymerization. Reversibility was achieved by switching between superhydrophobic doped or oxidized states and superhydrophilicity dedoped or neutral states with changing the applied electrochemical potential.

A stretching method can be used to produce a superhydrophobic surface. [Zhang et al. \(2004a\)](#) stretched a Teflon film and converted it into fibrous crystals with a large fraction of void space in the surface, leading to high roughness and the superhydrophobicity.

Deposition methods can also be used to make a substrate rough. There are several ways to make a rough surface including adsorption, dip coating, electrospinning, anodization, electrochemical, evaporation, chemical-vapor deposition (CVD), and plasma. Solidification of wax can be used to produce a superhydrophobic surface. [Shibuichi et al. \(1996\)](#) used alkylketene dimer (AKD) wax on a glass plate to spontaneously form a fractal structure in its surfaces. They obtained a surface with a contact angle larger than 170° without any fluorination treatments. [Klein et al. \(2003\)](#) obtained superhydrophobic surfaces by simply dip-coating a substrate with a slurry containing nano-silica spheres, which adhered to the substrate after a low temperature heat treatment. After reaction of the surface with a fluoroalkyltrichlorosilane, the hydrophobicity increased with a decreasing area fraction of spheres. [Ma et al. \(2005\)](#) produced block copolymer poly(styrene-b-dimethylsiloxane) fibers with submicrometer diameters in the range of 150–400 nm by electrospinning from a solution in tetrahydrofuran and dimethylformamide. They obtained superhydrophobic nonwoven fibrous mats with a contact angle of 163°. [Shiu et al. \(2004\)](#) produced self-organized close-packed superhydrophobic surfaces by spin-coating the monodispersed polystyrene beads solution on a substrate surface. [Abdelsalam et al. \(2005\)](#) studied the wetting of structured gold surfaces formed by electrodeposition through a template of submicrometer spheres and discussed the role of the pore size and shape in controlling wetting. [Bormashenko et al. \(2006\)](#) used evaporated polymer solutions of polystyrene (PS), polycarbonate (PC) and polymethylmethacrylate (PMMA) dissolved in chlorinated solvents, dichloromethane (CH_2Cl_2), and chloroform (CHCl_3) to obtain a self-assembled structure with hydrophobic properties. Chemical/physical vapor deposition (CVD/PVD) has been used for the modification of surface chemistry as well. [Lau et al. \(2003\)](#) created superhydrophobic carbon nanotube forests by modifying the surface of vertically aligned nanotubes with plasma-enhanced chemical-vapor deposition (PECVD). Superhydrophobicity was achieved down to the microscopic level where essentially spherical, micrometer-sized water droplets can be suspended on top of the nanotube forest. [Zhu et al. \(2005\)](#) and [Huang et al. \(2005\)](#) prepared surfaces with two-scale

roughness by the controlled growth of carbon nanotube (CNT) arrays by CVD. [Zhao et al. \(2006\)](#) also synthesized vertically aligned multiwalled carbon nanotube (MWCNT) arrays by chemical-vapor deposition on Si substrates using a thin film of iron (Fe) as catalyst layer and aluminum (Al) film.

Attempts to create superhydrophobic surfaces by casting and nanoimprint methods have been successful. [Yabu and Shimomura \(2005\)](#) prepared a porous superhydrophobic transparent membrane by casting a fluorinated block polymer solution under humid environment. Transparency was achieved because the honeycomb-patterned films had a sub-wavelength pore size. [Sun et al. \(2005\)](#) reported a nanocasting method to make a superhydrophobic PDMS surface. They first made a negative PDMS template using a Lotus leaf as an original template and then used the negative template to make a positive PDMS template—a replica of the original Lotus leaf. [Zhao et al. \(2005\)](#) prepared a superhydrophobic surface by casting a micellar solution of a copolymer poly(styrene-b-dimethylsiloxane) (PS-PDMS) in humid air based on the cooperation of vapor-induced phase separation and surface enrichment of PDMS block. [Lee et al. \(2004\)](#) produced vertically aligned PS nanofibers by using nanoporous anodic aluminum oxide as a replication template in a heat- and pressure-driven nanoimprint pattern transfer process. As the aspect ratio of the polystyrene (PS) nanofibers increased, the nanofibers could not stand upright but formed twisted bundles resulting in a three-dimensionally rough surface with a contact angle of about 155°.

5.2 Coating to Create One-Level Hydrophobic Structures

Modifying the surface chemistry with a hydrophobic coating widens the potential applications of superhydrophobic surfaces. There are several ways to modify the chemistry of a surface including sol–gel, dip coating, self-assembly, electrochemical, and chemical/physical vapor deposition. [Shirtcliffe et al. \(2005\)](#) prepared porous sol–gel foams from organo-triethoxysilanes which exhibited switching between superhydrophobicity and superhydrophilicity when exposed to different temperatures. [Hikita et al. \(2005\)](#) used colloidal silica particles and fluoroalkylsilane as the starting materials and prepared a sol–gel film with superliquid repellency by hydrolysis and condensation of alkoxy silane compounds. [Feng et al. \(2004\)](#) produced superhydrophobic surfaces using ZnO nanorods by sol–gel method. They showed that superhydrophobic surfaces can be switched into hydrophilic surfaces by alteration of ultraviolet (UV) irradiation. [Shang et al. \(2005\)](#) did not blend low surface energy materials in the sols, but described a procedure to make transparent superhydrophobic surfaces by modifying silica-based gel films with a fluorinated silane. In a similar way, [Wu et al. \(2005\)](#) made a microstructured ZnO-based surface via a wet-chemical process and obtained superhydrophobicity after coating the surface with long-chain alkanoic acids. [Chiou et al. \(2007\)](#) fabricated polyaniline nanofibers using chemical oxidative polymerization to produce uniform aligned

nanofibers and treated with CF₄ plasma treatment to create superhydrophobic surfaces with a contact angle of 175°.

Zhai et al. (2004) used a layer-by-layer (LBL) self-assembly technique to create a poly(allylamine hydrochloride)/poly(acrylic acid) (PAH/PAA) multilayer which formed a honeycomb-like structure on the surface after an appropriate combination of acidic treatments. After cross-linking the structure, they deposited silica nanoparticles on the surface via alternating dipping of the substrates into an aqueous suspension of the negatively charged nanoparticles and an aqueous PAH solution, followed by a final dipping into the nanoparticle suspension. Superhydrophobicity was obtained after the surface was modified by a chemical-vapor deposition of (tridecafluoro-1,1,2,2-tetrahydrooctyl)-1-trichlorosilane followed by a thermal annealing.

Zhang et al. (2004b) showed that the surface covered with dendritic gold clusters, which was formed by electrochemical deposition onto an indium tin oxide (ITO) electrode modified with a polyelectrolyte multilayer, showed superhydrophobic properties after further deposition of a *n*-dodecanethiol monolayer. Han et al. (2005) described the fabrication of lotus leaf-like superhydrophobic metal surfaces by using electrochemical reaction of Cu or Cu–Sn alloy plated on steel sheets with sulfur gas and subsequent perfluorosilane treatment. Chemical bath deposition (CBD) has also been used to make nanostructured surfaces; thus, Hosono et al. (2005) fabricated a nanopin film of brucite-type cobalt hydroxide (BCH) and achieved the contact angle of 178° after further modification of lauric acid (LA). Shi et al. (2006) described the use of galvanic cell reaction as a facile method to chemically deposit Ag nanostructures on the *p*-silicon wafer on a large scale. When the Ag-covered silicon wafer was further modified with a self-assembled monolayer of *n*-dodecanethiol, a superhydrophobic surface was obtained with a contact angle of about 154° and a tilt angle lower than 5°.

5.3 Methods to Create Two-Level (Hierarchical) Structures

Two-level (hierarchical) roughness structures are typical for superhydrophobic surfaces in nature, as was discussed above. Recently, many efforts have been devoted to fabricating these hierarchical structures in various ways. Shirtcliffe et al. (2004) prepared a hierarchical (double-roughened) copper surface by electrodeposition from acidic copper sulfate solution onto flat copper and a patterning technique of coating with a fluorocarbon hydrophobic layer. Another way to obtain a rough surface for superhydrophobicity is assembly from colloidal systems. Ming et al. (2005) prepared a hierarchical (double-roughened) surface consisting of silica-based raspberry-like particles. First is the attachment of epoxy and amino groups onto the silica microparticles of about 700 nm and nanoparticles of about 70 nm, respectively, using established synthetic procedures. Two suspensions in ethanol are created, one with microparticles and another one with nanoparticles. In the

next step, the suspension with the silica microparticles is added dropwise to the suspension with the nanoparticles. The nanoparticles attach to the microparticles due to the reaction between the epoxy and amino groups present on the surface of the particles. Then, the suspension is centrifuged to separate any unreacted particles. A next step involves depositing these micro-/nanostructured particles into an epoxy film (on silicon). Finally, since the resulting micro-/nanoparticle surface is initially hydrophilic, it is made hydrophobic by a deposition of monoepoxy-end-capped polydimethylsiloxane (PDMS). [Northen and Turner \(2005\)](#) fabricated arrays of flexible silicon dioxide platforms supported by single high-aspect-ratio silicon pillars down to $1\text{ }\mu\text{m}$ in diameter and with heights up to $\sim 50\text{ }\mu\text{m}$. When these platforms were coated with polymeric organorods of approximately $2\text{ }\mu\text{m}$ tall and $50\text{--}200\text{ nm}$ in diameter, it showed that the surface is highly hydrophobic with a water contact angle of 145° .

[Chong et al. \(2006\)](#) fabricated hierarchically ordered nanowire arrays with periodic voids at the microscale and hexagonally packed nanowires at the nanoscale. This hierarchical surface was created by selective electrodeposition using nanoporous anodic alumina as a template and a porous gold film as a working electrode that is patterned by microsphere monolayers. [Wang et al. \(2006\)](#) also developed a novel precursor hydrothermal redox method with Ni(OH)_2 as the precursor to fabricate a hierarchical structure consisting of nickel hollow microspheres with nickel nanoparticles in situ. The created hierarchical hollow structure exhibited enhanced coercivity and remnant magnetization as compared with hollow nickel submicrometer spheres, hollow nickel nanospheres, bulk nickel, and free Ni nanoparticles.

[Kim et al. \(2007\)](#) fabricated a hierarchical structure which looks like the same structures as the Lotus leaf. First, the nanoscale porosity was generated by anodic aluminum oxidation, and then, the anodized porous alumina surface was replicated by polytetrafluoroethylene. The polymer sticking phenomenon during the replication created the sub-microstructures on the negative polytetrafluoroethylene nanostructure replica. The contact angle of the created hierarchical structure was about 160° , and the tilting angle is less than 1° . [del Campo and Greiner \(2007\)](#) reported that SU-8 hierarchical patterns comprising of features with lateral dimensions ranging from 5 to 2 mm and heights from 10 to $500\text{ }\mu\text{m}$ were obtained by photolithography, which comprises of a step of layer-by-layer exposure in soft contact printed shadow masks which are embedded into the SU-8 multilayer.

[Bhushan et al. \(2008a, b, 2009a, b\)](#) and [Koch et al. \(2009b\)](#) produced hierarchical structures by replication of a micropatterned silicon surface and a Lotus leaf microstructure using an epoxy resin and by self-assembly of synthetic and plant waxes as thin hydrophobic three-dimensional crystals to create hydrophobic nanostructures. The fabrication technique used is a low-cost two-step process, which provides flexibility in the fabrication of a variety of hierarchical structures. They showed that a hierarchical structure has a high propensity of air pocket formation and leads to a static contact angle of 173° and contact angle hysteresis and tilt angle of $\sim 2^\circ$.

Zhao et al. (2008) fabricated a hierarchical structure by using layer-by-layer assembly of silica nanoparticles on a microsphere-patterned polyimide precursor substrate combined with the fluoroalkylsilane treatment. The microstructures were created by replica molding of polyamide using two-dimensional PS microsphere arrays. They obtained a superhydrophobic surface with a static contact angle of 160° and sliding angle of less than 10°. Cortese et al. (2008) applied plasma CF₄ treatment on micropattern PDMS and obtained contact angle of 170°. Kuan et al. (2009) produced a hierarchical structure by imprinting ZnO precursor films using gratings with 830-nm and 50 μm dimensions. They achieved a contact angle of 141° by nanostructures deposited on sawtooth patterns without modifying the surface chemistry. Lee and Bhushan (2012) fabricated a hierarchical structure made of polypropylene fibers using two stacked porous membranes as a template.

Jung and Bhushan (2009) produced mechanically durable carbon nanotube composite hierarchical structures with a static contact angle of 170° and a contact angle hysteresis of 2° by replication of a micropatterned silicon surface using an epoxy resin and by deposition of the carbon nanotube composite using a spray method. They showed that carbon nanotube composite structure had high mechanical strength and wear resistance led from the uniform distribution and strong bonding of carbon nanotube on substrates. Ebert and Bhushan (2012) produced a mechanically durable silica composite hierarchical structure with a static contact angle of 168° and a contact angle hysteresis of 1° fabrication using spray method.

References

- Abdelsalam ME, Bartlett PN, Kelf T, Baumberg J (2005) Wetting of regularly structured gold surfaces. *Langmuir* 21:1753–1757
- Bhushan B, Jung YC (2007) Wetting study of patterned surfaces for superhydrophobicity. *Ultramicroscopy* 107:1033–1041
- Bhushan B, Koch K, Jung YC (2008a) Nanostructures for superhydrophobicity and low adhesion. *Soft Matter* 4:1799–1804
- Bhushan B, Koch K, Jung YC (2008b) Biomimetic hierarchical structure for self-cleaning. *Appl Phys Lett* 93:093101
- Bhushan B, Jung YC, Niemietz A, Koch K (2009a) Lotus-like biomimetic hierarchical structures developed by the self-assembly of tubular plant waxes. *Langmuir* 25:1659–1666
- Bhushan B, Koch K, Jung YC (2009b) Fabrication and characterization of the hierarchical structure for superhydrophobicity. *Ultramicroscopy* 109:1029–1034
- Bormashenko E, Stein T, Whyman G, Bormashenko Y, Pogreb E (2006) Wetting properties of the multiscaled nanostructured polymer and metallic superhydrophobic surfaces. *Langmuir* 22:9982–9985
- Cappella B, Bonaccorso E (2007) Solvent-assisted nanolithography on polystyrene surfaces using the atomic force microscope. *Nanotechnology* 18:155307
- Chiou N, Lu C, Guan J, Lee LJ, Epstein AJ (2007) Growth and alignment of polyaniline nanofibres with superhydrophobic, superhydrophilic and other properties. *Nat Nanotechnol* 2:354–357

- Chong MAS, Zheng YB, Gao H, Tan LK (2006) Combinational template-assisted fabrication of hierarchically ordered nanowire arrays on substrates for device applications. *Appl Phys Lett* 89:233104
- Cortese B, Amone SD, Manca M, Viola I, Cingolani R, Gigli G (2008) Superhydrophobicity due to the hierarchical scale roughness of PDMS surfaces. *Langmuir* 24:2712–2718
- Coulson SR, Woodward I, Badyal JPS, Brewer SA, Willis C (2000) Super-repellent composite fluoropolymer surfaces. *J Phys Chem B* 104:8836–8840
- del Campo A, Greiner C (2007) SU-8: a photoresist for high-aspect-ratio and 3D submicron lithography. *J Micromech Microeng* 17:R81–R95
- Ebert D, Bhushan B (2012) Durable lotus-effect surfaces with hierarchical structure using micro- and nanosized hydrophobic silica particles. *J Colloid Interface Sci* 368:584–591
- Feng XJ, Feng L, Jin MH, Zhai J, Jiang L, Zhu DB (2004) Reversible Super-hydrophobicity to super-hydrophilicity transition of aligned ZnO nanorod films. *J Am Chem Soc* 126:62–63
- Fürstner R, Barthlott W, Neinhuis C, Walzel P (2005) Wetting and self-cleaning properties of artificial superhydrophobic surfaces. *Langmuir* 21:956–961
- Han JT, Jang Y, Lee DY, Park JH, Song SH, Ban DY, Cho K (2005) Fabrication of a bionic superhydrophobic metal surface by sulfur-induced morphological development. *J Mater Chem* 15:3089–3092
- Hikita M, Tanaka K, Nakamura T, Kajiyama T, Takahara A (2005) Superliquid-repellent surfaces prepared by colloidal silica nanoparticles covered with fluoroalkyl groups. *Langmuir* 21:7299–7302
- Hosono E, Fujihara S, Honma I, Zhou H (2005) Superhydrophobic perpendicular nanopin film by the bottom-up process. *J Am Chem Soc* 127:13458–13459
- Huang L, Lau SP, Yang HY, Leong ESP, Yu SF (2005) Stable superhydrophobic surface via carbon nanotubes coated with a ZnO thin film. *J Phys Chem* 109:7746–7748
- Jansen H, de Boer M, Legtenberg R, Elwenspoek M (1995) The black silicon method: a universal method for determining the parameter setting of a fluorine-based reactive ion etcher in deep silicon trench etching with profile control. *J Micromech Microeng* 5:115–120
- Jung YC, Bhushan B (2006) Contact angle, adhesion, and friction properties of micro- and nanopatterned polymers for superhydrophobicity. *Nanotechnology* 17:4970–4980
- Jung YC, Bhushan B (2009) Mechanically durable CNT-composite hierarchical structures with superhydrophobicity, self-cleaning, and low-drag. *ACS Nano* 3:4155–4163
- Khorasani MT, Mirzadeh H, Kermani Z (2005) Wettability of porous polydimethylsiloxane surface: morphology study. *Appl Surf Sci* 242:339–345
- Kim D, Hwang W, Park HC, Lee KH (2007) Superhydrophobic micro- and nanostructures based on polymer sticking. *Key Eng Mater* 334–335:897–900
- Klein RJ, Biesheuvel PM, Yu BC, Meinhart CD, Lange FF (2003) Producing super-hydrophobic surfaces with nano-silica spheres. *Z Metallkd* 94:377–380
- Koch K, Bhushan B, Jung YC, Barthlott W (2009b) Fabrication of artificial lotus leaves and significance of hierarchical structure for superhydrophobicity and low adhesion. *Soft Matter* 5:1386–1393
- Krupenkin TN, Taylor JA, Wang EN, Kolodner P, Hodes M, Salamon TR (2007) Reversible wetting-dewetting transitions on electrically tunable superhydrophobic nanostructured surfaces. *Langmuir* 23:9128–9133
- Kuan CY, Hon MH, Chou JM, Leu IC (2009) Wetting characteristics on micro/nanostructured zinc oxide coatings. *J Electrochem Soc* 156:J32–J36
- Lau KKS, Bico J, Teo KBK, Chhowalla M, Amarantunga GAJ, Milne WI, McKinley GH, Gleason KK (2003) Superhydrophobic carbon nanotube forests. *Nano Lett* 3:1701–1705
- Lee H, Bhushan B (2012) Fabrication and characterization of hierarchical nanostructured smart adhesion surfaces. (unpublished)
- Lee W, Jin M, Yoo W, Lee J (2004) Nanostructuring of a polymeric substrate with well-defined nanometer-scale topography and tailored surface wettability. *Langmuir* 20:7665–7669
- Ma M, Hill RM (2006) Superhydrophobic surfaces. *Curr Opin Colloid Interface Sci* 11:193–202

- Ma M, Hill RM, Lowery JL, Fridrikh SV, Rutledge GC (2005) Electrospun poly(styrene-block-dimethylsiloxane) block copolymer fibers exhibiting superhydrophobicity. *Langmuir* 21:5549–5554
- Martin C, Rius G, Borrise X, Perez-Murano F (2005) Nanolithography on thin layers of PMMA using atomic force microscopy. *Nanotechnology* 16:1016–1022
- Martines E, Seunarine K, Morgan H, Gadegaard N, Wilkinson CDW, Riehle MO (2005) Superhydrophobicity and superhydrophilicity of regular nanopatterns. *Nano Lett* 5:2097–2103
- Ming W, Wu D, van Benthem R, de With G (2005) Superhydrophobic films from raspberry-like particles. *Nano Lett* 5:2298–2301
- Nakajima A, Fujishima A, Hashimoto K, Watanabe T (1999) Preparation of transparent superhydrophobic boehmite and silica films by sublimation of aluminum acetylacetone. *Adv Mater* 11:1365–1368
- Northen MT, Turner KL (2005) A batch fabricated biomimetic dry adhesive. *Nanotechnology* 16:1159–1166
- Qian B, Shen Z (2005) Fabrication of superhydrophobic surfaces by dislocation-selective chemical etching on aluminum, copper, and zinc substrates. *Langmuir* 21:9007–9009
- Shang HM, Wang Y, Limmer SJ, Chou TP, Takahashi K, Cao GZ (2005) Optically transparent superhydrophobic silica-based films. *Thin Solid Films* 472:37–43
- Shi F, Song Y, Niu J, Xia X, Wang Z, Zhang X (2006) Facile method to fabricate a large-scale superhydrophobic surface by galvanic cell reaction. *Chem Mater* 18:1365–1368
- Shibuchi S, Onda T, Satoh N, Tsujii K (1996) Super-water-repellent surfaces resulting from fractal structure. *J Phys Chem* 100:19512–19517
- Shirtcliffe NJ, McHale G, Newton MI, Chabrol G, Perry CC (2004) Dual-scale roughness produces unusually water-repellent surfaces. *Adv Mater* 16:1929–1932
- Shirtcliffe NJ, McHale G, Newton MI, Perry CC, Roach P (2005) Porous materials show superhydrophobic to superhydrophilic switching. *Chem Commun* 3135–3137
- Shiu J, Kuo C, Chen P, Mou C (2004) Fabrication of tunable superhydrophobic surfaces by nanosphere lithography. *Chem Mater* 16:561–564
- Sun M, Luo C, Xu L, Ji H, Ouyang Q, Yu D, Chen Y (2005) Artificial lotus leaf by nanocasting. *Langmuir* 21:8978–8981
- Teshima K, Sugimura H, Inoue Y, Takai O, Takano A (2005) Transparent ultra water-repellent poly(ethylene terephthalate) substrates fabricated by oxygen plasma treatment and subsequent hydrophobic coating. *Appl Surf Sci* 244:619–622
- Wang Y, Zhu Q, Zhang H (2006) Fabrication and magnetic properties of hierarchical porous hollow nickel microspheres. *J Mater Chem* 16:1212–1214
- Wang S, Liu H, Liu D, Ma X, Fang X, Jiang L (2007) Enthalpy driven three state switching of a superhydrophilic/superhydrophobic surfaces. *Angew Chem Int Ed* 46:3915–3917
- Wu X, Zheng L, Wu D (2005) Fabrication of superhydrophobic surfaces from microstructured ZnO-based surfaces via a wet-chemical route. *Langmuir* 21:2665–2667
- Xu L, Chen W, Mulchandani A, Yan Y (2005) Reversible conversion of conducting polymer films from superhydrophobic to superhydrophilic. *Angew Chem Int Ed* 44:6009–6012
- Yabu H, Shimomura M (2005) Single-step fabrication of transparent superhydrophobic porous polymer films. *Chem Mater* 17:5231–5234
- Zhai L, Cebeci FC, Cohen RE, Rubner MF (2004) Stable superhydrophobic coatings from polyelectrolyte multilayers. *Nano Lett* 4:1349–1353
- Zhang JL, Li JA, Han YC (2004a) Superhydrophobic PTFE surfaces by extension. *Macromol Rapid Commun* 25:1105–1108
- Zhang X, Feng S, Yu X, Liu H, Fu Y, Wang Z, Jiang L, Li X (2004b) Polyelectrolyte multilayer as matrix for electrochemical deposition of gold clusters: toward super-hydrophobic surface. *J Am Chem Soc* 126:3064–3065
- Zhao N, Xie QD, Weng LH, Wang SQ, Zhang XY, Xu J (2005) Superhydrophobic surface from vapor-induced phase separation of copolymer micellar solution. *Macromolecules* 38:8996–8999

- Zhao Y, Tong T, Delzeit L, Kashani A, Meyyappan M, Majumdar A (2006) Interfacial energy and strength of multiwalled-carbon-nanotube-based dry adhesive. *J Vac Sci Technol B* 24:331–335
- Zhao Y, Li M, Lu Q, Shi Z (2008) Superhydrophobic polyimide films with a hierarchical topography: combined replica molding and layer-by-layer assembly. *Langmuir* 24:12651–12657
- Zhu L, Xiu Y, Xu J, Tamirisa PA, Hess DW, Wong C (2005) Superhydrophobicity on two-tier rough surfaces fabricated by controlled growth of aligned carbon nanotube arrays coated with fluorocarbon. *Langmuir* 21:11208–11212

Chapter 6

Fabrication and Characterization of Micro-, Nano-, and Hierarchical Structured Surfaces

6.1 Introduction

It has been demonstrated experimentally that roughness changes contact angle in accordance with the Wenzel model or the Cassie–Baxter model, depending upon whether the surface is hydrophilic or hydrophobic. Yost et al. (1995) found that roughness enhances wetting of a copper surface with Sn–Pb eutectic solder, which has a contact angle of 15–20° for a smooth surface. Shibuichi et al. (1996) measured the contact angle of various liquids (mixtures of water and 1,4-dioxane) on alkyl ketene dimer (AKD) substrate (contact angle not larger than 109° for a smooth surface). They found that for wetting liquids, the contact angle decreases with increasing roughness, whereas for non-wetting liquids, it increases. Semal et al. (1999) investigated the effect of surface roughness on contact angle hysteresis by studying a sessile droplet of squalene spreading dynamically on multilayer substrates (behenic acid on glass) and found that an increase in microroughness slows the rate of droplet spread. Erbil et al. (2003) measured the contact angle of polypropylene (contact angle of 104° for smooth surface) and found that the contact angle increases with increasing roughness. Burton and Bhushan (2005) and Jung and Bhushan (2006) measured the contact angle of various micro- and nanopatterned polymer surfaces with hydrophilicity and hydrophobicity. They found that in the case of hydrophilic surfaces, it decreases with increasing roughness factor, and for hydrophobic surfaces, it increases with increasing roughness factor. Nanopatterned surfaces benefit from air pocket formation. Jung and Bhushan (2008c) also studied the effect of submicron droplets on contact angle.

The contact angle on selected patterned surfaces has been measured to understand the role of pitch value on the contact angle as well as on the transition between the Cassie–Baxter regime and Wenzel regime (Bhushan and Jung, 2007, 2008; Jung and Bhushan, 2007, 2008a, b). Evaporation studies are useful in characterizing the role of droplet size. During evaporation, droplets with decreasing sizes exist which are used to evaluate the transition criterion on a given patterned surface (Bourges-Monnier and Shanahan, 1995; Rowan et al., 1995; Erbil et al., 2002;

McHale et al., 2005; Jung and Bhushan, 2007, 2008a; Nosonovsky and Bhushan, 2007a, c, 2008b, d, e; Bhushan et al., 2008a, 2009b, c, d). It is found that the wetting state changes from the Cassie–Baxter to the Wenzel state as the droplet becomes smaller than a critical value and the pitch value becomes larger than a critical value on patterned surfaces.

Another important phenomenon related to wetting behavior is the bouncing of droplets. When a droplet hits a surface, it can bounce, spread, or stick. In practical applications of superhydrophobic surfaces, surfaces should maintain their ability to repel penetrating droplets under dynamic conditions. The transition can occur by the impact of a droplet on a given patterned surface at a critical velocity with a critical geometric parameter (Richard et al., 2002; Lafuma and Quère, 2003; Bartolo et al., 2006; Reyssat et al., 2006; Jung and Bhushan, 2008b, 2009a; Nosonovsky and Bhushan, 2008e).

An environmental scanning electron microscope (ESEM) can be used to condense or evaporate water droplets on surfaces by adjusting the pressure of the water vapor in the specimen chamber and the temperature of the cooling stage. Transfer of the water droplet has been achieved by a specially designed micro-injector device on wool fibers and then imaged at room temperature in ESEM (Danilatos and Brancik, 1986). Images of water droplets show strong topographic contrast in ESEM such that reliable contact angle measurements can be made on the surfaces (Stelmashenko et al., 2001). Water condensation and evaporation studies on patterned surfaces have been carried out by Jung and Bhushan (2008a) where the change of static contact angle and contact angle hysteresis was related with the surface roughness; also see Nosonovsky and Bhushan (2007a, c, 2008b, d, e).

Bhushan and Jung (2007, 2008), Jung and Bhushan (2006, 2007, 2008a, b), Bhushan et al. (2007, 2008a, b, 2009b, c, d), and Koch et al. (2009) used nature's route to fabricate hierarchical structures, created by replication of micropatterns and by self-assembly of hydrophobic alkanes and plant wax. They studied their static contact angle, contact angle hysteresis, tilt angle, air pocket formation, and adhesive force, as well as efficiency of self-cleaning. Hierarchical structures exhibited superhydrophobicity with static contact angles of about 171° and low contact angle hysteresis of about 2° and self-cleaning properties comparable to that of the Lotus leaf. This verified their understanding of the wetting mechanisms of the Lotus leaf. Jung and Bhushan (2008b, 2009a) performed bouncing and vibrating droplet experiments to study the effect of impact velocity and vibration amplitude on the transition from the composite solid–air–liquid interface to the homogeneous solid–liquid interface.

By using smart materials and nanofabrication techniques, Jung and Bhushan (2009b) produced mechanically durable carbon nanotube (CNT) composite hierarchical structures with a static contact angle of 170° and a contact angle hysteresis of 2° by replication of a micropatterned silicon surface using an epoxy resin and by deposition of the CNT composite using a spray method. Based on durability experiments, they showed that the CNT composite structure had high mechanical strength and wear resistance from the uniform distribution and strong bonding of

CNT on substrates. [Ebert and Bhushan \(2012\)](#) have produced mechanically durable hierarchical structures using micro-/nanoparticles.

In this chapter, characterization of various micro-, nano-, and hierarchical patterned surfaces is provided to verify theoretical models and to understand the transition between the Wenzel and Cassie–Baxter wetting regimes and the role of contact angle hysteresis and hierarchical roughness. Details on fabricated surfaces using nature's route are presented which was used to verify one's understanding, and then details on optimum structures fabricated based on the models using smart materials and fabrication techniques are presented.

6.2 Experimental Techniques

6.2.1 Contact Angle, Surface Roughness, and Adhesion

The static and dynamic (advancing and receding) contact angles were measured using a Rame–Hart model 100 contact angle goniometer and droplets of DI water ([Burton and Bhushan, 2005; Bhushan and Jung, 2007, 2008; Jung and Bhushan, 2006, 2007; Bhushan et al., 2008a, b, 2009c, d; Koch et al., 2009](#)). For measurement of the static contact angle, the droplet size should be smaller than the capillary length but larger than the dimension of the structures present on the surfaces. Droplets of about $5 \mu\text{L}$ in volume (with the diameter of a spherical droplet about 2.1 mm) were gently deposited on the substrate using a microsyringe for measurement of the static contact angle. The advancing and receding contact angles were measured by the addition and removal of water from a DI water sessile droplet using a microsyringe. The contact angle hysteresis was calculated as the difference between the measured advancing and receding contact angles, and the tilt angle was measured by using a simple tilting stage ([Bhushan and Jung, 2007, 2008; Bhushan et al., 2008a, b, 2009c, d; Koch et al., 2009](#)). All measurements were made at five different points for each sample at $22 \pm 1^\circ\text{C}$ and $50 \pm 5\%$ RH. The measurements were reproducible to within $\pm 3^\circ$.

For surface roughness measurement, an optical profiler was used for different surface structures ([Burton and Bhushan, 2006; Bhushan and Jung, 2006, 2007, 2008](#)). The optical profiler has one advantage due to its greater Z-range (2 mm) over an atomic force microscope (AFM) (Z-range about 7 μm), but it has a maximum lateral resolution of only $\sim 0.6 \mu\text{m}$ ([Bhushan, 1999, 2002, 2011](#)).

Adhesive force was measured with an AFM using the force distance curve approach described earlier. Experiments were performed using three different radii tips to study the effect of scale dependence. A borosilicate ball with 15 μm radius and a silica ball with 3.8 μm radius were mounted on a gold-coated triangular Si_3N_4 cantilever with a nominal spring constant of 0.58 N/m. A square pyramidal Si_3N_4 tip with a nominal radius of 30–50 nm on a triangular Si_3N_4 cantilever with a nominal spring constant of 0.58 N/m was used for the smaller radius tip.

6.2.2 Droplet Evaporation Studies

Droplet evaporation was observed and recorded by a digital camcorder with a 10 \times optical and 120 \times digital zoom for every run of the experiment. Then the decrease in the diameter of the droplets with time was determined ([Jung and Bhushan, 2007, 2008a, Bhushan et al., 2008a](#) [2009c](#)). The frame speed of the camcorder was 0.03 s/frame. An objective lens placed in front of the camcorder during recording gave a total magnification of 10–20 times. Droplet diameter as small as a few hundred microns could be measured with this method. Droplets were gently deposited on the substrate using a microsyringe, and the whole process of evaporation was recorded. Images obtained were analyzed using Imagetool® software (University of Texas Health Science Center) for the contact angle. To find the dust trace remaining after droplet evaporation, an optical microscope with a charge-coupled device (CCD) camera was used. All measurements were made in a controlled environment at 22 \pm 1°C and 45 \pm 5% RH ([Jung and Bhushan, 2007, 2008a, Bhushan et al., 2008a, 2009c, d](#)).

6.2.3 Bouncing Droplet Studies

The process of dynamic impact was recorded by a highspeed camera (Kodak Ektapro HS Motion Analyzer, Model 4540) operated at 500 frames/s for each experimental run and then measuring the dynamic impact behavior of the droplet as a function of time. The impact velocity was calculated by varying the droplet release height. The size of the droplet was the same as that of a droplet for the static contact angle. All measurements were made in a controlled environment at 22 \pm 1°C and 45 \pm 5% RH ([Jung and Bhushan, 2008b](#)).

6.2.4 Vibrating Droplet Studies

The process of dynamic behavior was obtained by a system producing vertical vibrations ([Jung and Bhushan, 2009a](#)). The system consists of an electrodynamic shaker (Labworks Inc. Model ET-126A/B) connected with a signal generator and power amplifier, a digital camcorder with an objective lens, and a lamp for a light source. The specimen was placed on the top of the shaker, and a droplet was gently deposited using a microsyringe. The size of the droplet was the same as that of a droplet for the static contact angle as reported earlier. The vibration frequency was controlled between 0 and 300 Hz at 0.4 mm amplitude for measurement of the resonance frequency of a droplet. For wetting behavior of a droplet on the surface, a frequency of 30 Hz, which was less than the resonance frequency, was chosen, and the vibration amplitude was controlled between 0 and 3 mm. The vibration

time applied to the droplet was 1 min for each experiment. All measurements were made in a controlled environment at $22 \pm 1^\circ\text{C}$ and $45 \pm 5\%$ RH ([Jung and Bhushan, 2009a](#)).

6.2.5 Microdroplet Condensation and Evaporation Studies Using ESEM

A Philips XL30 ESEM equipped with a Peltier cooling stage was used to study smaller droplets ([Jung and Bhushan, 2008a](#)). ESEM uses a gaseous secondary electron detector (GSED) for imaging. The ESEM column is equipped with a multistage differential pressure-pumping unit. The pressure in the upper part is about 10^{-6} – 10^{-7} Torr, but a pressure of about 1–15 Torr can be maintained in the observation chamber. When the electron beam (primary electrons) ejects secondary electrons from the surface of the sample, the secondary electrons collide with gas molecules in the ESEM chamber, which in turn acts as a cascade amplifier, delivering the secondary electron signal to the positively biased GSED. The positively charged ions are attracted toward the specimen to neutralize the negative charge produced by the electron beam. Therefore, the ESEM can be used to examine electrically isolated specimens in their natural state. In ESEM, adjusting the pressure of the water vapor in the specimen chamber and the temperature of the cooling stage allows the water to condense on the sample in the chamber. For the measurement of the static and dynamic contact angles on patterned surfaces, video images were recorded. The voltage of the electron beam was 15 kV, and the distance of the specimen from the final aperture was about 8 mm. If the angle of observation is not parallel to the surface, the electron beam is not parallel to the surface but inclined at an angle; this will produce a distortion in the projection of the droplet profile. A mathematical model to calculate the real contact angle from the ESEM images was used to correct the tilting of the surfaces during imaging ([Brugnara et al., 2006; Jung and Bhushan, 2008a](#)).

6.2.6 Generation of Submicron Droplets

In order to generate submicron droplets, [Jung and Bhushan \(2008c\)](#) developed an AFM-based technique using a modified nanoscale dispensing (NADIS) probe as shown in Fig. 6.1. The NADIS probe was fabricated from modifying a commercially available silicon nitride (Si_3N_4) cantilever (Olympus OMCL-RC800) with lengths of 100 and 200 μm , spring constants of 0.8 and 0.1 N/m, and resonance frequencies of 68.94 and 122.02 kHz, respectively (Swiss Center for Electronics and Microtechnology). The probe consisted of a loading area (30 μm diameter) for the liquid on the upper side of the cantilever. The loading area was produced by removing the material locally in and around the tip with a reflective gold layer

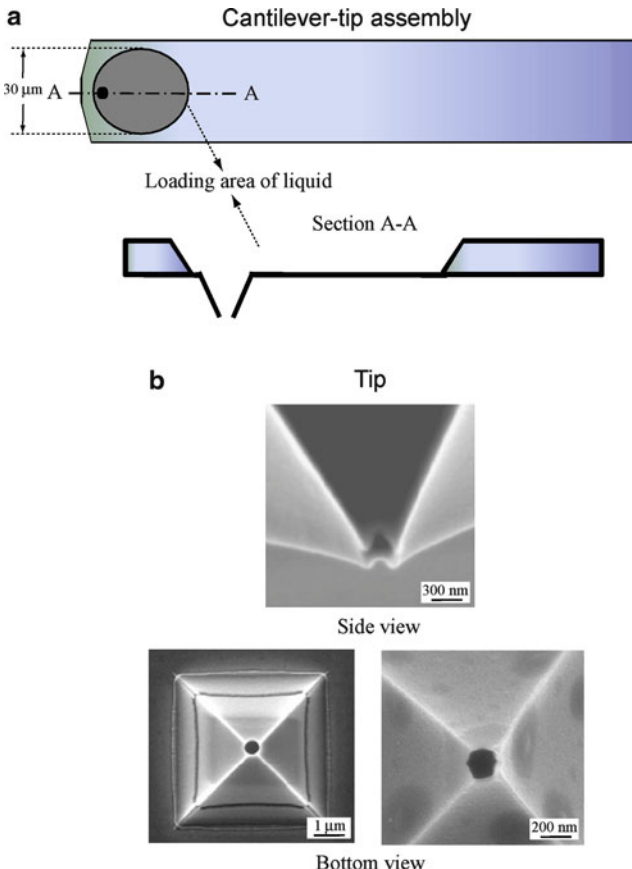


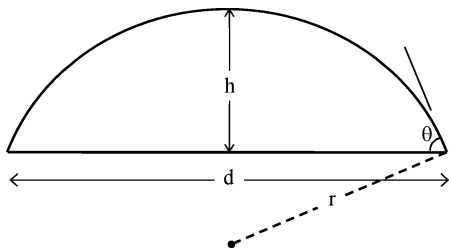
Fig. 6.1 (a) Schematic of modified nanoscale dispensing (NADIS) probe for generation of submicron-size droplets. The loaded liquid is limited to the loading area (30 μm diameter circle). (b) Scanning electron micrograph of tip in side view and bottom view with different aperture sizes (500 and 200 nm) at its apex (Jung and Bhushan, 2008c)

using focused ion beam milling. The remaining gold was made hydrophobic using hexadecanethiol (in liquid phase) whereas the bare silicon nitride in the milling area remained hydrophilic. The hydrophilic–hydrophobic transition prevents spreading of the loaded liquid over the entire cantilever.

A droplet of a certain volume V is deposited on the surface. Figure 6.2 shows an idealized spherical capped droplet. Based on the thickness of the droplet h and contact diameter d , the contact angle is obtained by the following equation for a simple spherical capped geometry of droplet (Jung and Bhushan, 2008c):

$$\theta = \sin^{-1} \left(\frac{3d}{2 \left(\frac{3V}{\pi h^2} + h \right)} \right). \quad (6.1)$$

Fig. 6.2 Droplet of liquid in contact with a surface, contact angle θ . The thickness of droplet is h . The contact diameter between droplet and surface is d . The radius of curvature of droplet is r (Jung and Bhushan, 2008c)



For calculation of the contact angle of the droplet, Jung and Bhushan (2008c) use the following three steps:

- (1) For the measurement of the volume of a droplet deposited on the surface, the change in resonance frequency of the cantilever before and after depositing the droplet on the surface is measured. The resonance frequency of the cantilever is measured by performing a frequency sweep of the voltage-driven oscillations by a thermal tune method (Palacio and Bhushan, 2010)
- (2) For the measurement of the thickness of a droplet deposited on the surface, the distance between the tip snap-in and the position where the tip is in contact with the surface is measured in the force calibration mode.
- (3) For the measurement of the contact diameter between a droplet and surface, the image of the droplet after evaporation is measured using a Si tip.

For the thickness of a droplet deposited on the surface, the force distance curve was used (Bhushan, 1999, 2002, 2011). The droplet was deposited in the first approach. The force distance curve was obtained during a second approach to measure the thickness of the droplet (Bhushan and Blackman, 1991; Chen and Bhushan, 2006; Lodge and Bhushan, 2006). The cantilever deflection is plotted on the vertical axis against the Z-position of the piezo scanner in a force distance curve as shown in Fig. 6.3. The measurement starts at a large separation (point A), where there is no deflection of the cantilever. As the piezo moves to the sample, a sudden mechanical instability occurs between point B and point C, and the droplet jumps into contact with the tip and wicks up around the tip to form a meniscus. The cantilever bends downward because of the attractive meniscus force acting on the tip. As the piezo further approaches the surface, the deflection of the cantilever increases while the tip travels the thickness of the droplet and eventually contacts the underlying surface at point D, and the cantilever starts to bend upward. Once the piezo reaches the end of its designated ramp size at point E, it is retracted to its starting position. The tip goes beyond zero deflection and enters the adhesion region. At point F, the elastic force of the cantilever becomes equivalent to the adhesive force, causing the cantilever to snap back to point G. As the tip travels in the liquid, it is deflected as well. The tip deflection occurs in the same direction as the piezo travels for the AFM used in this study. The liquid film thickness (h) is the sum of the travel distance of the piezo (described as h_1 in Fig. 6.3) and the deflection of the cantilever (described as h_2 in Fig. 6.3). Though previous studies show that h overestimates the actual liquid film thickness, it still provides a good measurement of the thickness

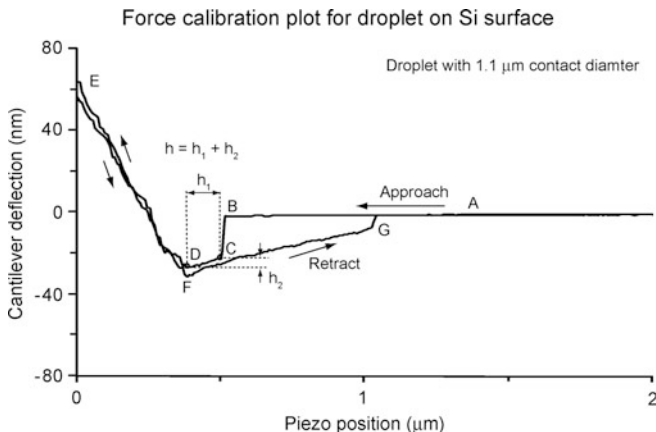


Fig. 6.3 Force calibration plot for a droplet with $1.1\text{ }\mu\text{m}$ contact diameter on Si surface. The h is a measure of droplet thickness on the surface

of the droplet (Bhushan and Blackman, 1991; Chen and Bhushan, 2006; Lodge and Bhushan, 2006).

The resolution of volume (mass), thickness, and contact diameter was about $1 \times 10^{-4}\text{ }\mu\text{m}^3$ (0.12 fg), 0.1 nm , and $<1\text{ nm}$, respectively. The resolution of volume was calculated with the measured data of the shift in the resonance frequency of the cantilever from 122.01 to 122.02 kHz during the evaporation time of 10 min . The resolutions of thickness and contact diameter measurements were from the calibration data of the z piezo and $x-y$ piezo by AFM vendor (Veeco), respectively. The accuracy of volume, thickness, and contact diameter measurement was about $\pm 10\%$, 10% , and $<1\text{ nm}$, respectively.

6.2.7 Waterfall/Jet Tests

To investigate the durability of the created surfaces in long-term exposure to water and different kinetic energies of water, a setup was constructed to provide a waterfall/jet flow as shown in Fig. 6.4 (Jung and Bhushan, 2009b). The water from the laboratory faucet flowed through a pipe. Specimens were fixed on the stage by using a double-sided adhesive tape. Specimens are placed 2 mm below the four holes in the pipe. In order to minimize flow interruption on the specimens, the runoff plate was tilted to 45° . Waterfall/jet experiments are composed of two different setups. First, water pressure was fixed at 10 kPa , and then specimens were exposed for 24 h . Next, in order to apply different kinetic energies of the water, the water pressure was controlled between 0 and 45 kPa . The exposure time applied to the specimens was 20 min for each experiment. During the tests, the change of static contact angle was measured using droplets of about $5\text{ }\mu\text{L}$ in volume (with

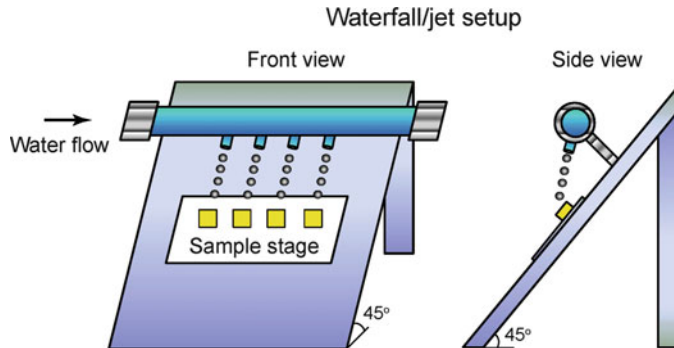


Fig. 6.4 Schematics of waterfall/jet setup shown in front and side views ([Jung and Bhushan, 2009c](#))

radius of a spherical droplet about 1 mm) gently deposited on the substrate using a microsyringe. For contact angle hysteresis, the advancing and receding contact angles were measured at the front and back of the droplet moving along the tilted surface, respectively. The image of the droplet is obtained by a digital camcorder with a 10 \times optical and 120 \times digital zoom. Images obtained were analyzed using *ImageTool®* software (University of Texas Health Science Center) for the contact angle.

6.2.8 Wear and Friction Tests

To investigate the durability of structured surfaces, wear tests on the surfaces were performed using a commercial AFM ([Jung and Bhushan, 2009b](#)). With the AFM in contact mode, the surfaces were worn using a 15 μm radius borosilicate ball that was mounted on a triangular Si_3N_4 cantilever with a nominal spring constant of 0.58 N/m. Wear scars with dimensions of $50 \times 50 \mu\text{m}^2$ were created and scanned for 1 cycle at two different loads of 100 nN and 10 μN . In order to analyze the changes in the morphology of structured surfaces before and after wear tests, surface height maps were obtained in dimensions of $100 \times 100 \mu\text{m}^2$ using a square pyramidal $\text{Si}(1\ 0\ 0)$ tip with a native oxide layer which has a nominal radius of 20 nm on a rectangular $\text{Si}(1\ 0\ 0)$ cantilever with a spring constant of 3 N/m and at a natural frequency of 76 kHz in tapping mode.

In order to investigate durability at a high load, macroscale wear and friction tests on the structured surfaces were conducted based on an established procedure of using a ball-on-flat tribometer under reciprocating motion ([Jung and Bhushan, 2009b](#)). A sapphire ball with a diameter of 3 mm and surface finish of about 2 nm RMS was fixed on a stationary holder. A normal load of 10 mN was applied, and the frictional forces were measured with semiconductor strain gauges, which were then digitized and collected on a computer. Typical test conditions were

stroke length = 800 μm , average linear speed = 1 mm/s, temperature = $22 \pm 1^\circ\text{C}$, and relative humidity = $45 \pm 5\%$. Wear was characterized by imaging the resulting scar with an optical microscope with a CCD camera before and after wear tests. The number of cycles to failure was determined by identifying the point where a sudden change in the friction force is observed.

6.3 Micro- and Nanopatterned Polymers

To investigate the effects of microstructure and nanostructure on contact angle and adhesion, [Jung and Bhushan \(2006\)](#) studied micr- and nanopatterned surfaces made with two types of polymers: poly(methyl methacrylate) (PMMA) and polystyrene (PS). PMMA and PS were chosen because they are widely used in MEMS/NEMS devices ([Bhushan, 2010](#)). Both hydrophilic and hydrophobic surfaces can be produced by using these two polymers, as PMMA has polar (hydrophilic) groups with high surface energy while PS has electrically neutral and nonpolar (hydrophobic) groups with low surface energy. Furthermore, a PMMA structure can be made hydrophobic by treating it appropriately, for example, by coating with a hydrophobic self-assembled monolayer (SAM).

Four types of surface patterns were fabricated from PMMA: a flat film, low aspect ratio asperities (LAR, 1:1 height-to-diameter ratio), high aspect ratio asperities (HAR, 3:1 height-to-diameter ratio), and a replica of the Lotus leaf (the Lotus pattern). Two types of surface patterns were fabricated from PS: a flat film and the Lotus pattern. Figure 6.5 shows SEM images of the two types of nanopatterned structures, LAR and HAR, and the one type of micropatterned structure, Lotus pattern, all on a PMMA surface ([Burton and Bhushan, 2005; Jung and Bhushan, 2006](#)). Both micro- and nanopatterned structures were manufactured using soft lithography. For nanopatterned structures, PMMA film was spin-coated on the silicon wafer. A UV-cured mold of polyurethane acrylate (PUA) resin with nanopatterns of interest was made which enables one to create sub-100-nm patterns with a high aspect ratio ([Choi et al., 2004](#)). The mold was placed on the PMMA film, and a slight pressure of $\sim 10 \text{ g/cm}^2$ ($\sim 1 \text{ kPa}$) was applied and annealed at 120°C . Finally, the PUA mold was removed from the PMMA film. For micropatterned structures, a polydimethylsiloxane (PDMS) mold was first made by casting PDMS against a Lotus leaf after the wax had been removed (left with only microstructure), followed by heating. Then, the mold was placed on the PMMA and PS film to create a positive replica of Lotus leaf. As shown in Fig. 6.5, it can be seen that only microstructures exist on the surface of Lotus pattern ([Jung and Bhushan, 2006](#)).

Since PMMA by itself is hydrophilic, in order to obtain a hydrophobic sample, a self-assembled monolayer (SAM) of perfluorodecyltriethoxysilane (PFDTES) was deposited on the sample surfaces using a vapor phase deposition technique. PFDTES was chosen because of its hydrophobic nature. The deposition conditions for PFDTES were 100°C temperature, 400 Torr pressure, 20 min deposition time, and 20 min annealing time. The polymer surface was exposed to an oxygen plasma

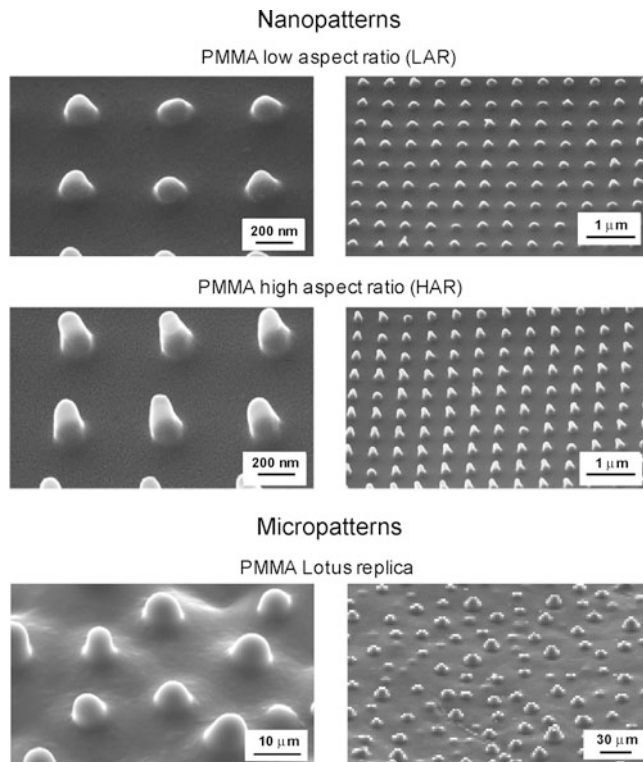


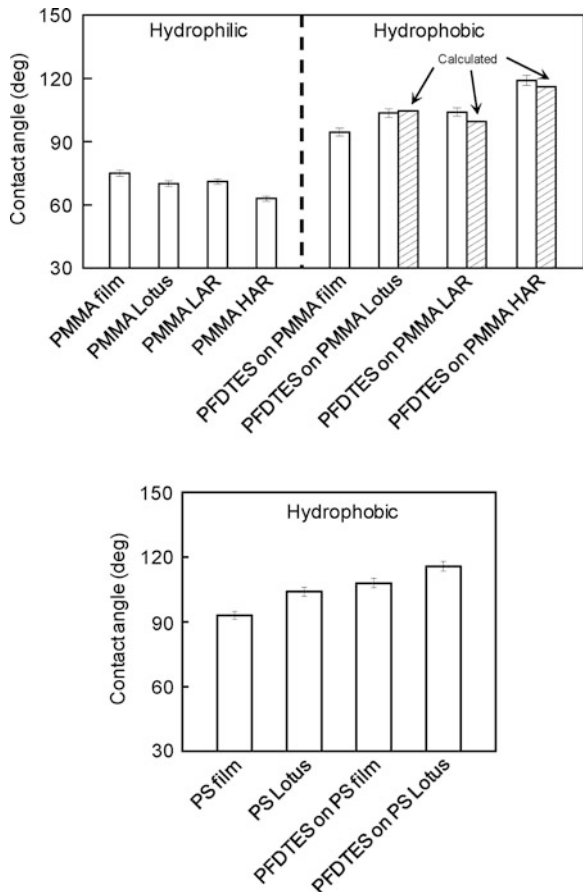
Fig. 6.5 Scanning electron micrographs of the two nanopatterned polymer surfaces (shown using two magnifications to see both the asperity shape and the asperity pattern on the surface) and the micropatterned polymer surface (Lotus pattern, which has only microstructures on the surface) (Burton and Bhushan, 2005; Jung and Bhushan, 2006)

treatment (40 W, O₂ 187 Torr, 10 s) prior to coating (Bhushan et al., 2006). The oxygen plasma treatment is necessary to oxidize any organic contaminants on the polymer surface and to also alter the surface chemistry to allow for enhanced bonding between the SAM and the polymer surface.

6.3.1 Contact Angle

Jung and Bhushan (2006) measured the static contact angle of water with the micro- and nanopatterned PMMA and PS structures; see Fig. 6.6. Since the Wenzel roughness factor is the parameter that often determines wetting behavior, the roughness factor was calculated, and it is presented in Table 6.1 for various samples. The data show that the contact angle of the hydrophilic materials decreases with an increase in the roughness factor, as predicted by the Wenzel model. When

Fig. 6.6 Contact angles for various micro- and nanopatterned surfaces on PMMA and PS polymers and calculated values using Wenzel equation (Jung and Bhushan, 2006)



the polymers were coated with PFDTES, the film surface became hydrophobic. Figure 6.6 also shows the contact angle for various PMMA samples coated with PFDTES. For a hydrophobic surface, the standard Wenzel model predicts an increase of contact angle with roughness factor, which is what happens in the case of patterned samples. The calculated values of the contact angle for various micro- and nanopatterned samples based on the contact angle of the smooth film and Wenzel equation are also presented. The measured contact angle values for the Lotus pattern were comparable with the calculated values, whereas for the LAR and HAR patterns, they are higher. It suggests that nanopatterns benefit from air pocket formation. Furthermore, pinning at the top of the nanopatterns may stabilize the droplet. For the PS material (hydrophobic), the contact angle of the Lotus pattern also increased with increased roughness factor.

Table 6.1 Roughness factor for micro- and nanopatterned polymers (Jung and Bhushan, 2006)

	LAR	HAR	Lotus
R_f	2.1	5.6	3.2

6.3.2 Effect of Submicron Droplet on Contact Angle

Wetting phenomena have been studied and understood at the macroscale; however, micro- and nanoscale wetting mechanisms require further investigation. The actual contact angle under which the liquid–vapor interface comes in contact with the solid surface at the micro- and nanoscale is expected to be a function of the droplet size. Jung and Bhushan (2008c) measured the contact angle of micro- and nanodroplets on various surfaces using the AFM-based technique. The contact angle for different droplet sizes on various hydrophilic and hydrophobic, nanopatterned surfaces is summarized in Fig. 6.7. The data for the microdroplets with 2.4–8.1 μm diameter, and nanodroplets with 0.22–1.1 μm diameter were compared with conventional contact angle measurements obtained with a droplet with 2.1 mm diameter (5 μL volume). The measured values of micro- and nanodroplets using an AFM were found to be lower than those of the macrodroplet (Pompe and Herminghaus, 2000; Checco et al., 2003). There are several reasons for the scale dependence, such as the effect of contact line tension of a three-phase system (solid–liquid–vapor), which is the excess free energy of a solid–liquid–vapor system per unit length of the contact line (Pompe and Herminghaus, 2000; Checco et al., 2003; Quere, 2004; Nosonovsky and Bhushan, 2007d). Another reason can be surface heterogeneity (Checco et al., 2003). For a thin fluid film present on a surface, disjoining pressure of a film is repulsive, analogous to the repulsive van der Waals force across a film, and it causes a film to spread on surfaces. It decreases with the liquid layer thickness (Israelachvili, 1992). This pressure may lead to a smaller contact angle at the nanoscale.

6.3.3 Adhesive Force

Adhesion force depends, among other factors, on the hydrophobic/hydrophilic nature of the surfaces, surface structure, and AFM tip radii. Figure 6.8 shows the scale dependence of adhesive force on tip radius for PMMA (hydrophilic) and PFDTES coated on PMMA (hydrophobic) surfaces with various micro- and nanopatterns (Jung and Bhushan, 2006). The left bar chart in Fig. 6.8 is for hydrophilic PMMA film and Lotus, LAR, and HAR patterns. For increasing radius, the adhesive force increases for each material. With a larger radius, the real area of contact and the meniscus contribution increase, resulting in increased adhesion. Adhesive force is the lowest for a nanopattern with the highest bump height. The right bar chart in Fig. 6.8 shows the results for hydrophobic PFDTES coated on each material. These samples show the same trends as the film samples, but the change

Contact angle for different droplet sizes on various surfaces

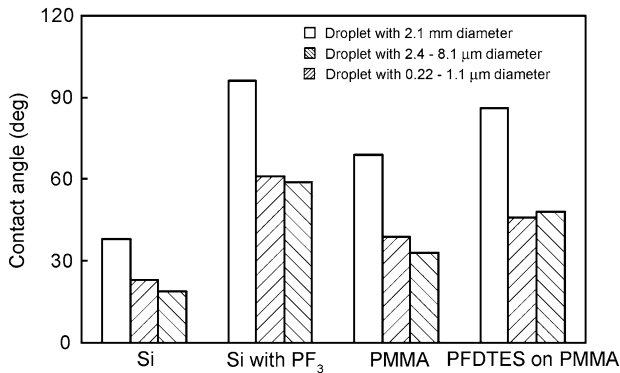


Fig. 6.7 Contact angle measurements for different droplet sizes on various nanopatterned surfaces (Jung and Bhushan, 2008c)

PMMA polymers with different surface roughness patterns (22 °C, 50% RH)

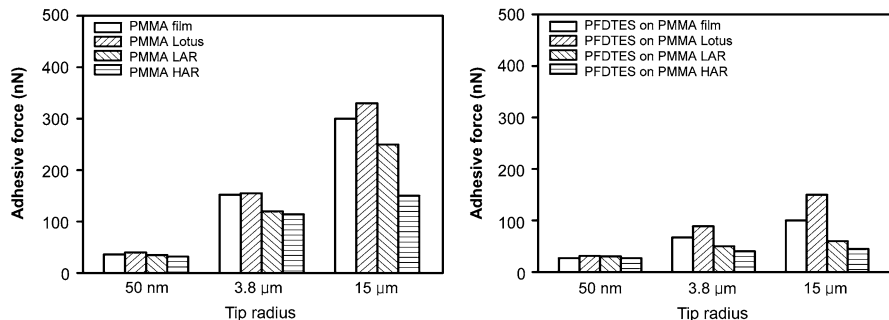


Fig. 6.8 Scale dependence of adhesive force for various micro- and nanopatterned surfaces measured using AFM tips of various radii (Jung and Bhushan, 2006)

in adhesion is not as dramatic. The hydrophobicity of PFDTES on material reduces meniscus forces, which in turn reduces adhesion from the surface. The dominant mechanism for the hydrophobic material is real area of contact and not meniscus force, whereas with hydrophilic material, there is a combination of real area of contact and meniscus forces (Jung and Bhushan, 2006).

6.3.4 Summary

The contact angle data on micro- and nanopatterned polymers show that in hydrophilic surfaces, contact angle decreases with roughness and in hydrophobic surfaces, it increases consistent with the Wenzel and Cassie–Baxter equations. The

measured contact angles of nanopatterned samples are higher than the calculated values using the Wenzel equation. It suggests that nanopatterns benefit from air pocket formation.

The contact angle for micro- and nanodroplets on various hydrophilic and hydrophobic nanopatterned surfaces was found to be scale dependent.

Adhesive force decreases with an increase of the contact angle. The AFM tip radius affects the adhesion because the tip/sample interfaces area changes with tip size. The adhesive force increases with tip size for all samples because of an increased number of contacting asperities (real area of contact) and increased meniscus contribution.

6.4 Micropatterned Si Surfaces

It was reported earlier that the Cassie–Baxter regime is desirable to achieve high contact angle and low contact angle hysteresis. The relevant regime is dependent upon the micro-/nanostructure and droplet radius. A criterion transition from the Cassie–Baxter to the Wenzel regime has been proposed. Using micropatterned surfaces, [Jung and Bhushan \(2007, 2008a\)](#) investigated the role of distance between micropillars (pitch) and droplet radius on the contact angle and contact angle hysteresis. The effect of droplet radius has been studied using evaporation studies. To provide insight into the formation of microdroplets on micropatterned surfaces, condensation and evaporation studies of microdroplets over patterned surfaces have been carried out using an ESEM. [Jung and Bhushan \(2008b\)](#) also studied the transition during the bouncing droplet.

Micropatterned surfaces produced from single-crystal silicon (Si) by photolithography and coated with a SAM were used by [Jung and Bhushan \(2007, 2008a, b\)](#) in their study. Silicon has traditionally been the most commonly used structural material for micro-/nanocomponents. A Si surface can be made hydrophobic by coating it with a SAM. One purpose of this investigation was to study the transition from the Cassie–Baxter to the Wenzel regime by changing the distance between the pillars. To create micropatterned Si, two series of nine samples each were fabricated using photolithography. Series 1 had 5 μm diameter and 10 μm height flat-top, cylindrical pillars with different pitch values (7, 7.5, 10, 12.5, 25, 37.5, 45, 60, and 75 μm), and series 2 had 14 μm diameter and 30 μm height flat-top, cylindrical pillars with different pitch values (21, 23, 26, 35, 70, 105, 126, 168, and 210 μm). The pitch is the spacing between the centers of two adjacent pillars. The SAM of 1, 1, -2, 2,-tetrahydroperfluorodecyltrichlorosilane (PF_3) was deposited on the Si sample surfaces using a vapor phase deposition technique. PF_3 was chosen because of the hydrophobic nature of the surface. The thickness and root mean square (RMS) roughness of the SAM of PF_3 were 1.8 and 0.14 nm, respectively ([Kasai et al., 2005](#)).

An optical profiler was used to measure the surface topography of the micropatterned surfaces ([Bhushan and Jung, 2007, 2008; Jung and Bhushan, 2008a, b](#)).

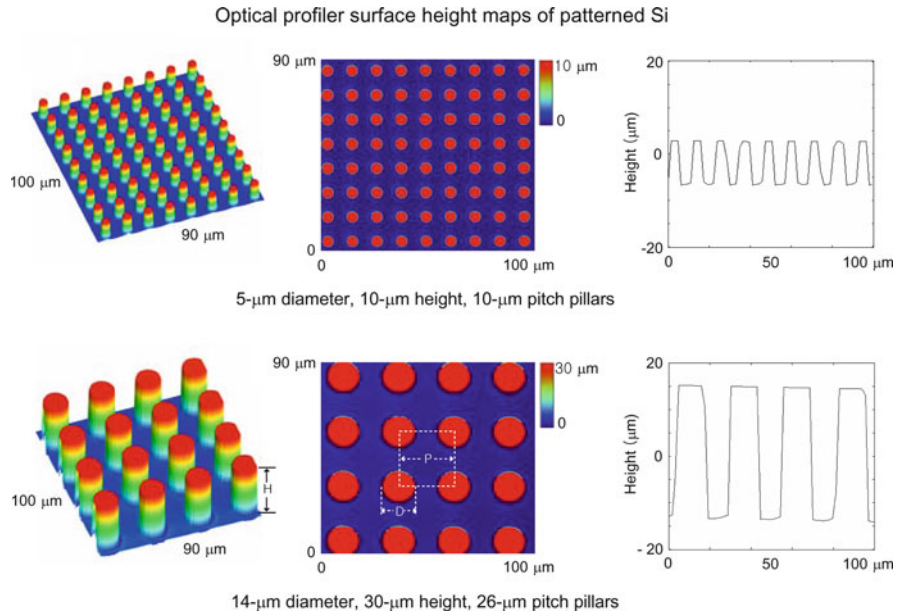


Fig. 6.9 Surface height maps and 2-D profiles of the micropatterned surfaces using an optical profiler (Bhushan and Jung, 2007)

One sample each from the two series was chosen to characterize the surfaces. Two different surface height maps can be seen for the micropatterned Si in Fig. 6.9. In each case, a 3-D map and a flat map along with a 2-D profile in a given location of the flat 3-D map are shown. A scan size of $100 \mu\text{m} \times 90 \mu\text{m}$ was used to obtain a sufficient amount of pillars to characterize the surface but also to maintain enough resolution to get an accurate measurement.

Consider the geometry of flat-top, cylindrical pillars of diameter D , height H , and pitch P , distributed in a regular square array as shown in Fig. 6.9. For the special case of a droplet size much larger than P (of interest in this study), a droplet contacts the flat-top of the pillars forming the composite interface, and the cavities are filled with air. For this case, $f_{\text{LA}} = 1 - \pi D^2 / 4P^2 = 1 - f_{\text{SL}}$. Further, assume that the flat-tops are smooth with $R_f = 1$. The contact angles for the Wenzel and Cassie–Baxter regimes are given by (3.6) and (3.9) (Bhushan and Jung, 2007):

$$\text{Wenzel : } \cos \theta = \left(1 + \frac{\pi DH}{P^2} \right) \cos \theta_0, \quad (6.2)$$

$$\text{Cassie-Baxter : } \cos \theta = \frac{\pi D^2}{4P^2} (\cos \theta_0 + 1) - 1, \quad (6.3)$$

Geometrical parameters of the flat-top, cylindrical pillars in series 1 and 2 are used for calculating the contact angle for the above-mentioned two cases. Figure 6.10

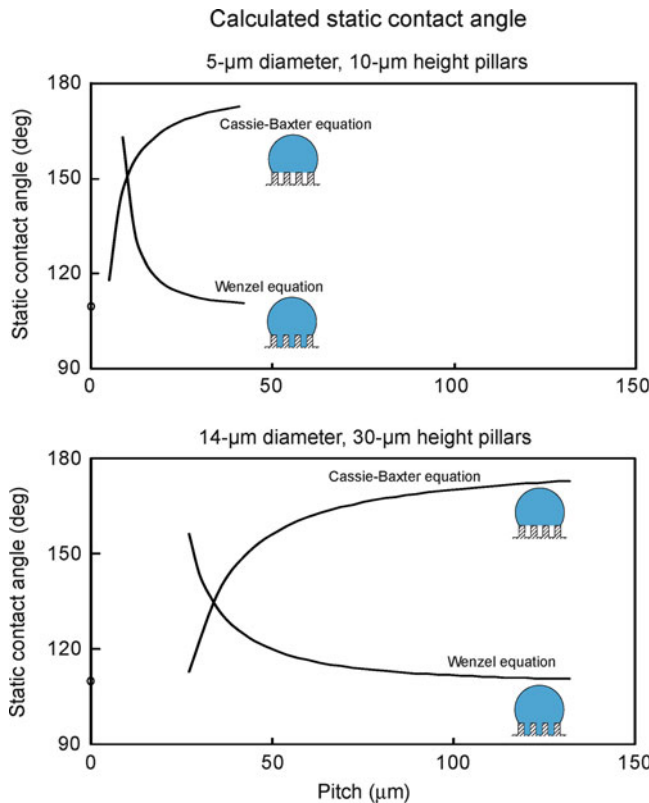


Fig. 6.10 Calculated static contact angle as a function of geometric parameters for a given value of θ_0 using the Wenzel and Cassie–Baxter equations for two series of the micropatterned surfaces with different pitch values (Bhushan and Jung, 2007)

shows the plot of the predicted values of the contact angle as a function of pitch between the pillars for the two cases. The Wenzel and Cassie–Baxter equations present two possible equilibrium states for a water droplet on the surface. This indicates that there is a critical pitch below which the composite interface dominates and above which the homogeneous interface dominates the wetting behavior. Therefore, one needs to find the critical point that can be used to design superhydrophobic surfaces. Furthermore, even in cases where the liquid droplet does not contact the bottom of the cavities, the water droplet can be in a metastable state and can become unstable, with the transition from the Cassie–Baxter to Wenzel regime occurring if the pitch is large.

6.4.1 Cassie–Baxter and Wenzel Transition Criteria

A stable composite interface is essential for the successful design of superhydrophobic surfaces. However, the composite interface is fragile, and it may transform into the homogeneous interface. What triggers the transition between the regimes remains a subject of argument, although a number of explanations have been suggested. [Nosonovsky and Bhushan \(2007b\)](#) have studied destabilizing factors for the composite interface and found that a convex surface (with bumps) leads to a stable interface and high contact angle. Also, they have suggested the effects of a droplet's weight and curvature among the factors which affect the transition.

[Bhushan and Jung \(2007, 2008\)](#) and [Jung and Bhushan \(2007, 2008a, b\)](#) investigated the effect of droplet curvature on the Cassie–Baxter and Wenzel regime transition. First, they considered a small water droplet suspended on a superhydrophobic surface consisting of a regular array of circular pillars with diameter D , height H , and pitch P as shown in Fig. 6.11. The local deformation for small droplets is governed by surface effects rather than gravity. The curvature of a droplet is governed by the Laplace equation, which relates the pressure inside the droplet to its curvature ([Adamson, 1990](#)). Therefore, the curvature is the same at the top and at the bottom of the droplet ([Nosonovsky and Bhushan, 2007d](#)). For the micropatterned surface considered here, the maximum droop of the droplet occurs in the center of the square formed by the four pillars as shown in Fig. 6.11a. Therefore, the maximum droop of the droplet (δ) in the recessed region can be found in the middle of two pillars which are diagonally across as shown in Fig. 6.11b, which is $(\sqrt{2}P - D)^2/(8R)$. If the droop is greater than the depth of the cavity, then the droplet will just contact the bottom of the cavities between pillars. If it is much greater, transition from the Cassie–Baxter to Wenzel regime occurs:

$$\frac{(\sqrt{2}P - D)^2}{R \geq H}, \quad (6.4)$$

Equation (6.4) shows that geometry (P and H) and droplet radius R govern the transition. A droplet with a large radius, lower pitch, or larger height is desirable for the Cassie–Baxter regime.

To investigate the dynamic effect of a bouncing water droplet on the Cassie–Baxter and Wenzel regime transition, [Jung and Bhushan \(2008b\)](#) considered a water droplet hitting a superhydrophobic surface as shown in Fig. 6.11. As the droplet hits the surface at velocity V , a liquid–air interface below the droplet is formed when the dynamic pressure is less than the Laplace pressure. The Laplace pressure can be written as

$$p_L = \frac{2\gamma}{R} = \frac{16\gamma\delta}{(\sqrt{2}P - D)^2}, \quad (6.5)$$

where γ is the surface tension of the liquid–air interface, and the dynamic pressure of the droplet is equal to

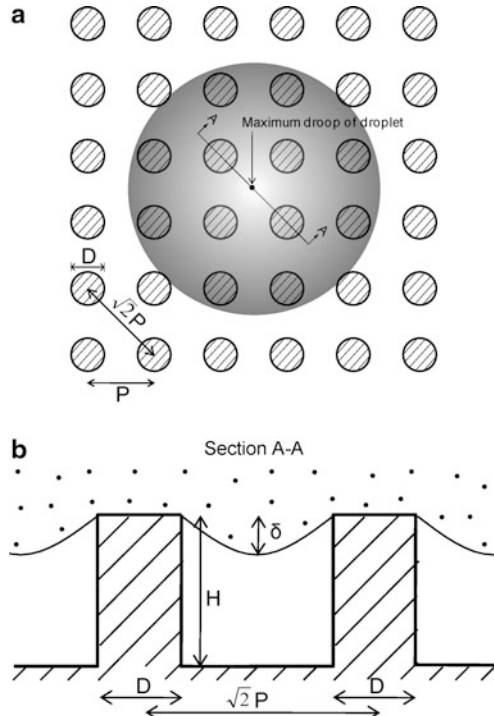


Fig. 6.11 A liquid droplet suspended on a superhydrophobic surface consisting of a regular array of circular pillars. **(a)** Plan view. The maximum droop of droplet occurs in the center of square formed by four pillars. **(b)** Side view in section A–A. The maximum droop of droplet (δ) can be found in the middle of two pillars which are diagonally across (Jung and Bhushan, 2007).

$$p_d = \frac{1}{2} \rho V^2, \quad (6.6)$$

where ρ is the mass density of the liquid droplet. If the maximum droop of the droplet (δ) is larger than the height of pillar (H), the droplet contacts the bottom of the cavities between pillars. Determination of the critical velocity at which the droplet touches the bottom is obtained by equating the Laplace pressure to the dynamic pressure. To develop a composite interface, velocity should be smaller than the critical velocity given as

$$V < \sqrt{\frac{32\gamma H}{\rho(\sqrt{2}P - D)^2}}. \quad (6.7)$$

Furthermore, in the case of large distances between the pillars, the liquid–air interface can easily be destabilized due to dynamic effects. This leads to the formation of the homogeneous solid–liquid interface (Nosonovsky and Bhushan, 2007b).

Equation (6.7) shows that critical velocity increases with a decrease of pitch or an increase of pillar height.

Nosonovsky and Bhushan (2008e) used the energy barrier approach to study the Cassie–Baxter and Wenzel transition. The energy barrier is given by the product of the height of the pillars, H ; pillar perimeter, πD ; pillar density, $1/P^2$; and the area, A_0 , required to initiate the transition, and the corresponding change in the surface energy

$$\Delta E = A_0 \frac{\pi HD}{P^2} (\gamma_{SL} - \gamma_{SA}) = -A_0 \frac{\pi HD}{P^2} \gamma_{LA} \cos \theta_0, \quad (6.8)$$

where, A_0 is $\pi(R \sin \theta)^2$.

For a short pitch, the net energy of the Cassie–Baxter state is lower than that of the Wenzel state, whereas for larger pitch values, the energy of the Wenzel state is lower (Fig. 3.10c). However, due to the energy barriers, a metastable Cassie–Baxter state with a higher energy than the Wenzel state may be found.

The energy barrier of the Cassie–Baxter and Wenzel transition can be estimated as the kinetic energy of the droplet. The kinetic energy of a droplet of radius R_0 , mass m , and density ρ with the velocity V is given by

$$E_{\text{kin}} = \frac{(4/3)\pi\rho R^3 V^2}{2}. \quad (6.9)$$

6.4.2 Effect of Pitch Value on the Transition

In order to study the effect of pitch value on the transition from the Cassie–Baxter to the Wenzel regime, the static contact angles were measured on the micropatterned Si coated with PF_3 , and the data are plotted as a function of pitch between the pillars in Fig. 6.12a (Bhushan and Jung, 2007, 2008; Jung and Bhushan, 2007, 2008a, b). A dotted line represents the transition criteria range obtained using (6.4). The flat Si coated with PF_3 showed a static contact angle of 109° . The contact angle of selected micropatterned surfaces is much higher than that of the flat surfaces. It first increases with an increase in the pitch values, then drops rapidly to a value slightly higher than that of the flat surfaces. In the first portion, it jumps to a high value of 152° corresponding to a superhydrophobic surface and continues to increase to 170° at a pitch of $45 \mu\text{m}$ in series 1 and $126 \mu\text{m}$ in series 2 because open air space increases with an increase in pitch, responsible for the propensity of air pocket formation. The sudden drop at about a pitch value of $50 \mu\text{m}$ in series 1 and $150 \mu\text{m}$ in series 2 corresponds to the transition from the Cassie–Baxter to the Wenzel regime. In series 1, the value predicted from the curvature transition criteria (6.4) is a little higher than the experimental observations. However, in series 2, there is a good agreement between the experimental data and the values theoretically predicted by Jung and Bhushan (2007, 2008a b) for the Cassie–Baxter and Wenzel transition.

Fig. 6.12 (a) Static contact angle [a dotted line represents the transition criteria range obtained using (6.4)] and (b) contact angle hysteresis and tilt angle as a function of geometric parameters for two series of the micropatterned surfaces with different pitch values for a droplet with 1 mm in radius ($5 \mu\text{L}$ volume). Data at zero pitch correspond to a flat sample (Bhushan and Jung, 2007; Jung and Bhushan, 2007)

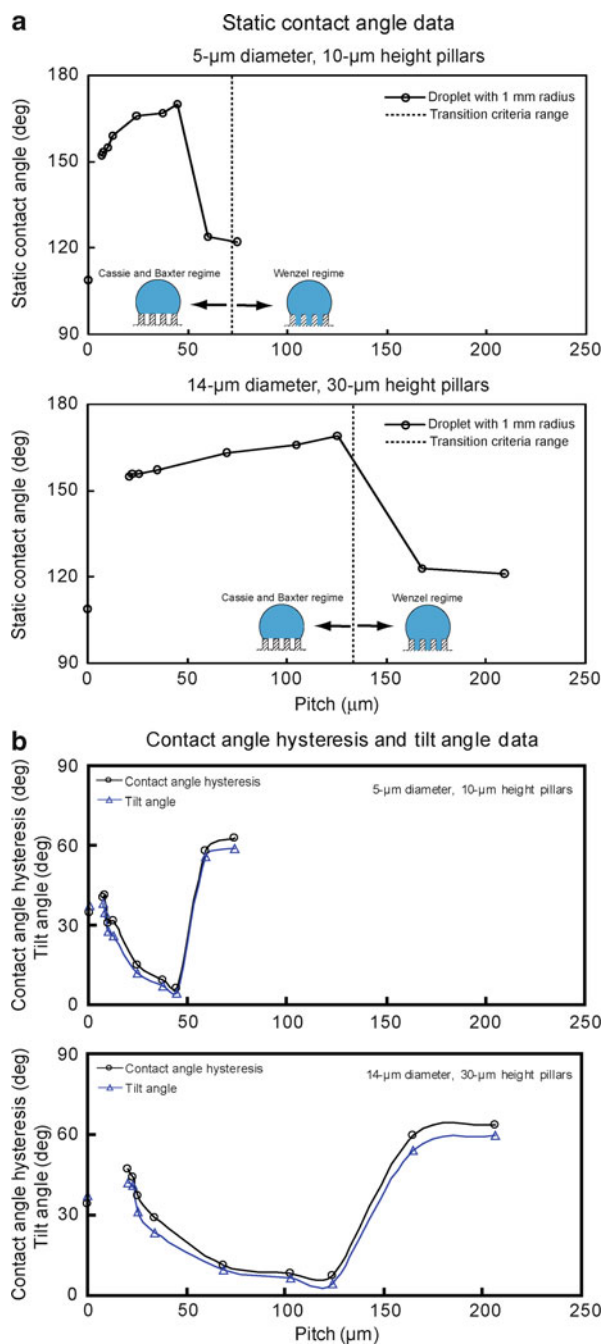


Figure 6.12b shows contact angle hysteresis and tilt angle as a function of pitch between the pillars (Bhushan and Jung, 2007, 2008). Both angles are comparable. The flat Si coated with PF₃ showed a contact angle hysteresis of 34° and tilt angle of 37°. The angle first increases with an increase of pitch value, which has to do with pinning of the droplet at the sharp edges of the micropillars. Figure 6.13 shows droplets on micropatterned Si with 5 μm diameter and 10 μm height pillars with different pitch values. The asymmetrical shape of the droplet signifies pinning. The pinning on the micropatterned surfaces can be observed as compared to the flat surface. The micropatterned surface with low pitch (7 μm) has more pinning than the micropatterned surface with high pitch (37.5 μm) because the micropatterned surface with low pitch has more sharp edges in contact with a droplet. As the pitch increases, there is a higher propensity of air pocket formation and fewer numbers of sharp edges per unit area, which is responsible for the sudden drop in the angle. The lowest contact angle hysteresis and tilt angle are 5° and 3°, respectively, which were observed on the micropatterned Si with 45 μm of series 1 and 126 μm of series 2. Above a pitch value of 50 μm in series 1 and 150 μm in series 2, the angle increases very rapidly because of transition to the Wenzel regime.

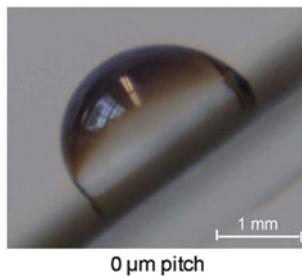
These results suggest that air pocket formation and the reduction of pinning in the micropatterned surface play an important role for a surface with both low contact angle hysteresis and tilt angle (Bhushan and Jung, 2007, 2008). Hence, to create superhydrophobic surfaces, it is important that they are able to form a stable composite interface with air pockets between solid and liquid.

6.4.3 *Observation of Transition During the Droplet Evaporation*

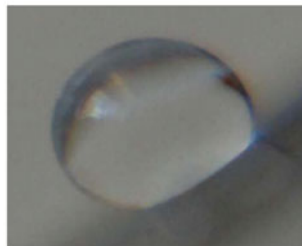
In order to study the effect of droplet size on the transition from a composite state to a wetted state, Jung and Bhushan (2007, 2008a) performed droplet evaporation experiments to observe the Cassie–Baxter and Wenzel transition on two different micropatterned Si surfaces coated with PF₃. The series of four images in Fig. 6.14 shows the successive photos of a droplet evaporating on the two micropatterned surfaces. The initial radius of the droplet was about 700 μm, and the time interval between first two photos was 180 s and between the latter two was 60 s. In the first three photos, the droplet is shown in a Cassie–Baxter state, and its size gradually decreases with time. However, as the radius of the droplet reached 360 μm on the surface with 5 μm diameter, 10 μm height, and 37.5 μm pitch pillars, and 423 μm on the surface with 14 μm diameter, 30 μm height, and 105 μm pitch pillars, the transition from the Cassie–Baxter to Wenzel regime occurred, as indicated by the arrow. The light passes below the first droplet, indicating that air pockets exist, so that the droplet is in the Cassie–Baxter state. However, an air pocket is not visible below the last droplet, so it is in the Wenzel state. This could result from an

Fig. 6.13 Optical micrographs of droplets on the inclined micropatterned surfaces with different pitch values. The images were taken when the droplet started to move down. Data at zero pitch correspond to a flat sample (Bhushan and Jung, 2007)

Patterned surfaces with 5- μm diameter and 10- μm height pillars with different pitch values



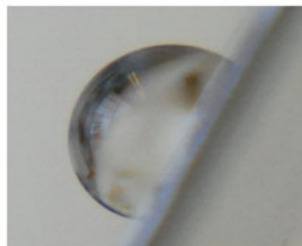
0 μm pitch



7 μm pitch



37.5 μm pitch



75 μm pitch

impalement of the droplet in the micropatterned surface, characterized by a smaller contact angle.

To find the contact angle before and after the transition, the values of the contact angle are plotted against the theoretically predicted value, based on the Wenzel [calculated using (3.6)] and Cassie–Baxter [calculated using (3.9)] models.

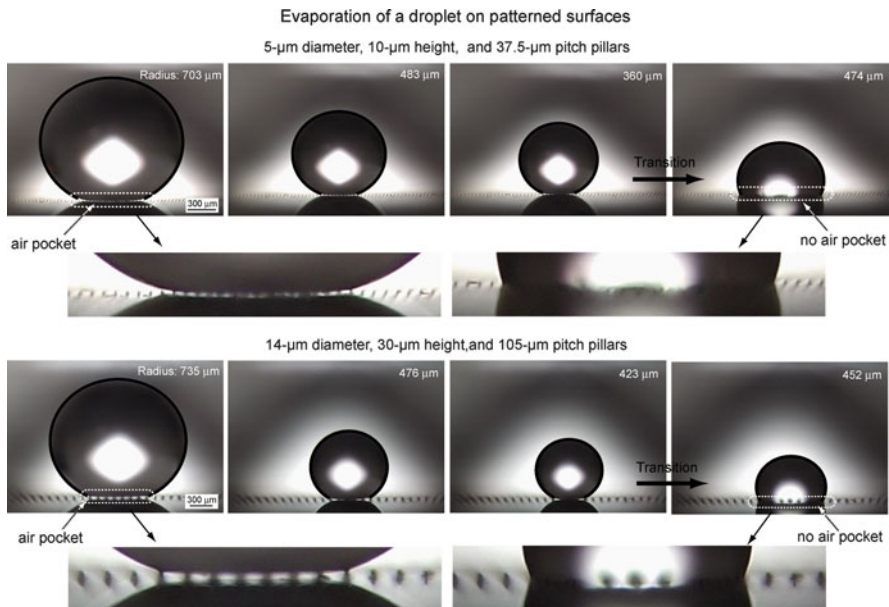


Fig. 6.14 Evaporation of a droplet on two different micropatterned surfaces. The initial radius of the droplet is about 700 μm , and the time interval between the first two photos was 180 s and between the latter two was 60 s. As the radius of the droplet reaches 360 μm on the surface with 5 μm diameter, 10 μm height, and 37.5 μm pitch pillars and 420 μm on the surface with 14 μm diameter, 30 μm height, and 105 μm pitch pillars, the transition from the Cassie–Baxter regime to Wenzel regime occurs, as indicated by the arrow. Before the transition, an air pocket is clearly visible at the bottom area of the droplet, but after the transition, an air pocket is not found at the bottom area of the droplet (Jung and Bhushan, 2008a)

Figure 6.15 shows the static contact angle as a function of geometric parameters for the experimental contact angles before (circle) and after (triangle) the transition compared to the Wenzel and Cassie–Baxter equations (solid lines) with a given value of θ for two series of micropatterned Si with different pitch values coated with PF_3 (Jung and Bhushan, 2008a). The fit is good between the experimental data and the theoretically predicted values for the contact angles before and after transition.

To prove the validity of the transition criteria in terms of droplet size, the critical radius of a droplet deposited on the micropatterned Si with different pitch values coated with PF_3 is measured during the evaporation experiment (Jung and Bhushan, 2007, 2008a). Figure 6.16 shows the radius of a droplet as a function of geometric parameters for the experimental results (circle) compared with the transition criterion (6.4) from the Cassie–Baxter regime to Wenzel regime (solid lines) for two series of micropatterned Si with different pitch values coated with PF_3 . It is found that the critical radius of impalement is in good quantitative agreement with the predictions. The critical radius of the droplet increases linearly with the geometric parameter (pitch). For the surface with small a pitch, the critical radius of droplet can become quite small.

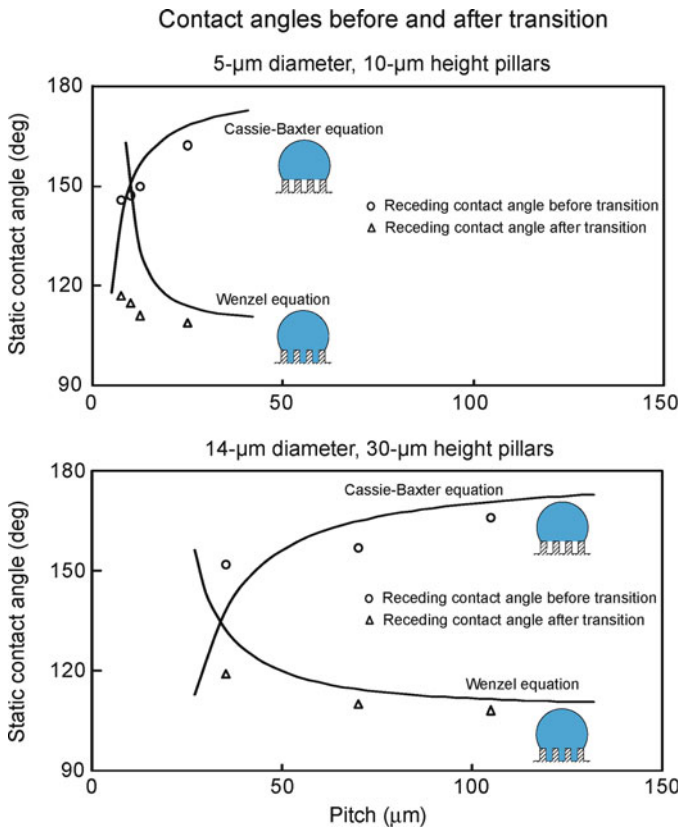


Fig. 6.15 Receding contact angle as a function of geometric parameters before (circle) and after (triangle) transition compared with predicted static contact angle values obtained using the Wenzel and Cassie–Baxter equations (solid lines) with a given value of θ_0 for two series of the micropatterned surfaces with different pitch values (Jung and Bhushan, 2008a)

To verify the transition, Jung and Bhushan (2007, 2008a) used another approach using dust mixed in water. Figure 6.17 presents the dust trace remaining after a droplet with 1 mm radius (5 μL volume) has evaporated on the two micropatterned Si surfaces. As shown in the top image, after the transition from the Cassie–Baxter regime to Wenzel regime, the dust particles remained not only at the top of the pillars but also at the bottom with a footprint size of about 450 μm . However, as shown in the bottom image, the dust particles remained on only a few pillars with a footprint size of about 25 μm until the end of the evaporation process. From Fig. 6.16, it is observed that the transition occurs at about 300 μm radius of droplet on the 5 μm diameter and 10 μm height with 37.5 μm pitch pillars, but the transition does not occur on the patterned Si surface with pitch of less than about 5 μm . These experimental observations are consistent with model predictions. In the literature, it has been shown that on superhydrophobic natural Lotus, the droplet remains

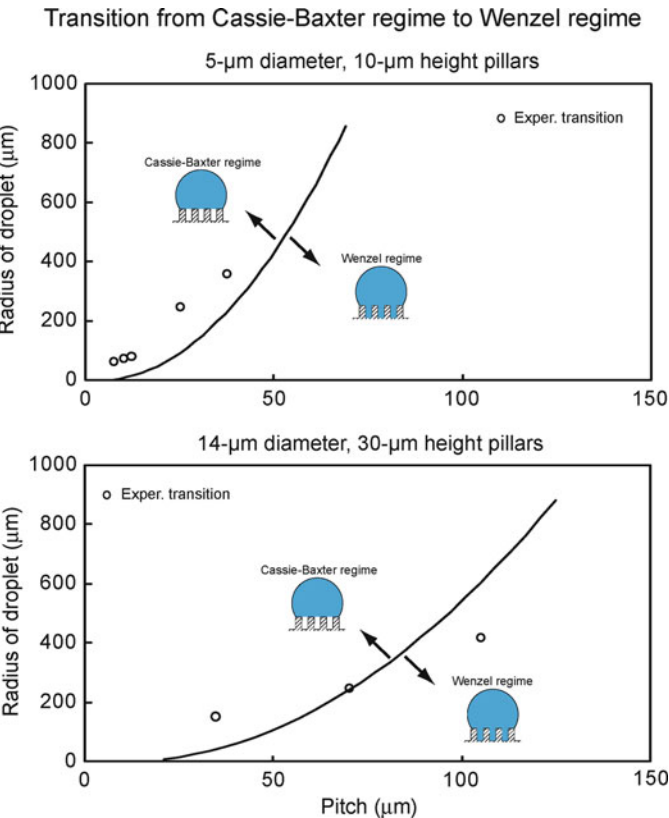


Fig. 6.16 Radius of droplet as a function of geometric parameters for the experimental results (circle) compared with the transition criteria from the Cassie–Baxter regime to Wenzel regime (solid lines) for two series of the micropatterned surfaces with different pitch values ([Jung and Bhushan, 2008a](#))

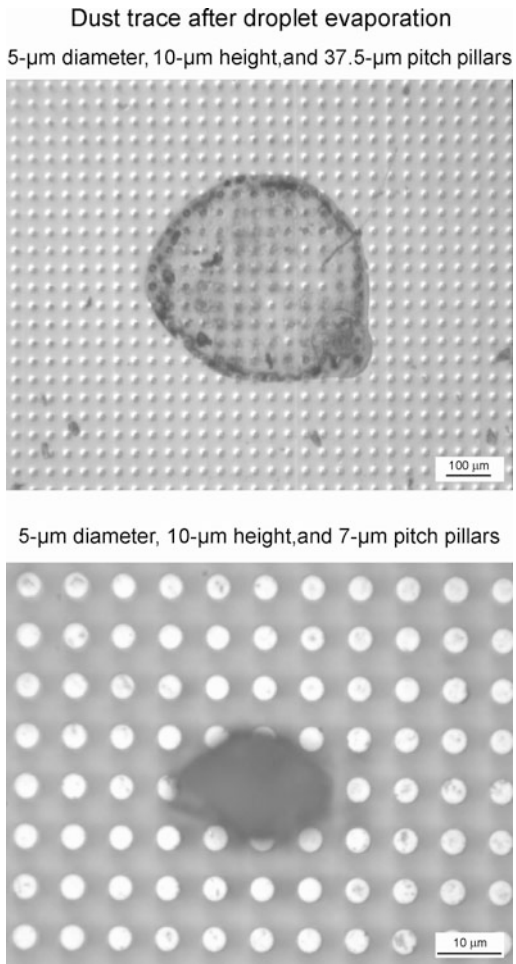
in the Cassie–Baxter regime during the evaporation process ([Zhang et al., 2006](#)). This indicates that the distance between the pillars should be minimized enough to improve the ability of the droplet to resist sinking.

6.4.4 Another Cassie–Baxter and Wenzel Transition for Different Series

Nosonovsky and Bhushan ([2007a, c, d, 2008b, d](#)) studied the data for the Cassie–Baxter and Wenzel transition with the two series of surfaces using the nondimensional spacing factor:

$$S_f = \frac{D}{P} \quad (6.10)$$

Fig. 6.17 Dust trace remained after droplet evaporation for the micropatterned surface. In the top image, the transition occurred at $360\text{ }\mu\text{m}$ radius of droplet, and in the bottom image, the transition occurred at about $20\text{ }\mu\text{m}$ radius of droplet during the process of droplet evaporation. The footprint size is about 450 and $25\text{ }\mu\text{m}$ for the top and bottom images, respectively (Jung and Bhushan, 2008a)



The values of the droplet radius at which the transition occurs during the evaporation plotted against the spacing factor scale well for the two series of the experimental results, yielding virtually the same straight line. Thus, the two series of micropatterned surfaces scale well with each other, and the transition occurs at the same value of the spacing factor multiplied by the droplet radius (Fig. 6.18a). The physical mechanism leading to this observation remains to be determined; however, it is noted that this mechanism is different from the one suggested by (6.4). The observation suggests that the transition is a linear 1-D phenomenon and that neither droplet droop (that would involve P^2/H) nor droplet weight (that would involve R^3) are responsible for the transition, but rather linear geometric relations are involved. Note that the experimental values approximately correspond to the values of the ratio $RD/P = 50\text{ }\mu\text{m}$ or the total area of the pillar tops under the droplet $(\pi D^2/4)\pi R^2/P^2 = 6,200\text{ }\mu\text{m}^2$.

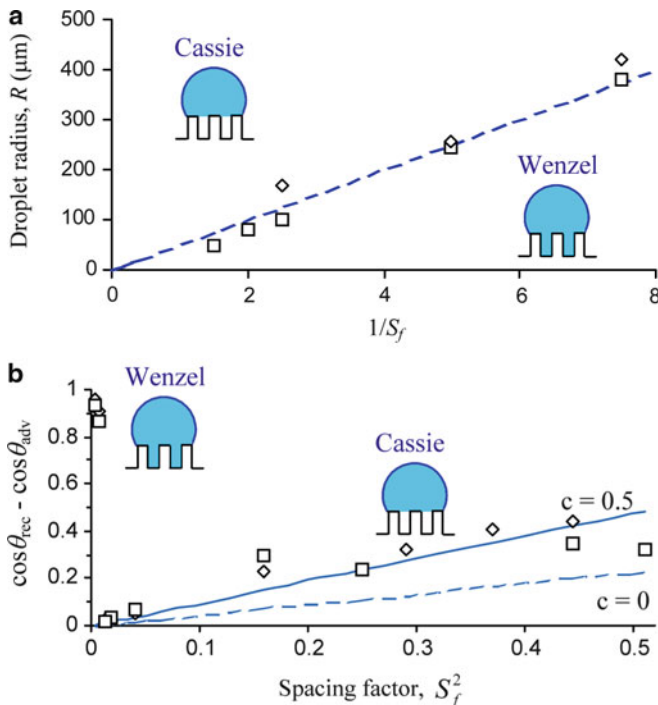


Fig. 6.18 (a) Droplet radius, R , for the Cassie–Baxter and Wenzel transition as a function of $P/D = 1S_f$. It is observed that the transition takes place at a constant value of $RD/P \sim 50 \mu\text{m}$ (dashed line). This shows that the transition is a linear phenomenon. (b) The difference $\cos \theta_{\text{rec}} - \cos \theta_{\text{adv}}$ as a function of S_f for the first (squares) and second (diamonds) series of the experiments compared with the theoretically predicted values of $\cos \theta_{\text{adv}} - \cos \theta_{\text{rec}} = (D/P)^2(p/4)(\cos \theta_{\text{adv}} - \cos \theta_{\text{rec}0}) + c(D/P)^2$, where c is a proportionality constant. It is observed that when only the adhesion hysteresis/interface energy term is considered ($c = 0$), the theoretical values are underestimated by about a half, whereas $c = 0.5$ provides a good fit. Therefore, the contribution of the adhesion hysteresis is of the same order of magnitude as the contribution kinetic effects (Nosonovsky and Bhushan, 2007c)

6.4.5 Contact Angle Hysteresis and Wetting–Dewetting Asymmetry

Contact angle hysteresis can be viewed as a result of two factors that act simultaneously. First, the changing contact area affects the contact angle hysteresis, since a certain value of contact angle hysteresis is inherent for even a nominally flat surface. Decreasing the contact area by increasing the pitch between the pillars leads to a proportional decrease of the contact angle hysteresis. This effect is clearly proportional to the contact area between the solid surface and the liquid droplet. Second, the edges of the pillar tops prevent the motion of the triple line. This roughness effect is proportional to the contact line density, and its contribution was,

in the experiment, comparable with the contact area effect. Interestingly, the effect of the edges is much more significant for the advancing than for the receding contact angle.

Nosonovsky and Bhushan (2007a, c, d, 2008b, d) studied the wetting of two series of micropatterned Si surfaces with different pitch values coated with PF₃ based on the spacing factor (6.10). They found that the contact angle hysteresis involves two terms (Fig. 6.18b): the term $S_f^2(\pi/4)(\cos \theta_{\text{adv}0} - \cos \theta_{\text{rec}0})$ corresponding to the adhesion hysteresis (which is found even in a nominally flat surface and is a result of molecular-scale imperfectness) and the term $H_r \propto D/P^2$ corresponding to microscale roughness and proportional to the edge line density. Thus, the contact angle hysteresis is given, based on (3.18) and (6.10), by using $R_f = 1 + (\pi DH/P^2)$ and $f_{\text{LA}} = 1 - (\pi D^2/4P^2) = 1 - f_{\text{SL}}$ (Bhushan et al., 2007, Nosonovsky and Bhushan, 2007b):

$$\cos \theta_{\text{adv}} - \cos \theta_{\text{rec}} = \frac{\pi}{4} S_f^2 (\cos \theta_{\text{adv}0} - \cos \theta_{\text{rec}0}) + H_r. \quad (6.11)$$

Besides the contact angle hysteresis, the asymmetry of the Wenzel and Cassie–Baxter states is the result of the wetting–dewetting asymmetry. While the fragile metastable Cassie–Baxter state is often observed, as well as its transition to the Wenzel state, the opposite transition never happens. Using (6.2) and (6.3), the contact angle with micropatterned surfaces is given by (Bhushan et al., 2007, Nosonovsky and Bhushan, 2007b):

$$\cos \theta = (1 + 2\pi S_f^2) \cos \theta_0 \quad (\text{Wenzel state}), \quad (6.12)$$

$$\cos \theta = \frac{\pi}{4} S_f^2 (\cos \theta_0 + 1) - 1 \quad (\text{Cassie–Baxter state}). \quad (6.13)$$

For a perfect macroscale system, the transition between the Wenzel and Cassie–Baxter states should occur only at the intersection of the two regimes (the point at which the contact angle and net energies of the two regimes are equal, corresponding to $S_f = 0.51$). It is observed, however, that the transition from the metastable Cassie–Baxter to stable Wenzel occurs at much lower values of the spacing factor $0.083 < S_f < 0.111$. As shown in Fig. 6.19a, the stable Wenzel state (1) can transform into the stable Cassie–Baxter state with increasing S_f (2). The metastable Cassie–Baxter state (3) can abruptly transform (4) into the stable Wenzel state (1). The transition points (1) and (2) correspond to equal free energies in the Wenzel and Cassie–Baxter states. Whereas the transition (4) corresponds to the Wenzel energy being much lower than the Cassie–Baxter energy and thus involves significant energy dissipation and is irreversible (Nosonovsky and Bhushan, 2007c). The solid and dashed straight lines correspond to the values of the contact angle, calculated from (6.12) and (6.13) using the contact angle for a nominally flat surface, $\theta_0 = 109^\circ$. The two series of the experimental data are shown with squares and diamonds.

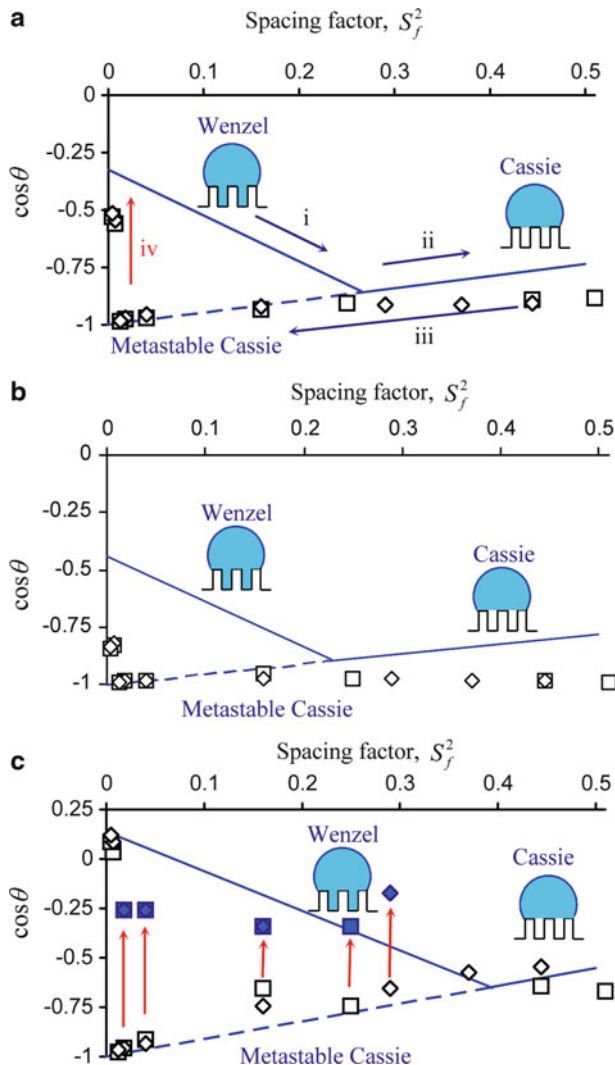


Fig. 6.19 Theoretical (solid and dashed) and experimental (squares for the first series, diamonds for the second series) (a) contact angle as a function of the spacing factor, (b) advancing contact angle, and (c) receding contact angle and values of the contact angle observed after the transition during evaporation (blue) (Nosonovsky and Bhushan, 2007c)

Figure 6.19b shows the values of the advancing contact angle plotted against the spacing factor (6.10). The solid and dashed straight lines correspond to the values of the contact angle for the Wenzel and Cassie–Baxter states, calculated from (6.12) and (6.13) using the advancing contact angle for a nominally flat surface, $\theta_{adv0} = 116^\circ$ (Nosonovsky and Bhushan, 2007c). It is observed that the

calculated values underestimate the advancing contact angle, especially for a large S_f (small distance between the pillars or pitch P). This is understandable because the calculation takes into account only the effect of the contact area and ignores the effect of roughness and edge line density (it corresponds to $H_r = 0$ in (6.11), while this effect is more pronounced for high pillar density (big S_f). In a similar manner, the contact angle is underestimated for the Wenzel state, since the pillars constitute a barrier for the advancing droplet.

Figure 6.19c shows the values of the contact angle after the transition took place (squares and diamonds), as it was observed during evaporation (Nosonovsky and Bhushan, 2007c). For both series, the values almost coincide. For comparison, the values of the receding contact angle measured for millimeter-sized water droplets are also shown (squares and diamonds), since evaporation constitutes removing liquid, and thus, the contact angle during evaporation should be compared with the receding contact angle. The solid and dashed straight lines correspond to the values of the contact angle, calculated from (6.12) and (6.13) using the receding contact angle for a nominally flat surface, $\theta_{\text{rec0}} = 82^\circ$. Figure 6.19c demonstrates a good agreement between the experimental data and (6.12)–(6.13).

In the analysis of the evaporation data of micropatterned surfaces, Nosonovsky and Bhushan (2008b) found several effects specific to the multiscale character of this process. First, they discussed the applicability of the Wenzel and Cassie–Baxter equations for average surface roughness and heterogeneity. These equations relate the local contact angle with the apparent contact angle of a rough/heterogeneous surface. However, it is not obvious what should be the size of roughness/heterogeneity averaging, since the triple line at which the contact angle is defined has two very different length scales: its width is of the molecular scale while its length is on the order of the size of the droplet (i.e., microns or millimeters). They presented an argument that in order for the averaging to be valid, the roughness details should be small compared to the size of the droplet (and not the molecular size). They showed that while for uniform roughness/heterogeneity the Wenzel and Cassie–Baxter equations can be applied, for a more complicated case of nonuniform heterogeneity, the generalized equations should be used. The proposed generalized Cassie–Baxter and Wenzel equations are consistent with a broad range of available experimental data. The generalized equations are valid both in the cases when the classical Wenzel and Cassie–Baxter equations can be applied as well as in the cases when the latter fail.

The macroscale contact angle hysteresis and Cassie–Baxter and Wenzel transition cannot be determined from the macroscale equations and are governed by micro- and nanoscale effects, so wetting is a multiscale phenomenon (Nosonovsky and Bhushan, 2007a, c, d, 2008b, d). The kinetic effects associated with contact angle hysteresis should be studied at the microscale, whereas the effects of adhesion hysteresis and the Cassie–Baxter and Wenzel transition involve processes at the nanoscale. Their theoretical arguments are supported by the experimental data on micropatterned surfaces. The experimental study of the contact angle hysteresis demonstrates that two different processes are involved: the changing solid–liquid area of contact and pinning of the triple line. The latter effect is more significant for

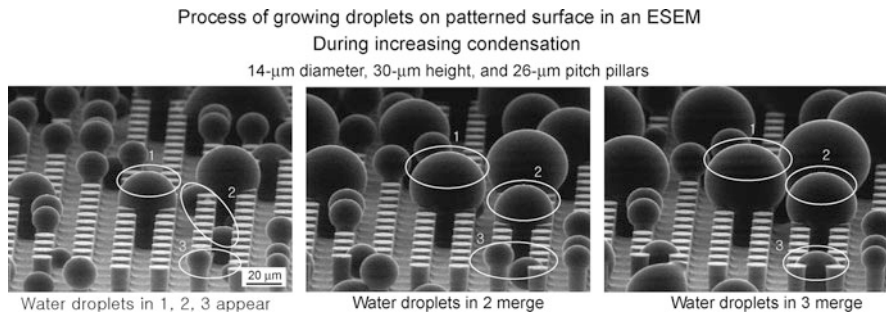


Fig. 6.20 Microdroplet (in dimensions of <1 mm diameter) growing and merging process under ESEM during increasing condensation by decreasing temperature. (*Left image*) Some small water droplets appear at the beginning, i.e., water droplets 1–3. (*Middle image*) Water droplets at locations 1 and 3 increase in size, and water droplets at location 2 merge together to form one big droplet. (*Right image*) Water droplets at locations 1 and 2 increase in size and water droplets at location 3 merge together to form one big droplet (Jung and Bhushan, 2008a)

the advancing than for the receding contact angle. The transition between wetting states was observed for evaporating microdroplets, and droplet radius scales well with the geometric parameters of the micropattern.

6.4.6 Contact Angle Measurements During Condensation and Evaporation of Microdroplets on Micropatterned Surfaces

To provide insight into the formation of microdroplets and detailed information about the contact angle on the micropatterned surfaces, ESEM experiments on micropatterned surfaces have been performed during condensation and evaporation. Figure 6.20 shows how water droplets grow and merge in an ESEM (Jung and Bhushan, 2008a) that was used as a contact angle analysis tool. Microdroplets (with a diameter less than 1 mm) were distributed on a micropatterned surface coated with PF₃ using condensation by decreasing temperature. At the beginning, some small water droplets appeared, i.e., the water droplets at locations 1–3 in the left image. During further condensation with decreasing temperature, the droplets at locations 1 and 3 gradually grew while the droplets at location 2 merged together. With further condensation, the droplets at locations 1 and 2 gradually grew while the droplets at location 3 merged together into one large droplet in the right image. In all cases, condensation was initiated at the bottom; therefore, the droplets were in the Wenzel regime.

Compared with the conventional contact angle measurement, ESEM is able to provide detailed information about the contact angle of microdroplets on micropatterned surfaces. The diameter of the water droplets used for the contact

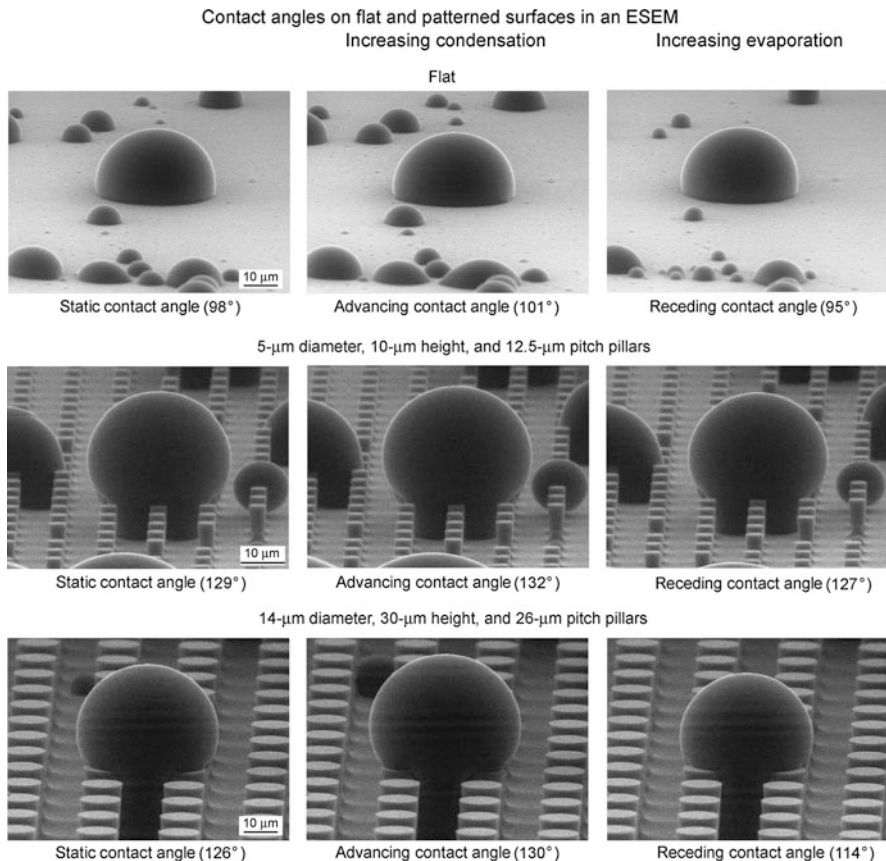


Fig. 6.21 Microdroplets on flat and two micropatterned surfaces using ESEM. Second set of images were taken during increasing condensation, and the third set of images were taken during increasing evaporation. Static contact angle was measured when the droplet was stable. Advancing contact angle was measured after increasing condensation by decreasing the temperature of the cooling stage. Receding contact angle was measured after decreasing evaporation by increasing the temperature of the cooling stage (Jung and Bhushan, 2008a)

angle measurement was $10 \mu\text{m}$, so that the size limit pointed out by Stelmashenko et al. (2001) was avoided. For a droplet size smaller than $1 \mu\text{m}$, substrate backscattering can distort the intensity profile such that the images are inaccurate.

As shown in Fig. 6.21, the static contact angle and contact angle hysteresis of the microdroplets on flat and micropatterned surfaces were obtained from the images using the methodology described earlier. Once the microdroplet's condensation and evaporation has reached a dynamic equilibrium, static contact angles were determined. The flat Si coated with PF_3 showed a static contact angle of 98° . The micropatterned surfaces coated with PF_3 increase the static contact angle compared to the flat surface coated with PF_3 due to the effect of roughness. Advancing

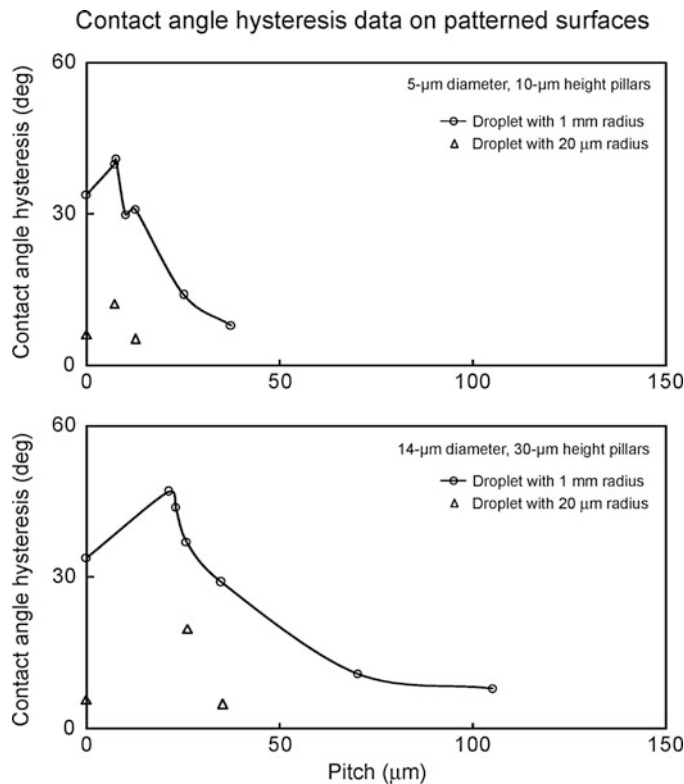


Fig. 6.22 Contact angle hysteresis as a function of pitch value for the microdroplet with about 20 μm radius from ESEM (*triangle*) compared with the droplet with 1 mm radius (5 μL volume) (*circle* and *solid lines*) for two series of micropatterned surfaces with different pitch values. Data at zero pitch correspond to a flat sample (Jung and Bhushan, 2008a)

and receding contact angles were measured during condensation/evaporation with decreasing/increasing the temperature of the cooling stage, and the contact angle hysteresis was then calculated (Jung and Bhushan, 2008a).

Figure 6.22 shows contact angle hysteresis as a function of pitch value for the microdroplets formed in the ESEM (triangles) for two series of micropatterned Si with different pitch values coated with PF_3 . Data at zero pitch correspond to a flat Si sample. The droplets with about 20 μm radii, which are larger than the pitch, were selected in order to look at the effect of pillars in contact with the droplet. These data were compared with conventional contact angle measurements with the droplet with 1 mm radius (5 μL volume) (Bhushan and Jung, 2007). When the distance between pillars increases above a certain value, the contact area between the micropatterned surface and the droplet decreases, resulting in a decrease of the contact angle hysteresis. Both droplets with 1 mm and 20 μm radii showed the same trend. The contact angle hysteresis for the micropatterned surfaces with low

pitch are higher compared to the flat surface due to the effect of sharp edges on the pillars, resulting in pinning ([Nosonovsky and Bhushan, 2005](#)). Contact angle hysteresis for a flat surface can arise from roughness and surface heterogeneity. For a droplet advancing forward on the micropatterned surfaces, the line of contact of the solid, liquid, and air will be pinned at the edge point until it is able to move, resulting in increasing contact angle hysteresis. The contact angle hysteresis for the microdroplet from ESEM is lower as compared to that for the droplet with 1 mm radius. The difference of contact angle hysteresis between a microdroplet and a droplet with 1 mm radius could come from the different pinning effects because the latter has more sharp edges in contact with a droplet compared to the former. The results show how droplet size can affect the wetting properties of micropatterned Si surfaces ([Jung and Bhushan, 2008a](#)).

6.4.7 Observation of Transition During the Bouncing Droplet

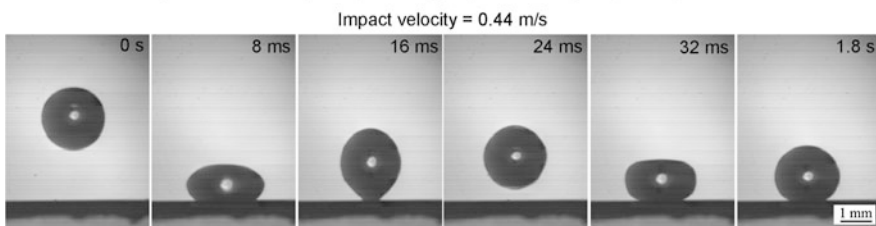
Dynamic effects such as bouncing of a droplet (e.g., rain droplets hitting the window glass) can destroy the composite interface. Based on [\(6.7\)](#), the relationship between the impact velocity of a droplet and geometric parameters affects the transition from the Cassie–Baxter to the Wenzel regime. Therefore, it is necessary to study the dynamic effect of droplets under various impact velocities.

[Jung and Bhushan \(2008b\)](#) performed bouncing droplet experiments to observe how impact velocity influences the Cassie–Baxter and Wenzel transition during the droplet hitting the surface on two different micropatterned Si surfaces with PF₃. Figure [6.23](#) shows snapshots of a droplet with 1 mm radius hitting the surfaces. The impact velocity was obtained just prior to the droplet hitting the surface. As shown in the images in the first row for the two sets of surfaces, the droplet hitting the surface under an impact velocity of 0.44 m/s first deformed and then retracted, and bounced off the surface. Finally, the droplet sat on the surface and had a high contact angle, which suggests the formation of a solid–air–liquid interface. Next, they repeated the impact experiment by increasing the impact velocity. The bounce off does not occur, and the wetting of the surface (and possibly pinning of droplet) occurred at an impact velocity of 0.88 and 0.76 m/s, respectively, referred to as the critical velocity (described earlier). The second row of the two sets of images show the droplet at the critical velocity. After the droplet hit the surface, it wetted the surface (possibly the droplet was also pinned) after the deformation of the droplet. This is because air pockets do not exist below the droplet as a result of droplet impalement by the pillars, characterized by a smaller contact angle. These observations indicate the transition from a Cassie–Baxter to a Wenzel regime.

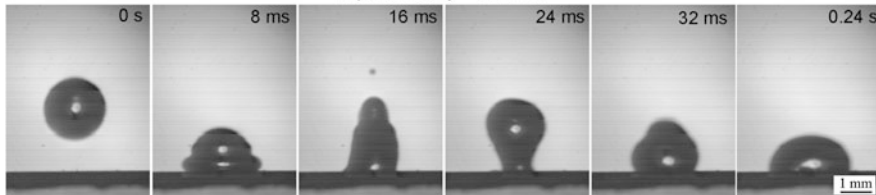
To identify whether one is in a Wenzel regime or a Cassie–Baxter regime, the contact angle data in the static condition and after bounce off were plotted ([Jung and Bhushan, 2008b](#)). Figure [6.24](#) shows the measured static contact angle as a function of pitch value for the droplet with 1 mm radius gently deposited on the surface and for the droplet with 1 mm radius after hitting the surface at 0.44 m/s. The data are

Dynamic effects of a droplet on micropatterned surfaces

5- μm diameter, 10- μm height, and 10- μm pitch pillars

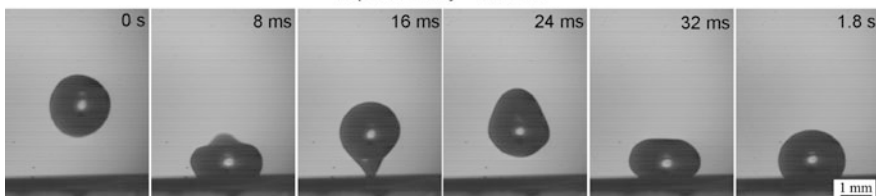


Impact velocity = 0.88 m/s



14- μm diameter, 30- μm height, and 26- μm pitch pillars

Impact velocity = 0.44 m/s



Impact velocity = 0.76 m/s

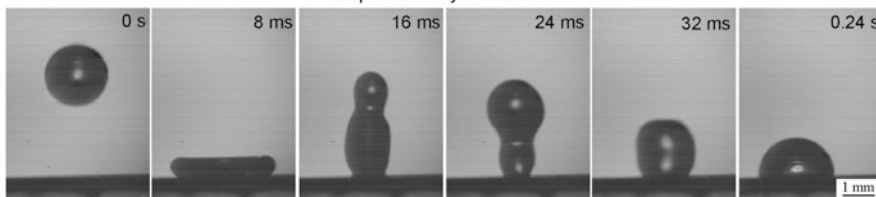


Fig. 6.23 Snapshots of a droplet with 1 mm radius hitting on two different micropatterned surfaces. The impact velocity was obtained just prior to the droplet hitting the surface. The pinning of the droplet on the surface with 5 μm diameter, 10 μm height, and 10 μm pitch pillars and on the surface with 14 μm diameter, 30 μm height, and 26 μm pitch pillars occurred at impact velocity of 0.88 m/s and 0.76 m/s, respectively (Jung and Bhushan, 2008b).

compared with predicted static contact angle values obtained using the Wenzel and the Cassie–Baxter equations with a given value of θ_0 (109°) for a smooth surface for two series of the micropatterned surfaces. In the case of the droplet gently deposited on the surface, as the pitch increases up to 45 μm in series 1 and 126 μm in series 2,

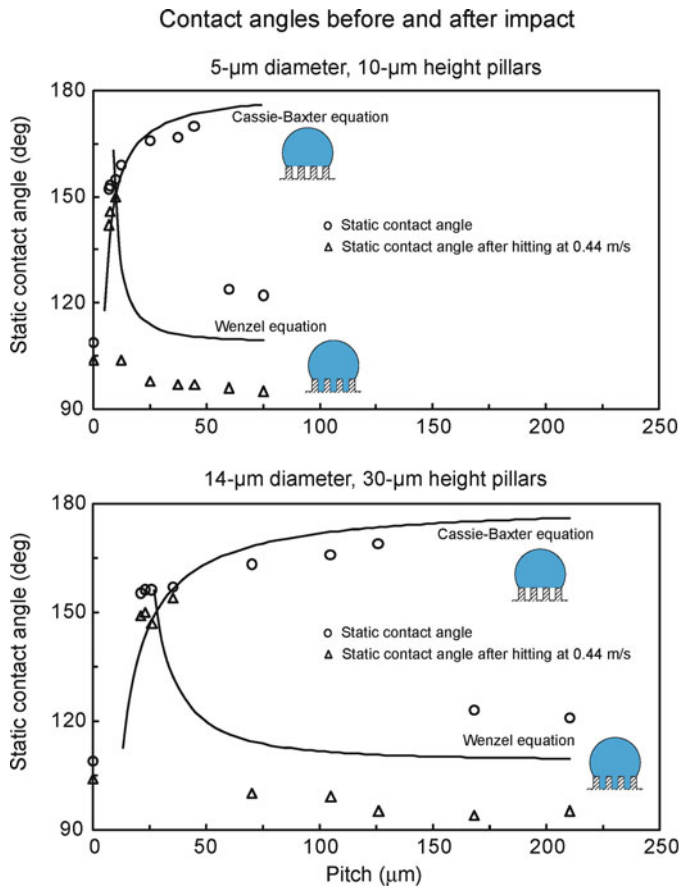


Fig. 6.24 Measured static contact angle as a function of pitch value for the droplet with 1 mm radius gently deposited on the surface (*circles*) and for the droplet with 1 mm radius after hitting the surface at 0.44 m/s (*triangles*). The data are compared with predicted static contact angle values obtained using Wenzel and Cassie–Baxter equations (*solid lines*) with a given value of θ_0 (109°) for a smooth surface for two series of the micropatterned Si with different pitch values (Jung and Bhushan, 2008b)

the static contact angle first increases gradually from 152° to 170° . Then, the contact angle starts decreasing sharply. The increase in the contact angle occurs because of an increase in the roughness factor and the formation of composite surface (Bhushan and Jung, 2007). The decrease in contact angle at pitch values higher than $60 \mu\text{m}$ for series 1 and $168 \mu\text{m}$ for series 2 occurs due to the transition from the composite interface to the solid–liquid interface. In the case of the droplet hitting the surface at 0.44 m/s, it is shown that the liquid–air interface can easily be destabilized due to dynamic impact on the surface with a pitch value higher than $12.5 \mu\text{m}$ for series 1 and $70 \mu\text{m}$ for series 2, although the droplet is in the Cassie–Baxter regime when it

is gently deposited on the surface. The static contact angle of the droplet after hitting at 0.44 m/s is lower than that of the droplet gently deposited. It can be interpreted that after hitting, the droplet contacts the bottom of the cavities between pillars and pushes out the entrapped air under the droplet, resulting in an abrupt increase of the solid–liquid surface area by dynamic impact. It will be shown in the following paragraph that the critical velocity at which wetting occurs for series 1 and series 2 samples is equal to about 0.44 m/s at pitch values larger than 12.5 and 70 μm , respectively. Thus, wetting at the velocity used here is expected.

To study the validity of the transition criterion (6.7), the critical impact velocity at which wetting of the surface (possibly pinning of droplet) occurs was measured (Jung and Bhushan, 2008b). For calculations, the surface tension of the water–air interface (γ) was taken at 0.073 N/m, the mass density (ρ) is 1,000 kg/m³ for water, and 1 kg m/s² = 1 N (Adamson, 1990). Figure 6.25 shows the measured critical impact velocity of a droplet with 1 mm radius as a function of pitch value. The trends are compared with the predicted curve. It is found that the critical impact velocity at which wetting occurs is in good quantitative agreement with the predictions. The critical impact velocity of the droplet decreases with the geometric parameter (pitch). For the surface with a small pitch, the critical impact velocity of droplet can be large.

The energy barrier of the Cassie–Baxter and Wenzel transition can be estimated as the kinetic energy of the droplets (Nosonovsky and Bhushan, 2008e). Figure 6.26 shows the dependence of the kinetic energy corresponding to the transition, E_{kin} , on $\Delta E/(A_0 \cos \theta_0)$ calculated from (6.8). It is observed that the dependence is close to linear; however, the series of smaller pillars has larger energies of transition. The value of A_0 is in the range $0.11 \text{ mm}^2 < A_0 < 0.18 \text{ mm}^2$ for series 1 and $0.05 \text{ mm}^2 < A_0 < 0.11 \text{ mm}^2$ for series 2, which is of the same order as the actual area under the droplet.

These results suggest that the energy barrier for the Cassie–Baxter and Wenzel transition is given by (6.8) and is proportional to the area under the droplet (Nosonovsky and Bhushan, 2008e). For droplets sitting on the surface or evaporating, the transition takes place when the size of the barrier decreases to the value of the vibrational energy, U . The vibrational energy of the droplet is the energy associated with the vibration of the droplet due to surface waves, thermal vibration, etc. Assuming $U = \text{const}$, the proportionality of P/D and R suggests that the energy barrier is proportional to the RD/P . This is indeed true, since the area under the droplet $A_0 = \pi(R \sin \theta)^2$. Substituting $\sin^2 \theta = 0.1$, $\cos \theta_0 = \cos 109^\circ = -0.33$, $\gamma_{\text{LA}} = 0.072 \text{ J/m}^2$ in (6.8) and taking the observed value $RD/P = 50 \mu\text{m}$ yields an estimated value of the vibrational energy $U = 1.2 \times 10^{-10} \text{ J}$. The transition happens because the size of the droplet is decreased or because the pitch between the pillars that cover the surface is increased. A different way to overcome the barrier is to hit the surface with a droplet with a certain kinetic energy.

Based on Nosonovsky and Bhushan (2008e), the vibrational energy U also plays a role in overcoming energy barriers that lead to contact angle hysteresis during liquid flow (Johnson and Dettre, 1964). To estimate the effect of the energy barriers

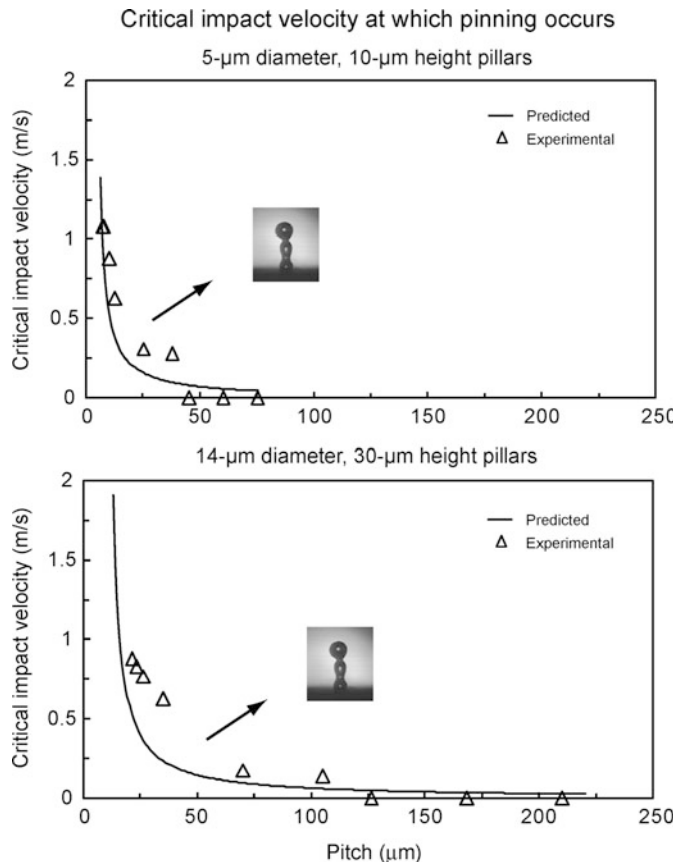


Fig. 6.25 Measured critical impact velocity of droplet with 1 mm radius as a function of pitch value (triangles). The data are compared with the criterion of impact velocity for the pinning of droplet (solid lines) for two series of the micropatterned Si with different pitch values (Jung and Bhushan, 2008b)

on contact angle hysteresis, it is assumed, based on (3.5), that the difference between the advancing and receding contact angle is given by

$$\cos \theta_{\text{rec}} - \cos \theta_{\text{adv}} = \frac{\Delta W}{\gamma_{\text{LA}}}, \quad (6.14)$$

where ΔW corresponds to the energy barrier associated with the wetting–dewetting cycle. Assuming that this energy barrier is of the same order as the vibrational energy per contact area, $\Delta W = U/A_0$, and taking $A_0 = 0.1 \text{ mm}^2$, $\Delta W = 10^{-3} \text{ J/m}^2$ is obtained. For water ($\gamma_{\text{LA}} = 0.072 \text{ J/m}^2$), (6.14) leads to a realistic value of hysteresis on a superhydrophobic surface $\cos \theta_{\text{rec}} - \cos \theta_{\text{adv}} = 0.014$. This number provides an estimate for contact angle hysteresis in the limit of small energy

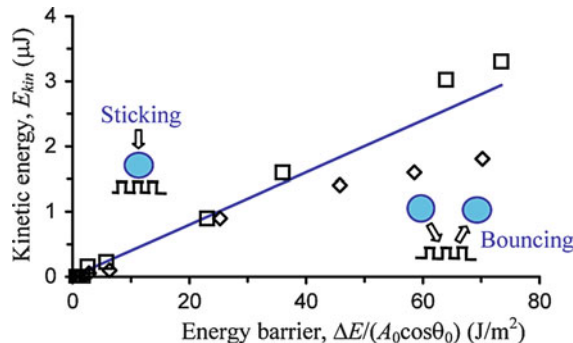


Fig. 6.26 Bouncing droplets dependency of the kinetic energy of a droplet corresponding to the regime transition upon the energy barrier calculated from (6.8) (squares for series 1 and diamonds for series 2). The fit (solid line) is shown for $A_0 = 0.12 \text{ mm}^2$ (Nosonovsky and Bhushan, 2008e)

barriers comparable with U . The actual values for a micropatterned surface are dependent upon the solid–liquid contact area (that provides energy barriers due to so-called adhesion hysteresis) and the density of the solid–air–liquid contact line (that provides additional pinning) and were found to be between 0.0144 and 0.440 (Bhushan et al., 2007), thus showing a good agreement with the value calculated based on U as the lower limit. This indicates that the value of U is relevant both for the Cassie–Baxter and Wenzel regime transition and contact angle hysteresis.

6.4.8 Summary

The presence of the Wenzel and Cassie–Baxter regimes is dependent upon the micro-/nanostructure and droplet radius. Cassie–Baxter and Wenzel transition criteria have been proposed. Bhushan and Jung (2007, 2008) and Jung and Bhushan (2007, 2008a, b) proposed a transition criterion based on the pitch distance between the pillars and the curvature of the droplet governed by the Laplace equation, which relates the pressure inside the droplet to its curvature. In addition, the transition can occur by applying external pressure to the droplet or by the impact of a droplet on the patterned surfaces (Jung and Bhushan, 2008b; Nosonovsky and Bhushan, 2008e). Alternatively, Bhushan et al. (2007) and Nosonovsky and Bhushan (2007c, d) found that the transition occurs at a critical value of the spacing factor, a nondimensional parameter which is defined as the diameter of the pillars divided by the pitch distance between them for patterned surfaces and its ratio to the droplet size.

The transition criteria were validated using micropatterned surfaces with various pitch values of micropillars and droplet radii. Droplet radii were varied by performing measurements during droplet evaporation. Contact angle measurements have also been made during condensation and evaporation of droplets.

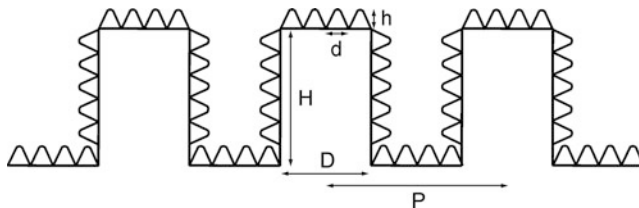


Fig. 6.27 Schematic of structure of an ideal hierarchical surface. Microasperities consist of the circular pillars with diameter D , height H , and pitch P . Nanoasperities consist of pyramidal nanoasperities of height h and diameter d with rounded tops

To study the dynamic effect of droplets under various impact velocities, bouncing of a droplet experiments over micropatterned surfaces have been performed. For a given micropattern geometry, as the droplet hits the surface, the droplet bounced off below a certain critical velocity. Above the critical velocity, after the droplet hits the surface, it does not bounce off and the liquid–air interface changes to the solid–liquid interface due to dynamic impact. A transition model is verified with measurement data.

6.5 Ideal Surfaces with Hierarchical Structure

It was reported earlier that a hierarchical surface is needed to develop a composite interface with high stability. The structure of an ideal hierarchical surface is shown in Fig. 6.27. The asperities should be high enough so that the droplet does not touch the valleys. As an example, for a structure with circular pillars, the following relationship should hold for a composite interface: $(\sqrt{2}P - D)^2/R < H$, (6.4). As an example, for a droplet with a radius on the order of 1 mm or larger, a value of H on the order of $30 \mu\text{m}$, D on the order of $15 \mu\text{m}$, a P on the order of $130 \mu\text{m}$ (Fig. 6.12) is optimum. Nanoasperities can pin the liquid–air interface and thus prevent liquid from filling the valleys between asperities. They are also required to support nanodroplets, which may condense in the valleys between large asperities. Therefore, nanoasperities should have a small pitch to handle nanodroplets, less than 1 mm down to few nm radius. The values of h on the order of 10 nm and d on the order of 100 nm can be easily fabricated.

The structures were first fabricated using nature’s route to verify that properties comparable to that of nature objects can be obtained (Sect. 6.6). Next, mechanically durable structures were fabricated guided by models and by using smart materials and fabrication techniques (Sect. 6.7).

6.6 Hierarchical Structured Surfaces with Wax Platelets and Tubules Using Nature's Route

A hierarchical structure is composed of at least two levels of structuring in different length scales. Bhushan et al. (2008a, b, 2009c, d, 2012) and Koch et al. (2009) used nature's route to create various structures and measured contact angle, contact angle hysteresis, adhesion, and self-cleaning efficiency and compared these with that of the Lotus leaf. They also performed experiments to study the dynamic effects of bouncing and vibrating droplets in order to observe their influence on transition from the composite interface to the homogeneous interface.

They fabricated surfaces with a hierarchical structure with micropatterned epoxy replicas and Lotus leaf microstructure and created a second level of structuring with wax tubules and wax platelets. Tubules and platelets are the most common wax morphologies found in plant surfaces and exist on superhydrophobic leaves. For example, Lotus and *Colocasia esculenta* leaves consist of tubules and platelets morphologies, respectively. The structures developed mimic the hierarchical structures of superhydrophobic leaves. Two steps of the fabrication process include the production of microstructured surfaces by soft lithography and the subsequent development of nanostructures on top by self-assembly of plant waxes and artificial wax components.

A two-step molding process was used to fabricate several structurally identical copies of micropatterned Si surface and Lotus leaves. The technique used is a fast, precise, and low cost molding process for biological and artificial surfaces (Koch et al., 2007, 2008). The technique was used to mold a microstructured Si surface with pillars of 14 μm diameter and 30 μm height with 23 μm pitch (Bhushan et al., 2008a, b, 2009c, d; Koch et al., 2009), fabricated by photolithography. Before replication of the Lotus leaf, the epicuticular wax tubules were removed in areas of approximately 6 cm^2 . For this purpose, a two-component fast hardening glue was applied on the upper side of the leaves and was carefully pressed onto the leaf. After hardening, the glue with the embedded waxes was removed from the leaf, and the procedure was repeated (Koch et al., 2009).

The replication is a two-step molding process, in which first a negative replica of a template is generated and then a positive replica is generated, as shown in Fig. 6.28a (Bhushan et al., 2009d). A polyvinylsiloxane dental wax (President Light Body® Gel, ISO 4823, Polyvinylsiloxan (PLB), Coltene Whaledent, Hamburg, Germany) was applied via a dispenser on the surface and immediately pressed down with a glass plate. After complete hardening of the molding mass (at room temperature for approximately 5 min at room temperature), the silicon master surface and the mold (negative) were separated. After a relaxation time of 30 min for the molding material, the negative replicas were filled with a liquid epoxy resin (Epoxydharz L®, No. 236349, Conrad Electronics, Hirschau, Germany) with hardener (Harter S, Nr 236365, Conrad Electronics, Hirschau, Germany). Specimens with microstructures were immediately transferred to a vacuum chamber at 750 mTorr (100 Pa) pressure for 10 s to remove trapped air and to increase resin infiltration.

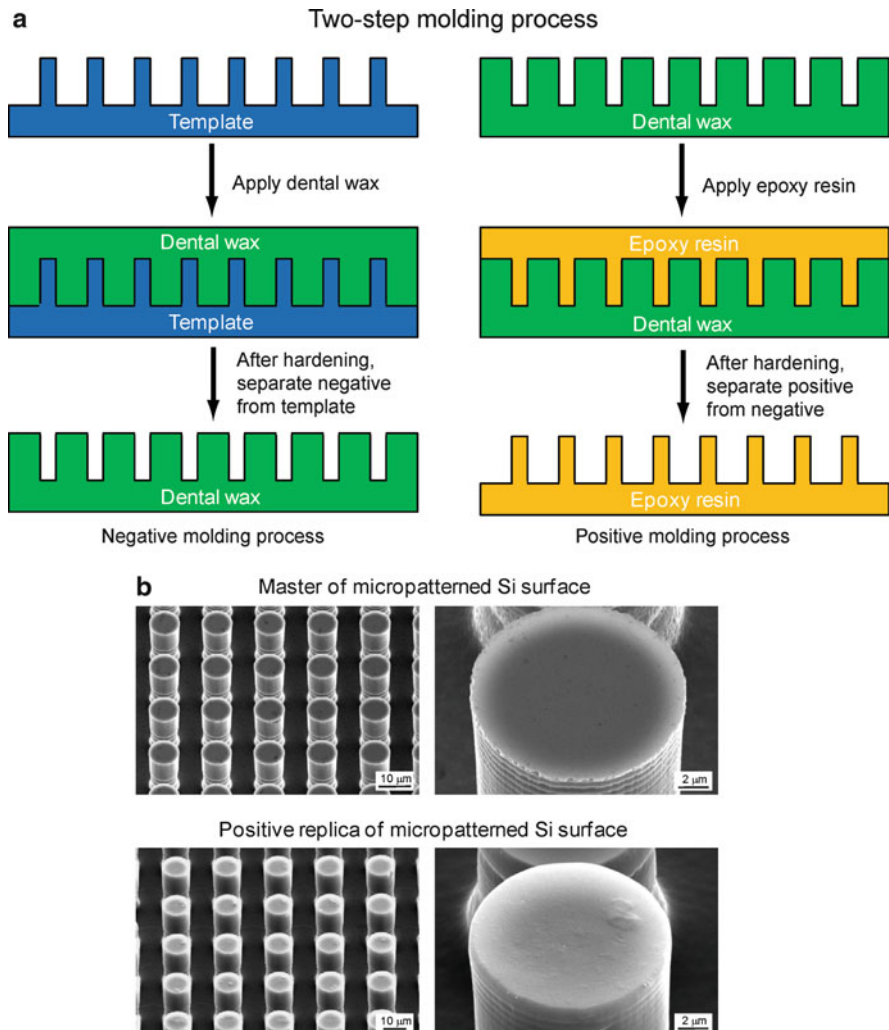


Fig. 6.28 (a) Schematic of two-step molding process used to fabricate microstructure, in which at first a negative is generated and then a positive, and (b) SEM micrographs of the master of micropatterned Si surface and positive replica fabricated from the master surface measured at 45° tilt angle (shown using two magnifications) (Bhushan et al., 2009d)

tration through the structures. After hardening at room temperature (24 h at 22°C), the positive replica was separated from the negative replica. The second step can be repeated to generate a number of replicas. The pillars of the master surface have been replicated without any morphological changes as shown in Fig. 6.28b (Bhushan et al., 2009d). The nanogrooves of a couple of 100 nm in lateral dimension present on the pillars of the master surface are shown to reproduce faithfully in the replica.

Table 6.2 Chemical structure of the major components of *n*-hexatriacontane, *T. majus*, and Lotus waxes

<i>n</i> -Hexatriacontane	$C_{36}H_{74}$
<i>Tropaeolum majus</i>	Nonacosan-10-ol $\text{CH}_3-(\text{CH}_2)_8-\overset{\text{OH}}{\underset{ }{\text{CH}}}-(\text{CH}_2)_{18}-\text{CH}_3$
	Nonacosane-4,10-diol $\text{CH}_3-(\text{CH}_2)_2-\overset{\text{OH}}{\underset{ }{\text{CH}}}-(\text{CH}_2)_5-\overset{\text{OH}}{\underset{ }{\text{CH}}}-(\text{CH}_2)_{18}-\text{CH}_3$
	Nonacosane-10,15-diol $\text{CH}_3-(\text{CH}_2)_8-\overset{\text{OH}}{\underset{ }{\text{CH}}}-(\text{CH}_2)_4-\overset{\text{OH}}{\underset{ }{\text{CH}}}-(\text{CH}_2)_{13}-\text{CH}_3$
Lotus	Nonacosan-10-ol $\text{CH}_3-(\text{CH}_2)_8-\overset{\text{OH}}{\underset{ }{\text{CH}}}-(\text{CH}_2)_{18}-\text{CH}_3$

The major component is shown first ([Bhushan et al., 2008a, 2009c; Koch et al., 2009](#))

Nanostructures have been created by self-assembly of synthetic and plant waxes deposited by thermal evaporation. The alkane *n*-hexatriacontane ($C_{36}H_{74}$) has been used for the development of platelet nanostructures ([Bhushan et al., 2008a, b, 2009d](#)). Tubule-forming waxes which were isolated from leaves of *Tropaeolum majus* (L.) and *Nelumbo nucifera*, in the following referred to as *T. majus* and Lotus, were used to create tubule structures ([Bhushan et al., 2009c; Koch et al., 2009](#)). The chemical structure of the major components of the wax forming tubule and alkane *n*-hexatriacontane are shown in Table 6.2. The complete chemistry of the plant waxes used is presented in [Koch et al. \(2006a\)](#). For a homogenous deposition of the waxes and alkane, a thermal evaporation system, as shown in Fig. 6.29, has been used ([Bhushan et al., 2009d](#)). Specimens of smooth surfaces (flat silicon replicas) and microstructured replicas were placed in a vacuum chamber at 30 mTorr (4 kPa), 20 mm above a heating plate loaded with waxes of *n*-hexatriacontane (300, 500, or 1,000 μg), *T. majus* wax (500, 1,000, 1,500, or 2,000 μg), and Lotus wax (2,000 μg) ([Bhushan et al., 2008a, b, 2009c, d; Koch et al., 2009](#)). The wax was evaporated by heating it up to 120°C. In a vacuum chamber, the evaporation from the point source to the substrate occurs in a straight line; thus, the amount of sublimated material is equal in a hemispherical region over the point of source ([Bunshah, 1994](#)). In order to estimate the amount of sublimated mass, the surface area of the half sphere was calculated by using the formula $2\pi r^2$, whereby the radius (r) represents the distance between the specimen to be covered and the heating plate with the substance to be evaporated. The amounts of wax deposited on the specimen surfaces were 0.12, 0.2, and 0.4 $\mu\text{g}/\text{mm}^2$ for *n*-hexatriacontane, and 0.2, 0.4, 0.6, and 0.8 $\mu\text{g}/\text{mm}^2$ for *T. majus* and 0.8 $\mu\text{g}/\text{mm}^2$ for Lotus waxes, respectively.

After coating, the specimens with *n*-hexatriacontane were placed in a desiccator at room temperature for 3 days for crystallization of the alkanes. A stable stage was indicated by no further increase of crystal sizes.

For the plant waxes which are a mixture of aliphatic components, different crystallization conditions have been chosen. It has been reported by [Niemietz et al. \(2009\)](#) that an increase of temperature from 21°C (room temperature)

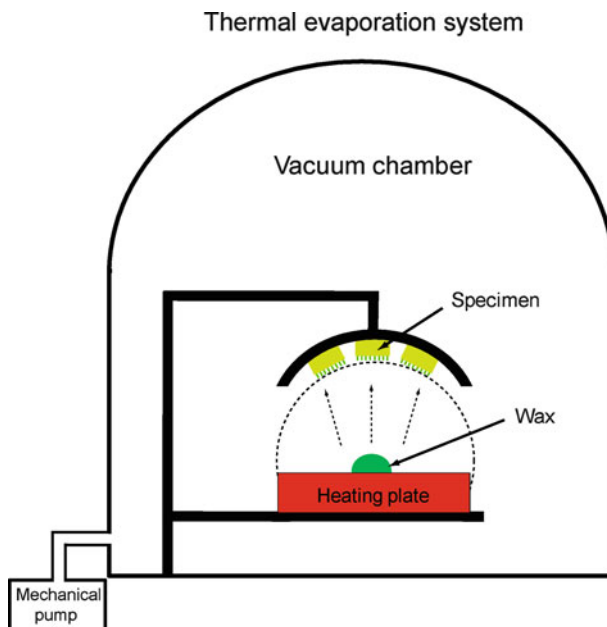


Fig. 6.29 Schematic of thermal evaporation system for self-assembly of a wax. Evaporation from the point source to the substrate occurs over hemispherical region (dotted line) (Bhushan et al., 2009d)

to 50°C had a positive effect on the mobilization and diffusion of wax molecules, required for separation of the tubule-forming molecules. It is also known that chemical ambient has an influence on the propensity of wax crystallization; thus, the specimens with evaporated plant waxes (*T. majus* and Lotus) were stored for 3 days at 50°C in a crystallization chamber, where they were exposed to a solvent (ethanol) in vapor phase (Fig. 6.30). Specimens were placed on metal posts, and a filter paper wetted with 20 mL of the solvent was placed below the specimens. Slow diffusive loss of the solvent in the chamber was provided by placing a thin filter paper between the glass body and the lid. After evaporation of the solvent, specimens were left in the oven at 50°C in total for seven days. Figure 6.31 shows the nanostructures formed by Lotus wax, 7 days after wax deposition on flat surfaces. Figure 6.31a shows the nanostructure after storage at 21°C; in these, no tubules were grown. Figure 6.31b shows that Lotus waxes exposed to ethanol vapor for 3 days at 50°C formed wax tubules. A detailed description of the nanostructure sizes and nanoroughness is given in the following.

Flat films of *n*-hexatriacontane and wax tubules were made by heating the substances above their melting point and rapidly cooling down. This procedure interrupts the crystallization and leads to smooth films (Bhushan et al., 2008a, b, 2009c, d; Koch et al., 2009).

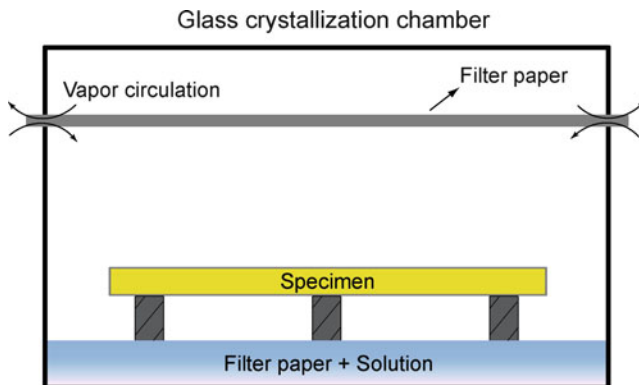


Fig. 6.30 Schematic of a glass recrystallization chamber used for tubules formation. The filter paper placed at the bottom of the chamber was wetted with 20 mL of the solvent, and slow evaporation of the solvent was provided by placing a thin filter paper between the glass body and the cap placed above. The total volume of the chamber is about 200 cm³ (Bhushan et al., 2009b)

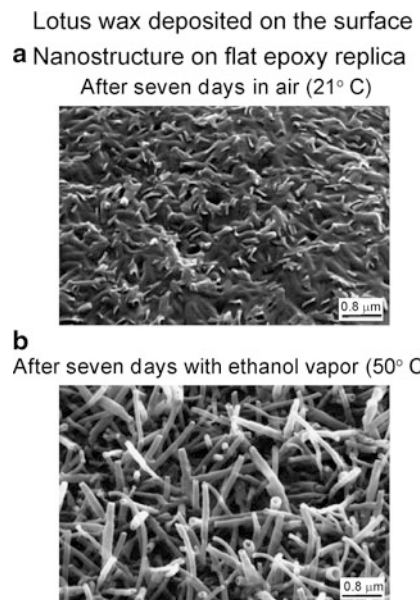


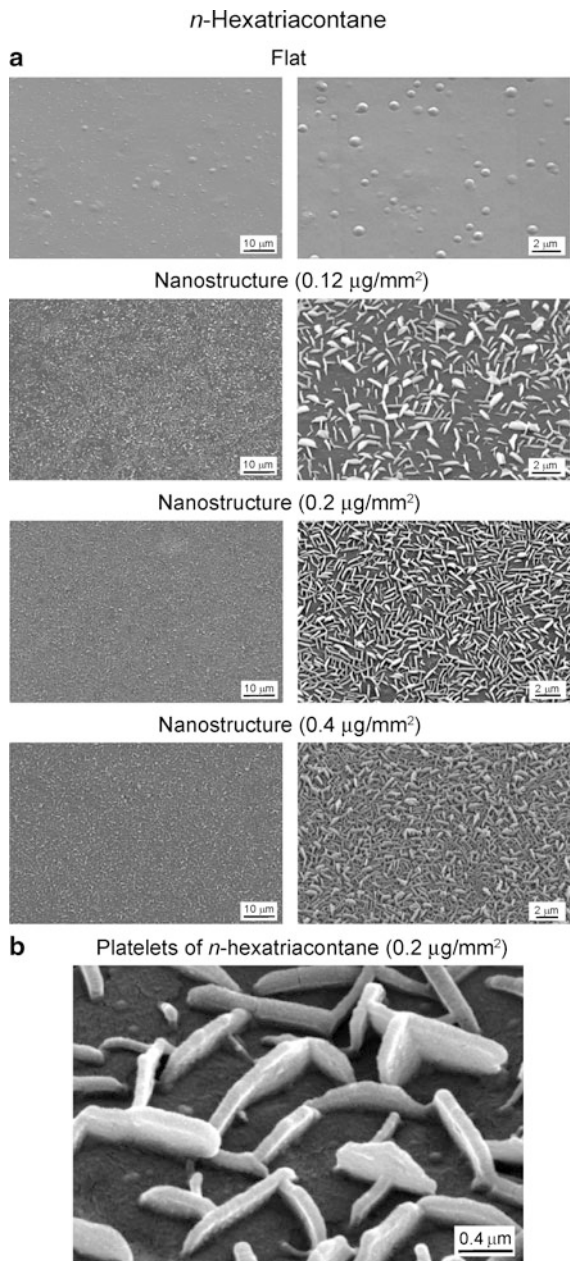
Fig. 6.31 SEM micrographs of morphology of the Lotus wax deposited on the flat epoxy replica surface after two treatments of specimens measured at 45° tilt angle, (a) after 7 days at 21° C (top), nanostructure on flat epoxy replica was found with no tubules, and (b) after seven days at 50° C with ethanol vapor (bottom), tubular nanostructures with random orientation were found on the surface (Koch et al., 2009)

6.6.1 Effect of Nanostructures with Various Wax Platelet Crystal Densities on Superhydrophobicity

Nanostructures with various wax platelet crystal densities were fabricated to study the effect of crystal density on superhydrophobicity. Figure 6.32a shows the SEM micrographs of a flat surface and nanostructures fabricated with various masses of *n*-hexatriacontane (Bhushan et al., 2008a). The nanostructure is formed by 3-D platelets of *n*-hexatriacontane, as shown in detail in Fig. 6.32b. Platelets are flat crystals, grown perpendicular to the substrate surface. They are randomly distributed on the surface, and their shapes and sizes show some variations. Some of the single platelets are connected to their neighboring crystals at their lateral ends. This arrangement leads to a kind of cross-linking of the single platelets. As shown in Fig. 6.32b, and based on additional specimens, the platelet thickness varied between 50 and 100 nm, and their length varied between 500 and 1,000 nm. The self-assembly of *n*-hexatriacontane and most other long-chain hydrocarbons leads to layered structures with a lamellae order. In these structures, the molecular axis is orientated parallel to the substrate surface. The growth of these layers results in an ordered, crystalline 3-D structure (Dorset et al., 1983). The created nanostructures are comparable to the wax crystal morphology found on superhydrophobic leaves, for example, *Colocasia esculenta* (Neinhuis and Barthlott, 1997) and *Triticum aestivum* (wheat) (Koch et al., 2006). SEM micrographs of the nanostructures fabricated with three different masses of *n*-hexatriacontane show different densities of crystals. An AFM was used to characterize the nanostructures. Statistical parameters of nanostructures [root mean square (RMS) height, peak to valley height, and summit density (η)] (Bhushan, 1999, 2002) were calculated and are presented in Table 6.3. A summit is defined as a point whose height is greater than its four nearest neighboring points above a threshold value of 10% of RMS height to avoid measurement errors. The measurement results were reproducible within $\pm 5\%$.

To study the effect of nanostructures with different crystal density on superhydrophobicity, static contact angle, contact angle hysteresis and tilt angle, and adhesive forces were measured (Bhushan et al., 2008a). For contact angle hysteresis, the advancing and receding contact angles were measured at the front and back of the droplet moving along the tilted surface, respectively. The data are shown in Fig. 6.33. The static contact angle of a flat surface coated with a film of *n*-hexatriacontane was 91° . It showed a contact angle hysteresis of 87° , and the droplet still adhered at a tilt angle of 90° . Nanostructuring of flat surfaces with *n*-hexatriacontane platelets creates superhydrophobic surfaces with a high static contact angle and a reduction of contact angle hysteresis and tilt angle. The values are a function of crystal density. Figure 6.34 shows a plot of static contact angle and contact angle hysteresis as a function of the mass of *n*-hexatriacontane deposited. As the mass of *n*-hexatriacontane increased, the static contact angle first increased and the contact angle hysteresis decreased. Then, above a mass of $0.2 \mu\text{g}/\text{mm}^2$, static contact angle and contact angle hysteresis gradually decreased and increased with increasing mass, respectively. The highest static contact angle and lowest contact

Fig. 6.32 SEM micrographs taken at 45° tilt angle (shown using two magnifications) of (a) the flat surface and nanostructures fabricated with various mass of *n*-hexatriacontane and (b) 3-D platelets forming nanostructures on the surface fabricated with 0.2 µg/mm² mass of *n*-hexatriacontane. All samples are fabricated with epoxy resin coated with *n*-hexatriacontane ([Bhushan et al., 2008a](#))



angle hysteresis are 158° and 23° at a mass of 0.2 µg/mm². As shown in Fig. 6.33, the adhesive force measured using a 15 µm radius borosilicate tip in an AFM also shows a similar trend as the wetting properties. Adhesive forces of the nanostructured surfaces were lower than for the flat surface because the contact between the

Table 6.3 Roughness statistics for a nanostructured surface measured using an AFM (scan size $10\text{ }\mu\text{m} \times 10\text{ }\mu\text{m}$)

	RMS height (nm)	Peak to valley height (nm)	η (/sq. μm)
<i>n</i> -Hexatriacontane			
Nanostructure ($0.12\text{ }\mu\text{g}/\text{mm}^2$)	46	522	0.78
Nanostructure ($0.2\text{ }\mu\text{g}/\text{mm}^2$)	65	663	1.39
Nanostructure ($0.4\text{ }\mu\text{g}/\text{mm}^2$)	82	856	1.73
<i>Tropaeolum majus</i> wax			
Nanostructure ($0.8\text{ }\mu\text{g}/\text{mm}^2$)	180	1,570	0.57
<i>Lotus</i> wax			
Nanostructure ($0.8\text{ }\mu\text{g}/\text{mm}^2$)	187	1,550	1.47

Nanostructures were fabricated with *n*-hexatriacontane, *T. majus*, and Lotus waxes (Bhushan et al., 2008a, 2009c; Koch et al., 2009)

RMS root mean square

η —summit density

tip and surface was lower than on the flat surface, because the contact between the tip and surface was reduced by surface structuring (Bhushan, 1999, 2002).

In order to identify wetting regimes (Wenzel or Cassie–Baxter) as well as to understand the effect of crystal density on the propensity of air pocket formation for the nanostructured surfaces, roughness factor (R_f) and fractional liquid–air interface (f_{LA}) are needed. The R_f for the nanostructures was calculated using the AFM map (Burton and Bhushan, 2006; Bhushan and Jung, 2006). The calculated results were reproducible within $\pm 5\%$. The R_f for the nanostructured surfaces with masses of 0.12 , 0.2 , and $0.4\text{ }\mu\text{g}/\text{mm}^2$ were found to be 3.4 , 4.9 , and 6.8 , respectively. For calculation of f_{LA} of the nanostructures, only the higher crystals are assumed to come in contact with a water droplet. The fractional geometrical area of the top surface for the nanostructures was calculated from SEM micrographs with top view (0° tilt angle). The SEM images were converted to high contrast black and white images using Adobe Photoshop. The increase of contrast in the SEM image eliminates the smaller platelet structures, which were visible in the original SEM image. The higher crystals led to white signals in the SEM figure. The fractional geometrical area of the top nanostructured surfaces with masses of 0.12 , 0.2 , and $0.4\text{ }\mu\text{g}/\text{mm}^2$ was found to be 0.07 , 0.15 , and 0.24 , leading to f_{LA} of 0.93 , 0.85 , and 0.76 , respectively. The calculated results were reproducible within $\pm 5\%$. The values of static contact angle in the Wenzel and Cassie–Baxter regimes for the nanostructured surfaces were calculated using the values of R_f and f_{LA} and presented in Fig. 6.33. The values of contact angle hysteresis in Cassie–Baxter regimes for various surfaces were calculated using (3.20). The data are presented in Fig. 6.33.

As shown in Fig. 6.33, the experimental static contact angle and contact angle hysteresis values for the two nanostructured surfaces with 0.2 and $0.4\text{ }\mu\text{g}/\text{mm}^2$ were comparable to the calculated values in the Cassie–Baxter regime. The results suggest that a droplet on two nanostructured surfaces should exist in the Cassie–Baxter regime. However, the experimental static contact angle and contact angle

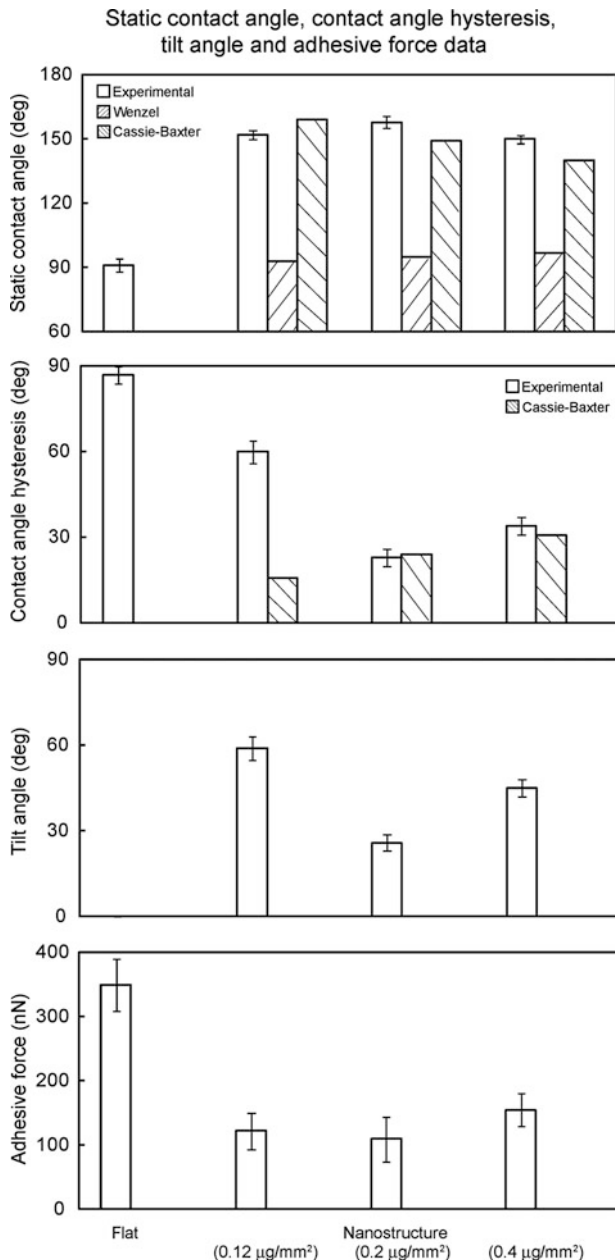


Fig. 6.33 Bar chart showing the measured static contact angle, contact angle hysteresis, and tilt angle; also shown are calculated static contact angles obtained using Wenzel and Cassie–Baxter equations with a given value of θ_0 and calculated contact angle hysteresis using Cassie–Baxter equation on flat surface and nanostructures fabricated with various mass of *n*-hexatriacontane. The droplet on flat surface does not move along the surface even at tilt angle of 90°. The bar chart also shows adhesive forces for various structures, measured using a 15 µm radius borosilicate tip (Bhushan et al., 2008a)

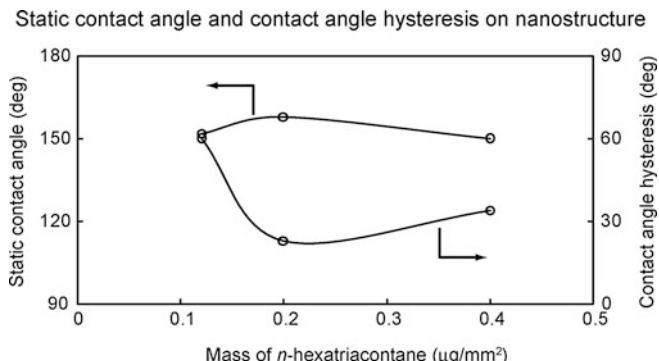


Fig. 6.34 Static contact angle and contact angle hysteresis as a function of mass of *n*-hexatriacontane deposited on nanostructures (Bhushan et al., 2008a)

hysteresis values for the nanostructured surface with $0.12 \mu\text{g}/\text{mm}^2$ were lower and higher than the calculated values in Cassie–Baxter regime, respectively. It is believed that neighboring crystals are separated at lower crystal density, and any trapped air can be squeezed out, whereas neighboring crystals are interconnected at higher densities and air remains trapped. At highest crystal density at a mass of $0.4 \mu\text{g}/\text{mm}^2$, there is less open volume compared to that at $0.2 \mu\text{g}/\text{mm}^2$, and that explains a droplet static contact angle going from 158° to 150° (Bhushan et al., 2008a).

6.6.2 Effect of Hierarchical Structure with Wax Platelets on the Superhydrophobicity

Bhushan et al. (2008b, 2009d) created surfaces with *n*-hexatriacontane of $0.2 \mu\text{g}/\text{mm}^2$ to study the influence of hierarchical structure on superhydrophobicity. Figure 6.35 shows the SEM micrographs of a flat surface and nano-, micro-, and hierarchical structures. To study the effect of structure on superhydrophobicity, static contact angle, contact angle hysteresis and tilt angle, and adhesive forces of the four structures were measured. The data are shown in Fig. 6.36. The static contact angle of a flat surface coated with a film of *n*-hexatriacontane was 91° and increased to 158° when *n*-hexatriacontane formed a nanostructure of platelets on it. The static contact angle on a flat specimen with a microstructure was 154° , but it increased to 169° for the hierarchical surface structure. Contact angle hysteresis and tilt angle for flat, micro-, and nanostructured surfaces show similar trends. The flat surface showed a contact angle hysteresis of 87° , and the droplet still adhered at a tilt angle of 90° . The superhydrophobic micro- and nanostructured surfaces showed a reduction of contact angle hysteresis and tilt angle, but a water droplet still needs a tilt angle of 26° and 51° , respectively, before sliding. Only the hierarchical surface

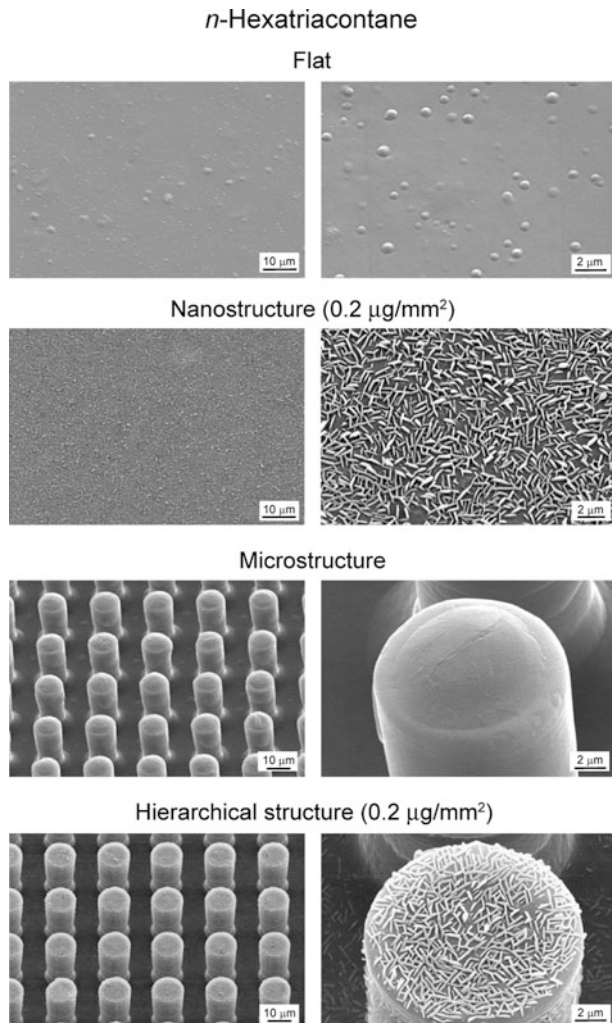


Fig. 6.35 SEM micrographs of the flat surface, nanostructure, microstructure, and hierarchical structure measured at 45° tilt angle (shown using two magnifications). All samples are fabricated with epoxy resin coated with *n*-hexatriacontane ([Bhushan et al., 2008b](#))

structure with static contact angle of 169° and low contact angle hysteresis of 2° exceeds the basic criteria for superhydrophobic and self-cleaning surfaces ([Bhushan and Jung, 2008](#)). Adhesive force measured using a $15 \mu\text{m}$ radius borosilicate tip in an AFM also shows a similar trend as the wetting properties. Adhesion force of the hierarchical surface structure was lower than that of both micro- and nanostructured surfaces because the contact between the tip and surface was lower as a result of contact area being reduced ([Bhushan, 1999, 2002](#)).

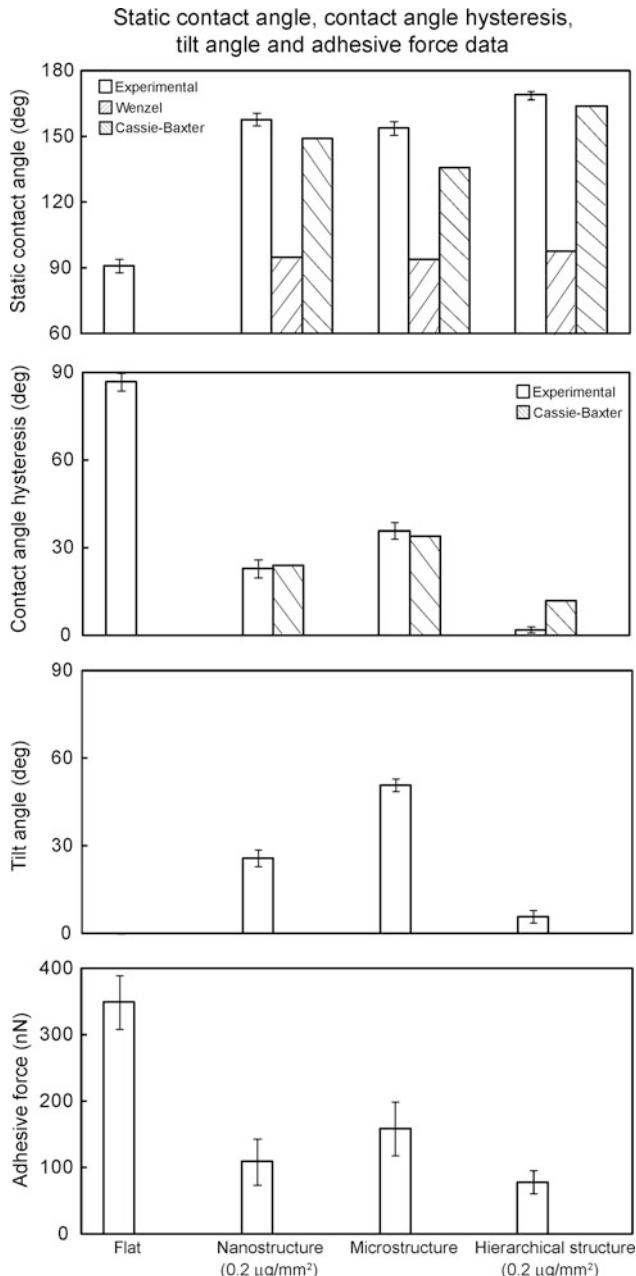


Fig. 6.36 Bar chart showing the measured static contact angle, contact angle hysteresis, and tilt angle; also shown are calculated static contact angles obtained using Wenzel and Cassie–Baxter equations with a given value of θ_0 and calculated contact angle hysteresis using Cassie–Baxter equation on various structures. The droplet on flat surface does not move along the surface even at tilt angle of 90° . The bar chart also shows adhesive forces for various structures, measured using a $15 \mu\text{m}$ radius borosilicate tip (Bhushan et al., 2008b)

Table 6.4 Summary of static contact angles and contact angle hysteresis measured and calculated for droplets in the Wenzel regime and the Cassie–Baxter regime on the various surfaces with *n*-hexatriacontane using the calculated values of R_f and f_{LA} (Bhushan et al., 2008b, 2009d)

R_f	f_{LA}	Static contact angle (deg)			Contact angle hysteresis (deg)	
		Measured	Calculated in Wenzel regime	Calculated in Cassie– Baxter regime	Measured	Calculated in Cassie– Baxter regime
Flat		91			87 ^a	
Nanostructure	4.9	0.85	158	95	23	24
Microstructure	3.5	0.71	154	94	36	34
Hierarchical structure	8.4	0.96	169	98	2	12

^aAdvancing and receding contact angles are 141° and 54°, respectively

In order to identify wetting regimes (Wenzel or Cassie–Baxter) for the various surfaces, roughness factor (R_f) and fractional liquid–air interface (f_{LA}) are needed. The R_f for the nanostructure was described earlier. The R_f for the microstructure was calculated for the geometry of flat-top, cylindrical pillars of diameter D , height H , and pitch P distributed in a regular square array. For this case, the roughness factor for the microstructure, $(R_f)_{\text{micro}} = (1 + \pi DH/P^2)$. The roughness factor for the hierarchical structure is the sum of $(R_f)_{\text{micro}}$ and $(R_f)_{\text{nano}}$. The values calculated for various surfaces are summarized in Table 6.4.

For the calculation of f_{LA} , the following assumptions are made. For the microstructure, consider that a droplet in size much larger than the pitch P contacts only the flat-top of the pillars in the composite interface, and the cavities are filled with air. For microstructure, fractional flat geometrical area of the liquid–air interface under the droplet, $(f_{LA})_{\text{micro}} = (1 - \pi D^2/4P^2)$ (Bhushan and Jung, 2008). The fractional geometrical area of the top surface for the nanostructure was described earlier. For the hierarchical structure, the fractional flat geometrical area of the liquid–air interface, $(f_{LA})_{\text{hierarchical}} = 1 - (\pi D^2/4P^2)[1 - (f_{LA})_{\text{nano}}]$. The values of contact angle hysteresis in Cassie–Baxter regimes for various surfaces were calculated using (3.20). The values are summarized in Table 6.4.

The values of static contact angle in the Wenzel and Cassie–Baxter regimes for various surfaces were calculated using the values of R_f and f_{LA} (Table 6.4). As shown in Fig. 6.36, the experimental static contact angle values for the three structured surfaces were larger than the calculated values in the Cassie–Baxter regime. The results suggest that the droplets on three of the structured surfaces were in the Cassie–Baxter regime. This indicates that the microstructure and nanostructure surface induce air pocket formation. For the contact angle hysteresis, there is a good agreement between the experimental data and the theoretically predicted values for the Cassie–Baxter regime. These results show that air pocket formation in the micro- and nanostructure decreases the solid–liquid contact (Koch et al., 2009). In hierarchical structured surfaces, the air pocket formation further decreases the solid–liquid contact and thereby reduces contact angle hysteresis and tilt angle (Bhushan et al., 2008b, 2009d).

6.6.3 Effect of Hierarchical Structure with Wax Tubules on Superhydrophobicity

6.6.3.1 *T. majus* Tubules

Figure 6.37a shows the SEM micrographs of the nanostructure and hierarchical structure fabricated with two different masses (0.6 and $0.8 \mu\text{g}/\text{mm}^2$) of *T. majus* wax (Bhushan et al., 2009c). SEM micrographs show an increase in the tubule amount on the flat and microstructure surfaces after deposition of higher masses of wax. The tubules of *T. majus* wax grown in an ethanol atmosphere are comparable to the wax morphology found on the leaves of *T. majus*. Surfaces show a homogenous distribution of the wax mass on the specimen surfaces, and tubules provide the desired nanostructure of 3-D tubules on the flat and microstructure surfaces. The tubule morphology of *T. majus* wax is shown in detail in Fig. 6.37b. The tubular crystals are hollow structures, randomly orientated on the surface and embedded into an amorphous wax layer. They are randomly distributed on the surface, and their shapes and sizes show some variations. As shown in Fig. 6.37b, and based on additional specimens, the tubular diameter varied between 100 and 300 nm and their length varied between 300 and $1,200 \text{ nm}$.

AFM was used to characterize the nanostructure fabricated using *T. majus* wax of $0.8 \mu\text{g}/\text{mm}^2$ after storage at 50°C with ethanol vapor (Bhushan et al., 2009c). Statistical parameters of the nanostructure [root mean square (RMS) height, peak to valley height, and summit density (η)] were calculated and are presented in Table 6.3 (Bhushan, 1999, 2002). A summit is defined as a point whose height is greater than that of its four nearest neighboring points above a threshold value of 10% of RMS height to avoid measurement errors. The measurement results were reproducible within $\pm 5\%$.

To study the effect of structures with various length scales on superhydrophobicity, static contact angle, contact angle hysteresis and tilt angle, and adhesive forces of the four structures produced using *T. majus* wax were measured (Bhushan et al., 2009c). Nanostructures formed on the flat and microstructured surfaces were fabricated using *T. majus* wax of $0.8 \mu\text{g}/\text{mm}^2$ after storage at 50°C with ethanol vapor. The data are shown in Fig. 6.38. The static contact angle of a flat surface coated with a film of *T. majus* wax was 112° , and increased to 164° when *T. majus* wax formed a nanostructure of tubules on it. On the flat specimen with a microstructure on it, the static contact angle was 154° but increased to 171° for the hierarchical surface structure. Contact angle hysteresis and tilt angle for flat, micro-, and nanostructured surfaces show similar trends. The flat surface showed a contact angle hysteresis of 61° and a tilt angle of 86° . The microstructured surface shows a reduction of contact angle hysteresis and tilt angle, but a water droplet still needs a tilt angle of 31° before sliding. As tubules are formed on the flat and microstructured surfaces, the nanostructured and hierarchical structure surfaces have low contact angle hysteresis of 5° and 3° , respectively. These properties are superior to plant leaves, including Lotus leaves. Adhesive force measured using a $15 \mu\text{m}$ radius

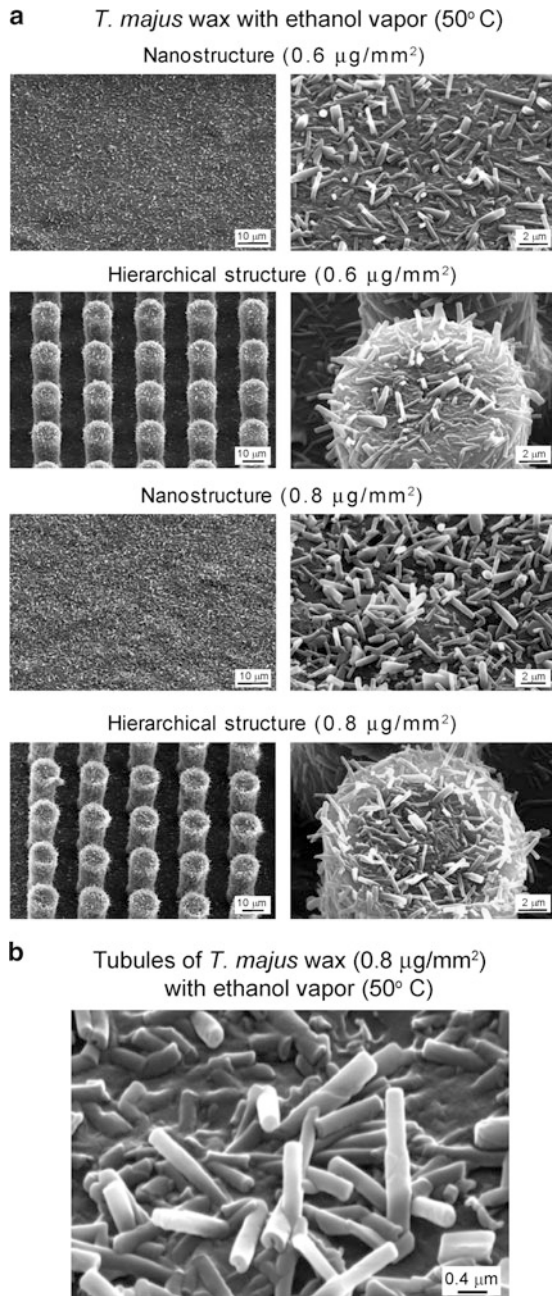


Fig. 6.37 SEM micrographs taken at 45° tilt angle (shown using two magnifications) of (a) the nanostructure and hierarchical structure fabricated with two different mass (0.6 and $0.8 \mu\text{g}/\text{mm}^2$) of *T. majus* wax after storage at 50°C with ethanol vapor and (b) 3-D tubules forming nanostructures on the surface fabricated with $0.8 \mu\text{g}/\text{mm}^2$ mass of *T. majus* wax after storage at 50°C with ethanol vapor (Bhushan et al., 2009c)

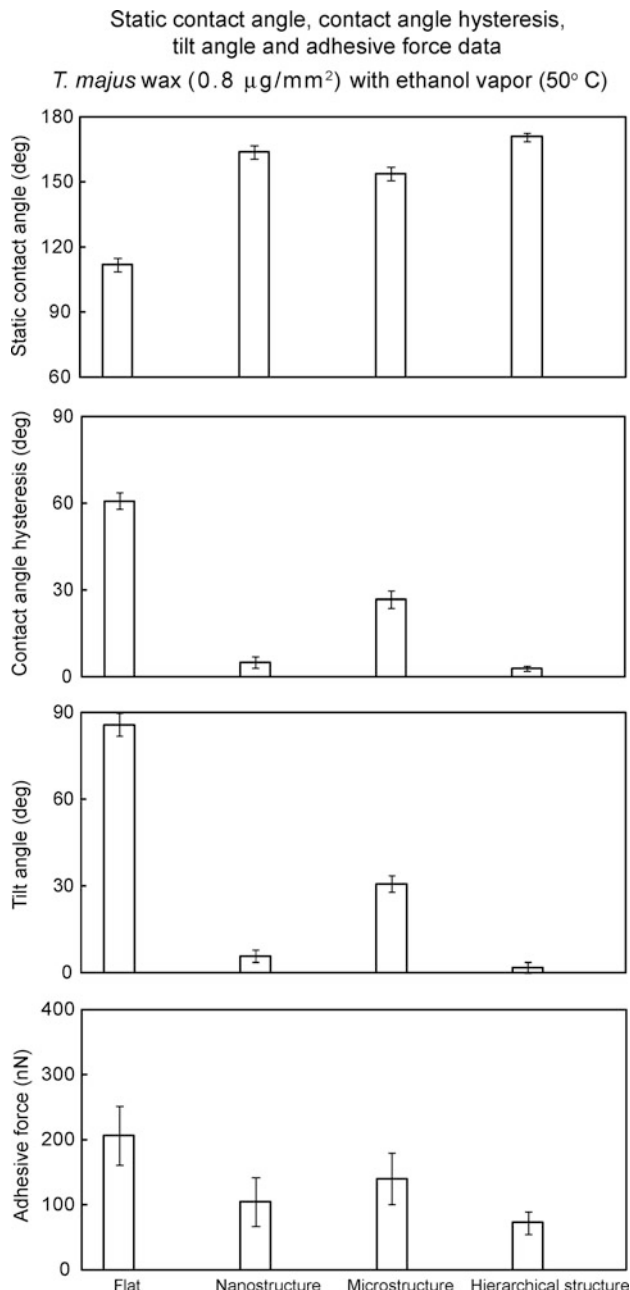


Fig. 6.38 Bar chart showing the measured static contact angle, contact angle hysteresis, and tilt angle on various structures fabricated with $0.8 \mu\text{m}/\text{mm}^2$ mass of *T. majus* wax after storage at 50°C with ethanol vapor. The bar chart also shows adhesive forces for various structures, measured using a $15 \mu\text{m}$ radius borosilicate tip (Bhushan et al., 2009c)

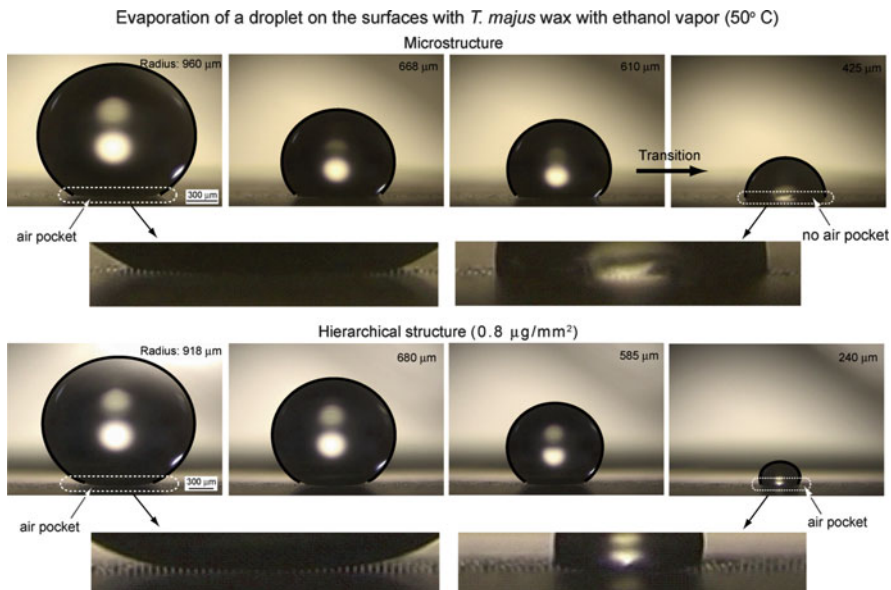


Fig. 6.39 Evaporation of a droplet on a microstructured and hierarchical structured surfaces fabricated with $0.8 \mu\text{m}/\text{mm}^2$ mass of *T. majus* wax after storage at 50°C with ethanol vapor. The initial radius of the droplet was about $950 \mu\text{m}$, and the time interval between first two photos was 180 s and between the latter was 60 s. As the radius of droplet reached $425 \mu\text{m}$ (foot print = $836 \mu\text{m}^2$) on the microstructured surface, the transition from Cassie–Baxter regime to Wenzel regime occurred, as indicated by the arrow. On the hierarchical structured surface, air pockets, visible at the bottom area of the droplet, exist until the droplet evaporated completely (Bhushan et al., 2009b)

borosilicate tip in an AFM also show a similar trend as the wetting properties. Adhesion force of the hierarchical surface structure was lower than that of micro- and nanostructured surfaces because the contact between the tip and surface was lower as a result of contact area being reduced (Bhushan, 1999, 2002).

To further verify the effect of hierarchical structure on the propensity of air pocket formation, Bhushan et al. (2009c) performed evaporation experiments with a droplet on a microstructure and hierarchical structure fabricated with $0.8 \mu\text{m}/\text{mm}^2$ mass of *T. majus* wax with ethanol vapor at 50°C . Figure 6.39 shows the successive photos of a droplet evaporating on the two structured surfaces. On the microstructured surface, the light passes below the droplet and air pockets can be seen, so to start with the droplet is in the Cassie–Baxter regime. When the radius of the droplet decreased to $425 \mu\text{m}$, the air pockets are not visible anymore and the droplet is in the Wenzel regime. This transition results from an impalement of the droplet in the patterned surface, characterized by a smaller contact angle. For the hierarchical structure, an air pocket was clearly visible at the bottom area of the droplet throughout, and the droplet was in a hydrophobic state until the droplet evaporated completely. This suggests that a hierarchical structure with nanostructures prevents liquid from filling the gaps between the pillars.

6.6.3.2 Lotus Tubules

For the development of nanostructures by tubule formation, Lotus wax was used (Koch et al., 2009). Figure 6.40a shows the scanning electron microscope (SEM) micrographs of flat surfaces with the tubules nanostructure. The microstructures shown in Fig. 6.40b are the Lotus leaf and the micropatterned Si replica covered with a Lotus wax film. Hierarchical structures were fabricated with microstructured Lotus leaf replicas and micropatterned Si replicas covered with a nanostructure of Lotus wax tubules, as shown in Fig. 6.40c. SEM micrographs show an overview (left column), a detail in higher magnification (middle column), and a large magnification of the created flat wax layers and tubules nanostructures (right column). The grown tubules provide the desired nanostructure on flat and microstructured surfaces. The recrystallized Lotus wax shows tubular hollow structures, with random orientation on the surfaces. Their shapes and sizes show only a few variations. The tubular diameter varied between 100 and 150 nm, and their length varied between 1,500 and 2,000 nm. Atomic force microscopy (AFM) was used to characterize the nanostructure of the Lotus wax tubules. The statistical parameters of the nanostructure [root mean square (RMS) height, peak to valley height, and summit density (η)] were calculated and are presented in Table 6.3.

To study the effect of Lotus wax tubule nanostructures on superhydrophobicity, static contact angle, contact angle hysteresis, and tilting angle were measured on flat, microstructured Lotus replica, micropatterned Si replica, and hierarchical surfaces. Hierarchical surfaces were made of the Lotus leaf replica and micropatterned Si replica with a nanostructure of wax tubules on top. Additionally, fresh Lotus leaves were investigated to compare the properties of the fabricated structures with the original biological model.

Figure 6.41 shows that the highest static contact angles of 173°, lowest contact angle hysteresis of 1°, and tilting angle varying between 1° and 2° were found for the hierarchical structured Si replica. The hierarchical structured Lotus leaf replica showed a static contact angle of 171° and the same contact angle hysteresis (2°) and tilt angles of 1–2° as the hierarchical Si replica. The fresh Lotus leaf surface investigated here showed a static contact angle of 164°, contact angle hysteresis of 3°, and a tilting angle of 3° which suggests that, the artificial hierarchical surfaces showed higher static contact angle and lower contact angle hysteresis. Structural differences between the original Lotus leaf and the artificial Lotus leaf produced here are limited to a difference in wax tubules length, which are 0.5–1 μm longer in the artificial Lotus leaf (Koch et al., 2009).

The melting of the wax led to a flat surface with a flat wax film with a much lower static contact angle (119°), a higher contact angle hysteresis (71°), and a high tilting angle of 66°. The data of a flat Lotus wax film on a flat replica show that the Lotus wax by itself is hydrophobic. The data demonstrate that the native, flat wax of Lotus leaves, with a static contact angle of 119°, is hydrophobic and can turn superhydrophobic (167°) by increasing the surface roughness after self-assembly into 3-D wax tubules. The static contact angle of the Lotus wax film is 119°, which

Lotus wax ($0.8 \mu\text{g}/\text{mm}^2$) after seven days with ethanol vapor (50°C)

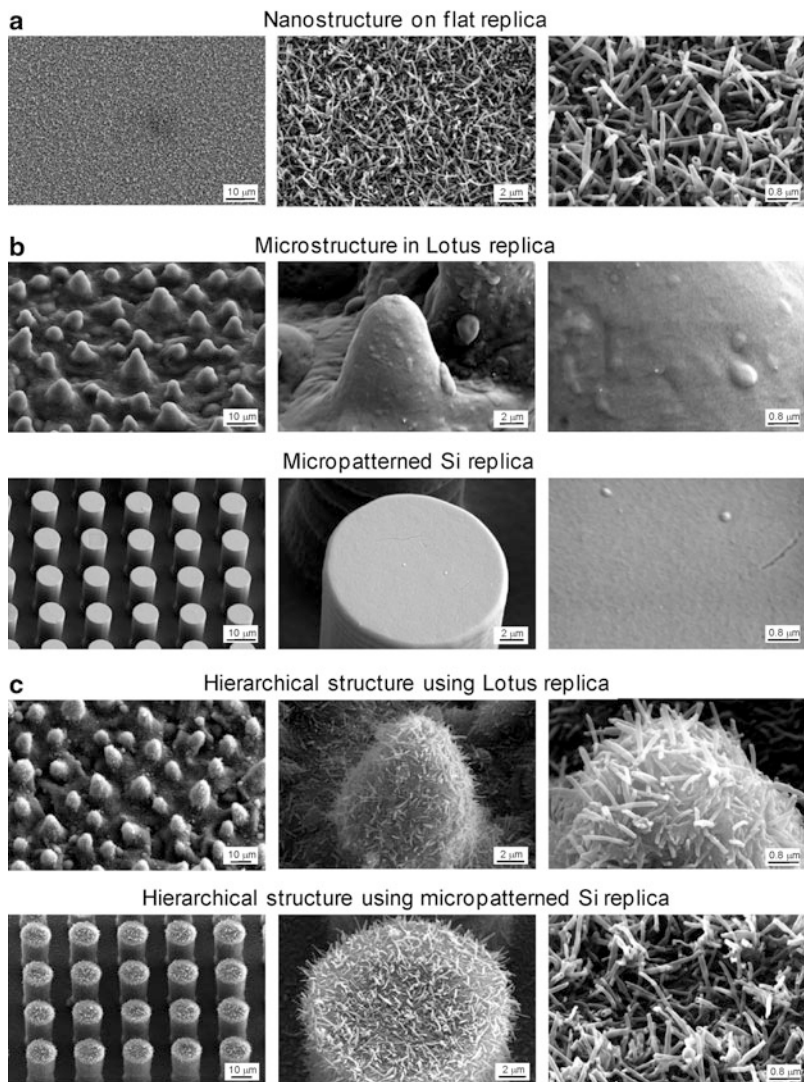


Fig. 6.40 SEM micrographs taken at 45° tilt angle (shown using three magnifications) of (a) nanostructure on flat replica, (b) microstructures in Lotus replica and micropatterned Si replica, and (c) hierarchical structure using Lotus and micropatterned Si replicas. Nano- and hierarchical structures were fabricated with mass $0.8 \mu\text{g}/\text{mm}^2$ of Lotus wax after storage for 7 days at 50°C with ethanol vapor. Flat epoxy resin and microstructure were covered with flat Lotus wax (Koch et al., 2009)

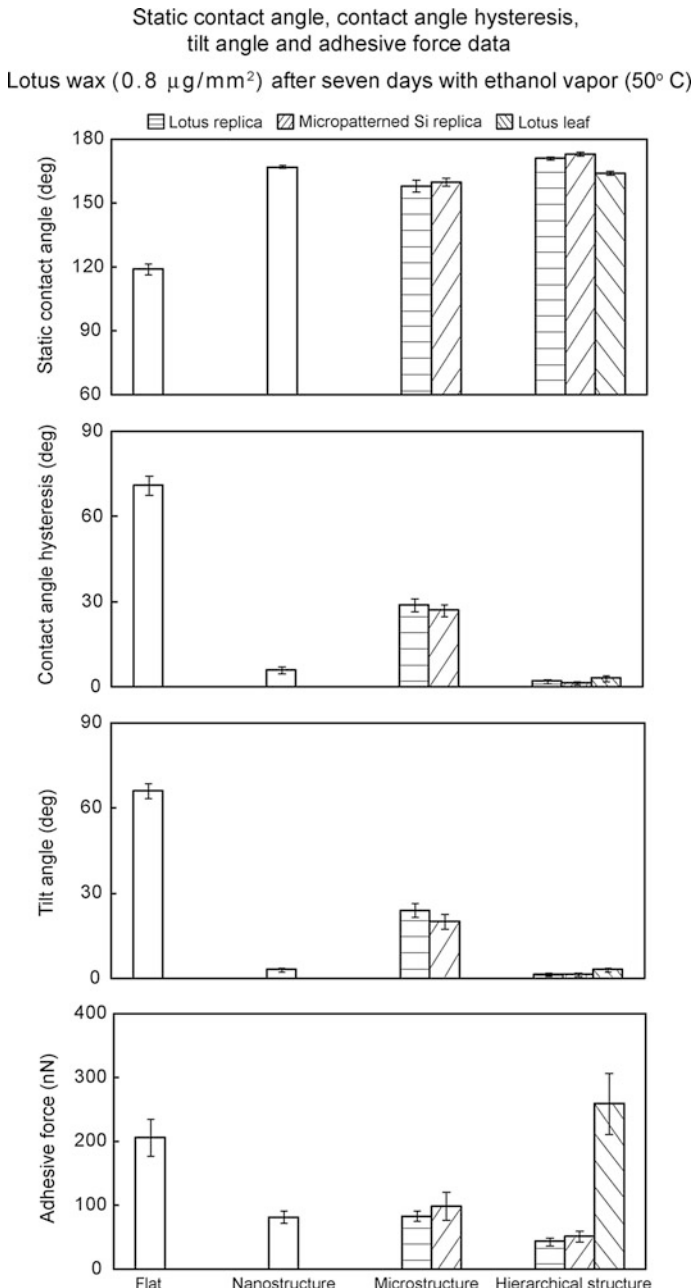


Fig. 6.41 Bar chart showing the measured static contact angle, contact angle hysteresis, and tilt angle on various structures fabricated with $0.8 \mu\text{g}/\text{mm}^2$ of Lotus wax after storage for 7 days at 50°C with ethanol vapor. The bar chart also shows adhesive forces for various structures, measured using a $15 \mu\text{m}$ radius borosilicate tip. The error bar represents ± 1 standard deviation (Koch et al., 2009)

is higher than that of the wax film made of *T. majus* of 112°. However, films made of *n*-hexatriacontane showed static contact angles of only 91°. SEM investigations, made directly after contact angle measurements, revealed no morphological differences between these films. Based on the chemical composition, it should be assumed that the nonpolar *n*-hexatriacontane molecules are more hydrophobic than the plant waxes, which contain high amounts of oxygen atoms. At this point, these differences cannot be explained by structural or chemical differences of the films but will be of interest for further studies.

Adhesive force measured using a 15 μm radius borosilicate tip in an AFM also shows a similar trend as the wetting properties for the artificial surfaces (Fig. 6.41) (Koch et al., 2009). Adhesion force of the hierarchical surface structure was lower than that of micro- and nanostructured and flat surfaces because the contact between the tip and surface was lower as a result of the contact area being reduced. However, for the fresh Lotus leaf, there is moisture within the plant material, which causes softening of the leaf, and so when the tip comes into contact with the leaf sample, the sample deforms and a larger area of contact between the tip and sample causes an increase in the adhesive force (Bhushan, 1999, 2002).

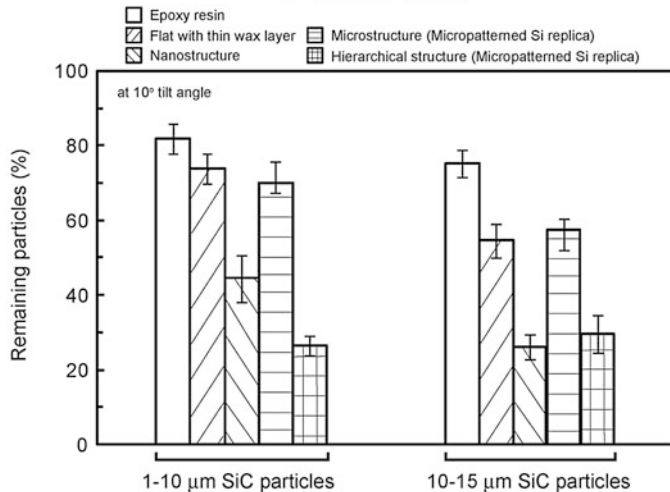
6.6.4 Self-Cleaning Efficiency of Hierarchical Structured Surfaces

For deposition of contamination on artificial surfaces, various structures were placed in a contamination glass chamber (Bhushan et al., 2009a). Silicon carbide (SiC) (Guillaume, Germany) particles in two different sizes ranges of 1–10 μm and 10–15 μm were used as the contaminants. The SiC particles have been chosen because of their similarity in shape, sizes, and hydrophilicity to natural dirt contaminants. The number of particles per area was determined by counting them from a 280 μm × 210 μm image taken by an optical microscope with a camera before and after water cleaning.

For the cleaning test, the specimens with the contaminants were subjected to water droplets of approximately 2 mm diameter, using two microsyringes (Bhushan et al., 2009a). In order to obtain a relative measure of the self-cleaning ability of hierarchical structures which exhibit the lowest contact angle hysteresis and tilt angle as compared to other structures (flat, nanostructures, and microstructures), the tilt angle chosen for the cleaning tests was slightly above the tilt angle for the hierarchical structures. Thus, experiments were performed with 10° for surfaces covered with *n*-hexatriacontane and 3° for surfaces with Lotus wax. The water cleaning test was carried out for 2 min (water quantity, 10 mL) with nearly zero kinetic energy of droplets. For watering with nearly zero kinetic energy, the distance between the microsyringes and surface was set to 0.005 m (nearly zero impact velocity). The chosen impact velocity represents a low value compared to a natural rain shower, where a water droplet of 2 mm diameter can reach an impact velocity of 6 m/s (measured under controlled conditions) (van Dijk et al., 2002).

Self-cleaning experiments using two different particle sizes

n-Hexatriacontane



Lotus wax

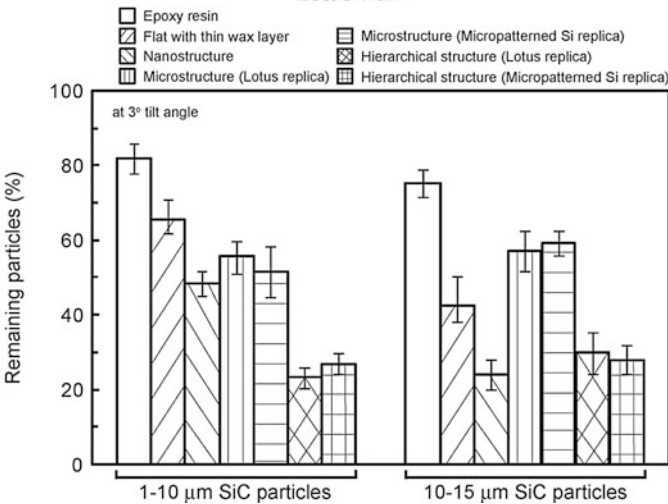


Fig. 6.42 Bar charts showing the remaining particles after applying droplets with nearly zero kinetic energy on various structures fabricated using *n*-hexatriacontane and Lotus wax using 1–10 μm and 10–15 μm SiC particles. The experiments on the surfaces with *n*-hexatriacontane and Lotus wax were carried out on tilted stages with 10° and 3°, respectively. The error bars represent ± 1 standard deviation (Bhushan et al., 2009a)

The cleaning tests were performed on various surfaces with *n*-hexatriacontane and Lotus wax (Bhushan et al., 2009a). The data represent the average of five different investigated areas for each experiment. Figure 6.42 shows that none of the investigated surfaces was fully cleaned by water rinsing. For Lotus wax,

which forms tubule nanostructures, and *n*-hexatriacontane, which forms platelet nanostructures, the same tendency of particle removal was found. With the exception of hierarchical structure on all surfaces, larger particles were removed more than small ones. Most particles (70–80%) remained on smooth surfaces, and 50–70% of particles were found on microstructured surfaces. Most particles were removed from the hierarchical structured surfaces, but ~30% of particles remained. A clear difference in particle removal, independent of particle sizes, was only found in flat and nanostructured surfaces where larger particles were removed with higher efficiency. Observations of the droplet behavior during the movement on the surfaces showed that droplets were rolling only on the hierarchical structured surfaces. On flat, micro-, and nanostructured surfaces, the droplets first applied were not moving, but the continuous application of water droplets increased the droplet volumes and led to a sliding of these large droplets. During this, some of the particles had been removed from the surfaces. However, the rolling droplets on hierarchical structures did not collect the dirt particles trapped in the cavities of the microstructures. The data clearly shows that hierarchical structures have superior cleaning efficiency.

6.6.5 Observation of Transition During the Bouncing Droplet

To observe how the impact velocity influences the transition from the composite solid–air–liquid interface to the homogeneous solid–liquid interface during droplet impact, [Jung and Bhushan \(2008b, 2009a\)](#) performed bouncing droplet experiments on various surfaces with *n*-hexatriacontane and *T. majus* and Lotus waxes. Figure 6.43 shows snapshots of a droplet of 1 mm radius hitting various surfaces fabricated with 0.2 and 0.4 $\mu\text{m}/\text{mm}^2$ of *n*-hexatriacontane after storage at room temperature. The impact velocity was obtained just prior to the droplet hitting the surface. First, on the flat surface, it was found that the droplet did not bounce off even though the impact velocity applied was up to 1.5 m/s. As shown in the images in the first row for each nano-, micro-, and hierarchical structured surface, the droplet hitting the surface under an impact velocity of 0.44 m/s first deformed and then retracted, and bounced off the surface. Finally, the droplet sat on the surface and had a high contact angle, which suggests the formation of a solid–air–liquid interface. Next, the impact experiment was repeated by increasing the impact velocity. As shown in the second row of images for the nanostructure ($0.4 \mu\text{g}/\text{mm}^2$) and microstructure, bounce off did not occur, and the wetting of the surface (and possibly pinning of droplet) occurred at impact velocities of 1.2 and 0.77 m/s, respectively, referred to as the critical impact velocity. This is because air pockets do not exist below the droplet as a result of droplet impalement by the structures, characterized by a smaller contact angle. These observations indicate the transition from the composite interface to the homogenous interface. However, as shown in the second row of images for the nanostructure ($0.2 \mu\text{g}/\text{mm}^2$) and hierarchical structure, during applying impact velocity of up to 1.5 m/s, the bounce off always occurred and the wetting of the surface did not occur.

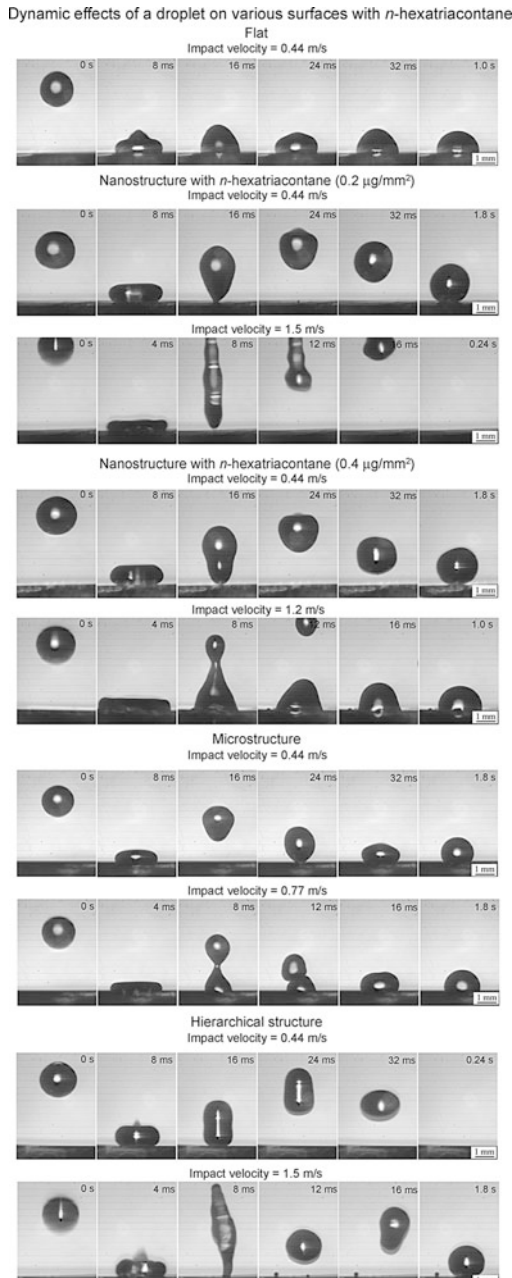


Fig. 6.43 Snapshots of a droplet with 1 mm radius hitting various surfaces fabricated with 0.2 and $0.4 \mu\text{g}/\text{mm}^2$ of *n*-hexatriacontane after storage at room temperature. The impact velocity was obtained just prior to the droplet hitting the surface. The pinning of droplet on the nanostructure with $0.4 \mu\text{g}/\text{mm}^2$ mass and on the microstructure occurred at impact velocities of 1.2 and 0.77 m/s, respectively (Jung and Bhushan, 2009a)

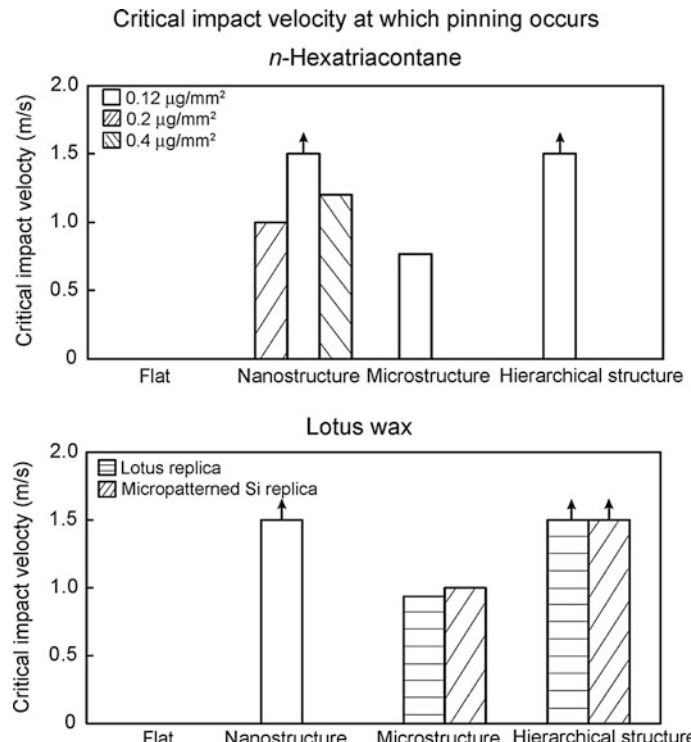


Fig. 6.44 Bar chart showing the measured critical impact velocity of a droplet with 1 mm radius at which transition occurs on various structures. The arrow indicates that the critical impact velocity can possibly be more than 1.5 m/s or the transition did not occur ([Jung and Bhushan, 2009a](#))

As shown in Fig. 6.44, the critical impact velocity of a droplet with 1 mm radius on various structures at which wetting of the surface (possibly pinning of droplet) occurs was measured ([Jung and Bhushan, 2009a](#)). The arrow indicates that the critical impact velocity can possibly be more than 1.5 m/s, or the transition has not occurred. As mentioned earlier, when the mass of *n*-hexatriacontane increased, the static contact angle of the nanostructure first increased followed by a decrease at a mass of 0.2 µg/mm². For the critical impact velocity, the same trends were found. It is believed that if neighboring crystals are separated on a sample with lower crystal density, any trapped air can be squeezed out whereas if the neighboring crystals are interconnected on a sample with higher density, air remains trapped. At the highest crystal density at a mass of 0.4 µg/mm², there is less open volume compared to that at 0.2 µg/mm². For all microstructures with *n*-hexatriacontane and Lotus wax, the critical impact velocities of the droplet are lower than those on nano- and hierarchical structures due to the larger distance between the pillars, and the solid–air–liquid interface can easily be destabilized from dynamic impact on the surface. Based on (6.7), the critical impact velocity of the droplet decreases

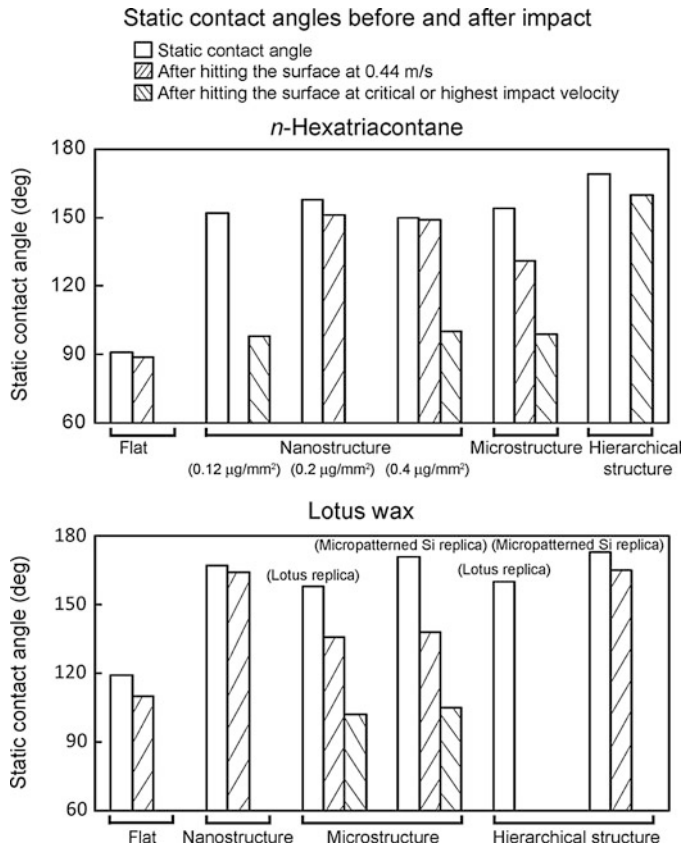


Fig. 6.45 Bar chart showing the measured static contact angle of a droplet on various surfaces. The contact angles of the *left* bar for each sample were measured using a droplet with 1 mm radius gently deposited on the surface. The contact angles of the *middle* and *right* bars for each sample were measured using the droplet after hitting the surface at 0.44 m/s and critical or highest impact velocity (Jung and Bhushan, 2009a)

with the geometric parameter (pitch). The theoretical critical impact velocity for a microstructure using (6.7) is 0.5 m/s. This value is lower than the experimental values of critical impact velocity for microstructures by about 30–50% depending on the structured surfaces. In these experiments, during applying an impact velocity of up to 1.5 m/s on nano- and hierarchical structures with *n*-hexatriacontane ($0.2 \mu\text{g}/\text{mm}^2$ for nanostructure) and Lotus wax, the wetting of the surface did not occur. The data clearly shows that nano- and hierarchical structures are superior to the microstructure in maintaining a stable composite solid–air–liquid interface.

To identify whether one is in a homogeneous solid–liquid interface or a composite solid–air–liquid interface, the contact angle data in the static condition and after bounce off were measured on various surfaces, as shown in Fig. 6.45 (Jung and Bhushan, 2009a). The contact angles of the left bar for each sample were

measured using the droplet with 1 mm radius gently deposited on the surface. The contact angles of the middle and right bars for each sample were measured using the droplet after hitting the surface at 0.44 m/s and critical or highest impact velocity. Missing bars mean that the droplet, after hitting the surface, bounced off without coming to sit on the surface. The static contact angle of the droplet after impact at 0.44 m/s is lower than that of the droplet gently deposited for all of the surfaces with *n*-hexatriacontane and Lotus wax. It can be interpreted that after hitting, the droplet pushes out the entrapped air of the cavities between the pillars under the droplet, resulting in an abrupt increase of the solid–liquid surface area by dynamic impact. As mentioned earlier, after hitting the surface at a critical impact velocity, the contact angles were close to 90° and much lower than that of the droplet gently deposited for the nanostructures with *n*-hexatriacontane (0.12 and 0.4 µg/mm²) and the microstructures with *n*-hexatriacontane and Lotus wax. Even though the droplet is in the composite interface when it is gently deposited on the surface, these observations indicate that the composite solid–air–liquid interface was destroyed due to dynamic impact on the surface.

6.6.6 Observation of Transition During the Vibrating Droplet

To observe how a vibrating droplet influences the transition from the composite solid–air–liquid interface to the homogeneous solid–liquid interface, [Jung and Bhushan \(2009a\)](#) performed vibrating droplet experiments on various surfaces with *n*-hexatriacontane and *T. majus* and Lotus waxes.

6.6.6.1 Model for the Adhesion and Inertia Forces of the Vibrating Droplet

[Jung and Bhushan \(2009a\)](#) presented a model for vibration. In this model, they calculated expressions for adhesion force and inertia force as a function of droplet properties and operating conditions. Consider a small droplet of liquid deposited on a surface. The liquid and surface come together under equilibrium at a characteristic angle, called the static contact angle θ , as shown in Fig. 6.46. When a droplet on a surface is vibrated, based on [Lamb \(1932\)](#), a general expression for the resonance frequency f_r of a free oscillating liquid droplet is given as

$$f_r = \sqrt{\frac{n(n-1)(n+2)\gamma}{3\pi\rho V}}, \quad (6.15)$$

where V is the volume of the droplet, and n represents the number of modes, with two being the first mode, etc. For a spherical droplet with a radius R with the distance between the center of droplet and the solid H , the volume of droplet V is given by

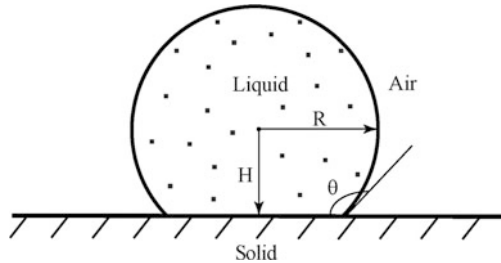


Fig. 6.46 Droplet of liquid in contact with a solid surface—contact angle θ ; radius of droplet R ; distance between the center of droplet and the solid H (Jung and Bhushan, 2009a)

$$\begin{aligned} V &= \frac{1}{3}\pi(R + H)^2(2R - H) \\ &= \frac{1}{3}\pi R^3(1 - \cos\theta)^2(2 + \cos\theta). \end{aligned} \quad (6.16)$$

Recent experimental studies were carried out by Noblin et al. (2004) and Celestini and Kofman (2006). They showed that the frequency decreases with the volume of the droplet, and the trends are compared with a theoretical model.

When liquid comes in contact with a surface, the energy gained for surfaces coming into contact is greater than the energy required for their separation (or the work of adhesion) by the quantity ΔW , which constitutes the adhesion hysteresis (Bhushan, 2003). For a surface, the difference between the two values of the interface energy (measured during loading and unloading) is given by ΔW . These two values are related to the advancing contact angle, θ_a , and receding contact angle, θ_r , of the surface. For example, a model based on Young's equation has been used to calculate the work of adhesion from contact angle hysteresis (Good, 1952; Chen et al., 1991; Nosonovsky and Bhushan, 2007a, 2008a):

$$\cos\theta_a - \cos\theta_r = \frac{\Delta W}{\gamma}. \quad (6.17)$$

From (6.17), the dominant force (adhesion force) responsible for the separation between the droplet and surface is given by (Joanny and de Gennes, 1984; Lee and Laibinis, 2000)

$$\begin{aligned} F_A &= L\gamma(\cos\theta_a - \cos\theta_r) \\ &= 2R\sin\theta(\gamma)(\cos\theta_a - \cos\theta_r), \end{aligned} \quad (6.18)$$

where L is the length of the triple contact line, referred to as line of contact of the solid, liquid, and air. The radius of a spherical droplet, R , depends on the contact angle and can be obtained from (6.16).

Vibration of a droplet on microstructured surface with *n*-hexatriacontane

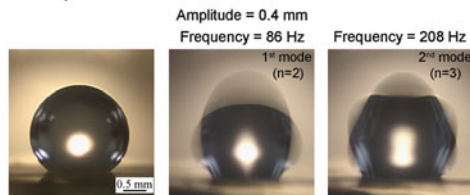


Fig. 6.47 Optical micrographs of droplets on the microstructured surface with *n*-hexatriacontane before and after vibration at amplitude of 0.4 mm for first mode ($n = 2$) and second mode ($n = 3$) of vibration. The frequencies for first mode and second mode were measured to be 86 and 208 Hz, respectively (Jung and Bhushan, 2009a)

From applying vertical vibration of a droplet on a surface, the inertia force of droplet F_I is given by

$$F_I = \rho V A \omega^2, \quad (6.19)$$

where A and ω are the amplitude and frequency of vibration, respectively. Bormashenko et al. (2007) showed that the transition occurred at a critical value of inertia force acting on the length of a triple line. However, if the inertia force of the droplet vibrated on the surface can overcome the adhesion force between the droplet and surface, which ΔF is positive value (Jung and Bhushan, 2009a),

$$\Delta F = F_I - F_A. \quad (6.20)$$

The droplet can be vertically separated from the surface (bouncing off) before the composite solid–liquid–air interface is destroyed.

6.6.6.2 Vibration Study Results

A droplet on various surfaces was vibrated by varying the frequency with a sinusoidal excitation of relatively low amplitude (0.4 mm) (Jung and Bhushan, 2009a). Based on (6.15), the experiments were performed in the first and second modes ($n = 2$ and 3). Figure 6.47 shows the optical micrographs of droplets on the microstructured surface with *n*-hexatriacontane before and after vibration at an amplitude of 0.4 mm for first mode ($n = 2$) and second mode ($n = 3$) of vibration. The frequencies for the first mode and second mode were measured to be 86 Hz and 208 Hz, respectively. The resonance frequencies on various surfaces were measured, and the data are summarized in Table 6.5. For comparison, the theoretical values for the two modes were calculated using (6.15). For calculations, the surface tension of the water–air interface (γ) was taken to be 0.073 N/m, the mass density (ρ) was 1,000 kg/m³ for water, and the volume of the droplet (V) was 5 µL. The theoretical

Table 6.5 Summary of the measured resonance frequency at the fixed amplitude value of 0.4 mm, the calculated inertia force of a vibrated droplet, and adhesive force between the droplet and surface on the various surfaces fabricated with *n*-hexatriacontane and Lotus wax

	Resonance frequency (Hz)		$F_A (\mu\text{N})$	$F_I (\mu\text{N})$ at transition or bouncing off	$\Delta F = F_I - F_A$ (mN)
	First mode ($n = 2$)	Second mode ($n = 3$)			
<i>n</i> -Hexatriacontane					
Flat	103	271	260 ± 3.7		
Nanostructure ($0.12 \mu\text{g}/\text{mm}^2$)	63	169	45 ± 2.2	11	-34 ± 2.2 (T)
Nanostructure ($0.2 \mu\text{g}/\text{mm}^2$)	50	147	10 ± 1.6	10	0 ± 1.6 (B)
Nanostructure ($0.4 \mu\text{g}/\text{mm}^2$)	54	149	13 ± 2.0	11	-2 ± 2.0 (B)
Microstructure	86	208	21 ± 1.7	9	-12 ± 1.7 (T)
Hierarchical structure	49	144	0.2 ± 0.06	3.6	3.4 ± 0.06 (B)
Lotus wax					
Flat	92	243	133 ± 3.3		
Nanostructure	47	138	0.8 ± 0.08	3.2	2.4 ± 0.08 (B)
Microstructure (Lotus replica)	63	179	14 ± 1.8	11	-3 ± 1.8 (T and B)
Microstructure (micropatterned Si replica)	66	183	10 ± 1.6	10	0 ± 1.6 (B)
Hierarchical structure (Lotus replica)	40	139	0.1 ± 0.04	3.6	3.5 ± 0.04 (B)
Hierarchical structure (micropatterned Si replica)	38	137	0.04 ± 0.01	2.7	2.6 ± 0.01 (B)

Positive value of ΔF means that the droplet bounced off before the transition occurred. The variation represents ± 1 standard deviation (Jung and Bhushan, 2009a)

B—bouncing off

T—transition

values for the first mode ($n = 2$) and second mode ($n = 3$) from (6.15) are 110 and 214 Hz, respectively. These values are similar to those of flat surfaces with *n*-hexatriacontane and Lotus wax. However, with the same volume, the resonance frequencies of the structured surfaces are lower than those of flat surfaces. Celestini and Kofman (2006) showed that the resonance frequency depends on the contact angle of the structured surfaces, and it decreases with increasing contact angle. The hierarchical structures with highest contact angle have the lowest resonance frequency, consistent with the results by Celestini and Kofman (2006).

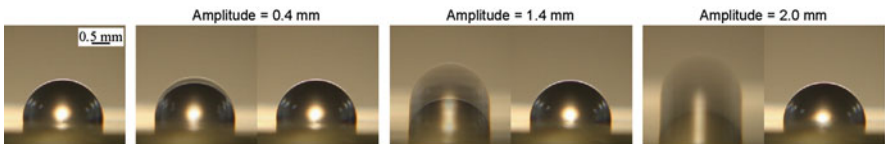
To observe how the vibration of the droplet influences the transition from the composite solid–air–liquid interface to the homogeneous solid–liquid interface, Jung and Bhushan (2009a) performed vibrating droplet experiments on various surfaces with *n*-hexatriacontane and Lotus wax. Figure 6.48 shows optical micrographs of droplets on various surfaces with *n*-hexatriacontane before and after vibrating at a frequency of 30 Hz, which is less than the resonance frequency for the first mode ($n = 2$). The vibration amplitude was increased until transition or until the droplet bounced off. First, on the flat surface, it was found that the droplet did not change much after applying vibration at amplitudes ranging from 0 to 3 mm. As shown in the images for the nanostructure ($0.12 \mu\text{g}/\text{mm}^2$) and microstructure, the static contact angles of the droplet before vibrating were 152° and 154° , respectively. After vibrating at amplitudes of 0.4 and 1.4 mm, the contact angles still have similar values (151° for nanostructure and 149° for microstructure), which suggests the formation of a solid–air–liquid interface. However, after vibrating at amplitudes of 2.4 mm for the nanostructure ($0.12 \mu\text{g}/\text{mm}^2$) and 2.0 mm for the microstructure, the static contact angles became 125° and 121° , respectively. This is because air pockets do not exist below the droplet as a result of droplet impalement by the structures, characterized by a smaller contact angle. These observations indicate the transition from the composite interface to the homogenous interface. Observations of vibration on two nanostructures (0.2 and $0.4 \mu\text{g}/\text{mm}^2$) and a hierarchical structure showed that the transition did not occur, but the droplet started to bounce off the surface from amplitudes of 2.2, 2.4, and 0.8 mm, respectively.

To study the validity of the proposed model (6.20), the adhesive force responsible for the separation between the droplet and surface and the inertia force of a droplet vibrated on various structures were calculated (Jung and Bhushan, 2009a). The adhesive force was obtained from (6.18) using static contact angle and contact angle hysteresis. The inertia forces were obtained from (6.19) using the amplitude and frequency of vibration as the transition or droplet bounce off occurred. The data are presented in Fig. 6.49 and summarized in Table 6.5. As shown in Fig. 6.48, it was observed that the transition occurred as a result of droplet impalement by the structures by increasing the inertia force of droplet on the surfaces. However, if the inertia force of the droplet vibrated on the surface can overcome the adhesion force between the droplet and surface (ΔF is positive), the droplet can be vertically separated from the surface (bouncing off) before the composite solid–liquid–air interface is destroyed. The experimental results for bouncing off of the droplet appear to have the same trend as the proposed model (6.20). It is shown that hierarchical structures have the positive value of the difference between the inertia force and adhesive force for droplet bounce off responsible for superior resistance to the dynamic effects and maintain a stable composite solid–air–liquid interface.

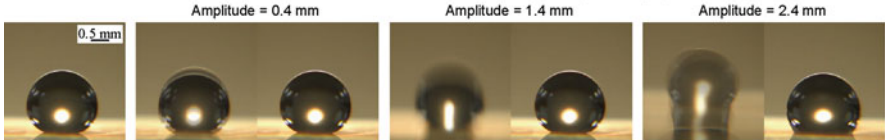
Vibration of a droplet on various surfaces with *n*-hexatriacontane

Frequency = 30 Hz

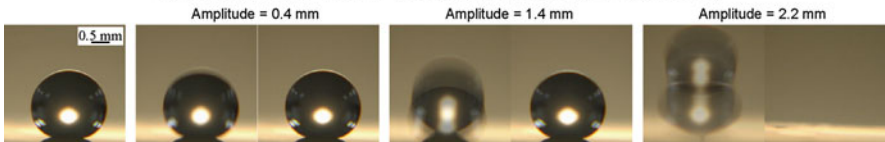
Flat



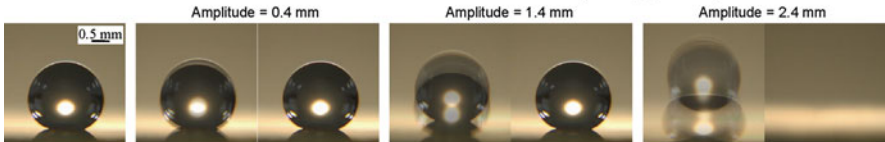
Nanostructure with *n*-hexatriacontane ($0.12 \mu\text{g}/\text{mm}^2$)



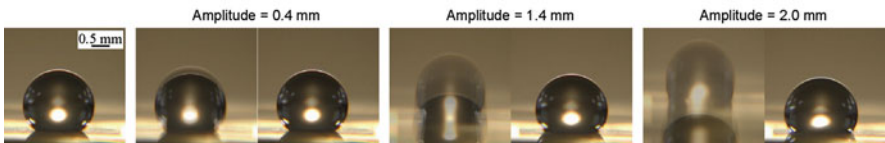
Nanostructure with *n*-hexatriacontane ($0.2 \mu\text{g}/\text{mm}^2$)



Nanostructure with *n*-hexatriacontane ($0.4 \mu\text{g}/\text{mm}^2$)



Microstructure



Hierarchical structure

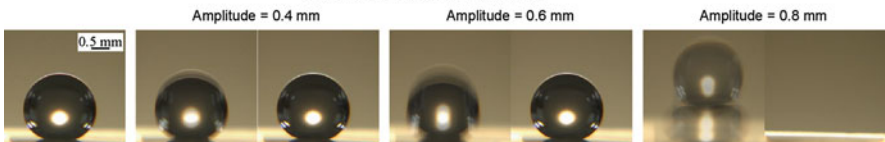


Fig. 6.48 Optical micrographs of droplets on various surfaces with *n*-hexatriacontane before and after vibrating at frequency of 30 Hz. The transition of a droplet on the nanostructure with $0.12 \mu\text{g}/\text{mm}^2$ mass of *n*-hexatriacontane and on the microstructure occurred at amplitudes of 2.4 and 2.0 mm, respectively (Jung and Bhushan, 2009a)

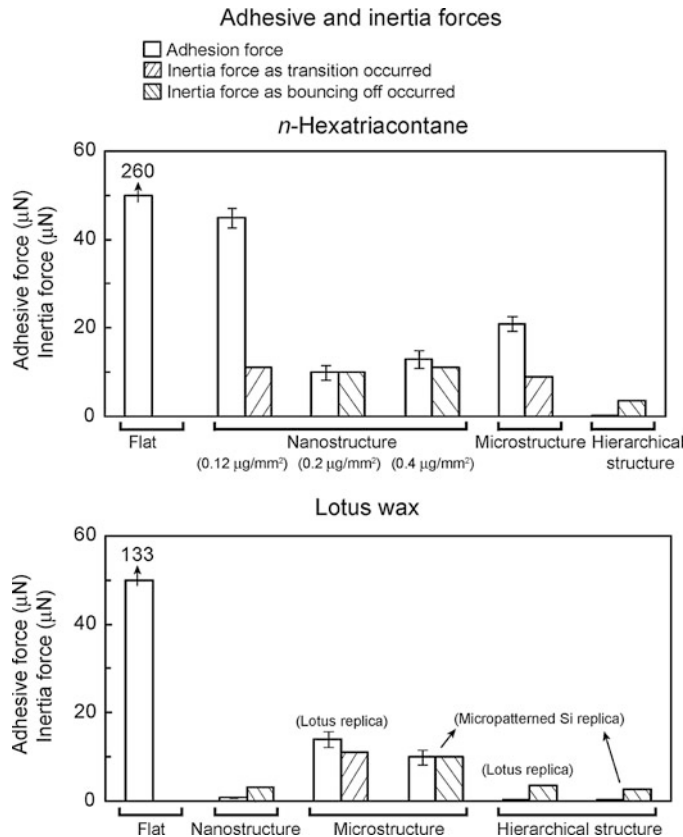


Fig. 6.49 Bar chart showing the calculated adhesive force responsible for the separation between the droplet and surface and inertia force^{1.1} of a droplet vibrated on various structures. The inertia forces were obtained as the transition or droplet bounce off occurred. If the inertia force of the droplet vibrated on the surface can overcome the adhesion force between the droplet and surface (ΔF is positive), the droplet can be vertically separated from the surface (bouncing off) before the composite solid–liquid–air interface is destroyed (Jung and Bhushan, 2009a)

6.6.7 Measurement of Fluid Drag Reduction

Superhydrophobicity reduces fluid slip and drag in fluid flow (Jung and Bhushan, 2010). The drag data and analysis will be presented in Sect. 10.5. It will be shown that fluid drag decreases with an increase in the degree of hydrophobicity.

6.6.8 Summary

Hierarchical structured surfaces using nature's route were fabricated to verify that properties comparable to that of natural objects can be obtained. Various structures

with two types of wax morphology with various crystal densities were fabricated for detailed analyses.

Nanostructures with different wax platelet crystal densities using *n*-hexatriacontane were deposited on a flat surface and a microstructure, and the effect of crystal density on the static contact angle, contact angle hysteresis, and air pocket formation as well as adhesive force was studied. High density of crystals with sufficient spacing between them leads to a propensity to form air pockets resulting in a high static contact angle. In hierarchical structured surfaces as compared to nanostructured and microstructured surfaces, the air pocket formation further increases contact angle and reduces both contact angle hysteresis and adhesive force.

The nanostructures with *T. majus* and Lotus wax tubules were deposited on flat surfaces. Nanostructures were formed by wax tubules. Tubules were hollow structures and randomly oriented on the surface. The tubular diameter varied between 100 and 150 nm, and their length varied between 1,500 and 200 nm. The created nanostructures were comparable to the wax crystal morphology found on the Lotus leaf. The influence of these nanostructures deposited on a flat surface and a microstructure was studied on the static contact angle, contact angle hysteresis, air pocket formation, and adhesive force as well as self-cleaning efficiency. The data were compared with that of a Lotus plant leaf. Hierarchical structured followed by nanostructured surfaces have high static contact angle, low contact angle hysteresis, and low adhesive force. These properties are superior to the Lotus leaf. Evidence of air pocket formation has been reported. Self-cleaning experiments performed by deposition of contaminant particles followed by cleaning with water droplets show that hierarchical structures have superior cleaning efficiency, comparable to that of Lotus leaf. To sum up, hierarchical structured surfaces using nature's route have been created, and contact angles, adhesive force, and self-cleaning efficiency are comparable to that of the Lotus leaf, which verifies the understanding of the mechanisms relevant to superhydrophobicity and self-cleaning in the Lotus leaf.

Bouncing and vibrating droplet studies were performed to investigate the transition from the composite interface to the homogeneous interface on nanostructures with *T. majus* and Lotus wax tubules deposited on flat surfaces and a microstructure. Bouncing and vibrating droplet experiments show that in hierarchical structured and nanostructured surfaces with certain crystal densities, wetting did not occur up to 1.5 m/s. In microstructured surfaces due to the larger distance between the pillars, composite interface was destroyed above a certain critical velocity in bouncing droplet experiments and above a certain inertia force of the droplet on the surfaces in vibrating droplet experiments.

6.7 Mechanically Durable Hierarchical Structured Surfaces

For commercial applications, Lotus-inspired mechanically durable surfaces are needed. Following are two examples of hierarchical structured surfaces fabricated with CNT composites and nanoparticle composites. As a benchmark, structured surfaces with Lotus wax were also prepared to compare with the durability of CNT

composite structures. Contact angle and contact angle hysteresis were measured. To compare the durability of the various fabricated surfaces, waterfall/jet tests were conducted to determine the loss of superhydrophobicity. Wear and friction studies were also performed using an AFM and a ball-on-flat tribometer.

6.7.1 CNT Composites

Various attempts have been made to fabricate mechanically durable structures using multiwalled carbon nanotube (CNT) arrays with high mechanical strength (Lau et al., 2003; Huang et al., 2005; Zhu et al., 2005; Hong and Uhm, 2006). A simpler approach is to use CNT composites. Jung and Bhushan (2009b) deposited CNT composite on flat epoxy resin and a microstructure using a spray method in order to create nano- and hierarchical structures, as shown in Fig. 6.50. CNTs were fabricated using catalyst-assisted chemical vapor deposition (CCVD) (Sun Nanotech Co Ltd., China). An iron catalyst was used to initiate growth of nanotubes using natural gas as a carbon source and Ar/H₂ as a buffer gas at 750°C. The contact angle of individual carbon nanotubes has been reported as 60° and higher. Microstructures were fabricated using a microstructured Si surface with pillars of 14 μm diameter and 30 μm height with 23 μm pitch by soft lithography, as described earlier (Bhushan et al., 2009b; Jung and Bhushan, 2009b). The first step of deposition of the CNT composite using the spray method was to disperse the CNT into a solvent in order to maintain a uniform distribution. Acetone was used as a solvent because it does not affect surface modification and is easily vaporized in ambient conditions. The dispersion process consisted of the sonification of 200 mg the CNT in 100 mL of acetone for 4 min using a Branson Digital Sonifier with a frequency of 20 kHz at an amplitude of 80%. During this process, the mixture was exposed to ultrasonic pressure waves in a sonifier in order to disperse the CNT into smaller aggregates. To provide strong bonding between CNT and the substrate, 200 mg EPON epoxy resin 1002F was added to the mixture of CNT and acetone, and then the mixture was sonicated for four more minutes. Next, the sonified mixture was poured into a spray gun and sprayed onto the specimen surfaces. The conditions for uniform deposition of the CNT on the surfaces were optimized by adjusting the concentration of CNT in the solvent. After spraying the CNT on the surfaces, the CNT composite structures were then cured at 120°C for 3 h (above the recommended curing temperature), which is above the melting point (80–88°C) and below the burning point (180°C) of EPON epoxy resin 1002F. At this temperature, the epoxy which initially covered the CNT was melted and moved to the interface between the CNT and substrates, resulting in exposed individual CNTs to provide the intended nanostructure which leads to high contact angle.

Figure 6.51 shows the SEM micrographs of nano- and hierarchical structures fabricated with CNT (Jung and Bhushan, 2009b). SEM micrographs show an overview (left column), a detail in higher magnification (middle column), and a large magnification of the nanostructures with CNT (right column). All surfaces show a homogenous distribution of CNT on the specimen. The CNTs were well dispersed

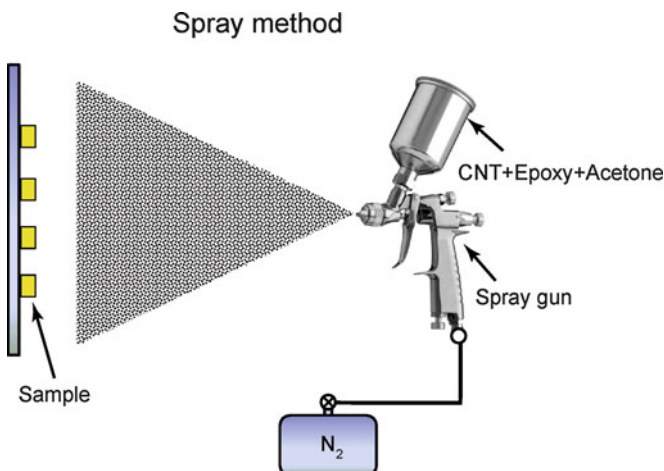


Fig. 6.50 Schematic of spray method to deposit a mixture of CNT, epoxy, and acetone on surfaces (Jung and Bhushan, 2009c)

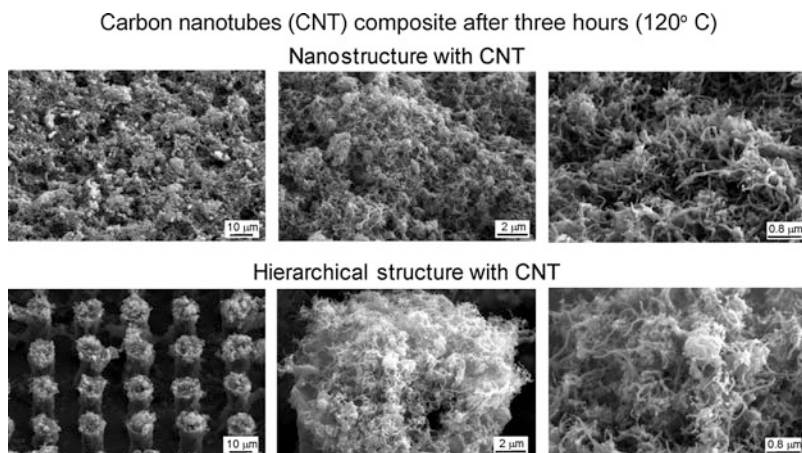


Fig. 6.51 SEM micrographs taken at 45° tilt angle show three magnifications of nano- and hierarchical structures fabricated with CNT after three hours at 120°C (Jung and Bhushan, 2009c)

and embedded on flat and microstructured surfaces for the desired nanostructure. The CNT diameter varied between 10 and 30 nm, and an aspect ratio varied between 160 and 200.

Lotus leaves have been the inspiration for the development of superhydrophobic and self-cleaning products. Therefore, as a benchmark for mechanical durability studies, Jung and Bhushan (2009b) used nano-, micro-, and hierarchical structures created by the self-assembly of Lotus wax with the amounts of $0.8 \mu g/mm^2$ deposited on flat epoxy resin and microstructure by thermal evaporation as shown in Fig. 6.40.

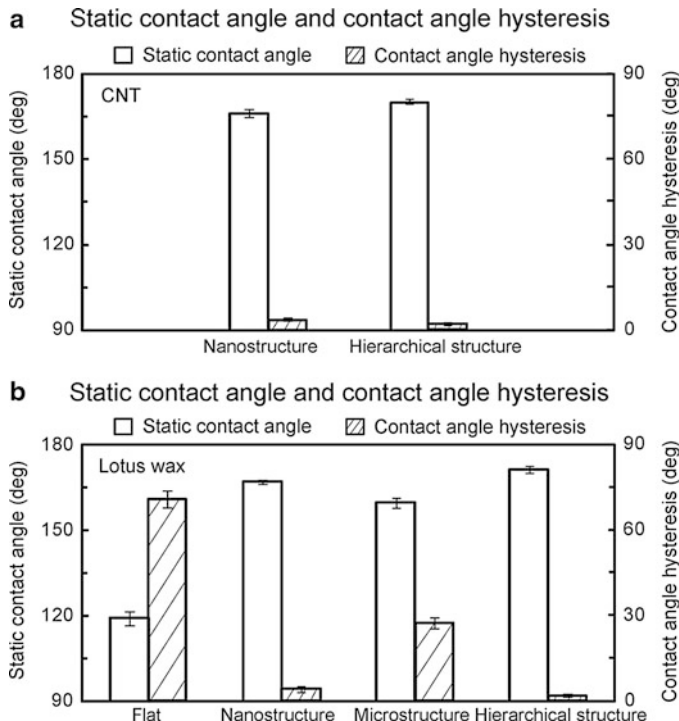


Fig. 6.52 Bar chart showing the measured static contact angle and contact angle hysteresis on (a) nano- and hierarchical structures fabricated with CNT after three hours at 120°C, and (b) various structures fabricated with 0.8 µg/mm² of Lotus wax after storage for 7 days at 50°C with ethanol vapor. The error bar represents ± 1 standard deviation (Jung and Bhushan, 2009c)

6.7.1.1 Contact Angle

To study the effect of CNT composite structures for superhydrophobicity, Jung and Bhushan (2009b) measured the static contact angle and contact angle hysteresis on nano- and hierarchical structures with CNT. For static contact angle and contact angle hysteresis, droplets of about 5 µL in volume (with the diameter of a spherical droplet about 2.1 mm) were gently deposited on the surface using a microsyringe. For contact angle hysteresis, the advancing and receding contact angles were measured at the front and back of the droplet moving along the tilted surface, respectively. Figure 6.52a shows that superhydrophobicity with a static contact angle of 166° and a contact angle hysteresis of 4° was found in the nanostructured surface with CNT. After introducing the CNT nanostructure to the top of the micropatterned Si replica, the higher static contact angle of 170° and lower contact angle hysteresis of 2° were found for the hierarchical structures with CNT. Both nano- and hierarchical structures created with CNT showed superhydrophobic and self-cleaning surface, which has a static contact angle of more than 150° and contact angle hysteresis of less than 10° (Jung and Bhushan, 2009b).

Figure 6.52b shows that for the hierarchical structure with Lotus wax, the highest static contact angles of 173° and lowest contact angle hysteresis of 1° were found. The recrystallized wax tubules are very similar to those of the original Lotus leaf, but are $0.5\text{--}1\ \mu\text{m}$ longer, the static contact angle is higher, and the contact angle hysteresis is lower than reported for the original Lotus leaf (static contact angle of 164° and contact angle hysteresis of 3°) (Koch et al., 2009). Superhydrophobicity with a static contact angle of 167° and a contact angle hysteresis of 5° was also found in the nanostructured surface with Lotus wax. The microstructured surface with a Lotus wax layer has a static contact angle of 160° but shows a much higher contact angle hysteresis of 29° than found in hierarchical structures. Melting of the Lotus wax led to a flat surface with a flat wax film and a much lower static contact angle of 119° and higher contact angle hysteresis of 71° . The data of a flat Lotus wax film on a flat replica show that the Lotus wax by itself is hydrophobic (Jung and Bhushan, 2009b).

6.7.1.2 Durability of Various Surfaces in Waterfall/Jet Tests

To investigate the durability of the created surfaces in long-term exposure to water and how different kinetic energies of the water hitting the surface affect wetting properties, Jung and Bhushan (2009b) conducted waterfall/jet tests on the surfaces created with CNT and Lotus wax. The nano- and hierarchical structures with CNT were exposed to water with pressure ranging from 0 to 45 kPa for 20 min. Figure 6.53(left) shows static contact angle and contact angle hysteresis as a function of water pressure. As water pressure hitting the surfaces increased, the static contact angle and contact angle hysteresis decreased and increased slightly, respectively, but a significant change was not found on both the nano- and hierarchical structures for superhydrophobicity. It can be interpreted that there was no deformation of CNT structures due to strong bonding with the substrate. As a result, superhydrophobic CNT composite structures showed good stability of wetting properties not only from long-term exposure to water but also high water pressure. In order to compare durability of the created surfaces with CNT and Lotus wax, Jung and Bhushan (2009b) also conducted waterfall/jet tests on the flat, nano-, micro-, and hierarchical structures with Lotus wax. Figure 6.53 (right side) shows static contact angle and contact angle hysteresis as a function of water pressure of exposure. As the water pressure increased up to 45 kPa, static contact angle and contact angle hysteresis of flat and microstructure with Lotus wax layer remained almost constant. However, as the water pressure increased up to 34 kPa, the static contact angle of nano- and hierarchical structures with Lotus wax first decreased slightly and then the contact angle started decreasing sharply. It was also observed that the corresponding large change in contact angle hysteresis was found above 34 kPa. It is usually known that wax structures on the leaves can easily be induced by touching the leaf surface or by mechanical wear during transport of the leaves. As expected, it is observed that the nanostructure with Lotus wax can be damaged by water with high pressure, resulting in a loss of superhydrophobicity.

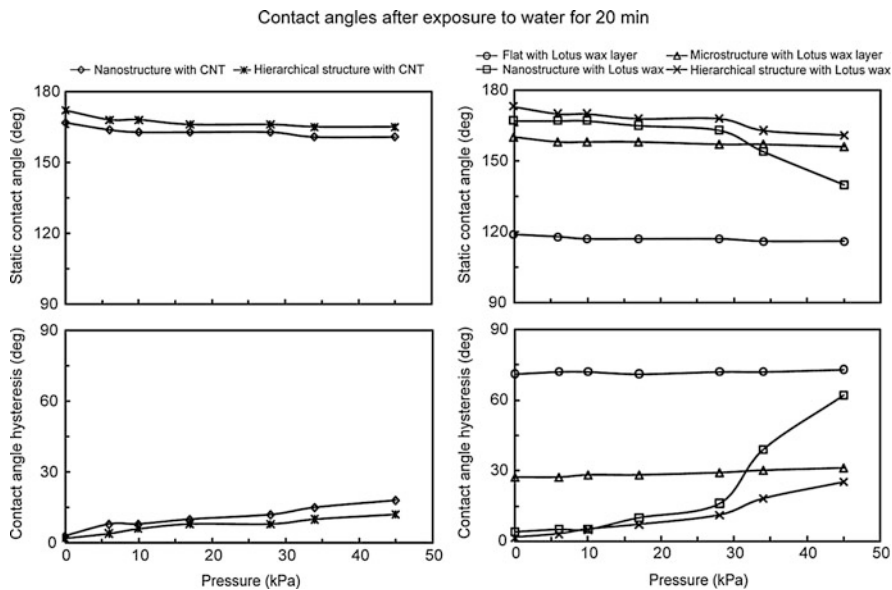


Fig. 6.53 Static contact angle and contact angle hysteresis as a function of water pressure of exposure for 20 min for the droplet with a 1 mm radius (5 μL volume) gently deposited on the surfaces with CNT and Lotus wax. The data are reproducible within $\pm 5\%$ (adapted from [Jung and Bhushan, 2009c](#))

6.7.1.3 Durability of Various Surfaces in AFM and Ball-On-Flat Tribometer Tests

To investigate the durability of the nanostructure fabricated using CNT, [Jung and Bhushan \(2009b\)](#) conducted wear tests by creating $50 \times 50 \mu\text{m}^2$ wear scars with a $15 \mu\text{m}$ radius borosilicate ball for 1 cycle at two normal loads of 100 nN and 10 μN using an AFM. Figure 6.54a shows surface height maps before and after wear tests for nanostructures with CNT. As the normal load of 100 nN was applied to the nanostructure with CNT, the wear scar induced on the surface after the 100 nN normal load tests was not found or was very low, and it was also hard to quantify a wear depth on the nanostructure with CNT scanned with a borosilicate ball. With increasing the normal load to 10 μN , it was found that the wear depth on the nanostructure with CNT was not significantly changed, but the morphology of the CNT differs slightly from that before the wear test. It can be interpreted that the individual CNT might be expected to slide or bend with the borosilicate ball applied by high normal load of 10 μN during the test process.

For comparison, [Jung and Bhushan \(2009b\)](#) also investigated the durability of the nanostructure fabricated using Lotus wax by applying two normal loads of 100 nN and 10 μN using AFM. Figure 6.54b shows surface height maps before and after wear tests for nanostructures with Lotus wax. As the normal load of 100 nN was

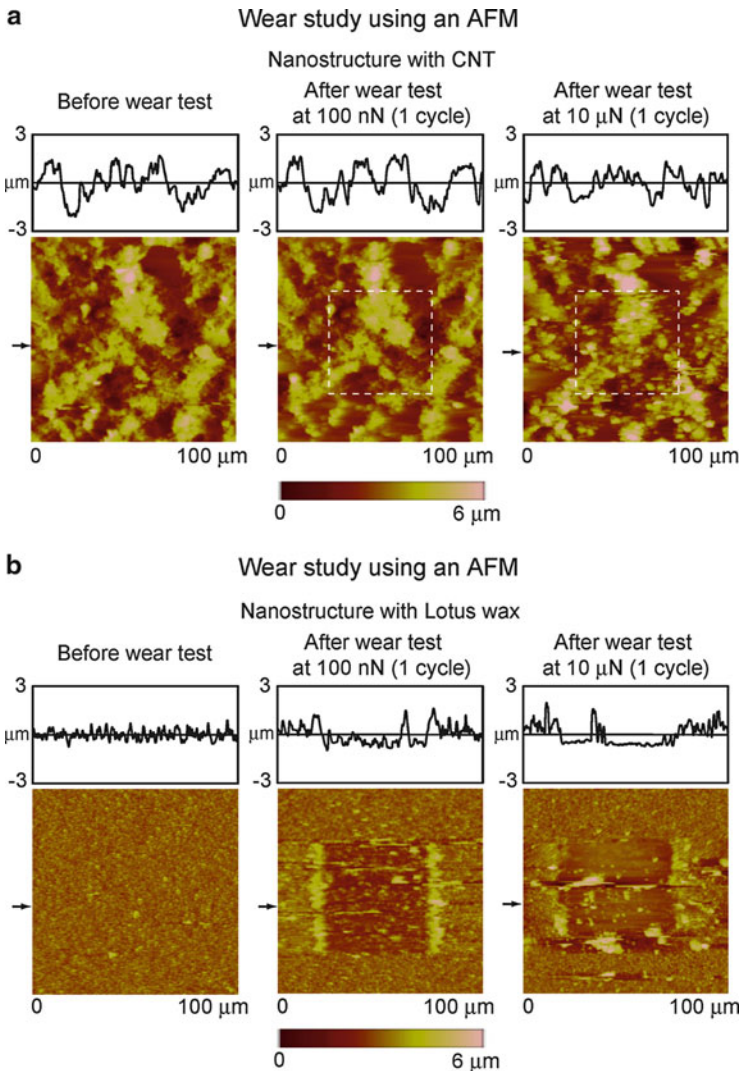


Fig. 6.54 Surface height maps before and after wear tests with a 15 μ m radius borosilicate ball at 100 nN and 10 μ N for nanostructures with (a) CNT and (b) Lotus wax using an AFM ([Jung and Bhushan, 2009c](#))

applied to the nanostructure with Lotus wax, the change in the morphology of the structured surface was observed, and a small amount of debris was generated compared to the surface before the wear test, indicating that the wax nanostructure has weak mechanical strength at even small loads. With increasing the normal load to 10 μ N, it was found that the depth of the wear mark increased and the nanostructure with Lotus wax was fully removed from the substrate. As expected,

the nanostructure with Lotus wax exhibited the greater amount of wear compared to the nanostructure with CNT, as evidenced by debris buildup around the edge of the wear test region. The damage of the structured surface can cause the sticking of water droplets in the wear region, resulting in low static contact angle and high contact angle hysteresis.

In order to investigate the durability of structured surfaces at a high load, [Jung and Bhushan \(2009b\)](#) conducted conventional ball-on-flat tribometer experiments for the surfaces with CNT. Figure 6.55a shows the coefficient of friction as a function of the number of cycles for the nano- and hierarchical structures with CNT. The data are reproducible within $\pm 5\%$ based on three measurements. The coefficients of friction on both the nano- and hierarchical structures with CNT first increased slightly for 20 cycles. Such a trend can be due to the elastic bending or buckling of CNT by contacting with a sapphire ball during the beginning of scan, resulting in an increase of the contact area. During the entire experiment, the coefficient of friction value of the nano- and hierarchical structures with CNT changed minimally, which indicates that the CNT was not being worn after 100 cycles. To investigate the change in the morphology of the surfaces after the wear test, optical microscope images were obtained before and after the wear test as shown in Fig. 6.56a. As expected, it was observed that there is no or low wear on the nano- and hierarchical structures after wear tests. No or low wear on the CNT composite structure can possibly be due to the significant increase in the mechanical strength and wear resistance led from the uniform distribution and strong bonding of CNT on flat epoxy resin and microstructure. The elastic bending or buckling exhibited by CNT make them exceedingly tough materials that may be absorbing some of the force at contact, acting as a compliant spring moderating the impact of the ball on the surface ([Dresselhaus et al., 2000](#); [Meyyappan, 2005](#); [Chen et al., 2006](#)).

Contact diameters and contact stresses of CNT at three loads used in AFM and ball-on-flat tribometer tests were calculated ([Jung and Bhushan, 2009b](#)). Table 6.6 lists the physical properties of various specimens. It is assumed that contacts are single-asperity elastic contacts. For this case, the contact diameter ([Bhushan, 1999, 2002](#)),

$$d = 2 \left(\frac{3WR}{4E^*} \right)^{1/3}, \quad (6.21)$$

where W is the total normal load, R is the asperity radius, and E^* is the effective elastic modulus. It should be noted that contact occurs on multiple asperities, and (6.21) gives an approximate value. The calculated contact diameter and contact stress are presented in Table 6.6. The deformation of CNT appears to be elastic at the three loads applied by the borosilicate ball and sapphire ball.

In order to compare the durability of the created surfaces with CNT and Lotus wax at a high load, [Jung and Bhushan \(2009b\)](#) conducted a wear study on the surfaces with Lotus wax using a conventional ball-on-flat tribometer. As shown in

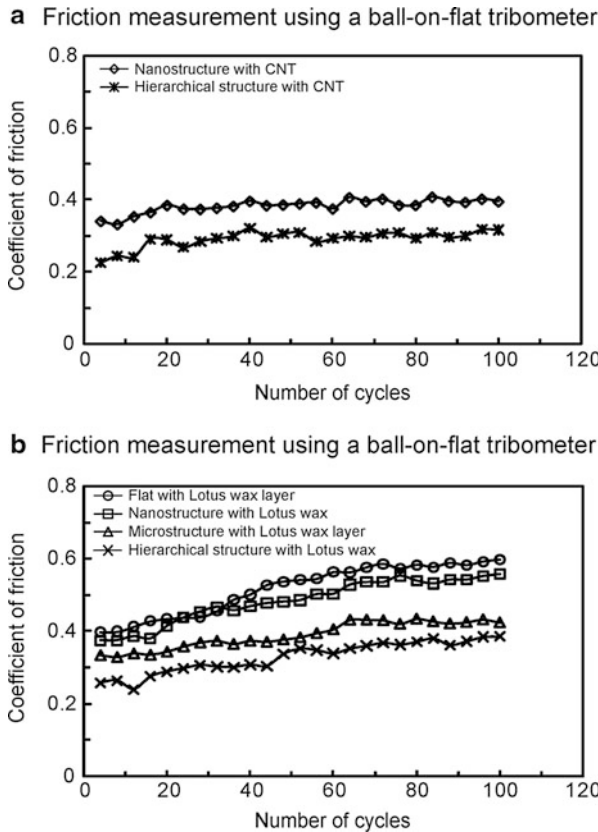


Fig. 6.55 Coefficient of friction as a function of number of cycles using a ball-on-flat tribometer for the surfaces with (a) CNT and (b) Lotus wax at room temperature ($22 \pm 1^\circ\text{C}$) and ambient air ($45 \pm 5\%$ RH). The data are reproducible within $\pm 5\%$ based on three measurements (Jung and Bhushan, 2009c)

Fig. 6.55b, the coefficient of friction value of the surfaces with Lotus wax exhibited a gradual increase when the sliding cycle increases up to about 70 cycles and then remains constant. This indicates that the wax nanostructure and flat wax layer could be undergoing some wear due to weak bonding between them and the substrates. The change in the morphology of the surfaces with Lotus wax was observed in optical microscope images as shown in Fig. 6.56b. As shown in the AFM study at low loads (Fig. 6.54b), it is clearly observed that the flat wax layer and wax nanostructure on the flat and microstructure were fully removed from the surfaces. As a result, superhydrophobic CNT composite structures showed better mechanical durability than the structured surfaces with Lotus wax to best withstand real world applications.

Fig. 6.56 Optical micrographs before and after wear test at 10 mN (100 cycle s) using a ball-on-flat tribometer for the surfaces with (a) CNT and (b) Lotus wax (Jung and Bhushan, 2009c)

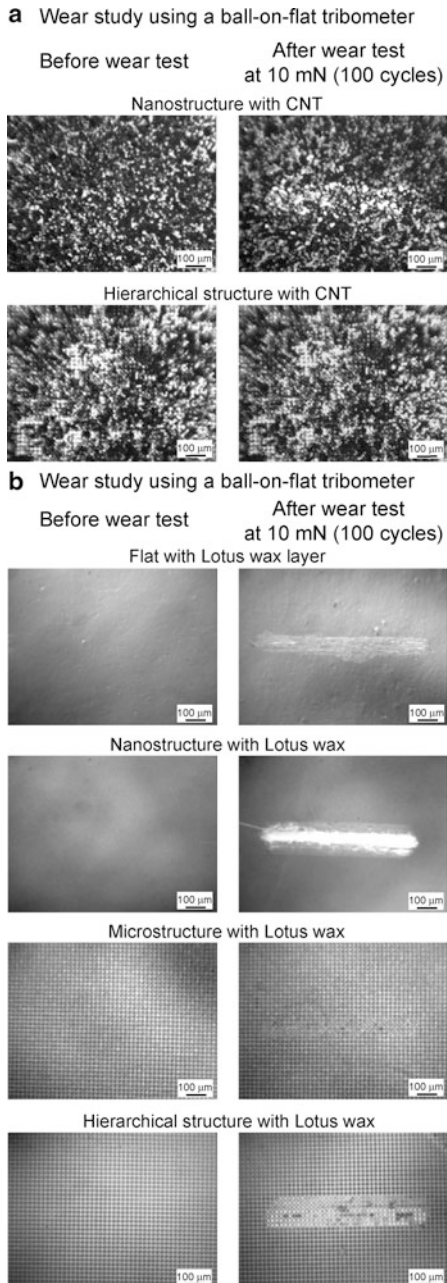


Table 6.6 Typical physical properties of various specimens and calculated contact diameters and contact stresses at three loads used in AFM and ball-on-flat tribometer measurements

	Borosilicate ball with a 15 μm radius	Sapphire ball with a 1.5-mm radius	Carbon nanotube			
Elastic modulus (GPa)	70 ^a	390 ^b	1,200 ^c			
Poisson's ratio	0.2 ^a	0.23 ^b	0.2 ^d			
Bending strength (GPa)			14.2 ^c			
Contact diameter (μm)			Mean contact pressure (GPa)			
	Borosilicate ball at 100 nN	Borosilicate ball at 10 μN	Sapphire ball at 10 mN	Borosilicate ball at 100 nN	Borosilicate ball at 10 μN	Sapphire ball at 10 mN
Carbon nanotube	0.05	0.24	6.62	0.076	0.33	0.44

It is assumed that contacts are single-asperity contact ([Jung and Bhushan, 2009c](#))

^a[Callister \(2000\)](#)

^b[Bhushan and Blackman \(1991\)](#)

^c[Wong et al. \(1997\)](#)

^d[Zhang et al. \(2008\)](#)

6.7.1.4 Summary

The hierarchical structure created with CNTs shows a high static contact angle of 170° and a low contact angle hysteresis of 2°. As a benchmark, the structures created using Lotus wax were used to compare the durability of CNT composite structures. It was found that superhydrophobic CNT composite structures showed good stability of wetting properties exposure to water. In contrast, it was observed that the nanostructure with Lotus wax can be damaged by water with high pressure, resulting in the loss of superhydrophobicity. From wear and friction studies, it was found that the nanostructure with Lotus wax can be easily damaged even at a small load. However, the CNT composite structure showed high wear resistance because of the uniform distribution and strong bonding of CNTs to the flat epoxy resin and microstructure.

6.7.2 Nanoparticle Composites

Superhydrophobic surfaces using silica particles have been created by drop casting, chemical deposition, and sol–gel processes ([Ming et al., 2005; Liu et al., 2006; Englert et al., 2006](#)). [Ebert and Bhushan \(2012\)](#) created hierarchical structures resistant to mechanical wear with silica particles using a spray method. First, silica nanoparticles of two different sizes were deposited onto micropatterned surfaces

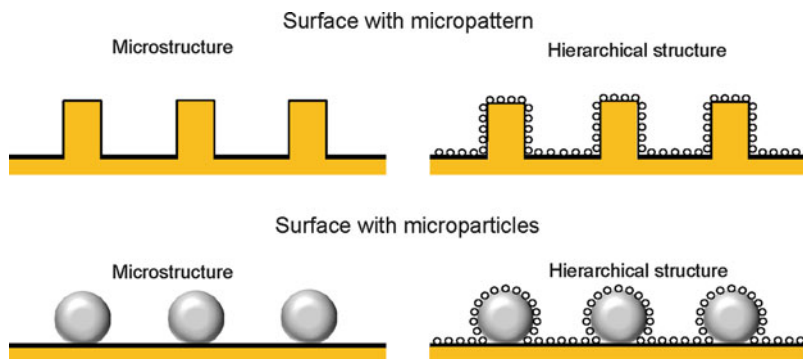


Fig. 6.57 Schematic examples of microstructured and hierarchically structured surfaces in which the microstructure is formed by both a uniform micropattern (*top*) and microparticles (*bottom*). In both cases, the hierarchical structure is achieved through addition of nanoparticles (adapted from Ebert and Bhushan, 2012)

to confirm superhydrophobicity and low CAH. Then, silica microparticles were substituted for the micropattern to create the microscale roughness. The pitch between pillars for the micropatterns was known, and the average pitch between microparticles on a surface was determined through SEM imaging. Figure 6.57 illustrates the use of both particles and a patterned surface to form microstructures and hierarchical structures. Knowing the geometry of the particles, the transition to the Wenzel regime can be predicted to occur above a certain pitch value.

6.7.2.1 Experimental Details

Silica nanoparticles of 10 nm (± 1 nm) and 50 nm (± 15 nm) were created through continuous flame hydrolysis of SiCl_4 and hydrophobized through silane treatment (Evonik-Degussa Corporation, Parsippany, New Jersey). In order to spray the particles onto the surfaces, they were first dispersed uniformly in solution. In 100 mL of acetone, 200 mg of particles were sonicated for 4 min with a Branson Sonifier 450A with a frequency of 20 kHz at 80% amplitude. For strong bonding of the nanoparticles to the substrates, 200 mg of EPON epoxy resin 1002F (Hexion Specialty Chemicals, Columbus, Ohio) was then added, and the solution was sonicated for another 4 min. The dispersion of particles in solution was then sprayed onto the sample surface using a spray gun. The samples were then annealed at 120°C for 3 h. Annealing at this temperature (above the melting point and below the burning point of EPON 1002F) was done so that the resin would melt and move to the interface between the particles and the surface. Figure 6.58 shows the SEM micrographs of hierarchical structures with silica nanoparticles and an epoxy micropattern. The hierarchical structures are shown at three magnifications: the lowest to show the pitch between pillars, the middle to show an individual pillar, and the highest to show surface nanoscale roughness.

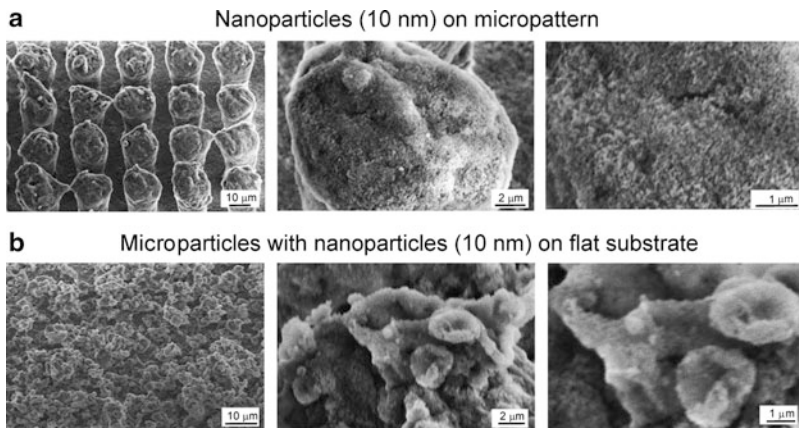


Fig. 6.58 SEM micrographs taken at 45° tilt angle showing (a) 10-nm particles on micropattern with a pitch value (P) of 23 m at three magnifications (bottom), and (b) microparticle with 10-nm particles with microparticle spray concentration of 1,400 mg/L with resulting average pitch value (P_{avg}) of 21 μm (adapted from [Ebert and Bhushan, 2012](#))

For samples using microparticles as the microscale roughness, the microparticles were sonicated in solution in the same manner and sprayed onto flat epoxy surfaces. The hydrophobic silica microparticles (diameter = $10 \mu\text{m} \pm 5 \mu\text{m}$) were obtained as a trimethylated silica gel powder from Dow Corning (Midland, Michigan). For hierarchically structured surfaces, an additional sonication and spray of nanoparticles was performed. Surfaces of varying pitch were created by changing the concentration of microparticles in the solution (400 or 1,400 mg/L). The value of the average pitch between microparticles was found by determining the number of particles in a 1 mm^2 area in five different locations on the sample by examining SEM images. Figure 6.58 shows the SEM micrographs of surfaces using microparticles with concentration of 1,400 mg/L resulting in P_{avg} of 21 μm .

6.7.2.2 Contact Angle of Structured Surfaces Using Micropattern

Contact angle and contact angle hysteresis data for the 10 and 50 nm particles on flat and micropatterned surfaces are shown in Fig. 6.59 ([Ebert and Bhushan, 2012](#)). Data for the micropattern without nanoparticles is shown for reference. In the cases of both flat and micropatterned surfaces, the difference in the data between the 10 and 50 nm particles was insignificant. Nanoparticles on a flat surface (nanostructure) showed a CA of $161^\circ (\pm 2^\circ)$ and CAH of $2^\circ (\pm 1^\circ)$. The CA and CAH of the epoxy micropattern alone were found to be $151^\circ (\pm 2^\circ)$ and $33^\circ (\pm 2^\circ)$, respectively. For nanoparticles on the micropattern (hierarchical structure), the highest CA of $168^\circ (\pm 2^\circ)$ and lowest CAH of $1^\circ (\pm 0.5^\circ)$ were found. The relative improvements

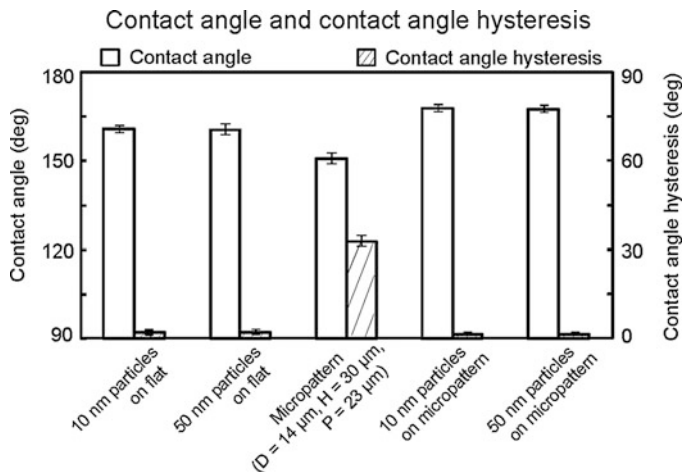


Fig. 6.59 Bar chart showing the measured static contact angle and contact angle hysteresis on nano-, micro-, and hierarchically structured surfaces using both 10 nm and 50-nm particles. The error bars represent ± 1 standard deviation (Ebert and Bhushan, 2012)

in CA and CAH seen in the nanostructured, microstructured, and hierarchically structured surfaces are in agreement using CNTs and Lotus wax, presented earlier.

6.7.2.3 Contact Angle of Surfaces Using Microparticles and Comparison to Micropattern

The CA and CAH of surfaces with $10 \mu\text{m}$ particles on flat and $10 \mu\text{m}/10\text{-nm}$ particles combined on flat are shown in Fig. 6.60 (Ebert and Bhushan, 2012) across a range of average pitch values. In addition, the CA/CAH of epoxy micropatterns of varying pitch are shown in order to provide a comparison of the trends seen with microparticles versus micropatterns. In this comparison, micropatterns with pillars with $D = 5 \mu\text{m}$ and $H = 10 \mu\text{m}$ were used, as the size is more comparable to the microparticles. It is seen that for $10 \mu\text{m}$ particles alone on flat, the trends in CA and CAH with pitch are similar to those of the micropatterns. The micropatterns maintain a contact angle above 150° from the lowest pitch value until a sharp drop at a pitch of $60 \mu\text{m}$. The surfaces with microparticles similarly show a steady CA above 150° , with a sharp drop at an average pitch of $40 \mu\text{m}$. For CAH, the micropattern shows a steady decrease with increasing pitch, until a large increase occurs at $60 \mu\text{m}$. For the $10 \mu\text{m}$ particles, an initial decrease is seen at low pitch, and very low CAH is seen until a large increase occurs, again at $40 \mu\text{m}$.

The sudden changes in CA/CAH, occurring at a pitch of $60 \mu\text{m}$ for the micropatterns and $40 \mu\text{m}$ for the microparticles, represent the transition to the Wenzel regime. At these pitch values, the droop of the water between microstructures is enough that the water fully penetrates between them, leaving no air pockets. For the

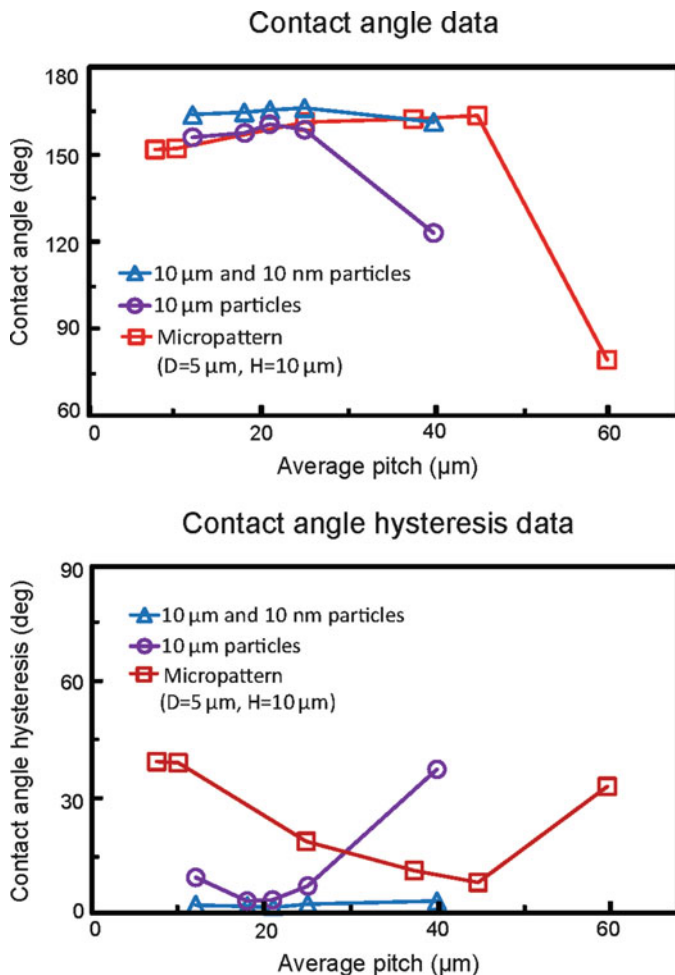
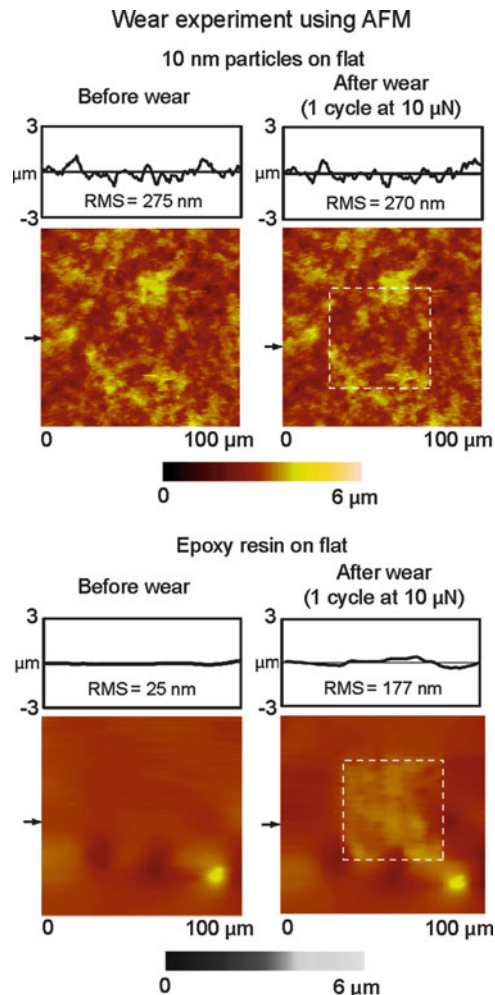


Fig. 6.60 Static contact angle and contact angle hysteresis as a function of average pitch for surfaces with 10 μm particles alone and with 10 μm /10-nm particles combined. Epoxy micropattern data is also shown for comparison of microstructure behavior. Reproducibility is $\pm 1^\circ$ for CAH of 10 μm /10-nm particles combined, $\pm 2^\circ$ for CAH of 10 μm particles and epoxy micropatterns, and $\pm 2^\circ$ for all CA data (Ebert and Bhushan, 2012)

micropatterns, the value of 60 μm is close to the value predicted by (6.4) (74 μm with $D = 5 \mu\text{m}$, $H = 10 \mu\text{m}$). The transition value for the surfaces with 10 μm particles is expected to be different since the pitch, diameter, and height are much less uniform compared to the micropatterns. However, the similarity of the overall trends in CA and CAH with pitch indicates that the microparticles are reasonably mimicking a micropatterned surface. In addition, the data for the 10 μm /10-nm particles combined shows an overall increase in CA and decrease in CAH compared

Fig. 6.61 Surface height maps and sample surface profiles (locations indicated by arrows) before and after AFM wear experiment with 15 μm radius borosilicate ball at load of 10 μN for 10-nm particles on flat surface (*top*) and epoxy resin on flat surface (*bottom*). RMS roughness values for surface profiles are displayed within surface profile boxes (Ebert and Bhushan, 2012)



to the 10 μm particles alone, indicating that the benefits of hierarchical structure can be realized using the 10 μm particles as the underlying microstructure. CA as high as 166°($\pm 2^\circ$) and CAH as low as 2°($\pm 1^\circ$) were seen for these surfaces.

6.7.2.4 Durability of Various Surfaces in AFM and Ball-on-Flat Tribometer Tests

The results of the AFM wear experiment for 10-nm particles as well as an epoxy resin are shown in Fig. 6.61 (Ebert and Bhushan, 2012). Surface height maps before and after the wear experiment are displayed, as well as sample scans across the middle of the image (position indicated by arrow) with root

mean square roughness (RMS) within the wear area displayed. After 1 cycle at 10 μN with the borosilicate ball, the morphology of the surface with 10-nm particles was not significantly changed, and RMS of the sample scan within the wear area was nearly identical (270 nm after compared with 275 nm before). However, the afterimage for the epoxy resin reveals some wear, as well as an overall swelling of the wear area. In addition, RMS of the sample scan increased from 25 to 177 nm within the wear area. This demonstrates that the durability of the nanoparticle-coated surfaces is superior to that of the surfaces with epoxy resin alone.

The ball-on-flat tribometer experimental results are shown in Fig. 6.62 for surfaces with 10 μm particles, 10 μm /10-nm particles combined, and an epoxy resin (Ebert and Bhushan, 2012). Before- and afterimages as well as a scan across the wear scar are displayed for 10 μm particles on flat, 10 μm with 10-nm particles on flat, and epoxy resin on flat. After 100 cycles at 10 mN, the 10 μm particles alone showed minimal wear (mainly in the form of burnishing of the tops of particles), and a microscale roughness is preserved. The 10 μm and 10-nm particles combined show similar results of minimal wear. However, the afterimage of the epoxy resin reveals a well-defined groove. The scan shows buildup along the sides of the groove, and the groove depth can be seen as approximately 300 nm. Thus, the surfaces with microparticles also showed resistance to wear superior to that of the surfaces with epoxy resin alone.

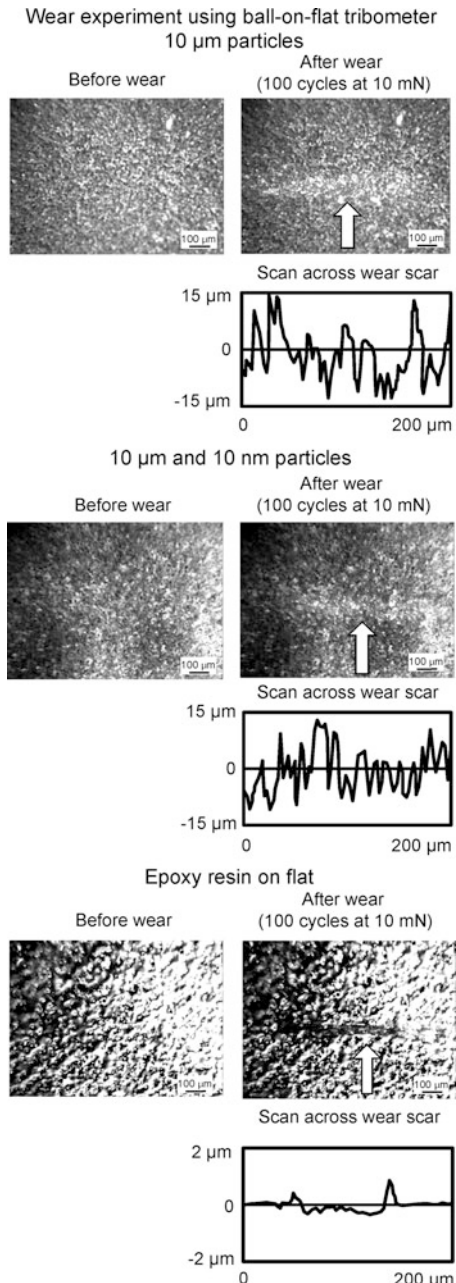
6.7.2.5 Summary

Mechanically durable, hierarchically structured surfaces with Lotus-effect characteristics have been produced using micro- and nanosized silica particles and a spray method. A comparison was made between the use of microparticles and micropatterns in terms of wettability across different pitch values. Results show similar trends in CA/CAH with pitch value whether the microstructure was formed with particles or a micropattern. Hierarchical surfaces using micro- and nanoparticles exhibited a CA of $166^\circ(\pm 2^\circ)$ and a CAH of $2^\circ(\pm 1^\circ)$ at optimum pitch. For hierarchical surfaces using micropatterns with nanoparticles, a nearly identical CA of $168^\circ(\pm 2^\circ)$ and CAH of $1^\circ(\pm 0.5^\circ)$ were measured. In addition, the surfaces demonstrated wear resistance superior to the epoxy resin on multiple length scales in the AFM and tribometer experiments, showing ability to preserve both nanoscale and microscale roughness.

6.8 Summary

In Chap. 4, various leaf surfaces on the micro- and nanoscale have been characterized and modeled to understand how nature provides functionality. Chapter 5 provided an overview of various fabrication techniques which have been used

Fig. 6.62 Optical micrographs before and after wear experiment using ball-on-flat tribometer at 10 mN for 10 μm particles (*top*), 10 μm particles with 10-nm particles (*middle*), and epoxy resin on flat surface (*bottom*). Sample profiles across wear areas are shown below after images (arrows indicate location of profile) (Ebert and Bhushan, 2012)



to fabricate one-level and hierarchical structures. In this chapter, micro-, nano-, and hierarchical patterned structures have been fabricated using soft lithography, photolithography, and techniques which involve the replication of micropatterns, self-assembly of hydrophobic alkanes and plant waxes, and a spray coating of carbon nanotubes and silica particles. They have been characterized to validate the models and to provide design guidelines for superhydrophobic and self-cleaning surfaces. To further examine the effect of meniscus force and real area of contact, scale dependence is considered with the use of AFM tips of various radii. To investigate how the effects of spacing between pillars, droplet size, and impact velocity influence the transition, wetting, evaporation, and bouncing studies were conducted on silicon surfaces patterned with pillars of two different diameters and heights and with varying pitch values and deposited with a hydrophobic coating. In order to generate submicron droplets, an atomic force microscopy-based technique using a modified nanoscale dispensing probe was used. An ESEM study on the wetting behavior for a microdroplet with about $20\text{ }\mu\text{m}$ radius on the micropatterned Si surfaces was carried out.

Hierarchical structures using nature's route were fabricated to verify the understanding of the mechanisms relevant to superhydrophobicity and self-cleaning in the Lotus leaf by comparing the superhydrophobicity and self-cleaning of fabricated surfaces and the Lotus leaf. For durable fabricated surfaces, surfaces with carbon nanotubes and silica particles were fabricated. The loss of superhydrophobicity as well as wear and friction was investigated).

References

- Adamson AV (1990) Physical chemistry of surfaces. Wiley, New York
- Bartolo D, Bouamrane F, Verneuil E, Buguin A, Silberzan P, Moulinet S (2006) Bouncing or sticky droplets: impalement transitions on superhydrophobic micropatterned surfaces. *Europhys Lett* 74:299–305
- Bhushan B (1999) Principles and applications of tribology. Wiley, New York
- Bhushan B (2002) Introduction to tribology. Wiley, New York
- Bhushan B (2003) Adhesion and stiction: mechanisms, measurement techniques and methods for reduction. *J Vac Sci Technol B* 21:2262–2296
- Bhushan B (2010) Springer handbook of nanotechnology, 3rd edn. Springer, Heidelberg
- Bhushan B (2011) Nanotribology and nanomechanics I—measurement techniques, II—nanotribology, biomimetics, and industrial applications, 3rd edn Springer, Heidelberg
- Bhushan B, Blackman GS (1991) Atomic force microscopy of magnetic rigid disks and sliders and its applications to tribology. *ASME J Tribol* 113:452–457
- Bhushan B, Gupta BK (1991) Handbook of tribology: materials, coatings, and surface treatments. McGraw-Hill, New York
- Bhushan B Jung YC (2006) Micro and nanoscale characterization of hydrophobic and hydrophilic leaf surface. *Nanotechnology* 17:2758–2772
- Bhushan B, Jung YC (2007) Wetting study of patterned surfaces for superhydrophobicity. *Ultramicroscopy* 107:1033–1041
- Bhushan B, Jung YC (2008) Wetting, adhesion and friction of superhydrophobic and hydrophilic leaves and fabricated micro/nanopatterned surfaces. *J Phys Condens Matter* 20:225010

- Bhushan B, Hansford D, Lee KK (2006) Surface modification of silicon and polydimethylsiloxane surfaces with vapor-phase-deposited ultrathin fluorosilane films for biomedical nanodevices. *J Vac Sci Technol A* 24:1197–1202
- Bhushan B, Nosonovsky M, Jung YC (2007) Towards optimization of patterned superhydrophobic surfaces *J R Soc Interface* 4:643–648
- Bhushan B, Koch K, Jung, YC (2008a) Nanostructures for superhydrophobicity and low adhesion. *Soft Matter* 4:1799–1804
- Bhushan B, Koch K, Jung YC (2008b) Biomimetic hierarchical structure for self-cleaning. *Appl Phys Lett* 93:093101
- Bhushan B, Jung YC, Koch K (2009a) Self-cleaning efficiency of artificial superhydrophobic surfaces. *Langmuir* 25:3240–3248
- Bhushan B, Jung YC, Koch K (2009b) Micro-, nano- and hierarchical structures for superhydrophobicity, self-cleaning and low adhesion. *Philos Trans Roy Soc A* 367:1631–1672
- Bhushan B, Jung YC, Niemietz A, Koch K (2009c) Lotus-like biomimetic hierarchical structures developed by the self-assembly of tubular plant waxes. *Langmuir* 25:1659–1666
- Bhushan B, Koch K, Jung YC (2009d) Fabrication and characterization of the hierarchical structure for superhydrophobicity. *Ultramicroscopy* 109:1029–1034
- Bhushan B, Jung YC, Nosonovsky M (2012) Hierarchical structures for superhydrophobic surfaces and methods of making. US Patent 8,137,751 B2, 20 March 2012
- Bormashenko E, Pogreb R, Whyman G, Erlich M (2007) Cassie–Wenzel wetting transition in vibrated drops deposited on the rough surfaces: is dynamic Cassie–Wenzel transition 2D or 1D affair? *Langmuir* 23:6501–6503
- Bourges-Monnier C, Shanahan MER (1995) Influence of evaporation on contact angle. *Langmuir* 11:2820–2829
- Brugnara M, Della Volpe C, Siboni S, Zeni D (2006) Contact angle analysis on polymethylmethacrylate and commercial wax by using an environmental scanning electron microscope. *Scanning* 28:267–273
- Bunshah RF (1994) Handbook of deposition technologies for films and coatings: science, technology and applications. Applied Science Publishers, Westwood, New Jersey
- Burton Z, Bhushan B (2005) Hydrophobicity, adhesion, and friction properties of nanopatterned polymers and scale dependence for micro- and nanoelectromechanical systems. *Nano Lett* 5:1607–1613
- Burton Z, Bhushan B (2006) Surface characterization and adhesion and friction properties of hydrophobic leaf surfaces. *Ultramicroscopy* 106:709–719
- Callister WD (2000) Materials science and engineering—an introduction, 5th edn. Wiley, New York
- Celestini F, Kofman R (2006) Vibration of submillimeter-size supported droplets. *Phys Rev E* 73:041602
- Checco A, Guenoun P, Daillant J (2003) Nonlinear dependence of the contact angle of nanodroplets on contact line curvatures. *Phys Rev Lett* 91:186101
- Chen N, Bhushan B (2006) Atomic force microscopy studies of conditioner thickness distribution and binding interactions on the hair surface. *J Microsc* 221:203–215
- Chen YL, Helm CA, Israelachvili JN (1991) Molecular mechanisms associated with adhesion and contact angle hysteresis of monolayer surfaces. *J Phys Chem* 95:10736–10747
- Chen XH, Chen CS, Xiao HN, Liu HB, Zhou LP, Li SL, Zhang G (2006) Dry friction and wear characteristics of nickel/carbon nanotube electroless composite deposits. *Tribol Int* 39:22–28
- Choi SE, Yoo PJ, Baek SJ, Kim TW, Lee HH (2004) An ultraviolet-curable mold for sub-100-nm lithography. *J Am Chem Soc* 126:7744–7745
- Danilatos GD, Brancik JV (1986) Observation of liquid transport in the ESEM. In: Proceedings of the 44th annual meeting EMSA, pp 678–679
- Dorset DL, Pangborn WA, Hancock AJ (1983) Epitaxial crystallization of alkane chain lipids for electron diffraction analysis. *J Biochem Biophys Meth* 8:29–40
- Dresselhaus MS, Dresselhaus G, Avouris Ph (2000) Carbon nanotubes: synthesis, structure, properties, and applications. Springer, Heidelberg

- Ebert D, Bhushan B (2012) Durable Lotus-effect surfaces with hierarchical structure using micro- and nanosized hydrophobic silica particles. *J Colloid Interface Sci* 368:584–591
- Englert BC, Xiu Y, Wong CP (2006) Deposition and surface treatment of microparticles to produce Lotus-effect surface. In: 11th international symposium on advanced packaging materials: processes, properties and interfaces, Atlanta, GA, March 15–17, pp 73–78
- Erbil HY, Demirel AL, Avci Y (2003) Transformation of a simple plastic into a superhydrophobic surface. *Science* 299: 1377–1380
- Erbil HY, McHale G, Newton MI (2002) Drop evaporation on solid surfaces: constant contact angle mode. *Langmuir* 18:2636–2641
- Good RJ (1952) A thermodynamic derivation of Wenzel's modification of Young's equation for contact angles; together with a theory of hysteresis. *J Am Chem Soc* 74:5041–5042
- Hong YC, Uhm HS (2006) Superhydrophobicity of a material made from multiwalled carbon nanotubes. *Appl Phys Lett* 88:244101
- Huang L, Lau SP, Yang HY, Leong ESP, Yu SF (2005) Stable superhydrophobic surface via carbon nanotubes coated with a zno thin film *J Phys Chem* 109:7746–7748
- Israelachvili JN (1992) Intermolecular and surface forces. 2nd edn., Academic, London
- Joanny JF, de Gennes PG (1984) A model for contact angle hysteresis. *J Chem Phys* 81:552–562
- Johnson RE, Dettre RH (1964). Contact angle hysteresis. In: Fowkes FM (ed) Contact angle, wettability, and adhesion. Adv. Chem. Ser., vol 43. American Chemical Society, Washington, DC, pp 112–135
- Jung YC, Bhushan B (2006) Contact angle, adhesion, and friction properties of micro- and nanopatterned polymers for superhydrophobicity. *Nanotechnology* 17:4970–4980
- Jung YC, Bhushan B (2007) Wetting transition of water droplets on superhydrophobic patterned surfaces. *Scripta Mater* 57:1057–1060
- Jung YC, Bhushan B (2008a) Wetting behavior during evaporation and condensation of water microdroplets on superhydrophobic patterned surfaces. *J Microsc* 229:127–140
- Jung YC, Bhushan B (2008b) Dynamic effects of bouncing water droplets on superhydrophobic surfaces. *Langmuir* 24:6262–6269
- Jung YC, Bhushan B (2008c) Technique to measure contact angle of micro/nanodroplets using atomic force microscopy. *J Vac Sci Technol A* 26:777–782
- Jung YC, Bhushan B (2009a) Dynamic effects induced transition of droplets on biomimetic superhydrophobic surfaces. *Langmuir* 25:9208–9218
- Jung YC, Bhushan B (2009b) Mechanically durable CNT-composite hierarchical structures with superhydrophobicity, self-cleaning, and low-drag. *ACS Nano* 3:4155–4163
- Jung YC, Bhushan B (2009c) Mechanically durable CNT-composite hierarchical structures with superhydrophobicity, self-cleaning, and low-drag. *ACS Nano* 3:4155–4163
- Jung YC, Bhushan B (2010) Biomimetic structures for fluid drag reduction in laminar and turbulent flows. *J Phys Condens Matter* 22:035104
- Kasai T, Bhushan B, Kulik G, Barbieri L, Hoffmann P (2005) Micro/nanotribological study of perfluorosilane SAMs for antistiction and low wear. *J Vac Sci Technol B* 23:995–1003
- Koch K, Dommissie A, Barthlott W (2006a) Chemistry and crystal growth of plant wax tubules of Lotus (*Nelumbo nucifera*) and Nasturtium (*Tropaeolum majus*) leaves on technical substrates. *Cryst Growth Des* 6:2571–2578
- Koch K, Barthlott W, Koch S, Hommes A, Wandelt K, Mamdouh W, De-Feyter S, Broekmann P (2006b) Structural analysis of wheat wax (*Triticum aestivum*, c.v. 'Naturastar' L.): from the molecular level to three dimensional crystals. *Planta* 223:258–270
- Koch K, Dommissie A, Barthlott W, Gorb S (2007). The use of plant waxes as templates for micro- and nanopatterning of surfaces. *Acta Biomater* 3:905–909
- Koch K, Schulte AJ, Fischer A, Gorb SN, Barthlott W (2008). A fast and low-cost replication technique for nano- and high-aspect-ratio structures of biological and artificial materials. *Bioinsp Biomim* 3:046002
- Koch K, Bhushan B, Jung YC, Barthlott W (2009). Fabrication of artificial lotus leaves and significance of hierarchical structure for superhydrophobicity and low adhesion. *Soft Matter* 5:1386–1393

- Lafuma A, Quéré D (2003) Superhydrophobic states. *Nature Mater* 2:457–460
- Lamb H (1932) Hydrodynamics. Cambridge University Press, Cambridge
- Lau KKS, Bico J, Teo KBK, Chhowalla M, Amarasinghe GAJ, Milne WI, McKinley GH, Gleason KK (2003) Superhydrophobic carbon nanotube forests. *Nano Lett* 3:1701–1705
- Lee S-W, Laibinis PE (2000) Directed movement of liquids on patterned surfaces using noncovalent molecular adsorption. *J Am Chem Soc* 122:5395–5396
- Liu Y, Chen X, Xin JH (2006) Super-hydrophobic surfaces from a simple coating method: a bionic nanoengineering approach. *Nanotechnology* 17:3259–3263
- Lodge RA, Bhushan B (2006) Surface characterization of human hair using tapping mode atomic force microscopy and measurement of conditioner thickness distribution. *J Vac Sci Technol A* 24:1258–1269
- McHale G, Aqil S, Shirtcliffe NJ, Newton MI, Erbil HY (2005) Analysis of droplet evaporation on a superhydrophobic surface. *Langmuir* 21:11053–11060
- Meyyappan M (2005) Carbon nanotubes—science and applications. CRC Press, Boca Raton, FL
- Ming W, Wu D, van Benthem R, de With G (2005) Superhydrophobic films from raspberry-like particles. *Nano Lett* 5:2298–2301
- Neinhuis C, Barthlott W (1997) Characterization and distribution of water-repellent, self-cleaning plant surfaces. *Ann Bot* 79:667–677
- Niemietz A, Wandelt K, Barthlott W, Koch K (2009) Thermal evaporation of multi-component waxes and thermally activated formation of nano-tubules for superhydrophobic surfaces. *Prog Org Coat* 66:221–227
- Noblin X, Buguin A, Brochard-Wyart F (2004) Vibrated sessile drops: transition between pinned and mobile contact line oscillations. *Eur Phys J E* 14:395–404
- Nosonovsky M, Bhushan B (2005) Roughness optimization for biomimetic superhydrophobic surfaces. *Microsyst Technol* 11:535–549
- Nosonovsky M, Bhushan B (2007a) Multiscale friction mechanisms and hierarchical surfaces in nano- and bio-tribology. *Mater Sci Eng R* 58:162–193
- Nosonovsky M, Bhushan B (2007b) Hierarchical roughness makes superhydrophobic surfaces stable. *Microelectron Eng* 84:382–386
- Nosonovsky M, Bhushan B (2007c) Biomimetic superhydrophobic surfaces: multiscale approach. *Nano Lett* 7:2633–2637
- Nosonovsky M, Bhushan B (2007d) Hierarchical roughness optimization for biomimetic superhydrophobic surfaces. *Ultramicroscopy* 107:969–979
- Nosonovsky M, Bhushan B (2008a) Multiscale dissipative mechanisms and hierarchical surfaces: friction, superhydrophobicity, and biomimetics. Springer, Heidelberg
- Nosonovsky M, Bhushan B (2008b) Roughness-induced superhydrophobicity: a way to design non-adhesive surfaces. *J Phys Condens Matter* 20:225009
- Nosonovsky M, Bhushan B (2008c) Patterned non-adhesive surfaces: superhydrophobicity and wetting regime transitions. *Langmuir* 24:1525–1533
- Nosonovsky M, Bhushan B (2008d) Capillary effects and instabilities in nanocontacts. *Ultramicroscopy* 108:1181–1185
- Nosonovsky M, Bhushan B (2008e) Energy transitions in superhydrophobicity: low adhesion, easy flow and bouncing. *J Phys Condens Matter* 20:395005
- Palacio M, Bhushan B (2010) Normal and lateral force calibration techniques for AFM cantilevers. *Crit Rev Solid State Mater Sci* 35:73–104
- Pompe T, Herminghaus S (2000) Three-phase contact line energetics from nanoscale liquid surface topographies. *Phys Rev Lett* 85:1930–1933
- Quere D (2004) Surface wetting model droplets. *Nature Mater* 3:79–80
- Reyssat M, Pepin A, Marty F, Chen Y, Quere D (2006) Bouncing transitions on microtextured materials. *Europhys Lett* 74:306–312
- Richard D, Clanet C, Quere D (2002) Contact time of a bouncing drop. *Nature* 417:811
- Rowan SM, Newton MI, McHale G (1995) Evaporation of microdroplets and the wetting of solid surfaces. *J Phys Chem* 99:13268–13271

- Semal S, Blake TD, Geskin V, de Ruijter ML, Castelein G, De Coninck J (1999) Influence of surface roughness on wetting dynamics. *Langmuir* 15:8765–8770
- Shibuchi S, Onda T, Satoh N, Tsujii K (1996) Super-water-repellent surfaces resulting from fractal structure. *J Phys Chem* 100:19512–19517
- Stelmashenko NA, Craven JP, Donald AM, Terentjev EM, Thiel BL (2001) Topographic contrast of partially wetting water droplets in environmental scanning electron microscopy. *J Microsc* 204:172–183
- van Dijk AIJM, Bruijnzeel LA, Rosewell CJ (2002) Rainfall intensity–kinetic energy relationships: a critical literature appraisal. *J Hydrology* 261:1–23
- Wong EW, Sheehan PE, Lieber CM (1997) Nanobeam mechanics: elasticity, strength, and toughness of nanorods and nanotubes. *Science* 277:1971–1975
- Yost FG, Michael JR, Eisenmann ET (1995) Extensive wetting due to roughness. *Acta Metall Mater* 45:299–305
- Zhang X, Tan S, Zhao N, Guo X, Zhang X, Zhang Y, Xu J (2006) Evaporation of sessile water droplets on superhydrophobic natural Lotus and biomimetic polymer surfaces. *Chem Phys Chem* 7:2067–2070
- Zhang YY, Wang CM, Tan VBC (2008) Examining the effects of wall numbers on buckling behavior and mechanical properties of multiwalled carbon nanotubes via molecular dynamics simulations. *J Appl Phys* 103:053505
- Zhu L, Xiu Y, Xu J, Tamirisa PA, Hess DW, Wong C (2005) Superhydrophobicity on two-tier rough surfaces fabricated by controlled growth of aligned carbon nanotube arrays coated with fluorocarbon. *Langmuir* 21:11208–11212

Part II

Salvinia Effect



Chapter 7

Fabrication and Characterization of Micropatterned Structures Inspired by *Salvinia molesta*

7.1 Introduction

One plant leaf of interest is the floating water fern of genus *Salvinia* because of its ability to trap and hold an air film under water for up to several months (Koch et al., 2009). The ability to retain air prevents wetting and submersion. Specifically, *Salvinia molesta* has been studied because of its complex structured surface. It is an aquatic fern commonly known as giant *Salvinia* and is native to southeastern Brazil. *S. molesta* is a free-floating plant that does not require soil and consists of leaves that are roughly 0.5–4 cm wide and long.

A mechanism for long-term air retention for the floating water fern *S. molesta* has been explored by Barthlott et al. (2010) and Hunt and Bhushan (2011). It has been shown that the hierarchical nature of the *S. molesta* leaf is predominantly composed of tiny eggbeater-shaped hairs, shown in Fig. 7.1, which are almost completely hydrophobic due to a coating of nanoscopic wax crystals, except for the terminal cells of each hair which lack the crystals, thus making them hydrophilic. These hydrophilic patches are located at the top of each hair where the individual follicles forming the eggbeater shape are joined together. Due to the hydrophilic patches at the tip of each hair, *S. molesta* exhibits a pinning effect of water against the top of the hairs which enables the formation of air pockets between each hair as shown in Fig. 7.2 (Hunt and Bhushan, 2011). The combination of hydrophilic patches coupled with an inner hydrophobic coating of the *S. molesta* hairs and the subsequent ability of *S. molesta* to pin water and retain air when submerged underwater is referred to as “*Salvinia Effect*.”

Air-retaining surfaces are of technological interest due to their ability to reduce drag when used for fluid transport, ship coatings, and other submersible industrial products in which drag is a concern. Superhydrophobic surfaces have been utilized to obtain the desired air film for the previously stated applications; however, the effect called “giant liquid slip” has been shown to deteriorate the presence of such air films in a matter of minutes (Balasubramanian et al., 2004; Choi and Kim, 2006; Henoch et al., 2006; Lee and Kim, 2009). Therefore, *S. molesta*’s unique ability to

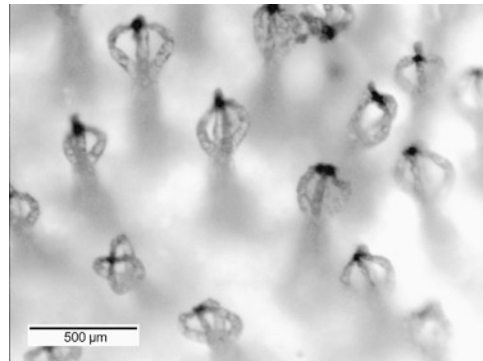


Fig. 7.1 Optical micrograph of *S. molesta* leaf (Hunt and Bhushan, 2011)

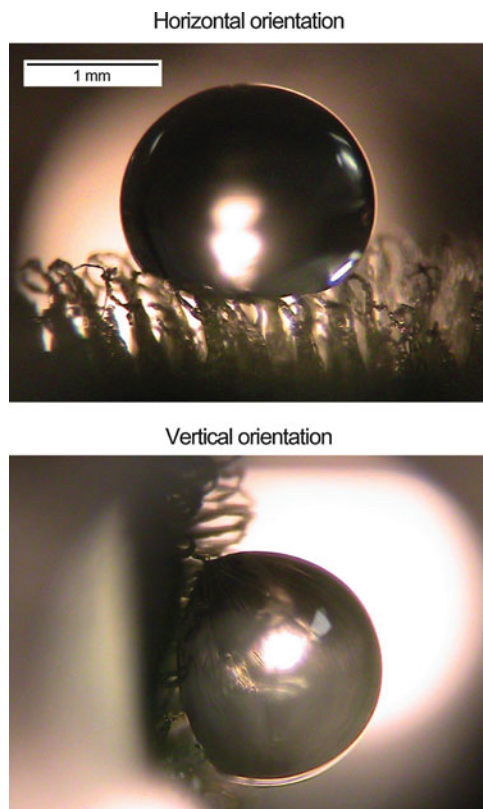


Fig. 7.2 Water droplet suspended by *S. molesta* hair at *horizontal* and *vertical* orientations demonstrating air pocket formation and water pinning at the hydrophilic tips where the terminal cells of each *S. molesta* hair is located (Hunt and Bhushan, 2011)

pin water and trap air is of importance in order to increase the durability and lifetime of air pocket formation for drag reduction in industrial use.

Hunt and Bhushan (2011) mimicked the air-trapping ability of *S. molesta* in order to prove that a structure can be created in the lab that can mimic the behavior of the fern as well as demonstrate microfabrication techniques that can be utilized in industry to produce such materials. To accomplish this, a micropattern was created in the lab with comparable dimensions to the *S. molesta* hairs. The micropattern was then treated with a hydrophobic coating which is then stripped away to produce a new microstructure which is hydrophobic everywhere except for the tips of the micropattern in the same manner as the *S. molesta* hairs themselves. The new micropattern was then studied to determine air-trapping ability as well as its ability to pin water in the same fashion as *S. molesta*.

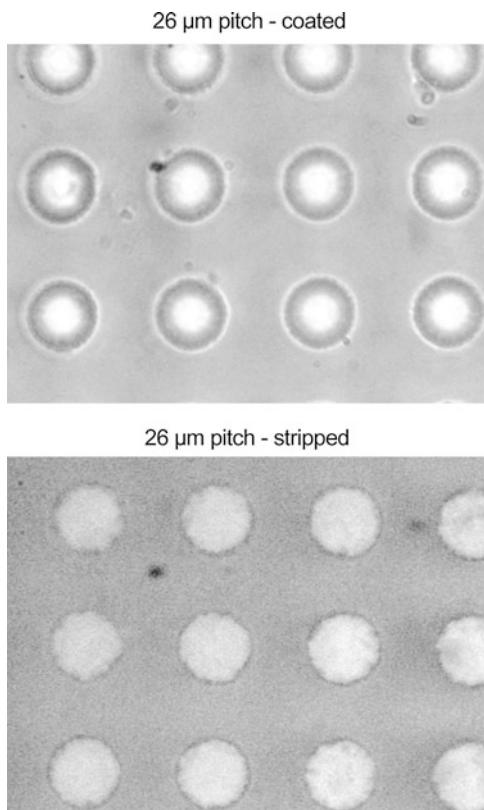
7.2 Characterization of Leaves and Fabrication of Inspired Structural Surfaces

To characterize the fern hair, an optical microscope was used to image *S. molesta* as well as determine the spacing of the fern hairs (Fig. 7.1). Using the microscope images, an average hair spacing of $490\text{ }\mu\text{m}$ with a range of $250\text{--}750\text{ }\mu\text{m}$ was observed. The apparent surface area of the tip of the *S. molesta* hair where the four eggbeater-shaped hairs come to a point was observed to be on the order of $20\text{ }\mu\text{m}\times 20\text{ }\mu\text{m}$. The height of the *S. molesta* hairs was about 2 mm.

To mimic the air-trapping ability of *S. molesta*, a micropatterned surface was fabricated. A two-step molding technique as discussed before was employed. The technique was used to create microstructures of $14\text{ }\mu\text{m}$ diameter (mimicking the surface area of the *S. molesta* hair tips) and $30\text{ }\mu\text{m}$ height with a pitch value of $26\text{ }\mu\text{m}$. The $30\text{ }\mu\text{m}$ pillar height, while much smaller than the observed 2-mm height of the *S. molesta* hairs, was selected based on the tallest pattern size readily available for the given pitch and diameter dimensions. The $26\text{ }\mu\text{m}$ pitch was selected to compensate for the low height of the micropillars as compared to the observed high height of the *S. molesta* hairs in order to reproduce a closer ratio between the height and pitch of the fern hairs to allow the ability to trap air.

Once the epoxy replicas were created, a coating of (tridecafluoro-1,1,2,2-tetrahydrooctyl) trichlorosilane (Gelest) was then applied by a syringe to the surface of the micropatterns to impart hydrophobicity. After coating, the micropatterns were placed in a vacuum at 500 mTorr for 1 min to remove air bubbles and to assist with saturation. Finally, the hydrophobic coating was removed using double-sided tape to strip away the trichlorosilane from the top of the microstructures, leaving the hydrophobic coating in between the micropillars. The tape was attached to a flat surface and then lowered onto the top of the micropattern using a motor-driven arm until the surface of the micropattern came into contact with the double-sided tape which ensured that the tape stayed flat and did not bend

Fig. 7.3 Micropillars created in lab (14 μm diameter, 30 μm height, 26 μm pitch) coated with (tridecafluoro-1,1,2,2-tetrahydrooctyl) trichlorosilane (Gelest) and stripped away ([Hunt and Bhushan, 2011](#))



while making contact with the tips of the micropattern. The hydrophobic coating was stripped from the tips of the micropillars, creating a microstructure which is hydrophobic with small patches at the tips of the micropillars which are hydrophilic. This was done in order to mimic the *S. molesta* hairs in which the surface of the leaf is almost completely hydrophobic except for tiny hydrophilic patches at the tips of the fern hairs. Optical microscope imaging of the microstructure is shown in Fig. 7.3 for the coated and stripped micropillars.

7.3 Measurement of Contact Angle and Adhesion

7.3.1 Observation of Pinning and Contact Angle

When submerged in water, a silvery layer is visible on the surface of the *S. molesta* leaf, indicating a layer of air trapped against the surface. To observe the effect that water pressure had on the ability of *S. molesta* to maintain an air layer when

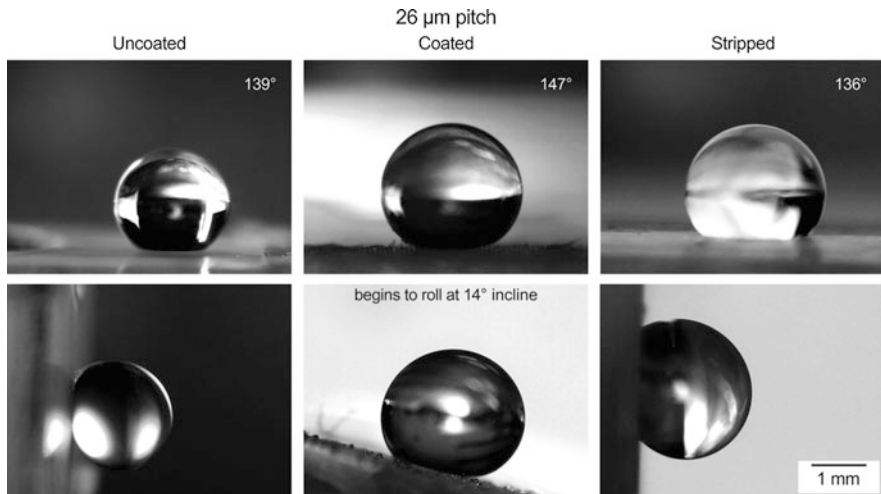


Fig. 7.4 Contact angle measurement for coated, uncoated, and stripped micropillars and samples turned to 90° vertical orientation to determine if water pinning occurs (adapted from [Hunt and Bhushan, 2011](#))

submerged in water, the leaf was subjected to a hydrostatic pressure test at a depth of 0.3 m under a column of water. When submerged, the fern was able to retain an air layer under a hydrostatic pressure of 3 kPa. With this result in mind, [Hunt and Bhushan \(2011\)](#) explored the interaction between water droplets and the micropatterns fabricated in their study to observe the micropatterns' ability to produce an air layer and pin water to its surface. This was accomplished by studying the contact angle and angle at which water will remain pinned to the surface of the micropatterns.

Results from the water contact angle test are shown in Fig. 7.4 ([Hunt and Bhushan, 2011](#)). Also shown in Fig. 7.4 are the results of the tilt test used to check for water pinning at vertical orientation. The uncoated 26 μm micropattern shows an increased contact angle of 139°. As predicted by the transition criteria discussed previously (6.4), the interface falls within the Cassie–Baxter regime, therefore creating air pockets between the water droplet and base of the micropattern. However, despite the higher contact angle observed on the 26 μm pitch, the water does not roll off of the epoxy microstructure due to the hydrophilic nature of the micropillars. The attraction between the micropillars and water droplet is high enough to pin the water to the surface of the microstructure at vertical orientation. The coated 26 μm micropattern displays a contact angle of 147° and is higher than the 139° contact angle of the uncoated sample. The water begins to roll off of the 26 μm pitch at an incline of 14°. When the microstructure is stripped, the contact angle is reduced to 136° which is on par with the uncoated 26 μm sample, and water remains pinned to the surface due to the hydrophilic nature of the now-exposed tips of the micropillars as a result of stripping. Because of the hydrophilic nature of

the surface of the microstructures, the water droplet remains pinned to the surface at vertical orientation despite the hydrophobic nature of the coating between the micropillars and air pocket resulting from the interface residing in the Cassie–Baxter regime.

To summarize, the micropattern traps air at the interface of the water droplet and also has a hydrophobic coating in between the micropillars while the tips of the pillars are hydrophilic in nature, thus exhibiting the same characteristics of *S. molesta*.

7.3.2 Adhesion

The force–distance curve resulting from the adhesion study of *S. molesta* is shown in Fig. 7.5 (top) (Hunt and Bhushan, 2011). The dip in Fig. 7.5 shows a vertical tip deflection in the retracting direction of 69 nm which is used to calculate the adhesive force (F_{ad}) by multiplying the vertical deflection of the tip by the cantilever spring constant (k) of 3 N/m. This corresponds with a resulting adhesive force of 207 nN. The force–distance curve for the stripped 26 μm micropattern is shown in Fig. 7.5 (middle). Similar to the *S. molesta* force–distance curve, a tip deflection of 67 nm is shown which corresponds with an adhesive force of 201 nN.

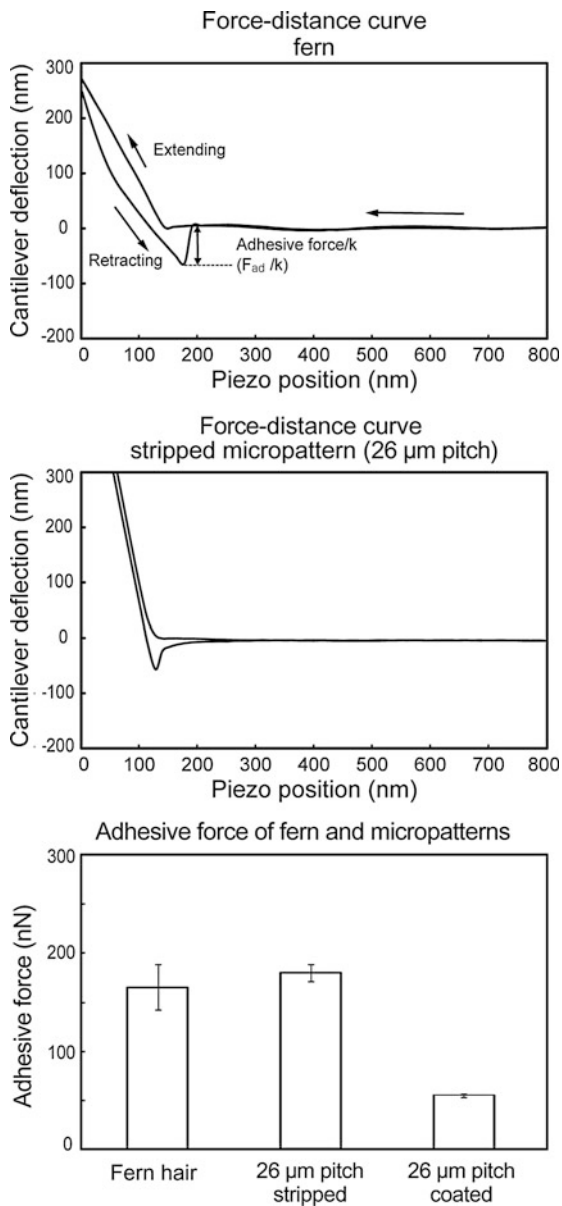
A comparison of the adhesive force for *S. molesta* and the 26 μm micropattern is shown in Fig. 7.5 (bottom) for both the coated and stripped micropatterns. As expected, the trichlorosilane-coated micropattern exhibits a much lower average adhesive force of 54 nN. The *S. molesta* hairs show an average adhesive force of 165 nN with a standard deviation of 47 nN, and the stripped 26 μm microstructure shows an average adhesive force of 180 nN with a standard deviation of 19 nN.

The similarity between the adhesive force of the stripped microstructure and the *S. molesta* hair is an important result because it shows that the stripped microstructure will exhibit similar surface characteristics as the *S. molesta* hair. The higher adhesive force of the stripped microstructure compared to the coated 26 μm microstructure explains why water will roll off of the coated sample at an incline of 14° whereas water will remain trapped at a vertical orientation for the stripped sample.

7.4 Summary

A 26 μm -pitch microstructure composed of micropillars has been created such that the surface is predominantly hydrophobic while still having hydrophilic tips. It exhibited a comparable wetting behavior to the *S. molesta* hair. The resultant microstructure is shown to create trapped air pockets between a water droplet and microstructure base due to the water droplet residing in the Cassie–Baxter state. Additionally, the newly created microstructure has been shown to exhibit similar

Fig. 7.5 Top plot shows force-distance curves for fern and striped microstructure showing extending and retracting motion of AFM tip and illustrating adhesive force calculation. The vertical deflection of the AFM tip is given by F_{ad}/k where F_{ad} is the adhesive force between AFM tip and the surface and k is the spring stiffness of the cantilever (3 N/m). F_{ad} is calculated by multiplying the tip deflection (read from the graph) and multiplying by the spring stiffness. The bottom bar chart presents adhesive force data for fern hairs and micropillars (coated and stripped) (Hunt and Bhushan, 2011)



adhesion as the *S. molesta* hair. As a result of the similar adhesive forces, water pinning on the microstructure has been observed up to vertical orientation in the same fashion as *S. molesta* (Hunt and Bhushan, 2011).

It has been shown that the Salvinia Effect of pinning water and creating air pockets at the water surface interface, as well as the necessary fabrication techniques

required for such a surface, is viable through the fabrication of hydrophobic micropatterns with a predefined level of hydrophilic patches. The commercial applications for such a technology include industrial uses in which fluid transport, drag reduction, and increased buoyancy are of interest, especially in applications in which giant liquid slip has been shown to deteriorate air films created by superhydrophobic surfaces.

References

- Balasubramanian AK, Miller AC, Rediniotis OK (2004) Microstructured hydrophobic skin for hydrodynamic drag reduction. *AIAA J* 42:411–414
- Barthlott W, Schimmel T, Wiersch S, Koch K, Brede M, Barczewski M, Walheim S, Weis A, Kaltenmaier A, Leder A, Bohn HF (2010) The salvinia paradox: superhydrophobic surfaces with hydrophilic pins for air retention under water. *Adv Mater* 22:2325–2328
- Choi C-H, Kim C-J (2006) Large slip of aqueous liquid flow over a nanoengineered superhydrophobic surface. *Phys Rev Lett* 96:066001-4
- Henoeh C, Krupenkin TN, Kolodner P, Taylor JA, Hodes MS, Lyons AM, Breuer K (2006) Turbulent drag reduction using superhydrophobic surfaces. In: 3rd AIAA flow control conference, San Francisco, CA, 5–8 June 2006, AIAA-2006-3192
- Hunt J, Bhushan B (2011) Nanoscale biomimetics studies of *Salvinia molesta* for micropattern fabrication. *J Colloid Interface Sci* 363:187–192
- Koch K, Bhushan B, Barthlott W (2009) Multifunctional surface structures of plants: an inspiration for biomimetics. *Prog Mater Sci* 54:137–178
- Lee C, Kim C-J (2009) Maximizing the giant liquid slip on superhydrophobic microstructures by nanostructuring their sidewalls. *Langmuir* 25:12812

Part III

Rose Petal Effect

Chapter 8

Characterization of Rose Petals and Fabrication and Characterization of Superhydrophobic Surfaces with High and Low Adhesion

8.1 Introduction

Unlike the Lotus leaf, some rose petals (*rosea Rehd*), scallions, and garlic exhibit superhydrophobicity with high contact angle hysteresis (Feng et al., 2008; Chang et al., 2009; Bhushan and Her, 2010). While a water droplet can easily roll off the surface of a Lotus leaf, it stays pinned to the surface of these leaves. The different behavior of wetting between the Lotus leaf and the rose petal can be explained by different designs in the surface hierarchical micro- and nanostructure. Since the rose petal's microstructure, possibly nanostructure, has a larger pitch value and lower height than the Lotus leaf, the liquid is allowed to impregnate between the microstructure and partially penetrates into the nanostructure, which increases the wetted surface area. As a result, contact angle hysteresis increases with increasing wetted surface area. In the case of scallion and garlic leaves, contact angle hysteresis is high due to hydrophobic defects responsible for contact line pinning. Such superhydrophobic surfaces with high adhesion have various potential applications, such as the transport of liquid microdroplets over a surface without sliding or rolling, the analysis of very small volumes of liquid samples, and for the inside of an aircraft surface to minimize the falling of condensed water droplets onto passengers. There have been few attempts to fabricate such surfaces in the laboratory (Jin et al., 2005; Hong et al., 2007; Bhushan and Her, 2010).

Bhushan and Her (2010) have reported that rose petals can have either high or low adhesion. They studied two superhydrophobic rose petals with high and low adhesion and proposed relevant mechanisms. Based on the understanding, they fabricated artificial superhydrophobic surfaces with high and low adhesions to verify mechanisms. Bhushan and Nosonovsky (2010) have studied wetting regimes in the two kinds of rose petals.

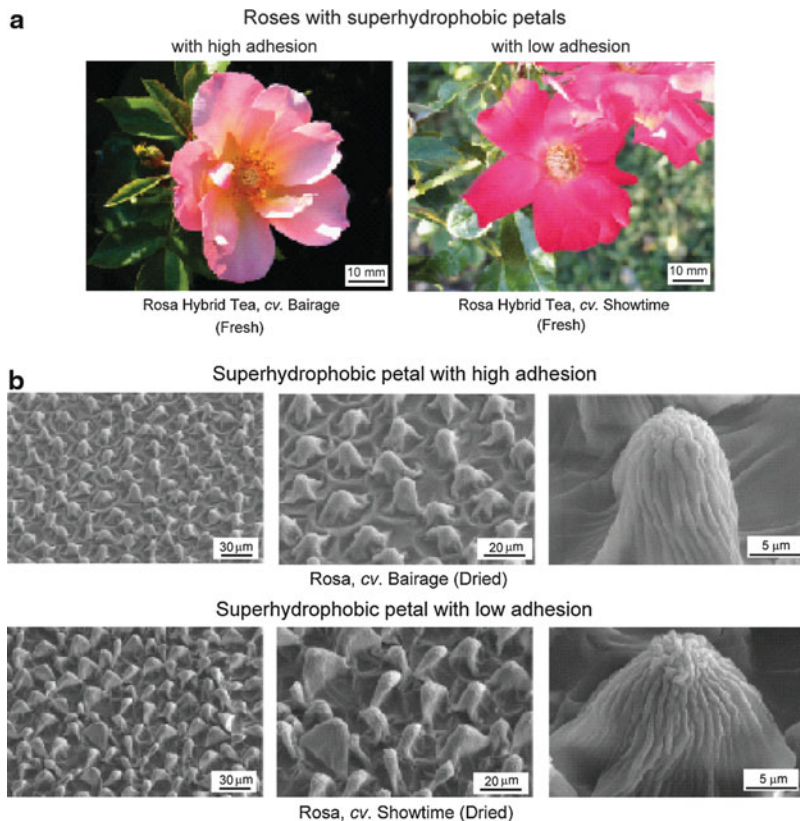


Fig. 8.1 (a) Optical micrographs and (b) SEM micrographs of two roses which have different adhesion properties on its petals—*Rosa Hybrid Tea* cv. *Bairage* (*Rosa* cv. *Bairage*) and *Rosa Hybrid Tea* cv. *Showtime* (*Rosa* cv. *Showtime*) ([Bhushan and Her, 2010](#))

8.2 Characterization of Two Kinds of Rose Petals and Their Underlying Mechanisms

Two kinds of rose petals with superhydrophobicity were studied by [Bhushan and Her \(2010\)](#). One is *Rosa Hybrid Tea* cv. *Bairage* for surfaces with high adhesion, and the other is *Rosa Hybrid Tea* cv. *Showtime* for low adhesion, referred to as *Rosa* cv. *Bairage* and *Rosa* cv. *Showtime*, respectively. Figure 8.1 shows optical and SEM micrographs of two rose petals. In their study, to get stable samples, they air-dried the petals for SEM measurement. [Koch et al. \(2008\)](#) reported that during the measurement of real petals using SEM, loss of water from the cell occurred, leading to shrinkage on the hierarchical micro- and nanostructures on petals in a high vacuum chamber. The specimen shown in the right image in Fig. 8.2 has been taken from the dried leaf, and the loss of the water from the cells led them to shrink. These figures demonstrate that the drying process has a great influence on

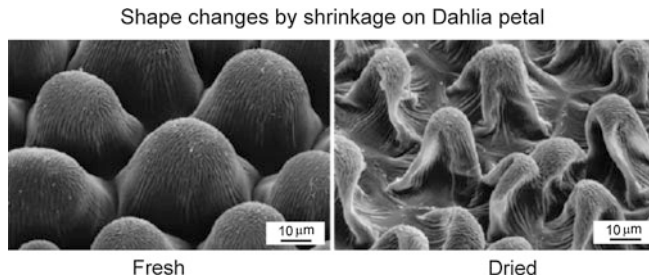


Fig. 8.2 SEM micrographs of *Dahlia* petal. These images have been taken from the same petal. Left one is fresh, and right one is air dried (Koch et al., 2008)

Table 8.1 Microbump map statistics for rose petals with high adhesion and low adhesion, measured in dried leaves using AFM (Bhushan and Her, 2010)

	Peak-to-base (P–B) height (μm)	Mid-width (μm)	Peak radius (μm)	Bump density ($1/10,000 \mu\text{m}^2$)
Rosa cv. Bairage (High adhesion)	6.8	16.7	5.8	23
Rosa cv. Showtime (Low adhesion)	8.4	15.3	4.8	34

the cell morphology. From the figures, it is noted that the height and width of the microstructures have changed, but the number of microstructures per unit area is unchanged by shrinkage.

Figure 8.1b shows that both petals have hierarchical structure, which means their surface structure consists of nanostructures on microstructures. The low magnification micrographs show a convex cell form with irregular cuticular folding in the central fields and parallel folding in the anticlinal field of the cells (Koch et al., 2008). It is observed that the two rose petals have different spacing (pitch value, P), peak-to-base (P–B) height of microstructure, and density of nanostructure. Based on Table 8.1 to be presented later, in the case of Rosa cv. Showtime, the pitch value is smaller than Rosa cv. Bairage, and the P–B height is larger than Rosa cv. Bairage, which is expected to lead to a superhydrophobic surface with low adhesion (to be discussed later).

Figure 8.3 shows optical micrographs of water droplets on the Rosa cv. Bairage petal in the fresh state (Bhushan and Her, 2010). As a water droplet is deposited on its surface, a high static contact angle (152°) is observed on the petal. When the petal is turned upside down, the water droplet does not drop down, which suggests high adhesion. In the case of a droplet on the Rosa cv. Showtime, it also has a high static contact angle (167°), but the droplet easily rolls off the surface with a small tilt angle (6°).

Figure 8.4a shows the static contact angle and contact angle hysteresis for the superhydrophobic rose petals when fresh and dried and after using chloroform (Bhushan and Her, 2010). Chloroform is a solvent which can be used to remove

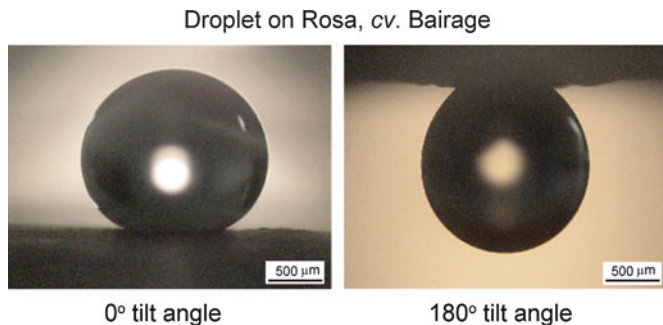


Fig. 8.3 Optical micrographs of water droplets on Rosa cv. Bairage at 0° and 180° tilt angles. Droplet is still suspended when the petal is turned upside down (Bhushan and Her, 2010)

wax compounds (Thomas et al., 1993). The contact angle reduced to less than 10° after chloroform treatment, which suggests that superhydrophobic rose petals have only a thin wax film (2D wax) on the surface (Koch et al., 2008). There is a small decrease in the static contact angle for both superhydrophobic petals when they are dried. Because a fresh petal has larger microstructure than a dried petal, this gives a higher contact angle according to Eq. (3.6). For contact angle hysteresis, there is a decrease of about 40° on the Rosa cv. Bairage between the fresh and dried state. Since a fresh petal has a higher P–B height of microstructure, this may lead to a higher pinning of the water droplet as compared to that of a dried leaf (McHale et al., 2004; Nosonovsky and Bhushan, 2008).

Figure 8.4b shows adhesive force measured using a $15\text{ }\mu\text{m}$ -radius borosilicate tip in an AFM for fresh and dried petals (Bhushan and Her, 2010). The adhesive force of the Rosa cv. Bairage is higher than that of the Rosa cv. Showtime. Adhesive force arises from several sources: the presence of a thin liquid film, such as an adsorbed water layer, that causes meniscus bridges to build up around the contacting and near contacting bumps and real area of contact and surface energy effects (Bhushan, 2002). For the fresh petals, there is moisture within the plant material, which causes softening of the petal, and so when the tip comes into contact with the petal sample, the sample deforms, and a larger area of contact between the tip and sample causes an increase in the adhesive force (Koch et al., 2009).

The coefficient of friction measured at a sliding velocity of $2\text{ }\mu\text{m/s}$ for the superhydrophobic surface with low adhesion is lower than that for the superhydrophobic surface with high adhesion due to the lower real area of contact between the tip and petal sample. The coefficient of friction is decreased in the dried state for both petals, since moisture on the petal leads to a higher friction force similar to that with adhesive force results.

Figure 8.5 shows AFM topography images and 2D profiles of the surfaces for different scan sizes (Bhushan and Her, 2010). As mentioned earlier, the AFM has a Z-range on the order of $7\text{ }\mu\text{m}$ and cannot be used for measurements in a conventional way because of the high P–B height of rose petals. In order to compensate for the large P–V distance, two scans were made for each height: one

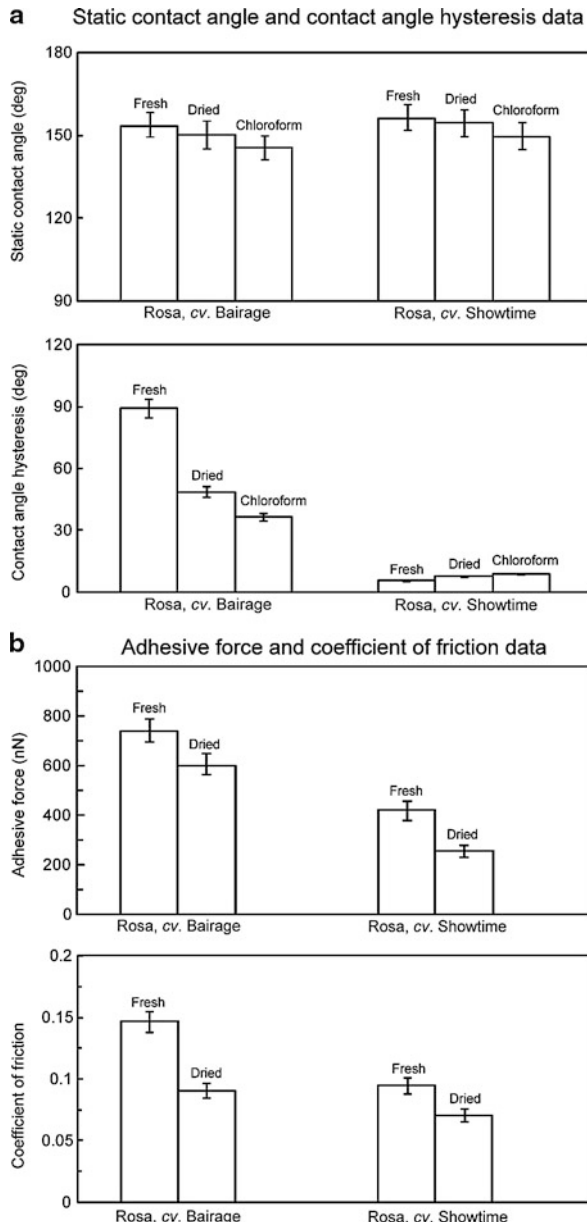


Fig. 8.4 (a) Bar charts showing the static contact angle and contact angle hysteresis measured on two rose petal surfaces when fresh and dried and after dip into chloroform for 10 s and (b) adhesive force and coefficient of friction for both fresh and dried petals, measured using 15 μm radius of borosilicate tip ([Bhushan and Her, 2010](#))

measurement that scans the tops of the bumps and another measurement that scans the base of the bumps. The total height of the bumps is embedded within the two scans. The two scans can be spliced together in the 2D profile to create the full profile of the petal surface. Figure 8.5a shows the $100\text{ }\mu\text{m} \times 100\text{ }\mu\text{m}$ and $10\text{ }\mu\text{m} \times 10\text{ }\mu\text{m}$ top row surface height maps obtained using this method for the Rosa cv. Bairage. Two-dimensional profiles in the right hand column take the profiles from the top scan and the bottom scan and splice them to get the total profile of the petal surface. Figure 8.5b shows the 100×100 and $10 \times 10\text{ }\mu\text{m}$ surface height maps for the Rosa cv. Showtime. These AFM images for microstructure and nanostructure show similar morphology to that in the SEM images in Fig. 8.1b. Using the AFM surface height maps, different statistical parameters of microstructure and nanostructure can

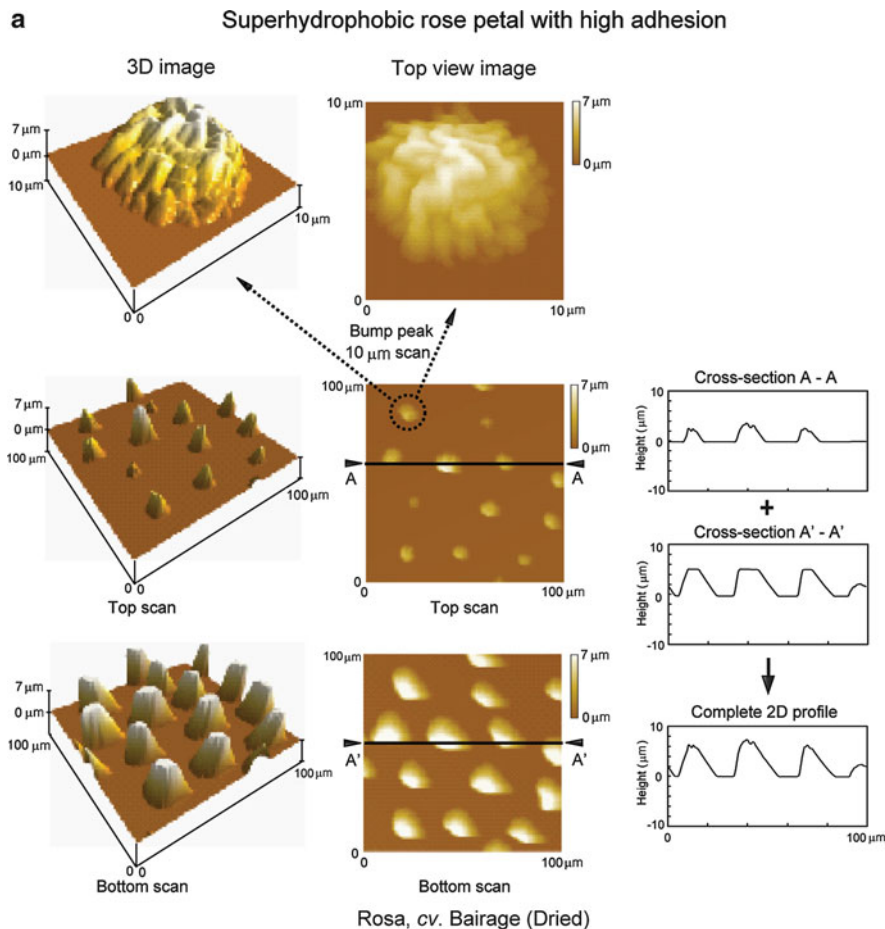


Fig. 8.5 Continued

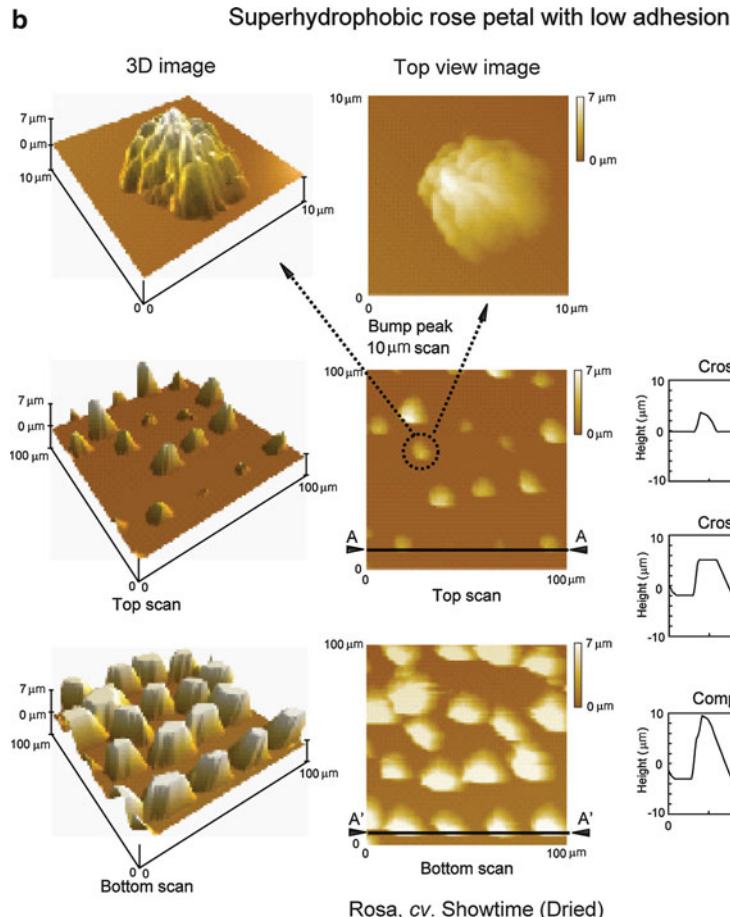


Fig. 8.5 Surface height maps and 2D profiles of (a) Rosa cv. Bairage (dried) and (b) Rosa cv. Showtime (dried) using an AFM. Top and bottom scans have been made using a 100 μm scan size, and the bump peak scans have been made using a 10 μm scan size in tapping mode (Bhushan and Her, 2010)

be obtained which include P-B height, mid-width, peak radius, and bump density (or pitch). Here, mid-width is defined as the width of the bump at a height equal to half of peak-to-mean value. Peak radius is defined as the radius of curvature which is calculated from the parabolic curve fit of the bump. Bump density is defined as the average number of bumps in the area of $100 \times 100 \mu\text{m}^2$. These quantities for the two petals are listed in Table 8.1. From the measured data of microbumps, it is found that the superhydrophobic rose petal with high adhesion has a smaller P-B height and bump density value than those of the superhydrophobic rose petal with low adhesion.

In order to understand the mechanisms for the microstructures of the two superhydrophobic rose petals with different adhesive force, Fig. 8.6 shows schematics

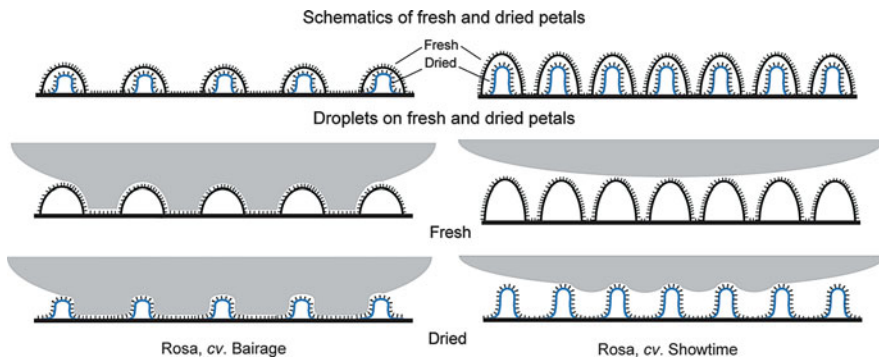


Fig. 8.6 Schematic illustrations of shape changes between fresh and dried petals' hierarchical structure and schematics of a water droplet contacting fresh and dried rose petal surfaces. *Left column* shows the schematic for Rosa cv. Bairage with a superhydrophobic and high adhesion surface and *right column* shows Rosa cv. Showtime with a superhydrophobic and low adhesion (Bhushan and Her, 2010)

of shape changes between fresh and dried hierarchical structures, which consist of a microstructure with a nanostructure, and also schematics of water droplet contact with rose petal surfaces which include dried and fresh conditions (Bhushan and Her, 2010). It is important to recognize the shape change after drying which was done to obtain stable samples for measurements. Pitch value (bump density) and P–B height of microstructures are different in the two petals. On the superhydrophobic surface with low adhesion (Rosa cv. Showtime), its microstructure has a smaller pitch value and a larger P–B height compared to the superhydrophobic surface with high adhesion (Rosa cv. Bairage). A smaller value of the ratio of pitch value (P) and P–B height (H) may lead to the Cassie–Baxter regime. If the value of P/H is decreased, it leads to an increase in the propensity of air pocket formation between microstructures, so the water droplet cannot touch its bottom and minimize the contact area between the droplet and surface, resulting in high static contact angle, low contact angle hysteresis, and low adhesion (Nosonovsky and Bhushan, 2008; Bhushan et al., 2009; Bhushan and Jung, 2011). In the case of the superhydrophobic surface with high adhesion, its large pitch value and small P–B height lead to a decrease in contact area, and water can penetrate to the bottom. This is responsible for a decrease in the static contact angle and an increase in contact angle hysteresis and high adhesion.

8.3 Fabrication of Surfaces with High and Low Adhesion

From the understanding of real rose petals, Bhushan and Her (2010) fabricated artificial superhydrophobic surfaces with high and low adhesion using the methodology presented earlier, in Sect. 6.6.2, used for the fabrication of artificial Lotus structures. In order to realize a microstructure with different pitch values, micropatterned pillars with 23- and 105 μm pitch values with the same diameter (14 μm) and height (30 μm) were used for replication. To fabricate the nanostructure with different pitch

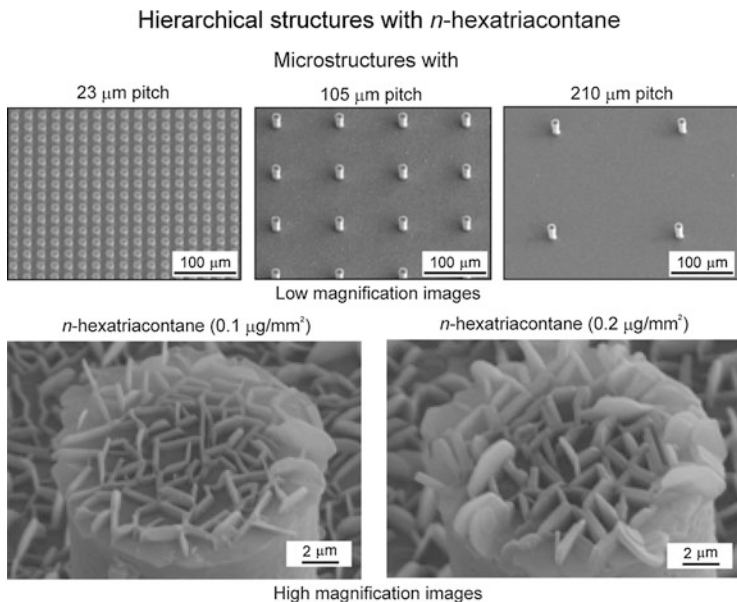


Fig. 8.7 SEM micrographs of the microstructures and nanostructures fabricated with two different masses of *n*-hexatriacontane for hierarchical structure. All images were taken at 45° tilt angle. All samples are positive replicas, obtained from negative replica with dental wax and Si micropatterned master template (14 μm diameter and 30 μm height) fabricated with epoxy resin coated with *n*-hexatriacontane (Bhushan and Her, 2010)

values, various masses of *n*-hexatriacontane ($\text{CH}_3(\text{CH}_2)_{34}\text{CH}_3$) (purity of >99.5%, Sigma-Aldrich, USA) were coated on a microstructure using thermal evaporation. The nanostructure is formed by three-dimensional platelets of *n*-hexatriacontane by self-assembly. Platelets are flat crystals, grown perpendicular to the surface. They are randomly distributed on the surface, and their shapes and sizes show some variation. Figure 8.7 shows selected images (Bhushan and Her, 2010). When different masses (0.1 and $0.2 \mu\text{g}/\text{mm}^2$) of wax are applied, the density of the nanostructure is changed, as shown in the bottom row of Fig. 8.7. Different pitch values and masses of wax were used to provide hierarchical structured surfaces with high and low adhesion.

To identify optimized superhydrophobic surfaces with high and low adhesion, Bhushan and Her (2010) studied the static contact angle and contact angle hysteresis as a function of the mass of *n*-hexatriacontane on hierarchical structures with different pitch values as shown in Fig. 8.8a. In the surface with a $23 \mu\text{m}$ pitch value, while the mass of *n*-hexatriacontane is changed, there are only small changes in the static contact angle and contact angle hysteresis values, which means that they are always in the Cassie–Baxter wetting regime. In the surface with a $105 \mu\text{m}$ pitch value, high contact angle hysteresis (87°) with a superhydrophobic (static contact angle is 152°) state at $0.1 \mu\text{g}/\text{mm}^2$ mass of *n*-hexatriacontane is found.

Static contact angle and contact angle hysteresis on hierarchical structure

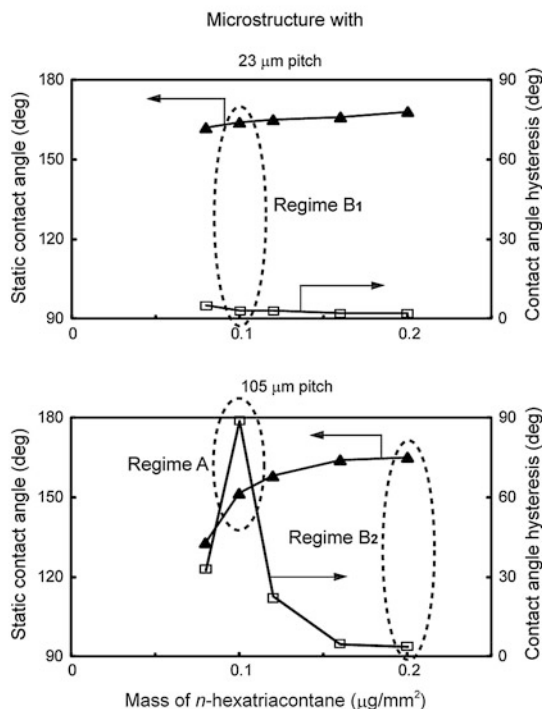
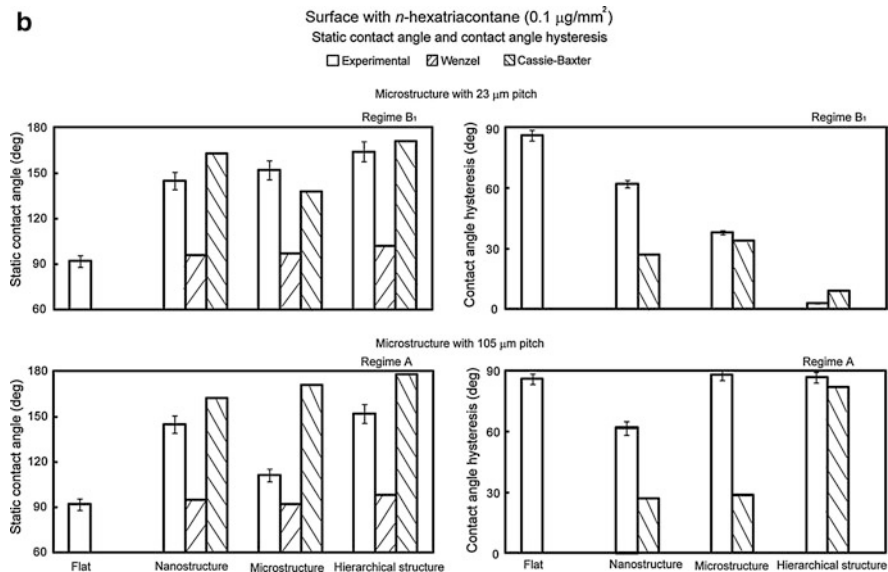
a**b**

Fig. 8.8 Continued

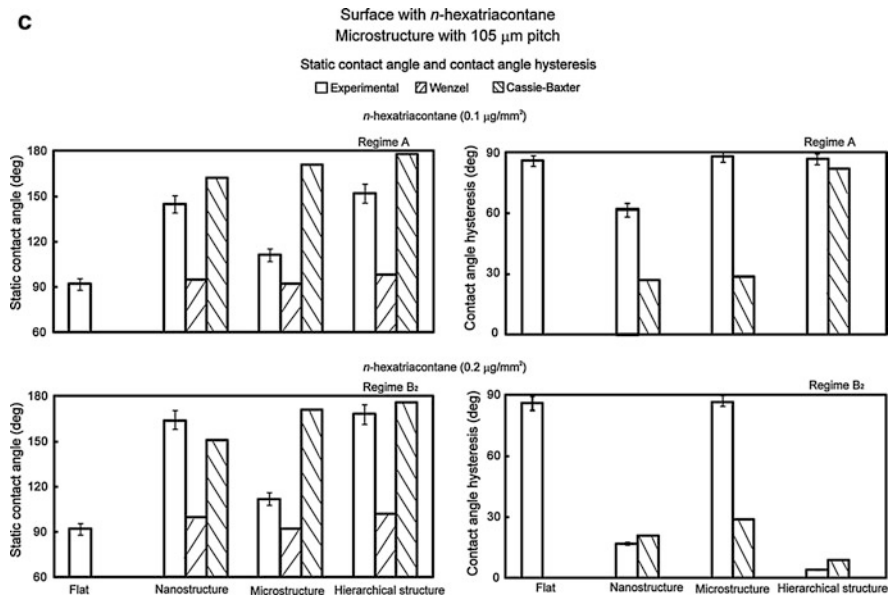


Fig. 8.8 (a) Static contact angle and contact angle hysteresis measured as a function of mass of *n*-hexatriacontane for hierarchical structures with two different pitch values (23 and 105 μm) and (b and c) charts showing the measured static contact angle and contact angle hysteresis, calculated contact angles obtained using the Wenzel and Cassie–Baxter equations with a given value of θ_0 , and calculated contact angle hysteresis angles using the Cassie–Baxter equation on a flat, nanostructure, microstructure, and hierarchical structure fabricated. (b) shows the comparison between regimes B₁ and A for the hierarchical structure from (a), and (c) shows comparison between regimes A and B₂ for the hierarchical structure from (a). All samples were made from epoxy resin using two-step molding process and coated with *n*-hexatriacontane (0.1 or 0.2 $\mu\text{g}/\text{mm}^2$). Micro- and hierarchical structures had a micropattern with 23- and 105 μm pitch value, 14 μm diameter, and 30 μm height (Adapted from Bhushan and Her, 2010)

To study the effect of microstructures and nanostructures with different densities on superhydrophobicity, static contact angle and contact angle hysteresis were measured on flat, nanostructured, microstructured, and hierarchical structured surfaces. All samples were coated with *n*-hexatriacontane, but the flat and microstructured samples do not have a nanostructure on top of the surface. All measurements were repeated five times, and values are presented in Fig. 8.8b, c and Table 8.2. The static contact angle and contact angle hysteresis of the flat and microstructured surfaces in regime A and B₂ were same in both cases. These values are 92° (CA) and 86° (CAH) for flat surface and 112° (CA) and 88° (CAH) for the microstructured surface, and the droplet still adhered at a tilt angle of 90°. The highest static contact angle of 168° and lowest contact angle hysteresis of 4° were found for the hierarchical structured surface with *n*-hexatriacontane (0.2 $\mu\text{g}/\text{mm}^2$). The nanostructured surface with *n*-hexatriacontane (0.2 $\mu\text{g}/\text{mm}^2$) showed a static contact angle of 162° and contact angle hysteresis of 17°. Static contact angle values

Table 8.2 Summary of static contact angles and contact angle hysteresis measured and calculated for droplets in Wenzel regime and Cassie–Baxter regime on the various surfaces using the values of R_f and f_{LA}

R_f	f_{LA}	Static contact angle (deg)			Contact angle hysteresis (deg)	
		Measured	Calculated using Wenzel equation	Calculated using Cassie–Baxter equation	Measured	Calculated using Cassie–Baxter equation
		23 μm pitch with <i>n</i> -hexatriacontane ($0.1 \mu\text{g}/\text{mm}^2$)				
Flat		92			86 ^a	
Nanostructure	2.8	0.95	145	96	163	62
Microstructure	3.5	0.71	152	97	138	38
Hierarchical structure (regime B ₁)	6.3	0.99	164	102	171	3
105 μm pitch with <i>n</i> -hexatriacontane ($0.1 \mu\text{g}/\text{mm}^2$)						
Flat		92			86 ^a	
Nanostructure	2.8	0.95	145	95	162	62
Microstructure	1.1	0.98	112	92	171	88
Hierarchical structure (regime A)	3.9	0.99	152	98	178	87
105 μm pitch with <i>n</i> -hexatriacontane ($0.2 \mu\text{g}/\text{mm}^2$)						
Flat		92			86 ^a	
Nanostructure	4.9	0.85	162	100	151	17
Microstructure	1.1	0.98	112	92	171	88
Hierarchical structure (regime B ₂)	6.0	0.99	168	102	176	4

The measurement results were reproducible within $\pm 5\%$ (Bhushan and Her, 2010)

^aAdvancing and receding contact angles are 141° and 55° , respectively

of nanostructured and hierarchical structured surfaces changed with a decrease in the mass of evaporated *n*-hexatriacontane ($0.1 \mu\text{g}/\text{mm}^2$). The nanostructure with wax ($0.1 \mu\text{g}/\text{mm}^2$) showed a static contact angle of 145° and contact angle hysteresis of 62° . The hierarchical structure with wax ($0.1 \mu\text{g}/\text{mm}^2$) shows a static contact angle of 152° and contact angle hysteresis of 87° , and the droplet still adhered to the surface at a tilt angle of 90° or turned upside down. To compare the nanostructured surface and flat surface, melting of the wax led to a flat surface with a flat wax film and a lower static contact angle (92°) and higher contact angle hysteresis (86°).

In order to identify wetting regimes (Wenzel or Cassie–Baxter), as well as to understand the effect of microstructure and nanostructure density on the propensity of air pocket formation, a roughness factor (R_f) and a fractional liquid–air interface (f_{LA}) are needed. For the microstructured surfaces, the R_f for the microstructure

was calculated for the geometry of flat-top pillars of diameter (D), height (H), and pitch value (P) distributed in a regular square array. In this case, the roughness factor for the microstructure is (Bhushan and Her, 2010)

$$(R_f)_{\text{micro}} = (1 + \pi DH/P^2). \quad (8.1)$$

The R_f for the nanostructures was calculated using the AFM map (Burton and Bhushan, 2006). The R_f for the nanostructured surfaces with masses of 0.1 and 0.2 $\mu\text{g}/\text{mm}^2$ was found to be 2.8 and 4.9, respectively. For calculation of f_{LA} , the following assumption was made. For a microstructure, consider that a droplet much larger in size than the pitch contacts only the flat top of the pillars in the composite interface, and the cavities are filled with air. For a microstructure, the fractional flat geometrical areas of the solid–liquid and liquid–air interfaces under the droplet are (Bhushan and Her, 2010)

$$(f_{\text{LA}})_{\text{micro}} = (1 - \pi D^2/4P^2). \quad (8.2)$$

For calculation of the f_{LA} of nanostructures, the fractional geometrical area of the top surface for the nanostructures was calculated from top view SEM micrographs (0° tilt angle). The SEM images were converted to high-contrast black and white images using Adobe Photoshop. The fractional geometrical area of the top of the nanostructured surfaces with masses of 0.1 and 0.2 $\mu\text{g}/\text{mm}^2$ gives f_{LA} values of 0.95 and 0.85, respectively. The roughness factor for the hierarchical structure ($R_f)_{\text{hierarchical}}$ is the sum of $(R_f)_{\text{micro}}$ and $(R_f)_{\text{nano}}$. For the hierarchical structure, the fractional flat geometrical area of the liquid–air interface is $(f_{\text{LA}})_{\text{hierarchical}} = 1 - (\pi D^2/4P^2)[1 - (f_{\text{LA}})_{\text{nano}}]$.

The values of contact angle hysteresis in Cassie–Baxter regimes for various surfaces were calculated using (3.20).

Figure 8.8b, c and Table 8.2 include the measured and calculated static contact angle and contact angle hysteresis using R_f and f_{LA} . Contact angles were calculated using the Wenzel and Cassie–Baxter equations with a given value of θ_0 and calculated contact angle hysteresis using the Cassie–Baxter equation on a nanostructure, microstructure, and hierarchical structure fabricated with two different masses of *n*-hexatriacontane. R_f and f_{LA} of the hierarchical structure are higher than those of the nano- and microstructures. These results show that air pocket formation in hierarchical structured surfaces might occur, which further decreases the solid–liquid contact and thereby reduces contact angle hysteresis.

Figure 8.8b shows the charts for surfaces with two microstructures in hierarchical structures (regimes B₁ and A defined in Fig. 8.8a). The effect of the microstructure could be briefly explained from the comparison between regimes B₁ and A. Those two regimes have the same nanostructure with *n*-hexatriacontane of 0.1 $\mu\text{g}/\text{mm}^2$ and different microstructure (pitch values with 23 and 105 μm). For a microstructured surface with a 23 μm pitch value, the experimental static contact angle and contact angle hysteresis value are comparable to the calculated values in the Cassie–Baxter regime. The data suggests that this microstructured surface leads to higher

propensity of air pocket formation between water droplet and the surface. Whereas the microstructured surface with a 105 μm pitch value leads to complete wetting between water droplet and the surface. There is a good agreement between the proposed mechanism in Fig. 8.6 and the measured and calculated data in Fig. 8.8b. These results show that a larger pitch value of microstructure increases the solid–liquid contact and thereby increases the contact angle hysteresis and high adhesion.

Figure 8.8c shows the charts for surfaces with two nanostructures in hierarchical structures (regimes A and B₂ defined in Fig. 8.8a). The experimental static contact angle and contact angle hysteresis values for the nanostructured surface with *n*-hexatriacontane of 0.2 $\mu\text{g}/\text{mm}^2$ are comparable to the calculated values in the Cassie–Baxter regime. The results suggest that a droplet on the nanostructured surface should exist in the Cassie–Baxter regime. However, the experimental static contact angle and contact angle hysteresis values for the nanostructured surface with 0.1 $\mu\text{g}/\text{mm}^2$ were lower and higher than the calculated values in the Cassie–Baxter regime, respectively. It is believed that the nanostructure has lower density and any trapped air can be squeezed out, whereas neighboring nanostructures are interconnected at higher densities, and air remains trapped. For a microstructured surface, the experimental static contact angle and contact angle hysteresis values are comparable to the calculated values in the Wenzel regime. This result shows that a microstructured surface leads to complete wetting between the water droplet and the surface. For a hierarchical structured surface, at higher nanostructure density at a mass of 0.2 $\mu\text{g}/\text{mm}^2$, the experimental static contact angle and contact angle hysteresis values are comparable to the calculated values in the Cassie–Baxter regime. However, the experimental static contact angle (152°) and contact angle hysteresis (87°) values for the hierarchical structured surface with 0.1 $\mu\text{g}/\text{mm}^2$ were lower and higher than the calculated values in the Cassie–Baxter regime, respectively. This surface consists of lower nanostructure density and microstructure without trapped air pockets. Hence, it is believed that the hierarchical structured surface with 0.1 $\mu\text{g}/\text{mm}^2$ is between Wenzel and Cassie–Baxter regime.

Schematics of the effect of nanostructure on the propensity of air pocket formation are shown in Fig. 8.9 (regimes A and B₂ in Fig. 8.8a) (Bhushan and Her, 2010). When a microstructure has same the pitch value and a nanostructure has low density (regime A in Fig. 8.8a), water could penetrate between the microstructures, but it is still not completely wetted into the nanostructure, resulting in increasing static contact angle and adhesion. However, high density of nanostructure prevents the transition from Cassie–Baxter to Wenzel regime and an increased propensity of air pocket formation between micro- and nanostructures. Bhushan and Nosonovsky (2010) have considered various wetting regimes and suggested that a rose petal with high adhesion can be in the Cassie impregnating wetting regime.

Next, optical images are examined of a water droplet on surfaces in regimes A, B₁, and B₂ defined in Fig. 8.8a. Figure 8.10 shows the shape of the droplets on a hierarchical structure with a 23- and 105 μm pitch value (Bhushan and Her, 2010). In regimes B₁ and B₂ (from Fig. 8.8a), a superhydrophobic surface with low adhesion and trapped air pockets is obtained. Figure 8.10a displays droplets on a horizontal substrate (23 μm pitch value) with *n*-hexatriacontane

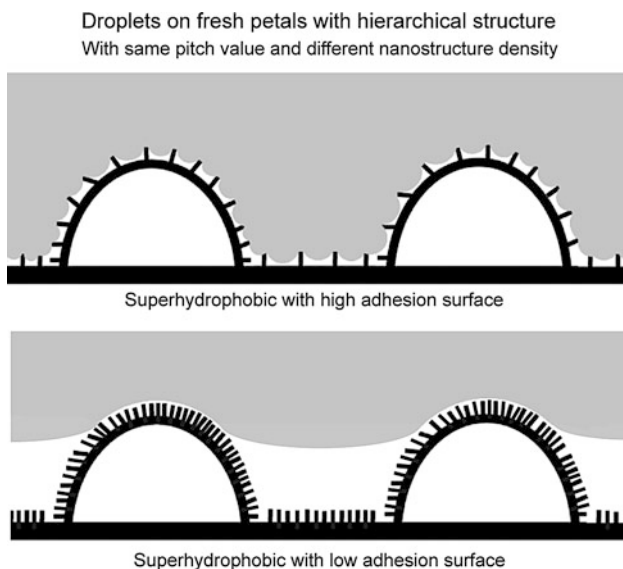


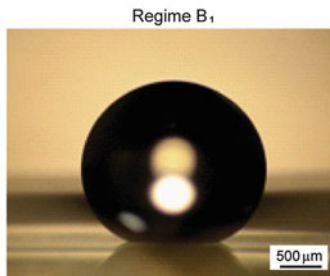
Fig. 8.9 Schematic illustrations of droplets on hierarchical structure with two nanostructures. As an example, mass of *n*-hexatriacontane changes the density of nanostructure (regimes A and B₂ in Fig. 8.8a). Nanostructures play an important role in contact formation between water and underlying substrate (Bhushan and Her, 2010)

(0.1 µg/mm²). Droplets on the surface (regime B₁) have a high contact angle (164°) with low contact angle hysteresis (3°), and trapped air pockets can be seen. When *n*-hexatriacontane (0.2 µg/mm²) is applied on a microstructure (105 µm pitch value), the droplet on the surface (regime B₂) also reveals high static contact angle (168°) with low contact angle hysteresis (4°) and trapped air pockets can be seen clearly, as shown in right side of top row Fig. 8.10b. However, by applying *n*-hexatriacontane (0.1 µg/mm²) on a surface with a 105 µm pitch value (regime A), a superhydrophobic surface with high adhesion but with no air pocket between the microstructures was fabricated (left side of top row in Fig. 8.10b). It is observed that this surface has high adhesion since the droplet does not drop down when the substrate is vertically inclined or turned upside down (bottom row of Fig. 8.10b).

To further verify the effect of wetting states on the surfaces, evaporation experiments with a droplet on a hierarchical structure coated with two different amounts of *n*-hexatriacontane were performed (Bhushan et al., 2008). Figure 8.11 shows the optical micrographs of a droplet evaporating on two different hierarchical structured surfaces (Bhushan and Her, 2010). On the *n*-hexatriacontane (0.1 µg/mm²)-coated surface, an air pocket was not visible at the bottom area of the droplet. However, the droplet on the surface has a high static contact angle (152°) since the droplet still cannot completely impregnate into the nanostructure. The footprint size of the droplet on the surface has only small changes from 1,820 to 1,791 µm. During evaporation, the initial contact area between the droplet and hierarchical

a Shape of droplets on hierarchical structure with 23 μm pitch

Horizontal surface with *n*-hexatriacontane ($0.1 \mu\text{g}/\text{mm}^2$)



Regime B₁

b Shape of droplets on hierarchical structure with 105 μm pitch

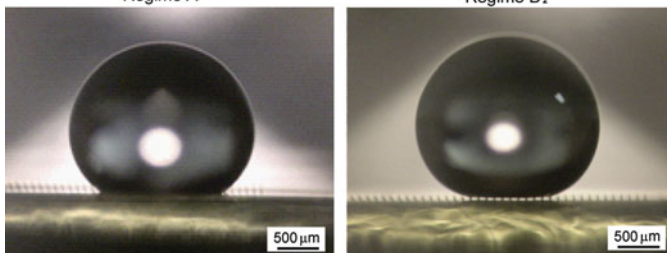
Horizontal surface with different mass of *n*-hexatriacontane

n-hexatriacontane ($0.1 \mu\text{g}/\text{mm}^2$)

n-hexatriacontane ($0.2 \mu\text{g}/\text{mm}^2$)

Regime A

Regime B₂



Inclined surface with *n*-hexatriacontane ($0.1 \mu\text{g}/\text{mm}^2$)

Regime A

vertical

upside down

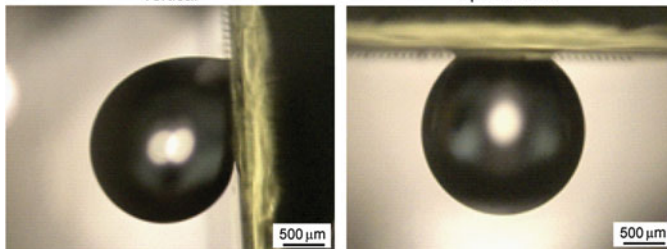


Fig. 8.10 (a) Droplet on a *horizontal* surface of hierarchical structure with $23 \mu\text{m}$ pitch and *n*-hexatriacontane ($0.1 \mu\text{g}/\text{mm}^2$) showing air pocket formation and (b) droplet on a hierarchical structure with $105 \mu\text{m}$ pitch and *n*-hexatriacontane ($0.1 \mu\text{g}/\text{mm}^2$) (regime A in Fig. 8.8a) and $0.2 \mu\text{g}/\text{mm}^2$ (regime B₂ in Fig. 8.8a) showing no air pocket and air pocket formation, respectively. Also shown is the image taken on the inclined surface with hierarchical structure with $0.1 \mu\text{g}/\text{mm}^2$ showing that droplet is still suspended (Bhushan and Her, 2010)

structured surface does not decrease until the droplet evaporates completely, which means complete wetting between the droplet and microstructures. For the *n*-hexatriacontane ($0.2 \mu\text{g}/\text{mm}^2$)-coated surface, the light passes below the droplet,

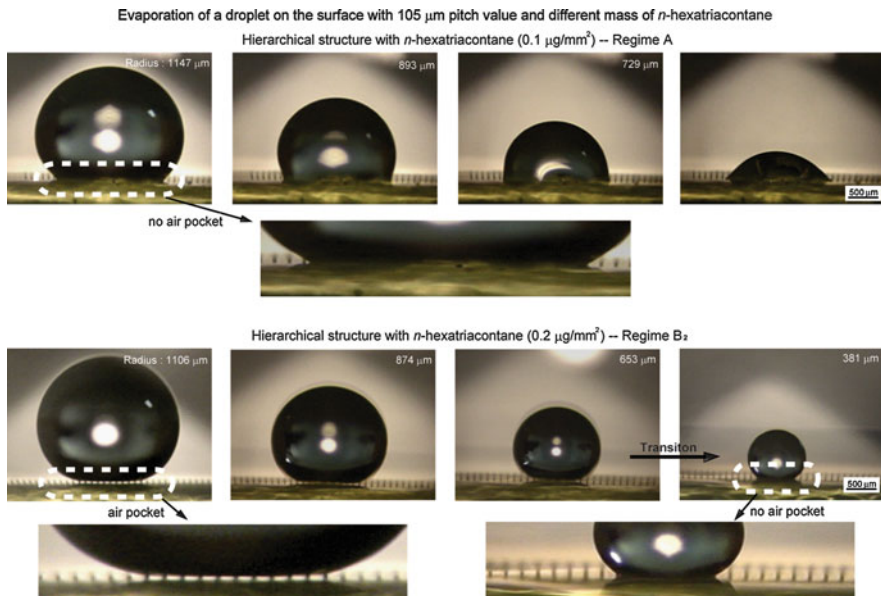


Fig. 8.11 Optical micrographs of droplet evaporation on the hierarchical structured surfaces with 105 μm pitch value. *n*-Hexatriacontane ($0.1 \mu\text{g}/\text{mm}^2$)-coated sample (regime A in Fig. 8.8a) has no air pocket formed between the pillars in the entire contact area until evaporation was completed. Hierarchical structure with *n*-hexatriacontane ($0.2 \mu\text{g}/\text{mm}^2$) (regime B₂ in Fig. 8.8a) has air pocket, and then the transition from Cassie–Baxter regime to Wenzel regime occurred (Bhushan and Her, 2010)

and air pockets can be seen, so to start with, the droplet is in the Cassie–Baxter regime. When the radius of the droplet decreased to 381 μm , the air pockets are no longer visible. The footprint size of the droplet on the surface is changed from 1,177 μm to 641 μm , since droplet remained on only a few pillars until the end of the evaporation process. Based on the transition criteria proposed by Bhushan and Jung (2007) and Jung and Bhushan (2008), the air pockets cease to exist below a certain ratio of the radius of the droplet to the pitch value.

8.4 Summary

Bhushan and Her (2010) found that two species of superhydrophobic rose petals have different surface micro- and nanostructures, therefore exhibiting high and low adhesion. Both rose petals have hierarchical structures, but their spacing (pitch value) and the P–B height of the microstructure, and most likely of the nanostructure, are different from each other. Superhydrophobic rose petals with high adhesion have a smaller P–B height and bump density value than those with low

adhesion. For a microstructure with large pitch value and small P–B height and a nanostructure with low density, water could impregnate between microstructures, but it is still not completely wetted into nanostructure, resulting in high adhesion while maintaining high static contact angle.

References

- Bhushan B (2002) Introduction to tribology. Wiley, New York
- Bhushan B, Her EK (2010) Fabrication of superhydrophobic surfaces with high and low adhesion inspired from rose petal *Langmuir* 26:8207–8217
- Bhushan B, Jung YC (2007) Wetting study of patterned surfaces for superhydrophobicity. *Ultramicroscopy* 107:1033–1041
- Bhushan B, Jung YC (2011) Natural and biomimetic artificial surfaces for superhydrophobicity, self-cleaning, low adhesion, and drag reduction. *Prog Mater Sci* 56:1–108
- Bhushan B, Nosonovsky M (2010) The rose petal effect and the modes of superhydrophobicity. *Philos Trans R Soc A* 368:4713–4728
- Bhushan B, Koch K, Jung YC (2008) Nanostructures for superhydrophobicity and low adhesion. *Soft Matter* 4:1799–1804
- Bhushan B, Jung YC, Koch K (2009) Micro-, nano- and hierarchical structures for superhydrophobicity, self-cleaning and low adhesion. *Philos Trans R Soc* 367:1631–1672
- Burton Z, Bhushan B (2006) Surface characterization and adhesion and friction properties of hydrophobic leaf surfaces. *Ultramicroscopy* 106:709–719
- Chang FM, Hong SJ, Sheng YJ, Tsao HK (2009) High contact angle hysteresis of superhydrophobic surfaces: hydrophobic defects. *Appl Phys Lett* 95:064102
- Feng L, Zhang Y, Xi J, Zhu Y, Wang N, Xia F, Jiang L (2008) Petal effect: a superhydrophobic state with high adhesive force. *Langmuir* 24:4114–4119
- Hong X, Gao X, Jiang L (2007) Application of superhydrophobic surface with high adhesive force in no lost transport of superparamagnetic microdroplet. *J Am Chem Soc* 129:1478–1479
- Jin M, Feng X, Feng L, Sun T, Zhai J, Li T, Jiang L (2005) Superhydrophobic aligned polystyrene nanotube films with high adhesive force. *Adv Mater* 17:1977–1981
- Jung YC, Bhushan B (2008) Wetting behavior during evaporation and condensation of water microdroplets on superhydrophobic patterned surfaces. *J Microsc* 229:127–140
- Koch K, Bhushan B, Barthlott W (2008) Diversity of structure, morphology and wetting of plant surfaces. *Soft Matter* 4:1943–1963
- Koch K, Bhushan B, Jung YC, Barthlott W (2009) Fabrication of artificial lotus leaves and significance of hierarchical structure for superhydrophobicity and low adhesion. *Soft Matter* 5:1386–1393
- McHale G, Shirtcliffe NJ, Newton MI (2004) Contact-angle hysteresis on super-hydrophobic surfaces. *Langmuir* 20:10146–10149
- Nosonovsky M, Bhushan B (2008) Multiscale dissipative mechanisms and hierarchical surfaces: friction, superhydrophobicity, and biomimetics. Springer, Heidelberg
- Thomas AB, Donn GS, Robert Q (1993) Evaluation of epicuticular wax removal from whole leaves with chloroform. *Weed Technol* 7(3):706–716

Part IV
Oleophobic/Oleophilic Surfaces

Chapter 9

Modeling, Fabrication, and Characterization of Oleophobic/Oleophilic Surfaces

9.1 Introduction

Oleophobic surfaces have the potential for self-cleaning and antifouling from biological and organic contaminants both in air and underwater applications. A model surface for superoleophobicity and self-cleaning is provided by sea animals such as fish and sharks, which are known to be well protected from contamination by oil pollution although they are wetted by water (Bhushan, 2009). Fish scales have a hierarchical structure consisting of sector-like scales with diameters of 4–5 mm covered by papillae 100–300 μm in length and 30–40 μm in width (Liu et al., 2009). Sharkskin, which is a model from nature for a low drag surface, is covered by small individual tooth-like scales called dermal denticles (little skin teeth) shaped like small riblets, with longitudinal grooves (aligned parallel to the local flow direction of the water). In turbulent flow, vortices are formed on the surface which increases fluid drag. Riblets lift and constrain the naturally occurring vortices, which reduces the transfer of momentum and shear stress (Bechert et al., 2000; Bhushan, 2009). The water surrounding these complex structures can lead to protection from marine fouling and play a role in the defense against adhesion and growth of marine organisms, e.g., bacteria and algae (Genzer and Efimenco, 2006; Bixler and Bhushan, 2012).

The surface tension of oil and organic liquids is lower than that of water, so to create a superoleophobic surface, the surface energy of the solid surface in air should be lower than that of oil. For underwater applications, if an oil droplet is placed on a solid surface in water, the solid–water–oil interface exists. The nature of oleophobicity/oleophilicity of an oil droplet in water can be determined from the values of surface energies of various interfaces and contact angles of water and oil in air.

Many superoleophobic surfaces have been developed by modifying the surface chemistry with a coating of extreme low surface energy materials (Shibuichi et al., 1998; Li et al., 2001; Kiuru and Alakoski, 2004; Xie et al., 2004; Nicolas et al., 2006; Hoefnagels et al., 2007; Tuteja et al., 2007; Jung and Bhushan, 2009).

Jung and Bhushan (2009) and Liu et al. (2009) performed experiments in a solid–water–oil interface. They found that hydrophilic and oleophilic surfaces (solid–air–water interface and solid–air–oil interface) can switch into an oleophobic surface in water (solid–water–oil interface). As a result, oil contaminants are washed away when immersed in water. This effect can be employed for underwater oleophobicity and self-cleaning that can be used against marine ship fouling (Jung and Bhushan, 2009).

In this chapter, a model advanced by Jung and Bhushan (2009) for predicting the oleophobic/oleophilic nature of surfaces is presented. To validate the model, it has been investigated how the water and oil droplets in three-phase interfaces influence the wetting behavior on flat surfaces as well as micropatterned surfaces with varying pitch values. Micropatterned surfaces have been selected to study the effect of geometry. For creating hydrophobic and oleophobic surfaces, *n*-perfluoroeicosane ($C_{20}F_{42}$) with surface energy lower than that of oil was deposited on flat and micropatterned surfaces, and the trends were explained in terms of the measured contact angle and the predicted values of models. The wetting behavior of the nano- and hierarchical structures found in Lotus plant surfaces and sharkskin replica as an example of aquatic animal has also been studied.

9.2 Modeling of Contact Angle for Various Surfaces

In this section, expressions are developed for contact angles for various interfaces—solid–air–water interface, solid–air–oil interface, and solid–water–oil interface. If a water droplet is placed on a solid surface in air, the solid–air and water–air interfaces come together with a static contact angle, θ_W . The value of θ_W can be determined from the condition of the total energy of the system being minimized (Adamson, 1990; Israelachvili, 1992) and is given by the Young's equation for the contact angle, θ_W ,

$$\cos \theta_W = \frac{\gamma_{SA} - \gamma_{SW}}{\gamma_{WA}}, \quad (9.1)$$

where γ_{SW} , γ_{SA} , and γ_{WA} are surface tensions of the solid–water, solid–air, and water–air interfaces, respectively. If an oil droplet is placed on a solid surface in air, the Young's equation for the contact angle, θ_O , can be expressed by

$$\cos \theta_O = \frac{\gamma_{SA} - \gamma_{SO}}{\gamma_{OA}}, \quad (9.2)$$

where γ_{SO} , γ_{SA} , and γ_{OA} are surface tensions of the solid–oil, solid–air, and oil–air interfaces, respectively. As predicted by (9.2), if γ_{SO} is higher than γ_{SA} , an oleophobic surface can be achieved.

To create an oleophobic surface in water, consider the solid–water–oil interface. If an oil droplet is placed on a solid surface in water, the contact angle of an oil droplet in water, θ_{OW} , is given by Young's equation:

$$\cos \theta_{\text{OW}} = \frac{\gamma_{\text{SW}} - \gamma_{\text{SO}}}{\gamma_{\text{OW}}}, \quad (9.3)$$

where γ_{SO} , γ_{SW} , and γ_{OW} are the surface tensions of the solid–oil, solid–water, and oil–water interfaces, respectively. Combining (9.1), (9.2), and (9.3), the equation for the contact angle, θ_{OW} , of an oil droplet in water is given as (Jung and Bhushan, 2009)

$$\cos \theta_{\text{OW}} = \frac{\gamma_{\text{OA}} \cos \theta_{\text{O}} - \gamma_{\text{WACOS}} \cos \theta_{\text{W}}}{\gamma_{\text{OW}}}. \quad (9.4)$$

As predicted by (9.4), for a hydrophilic surface ($\gamma_{\text{SA}} > \gamma_{\text{SW}}$), an oleophobic surface in the solid–water–oil interface can be created if $\gamma_{\text{OA}} \cos \theta_{\text{O}}$ is lower than $\gamma_{\text{WACOS}} \cos \theta_{\text{W}}$. Since the surface tension of oil and organic liquids is much lower than that of water, most hydrophilic surfaces can be made oleophobic in a solid–water–oil interface. For a hydrophobic surface ($\gamma_{\text{SA}} < \gamma_{\text{SW}}$) and an oleophobic surface in a solid–air–oil interface ($\gamma_{\text{SA}} < \gamma_{\text{SO}}$), an oleophobic surface in a solid–water–oil interface can be created if $\gamma_{\text{OA}} \cos \theta_{\text{O}}$ is higher than $\gamma_{\text{WACOS}} \cos \theta_{\text{W}}$ and vice versa. For a hydrophobic and an oleophilic surface in solid–air–oil interface, an oleophobic surface in solid–water–oil interface cannot be created. Schematics are shown in Fig. 9.1, and the summary of philic/phobic nature in various interfaces is shown in Table 9.1. For an oleophobic surface, oil contaminants are washed away when immersed in water. This effect leads to self-cleaning that can be used against marine ship fouling (Jung and Bhushan, 2009).

9.3 Experimental Techniques

For the measurement of static contact angle, deionized water was used for water droplets and hexadecane was used for oil droplets by Jung and Bhushan (2009). The surface tensions of the water–air interface (γ_{WA}), oil–air interface (γ_{OA}), and oil–water interface (γ_{OW}) are 73 (Lide, 2009), 27.5 (Lide, 2009), and 51.4 mN/m (Tajima et al., 1980), respectively. The mass densities are 1,000 and 773 kg/m³ for water and hexadecane, respectively. Water and oil droplets of about 5 µL in volume (with radius of a spherical droplet about 1 mm) in air environment were gently deposited on the specimen using a microsyringe. The process of wetting behavior of an oil droplet in water was obtained in a solid–water–oil interface system as shown in Fig. 9.2 (Jung and Bhushan, 2009). A specimen was first immersed in water phase. Then an oil droplet was gently deposited using a microsyringe from the bottom of the system because the density of oil (hexadecane) is lower than that of water. The image of the droplet was obtained by a digital camcorder with a 10 × optical and 120 × digital zoom. The images obtained were analyzed for the contact angle using ImageTool® software (University of Texas Health Science Center). The measurements were reproducible to within ±2°.

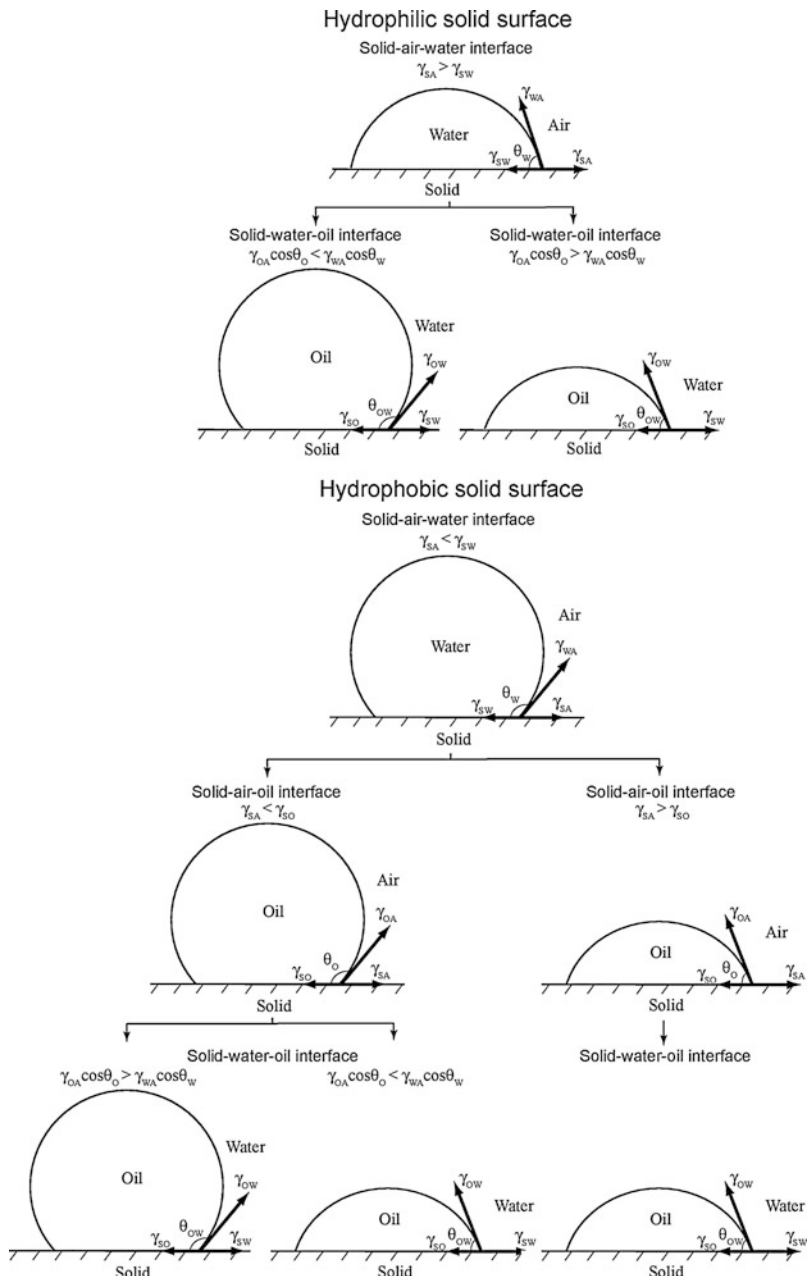


Fig. 9.1 Schematics of a droplet of liquid showing philic/phobic nature in three different phase interface on the surface— θ_W , θ_O , and θ_{OW} are static contact angles of water droplet, oil droplet, and oil droplet in water, respectively (Jung and Bhushan, 2009)

Table 9.1 Summary of philic/phobic nature in various interfaces (Jung and Bhushan 2009)

Solid-air-water interface	Solid-water-oil interface	
Hydrophilic $(\gamma_{SA} > \gamma_{SW})$	→	Oleophobic if $\gamma_{OA}\cos\theta_O < \gamma_{WA}\cos\theta_W$ Oleophilic if $\gamma_{OA}\cos\theta_O > \gamma_{WA}\cos\theta_W$
Solid-air-water interface	Solid-air-oil interface	Solid-water-oil interface
Hydrophobic $(\gamma_{SA} < \gamma_{SW})$	→ Oleophobic if $\gamma_{SA} < \gamma_{SO}$ Oleophilic if $\gamma_{SA} > \gamma_{SO}$	→ Oleophobic if $\gamma_{OA}\cos\theta_O > \gamma_{WA}\cos\theta_W$ Oleophilic if $\gamma_{OA}\cos\theta_O < \gamma_{WA}\cos\theta_W$

Solid-water-oil interface system

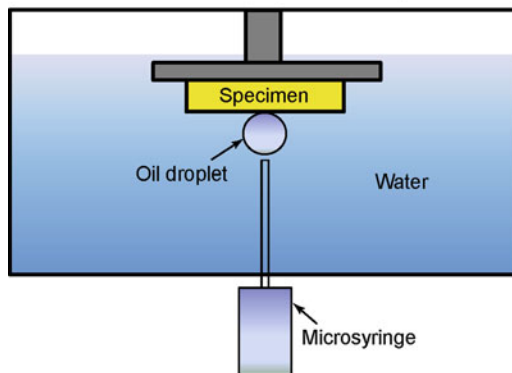


Fig. 9.2 Schematics of a solid–water–oil interface system. A specimen is first immersed in water phase, and then, an oil droplet is gently deposited using a microsyringe, and the static contact angle in the system is measured (Jung and Bhushan, 2009)

9.4 Fabrication and Characterization of Oleophobic Surfaces

A two-step molding process was used to replicate microstructures with varying pitch values, as described earlier. As a master template for the flat and micropatterned surfaces, a flat Si surface and micropatterned Si surfaces with pillars of $14\text{ }\mu\text{m}$ diameter and $30\text{ }\mu\text{m}$ height with different pitch values (21, 23, 26, 35, 70, 105, 126, 168, and $210\text{ }\mu\text{m}$), fabricated by photolithography, were used (Jung and Bhushan, 2009).

To study surfaces with some oleophobicity, a surface coating which has a lower surface tension than that of oil is needed. For this purpose, Jung and Bhushan (2009) deposited *n*-perfluoroeicosane ($\text{C}_{20}\text{F}_{42}$) (268828, Sigma-Aldrich, USA) on the epoxy surfaces by thermal evaporation. The surface energy of *n*-perfluoroeicosane is 6.7 mJ/m^2 (6.7 mN/m) (Nishino et al., 1999). The specimens

were mounted on a specimen holder with double-sided tape and placed in a vacuum chamber at 30 mTorr (4 kPa pressure), 2 cm above a heating plate loaded with 6,000 μg *n*-perfluoroeicosane (Bhushan et al., 2009). The *n*-perfluoroeicosane was evaporated by heating it up to 170°C. In a vacuum chamber, the evaporation from the point source to the substrate occurs in a straight line; thus, the amount of sublimated material is equal in a hemispherical region over the point of source (Bunshah, 1994). In order to estimate the amount of sublimated mass, the surface area of the half sphere was calculated by using the formula $2\pi r^2$, whereby the radius (r) represents the distance between the specimen to be covered and the heating plate with the substance to be evaporated. The calculated amount of *n*-perfluoroeicosane deposited on the surfaces was 2.4 $\mu\text{g}/\text{mm}^2$ (amount of *n*-perfluoroeicosane loaded on a heating plate divided by surface area).

Hierarchical structures were fabricated using a two-step fabrication process, including the production of microstructured surfaces by soft lithography and the subsequent development of nanostructures on top by self-assembly of *n*-hexatriacontane with the amounts of 0.2 $\mu\text{g}/\text{mm}^2$ deposited by thermal evaporation, as described earlier (Bhushan et al., 2008, 2009). Jung and Bhushan (2009) also used a sharkskin replica described earlier (L., Squalidae).

Figure 9.3a shows the SEM micrographs taken at a 45° tilt angle, showing two magnifications of the micropatterned surface. Figure 9.3b shows the hierarchical structures and nanostructures covered with *n*-hexatriacontane platelets. The nanostructure is formed by three-dimensional platelets of *n*-hexatriacontane. Platelets are flat crystals, grown perpendicular to the substrate surface. The platelet thickness varied between 50 and 100 nm, and their length varied between 500 and 1,000 nm. Figure 9.3c shows the sharkskin replica and shows only three ribs on each scale. It is clearly visible that the V-shaped ribs' height varies between 200 and 500 μm , and their spacing varies between 100 and 300 μm (Jung and Bhushan, 2009).

9.4.1 Wetting Behavior on Flat and Micropatterned Surfaces

To observe the wetting behavior of water and oil droplets for philic/phobic nature in three-phase interfaces, Jung and Bhushan (2009) performed experiments with droplets on hydrophilic, hydrophobic, and oleophilic surfaces in air. Figure 9.4 shows the optical micrographs of droplets in three different phase interfaces on flat epoxy resin and micropatterned surfaces. In a solid–air–water interface, the water droplet was hydrophilic for the flat epoxy resin and was superhydrophobic for the micropatterned surface with 23 μm pitch. Jung and Bhushan (2009) reported evidence of air pocket formation between the pillars which results in a high static contact angle for a micropatterned surface. However, in a solid–air–oil interface, the oil droplet was oleophilic for both surfaces. In the solid–water–oil interface system, in which the oil droplet sits on water trapped in the pillars, it is observed that the

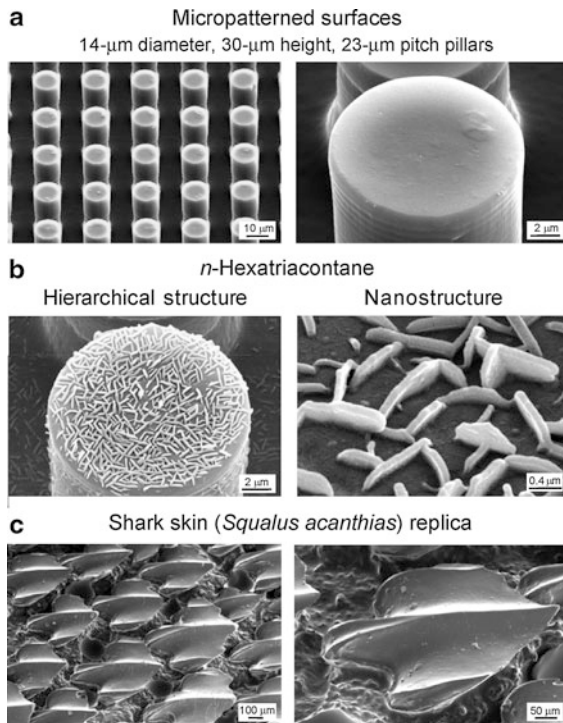


Fig. 9.3 SEM micrographs taken at a 45° tilt angle showing two magnifications of (a) the micropatterned surface, (b) hierarchical structure and nanostructure with three-dimensional platelets on the surface fabricated with 0.2 $\mu\text{g}/\text{mm}^2$ mass of *n*-hexatriacontane, and (c) sharkskin (*Squalus acanthias*) replica. The sharkskin replica shows only three ribs on each scale. It is clearly visible that the V-shaped ribs' height varies between 200 and 500 μm and their space varies between 100 and 300 μm (Jung and Bhushan, 2009)

oil droplet in water was oleophobic and had contact angles of 109° and 151° for flat epoxy resin and micropatterned surface with 23 μm pitch, respectively.

To study optimization of oleophobicity in the two solid–air–water and solid–air–oil interfaces, the static contact angles for water and oil droplets were measured on the micropatterned surfaces (Jung and Bhushan, 2009). Figure 9.5 (top) shows the measured static contact angle as a function of pitch between the pillars for a water droplet (circle) and an oil droplet (cross) in air. The data are compared with predicted static contact angle values obtained using the Wenzel and Cassie–Baxter equations (6.2) and (6.3) (solid lines) with a measured value of θ_0 for the micropatterned surfaces. In a solid–air–water interface for a water droplet, the flat epoxy resin showed a static contact angle of 76°. The static contact angle on micropatterned surfaces is higher than that of the flat surfaces. It first increases with an increase in the pitch values, then starts to drop rapidly to a value slightly higher than that of the flat surfaces. In the first portion, it jumps to a high value

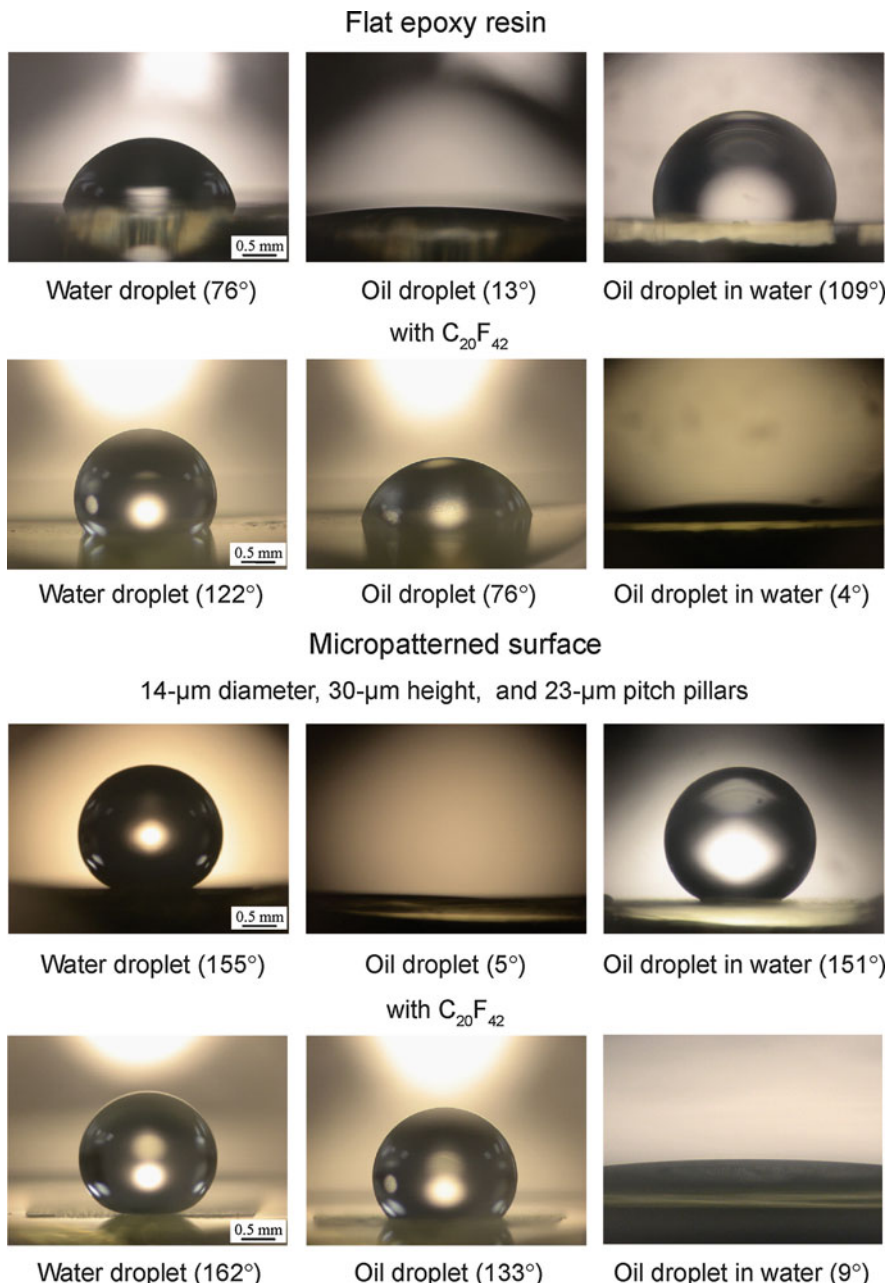


Fig. 9.4 Optical micrographs of droplets in three different phase interfaces on flat epoxy resin and micropatterned surface without and with $C_{20}F_{42}$. *Left image*: a water droplet is placed on a surface in air. *Middle image*: an oil droplet is placed on a surface in air. *Right image*: an oil droplet is placed on a solid surface in water (Jung and Bhushan, 2009)

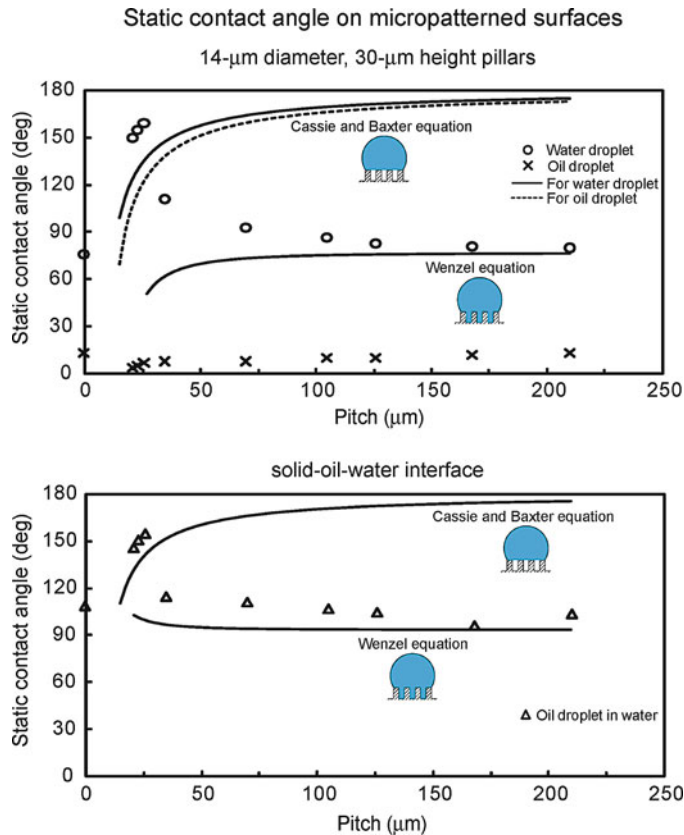


Fig. 9.5 Static contact angle as a function of pitch value for water droplet (circle) and oil droplet (cross) in air (top), and oil droplet in water (triangle) (bottom) compared with predicted static contact angle values obtained using Wenzel and Cassie–Baxter equations (solid lines) with a measured value of θ_0 for the micropatterned surfaces (Jung and Bhushan, 2009)

of 150° corresponding to a superhydrophobic surface and continues to increase to 160° at a pitch of $26 \mu\text{m}$ because open air space increases with an increase in pitch responsible for propensity of air pocket formation. The sudden drop at a pitch value of about $30 \mu\text{m}$ corresponds to the transition from the Cassie–Baxter to the Wenzel regime. The experimental observations for the transition are comparable to the value predicted from Wenzel and Cassie–Baxter equations.

At a solid–air–oil interface for an oil droplet, the flat epoxy resin showed a static contact angle of 13° . As shown in Fig. 9.5 (top), the oil droplets on all micropatterned surfaces were oleophilic, and the contact angle was lower than that of the flat surfaces. It increases with an increase in the pitch values as predicted from Wenzel equation. As mentioned earlier, the surface tension of the oil–air interface is very low for hexadecane. Therefore, it is observed that from (9.3) that the surface

tension of solid–oil interface (γ_{SO}) is lower than that of solid–water interface (γ_{SW}), resulting in oleophilic state for all micropatterned surfaces.

To study optimization of oleophobicity in a solid–water–oil interface, the static contact angles for oil droplets in water were measured on the micropatterned surfaces (Jung and Bhushan, 2009). Figure 9.5 (bottom) shows the measured static contact angle as a function of pitch between the pillars for an oil droplet in water (triangle). The data are compared with the predicted static contact angle values obtained using the Wenzel and Cassie–Baxter equations (6.2) and (6.3) (solid lines), with a measured value of θ_0 for the micropatterned surfaces. In a solid–water–oil interface, the oil droplet on the flat epoxy resin was oleophobic and had a static contact angle of 109°. The static contact angle of micropatterned surfaces in the solid–water–oil interface showed a similar trend to that in the solid–air–water interface. As the pitch increases up to 26 μm, the static contact angle first increases gradually from 146° to 155° because the oil droplet sits on water trapped in the pillars, and open space increases with an increase in pitch. Then, the contact angle starts decreasing rapidly due to the transition from the Cassie–Baxter to the Wenzel regime. The experimental observations for the transition are comparable to the values predicted from Wenzel and Cassie–Baxter equations. The micropatterned surfaces studied here were either hydrophilic or hydrophobic, and both were oleophilic. In the solid–water–oil interface, they were oleophobic. As shown in Fig. 9.1 and Table 9.1, it is observed that the data are not consistent with the model for hydrophobic surfaces. However, hydrophilic surfaces became oleophobic in the solid–water–oil interface because $\gamma_{OA}\cos\theta_O$ is higher than $\gamma_{WA}\cos\theta_W$.

9.4.2 Wetting Behavior on Flat and Micropatterned Surfaces with C₂₀F₄₂

To study surfaces with some oleophobicity, *n*-perfluoroeicosane (C₂₀F₄₂), which has a lower surface tension than that of oil, was deposited on the surfaces, and experiments with droplets on hydrophobic and both oleophilic and oleophobic surfaces in air were performed (Jung and Bhushan, 2009). Figure 9.4 shows the optical micrographs of droplets in three different phase interfaces on a flat epoxy resin and a micropatterned surface with C₂₀F₄₂. In a solid–air–water interface and a solid–air–oil interface, the water droplet and oil droplet showed contact angles of 122° and 76° for the flat epoxy resin with C₂₀F₄₂ and contact angles of 162° and 133° for the micropatterned surface with 23 μm pitch with C₂₀F₄₂, respectively. However, in a solid–water–oil interface, the oil droplet in water was oleophilic and had contact angles of 4° and 9° for both surfaces, respectively. To explain why the oleophobic surfaces in air became oleophilic in water, the theoretical values for both surfaces were calculated using Eq. 9.4. For calculations, the surface tensions of the water–air interface (γ_{WA}), oil–air interface (γ_{OA}), and oil–water

interface (γ_{OW}) were taken to be 73, 27.5, and 51.4 mN/m, and the contact angles for water and oil droplets in air were taken from the measured values. The theoretical values for the flat epoxy resin and the micropatterned surface with 23 μm pitch with $\text{C}_{20}\text{F}_{42}$ are 28° and 10° , respectively. These values are similar to those from the experiments. This indicates that the oleophobic surfaces become oleophilic in water.

To study optimization of oleophobicity in two solid–air–water and solid–air–oil interfaces, the static contact angles for water and oil droplets were measured on the micropatterned surfaces with different pitch values and with $\text{C}_{20}\text{F}_{42}$ (Jung and Bhushan, 2009). Figure 9.6 shows the measured static contact angle as a function of pitch between the pillars for a water droplet (circle) and an oil droplet (cross) in air. The data are compared with the predicted static contact angle values obtained using the Wenzel and Cassie–Baxter equations (6.2) and (6.3) (solid lines) with a measured value of θ_0 for the micropatterned surfaces with $\text{C}_{20}\text{F}_{42}$. In a solid–air–water interface for the water droplet, the flat epoxy resin with $\text{C}_{20}\text{F}_{42}$ showed a static contact angle of 122° . The static contact angle of micropatterned surfaces with $\text{C}_{20}\text{F}_{42}$ first increases from 158° to 169° with an increase in the pitch values, then starts to drop rapidly at a pitch value of 110 μm . From comparison of the experimental data to the Wenzel and Cassie–Baxter equations, this corresponds to the transition from Cassie–Baxter to Wenzel regime. All surfaces with $\text{C}_{20}\text{F}_{42}$ had an increase in contact angle, and the transition took place at higher pitch value than that of the micropatterned surfaces (Fig. 9.5).

At a solid–air–oil interface for an oil droplet, the flat epoxy resin with $\text{C}_{20}\text{F}_{42}$ showed a static contact angle of 76° . As shown in Fig. 9.6, the highest contact angle of micropatterned surfaces with $\text{C}_{20}\text{F}_{42}$ was 133° at a pitch value of 23 μm . Then, it decreases with an increase in the pitch values, and these values are comparable with the values predicted by the Wenzel equations. The contact angles of all micropatterned surfaces with $\text{C}_{20}\text{F}_{42}$ are higher than that of the flat surfaces.

To study optimization of oleophobicity in a solid–water–oil interface, the static contact angles for oil droplets in water were measured on the micropatterned surfaces with different pitch values and with $\text{C}_{20}\text{F}_{42}$ (Jung and Bhushan, 2009). Figure 9.6 shows the measured static contact angle as a function of pitch between the pillars for an oil droplet in water (triangle). The data are compared with the predicted static contact angle values obtained using the Wenzel and Cassie–Baxter equations (6.2) and (6.3) (solid lines) with a measured value of θ_0 for the micropatterned surfaces with $\text{C}_{20}\text{F}_{42}$. In a solid–water–oil interface, the flat epoxy resin with $\text{C}_{20}\text{F}_{42}$ was oleophilic and had a static contact angle of 4° . All micropatterned surfaces with $\text{C}_{20}\text{F}_{42}$ were oleophilic and had contact angle lower than 10° . The reason why hydrophobic and oleophobic surfaces in air became oleophilic in water can be explained from Fig. 9.1 and Table 9.1. The contact angle for a water droplet is higher than that for an oil droplet on all surfaces with $\text{C}_{20}\text{F}_{42}$, and the surface tension of the water–air interface (γ_{WA}) is higher than that of the oil–air interface (γ_{OA}). Therefore, it is observed that $\gamma_{WA}\cos\theta_W$ is higher than $\gamma_{OA}\cos\theta_O$, and then the surfaces become oleophilic in the solid–water–oil interface.

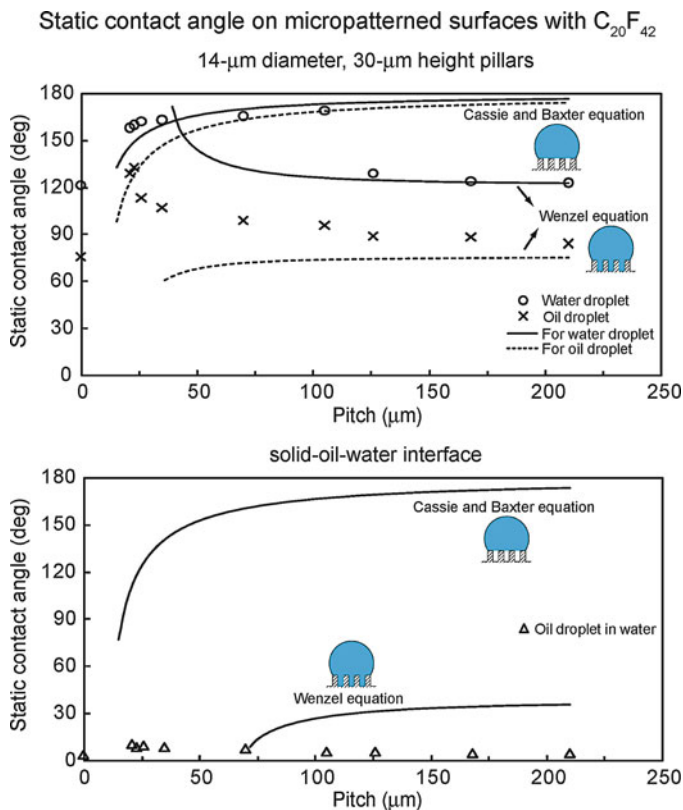


Fig. 9.6 Static contact angle as a function of pitch value for water droplet (circle) and oil droplet (cross) in air, and oil droplet in water (triangle) compared with predicted static contact angle values obtained using Wenzel and Cassie–Baxter equations (solid lines) with a measured value of θ_0 for the micropatterned surfaces with C₂₀F₄₂ (Jung and Bhushan, 2009)

9.4.3 Wetting Behavior on Nano- and Hierarchical Structures and Sharkskin Replica

To observe the wetting behavior of water and oil droplets for nano- and hierarchical structures found from Lotus plant surfaces, experiments with the droplets on the surfaces were performed in the three-phase interface (Jung and Bhushan, 2009). Figure 9.7 shows the optical micrographs of droplets in three different phase interfaces on a nanostructure and a hierarchical structure fabricated with 0.2 μg/mm² mass of *n*-hexatriacontane. Both nano- and hierarchical structures were superhydrophobic and had a static contact angle of 158° and 169° in the solid–air–water interface, respectively. However, they are oleophilic in the solid–air–oil interface because the surface energy of *n*-hexatriacontane is 31.4 mJ/m² (31.4 mN/m) (Wu, 1979), and this value is higher than that of an oil droplet

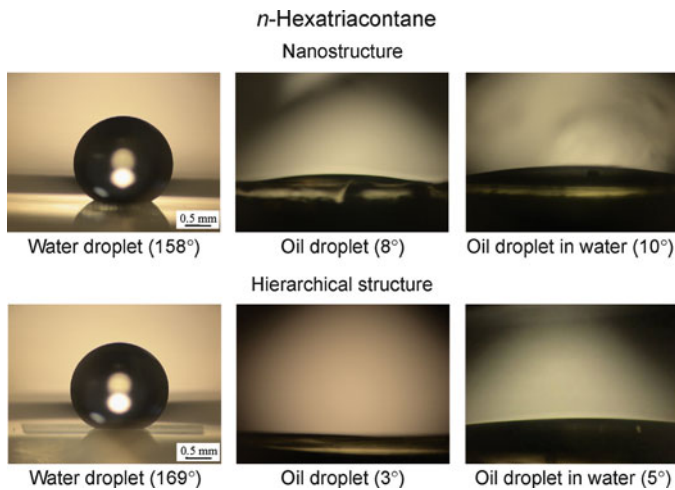


Fig. 9.7 Optical micrographs of droplets in three different phase interfaces on nanostructure and hierarchical structure fabricated with $0.2 \mu\text{g}/\text{mm}^2$ mass of *n*-hexatriacontane. *Left image*: a water droplet is placed on a surface in air. *Middle image*: an oil droplet is placed on a surface in air. *Right image*: an oil droplet is placed on a solid surface in water (Jung and Bhushan, 2009)

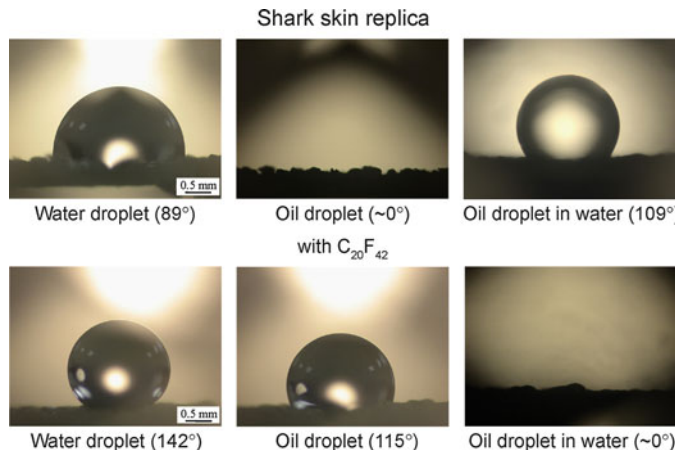


Fig. 9.8 Optical micrographs of droplets in three different phase interfaces on sharkskin replica without and with C₂₀F₄₂. *Left image*: a water droplet is placed on a surface in air. *Middle image*: an oil droplet is placed on a surface in air. *Right image*: an oil droplet is placed on a solid surface in water (Jung and Bhushan, 2009)

(hexadecane). In the solid–water–oil interface, nano- and hierarchical structures had a static contact angle of 10° and 5° , respectively. Based on Fig. 9.1 and Table 9.1, it is observed that both surfaces are oleophilic in solid–water–oil interface.

To study the surface structure on an aquatic animal, experiments with water and oil droplets on the sharkskin replica were performed in a three-phase interface ([Jung and Bhushan, 2009](#)). Figure 9.8 shows the optical micrographs of droplets in three different phase interfaces on a sharkskin replica without and with C₂₀F₄₂. First, the sharkskin replica had contact angles of 89° and ~0° for water and oil droplets, respectively. After the surface was coated with C₂₀F₄₂, the contact angles of water and oil droplets became 142° and 115°, respectively. In the solid–water–oil interface, the oil droplet in water on the sharkskin replica became oleophobic and had a contact angle of 109°. Based on [\(9.4\)](#), the calculated value was 59° for the oil droplet in water on a sharkskin replica. This difference may come from the open space under the scales of the sharkskin replica (Fig. 9.3) responsible for the propensity of trapped water pocket formation. Sharkskin replica with C₂₀F₄₂ was oleophilic and had a contact angle of ~0°. This state is the same as the micropatterned surfaces with C₂₀F₄₂ based on Fig. 9.1 and Table 9.1.

9.5 Summary

The wetting behavior of water and oil droplets for hydrophobic/hydrophilic and oleophobic/oleophilic surfaces in three-phase interfaces has been studied. In under-water applications, oleophobicity/oleophilicity of an oil droplet in water was studied on the surfaces with different surface energies of various interfaces and contact angles of water and oil droplets in air. Based on the model, it is found that for a hydrophilic surface, an oleophobic surface in the solid–water–oil interface can be created if $\gamma_{OAC}\cos\theta_O$ is lower than $\gamma_{WAC}\cos\theta_W$. For a hydrophobic surface and an oleophobic surface in solid–air–oil interface, an oleophobic surface in solid–water–oil interface can be created if $\gamma_{OAC}\cos\theta_O$ is higher than $\gamma_{WAC}\cos\theta_W$.

To validate the model for predicting the oleophobic/oleophilic nature of the surfaces, flat and micropatterned surfaces with varying pitch values were produced by soft lithography. *n*-Perfluorooctane (C₂₀F₄₂) with low surface energy (6.7 mN/m) was deposited by thermal evaporation to produce superhydrophobic and oleophobic flat and micropatterned surfaces. For water and oil droplets in three-phase interfaces, the experimental observations showed that there is a good agreement between the measured contact angle and the predicted values of models. It is also found that the transition can occur for hydrophobic and oleophobic micropatterned surfaces with a larger distance between pillars. The wetting behavior of the nano- and hierarchical structures found in Lotus plant surfaces and the sharkskin replica as an example of aquatic animal has also been investigated. It is found that the nano- and hierarchical structures with *n*-hexatriacontane were oleophilic due to the high surface energy of *n*-hexatriacontane. The structure of the sharkskin replica showed the higher propensity of trapped water pocket formation, resulting in a higher contact angle than the theoretical value, whereas the sharkskin replica with C₂₀F₄₂ had a contact angle of ~0° in the solid–water–oil interface as predicted by the model. For self-cleaning and antifouling, an oleophobic surface can be created based on this study.

References

- Adamson AV (1990) Physical chemistry of surfaces. Wiley, New York
- Bechert DW, Bruse M, Hage W (2000) Experiments with three-dimensional ripples as an idealized model of shark skin. *Exp Fluids* 28:403–412
- Bhushan B (2009) Biomimetics: lessons from nature – an overview. *Philos Trans R Soc A* 367:1445–1486
- Bhushan B, Koch K, Jung YC (2008) Nanostructures for superhydrophobicity and low adhesion. *Soft Matter* 4:1799–1804
- Bhushan B, Jung YC, Koch K (2009) Micro-, nano- and hierarchical structures for superhydrophobicity, self-cleaning and low adhesion. *Philos Trans R Soc A* 367:1631–1672
- Bixler GD, Bhushan B (2012) Biofouling: lessons from nature. *Philos Trans R Soc A* (in press)
- Bunshah RF (1994) Handbook of deposition technologies for films and coatings: science, technology and applications. Applied Science, Westwood, NJ
- Genzer J, Efimenko K (2006) Recent developments in superhydrophobic surfaces and their relevance to marine fouling: a review. *Biofouling* 22:339–360
- Hoefnagels HF, Wu D, de With G, Ming W (2007) Biomimetic superhydrophobic and highly oleophobic cotton textiles. *Langmuir* 23:13158–13163
- Israelachvili JN (1992) Intermolecular and surface forces, 2nd edn. Academic, London
- Jung YC, Bhushan B (2009) Wetting behavior of water and oil droplets in three phase interfaces for hydrophobicity/phobicity and oleophobicity/phobicity. *Langmuir* 25:14165–14173
- Kiuru M, Alakoski E (2004) Low sliding angles in hydrophobic and oleophobic coatings prepared with plasma discharge method. *Mater Lett* 58:2213–2216
- Li H, Wang X, Song Y, Liu Y, Li Q, Jiang L, Zhu D (2001) Super-“amphiphobic” aligned carbon nanotube films. *Angew Chem Int Ed* 40:1743–1746
- Lide DR (2009) CRC handbook of chemistry and physics, 89 edn. CRC, Boca Raton, FL
- Liu M, Wang S, Wei Z, Song Y, Jiang L (2009) Bioinspired design of a superoleophobic and low adhesive water/solid interface. *Adv Mater* 21:665–669
- Nicolas M, Guittard F, Geribaldi S (2006) Synthesis of stable super water- and oil-repellent polythiophene films. *Angew Chem Int Ed* 45:2251–2254
- Nishino T, Meguro M, Nakamae K, Matsushita M, Ueda Y (1999) The lowest surface free energy based on $-CF_3$ alignment. *Langmuir* 15:4321–4323
- Shibuichi S, Yamamoto T, Onda T, Tsujii K (1998) Super water- and oil-repellent surfaces resulting from fractal structure. *J Colloid Interface Sci* 208:287–294
- Tajima K, Tsutsui T, Murata H (1980) Thermodynamic relation of interfacial tensions in three fluid phases. *Bull Chem Soc Jpn* 53:1165–1166
- Tuteja A, Choi W, Ma M, Mabry JM, Mazzella SA, Rutledge GC, McKinley GH, Cohen RE (2007) Designing superoleophobic surfaces. *Science* 318:1618–1622
- Wu S (1979) Surface-tension of solids-equation of state analysis. *J Colloid Interface Sci* 71: 605–609
- Xie Q, Xu J, Feng L, Jiang L, Tang W, Luo X, Han CC (2004) Facile creation of a super-amphiphobic coating surface with bionic microstructure. *Adv Mater* 16:302–305

Part V

Shark skin Effect

Chapter 10

Shark skin Surface for Fluid-Drag Reduction in Turbulent Flow

10.1 Introduction

Nature has created ways of reducing drag in fluid flow, evident in the efficient movement of fish, dolphins, and sharks. The mucus secreted by fish causes a reduction in drag as they move through water, protects the fish from abrasion by making the fish slide across objects rather than scrape, and prevents disease by making the surface of the fish difficult for microscopic organisms to adhere to (Shephard, 1994). [Accumulation of unwanted biological matter on surfaces with biofilms created by microorganisms is referred to as biofouling (Bixler and Bhushan, 2012).] It has been known for many years that by adding as little as a few hundred parts per million guar, a naturally occurring polymer, friction in pipe flow, can be reduced by up to two thirds. Other synthetic polymers provide an even larger benefit (Hoyt, 1975). The compliant skin of the dolphin has also been studied for drag-reducing properties. By responding to the pressure fluctuations across the surface, a compliant material on the surface of an object in a fluid flow has been shown to be beneficial. Though early studies showed dramatic drag reduction benefits, later studies have only been able to confirm 7% drag reduction (Choi et al., 1997).

Another set of aquatic animals which possesses multipurpose skin are fast-swimming sharks. The skin of fast-swimming sharks reduces the drag experienced by sharks and protects against biofouling as they swim through water. The tiny scales covering the skin of fast-swimming sharks, known as dermal denticles (skin teeth), are shaped like small riblets and aligned in the direction of fluid flow. Slower sharks are covered in dermal denticles as well, but not those which are shaped like riblets or provide any drag reduction benefit. The cross-sectional shape of riblets on fast-swimming sharks varies greatly, even at different locations on the same shark. Figure 10.1 shows the difference between the separated blade riblets on the tail of a Shortfin Mako shark, *Isurus oxyrinchus*, with the scale-grouped riblets on its front section, as well as the morphology that exists on various other fast-swimming sharks. Shark skin inspired riblets have been shown to provide a drag reduction

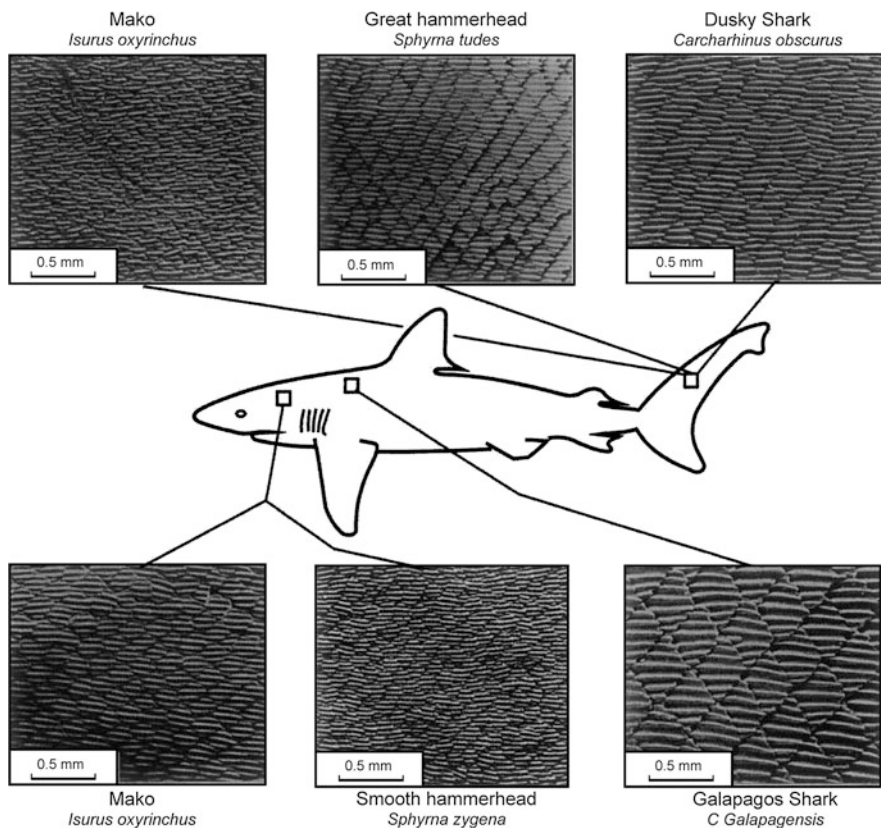


Fig. 10.1 Scale patterns on fast-swimming sharks (adapted from [Reif, 1985](#); [Bechert et al., 2000a](#))

benefit up to 9.9% ([Bechert et al., 1997b](#)). In addition to low drag, the spacing between these dermal denticles is such that microscopic aquatic organisms have difficulty adhering to and colonizing the surface ([Carman et al., 2006](#); [Genzer and Efimenko, 2006](#); [Kesel and Liedert, 2007](#); [Ralston and Swain, 2009](#)). Many sea animals, including fish and sharks, are known to be oleophobic underwater.

The effect of riblet structures on the behavior of fluid flow, as well as the optimization of their morphology, is the focus of this chapter ([Dean and Bhushan, 2010](#), [2012](#)). To understand the mechanism of shark skin drag reduction, it is first important to understand the nature of fluid flow over an effective shark skin surface. Flow characteristics and the mechanism of fluid drag will be discussed for fluid flowing over a flat plate. Mechanisms of drag reduction by riblet geometries will then be discussed, followed by a review of experimental riblet studies which have been performed, a discussion of optimization data for common riblet geometries, and other factors in riblet selection. Large-scale and commercial applications of riblets will then be explored.

10.2 Mechanisms of Fluid Drag

Fluid drag comes in several forms, the most basic of which are pressure drag and friction drag (Dean and Bhushan, 2010). Pressure or form drag is the drag associated with the energy required to move fluid out from in front of an object in the flow and then back in place behind the object. Much of the drag associated with walking through water is pressure drag, as the water directly in front of a body must be moved out and around the body before the body can move forward. The magnitude of pressure drag can be reduced by creating streamlined shapes. Friction or viscous drag is caused by the interactions between the fluid and a surface parallel to the flow, as well as the attraction between molecules of the fluid. Friction drag is similar to the motion of a deck of cards sliding across a table. The frictional interactions between the table and the bottom card, as well as between each successive card mimic the viscous interactions between molecules of fluid. Moving away from the surface of an object in a fluid flow, each fluid layer has a higher velocity until a layer is reached where the fluid has velocity equal to the mean flow. Fluids of higher viscosity—the attraction between molecules—have higher apparent friction between fluid layers, which increases the thickness of the fluid layer distorted by an object in a fluid flow. For this reason, more viscous fluids have relatively higher drag than less viscous fluids. A similar increase in drag occurs as fluid velocity increases. The drag on an object is in fact a measure of the energy required to transfer momentum between the fluid and the object to create a velocity gradient in the fluid layer between the object and undisturbed fluid away from the object's surface.

The above discussion of friction drag assumes all neighboring fluid molecules move in the same relative direction and momentum transfer occurs between layers of fluid flowing at different velocities. Figure 10.2 shows an image of the transition between laminar flow and turbulent flow, in which molecules move in swirling and cross-stream motions such that an average velocity is maintained in the direction of flow. The inclusion of cross-flow and nonparallel relative velocities between molecules in turbulent flow causes a dramatic increase in momentum transfer. The cross-flow momentum transfer is of particular interest, as all momentum transferred parallel to the surface of an object results in a corresponding increase in drag. Natural transition occurs from laminar to turbulent flow regimes near a Reynolds number around 4,000 for pipe flow and 500,000 for flow over a flat plate. Reynolds number, Re , is a ratio of the inertial forces to viscous forces in a given flow. For pipe flow, $Re = \rho V D / \mu$, where ρ = fluid density, V = velocity, D = pipe diameter, and μ = dynamic viscosity. For flow over a flat plate, $Re = \rho V L / \mu$, where L = length. For values of Re much less than the transition values above, flow is laminar—dominated by viscous forces between the molecules. For larger values of Re , the flow is turbulent—dominated by inertial forces of the system (Munson et al., 2005).

Fully developed turbulent flow is commonly said to exhibit complete randomness in its velocity distribution, but there exist distinct regions within fully developed turbulent flow that exhibits different patterns and flow characteristics

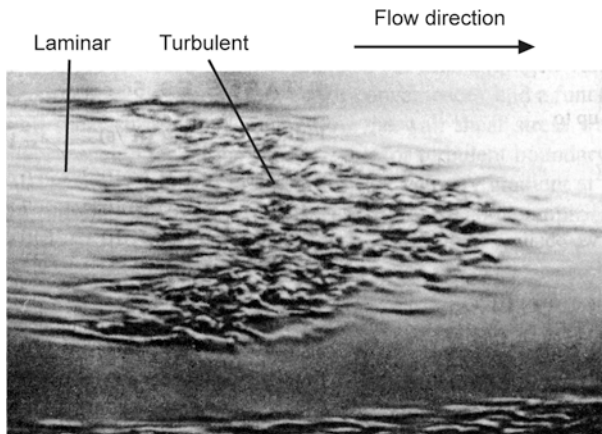


Fig. 10.2 Transition between laminar and turbulent flow in fluid over a flat plate (adapted from Munson et al., 2005)

(Kline et al., 1967). While organization is evident in the viscous sublayer, the layer closest to the surface, the outer layers of the turbulent boundary layer are chaotic and disorganized. Much of this chaotic motion above the viscous sublayer is caused by the outward bursting of the streamwise vortices that form at the surface in the viscous sublayer. Streamwise vortices (vortices which rotate about axes in the direction of mean velocity) dominate the viscous sublayer. As these vortices rotate and flow along the surface, they naturally translate across the surface in the cross-flow direction. The interaction between the vortices and the surface, as well as between neighboring vortices that collide during translation initiate bursting motions where vortices are rapidly ejected from the surface and into the outer boundary layers. As vortices are ejected, they tangle with other vortices and twist such that transient velocity vectors in the cross-stream direction can become as large as those in the average flow direction (Kline et al., 1967). The translation, bursting of vortices out of the viscous sublayer, and chaotic flow in the outer layers of the turbulent boundary-layer flow are all forms of momentum transfer and are large factors in fluid drag. Reducing the bursting behavior of the streamwise vortices is a critical goal of drag reduction, as the drag reduction possibilities presented by this are sizable.

The vortices were first visualized from a horizontal cross section and were seen as high and low-speed streaks aligned in the mean flow direction (Coles, 1978). Later, a full Navier–Stokes simulation was used to replicate the high- and low-speed streaks (Robinson, 1991), and more recently flow visualization techniques were used to capture cross-sectional images, shown in Fig. 10.3, of the streamwise vortex formations above both flat-plate and riblet surfaces (Lee and Lee, 2001). The streaky structure that was seen in the horizontal cross section was representative of local average velocity flows and is caused by the interactions between the neighboring vortices.

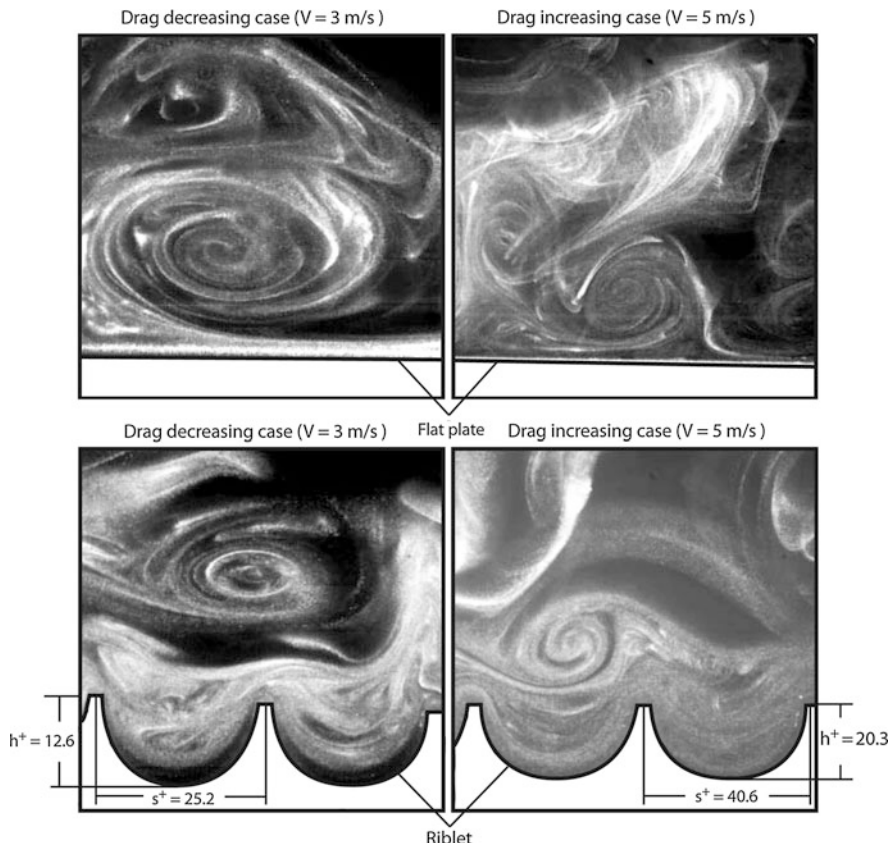


Fig. 10.3 Turbulent flow visualization of streamwise vortices in a vertical cross section over flat-plate and riblet surfaces using atomized olive oil in air (Adapted from Lee and Lee, 2001)

It is important to understand the dimensions used to characterize these vortices as well as riblet structures. As flow properties change, the dimensions of the turbulent flow structures change as well. As such, it is useful to use non-dimensional length values to better compare studies performed in different flow conditions. Dimensionless wall units, marked $^+$, are used for all length scales, which are calculated by multiplying the dimensional length by V_τ / ν . For example, $s^+ = s V_\tau / \nu$, where s^+ is the nondimesional riblet spacing, s is the dimensional riblet spacing, ν is the kinematic viscosity, and $V_\tau = (\tau_0 / \rho)^{0.5}$ is the wall stress velocity, for which ρ is the fluid density and τ_0 is the wall shear stress. Wall shear stress can be estimated for round pipe flow using the equation $\tau_0 = 0.03955 \nu^{1/4} \rho V^{7/4} d^{-1/4}$, where V is the average flow velocity and d is the hydraulic diameter. For flow in rectangular pipes, the equation for hydraulic diameter $d = 4A/c$ can be applied, where A is the cross sectional area and c is the wetted perimeter. The average cross-stream wavelength of the high and low speed streaks—the added widths of one high speed streak and

one low speed streak—is equal to the added diameters of two neighboring vortices and has been measured at 70–100 wall units (Kline et al., 1967; Wilkinson, 1983; Bechert et al., 2000a). This corresponds to a vortex diameter of 35–50 wall units. Flow visualizations shown in Fig. 10.3 show vortex cross sections and relative length scales, demonstrating vortex diameters smaller than 40 wall units (Lee and Lee, 2001).

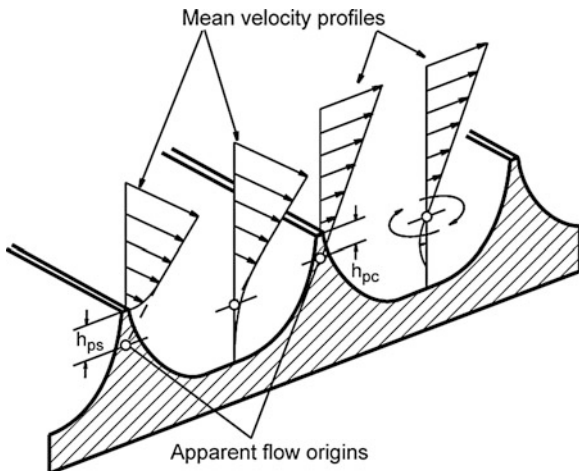
10.3 Role of Rilets in Drag Reduction

The small rilets which cover the skin of fast-swimming sharks work to reduce the increased drag present in turbulent flow in two ways: by impeding the cross-stream translation of the streamwise vortices in the viscous sublayer and by elevating the high-velocity vortices above the surface, reducing the shear stress and momentum transfer. The first mechanism, in which the rilets interact with and impede vortex translation, is complex, and the entirety of the phenomena is not yet fully understood. On a practical level, impeding the translation of vortices reduces the occurrence of vortex ejection into the outer boundary layers and momentum transfer caused by tangling and twisting of vortices in the outer boundary layers (Dean and Bhushan, 2010).

The addition of rilets protruding from a surface is not at first an obvious option for the reduction of drag. One classical drag-increasing feature which rilets exhibit is an increase in total wetted surface area. In the turbulent flow regime, fluid drag typically increases dramatically with an increase in surface area due to the shear stresses at the surface acting across the new, larger surface area. However, as vortices form above a rilet surface, they are held off of the lower structures by the rilet tips, interacting with the tips only and allowing lower velocity flow to dominate the valleys of the rilets. Since the higher velocity vortices interact only with a small surface area at the rilet tips, only this localized area experiences high shear stresses. The low-velocity fluid flow in the valleys of the rilets produces very low shear stresses across the majority of the surface of the rilet. By keeping the vortices above the rilet tips, the cross-stream velocity fluctuations inside the rilet valleys are much lower than the cross-stream velocity fluctuations above a flat plate (Lee and Lee, 2001). This difference in cross-stream velocity fluctuations is evidence of a reduction in shear stress and momentum transfer near the surface, which minimizes the effect of the increased surface area. Though the vortices remain above the rilet tips, some secondary vortex formations do occur that enter the rilet valleys transiently. The flow velocities of these transient secondary vortices are such that the increase in shear stress caused by their interaction with the surface of the rilet valleys is small.

Additionally, the protrusion of the rilets into the bulk flow increases the overall cross-sectional area of the object which has been covered with rilets. In external flows, this increase in cross-sectional area is minimal, and the drag-increasing effects are easily overcome by the rilets. Protruding into the flow without greatly

Fig. 10.4 Schematic representation of the mean velocity profiles and effective protrusion heights for flow in both the streamwise direction, h_{ps} , and in the cross-flow direction, h_{pc} (adapted from Bechert et al., 1997b)



increasing fluid drag allows the riblets to interact with the vortices to reduce the cross-stream translation and related effects. This is the second mechanism of drag reduction which riblets are known to provide. By reducing the non-streamwise momentum transfer, less energy is wasted in the flow. Though the underlying mechanisms are not completely understood, the riblets which protrude into the flow cause an increase in cross-flow shear stress (Bechert et al., 1997b). This increase in cross-flow resistance causes a tendency for riblets to become pinned at one location on the surface, reducing the occurrence of vortex translation. This in turn decreases their likelihood to interact, eject, tangle, and increase outer-layer turbulence. The momentum carried in ejected vortices and transferred in non-streamwise directions is purely wasteful and deleterious to the efficiency of the flow. By reducing the translation and ejection of vortices on the surface, large gains in energy efficiency can be made.

As the riblets protrude into the flow field, they raise the effective flow origin by some distance. The amount by which the height of the riblets is greater than the apparent vertical shift of the flow origin is referred to as the effective protrusion height. By calculating the average streamwise velocity in laminar flow at heights over riblet surfaces and comparing them to the average streamwise velocities in laminar flow at heights over a flat plate, the effective streamwise protrusion height, h_{ps} , is found for laminar flow. The effective cross-stream protrusion height, h_{pc} , is similarly found for laminar flow by comparing the cross-stream velocities over a riblet surface to those over a flat plate. A schematic of streamwise and cross-stream flow velocity profiles and effective protrusion heights is shown in Fig. 10.4. The difference between the vertical shifts in the streamwise and cross-stream origin, $\Delta h = h_{ps} - h_{pc}$, for any riblet geometry has been proposed to be the degree to which that riblet geometry will reduce vortex translation for low Re flows (Bechert et al., 1997b). As Re increases, the degree to which increased surface area affects the overall fluid drag increases, and the drag reduction correlation to these laminar flow theories deteriorates.

Numerical modeling of turbulent flow over riblet systems has also been done ([Goldstein et al., 1995](#)). Using an immersed boundary technique, a virtual riblet surface was created in turbulent flow inside a duct. This technique involves the insertion of point forces in the flow arranged in the shape of the desired riblet surface, which exert a stalling force opposite the direction of flow. Due to the random nature of fluid velocities in turbulent flow, a feedback loop must be used to adjust each point force to create an equilibrium state of zero velocity fluid in the shape of the riblet surface. Using this modeling method, the response of inserting a riblet surface into a turbulent flow can be monitored to better understand the mechanisms of drag reduction. In their study, [Goldstein et al. \(1995\)](#) first inserted virtual flat-plate boundaries in laminar and turbulent flow over a flat plate. These tests benchmarked the capability of the point forces to accurately represent a stagnant boundary in steady flow and the capability of the feedback loop to accurately model a boundary in unsteady flow, respectively. Building from these platforms, two virtual riblet surfaces were tested in turbulent flow. Velocity contours from one of these virtual riblet surfaces can be seen in Fig. 10.5. These surfaces performed similarly to similar physical riblet surfaces and showed up to 3.3% drag reduction when compared to flat a surface. Analysis of the modeled flow fields over the riblet surfaces is in consensus with existing theories of drag reduction mechanisms. As vortices form on the surface, they remain above the riblet tips, which creates a low-velocity channel in the riblet valleys. The low-velocity channel between riblet tips has a lower velocity gradient than flow over a flat plate, which reduces shear stresses over most of the riblet surface. Velocity gradients are higher at the riblet tips, and shear stresses are correspondingly higher. The net result of this shear stress distribution is a favorable decrease in overall drag. Also, vortex translation across the riblet surface during animations was noticeably damped in comparison to flow over a flat plate. Damped vortex translation serves to reduce the occurrence of vortex bursting, tangling, and outer-layer turbulence.

10.4 Studies with Various Riblet Geometries

Many types of riblets have been studied, from riblets which have a shape resembling natural riblets to those which bear little resemblance to the riblets on shark skin but sought to test all facets of riblet drag reduction. Sometimes, riblet shapes have been chosen for their ease of fabrication. A review of riblet optimization studies has been provided to summarize the findings of various researchers ([Dean and Bhushan, 2010](#)).

Two-dimensional (2D) riblets, which have a continuous extrusion of a simple cross section in the streamwise direction, have been most extensively characterized. The most thorough characterization has been completed for symmetrical 2D riblets with sawtooth, scalloped, and blade cross sections as shown in Fig. 10.6 ([Walsh, 1980, 1982; Bechert et al., 1985; Bechert et al., 1986, 1997a, 2000a, b; Walsh and Lindemann, 1984; Wilkinson and Lazos, 1988; Wilkinson et al., 1988;](#)

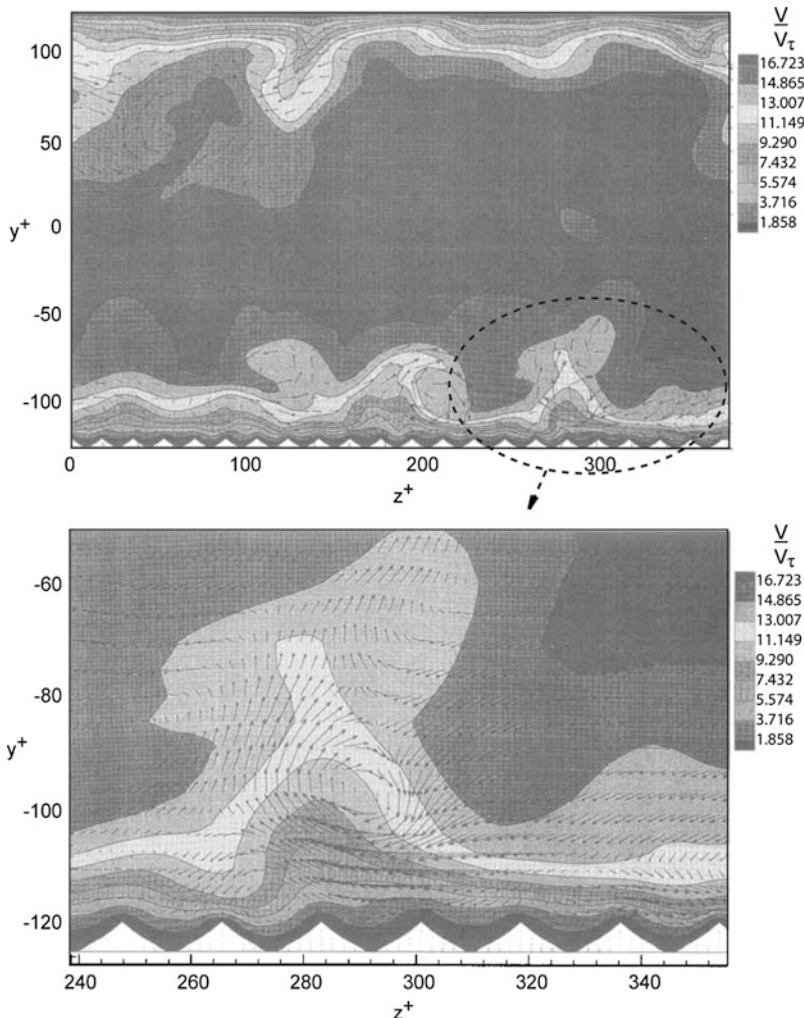


Fig. 10.5 Plots showing numerically simulated flow through a duct with virtual riblet surface on bottom and flat surface on top. A magnified view of a region of interest from the duct is shown below. Virtual riblets have sawtooth cross section with $h/s \sim 0.29$. Nondimensionalized length scales used for dimensions parallel and normal to surface are z^+ and y^+ , respectively. Lines of constant velocity are shown, as well as velocity vectors. Regions of similar flow velocity are plotted using a ratio of velocity, V , to wall stress velocity $V_\tau = (\tau_0/\rho)^{0.5}$ (adapted from Goldstein et al., 1995)

Walsh and Anders, 1989). Alternative riblet geometries have, in general, shown no increased benefit. These riblets, including asymmetrical riblets, hierarchical riblets, and riblets with rounded or notched peaks, have been studied in detail and do not improve upon the benefit of standard riblet geometries (Walsh, 1980, 1982; Walsh

and Lindemann, 1984). Other 2D riblet shapes which have been studied include alternating brother-sister-type riblets (Bechert et al., 1997a) and hierarchical riblets with small riblets on top of larger riblets (Wilkinson and Lazos, 1988). Three-dimensional (3D) riblets, which include segmented 2D riblets as well as shark skin moldings and replicas, have also been studied. Riblet types characterized include aligned segmented-blade riblets (Wilkinson and Lazos, 1988), offset segmented-blade riblets (Bechert et al., 2000a), offset 3D blade riblets (Bechert et al., 2000a), and 3D shark skin replicas (Bechert et al., 2000b; Lang et al., 2008; Jung and Bhushan, 2010).

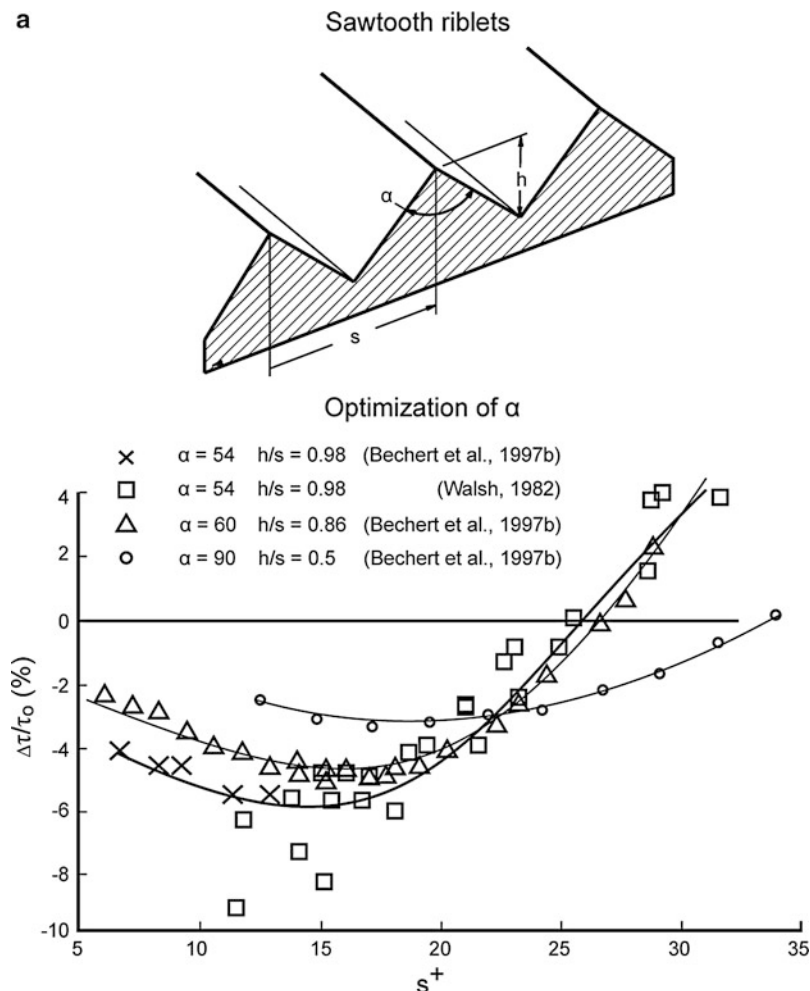
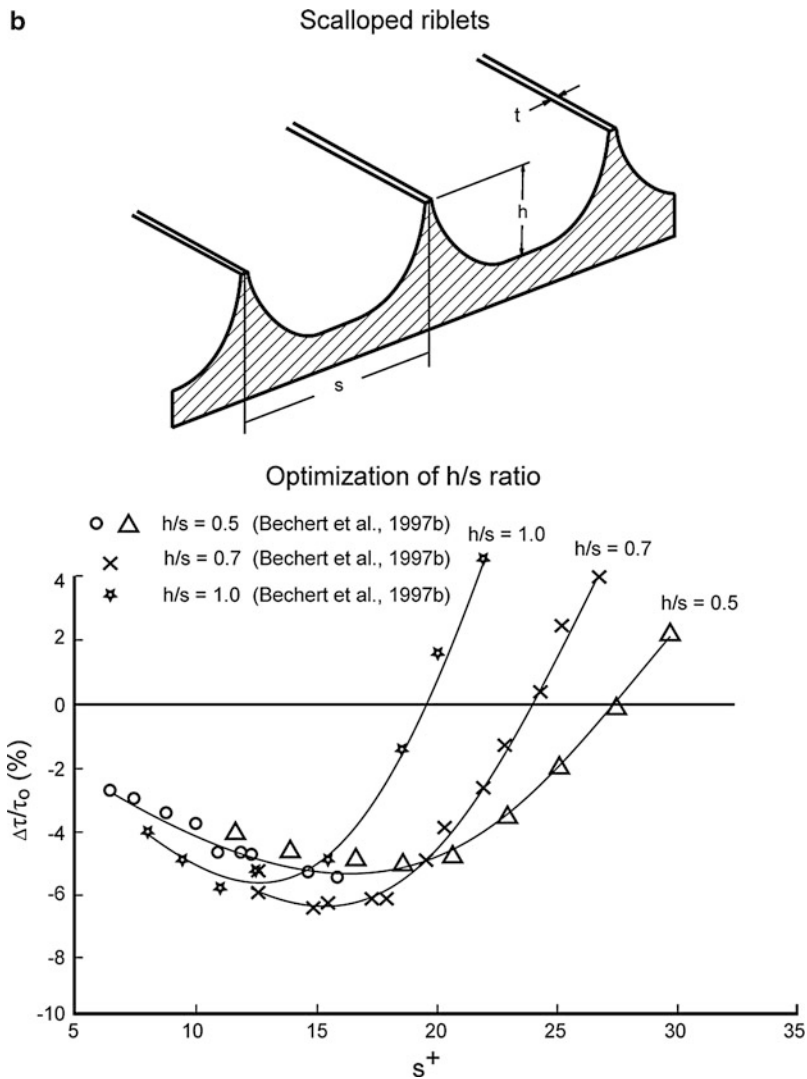
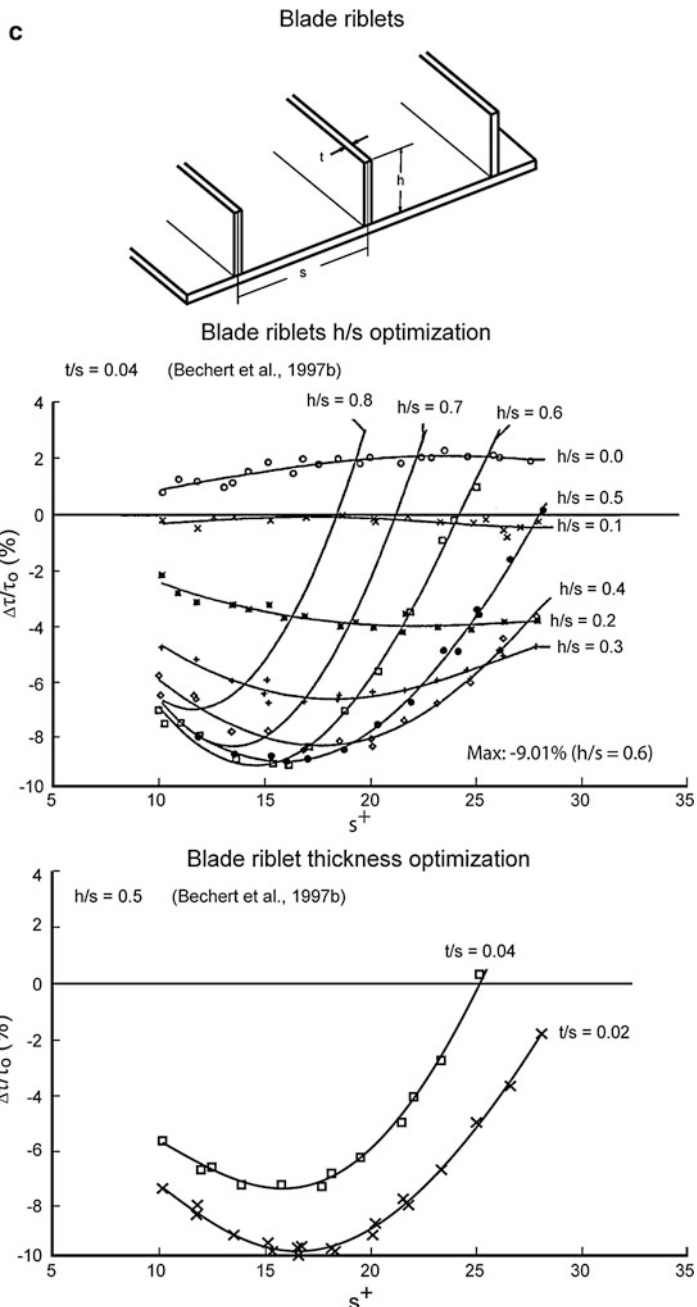


Fig. 10.6 (continued)

**Fig. 10.6** (continued)



Most studies are done by changing the nondimensionalized spacing, s^+ , by varying only fluid velocity and collecting shear stress data from a shear stress balance in a wind tunnel or fluid flow channel. Measured shear stress is compared to shear stress over a flat plate and plotted against the calculated s^+ value for the flow conditions. In this manner, a performance curve is created for a riblet array with a specific set of characteristic dimensions. The use of nondimensional characteristic dimensions for riblet studies, namely, nondimensional spacing, s^+ , is important for comparison between studies performed under different flow conditions. Nondimensionalization accounts for the change in size of flow structures like vortex diameter, which is the critical value to which riblets must be matched. Experiments have been carried out with various surface materials and in air using wind tunnel and oil and water using open flow channel. Under the same nondimensionalized flow conditions, riblet arrays sharing characteristic dimension ratios create similar performance curves whether they are made of different materials, are tested in different fluids, or are fabricated at a different scale.

10.4.1 Studies with 2D Riblets

Sawtooth riblets are the most commonly studied riblets. A schematic with characteristic dimensions and optimization data is shown in Fig. 10.6a. Sawtooth riblets are defined either by their height-to-spacing (h/s) ratio or their peak angle, α . Figure 10.6a shows the optimization data for sawtooth riblets. The best-fit line for riblets with $\alpha \sim 54^\circ$ was drawn spanning overlapping data sets from different sources. From available data, the optimal sawtooth riblets provide about 5% drag reduction at $h/s \sim 1.0$ and $\alpha = 54^\circ$ (Bechert et al., 1997b).

Fig. 10.6 (a) Schematic representation of riblet dimensions and drag reduction dependence on α for sawtooth riblets. The optimum drag reduction for sawtooth riblets is around $\alpha = 54^\circ$. For $\alpha = 54^\circ$, the best-fit line spans two data sets which overlap. All experiments performed using baby oil (kinetic viscosity = $1.2 \times 10^{-5} \text{ m}^2/\text{s}$) as the test fluid in an open channel with the exception of the $\alpha = 54^\circ$ by Walsh who tested in air in a wind tunnel. $\Delta\tau/\tau_0$ represents reduction or increase in drag compared to flat plate study. (b) Schematic representation of riblet dimensions and drag reduction dependence on h/s ratio for scalloped riblets. The optimum drag reduction for scalloped riblets is around $h/s = 0.7$. For $h/s = 0.5$, the best-fit line spans two data sets which overlap. All experiments performed using oil as the test fluid in an open channel. $\Delta\tau/\tau_0$ represents reduction or increase in drag compared to flat plate study. (c) Schematic representation of riblet dimensions and drag reduction dependence on h/s ratio and thickness for blade riblets. Optimum drag reduction for blade riblets occurs at $h/s = 0.5$. Riblet thickness experiments carried out at $h/s = 0.5$ show thinner riblets provide an improved drag reduction benefit. Blade thickness was changed by inserting thinner blades in place of original blades. All experiments performed using oil as the test fluid in an open channel. $\Delta\tau/\tau_0$ represents reduction or increase in drag compared to flat plate study (adapted from Walsh, 1982; Bechert et al., 1997b)

Table 10.1 Summary and comparison of optimum riblet geometry for various riblet shapes

Riblet shape	Relative rank ^a	Maximum drag reduction ^b (%)	Optimum geometry ^b	Comments
Sawtooth	3	5	$h/s \sim 1, \alpha \sim 60^\circ$	Most durable
Scalloped	2	6.5	$h/s \sim 0.7$	
Blade	1	9.9	$h/s \sim 0.5$	Drag reduction increases as riblet thickness decreases. Durability is an issue

^a1 corresponds to greatest drag reduction

^bBased on published data in [Bechert et al. \(1997b\)](#)

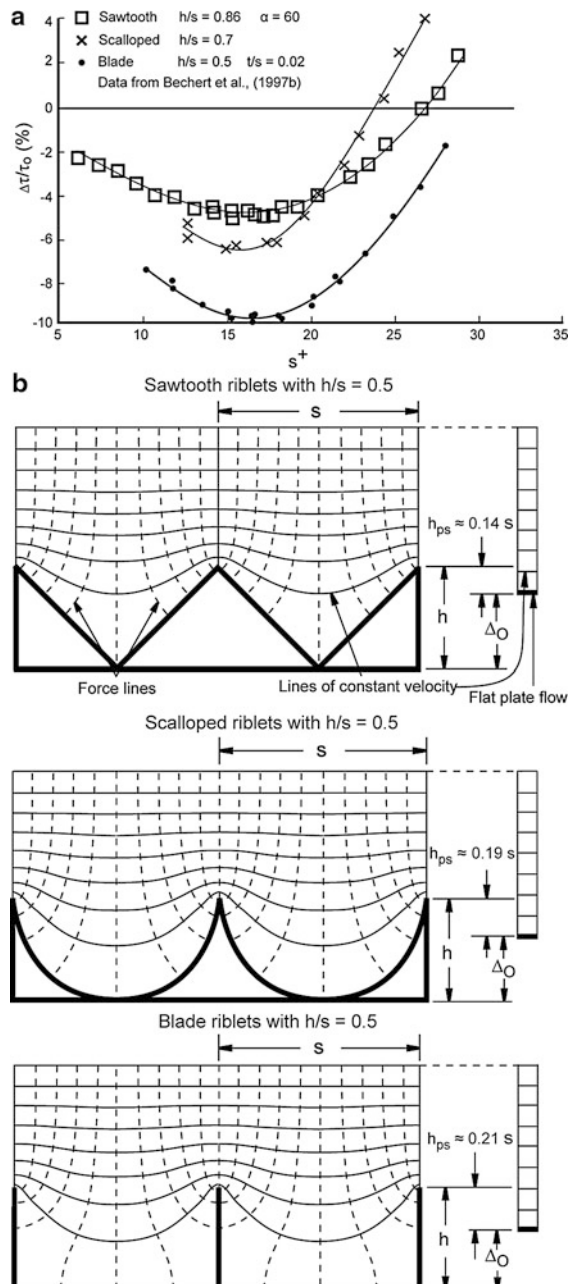
Scalloped riblets are most commonly defined by their h/s ratio, but test shapes have varied between research groups. While the basic shapes are similar, no consensus has been formed about a standard scalloped profile. Generally, any concave shape may be referred to as scalloped, and comparing data between sawtooth, scalloped, and blade riblet optimizations will support a generalization of comparable shapes. Ideally, the tip of the riblet is thin and sharp, but scalloped riblets with measurable tip thicknesses have also produced favorable results. Figure 10.6b shows optimization data for scalloped riblets. A maximum drag reduction of 6.5% has been achieved for scalloped riblets with $h/s \sim 0.7$ ([Bechert et al., 1997b](#)).

Blade riblets have been rigorously studied in their characteristic dimension ratios. A schematic with characteristic dimensions and optimization data for blade riblets is in Fig. 10.6c. By fabricating an adjustable blade riblet test stand, 9.9% drag reduction was achieved, and optimized dimensions of $h/s \sim 0.5$ and $t/s = 0.02$ were found ([Bechert et al., 1997b](#)). Due to their inherent weak structure, optimal blade riblet thickness is limited by strength, not fluid dynamics. Blades that are too thin will warp in fluid flow and allow vortices to translate as a result.

When comparing the optimal drag reduction geometries for sawtooth, scalloped, and blade riblets shown in Fig. 10.7a, it is clear that blade riblets provide the highest level of drag reduction, scalloped riblets provide the second most, and sawtooth riblets provide the least benefit. A summary of comparison features for sawtooth, scalloped, and blade riblets is in Table 10.1. In general, it can be seen in Fig. 10.6 that each type of riblet is most beneficial near $s^+ \sim 15$, which is between 1/3 and 1/2, the width of the streamwise vortices. Larger s^+ will cause vortices to begin falling into the gap between the riblets, which increases the shear stress at the surface between riblets. As s^+ decreases below optimum, the overall size of the riblets decreases to a point below which they cannot adequately impede vortex translation.

Comparing drag reduction benefit potential to effective protrusion height in the streamwise direction, it is apparent that increased protrusion height is correlated to drag reduction potential. Figure 10.7b shows the effective streamwise protrusion height for sawtooth, scalloped, and blade riblets. For the same h/s , blade riblets have the smallest shift in the effective flow origin due to their small cross-sectional

Fig. 10.7 (a) Drag reduction comparison for sawtooth, scalloped, and blade riblets with optimum values $h/s = 0.5$. All experiments were performed using oil as the test fluid in an open channel. (b) Schematic representations of lines of constant velocity above riblet and flat-plate surfaces in laminar flow allow for a comparison of effective protrusion height, h_p , of sawtooth, scalloped, and blade riblets. The effective protrusion height, which is favorable for the reduction of vortex translation reduction, is the difference between the riblet height, h , and the upward shift in the effective flow origin, Δ_O ; $h_p = \Delta_O - h$. To find the upward shift in the effective flow origin, the height and velocity of the lowest undisturbed line of constant velocity above a riblet surface are determined. Next, the height at which flow over a flat plate reaches the same velocity is determined. The difference between these two heights is the upward shift in the effective flow origin. Blade riblets have the largest effective protrusion height. Scalloped riblets have the second largest, and sawtooth riblets have the lowest of the three (adapted from Bechert et al., 1986, 1997b)



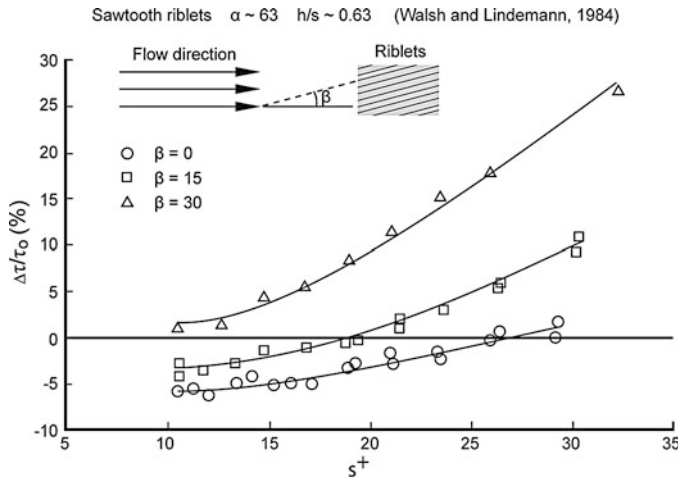


Fig. 10.8 Drag reduction dependence on yaw angle, β , of sawtooth riblets in free stream for $h/s \approx 0.62$. All experiments were performed using air as the test medium in a wind tunnel (adapted from [Walsh and Lindemann, 1984](#))

area, and sawtooth have the largest shift in the effective flow origin. Though all three profiles share a calculated maximum streamwise protrusion height of 0.2206 s at separate values of h/s , an increase in overall drag is experienced at these values due to the increased drag contributions of surface shear stress effects on the increased surface area in the turbulent regime ([Bechert et al., 1986](#)). The height at which h_p is maximized causes such an increase in effective flow origin shift that the drag reduction benefits are outweighed.

An additional concern to the application of riblets is the sensitivity of drag reduction to yaw angle. Yaw angle, the angle between the average flow direction and the riblet orientation, has a deleterious effect on the drag reduction benefits of riblet surfaces. Riblet surfaces become drag inducing above $\beta = 30^\circ$, but small drag reductions can still be seen up to $\beta = 15^\circ$ ([Walsh and Lindemann, 1984](#)). Figure 10.8 shows the effects of yaw angle on riblet performance for flow over sawtooth riblets.

10.4.2 Studies with 3D Riblets

Riblets on shark skin exist in short segments and groups, not as continuous structures. Riblets with 3D features have been created to better approximate the performance of actual shark skin and to determine if there are methods of drag reduction not yet understood from 2D riblet studies. Studies have explored the effects of compound riblet structures and 3D riblets comprised of aligned, segmented-blade riblets ([Wilkinson et al., 1988](#)). No improvement in net drag reduction was realized when compared to the corresponding performance of continuous

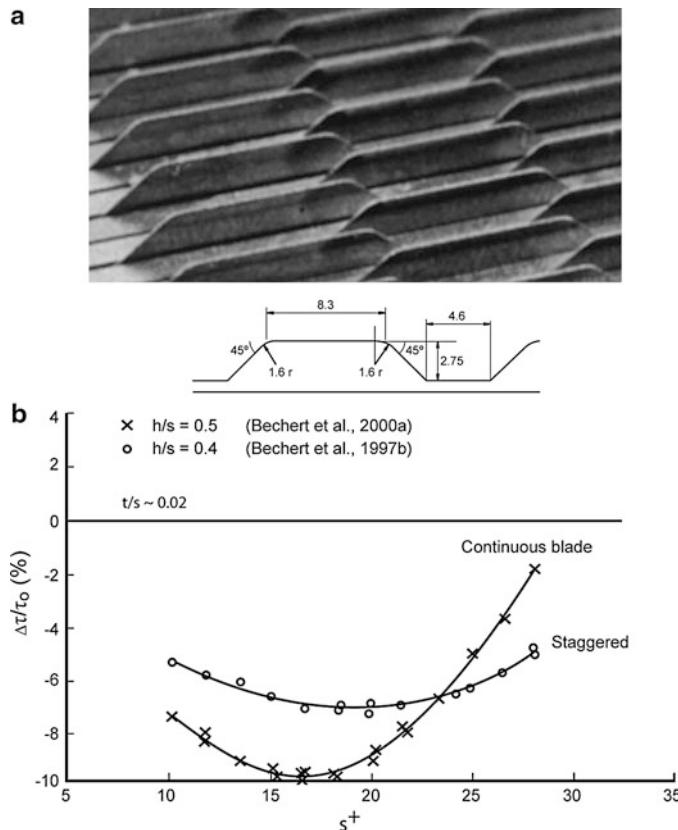
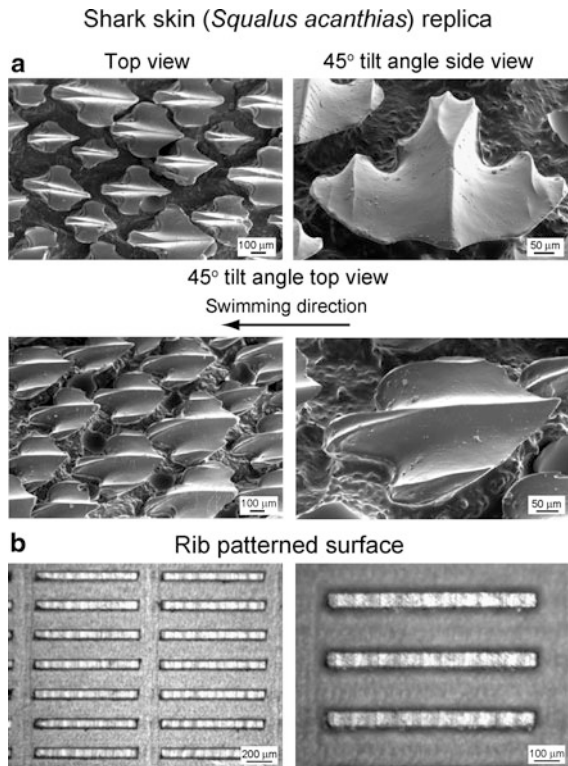


Fig. 10.9 Comparison of drag reduction over optimum continuous blade riblets with optimum segmented trapezoidal blade riblets. (a) Segmented riblets were staggered as shown. Spacing between offset rows is $s/2$, while spacing between corresponding rows is s . (b) Optimal h/s ratio for staggered blade riblets is 0.4. Staggered blade riblets provide less drag reduction benefit than continuous blade riblets. All experiments were performed using oil as the test fluid in an open channel (adapted from [Bechert et al., 1997b, 2000a](#))

riblet geometries. More recently, experiments with similarly shaped segmented-blade riblets at spacing s with a matching set of segmented-blade riblets staggered between each row of blades at a spacing of $s/2$ from either side have been performed ([Bechert et al., 1997b](#)). A schematic and image of staggered trapezoidal blade riblets are shown in Fig. 10.9a. Using these and other staggered riblets, [Bechert et al. \(1997b\)](#) hoped to achieve the same vortex elevation and anti-translation effects of continuous riblets with less effect on the flow origin. Experimental data comparing the largest drag reduction achieved with staggered segmented-blade riblets to optimum continuous blade riblets can be seen in Fig. 10.9b. Again, no net benefit in drag reduction was achieved, and after comparison of data, the conclusion was made that it is unlikely that 3D riblets comprised of segmented 2D riblets will greatly outperform continuous 2D riblets.

Fig. 10.10 (a) SEM micrographs taken at *top view*, 45° -tilt-angle *side view*, and 45° -tilt-angle *top view* show shark skin (*Squalus acanthias*) replica. The shark skin replica shows only three ribs on each scale. It is clearly visible that the V-shaped riblets' height varies between 200 and 500 μm , and their space varies between 100 and 300 μm , and (b) optical microscope images (shown using two magnifications) show the rib-patterned surface fabricated as a model of artificial shark skin surfaces (Jung and Bhushan, 2010)



In the true 3D realm, it has been theorized for some time that scales on which shark skin riblets are commonly grouped contribute to the performance of some shark skin varieties. By creating a pressure-exchange system below the scale surface, it was theorized that injection methods may have a pressure streak cancellation effect in the viscous sublayer, but concluded that the increased momentum exchange created would have deleterious effects (Wilkinson, 1983; Bechert et al., 1985, 1986). More recently, there have been studies which have investigated the drag reduction properties of riblet-topped shark scales as both a static structure (Jung and Bhushan, 2010) and a flexible—possibly controllable—member (Lang et al., 2008).

Jung and Bhushan (2010) studied scales molded in epoxy resin from the skin of the spiny dogfish (*Squalus acanthias*, L. Squalidae) and segmented-blade-type riblets fabricated on acrylic, shown in Fig. 10.10. Pressure drop from inlet to outlet of a channel is a measure of drag with large pressure drop occurring as a result of high drag. For measurements of pressure drop using water flow, a flow cell with closed rectangular channels was used. Fabrication procedure of the test samples and details of flow cell are presented in Appendix. Pressure drop data of the molded epoxy scale study are shown in Fig. 10.11a, and data from the segmented-blade riblet study are shown in Fig. 10.11b. For the scales molded in epoxy resin, a decrease in pressure drop of about 30% in turbulent flow—corresponding to a decrease in fluid drag—versus a smooth surface in a rectangular flow cell flow

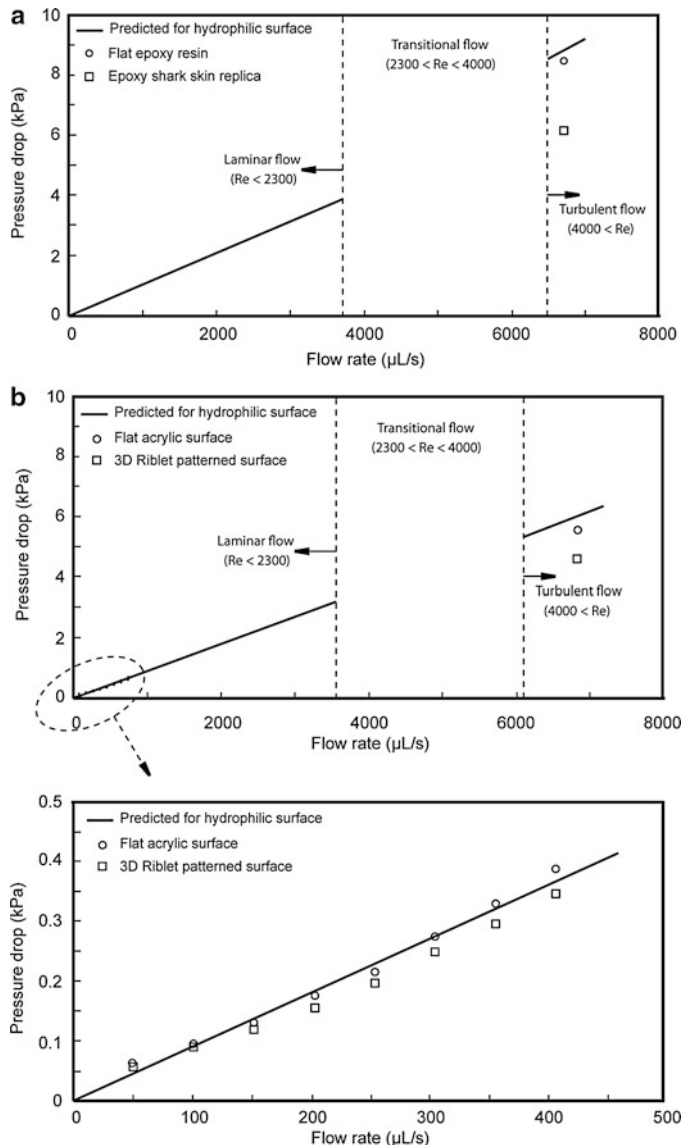


Fig. 10.11 (a) Comparison of pressure drop of water flow in a closed rectangular flow channel over flat epoxy surface and shark skin replica surface. (b) Comparison of pressure drop in flow over flat acrylic surface and segmented-blade riblets. Data are compared with the predicted pressure drop for a hydrophilic surface (solid lines) (adapted from [Jung and Bhushan, 2010](#))

experiment. The pressure drop in the laminar flow was negligible. A decrease of about 23% in pressure drop was also realized in a similar experiment using segmented aligned riblets fabricated on acrylic compared to a smooth acrylic test section.

Certain sharks are known to exhibit riblet-topped scales that are attached somewhat flexibly to the underlying surface of the shark skin. These scales are able to change their pitch angle by bristling. As the pressure beneath the scale attachments changes, the flexible member changes position, and the trailing edge of the scales can lift up. Alternatively, the scales may bristle at concave skin locations that occur during the natural swimming. In an experiment simulating the bristling of flexible riblet-covered scales into the boundary layer as a possible mechanism of control and drag reduction, no drag reduction benefit was achieved through extreme scale bristling. However, notable flow phenomena were found to occur as a result of scale bristling, including the formation of three distinct vortex shapes ([Lang et al., 2008](#)).

10.4.3 Riblet Trends in Pipe Flow

Riblet effects in pipe flow have been studied as well, and general patterns exist in the drag reduction benefit of sawtooth riblets. Due to the difficulty of riblet application in pipes, data is generally limited to applications of sawtooth riblet film produced by 3M ([Liu et al., 1990; Rohr et al., 1992; Enyutin et al., 1995; Koury and Virk, 1995](#)). Drag reduction tests in pipe flow are carried out by comparing the pressure drop in a riblet-lined pipe with that of a similar pipe with a smooth surface. Drag reduction data for sawtooth riblets on a flat plate are shown in Fig. 10.12a, and drag reduction data for water flow in sawtooth riblet-lined pipes are shown in Fig. 10.12b. As riblets are applied to the inside surface of a pipe, the riblet tips are shifted together due to the curve of the pipe wall. Consequently, the optimized s^+ range for riblets in pipe flow is lower than that for the same riblets in flow over a flat surface ([Liu et al., 1990](#)). Additionally, the decrease in s^+ suggests that an increased drag reduction in round pipes might be seen with a larger characteristic angle, α , than for flow over riblets on a flat surface.

10.5 Riblet Fabrication and Applications

Riblet manufacture for study and large-scale applications has been one of the main difficulties in the field ([Dean and Bhushan, 2010](#)). Typical microscale manufacturing techniques are ill-fitted for large-scale application due to the associated costs. Even for study, most researchers have opted for traditional milling or molding methods over the microfabrication techniques used in the microtechnology industry. Though nondimensional units allow for comparison between flow fields of different fluids and at different conditions, the accurate microscale manufacture of riblets for experimentation has been a field of study in its own right. The largest difficulty in optimizing riblet geometries has been the fabrication of riblet series with incremental changes in characteristic dimension. Riblets used in airflow require spacings at or below 1 mm due to the low viscosity of air and the high speed at

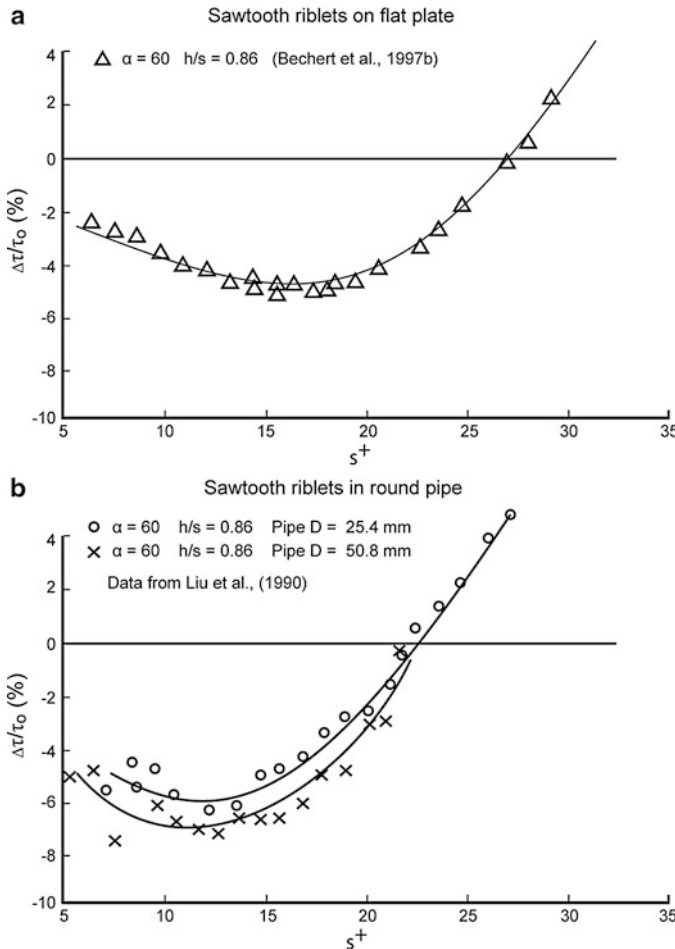


Fig. 10.12 Comparison of riblet performance curves over sawtooth riblets on a flat-plate surface and inside round pipes of 25.4- and 50.8-mm diameters. Peak drag reduction for riblets in pipe flow occurs near $s^+ = 12$, which is lower than the flat-plate optimal value of $s^+ = 15$. Bechert experiments were performed using oil as the test fluid, and Liu experiments were performed using water as the test fluid in an open channel (adapted from Liu et al., 1990; Bechert et al., 1997b)

which wind tunnels must operate to create accurately measurable shear stresses on a test surface. Conversely, studies in an oil channel are carried out in flow that is both highly viscous and slower moving. This allows for riblets to be made with spacings in the 3–10-mm range (Bechert et al., 1992).

Commercial and experimental application of riblets outside wind tunnels and test stands is also limited by the high costs for less-than-optimal riblet performance. Application of riblets on a large scale has been done for several studies as well as for competition and retail purposes. Sawtooth riblets on vinyl films including the ones produced by 3M have been applied to surfaces ranging from boat hulls to

airplanes. Racing swimsuits produced by Speedo and others also employ a riblet pattern on the surface to reduce drag during the streamline portion of each lap of a race. Additionally, a novel surface scratching technique has been applied to the inside surface of pipelines to create a faux-riblet surface.

10.5.1 Riblet Dimension Selection

Though the turbulent flow regime is characterized by completely random flow, the thickness of the viscous sublayer and the width of the streamwise vortices—and therefore the optimal riblet spacing—are dependent on properties of the fluid flow. Riblet spacing is the basis of other riblet dimensions, so the calculation of proper spacing is critical in riblet design. To calculate riblet spacing, wall shear stress must be known. Approximation of wall shear stress in rectangular channels can be done by combining Blasius' law for the friction coefficient with the Fanning friction factor and solving for wall shear stress. Blasius' law for the friction coefficient is defined as $c_f = 0.0791(Vd/\nu)^{-1/4}$, where ν is the kinematic viscosity and $d = 4A/p$ is the hydraulic diameter of the channel where A is the cross-sectional area and p is the wetted perimeter. The Fanning friction factor is a dimensionless number defined as $c_f = 2\tau_0/\rho V^2$, where τ_0 is the wall shear stress, ρ is the fluid density, and V is the average flow velocity. Combining equations, wall shear stress can be approximated by $\tau_0 = 0.03955\nu^{1/4}\rho V^{7/4}d^{-1/4}$.

Using the optimization comparison data in Fig. 10.7a, a nondimensionalized spacing should be chosen in the range $15 < s^+ < 18$. It is recommended that s^+ values for pipe flow be chosen slightly low, in the range $12 < s^+ < 14$, as shown in Fig. 10.12. To calculate physical spacing, s , from s^+ , the nondimensionalization factor is used such that $s = s^+ \nu / V_\tau$, where $V_\tau = (\tau_0/\rho)^{0.5}$ is the wall stress velocity. Using the optimization curves for each riblet shape in Fig. 10.6, the optimal spacing-based characteristic dimensions can be used to solve for optimal physical riblet dimensions.

10.5.2 Application of Riblets for Drag Reduction and Antifouling

The transition between research and the application of technologies is often slow, and riblet surfaces have been no different. Because of the limitations of past riblet technologies, both benefit in commercial applications and the methods of application have been limited. Because riblets provide drag reduction on objects where the dominant form of drag is caused by turbulent flow at the surface, only objects of a certain form factor will show any measurable benefit. A large portion of the total drag on long objects with relatively flat sides usually comes from turbulence

at the wall, so riblets will have an appreciable effect. However, for objects like automobiles, where pressure drag or flow separation is the dominant form of drag, application of riblets would have minimal effect.

Beginning in the mid-1980s, vinyl film sawtooth riblets have been applied to boat hulls for racing. Both an Olympic rowing boat and an Americas Cup sailing yacht have been covered with riblets during competition. Because skin friction of an airplane accounts for as much as 48% of total drag, vinyl film riblets have also been applied to test planes of both Boeing and Airbus. These films have not been used on standard commercial flights yet, but the benefits seen in testing should not go unmentioned. Application of riblets to an airplane requires that several concessions are made. Several locations that would be covered by riblets must be left uncovered due to environmental factors: windows are not covered for the sake of visibility, several locations where dust and debris contact the airplane during flight are left bare because the riblets would be eroded during flight, and locations where deicing, fuel, or hydraulic fluid would come in contact with the riblets are left bare. After these concessions, the riblets covering the remaining 70% of the aircraft have provided 3% total drag reduction. This 3% drag reduction correlates to a similar 3% savings in fuel costs ([Bechert et al., 1997a](#)).

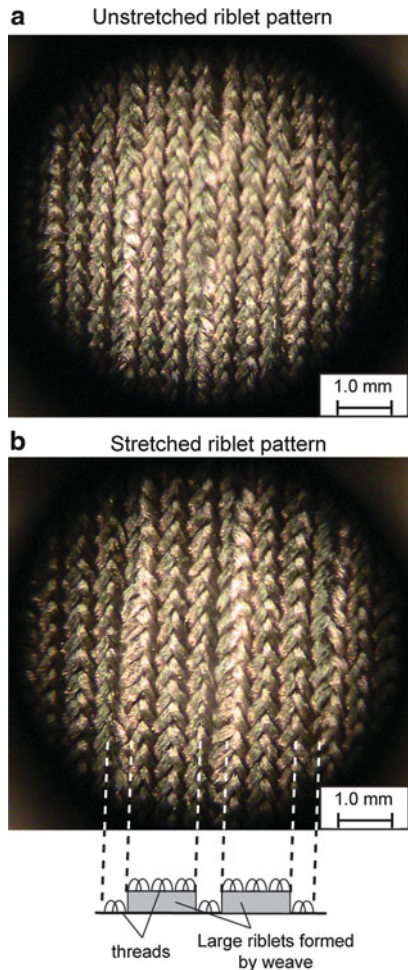
Another large commercial application for riblet technologies is drag reduction in pipe flow. Machining the surface or applying vinyl film riblets proves difficult for most pipes, and an alternate solution must be used. Experimental application of a scratching technique to the inside surface of pipes has created a riblet-like roughness that has provided more than 5% drag reduction benefit ([Weiss, 1997](#)). Stemming from an old sailors' belief that ships sail faster when their hulls are sanded in the longitudinal direction, [Weiss \(1997\)](#) fabricated these riblets by using a steel brush moved through the pipeline to create a ridged surface. Studies have shown as much as a 10% reduction in fluid flow with the combined effect of cleaning the pipe and ridging the surface. Tests on a 10-mile gas pipeline section have confirmed this benefit during commercial operation ([Bechert et al., 1997a](#)).

Wind turbines are being used for harnessing wind energy which is an important source for renewable energy. Riblet technology can be used on the turbine blades to reduce drag. Riblets can be either fabricated on the blades during production, or vinyl film riblets could be applied on the blades.

The only commercial application of riblet technology for drag reduction is competitive swimwear. The FastSkin® suits were introduced by Speedo in 2004 ([Krieger, 2004](#)). Speedo claimed a drag reduction of several percent in a static test compared to other race suits. However, given the compromises of riblet geometry made during manufacturing, it is hard to believe the full extent of the drag reduction. These suits were worn by American swimmer Michael Phelps who set Olympic records and won several gold medals.

It is clear that creating surface structures by weaving threads is difficult. As a result, riblet geometries woven from thread have limited options of feasible riblet shapes. By the pattern woven into the FastSkin® swimsuits, riblets are formed which resemble wide blade riblets with small grooves on top. The larger riblets are formed by the macro weaving pattern, and the smaller riblets are created by the

Fig. 10.13 Images of riblet geometries on (a) unstretched and (b) stretched Speedo FastSkin® swimsuit. (c) Schematic showing apparent hierarchical riblet structure formed by threads



individual weaves of thread aligned with the macro riblets. Both of these riblet-like shapes are distinguishable in Fig. 10.13. As shown in Fig. 10.13a, unstretched riblets are tightly packed. As the fabric stretches, the riblet width and spacing increase (Fig. 10.13b). The associated decrease in h/s ratio depends on the dimensions of each swimmer's body, which is another compromising factor in the design. Riblet thickness is also a factor considered in the design. Aside from the limitations imposed by the weaving patterns available, flexibility in the riblet tips will hinder the fabric's ability to impede the cross-stream translation of streamwise vortices. Thicker riblets are probably needed, used for strength, and cause a decrease in the peak drag reduction capability compared to thinner riblets.

Drag reduction is also beneficial in antifouling. Low-drag and low-adhesion surfaces reduce biofouling. In addition, as indicated earlier, spacing between the dermal denticles is such that microscopic aquatic organisms have difficulty adhering to and colonizing the surface. A microtexture film with riblet-inspired antifouling properties includes the Sharklet AFTM, which operates on the principle that microorganisms are deterred from hydrophobic surfaces and crevices slightly smaller than themselves. Research suggests that appropriately sized topographies prevent colonization by various microorganisms including *Ulva* sports and *Balanus amphitrite* cyprids (Carman et al., 2006; Schumacher et al., 2007).

10.5.3 Riblet Fabrication Methods for Study and Applications

For experimentation, many riblet geometries have been made through careful machining of riblets from stock, but standard machining techniques lack the precision required to make riblets for use in high-speed airflow. Additionally, machining lacks the flexibility to fabricate small-scale riblets with enough resolution to create incrementally different samples for true optimization of sawtooth and scalloped riblets. Using a small-scale computer numerically controlled (CNC) mill, segmented-blade riblets have been fabricated in acrylic with a thickness of only 38 μm and a height of 90 μm (Jung and Bhushan, 2010). Scalloped and sawtooth riblets have been machined in aluminum at spacings in the submillimeter range (Walsh and Lindemann, 1984).

Another method used to construct blade riblets is to assemble separately fabricated parts. By fabricating thin-element blades and spacers, stacked assemblies with adjustable geometry were created (Bechert et al., 1997b). By manufacturing blades in this separate manner, thinner blades can be fabricated using rolling techniques that eliminate the concern of milling errors ruining test plates. Riblet spacing is controlled by the added tolerances of each blade and spacer, which allows for an increase in overall fabrication tolerance. The major advantages of this method of assembly are ease of adjustment and less danger of milling errors destroying test plates. Optical images of assembled riblets can be seen in Fig. 10.9a.

For scale replicas and 3D riblets, the complex shapes required usually afford molding as the fabrication method. Micro-molding and micro-embossing have been evaluated using polymethyl methacrylate (PMMA) as the mold material and a silicone rubber as the replica material (Xin and Zhang, 2008). Replicas were shown to lack resolution by 2.2% and 5.5% of the groove spacing and 8.3% and 5.9% of the height, respectively. Alternatively, epoxy replicas of shark skin have been molded in dental wax reliefs taken from shark skin and studied in flow cell experiments in a rectangular pipe section (Jung and Bhushan, 2010). SEM images of these replicas can be seen in Fig. 10.10a.

Many of these fabrication methods are not suitable for use outside laboratory settings. The wear experienced in a physical environment where riblets would provide measurable drag benefits would quickly render many of the above models

non-beneficial. Additionally, fabrication for application on large scale is a concern with most of these methods. Other methods of riblet manufacturing have been studied for use in production environments. 3M vinyl film riblets have been used in myriad riblet performance studies, and the fabrication of riblets by microprofile grinding and incremental rolling processes has been investigated.

3M vinyl film riblets (Marentic and Morris, 1992) have been applied to many test surfaces, including the inside of various pipes for pipe flow studies (Liu et al., 1990; Rohr et al., 1992; Enyutin et al., 1995; Koury and Virk, 1995), flat plates in flow channels and wind tunnels, boat hulls in towing tanks (Choi et al., 1989), airplane wings (Han et al., 2002), and airplane fuselages. Similar riblet films have been fabricated using bulk micromachining of silicon to create a master for molding of polydimethylsiloxane (PDMS) to create a thin, flexible riblet film. This film has been used in flow visualization tests (Lee and Choi, 2008).

Grinding and rolling methods of riblet fabrication have been studied for application in both research and large-scale application. A profiled grinding wheel has been used to fabricate several riblet geometries based on sawtooth riblets with $h = 20 \mu\text{m}$ and $s = 50 \mu\text{m}$ (Denkena et al., 2009). Dressing of the grinding wheel was done with diamond-profile roller used in a two-step process in which the profile roller dresses every second tooth on the first pass, shifts axially the distance of one riblet spacing, and dresses the remaining teeth on a second pass. One downside of the grinding process is the lack of hardening on the final riblet surface. Alternatively, rolling methods can be used to strain harden the riblets during fabrication. Using a roller with the profile of two riblets on its outer face, a linearly patterned rolling process has been used to fabricate scalloped riblets in a titanium alloy with $h = 162 \mu\text{m}$ and $s = 340 \mu\text{m}$ (Klocke et al., 2007). The strain hardening, favorable grain patterns, and residual compressive stresses in the riblet surface after fabrication provide advantages in riblet strength for production applications.

10.6 Effect of Fluid Slip and Polymer Additives on Fluid Drag

Surfaces form molecular bonds with fluid molecules traveling across them. This attraction is not the same for all surface–fluid pairs, due to the different chemical structures of different fluid molecules. For this reason, classical nondimensionalization of these riblet tests does not allow for perfect comparison between studies done with different surface materials or fluids (Dean and Bhushan, 2010). Figure 10.14 shows a comparison between riblet performance studies which use similar riblet geometries tested with different surface material–fluid pairs. It is clear that a similar behavior is exhibited in both studies, but the curves do not match. The interactions between fluid molecules and the surface material, in addition to measurement resolution and accuracy, cause the experimental data to vary greatly at both the high and low ranges of s^+ .

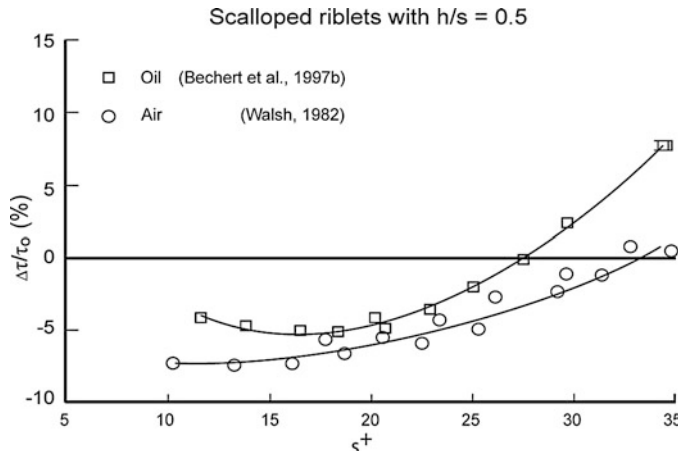


Fig. 10.14 Comparison of drag reduction with oil and air on similar sawtooth surfaces (adapted from Walsh, 1982; Bechert et al., 1997b)

Another factor important to the drag experienced in fluid flow is the presence of polymer additives to the flow. The interaction between polymeric agents and the molecules of fluid in turbulent flow causes a large reduction in drag to occur. Fish secrete a small amount of mucus as they swim, which mixes with the fluid in the boundary layer and reduces the drag effects on the fish. Though sharks do not secrete enough mucus to use this mechanism for drag reduction, small amounts of mucus are present on the skin of sharks (Bechert et al., 1986).

10.6.1 The Effect of Fluid Slip on Drag Reduction

It is generally assumed that the relative velocity between a hydrophilic solid wall and liquid is zero at the solid–liquid interface, which is the so-called no-slip boundary condition (Fig. 10.15). However, for hydrophobic surfaces, fluid film exhibits a phenomenon known as slip, which means that the fluid velocity near the solid surface is not zero (Maali and Bhushan, 2008; Wang et al., 2009; Wang and Bhushan, 2010). The degree of boundary slip at the solid–liquid interface is characterized by a slip length. Slip length b is defined as the length of the vertical intercept along the axis orthogonal to the interface when a tangent line is drawn along the velocity profile at the interface (Fig. 10.15). With an increase in the degree of hydrophobicity, the slip length increases, and the fluid drag decreases.

Pipes coated in low surface energy materials exhibit a decrease in pressure drop compared with similar pipes which have higher surface energy coatings. Jung and Bhushan (2010) measured pressure drop in a flow cell (described in Appendix) on hydrophilic, hydrophobic, and superhydrophobic surfaces (used for fabrication of artificial Lotus structures, Sect. 6.6.3.2). The contact angle data are presented in Table 10.2. Figure 10.16 shows laminar and turbulent pressure drop comparisons

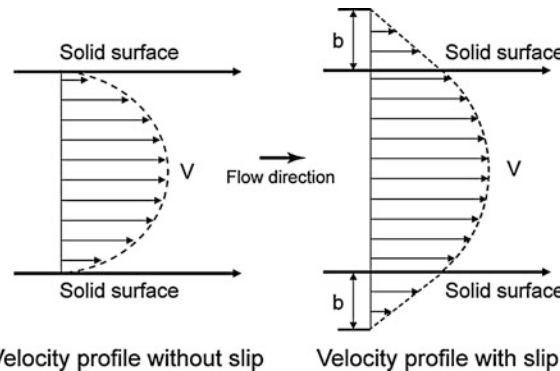


Fig. 10.15 Schematic of velocity profiles of fluid flow without and with boundary slip. The definition of slip length b characterizes the degree of boundary slip at the solid–liquid interface. The arrows represent directions for fluid flow

Table 10.2 Summary of the static contact angles and contact angle hysteresis measured on the various surfaces

	Static contact angle (deg)	Contact angle hysteresis (deg)	Pressure drop in turbulent flow (%)	Calculated slip length (μm)
(a) Epoxy resin				
Hydrophilic (flat epoxy resin)	76 ± 0.9	$67 \pm 2.9(151^{\text{a}}, 84^{\text{b}})$	~ 0	~ 0
Hydrophobic (flat with thin Lotus wax layer)	119 ± 2.4	$56 \pm 3.2(148^{\text{a}}, 92^{\text{b}})$	~ 21	~ 24
Superhydrophobic (hierarchical structure—micropatterned with thin Lotus wax layer)	173 ± 0.8	$1 \pm 0.6(174^{\text{a}}, 173^{\text{b}})$	~ 33	~ 103
Shark skin replica	89 ± 1.7	$66 \pm 3.4(155^{\text{a}}, 89^{\text{b}})$	~ 30	~ 35
(b) Acrylic resin				
Flat acrylic resin	82 ± 1.8	$71 \pm 2.6(122^{\text{a}}, 51^{\text{b}})$	~ 0	—
Rib-patterned surface	146 ± 1.2	$43 \pm 1.2(158^{\text{a}}, 115^{\text{b}})$	~ 23	—

Hierarchical structures were fabricated with $0.8 \mu\text{g}/\text{mm}^2$ of Lotus wax after storage at 50°C with ethanol vapor. Flat epoxy resin was covered with flat Lotus wax. The variation represents ± 1 standard deviation (adapted from [Jung and Bhushan, 2010](#))

^aAdvancing contact angle

^bReceding contact angle

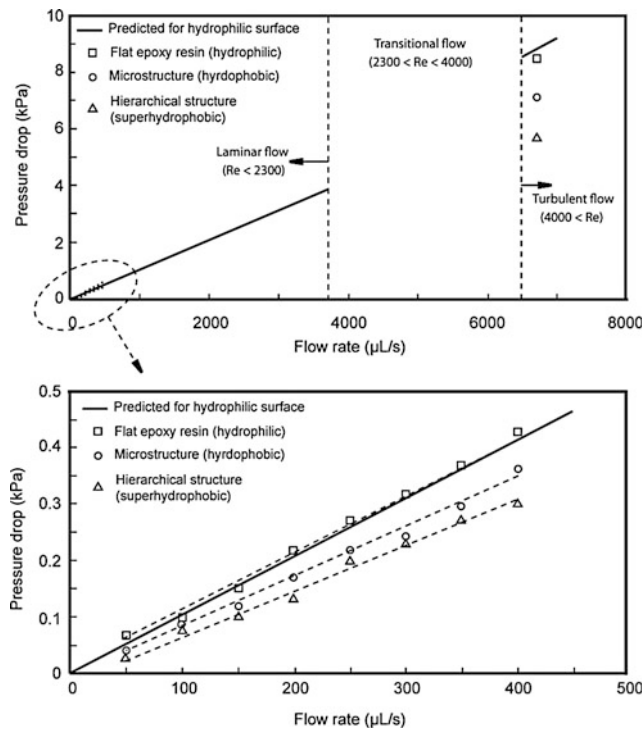


Fig. 10.16 Comparison of pressure drop of water flow in a closed rectangular channel with hydrophilic, hydrophobic, and superhydrophobic surfaces in laminar and turbulent flow regimes. Data are compared with the predicted pressure drop for a hydrophilic surface (solid lines). Decreased pressure drop in pipe flow corresponds to decreased drag (adapted from [Jung and Bhushan, 2010](#))

for a flow cell experiment for these surfaces in water flow. There is a slight decrease in pressure drop in laminar flow as compared to turbulent flow. The greatest decrease in pressure drop and fluid drag happens for the superhydrophobic surface. Reducing the strength of bonding between the fluid molecules and the surface causes a corresponding reduction in fluid drag in both the laminar and turbulent regimes.

Based on the pressure drop data, the slip lengths on the surfaces with different degrees of hydrophobicity were calculated surfaces using water flow in laminar flow ($0 < Re < 300$) using (10.8). For calculations, it was assumed that there is a no-slip boundary condition on hydrophilic surface (flat epoxy resin) as verified from the experiments ([Maali et al., 2009](#)). The average values of slip length on the surfaces were calculated over all the experimental flow rates, and data for various samples are presented in Table 10.2. The data suggests that the boundary slip increases with increasing hydrophobicity of solid surfaces. Slip length of a liquid droplet sitting on these surfaces has been measured on the nanoscale using tapping mode atomic force microscopy by [Wang et al. \(2009\)](#). They reported the slip length for hydrophobic and

superhydrophobic surfaces as 44 and 257 nm, respectively. These values are small as compared to the ones obtained using the flow. [Zhu and Granick \(2001\)](#) have reported that the slip length increases from nanometer range to micrometer range as the flow rate increases.

10.6.2 Effect of Fish Mucus and Polymers on Fluid Drag

Fish are known to secrete mucus during swimming. Though it is not known whether the mucus is present at all times, it is known that certain environmental factors cause, alter, or enhance the production of mucus. These environmental stressors may present a need for increased swimming speed to catch or avoid becoming prey, protection against non-predatory threats such as microorganisms, or resist abrasion while swimming near rocky surfaces. Regardless of which events cause fish to secrete mucus, the drag reduction benefits during mucus-assisted swimming are known. Numerous experiments have demonstrated the drag reduction possible with fish-covered mucus compared to non-mucus-covered shapes ([Hoyt, 1975](#)). In an experiment comparing the drag on wax models to a mucus-covered fish, a reduction in skin friction drag of 50% was seen ([Daniel, 1981](#)).

Similar to these fish mucus experiments, polymer additives in pipe flows have been known for many years to reduce the drag in fluid flows by extreme amounts. In a pipe flow study comparing various injection techniques of polymer solutions into water, drag reductions of up to 80% were achieved ([Frings, 1988](#)). Additionally, the drag reduction benefit increases with increased Reynolds number. While this works well for pipe flows, in which the polymer remains mixed and active throughout the length of the pipe, its application to external flows is much more difficult. Mucus on fish does not mix well with water in static contact, but does mix and provide drag reduction during dynamic contact. By this feature, the mucus use of fish is minimized. Unfortunately for any long-range application of polymer drag reduction on an external flow, the polymer solution must be continuously injected. This would cause large quantities of the solution to be used and likely render the strategy inefficient in terms of overall energy use.

Though sharks do not secrete enough mucus to use this mechanism for drag reduction, small amounts of mucus are present on the skin of sharks ([Bechert et al., 1986](#)). It is possible that shark skin mucus secretion is similar to fish, where only environmental stressors or swimming causes an increase in output, but the total quantity of mucus on the surface at any given time is likely quite low. One possible mechanism by which this trace quantity of mucus could be useful is in changing the flow characteristics in the riblet valleys or at the riblet peaks, where shear stresses are highest. In the riblet valleys, a trace secretion of mucus could increase flow velocity and decrease the overall momentum transfer from the shark to the surrounding water by condensing the overall structure of the velocity gradient. Alternatively, injection at the riblet peaks may cause a reduction in shear stresses where they are at their maximum and again cause a reduction in drag. These small effects near the surface

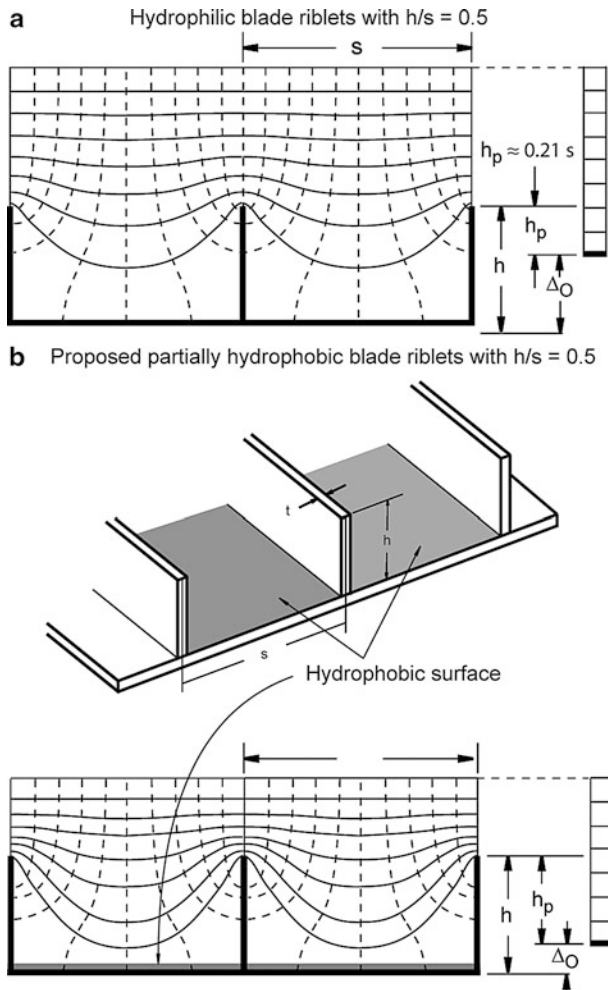


Fig. 10.17 (a) Behavior of hydrophilic surface in fluid flow. (b) Proposed deposition of hydrophobic surface on portions of blade riblet surface should increase the protrusion height of riblets and increase drag reduction benefit ([Dean and Bhushan, 2010](#))

may propagate into a larger benefit as the lines of constant velocity in the flow shift and condense as shown speculatively in Fig. 10.17. The localized effect of mucus secretion in the valleys or at the peaks would be similar to the effects of a partially hydrophobic surface. By coating a riblet surface with a hydrophobic layer in the valleys (Fig. 10.17b), at the peaks, and as a whole, comparisons can be drawn between the drag reduction effects of trace amounts of mucus found on shark skin ([Dean and Bhushan, 2010](#)).

10.7 Summary

The skin of fast-swimming sharks reduces the drag experienced by sharks and protects against biofouling as they swim through water. Shark skin is covered by very small individual toothlike scales called dermal denticles (little skin teeth), ribbed with longitudinal grooves (aligned parallel to the real flow direction of the water). Fluid drag in the turbulent boundary layer is in large part due to the effects of the streamwise vortices formed in the fluid closest to the surface. Turbulence and associated momentum transfer in the outer boundary layers are in large part due to the translation, ejection, and twisting of these vortices. Additionally, the vortices also cause high velocities at the surface which create large shear stresses on the surface. Numerical simulation has supported riblet drag reduction theories by showing two mechanisms of riblet drag reduction. First, riblets impede the translation of the streamwise vortices, which causes a reduction in vortex ejection and outer-layer turbulence. Second, riblets lift the vortices off of the surface and reduce the amount of surface area exposed to the high-velocity flow. By modifying the velocity distribution, riblets facilitate a net reduction in shear stress at the surface ([Dean and Bhushan, 2010](#)). In addition to low drag, the spacing between these dermal denticles is such that microscopic aquatic organisms have difficulty adhering to and colonizing the surface.

Various riblet shapes have been studied for their drag-reducing capabilities, but sawtooth, scalloped, and blade riblets are most common. By varying flow properties or riblet geometries, optimization studies have been performed. Drag reduction by riblet surfaces has been shown to be as high as nearly 10% given an optimal geometry of $h/s \sim 0.5$ for blade riblets with a no-slip condition. The maximum reliable drag reduction provided by scalloped riblets and sawtooth riblets is about 6% at $h/s \sim 0.7$ and 5% at $\alpha \sim 60^\circ$, respectively. Experimentation of other shapes has provided similar benefits of around 5% drag reduction. Additional experimentation with simple 3D shapes, such as offset segmented-blade riblets, has shown comparable performance to standard-blade riblets, but hierarchical structures and complex 3D shapes have yet to show improved benefit. The behavior of static and dynamic versions of complex 3D replicas has been minimally investigated, and much work remains in understanding the complexities that are involved. To date, no improved drag reduction has been accomplished using replica models, but hypothesized control mechanisms for dynamic replicas have been proposed. Though the optimum shape for drag reduction performance is blade riblets, the fragile nature of these blades makes their commercial application of little use. Scalloped and sawtooth riblets, which provide considerably less drag reduction benefit, are much stronger shapes mechanically speaking and should be used for application in environments where contact may occur with non-fluid materials ([Dean and Bhushan, 2010](#)).

Commercial applications of riblets include competition swimsuits, which use a thread-based riblet geometry, as well as experimental applications to airplanes and boats. Drag reductions in riblet application have been accomplished, and flight applications have seen a fuel savings of as much as three percent.

Drag reduction is also helpful in antifouling. Low-drag and low-adhesion surfaces reduce biofouling. Spacing between the dermal denticles is such that microscopic aquatic organisms have difficulty adhering to and colonizing the surface.

Manufacturing techniques for riblets must be chosen specific to their application. Vinyl film riblets are the easiest method, as application of a film to a surface requires less work for small-scale application than other methods. Rolling or grinding methods of riblet application can be used for turbine blades or high-volume commercially sold pieces. Laser machining, a two-step molding process using a photolithographically produced master can also be used for high-volume products. Machining methods are unfavorable in most instances and should be avoided in most instances of non-research riblet application.

Appendix

Fabrication Details of a Flow Cell and Shark skin Replica and Segmented-Blade-Type Riblets

Flow Cell

For the measurement of pressure drop using water flows, a flow cell with a closed rectangular channel was designed and fabricated as shown in Fig. 10.18 (Jung and Bhushan, 2010). The fabricated surfaces were used for the upper and lower walls of the flow channel. Two pieces of plastic were glued between the upper and lower samples and at each end to prevent flow leak. For the measurement of pressure drop, the upper sample had two opening holes connected with a differential manometer (Model A 1000-13, Differential Pressure Plus Inc., USA). The thickness, width, and length of the resulting channel are designated as H , W , and L , respectively.

The inlet and outlet ports were machined and connected with the plastic tubes. To introduce water into the channel in laminar flow, a syringe pump (Model NE-300, New Era Pump Systems Inc., USA) was used at a range of flow rates between 50 and 400 $\mu\text{L/s}$ (a range of flow velocity between 0.03 and 0.23 m/s). The Reynolds number of the flow applied by the syringe pump was less than 300, which is the laminar flow. To create a turbulent flow, a larger flow rate is needed than cannot be accomplished with the syringe pump. To accomplish high fluid flow, a separate plastic chamber filled with a measured amount of water was used to allow flow through the channel under the force of gravity. From measuring the amount of water and time to flow the water from a starting fluid level to an ending fluid level, the Reynolds number was calculated as 4,200 (flow velocity of 3.8 m/s), which indicates that the flow is turbulent using this setup.

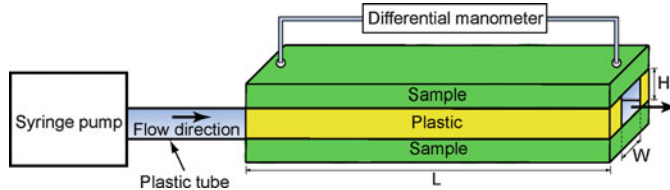


Fig. 10.18 Schematic of a flow cell connected with a differential manometer. The thickness, width, and length of the channel are H , W , and L , respectively (Jung and Bhushan, 2010)

Model for Calculation of Friction and Slip Length

The pressure drop, Δp , of an incompressible fluid flow between two points along the channel of thickness, H , width, W , and length, L , for a hydrophilic flat surface can be calculated by (Blevins, 1984)

$$\Delta p = \frac{\rho V^2 f L}{2 D_H}, \quad (10.1)$$

where ρ is the fluid density, V is the flow velocity obtained from flow rate (Q) divided by cross-sectional area of the channel, and f is the friction factor which specifies the loss in pressure required to impel a flow over the surface or through the channel. The friction factor is generally a function of Reynolds number, surface roughness, and the geometry of the surface. D_H is the hydraulic diameter which is proportional to four times the flow area divided by the perimeter of the surface containing the flow. For the rectangular channel, the hydraulic diameter is

$$D_H = \frac{2WH}{W + H}. \quad (10.2)$$

The friction factor for laminar flow is inversely proportional to the Reynolds number as (Blevins, 1984)

$$f = \frac{k}{Re} \quad \text{for laminar flow} \quad (10.3)$$

$$Re = \frac{\rho V D_H}{\eta}, \quad (10.4)$$

where η is the dynamic fluid viscosity. The Reynolds number can be used to determine whether the fluid flow will be within the laminar, turbulent, or transitional flow regimes. Since the Reynolds number is proportional to flow velocity, the pressure drop in laminar flow increases with flow velocity. k is the friction coefficient which can be found by the solution of Poisson's equation over the cross section as (Blevins, 1984)

$$k = \frac{64}{\frac{2}{3} + \frac{11}{23} \frac{H}{W} \left(2 - \frac{H}{W}\right)}. \quad (10.5)$$

From (10.5), the friction coefficient is dependent only on the shapes of the cross section, but it is independent of surface roughness.

To improve the calculation of the friction factor for turbulent flow in a rectangular channel, Jones (1976) developed an improved equivalent diameter, $D_e = 64D_H/k$, and the friction factor for turbulent flow can be modified as

$$f = \frac{64}{Re}, \quad \text{for turbulent flow.} \quad (10.6)$$

Next, an analysis is presented to calculate slip length in the laminar flow. Using the Navier slip boundary condition, the slip length b of the two infinite parallel and smooth plates can be obtained as (Blevins, 1984; Ou et al., 2004)

$$b = \frac{4\eta QL}{\Delta p WH^2} - \frac{H}{3}. \quad (10.7)$$

For a rectangular channel, the slip length would have the following general form (Ou et al., 2004)

$$b = \frac{c\eta QL}{\Delta p WH^2} - \frac{H}{3}, \quad (10.8)$$

where c is a constant which needs to be obtained empirically. In order to obtain the constant, pressure drop measurement on a hydrophilic channel needs to be made. Equation (10.8) is then fitted under the assumption of zero slip length with the measured pressure drop data to obtain c . It was equal to 5 for the channel ($H = 0.7$ mm, $W = 2.5$ mm, $L = 60$ mm) used in the study. The ρ and η for water taken to be 1,000 kg/m³ and 0.001 Pa s, respectively. This equation was used to calculate the slip length for hydrophobic surfaces (Jung and Bhushan, 2010).

Fabrication of Shark skin Replica and Segmented-Blade-Type Riblets

A shark (*Squalus acanthias*, L. Squalidae) was used for creating a shark skin replica (Jung and Bhushan, 2010). A shark is an aquatic animal, and its skin is permanently exposed to contamination from marine organisms, e.g., bacteria and algae. The shark was conserved in formaldehyde–acetic acid–ethanol (FAA) solution. The detailed structure varies from one location to another for the shark. The scales are present over most of the shark's body. To create a replica, the right front of shark body was selected. Before replicating the conserved shark skin, the selected area was first cleaned with acetone and then washed with deionized water. This process was repeated twice. The cleaned skin was placed in air for 1 h for drying. For the negative replica, a polyvinylsiloxane dental wax was applied via a dispenser on the

upper side of the shark skin and immediately pressed down with a glass plate. After complete hardening of the molding mass (at room temperature, 3–5 min), the master surface and the mold (negative) were separated. The first negative replica was made only to remove any remaining contaminations from the shark surface by embedding the dirt into the replica material. A second and a third replica of the same area were made to obtain negatives without contamination. For the positive replica, a liquid epoxy resin was used in the molding process.

To simulate a shark skin structure, a rib-patterned surface was created using a FlashCut CNC milling machine ([Jung and Bhushan, 2010](#)). [Bechert et al. \(1997b\)](#) have reported that optimal groove depth for the rib surface should be about half of the lateral rib spacing for low drag. In the rib pattern design selected here, multiple stacks of ribs oriented along an axis were fabricated. For the fabrication, first a model of a rib-patterned surface was designed in SolidWorks, and then the code for the rib's height, width, spacing and lengths, and channel dimensions was written using FeatureCAM in order to fabricate structures using the CNC milling machine. An acrylic resin was clamped onto the table of the CNC mill, and a fly cutter was used to make the top of the surface flat. The code was opened with FlashCut CNC, and then the rib patterns were milled using an end mill with 130 μm bit.

Figure [10.10a](#) presented earlier shows the SEM micrographs of the shark skin (*Squalus acanthias*) replica taken at a top view, a 45°-tilt-angle side view, and a 45°-tilt-angle top view. The shark skin replica shows that scales are lifted up at the end, and there are only three ribs on each scale. It is clearly visible that the V-shaped riblets' height varies between 200 and 500 μm , and their space varies between 100 and 300 μm . The ribs were oriented nearly parallel to swimming direction of the sharks. Figure [10.10b](#) shows the optical microscope images of the rib-patterned surface fabricated as a model of artificial shark skin surfaces. The height, width, and length of the created ribs were 90, 38, and 850 μm , respectively. The spacing between the ribs was 180 μm .

To measure wetting properties, contact angles of the samples were measured, and data are presented in Table [10.2](#). The shark skin replica made with epoxy resin had a static contact angle of 89° and a contact angle hysteresis of 66° for a water droplet. For acrylic resin material, a static contact angle of 82° and a contact angle hysteresis of 71° were found for flat acrylic resin. Introduction of the rib patterns on the flat surface led to a higher static contact angle of 146° and lower contact angle hysteresis of 43°.

References

- Bechert DW, Hoppe G, Reif WE (1985) On the drag reduction of the shark skin. In: Paper presented at AIAA Shear Flow Control Conference, Boulder, CO, Paper # AIAA-85-0564, AIAA, New York
- Bechert DW, Bartenwerfer M, Hoppe G, Reif W-E (1986) Drag reduction mechanisms derived from shark skin. In: Proceedings of 15th ICAS congress, vol 2 (A86-48-97624-01), Paper # ICAS-86-1.8.3. AIAA, New York, pp 1044–1068

- Bechert DW, Hoppe G (1985) On the drag reduction of the shark skin. Paper presented at AIAA Shear Flow Control Conference, Boulder, CO, March 12–14 Mar 1985, # AIAA-85-0564
- Bechert DW, Bartenwerfer M, Hoppe G, Reif W-E (1986) Drag Reduction mechanisms derived from shark skin. In: Proceedings of 15th ICAS congress, vol 2 (A86-48-97624-01), pp 1044–1068, AIAA, New York, Paper # ICAS-86-1.8.3
- Bechert DW, Hoppe G, van der Hoven JGTh, Makris R (1992) The Berlin oil channel for drag reduction research. *Exp Fluids* 12:251–260
- Bechert DW, Bruse M, Hage W, Meyer R (1997a) Biological surfaces and their technological application—laboratory and flight experiments on drag reduction and separation control. Paper presented at AIAA 28th Fluid Dynamics Conference, Snowmass Village, CO, AIAA, New York, # AIAA-1997-1960
- Bechert DW, Bruse M, Hage W, van der Hoeven JGTh, Hoppe G (1997b) Experiments on drag reducing surfaces and their optimization with an adjustable geometry. *J Fluid Mech* 338:59–87
- Bechert DW, Bruse M, Hage W (2000a) Experiments with three-dimensional riblets as an idealized model of shark skin. *Exp Fluids* 28:403–412
- Bechert DW, Bruse M, Hage W, Meyer R (2000b) Fluid mechanics of biological surfaces and their technological application. *Naturwissenschaften* 87:157–171
- Bixler GD, Bhushan B (2012) Biofouling: lessons from nature. *Philos Trans R Soc A* 370:2381–2417
- Blevins RD (1984) Applied fluid dynamics handbook. Van Nostrand Reinhold, New York
- Carman ML, Estes TG, Feinburg AW, Schumacher JF, Wilkerson W, Wilson LH, Callow ME, Callow JA, Brennan AB (2006) Engineered antifouling microtopographies—correlating wettability with cell attachment. *Biofouling* 22:11–21
- Choi KS, Gadd GE, Pearcey HH, Savill AM, Svensson S (1989) Tests of drag-reducing polymer coated on a riblet surface. *Appl Sci Res* 46:209–216
- Choi KS, Yang X, Clayton BR, Glover EJ, Altar M, Semenov BN, Kulik VM (1997) Turbulent drag reduction using compliant surfaces. *Proc R Soc A* 453:2229–2240
- Coles D (1978) A model for flow in the viscous sublayer. In: Smith CR, Abbott DE (eds) Proceedings of the workshop on coherent structure of turbulent boundary layers. Lehigh University, Bethlehem, PA, pp 462–475
- Daniel TL (1981) Fish mucus: in situ measurements of polymer drag reduction. *Biol Bull* 160: 376–382
- Dean BD, Bhushan B (2010) Shark-skin surfaces for fluid-drag reduction in turbulent flow: a review. *Philos Trans R Soc A* 368:4775–4806
- Dean BD, Bhushan B (2012) The effect of riblets in rectangular duct flow. *Appl Surf Sci* 258:3936–3947
- Denkena B, de Leon L, Wang B (2009) Grinding of microstructures functional surfaces: a novel strategy for dressing of micropatterns. *Prod Eng* 3:41–48
- Enyutin GV, Lashkov YuA, Samoilova NV (1995) Drag reduction in riblet-lined pipes. *Fluid Dyn* 30:45–48
- Frings B (1988) Heterogeneous drag reduction in turbulent pipe flows using various injection techniques. *Rheol Acta* 27:92–110
- Genzer J, Efimenco K (2006) Recent developments in superhydrophobic surfaces and their relevance to marine fouling: a review. *Biofouling* 22:339–360
- Goldstein D, Handler R, Sirovich L (1995) Direct numerical simulation of turbulent flow over a modeled riblet covered surface. *J Fluid Mech* 302:333–376
- Han M, Huh JK, Lee SS, Lee S (2002) Micro-Riblet film for drag reduction. In: Proceedings of the Pacific Rim workshop on transducers and micro/nano technologies, Xiamen, China
- Hoyt JW (1975) Hydrodynamic drag reduction due to fish slimes. In: Swimming and flying in nature, vol 2. Plenum, New York, pp 653–672
- Jones OC (1976) An improvement in the calculation of turbulent friction in rectangular ducts. *J Fluids Eng* 98:173–180
- Jung YC, Bhushan B (2010) Biomimetic structures for fluid drag reduction in laminar and turbulent flows. *J Phys Condens Matter* 22:035104

- Kesel A, Liedert R (2007) Learning from nature: non-toxic biofouling control by shark skin effect. *Comp Biochem Physiol A* 146:S130
- Kline SJ, Reynolds WC, Schraub FA, Runstadler PW (1967) The structure of turbulent boundary layers. *J Fluid Mech* 30:741–773
- Klocke F, Feldhaus B, Mader S (2007) Development of an incremental rolling process for the production of defined Riblet surface structures. *Prod Eng* 1:233–237
- Koury E, Virk PS (1995) Drag reduction by polymer solutions in a Riblet-lined pipe. *Appl Sci Res* 54:323–347
- Krieger K (2004) Do pool sharks really swim faster? *Science* 305:636–637
- Lang AW, Motta P, Hidalgo P, Westcott M (2008) Bristled shark skin: a microgeometry for boundary layer control? *Bioinspir Biomim* 3:1–9
- Lee SJ, Choi YS (2008) Decrement of spanwise vortices by a drag-reducing Riblet surface. *J Turbulence* 9:1–15
- Lee S-J, Lee S-H (2001) Flow field analysis of a turbulent boundary layer over a Riblet surface. *Exp Fluids* 30:153–166
- Liu KN, Christodoulou C, Riccius O, Joseph DD (1990) Drag reduction in pipes lined with riblets. *AIAA J* 28:1697–1699
- Maali A, Bhushan B (2008) Nanorheology and boundary slip in confined liquids using atomic force microscopy. *J Phys Condes Matter* 20:315201
- Maali A, Wang Y, Bhushan B (2009) Evidence of the no-slip boundary condition of water flow between hydrophilic surfaces using atomic force microscopy. *Langmuir* 25:12002–12005
- Marentic FJ, Morris TL (1992) Drag reduction article. United States Patent, No. 5,133,516
- Munson B, Young D, Okiishi T (2005) Fundamentals of fluid mechanics, 5th edn. Wiley, New York
- Ou J, Perot B, Rothstein JP (2004) Laminar drag reduction in microchannels using ultrahydrophobic surfaces. *Phys Fluids* 16:4635–4643
- Ralston E, Swain G (2009) Bioinspiration – the solution for biofouling control? *Bioinspir Biomim* 4:1–9
- Reif W-E (1985) Squamation and ecology of sharks, vol 78. Courier Forschungsinstitut Senckenberg, Frankfurt, pp 1–255
- Robinson SK (1991) The kinematics of turbulent boundary layer structure. NASA TM 103859, NASA, Washington, DC
- Rohr JJ, Anderson GW, Reidy LW, Hendricks EW (1992) A comparison of the drag-reducing benefits of Riblets in internal and external flows. *Exp Fluids* 13:361–368
- Schumacher JF, Aldred N, Callow ME, Finlay JA, Callow JA, Clare AS, Brennan AB (2007) Species-specific engineered antifouling topographies: correlations between the settlement of algal zoospores and barnacle cyprids. *Biofouling* 23:307–317
- Shephard KL (1994) Functions for fish mucus. *Rev Fish Biol Fish* 4:401–429
- Walsh MJ (1980) Drag characteristics of V-groove and transverse curvature riblets. *Visc Flow Drag Reduct* 72:169–184
- Walsh MJ (1982) Turbulent boundary layer drag reduction using riblets. Paper presented at AIAA 20th aerospace sciences meeting, Orlando, FL, AIAA, New York, Paper # AIAA-82-0169
- Walsh MJ, Anders JB (1989) Riblet/LEBU research at NASA Langley. *Appl Sci Res* 46:255–262
- Walsh MJ, Lindemann AM (1984) Optimization and application of riblets for turbulent drag reduction. Paper presented at AIAA 22nd aerospace sciences meeting, Reno, NV, AIAA, New York, Paper # AIAA-84-0347
- Wang Y, Bhushan B (2010) Boundary slip and nanobubble study in micro/nanofluidic using atomic force microscopy. *Soft Matter* 6:29–66
- Wang Y, Bhushan B, Maali A (2009) Atomic force microscopy measurement of boundary slip on hydrophilic, hydrophobic, and superhydrophobic surfaces. *J Vac Sci Technol A* 27:754–760
- Weiss MH (1997) Implementation of drag reduction techniques in natural gas pipelines. Paper presented at 10th European drag reduction working meeting, Berlin, Germany, 19–21 Mar 1997
- Wilkinson SP (1983) Influence of wall permeability on turbulent boundary-layer properties. Paper presented at 21st aerospace sciences meeting of the american institute of aeronautics and astronautics, Reno, NV, 10–13 Jan 1983, Paper # AIAA 83–0294

- Wilkinson SP, Lazos BS (1988) Direct drag and hot-wire measurements on thin-element riblet arrays. In: Liepmann HW, Narasimha R (eds) Proceedings of Turbulence Management and Relaminarization. Springer, Berlin
- Wilkinson SP, Anders JB, Lazos BS, Bushnell DM (1988) Turbulent drag reduction research at NASA Langley: progress and plans. *Int J Heat Fluid Flow* 9:266–277
- Xin H, Zhang D (2008) Study on the micro-replication of shark skin. *Sci China Ser E Technol Sci* 51:890–896
- Zhu Y, Granick S (2001) Rate-dependent slip of Newtonian liquid at smooth surfaces. *Phys Rev Lett* 87:096105

Part VI

Gecko Adhesion

Chapter 11

Gecko Adhesion

11.1 Introduction

The leg attachment pads of several animals including many insects, spiders, and lizards are capable of attaching to and detaching from a variety of surfaces and are used for locomotion, even on vertical walls or across the ceiling (Gorb, 2001; Bhushan, 2007). Biological evolution over a long period of time has led to the optimization of their leg attachment systems. This dynamic attachment ability is referred to as reversible adhesion or smart adhesion (Bhushan et al., 2006). Many insects (e.g., beetles and flies) and spiders have been the subject of investigation. However, the attachment pads of geckos have been the most widely studied due to the fact that they have the highest body mass and exhibit the most versatile and effective adhesive known in nature. As a result, most of this chapter will be concerned with gecko adhesion.

Although there are over 1,000 species of geckos (Kluge, 2001; Han et al., 2004) that have attachment pads of varying morphology (Ruibal and Ernst, 1965), the Tokay gecko (*Gekko gecko*) which is native to Southeast Asia has been the main focus of scientific research (Hiller, 1968; Irschick et al., 1996; Autumn, 2006). The Tokay gecko is the second largest gecko species, attaining lengths of approximately 0.3–0.4 m and 0.2–0.3 m for males and females, respectively. They have a distinctive blue or gray body with orange or red spots and can weigh up to 300 g (Tinkle, 1992). These have been the most widely investigated species of gecko due to the availability and size of these creatures.

Almost 2,500 years ago, the ability of the gecko to “run up and down a tree in any way, even with the head downwards” was observed by Aristotle (Aristotle/Thompson, 1918, Book IX, Part 9). Even though the adhesive ability of geckos has been known since the time of Aristotle, little was understood about this phenomenon until the late nineteenth century when the microscopic hairs covering the toes of the gecko were first noted. The development of electron microscopy in the 1950s enabled scientists to view the complex hierarchical morphology that covers the skin on the gecko’s toes. Over the past century and a half, scientific

studies have been conducted to determine the factors that allow the gecko to adhere to and detach from surfaces at will, including surface structure (Ruibal and Ernst, 1965; Russell, 1975, 1986; Williams and Peterson, 1982; Schleich and Kästle, 1986; Irschick et al., 1996; Autumn and Peattie, 2002; Arzt et al., 2003), the mechanisms of adhesion (Wagler, 1830; Simmernacher, 1884; Schmidt, 1904; Hora, 1923; Dellit, 1934; Ruibal and Ernst, 1965; Hiller, 1968; Gennaro, 1969; Stork, 1980; Autumn et al., 2000, 2002; Bergmann and Irschick, 2005; Huber et al., 2005b), and adhesion strength (Hiller, 1968; Irschick et al., 1996; Autumn et al., 2000; Arzt et al., 2003; Huber et al., 2005a, b). Modeling the gecko attachment system as a system of springs (Bhushan et al., 2006; Kim and Bhushan, 2007a, b, c, 2008) has provided valuable insight into adhesion enhancement. Van der Waals forces are widely accepted in literature as the dominant adhesion mechanism utilized by hierarchical attachment systems. Capillary forces created by humidity naturally present in the air can further increase the adhesion force generated by the spatulae (Kim and Bhushan, 2008). Both experimental and theoretical works support these adhesion mechanisms.

There is great interest among the scientific community to further study the characteristics of gecko feet in the hope that this information could be applied to the production of micro-/nanosurfaces capable of recreating the adhesion forces generated by these lizards (Bhushan, 2007). Common man-made adhesives such as tape or glue involve the use of wet adhesives that permanently attach two surfaces. However, replication of the characteristics of gecko feet would enable the development of a superadhesive tape capable of clean, dry adhesion. These structures can bind components in microelectronics without the high heat associated with various soldering processes. These structures will never dry out in a vacuum—a common problem in aerospace applications. They have the potential for use in everyday objects such as adhesive tapes, fasteners, and toys and in high technology such as microelectronic and space applications. Replication of the dynamic climbing and peeling ability of geckos could find use in the treads of wall-climbing robots.

This chapter first introduces various hairy attachment systems. Then, it introduces the Tokay Gecko and its construction and some details on adhesion, peeling, and self-cleaning mechanisms. The next section describes in detail the attachment mechanisms followed by adhesion measurements and data, adhesion modeling, and adhesion database of fibrillar structures. The last section presents various fabrication techniques to create structures in the lab.

11.2 Hairy Attachment Systems

There are two kinds of attachment pads—relatively smooth and hairy. The first kind are relatively smooth pads, so-called arolia and euplantulae, which are soft and deformable and are found in some amphibians, such as tree frogs, torrent frogs, cockroaches, grasshoppers, and bugs. They are able to attach to and move over wet or even flooded environments without falling (Federle et al., 2006). Tree frog toe attachment pads consist of a hexagonal array of flat-topped epidermal cells about

$10\text{ }\mu\text{m}$ in size separated by approximately $1\text{ }\mu\text{m}$ -wide mucus-filled channels; the flattened surface of each cell consists of submicron array of nanopillars or pegs of approximately $100\text{--}400\text{ nm}$ diameter. The toe pads are made of an extremely soft, inhomogeneous material; epithelium itself has an effective elastic modulus of about 15 MPa , equivalent to silicone rubber. The pads are permanently wetted by mucus secreted from glands that open into the channels between epidermal cells. They attach to mating surfaces by wet adhesion (Federle et al., 2006). They are capable of climbing on wet rocks even when water is flowing over the surface (Barnes et al., 2002). During walking, the squeezing is expected to occur rapidly. Torrent frogs can resist sliding even on flooded surfaces. The surface of their toe pads is similar to that of tree frogs with some changes in the structure to handle the large flow of water (Ohler, 1995).

The second kind are the hairy types which consist of long deformable setae and are found in many insects (e.g., beetles, flies), spiders, and lizards. The microstructures utilized by beetles, flies, spiders, and geckos have similar structures and can be seen in Fig. 11.1a. As the size (mass) of the creature increases, the radius of the terminal attachment elements decreases. This allows a greater number of setae to be packed into an area, hence increasing the linear dimension of contact and the adhesion strength. Arzt et al. (2003) determined that the density of the terminal attachment elements, ρ_A , per m^{-2} strongly increases with increasing body mass, m , in g. In fact, a master curve can be fitted for all the different species (Fig. 11.1b):

$$\log \rho_A = 13.8 + 0.669 \log m. \quad (11.1)$$

The correlation coefficient of the master curve is equal to 0.919. Beetles and flies have the largest attachment pads and the lowest density of terminal attachment elements. Spiders have highly refined attachment elements that cover its legs. Geckos have both the highest body mass and greatest density of terminal elements (spatulae). Spiders and geckos can generate high dry adhesion, whereas beetles and flies increase adhesion by secreting liquid stored generally within a spongy layer of cuticle and delivered at the contacting surface through a system of porous channels (Gorb, 2001; Arzt et al., 2003; Kesel et al., 2003). It should be noted that in the smooth attachment system discussed earlier, the secretion is essential for attachment.

It should be noted that Peattie and Full (2007) have revisited the scaling of terminal attachment elements with the body mass using a phylogenetic approach. In their work, a larger set of species (81) over a wider range of body mass and setal morphology were considered. They found that fiber morphology is better predicted by evolutionary history and adhesion mechanism (dry or wet) than by body mass.

Figure 11.2 shows the scanning electron micrographs of the end of the legs of two flies—the fruit fly (*Drosophila melanogaster*) and the syrphid fly. The fruit fly uses setae with flattened tips (spatulae) on the two hairy rods for attachment to smooth surfaces and two front claws for attachment to rough surfaces. The front claws are also used for locomotion. The syrphid fly uses setae on the legs for attachment. In both cases, fluid is secreted at the contacting surface to increase adhesion.

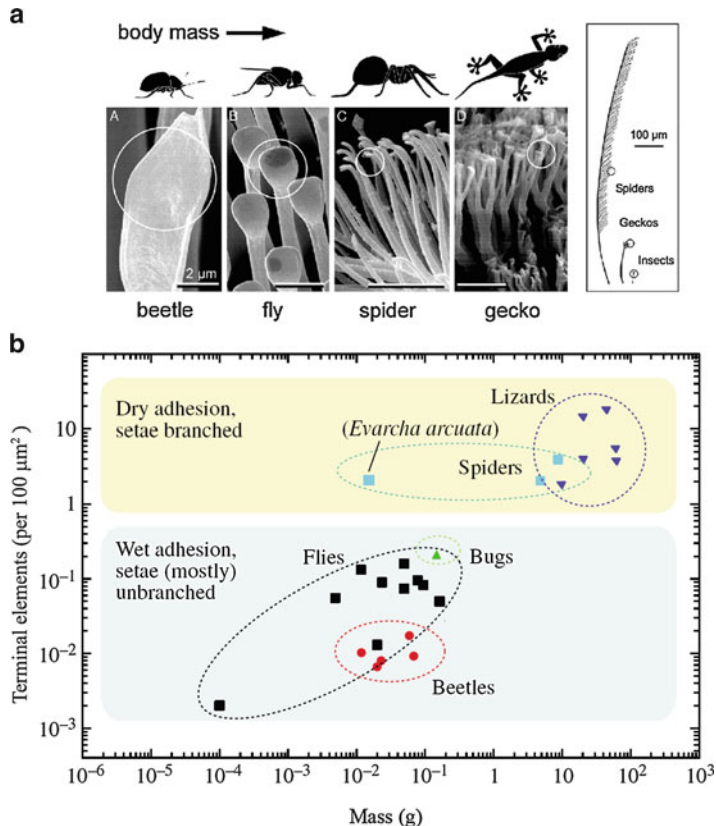


Fig. 11.1 (a) Terminal elements of the hairy attachment pads of a beetle, fly, spider, and gecko shown at two different scales (Arzt et al., 2003) and (b) the dependence of terminal element density on body mass (Federle, 2006). Data are from Arzt et al. (2003) and Kesel et al. (2003)

11.3 Tokay Gecko

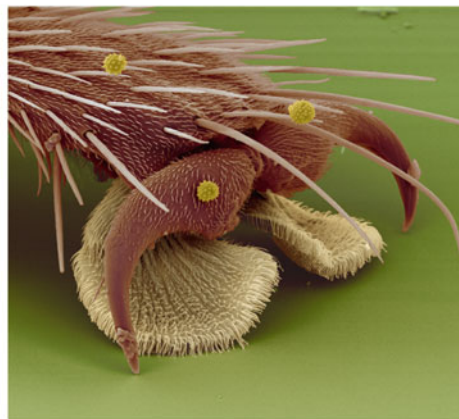
11.3.1 Construction of Tokay Gecko

The explanation for the adhesion properties of gecko feet can be found in the surface morphology of the skin on the toes of the gecko. The skin is comprised of a complex hierarchical structure of lamellae, setae, branches, and spatulae (Ruibal and Ernst, 1965). Figure 11.3 shows various SEM micrographs of a gecko foot, showing the hierarchical structure down to the nanoscale. Figure 11.4 shows a schematic of the structure, and Table 11.1 summarizes the surface characteristics. The gecko attachment system consists of an intricate hierarchy of structures beginning with lamellae, soft ridges 1–2 mm in length (Ruibal and Ernst, 1965) that are located

Fig. 11.2 SEM micrographs of the end of the legs of fruit fly (*Drosophila melanogaster*) and syrphid fly (Gorb, 2001)



End of the legs of fruit fly (*drosophila melanogaster*)



End of the leg of syrphid fly

on the attachment pads (toes) that compress easily so that contact can be made with rough bumpy surfaces. Tiny curved hairs known as setae extend from the lamellae with a density of approximately 14,000 per square millimeter (Schleich and Kästle, 1986). These setae are typically 30–130 µm in length, 5–10 µm in diameter (Ruibal and Ernst, 1965; Hiller, 1968; Russell, 1975; Williams and Peterson, 1982), and are composed primarily of β-keratin (Maderson, 1964; Russell, 1986) with some α-keratin component (Rizzo et al., 2006). At the end of each seta, 100–1,000 spatulae (Ruibal and Ernst, 1965; Hiller, 1968) with typically 2–5 µm in length and a diameter of 0.1–0.2 µm (Ruibal and Ernst, 1965) branch out and form the points of contact with the surface. The tips of the spatulae are approximately 0.2–0.3 µm in width (Ruibal and Ernst, 1965), 0.5 µm in length, and 0.01 µm in thickness (Persson and Gorb, 2003) and garner their name from their resemblance to a spatula.

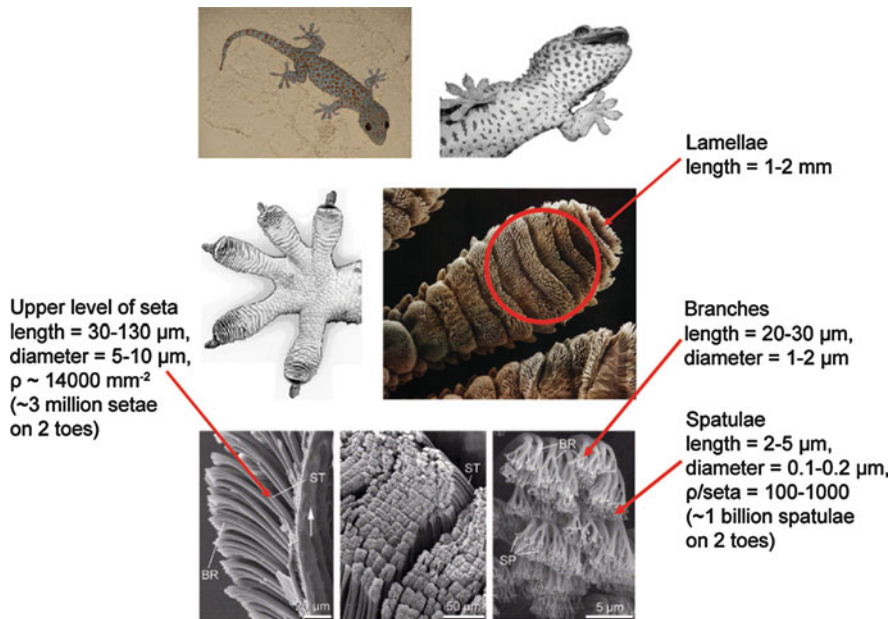


Fig. 11.3 The hierarchical structures of a Tokay gecko foot: a gecko foot (Autumn et al., 2000) and a gecko toe (Autumn, 2006). The two feet with an area of 220 mm^2 consist of about three million setae on their toes that branch off into about three billion spatulae. Scanning electron microscope (SEM) micrographs of the setae and the spatulae are shown in the bottom row (Gao et al., 2005). ST seta, SP spatula, BR branch

The attachment pads on two feet of the Tokay gecko have an area of about 220 mm^2 . About three million setae on their toes that branch off into about three billion spatulae on two feet can produce a clinging ability of about 20 N (vertical force required to pull a lizard down a nearly vertical (85°) surface) (Irschick et al., 1996) and allow them to climb vertical surfaces at speeds over 1 m/s with the capability to attach and detach their toes in milliseconds. In isolated setae, a $2.5 \mu\text{N}$ preload yielded adhesion of $20-40 \mu\text{N}$, and thus, the adhesion coefficient, which represents the strength of adhesion as a function of preload, ranges from 8 to 16 (Autumn et al., 2002).

11.3.2 Adhesion Enhancement by Division of Contacts and Multilevel Hierarchical Structure

Typical rough, rigid surfaces are able to make intimate contact with a mating surface only over a very small portion of the perceived apparent area of contact. In fact, the real area of contact is typically two to six orders of magnitude less than the apparent

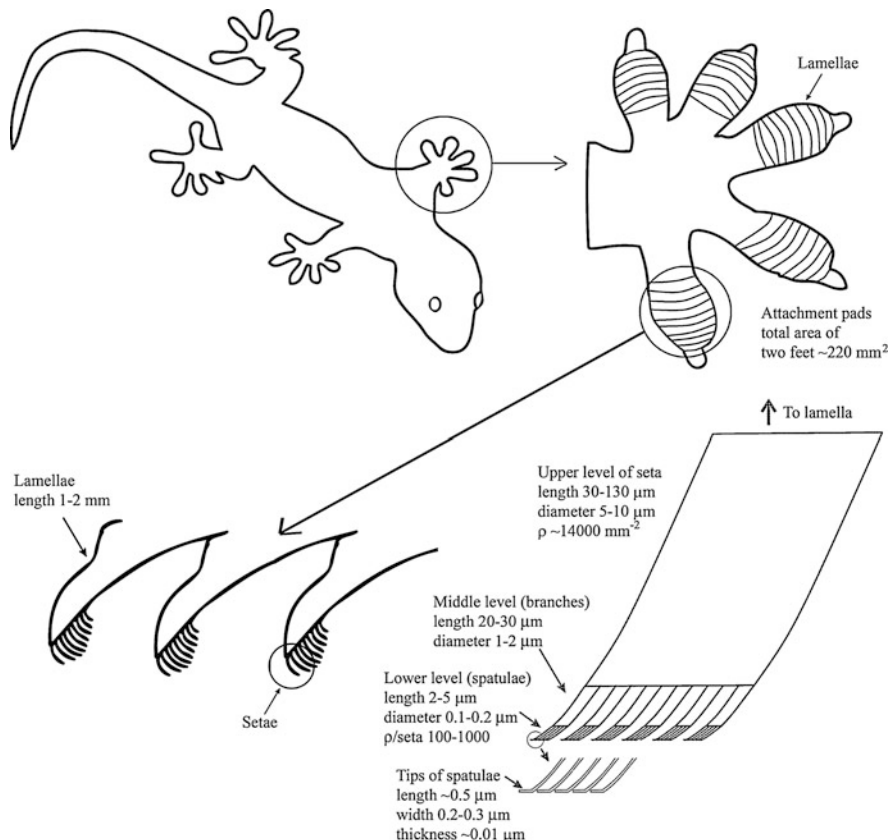


Fig. 11.4 Schematic drawings of a Tokay gecko including the overall body, one foot, a cross-sectional view of the lamellae, and an individual seta. ρ represents number of spatulae

Table 11.1 Physical dimensions of fibrillar structures on Tokay gecko feet and measured adhesive force data. Young's modulus of surface material, keratin = 1–20 GPa^{1,2}

Component	Size	Density	Adhesive force
Seta	$30-130^3-6/5-10^{3-6}$	$\sim 14,000^{8,9}$	$194 \mu\text{N}^{10}$ (in shear)
	Length/diameter (μm)	Setae/ mm^2	$\sim 20 \mu\text{N}^{10}$ (normal)
Branch	$20-30^3/1-2^3$	—	—
	Length/diameter (μm)		
Spatula	$2-5^3/0.1-0.2^{3,7}$	$100-1,000^{3,4}$	—
	Length/diameter (μm)	Spatulae per seta	
Tip of spatula	$\sim 0.5^{3,7}/0.2 - 0.3^{3,6}/\sim 0.01^7$	—	11nN^{11} (normal)
	Length/width/thickness (μm)		

¹Russell (1986); ²Bertram and Gosline (1987); ³Ruibal and Ernst (1965); ⁴Hiller (1968); ⁵Russell (1975); ⁶Williams and Peterson (1982); ⁷Persson and Gorb (2003); ⁸Schleich and Kästle (1986);

⁹Autumn and Peattie (2002); ¹⁰Autumn et al. (2000); ¹¹Huber et al. (2005a)

area of contact (Bhushan, 1999, 2002, 2011). Autumn et al. (2002) proposed that divided contacts serve as a means for increasing adhesion. The surface energy approach can be used to calculate adhesion force in a dry environment in order to calculate the effect of division of contacts. If the tip of a spatula is considered as a hemisphere with radius, R , adhesion force of a single contact, F_{ad} , based on the so-called JKR (Johnson–Kendall–Roberts) theory (Johnson et al., 1971) is given as

$$F_{\text{ad}} = \frac{3}{2}\pi W_{\text{ad}}R, \quad (11.2)$$

where W_{ad} is the work of adhesion (units of energy per unit area). Equation (11.2) shows that the adhesion force of a single contact is proportional to a linear dimension of the contact. For a constant area divided into a large number of contacts or setae, n , the radius of a divided contact, R_1 , is given by $R_1 = R/\sqrt{n}$ (self-similar scaling) (Arzt et al., 2003). Therefore, the adhesion force of (11.2) can be modified for multiple contacts such that

$$F'_{\text{ad}} = \frac{3}{2}\pi W_{\text{ad}} \left(\frac{R}{\sqrt{n}} \right) n = \sqrt{n} F_{\text{ad}}, \quad (11.3)$$

where F'_{ad} is the total adhesion force from the divided contacts. Thus, the total adhesive force is simply the adhesion force of a single contact multiplied by the square root of the number of contacts.

For contact in a humid environment, the meniscus (or capillary) forces further increase the adhesion force (Bhushan, 1999, 2002, 2011). The attractive meniscus force (F_m) consists of a contribution by both Laplace pressure and surface tension; see Sect. 11.4.2 (Orr et al., 1975; Bhushan, 2002). The contribution by Laplace pressure is directly proportional to the meniscus area. The other contribution is from the vertical component of surface tension around the circumference. This force is proportional to the circumference, as is the case for the work of adhesion (Bhushan, 2002). Going through the analysis presented earlier, one can show that the contribution from the component of surface tension increases with splitting into a larger number of contacts. It increases linearly with the square root of the number of contacts n (self-similar scaling) (Bhushan, 2007; Cai and Bhushan, 2007, 2008):

$$(F'_m)_{\text{surface tension}} = \sqrt{n} (F_m)_{\text{surface tension}}, \quad (11.4a)$$

where F'_m is the force from the divided contacts and F_m is the force of an individual contact. This component of meniscus force is significant if the meniscus radius is very small and the contact angles are relatively large.

During separation of two surfaces, the viscous force, F_v , of the divided contacts is given as (Cai and Bhushan, 2007, 2008)

$$F'_v = F_v/n, \quad (11.4b)$$

where F'_v is the force from the divided contacts and F_v is the force of an individual contact.

Table 11.2 Young's modulus of gecko skin and other materials for comparison

Material	Young's modulus
β -Keratin, mostly present in gecko skin	1–20 GPa
Steel	210 GPa
Cross-linked rubber	1 MPa
Consumer adhesive tape (uncross-linked rubber)	1 kPa

The models just presented only consider contact with a flat surface. Multilevel hierarchical structure of the gecko provides compliance and conformability to rough surfaces in order to achieve high adhesion. The flexibility of the body provides conformability at the cm scale. Several toes on the feet provide conformability independently at the several mm scale. Lamellae on the bottom surfaces of the toes provide conformability at the mm scale. The setae on the lamellae provide conformability at the several μm scale. The tips of the setae are divided into spatulae which provide conformability at the few to several hundred nm scale. To summarize, on natural rough surfaces, the compliance and adaptability of the hierarchical structure of gecko setae allows for greater contact with a natural rough surface than a non-branched attachment system (Sitti and Fearing, 2003; Bhushan et al., 2006; Kim and Bhushan, 2007a, b, c, 2008). Modeling of the contact between gecko setae and rough surfaces is discussed in detail in Sect. 11.6.

Material properties also play an important role in adhesion. A soft material is able to achieve greater contact with a mating surface than a rigid material. Although gecko skin is primarily comprised of β -keratin, a stiff material with a Young's modulus in the range of 1–20 GPa (Russell, 1986; Bertram and Gosline, 1987), the effective modulus of the setal arrays on gecko feet is about 100 kPa (Autumn et al., 2006a), which is approximately four orders of magnitude lower than the bulk material. Young's modulus of the gecko skin is compared with that of various materials in Table 11.2. The surface of consumer adhesive tape has been selected to be very compliant to increase the contact area for high adhesion. Nature has selected a relatively stiff material to avoid clinging to adjacent setae. Nonorthogonal attachment angle of the seta increases the bending stiffness. Division of contacts and hierarchical structure, as discussed earlier, provide high adhesion. By combining optimal surface structure and material properties, Mother Nature has created an evolutionary superadhesive.

11.3.3 Peeling

Although geckos are capable of producing large adhesion forces, they retain the ability to remove their feet from an attachment surface at will by peeling action. The orientation of the spatulae facilitates peeling. Autumn et al. (2000) were the first to experimentally show that the adhesion force of gecko setae is dependent on

the three-dimensional orientation as well as the preload applied during attachment (see Sect. 11.5.1.1). Due to this fact, geckos have developed a complex foot motion during walking. First, the toes are carefully uncurled during detachment. The maximum adhesion occurs at an attachment angle of 30° —the angle between a seta and mating surface. The gecko is then able to peel its foot from surfaces one row of setae at a time by changing the angle at which its setae contact a surface. At an attachment angle greater than 30° , the gecko will detach from the surface. Two diagonally opposite feet participate in the movement.

[Shah and Sitti \(2004\)](#) determined the theoretical preload required for adhesion as well as the adhesion force generated for setal orientations of 30° , 40° , 50° , and 60° . Consider a solid material (elastic modulus, E , Poisson's ratio, ν) to make contact with the rough surface described by

$$f(x) = H \sin^2\left(\frac{\pi x}{\lambda}\right), \quad (11.5)$$

where H is the amplitude and λ is the wavelength of the roughness profile. For a solid adhesive block to achieve intimate contact with the rough surface neglecting surface forces, it is necessary to apply a compressive stress, σ_c ([Jagota and Bennison, 2002](#)):

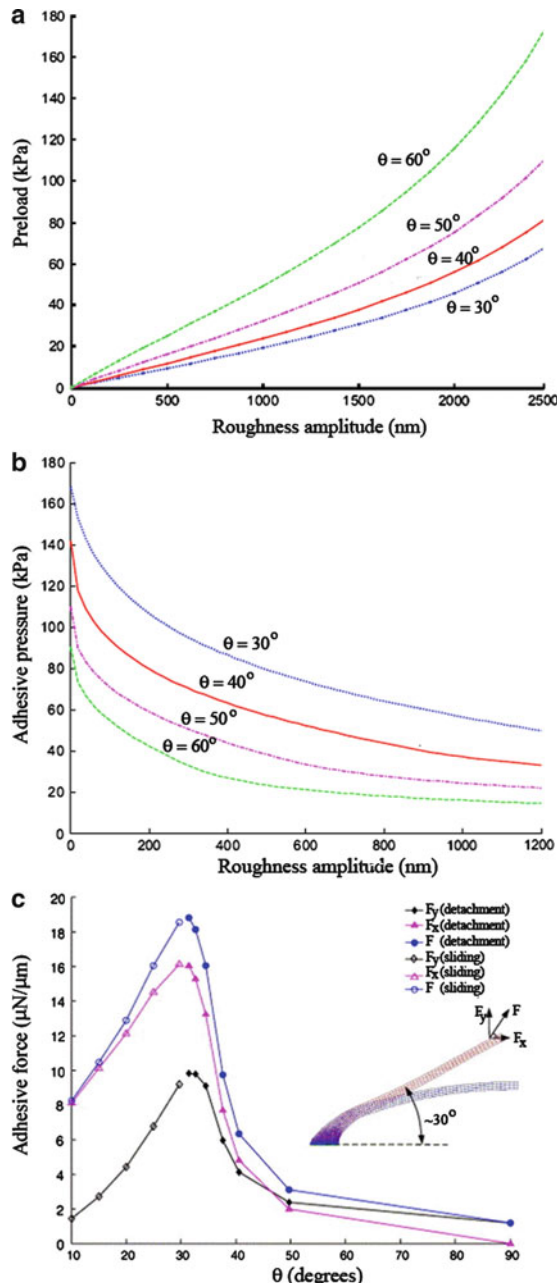
$$\sigma_c = \frac{\pi E H}{2\lambda(1-\nu^2)}. \quad (11.6)$$

Equation (11.6) can be modified to account for fibers oriented at an angle, θ . The preload required for contact is summarized in Fig. 11.5a. As the orientation angle decreases, so does the required preload. Similarly, adhesion strength is influenced by fiber orientation. As seen in Fig. 11.5b, the greatest adhesion strength occurs at $\theta = 30^\circ$.

[Gao et al. \(2005\)](#) created a finite element model of a single gecko seta in contact with a surface. A tensile force was applied to the seta at various angles, θ , as shown in Fig. 11.5c. Maximum adhesion again occurs at an angle of 30° . For forces applied at an angle of less than 30° , the dominant failure mode was sliding. On the contrary, the dominant failure mode for forces applied at angles greater than 30° was detachment. This verifies the results of [Autumn et al. \(2000\)](#) that detachment occurs at attachment angles greater than 30° .

[Tian et al. \(2006\)](#) studied the attachment and detachment process in detail. Schematics of various configurations are shown in Fig. 11.6. In their natural configuration, shown in Fig. 11.6a, the spatula pads are at an angle of about 30° to the seta shaft and are approximately normal to the spatula shafts. This corresponds to a weak adhesion force. When geckos roll in and grip their toes inward, shown in Fig. 11.6b, the pulling angle, θ_s , of the seta shaft to the substrate will range from 0 to 30° , whereas the pulling angles, θ , of the spatula shafts to the substrate will range from 0 to 90° . Pulling in of the toes leads to smaller θ and θ_s , with a larger number of spatulae in contact with the substrate. This results in both higher friction and adhesion at the seta shaft. During the rolling out of the toes to detach from a substrate, shown in Fig. 11.6c, the setae move back to their initial free state with $\theta_s \sim 30^\circ$ and $\theta \sim 90^\circ$.

Fig. 11.5 Contact mechanics results for the effect of fiber orientation on (a) preload required for contact and (b) adhesive pressure for roughness amplitudes ranging from 0 to 2,500 nm (Shah and Sitti, 2004). (c) Finite element analysis of the adhesive force of a single seta as a function of pull direction (Gao et al., 2005)



Pesika et al. (2007) developed a tape-peeling model based on the geometry of the peeling zone. They considered geometrical changes within the peel zone. The increased radius of curvature, R , increases the length of the peel zone, which in turn increases the peel force, F , in the peel direction. Figure 11.7a shows a schematic of

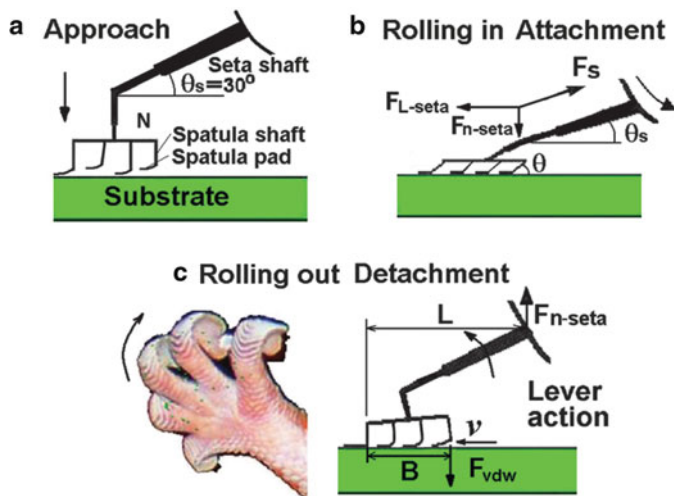


Fig. 11.6 Sketches of attachment and detachment of a single seta by (a) approaching the substrate rolling (or gripping) in (b) and rolling (or peeling) out the toes in (c). The image in (c) left is from the left back foot (Tian et al., 2006)

the peel zone for two peel regimes: peel angles between cases I and II (constant peel-zone regime) and between cases II and III (variable peel-zone regime). In the constant peel-zone regime, the geometry of the peel zone (i.e., length of the peel zone and the curvature of the tape backing) remains constant, while the peel angle, θ , is changed. In contrast, in the variable peel-zone regime, the length of the peel zone and curvature of the tape backing both increase as the peel angle, θ , is changed. Figure 11.7b shows a plot of predicted value of peel force, F , as a function of the peel angle, θ . During detachment, θ increases, resulting in a lower peel force (Fig. 11.5c). The measured peel force for a model tape over glass surface as a function of peel angle is also plotted. The measured data correlate well with the predicted values.

11.3.4 Self-Cleaning

Natural contaminants (dirt and dust) as well as man-made pollutants are unavoidable and have the potential to interfere with the clinging ability of geckos. Particles found in the air consist of particulates that are typically less than $10 \mu\text{m}$ in diameter, while those found on the ground can often be larger (Hinds, 1982; Jaenicke, 1998). Intuitively, it seems that the great adhesion strength of gecko feet would cause dust and other particles to become trapped in the spatulae and that they would have no way of being removed without some sort of manual cleaning action on

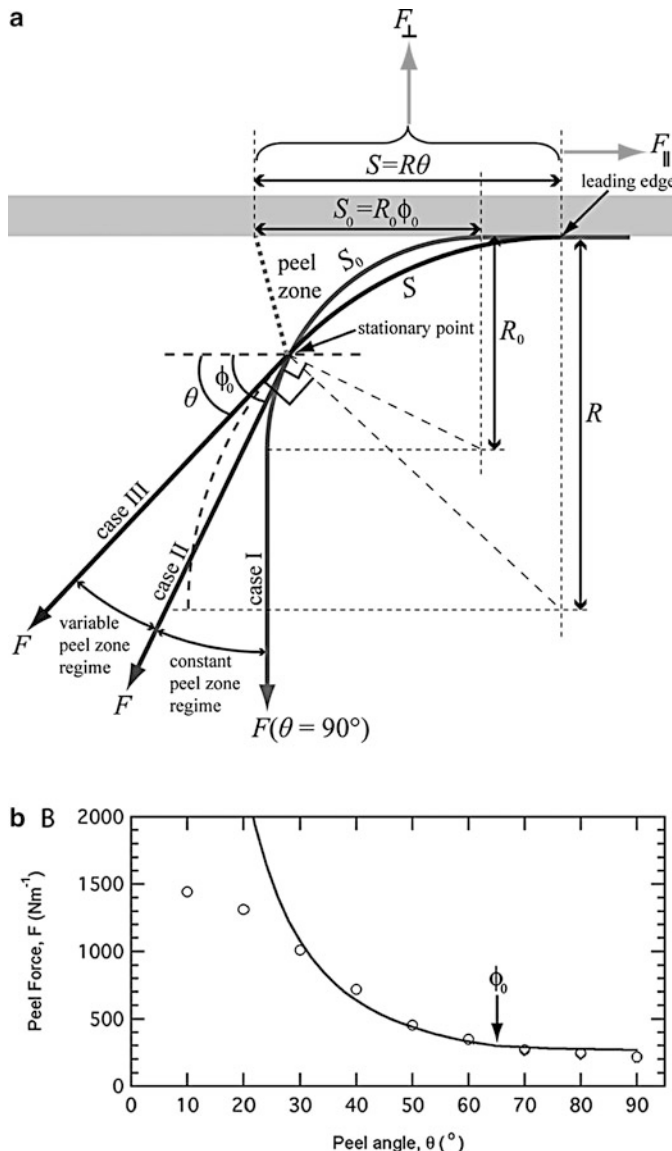


Fig. 11.7 (a) Schematic illustration of the peel zone showing the two peel regimes: constant peel-zone regime and variable peel-zone regimes and (b) plots of predicted (solid line) and measured (data for a tape) peel force, F , as a function of peel angle, θ (Pesika et al., 2007)

behalf of the gecko. However, geckos are not known to groom their feet like beetles (Stork, 1983), nor do they secrete sticky fluids to remove adhering particles like ants (Federle et al., 2002) and tree frogs (Hanna and Barnes, 1991), yet they retain adhesive properties. One potential source of cleaning is during the time when

the lizards undergo molting, or the shedding of the superficial layer of epidermal cells. However, this process only occurs approximately once per month (Van der Kloot, 1992). If molting were the sole source of cleaning, the gecko would rapidly lose its adhesive properties as it was exposed to contaminants in nature (Hansen and Autumn, 2005).

Hansen and Autumn (2005) tested the hypothesis that gecko setae become cleaner with repeated use—a phenomenon known as self-cleaning. The cleaning ability of gecko feet was first tested experimentally by applying 2.5 μm -radius silica–alumina ceramic microspheres to clean setal arrays. Figure 11.8a shows the setal arrays immediately after dirtying and after five simulated steps. It is noted that a significant fraction of the particles has been removed after five steps. The maximum shear stress that these “dirty” arrays could withstand was measured using a sensor. After each step that the gecko took, the shear stress was once again measured. As seen in Fig. 11.8b, after four steps, the gecko foot was clean enough to withstand its own body weight.

In order to understand this cleaning process, substrate–particle interactions must be examined. The interaction energy between a dust particle and a wall and spatulae can be modeled as shown in Fig. 11.9 (Hansen and Autumn, 2005). The interaction energy between a spherical dust particle and the wall, W_{pw} , can be expressed as (Israelachvili, 1992)

$$W_{\text{pw}} = \frac{-H_{\text{pw}} R_p}{6D_{\text{pw}}}, \quad (11.7)$$

where p and w refer to the particle and wall, respectively. H is the Hamaker constant, R_p is the radius of the particle, and D_{pw} is the separation distance between the particle and the wall. Similarly, the interaction energy between a spherical dust particle and a spatula, s , assuming that the spatula tip is spherical is (Israelachvili, 1992)

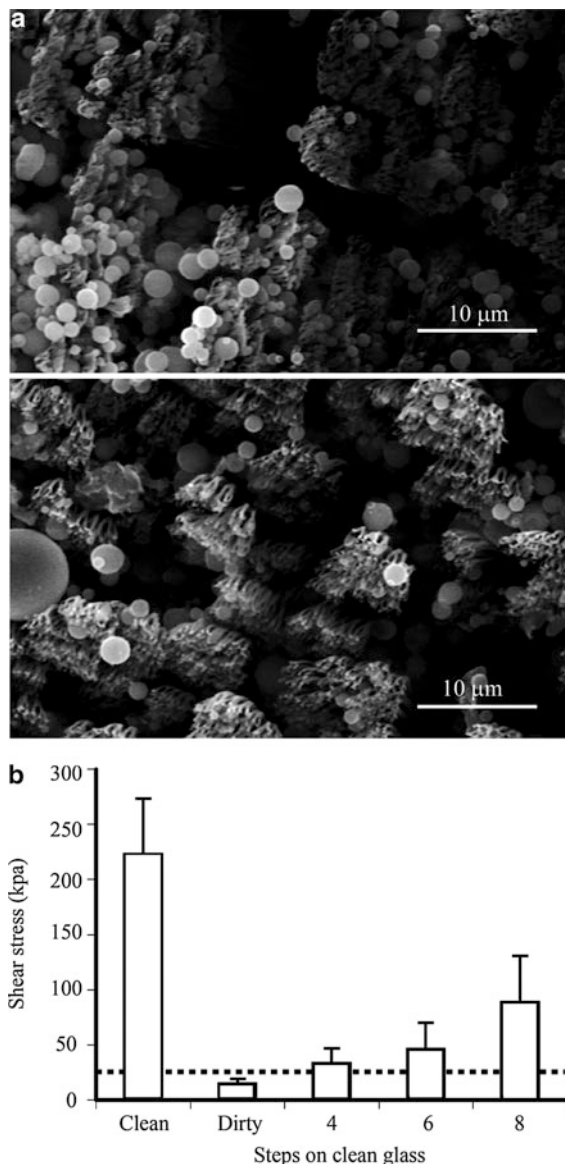
$$W_{\text{ps}} = \frac{-H_{\text{ps}} R_p R_s}{6D_{\text{ps}} (R_p + R_s)}. \quad (11.8)$$

The ratio of the two interaction energies, Z , can be expressed as

$$Z = \frac{W_{\text{pw}}}{W_{\text{ps}}} = \left(1 + \frac{R_p}{R_s}\right) \frac{H_{\text{pw}} D_{\text{ps}}}{H_{\text{ps}} D_{\text{pw}}}. \quad (11.9)$$

When the energy required to separate a particle from the wall is greater than that required to separate it from a spatula ($Z > 1$), self-cleaning will occur. For small contaminants ($R_p < 0.5 \mu\text{m}$), there are not enough spatulae available to adhere to the particle. For larger contaminants, the curvature of the particles makes it impossible for enough spatulae to adhere to it. As a result, Hansen and Autumn (2005) concluded that self-cleaning should occur for all spherical spatulae interacting with all spherical particles.

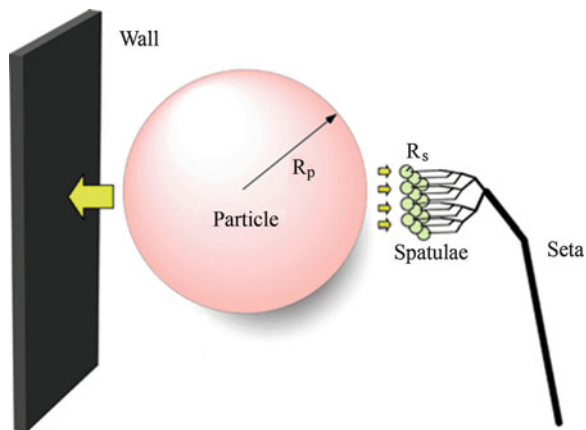
Fig. 11.8 (a) SEM image of spatulae after dirtying with microspheres (*top*) and after five simulated steps (*bottom*) and (b) mean shear stress exerted by a gecko on a surface after dirtying. The *dotted line* represents sufficient recovery to support weight by a single toe (Hansen and Autumn, 2005)



11.4 Attachment Mechanisms

When asperities of two solid surfaces are brought into contact with each other, chemical and/or physical attractions occur. The force developed that holds the two surfaces together is known as adhesion. In a broad sense, adhesion is considered to be either physical or chemical in nature (Bikerman, 1961; Zisman, 1963; Houwink

Fig. 11.9 Model of interactions between gecko spatulae of radius R_s , a spherical dirt particle of radius R_p , and a planar wall that enable self-cleaning (Hansen and Autumn, 2005)



and Salomon, 1967; Israelachvili, 1992; Bhushan, 1996, 1999, 2002, 2010, 2011). Chemical interactions such as electrostatic attraction charges (Schmidt, 1904) as well as intermolecular forces (Hiller, 1968) including van der Waals and capillary forces have all been proposed as potential adhesion mechanisms in gecko feet. Others have hypothesized that geckos adhere to surfaces through the secretion of sticky fluids (Wagler, 1830; Simmermacher, 1884), suction (Simmermacher, 1884), increased frictional force (Hora, 1923), and microinterlocking (Dellit, 1934).

Through experimental testing and observations conducted over the last century and a half, many potential adhesive mechanisms have been eliminated. Observation has shown that geckos lack any glands capable of producing sticky fluids (Wagler, 1830; Simmermacher, 1884), thus ruling out the secretion of sticky fluids as a potential adhesive mechanism. Furthermore, geckos are able to create large adhesive forces normal to a surface. Since friction only acts parallel to a surface, the attachment mechanism of increased frictional force has been ruled out. Dellit (1934) experimentally ruled out suction and electrostatic attraction as potential adhesive mechanisms. Experiments carried out in vacuum did not show a difference between the adhesive force at low pressures compared to ambient conditions. Since adhesive forces generated during suction are based on pressure differentials, which are insignificant under vacuum, suction was rejected as an adhesive mechanism (Dellit, 1934). Additional testing utilized X-ray bombardment to create ionized air in which electrostatic attraction charges would be eliminated. It was determined that geckos were still able to adhere to surfaces in these conditions, and therefore, electrostatic charges could not be the sole cause of attraction (Dellit, 1934). Autumn et al. (2000) demonstrated the ability of a gecko to generate large adhesive forces when in contact with a molecularly smooth SiO_2 microelectromechanical system (MEMS) semiconductor. Since surface roughness is necessary for microinterlocking to occur, it has been ruled out as a mechanism of adhesion. Two mechanisms, van der Waals forces and capillary forces, remain as the potential sources of gecko adhesion. These attachment mechanisms are described in detail in the following sections.

11.4.1 van der Waals Forces

van der Waals bonds are secondary bonds that are weak in comparison to other physical bonds such as covalent, hydrogen, ionic, and metallic bonds. Unlike other physical bonds, van der Waals forces are always present regardless of separation and are effective from very large separations (~ 50 nm) down to atomic separation (~ 0.3 nm). The van der Waals force per unit area between two parallel surfaces, f_{vdW} , is given by (Hamaker, 1937; Israelachvili and Tabor, 1972; Israelachvili, 1992)

$$f_{\text{vdW}} = \frac{H}{6\pi D^3} \quad \text{for } D < 30 \text{ nm}, \quad (11.10)$$

where H is the Hamaker constant and D is the separation between surfaces.

Hiller (1968) showed experimentally that the surface energy of a substrate is responsible for gecko adhesion. One potential adhesion mechanism would then be van der Waals forces (Stork, 1980; Autumn et al., 2000). Assuming van der Waals forces to be the dominant adhesion mechanism utilized by geckos, the adhesion force of a gecko can be calculated. Typical values of the Hamaker constant range from 4×10^{-20} to 4×10^{-19} J (Israelachvili, 1992). In calculation, the Hamaker constant is assumed to be 10^{-19} J, the surface area of a spatula is taken to be 2×10^{-14} m² (Ruibal and Ernst, 1965; Williams and Peterson, 1982; Autumn and Peattie, 2002), and the separation between the spatula and contact surface is estimated to be 0.6 nm. This equation yields the force of a single spatula to be about 0.5 μ N. By applying the surface characteristics of Table 11.1, the maximum adhesion force of a gecko is 150–1,500 N for varying spatula density of 100–1,000 spatulae per seta. If an average value of 550 spatulae/seta is used, the adhesion force of a single seta is approximately 270 μ N, which is in agreement with the experimental value obtained by Autumn et al. (2000), which will be discussed in Sect. 11.5.1.1.

Another approach to calculate adhesion force is to assume that spatulae are cylinders that terminate in hemispherical tips. By using (11.2) and assuming that the radius of each spatula is about 100 nm and that the surface energy is expected to be 50 mJ/m² (Arzt et al., 2003), the adhesive force of a single spatula is predicted to be 0.02 μ N. This result is an order of magnitude lower than the first approach calculated for the higher value of A . For a lower value of 10^{-20} J for the Hamaker constant, the adhesive force of a single spatula is comparable to that obtained using the surface energy approach.

Several experimental results favor van der Waals forces as the dominant adhesive mechanism, including temperature testing (Bergmann and Irschick, 2005) and adhesion force measurements of a gecko seta with both hydrophilic and hydrophobic surfaces (Autumn et al., 2000). This data will be presented in the Sects. 11.5.2–11.5.4.

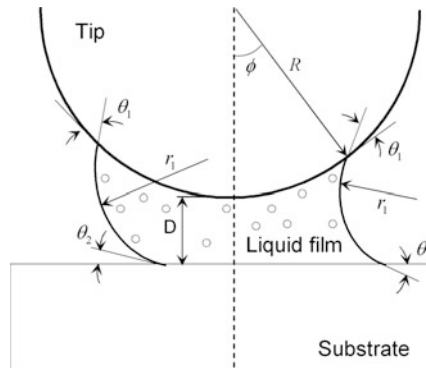


Fig. 11.10 Schematic of a sphere on a plane at distance D with a liquid film in between, forming menisci. In this figure, R is the tip radius, ϕ is the filling angle, θ_1 and θ_2 are contact angles on sphere and plane, respectively, and r_1 and r_2 are the two principal radii of the curved surface in two orthogonal planes (Kim and Bhushan, 2008)

11.4.2 Capillary Forces

It has been hypothesized that capillary forces that arise from liquid-mediated contact could be a contributing or even the dominant adhesive mechanism utilized by gecko spatulae (Hiller, 1968; Stork, 1980). Experimental adhesion measurements (presented later in Sects. 11.5.3 and 11.5.4) conducted on surfaces with different hydrophobicities and at various humidities (Huber et al., 2005b) as well as numerical simulations (Kim and Bhushan, 2008) support this hypothesis as a contributing mechanism. During contact, any liquid that wets or has a small contact angle on surfaces will condense from vapor in the form of an annular-shaped capillary condensate. Due to the natural humidity present in the air, water vapor will condense to liquid on the surface of bulk materials. During contact, this will cause the formation of adhesive bridges (menisci) due to the proximity of the two surfaces and the affinity of the surfaces for condensing liquid (Zimon, 1969; Fan and O'Brien, 1975; Phipps and Rice, 1979).

In the adhesion model with capillarity by Kim and Bhushan (2008), the tip of the spatula in a single contact was assumed as spherical; see Fig. 11.10. The total adhesion force between a spherical tip and a plane consists of the capillary force and the solid-to-solid interaction. Capillary force can be divided into two components: the Laplace force F_L and the surface tension force F_s , such that the total capillary force F_c

$$F_c = F_L + F_s. \quad (11.11)$$

The Laplace force is caused by the pressure difference across the interface of a curved liquid surface (Fig. 11.10) and depends on the pressure difference multiplied by the meniscus area, which can be expressed as (Orr et al. 1975)

$$F_L = -\pi\kappa\gamma R^2 \sin^2 \phi, \quad (11.12)$$

where γ is the surface tension of the liquid, R is the tip radius, ϕ is the filling angle, and κ is the mean curvature of the meniscus. From the Kelvin equation ([Israelachvili, 1992](#)), which is the thermal equilibrium relation, the mean curvature of the meniscus can be determined as

$$\kappa = \frac{\mathfrak{R}T}{V\gamma} \ln \left(\frac{p}{p_0} \right), \quad (11.13)$$

where \mathfrak{R} is the universal gas constant, T is the absolute temperature, V is the molecular volume, p_0 is the saturated vapor pressure of the liquid at T , and p is the ambient pressure acting outside the curved surface (p/p_0 is the relative humidity). [Orr et al. \(1975\)](#) formulated the mean curvature of a meniscus between a sphere and a plane in terms of elliptic integrals. The filling angle ϕ can be calculated from the expression just mentioned and (11.13) using the iteration method. Then, the Laplace force is calculated at a given environment using (11.12).

The surface tension of the liquid results in the formation of a curved liquid–air interface. The surface tension force acting on the sphere is ([Orr et al. 1975](#))

$$F_s = 2\pi R\gamma \sin \phi \sin(\theta_1 + \phi), \quad (11.14)$$

where θ_1 is the contact angle on the sphere.

Hence, the total capillary force on the sphere is

$$F_c = \pi R\gamma \{2 \sin \phi \sin(\theta_1 + \phi) - \kappa R \sin^2 \phi\}. \quad (11.15)$$

The effect of capillarity on gecko adhesion results will be presented in Sect. [11.6.4](#).

11.5 Adhesion Measurements and Data

Experimental measurements of the adhesion force of a single gecko seta ([Autumn et al., 2000](#)) and single gecko spatula ([Huber et al., 2005a](#)) have been made. The effect of the environment including temperature ([Losos, 1990; Bergmann and Irschick, 2005](#)) and humidity ([Huber et al., 2005b](#)) has been studied. Some of the data has been used to understand the adhesion mechanism utilized by the gecko attachment system—van der Waals or capillary forces. The majority of experimental results point toward van der Waals forces as the dominant mechanism of adhesion ([Autumn et al., 2000; Bergmann and Irschick, 2005](#)). Some research suggests that capillary forces can be a contributing adhesive factor ([Huber et al., 2005b; Kim and Bhushan, 2008](#)).

11.5.1 Adhesion Under Ambient Conditions

Two feet of a Tokay gecko are capable of producing about 20 N of adhesive force with a pad area of about 220 mm² (Irschick et al., 1996). Assuming that there are about 14,000 setae per mm², the adhesion force from a single hair should be approximately 7 μN. It is likely that the magnitude is actually greater than this value because it is unlikely that all setae are in contact with the mating surface (Autumn et al., 2000). Setal orientation greatly influences adhesive strength. This dependency was first noted by Autumn et al. (2000). It was determined that the greatest adhesion occurs at 30°. In order to determine the adhesion mechanism(s) utilized by gecko feet, it is important to know the adhesion force of a single seta. Hence, the adhesion force of gecko foot hair has been the focus of several investigations (Autumn et al., 2000; Huber et al., 2005a).

11.5.1.1 Adhesion Force of a Single Seta

Autumn et al. (2000) used both a microelectromechanical (MEMS) force sensor and a wire as a force gauge to determine the adhesion force of a single seta. The MEMS force sensor is a dual-axis atomic force microscope (AFM) cantilever with independent piezoresistive sensors which allows simultaneous detection of vertical and lateral forces (Chui et al., 1998). The wire force gauge consisted of an aluminum bonding wire that displaced under a perpendicular pull. Autumn et al. (2000) discovered that setal force actually depends on the three-dimensional orientation of the seta as well as the preloading force applied during initial contact. Setae that were preloaded vertically to the surface exhibited only one-tenth of the adhesive force ($0.6 \pm 0.7 \mu\text{N}$) compared to setae that were pushed vertically and then pulled horizontally to the surface ($13.6 \pm 2.6 \mu\text{N}$). The dependence of the adhesion force of a single gecko spatula on perpendicular preload is illustrated in Fig. 11.11. The adhesion force increases linearly with the preload, as expected (Bhushan, 1996, 1999, 2002). The maximum adhesion force of a single gecko foot hair occurred when the seta was first subjected to a normal preload and then slid 5 μm along the contacting surface. Under these conditions, adhesion force measured $194 \pm 25 \mu\text{N}$ (~10 atm adhesive pressure).

11.5.1.2 Adhesive Force of a Single Spatula

Huber et al. (2005a) used atomic force microscopy to determine the adhesion force of an individual gecko spatulae. A seta with four spatulae was glued to an AFM tip. The seta was then brought in contact with a surface, and a compressive preload of 90 nN was applied. The force required to pull the seta off of the surface was then measured. As seen in Fig. 11.12, there are two distinct peaks on the graph—one at 10 nN and the other at 20 nN. The first peak corresponds to one of the four spatulae

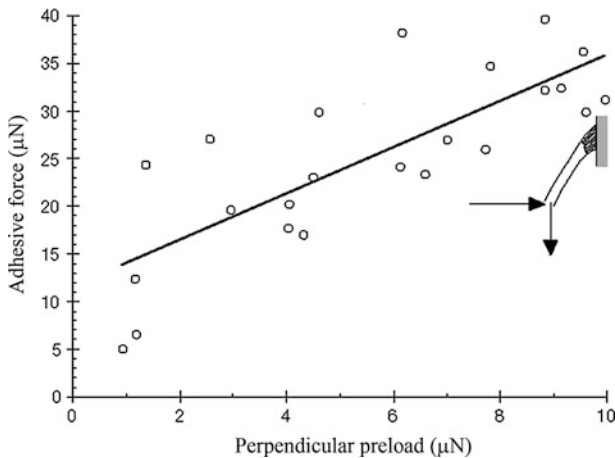


Fig. 11.11 Adhesive force of a single gecko seta as a function of applied preload. The seta was first pushed perpendicularly against the surface and then pulled parallel to the surface (Autumn et al., 2000)

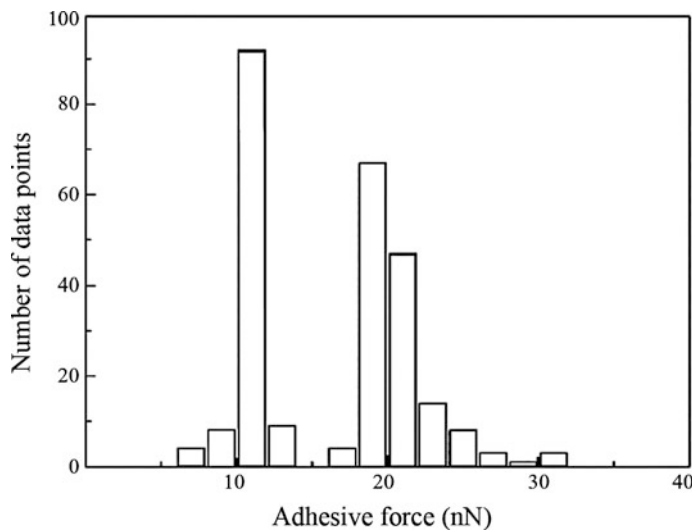


Fig. 11.12 Adhesive force of a single gecko spatula. The peak at 10 nN corresponds to the adhesive force of one spatula, and the peak at 20 nN corresponds to the adhesive force of two spatulae (Huber et al., 2005a)

adhering to the contact surface, while the peak at 20 nN corresponds to two of the four spatulae adhering to the contact surface. The average adhesion force of a single spatula was found to be 10.8 ± 1 nN. The measured value is in agreement with the measured adhesive strength of an entire gecko (on the order of 10^9 spatulae on a gecko).

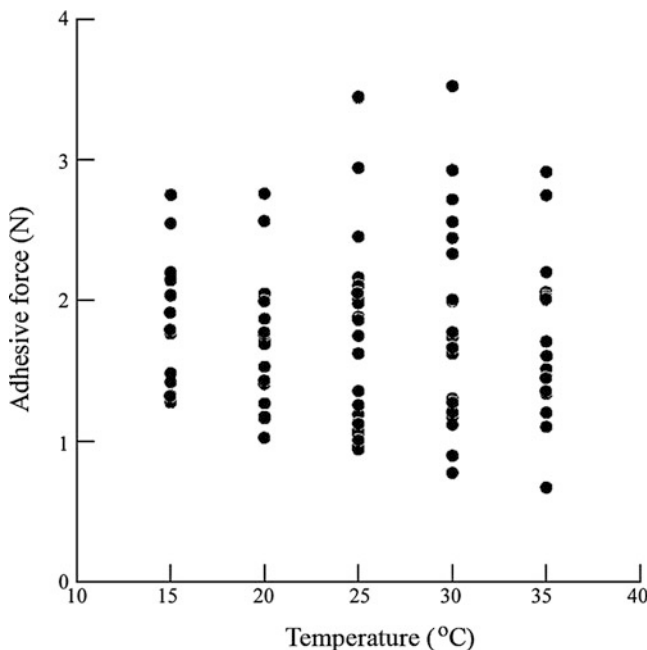


Fig. 11.13 Adhesive force of a gecko as a function of temperature (Bergmann and Irschick, 2005)

11.5.2 Effects of Temperature

Environmental factors are known to affect several aspects of vertebrate function, including speed of locomotion, digestion rate, and muscle contraction, and as a result, several studies have been completed to investigate environmental impact on these functions. Relationships between the environment and other properties such as adhesion are far less studied (Bergmann and Irschick, 2005). Only two known studies exist that examine the effect of temperature on the clinging force of the gecko (Losos, 1990; Bergmann and Irschick, 2005). Losos (1990) examined the adhesion ability of large live geckos at temperatures up to 17°C. Bergmann and Irschick (2005) expanded upon this research for body temperatures ranging from 15 to 35°C. The geckos were incubated until their body temperature reached a desired level. The clinging ability of these animals was then determined by measuring the maximum exerted force by the geckos as they were pulled off a custom-built force plate. The clinging force of a gecko for the experimental test range is plotted in Fig. 11.13. It was determined that variation in temperature is not statistically significant in the adhesion force of a gecko. From these results, it was concluded that the temperature independence of adhesion supports the hypothesis of clinging as a passive mechanism (i.e., van der Waals forces). Both studies only measured the overall clinging ability on the macroscale. There have not been any

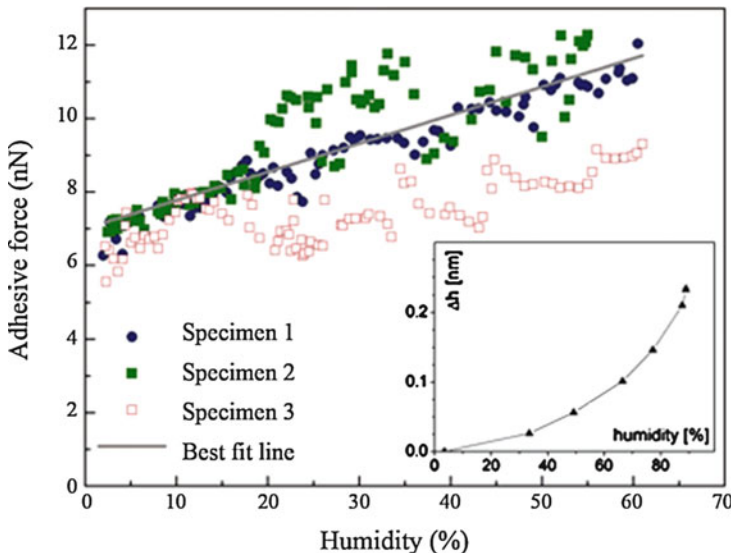


Fig. 11.14 Humidity effects on spatular pull-off force (inset). The increase in water film thickness on a Si wafer with increasing humidity (Huber et al., 2005b)

investigations into the effects of temperature on the clinging ability of a single seta on the microscale, and therefore, testing in this area would be extremely important.

11.5.3 Effects of Humidity

Huber et al. (2005b) employed similar methods to Huber et al. (2005a) (discussed previously in Sect. 11.5.1.2) in order to determine the adhesive force of a single spatula at varying humidity. Measurements were made using an AFM placed in an air-tight chamber. The humidity was adjusted by varying the flow rate of dry nitrogen into the chamber. The air was continuously monitored with a commercially available hygrometer. All tests were conducted at ambient temperature.

As seen in Fig. 11.14, even at low humidity, adhesion force is large. An increase in humidity further increases the overall adhesion force of a gecko spatula. The pull-off force roughly doubled as the humidity was increased from 1.5% to 60%. This humidity effect can be explained in two possible ways (1) by standard capillarity or (2) by a change of the effective short-range interaction due to absorbed monolayers of water—in other words, the water molecules increase the number of van der Waals bonds that are made. Based on this data, van der Waals forces are the primary adhesion mechanism, and capillary forces are a secondary adhesive mechanism.

11.5.4 Effects of Hydrophobicity

To further test the hypothesis, the capillary forces play a role in gecko adhesion, the spatular pull-off force was determined for contact with both hydrophilic and hydrophobic surfaces. As seen in Fig. 11.15a, the capillary adhesion theory predicts that a gecko spatula will generate a greater adhesion force when in contact with a hydrophilic surface as compared to a hydrophobic surface, while the van der Waals adhesion theory predicts that the adhesion force between a gecko spatula and a surface will be the same regardless of the hydrophobicity of the surface (Autumn et al., 2002). Figure 11.15b shows the shear stress of a whole gecko and adhesive force of a single seta on hydrophilic and hydrophobic surfaces. The data shows that the adhesion values are the same on both surfaces. This supports the van der Waals prediction of Fig. 11.15a. Huber et al. (2005b) found that the hydrophobicity of the attachment surface had an effect on the adhesion force of a single gecko spatula as shown in Fig. 11.15c. These results show that adhesion force has a finite value for a superhydrophobic surface and increases as the surface becomes hydrophilic. It is concluded that van der Waals forces are the primary mechanism, and capillary forces further increase the adhesion force generated.

11.6 Adhesion Modeling of Fibrillar Structures

With regard to the natural living conditions of the animals, the mechanics of gecko attachment can be separated into two parts: the mechanics of adhesion of a single contact with a flat surface and an adaptation of a large number of spatulae to a natural, rough surface. Modeling of the mechanics of adhesion of spatulae to a smooth surface, in the absence of meniscus formation, was developed by Autumn et al. (2002), Jagota and Bennison (2002), and Arzt et al. (2003). As discussed previously in Sect. 11.3.2, the adhesion force of multiple contacts F'_{ad} can be increased by dividing the contact into a large number (n) of small contacts, while the nominal area of the contact remains the same, $F'_{\text{ad}} \sim \sqrt{n} F_{\text{ad}}$. However, this model only considers contact with a flat surface. On natural, rough surfaces, the compliance and adaptability of setae are the primary sources of high adhesion. As stated earlier, the hierarchical structure of gecko setae allows for a greater contact with a natural, rough surface than a non-branched attachment system (Sitti and Fearing, 2003).

Bhushan et al. (2006) and Kim and Bhushan (2007a, b, c, 2008) have approximated a gecko seta in contact with random rough surfaces using a hierarchical spring model. Each level of springs in their model corresponds to a level of seta hierarchy. The upper level of springs corresponds to the thicker part of gecko seta, the middle spring level corresponds to the branches, and the lower level of springs corresponds to the spatulae. The upper level is the thickest branch of the seta. It is 75 μm in length and 5 μm in diameter. The middle level, referred to as a branch, has a length of 25 μm and a diameter of 1 μm . The lower level, called a spatula, is the thinnest

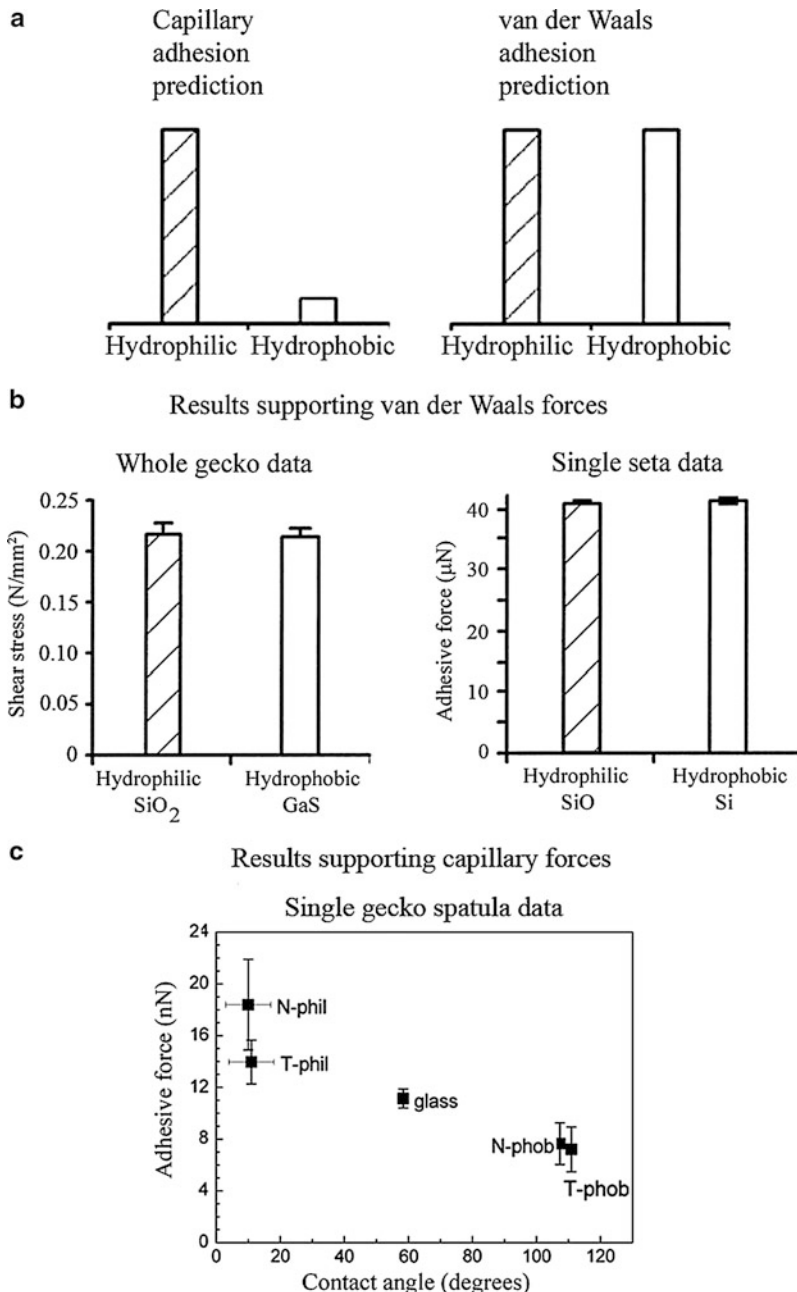


Fig. 11.15 (a) Capillary and van der Waals adhesion predictions for the relative magnitude of the adhesive force of gecko setae with hydrophilic and hydrophobic surfaces (Autumn et al., 2002). (b) Results of adhesion testing for a whole gecko and single seta with hydrophilic and hydrophobic surfaces (Autumn et al., 2002) and (c) results of adhesive force testing of a single gecko spatula with surfaces with different contact angles (Huber et al., 2005b)

Table 11.3 Geometrical size, calculated stiffness, and typical densities of branches of seta for *Tokay gecko* (Kim and Bhushan, 2007a)

Level of seta	Length (μm)	Diameter (μm)	Bending stiffness ^a (N/m)	Typical density (#/ mm^2)
III upper	75	5	2.908	14×10^3
II middle	25	1	0.126	—
I lower	2.5	0.1	0.0126	$1.4 - 14 \times 10^6$

^aFor elastic modulus of 10 GPa with load applied at 60° to spatula long axis

branch with a length of $2.5 \mu\text{m}$ and a diameter of about $0.1 \mu\text{m}$ (Table 11.3). As reported earlier, Autumn et al. (2000) showed that the optimal attachment angle between the substrate and a gecko seta is 30° in the single seta pull-off experiment. This finding is supported by the adhesion models of setae as cantilever beams (Shah and Sitti, 2004; Gao et al. 2005) (see Sect. 11.3.3 for more details). Therefore, θ was fixed at 30° in the studies by Bhushan et al. (2006) and Kim and Bhushan (2007a, b, c, 2008) presented below.

11.6.1 Single Spring Contact Analysis

In their analysis, Bhushan et al. (2006) and Kim and Bhushan (2007a, b, c, 2008) assumed the tip of the spatula in a single contact to be spherical. The springs on every level of hierarchy have the same stiffness as the bending stiffness of the corresponding branches of seta. If the beam is oriented at an angle, θ , to the substrate and the contact load F is aligned normal to the substrate, its components along and tangential to the direction of the beam, $F \cos \theta$ and $F \sin \theta$, give rise to bending and compressive deformations, δ_b and δ_c , respectively, as (Young and Budynas, 2001)

$$\delta_b = \frac{F \cos \theta l_m^3}{3EI}, \quad \delta_c = \frac{F \sin \theta l_m}{A_c E}, \quad (11.16)$$

where $I = \pi R_m^4 / 4$ and $A_c = \pi R_m^2$ are the moments of inertia of the beam and the cross-sectional area, respectively, l_m and R_m are the length and the radius of seta branches, respectively, and m is the level number. The net displacement, δ_\perp normal to the substrate, is given by

$$\delta_\perp = \delta_c \sin \theta + \delta_b \cos \theta. \quad (11.17)$$

Using (11.16) and (11.17), the stiffness of seta branches, k_m , is calculated as (Glassmaker et al., 2004)

$$k_m = \frac{\pi R_m^2 E}{l_m \sin^2 \theta \left(1 + \frac{4l_m^2 \cot^2 \theta}{3R_m^2} \right)}. \quad (11.18)$$

For an assumed elastic modulus, E , of seta material of 10 GPa with a load applied at an angle of 60° to spatulae long axis, Kim and Bhushan (2007a) calculated the stiffness of every level of seta as given in Table 11.3.

In the model, both the tips of a spatula and the asperity summits of the rough surface are assumed to be spherical with a constant radius (Bhushan et al., 2006). As a result, a single spatula adhering to a rough surface was modeled as the interaction between two spherical tips. Because β -keratin has a high elastic modulus (Russell, 1986; Bertram and Gosline, 1987), the adhesion force between two round tips was calculated according to the Derjaguin–Muller–Toporov (DMT) theory (Derjaguin et al., 1975) as

$$F_{\text{ad}} = 2\pi R_c W_{\text{ad}}, \quad (11.19)$$

where R_c is the reduced radius of contact, which is calculated as $R_c = (1/R_1 + 1/R_2)^{-1}$; R_1, R_2 —radii of contacting surfaces; and $R_1 = R_2$, $R_c = R/2$. The work of adhesion, W_{ad} , is then calculated using the following equation for two flat surfaces separated by a distance, D , (Israelachvili, 1992):

$$W_{\text{ad}} = -\frac{H}{12\pi D^2}, \quad (11.20)$$

where H is the Hamakar constant which depends on the medium between the two surfaces. Typical values of the Hamakar constant for polymers are $H_{\text{air}} = 10^{-19}$ J in the air and $H_{\text{water}} = 3.7 \times 10^{-20}$ J in the water (Israelachvili, 1992). For a gecko seta, which is composed of β -keratin, the value of H is assumed to be 10^{-19} J. The works of adhesion of two surfaces in contact separated by an atomic distance $D \approx 0.2$ nm is approximately equal to 66 mJ/m² (Israelachvili, 1992). By assuming that the tip radius, R , is 50 nm, using (11.19), the adhesion force of a single contact is calculated as 10 nN (Kim and Bhushan, 2007a). This value is identical to the adhesion force of a single spatula measured by Huber et al. (2005a). This adhesion force is used as a critical force in the model for judging whether the contact between the tip and the surface is broken or not during pull-off cycle (Bhushan et al., 2006). If the elastic force of a single spring is less than the adhesion force, the spring is regarded as having been detached.

11.6.2 The Multilevel Hierarchical Spring Analysis

In order to study the effect of the number of hierarchical levels in the attachment system on attachment ability, models with one (Bhushan et al., 2006; Kim and Bhushan, 2007a, b), two (Bhushan et al., 2006; Kim and Bhushan, 2007a, b), and three (Kim and Bhushan, 2007a, b) levels of hierarchy were simulated (Fig. 11.16). The one-level model has springs with length $l_1 = 2.5 \mu\text{m}$ and stiffness $k_1 = 0.0126 \text{ N/m}$. The length and stiffness of the springs in the two-level model are $l_1 = 2.5 \mu\text{m}$, $k_1 = 0.0126 \text{ N/m}$ and $l_{II} = 25 \mu\text{m}$, $k_{II} = 0.126 \text{ N/m}$ for levels

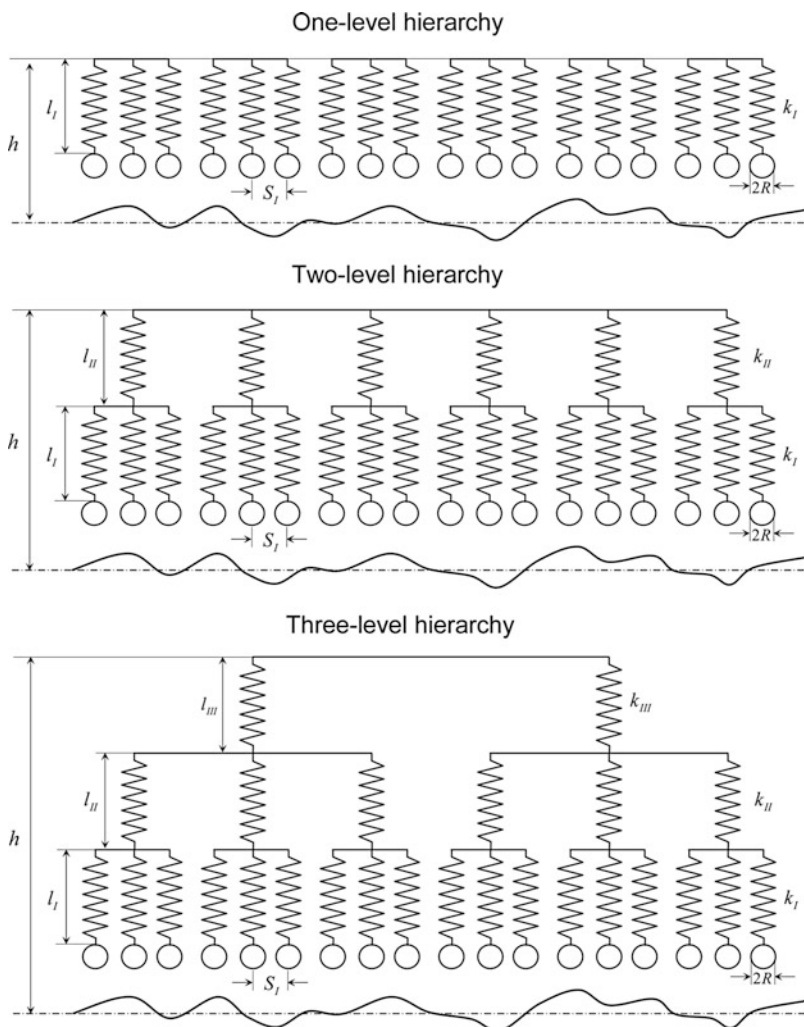


Fig. 11.16 One-, two-, and three-level hierarchical spring models for simulating the effect of hierarchical morphology on interaction of a seta with a rough surface. In this figure, $l_{I,II,III}$ are lengths of structures; s_I is space between spatulae; $k_{I,II,III}$ are stiffnesses of structures; I, II, and III are level indexes; R is radius of tip; and h is distance between upper spring base of each model and mean line of the rough profile (Kim and Bhushan, 2007a)

I and II, respectively. The three-level model has additional upper level springs with $l_{III} = 75 \mu\text{m}$, $k_{III} = 2.908 \text{ N/m}$ on the springs of the two-level model, which is identical to gecko setae. The base of the springs and the connecting plate between the levels are assumed to be rigid. The distance S_I between the neighboring structures of level I is $0.35 \mu\text{m}$, obtained from the average value of measured

spatula density, $8 \times 10^6 \text{ mm}^{-2}$, calculated by multiplying 14,000 setae/mm² by an average of 550 spatula/seta (Schleich and Kästle, 1986) (Table 11.3). A 1:10 proportion of the number of springs in the upper level to that in the level below was assumed (Bhushan et al., 2006). This corresponds to one spring at level III which is connected to ten springs on level II, and each spring on level II is connected with ten springs on level I. The number of springs on level I considered in the model is calculated by dividing the scan length (2,000 μm) with the distance S_I (0.35 μm), which corresponds to 5,700.

The spring deflection Δl was calculated as

$$\Delta l = h - l_0 - z, \quad (11.21)$$

where h is the position of the spring base relative to the mean line of the surface; l_0 is the total length of a spring structure which is $l_0 = l_I$ for the one-level model, $l_0 = l_I + l_{II}$ for the two-level model, and $l_0 = l_I + l_{II} + l_{III}$ for the three-level model; and z is the profile height of the rough surface. The elastic force F_{el} arisen in the springs at a distance h from the surface was calculated for the one-level model as (Bhushan et al., 2006)

$$F_{\text{el}} = -k_I \sum_{i=1}^p \Delta l_i u_i \quad u_i = \begin{cases} 1 & \text{if contact} \\ 0 & \text{if no contact} \end{cases}, \quad (11.22)$$

where p is the number of springs in level I of the model. For the two-level model, the elastic force was calculated as (Bhushan et al., 2006)

$$F_{\text{el}} = - \sum_{j=1}^q \sum_{i=1}^p k_{ji} (\Delta l_{ji} - \Delta l_j) u_{ji} \quad u_{ji} = \begin{cases} 1 & \text{if contact} \\ 0 & \text{if no contact} \end{cases}, \quad (11.23)$$

where q is the number of springs in level II of the model. For the three-level model, the elastic force was calculated as (Kim and Bhushan, 2007a)

$$F_{\text{el}} = - \sum_{k=1}^r \sum_{j=1}^q \sum_{i=1}^p k_{kji} (\Delta l_{kji} - \Delta l_{kj} - \Delta l_j) u_{kji} \quad u_{kji} = \begin{cases} 1 & \text{if contact} \\ 0 & \text{if no contact} \end{cases}, \quad (11.24)$$

where r is the number of springs in level III of the model. The spring force when the springs approach the rough surface is calculated using either (11.22), (11.23), or (11.24) for one-, two-, and three-level models, respectively. During pull-off, the same equations are used to calculate the spring force. However, when the applied load is equal to zero, the springs do not detach due to the adhesion attraction given by (11.19). The springs are pulled apart when pull-off force is equal to adhesion force at the interface. The adhesion force is the lowest value of elastic force F_{el} when the seta has detached from the contacting surface.

The adhesion energy is calculated as

$$W_{\text{ad}} = \int_{\bar{D}}^{\infty} F_{\text{el}}(D) dD, \quad (11.25)$$

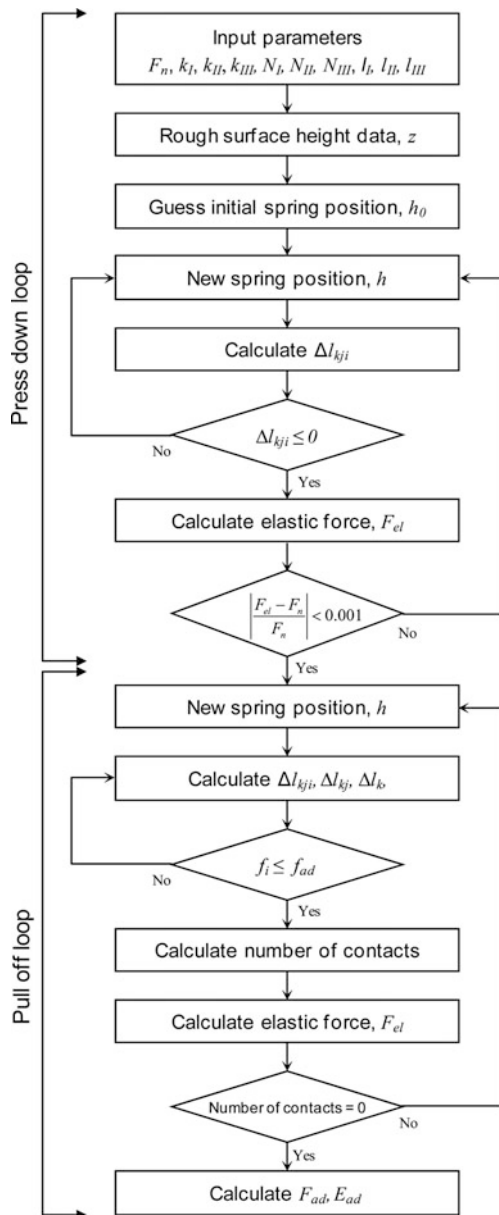
where D is the distance that the spring base moves away from the contacting surface. The lower limit of the distance \bar{D} is the value of D where F_{el} is first zero when the model is pulled away from the contacting surface. Also, although the upper limit of the distance is infinity, in practice, the $F_{\text{el}}(D)$ curve is integrated to an upper limit where F_{el} increases from a negative value to zero. Figure 11.17 shows the flow chart for the calculation of the adhesion force and the adhesion energy employed by [Kim and Bhushan \(2007a\)](#).

The random rough surfaces used in the simulations were generated on a computer ([Bhushan, 1999, 2002](#)). Several natural (sycamore tree bark and siltstone) and artificial (drywall, wood, laminate, steel, aluminum, and glass) surfaces were chosen to determine the surface parameters of typical rough surfaces that a gecko might encounter. Two-dimensional profiles of surfaces were obtained using a stylus profiler for two scan lengths: 80 μm , which is approximately the size of a single gecko seta and 2,000 μm , which is close to the size of a gecko lamellae ([Bhushan et al., 2006](#)). Surface roughness parameters (root mean square (RMS) amplitude σ and correlation length β^*) for scan lengths of 80 and 2,000 μm are presented in Table 11.4. The roughness parameters are scale dependent, and therefore, adhesion values also are expected to be scale dependent. As the scan length was increased, the measured values of RMS amplitude and correlation length both increased. At a scale length of 80 μm (size of seta), the roughness amplitude does not exceed 5 μm , while at a scale length of 2,000 μm (size of lamella), the roughness amplitude is as high as 30 μm . This suggests that setae should adapt to surfaces with roughness on the order of several microns, while lamellae should adapt to roughness on the order of tens of microns. Larger roughness values would be adapted to by the skin of the gecko. The range of values of σ from 0.01 μm to 30 μm and a fixed value of $\beta^* = 200 \mu\text{m}$ were used for modeling the contact of a seta with random rough surfaces. The chosen range covers values of roughnesses for relatively smooth, artificial surfaces to natural, rough surfaces.

11.6.3 Adhesion Results of the Multilevel Hierarchical Spring Model

The multilevel hierarchical spring model was developed by [Kim and Bhushan \(2007a\)](#). They obtained various useful results which will be presented next. Figure 11.18a shows the calculated spring force-distance curves for the one-, two-, and three-level hierarchical models in contact with rough surfaces of different values of root mean square (RMS) amplitude σ ranging from $\sigma = 0.01 \mu\text{m}$ to $\sigma = 30 \mu\text{m}$ at an applied load of 1.6 μN which was derived from the gecko's weight. When the

Fig. 11.17 Flowchart for the calculation of the adhesion force (F_{ad}) and the adhesion energy (E_{ad}) for three-level hierarchical spring model. In this figure, F_n is an applied load; $k_{I,II,III}$ and $l_{I,II,III}$ are stiffnesses and lengths of structures; Δl_{kji} , Δl_{ki} , and Δl_k are the spring deformations on level I, II, and III, respectively; i , j , and k are spring indexes on each level; f_i is the elastic force of a single spring; and f_{ad} is the adhesion force of a single contact (Kim and Bhushan, 2007a)



spring model is pressed against the rough surface, contact between the spring and the rough surface occurs at point A; as the spring tip presses into the contacting surface, the force increases up to point B, B', or B''. During pull-off, the spring relaxes, and the spring force passes an equilibrium state (0 N); tips break free of adhesion forces at point C, C', or C'' as the spring moves away from the surface.

Table 11.4 Scale dependence of surface parameters σ and β^* for rough surfaces at scan lengths of 80 μm and 2,000 μm (Bhushan et al., 2006)

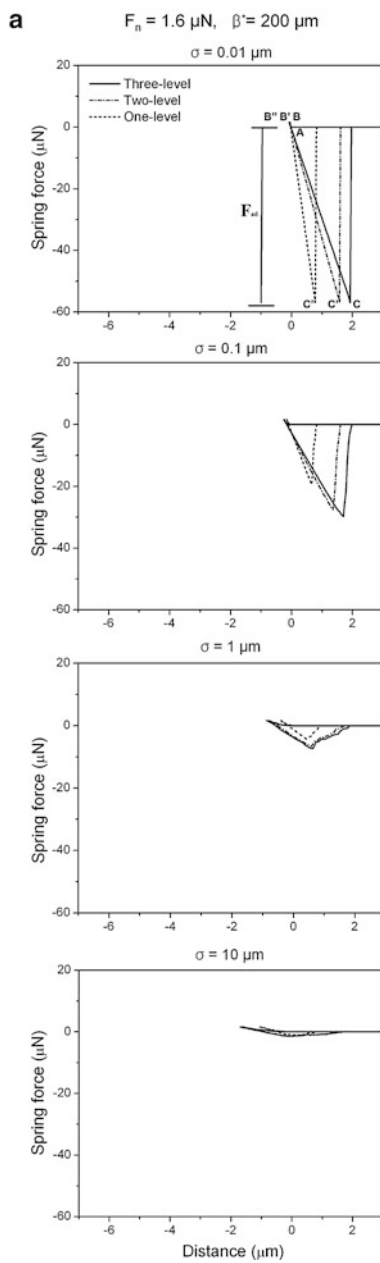
Scan length	80 μm		2,000 μm		
	Surface	$\sigma(\mu\text{m})$	$\beta^*(\mu\text{m})$	$\sigma(\mu\text{m})$	$\beta^*(\mu\text{m})$
Sycamore tree bark	4.4	17	27	251	
Siltstone	1.1	4.8	11	268	
Painted drywall	1	11	20	93	
Wood laminate	0.11	18	3.6	264	
Polished steel	0.07	12	0.40	304	
Polished 2024 aluminum	0.40	6.5	0.50	222	
Glass	0.01	2.2	0.02	152	

The perpendicular distance from C, C' or C'' to zero is the adhesion force. The data in Fig. 11.5 show that adhesion forces for various levels of hierarchy are comparable when in contact with a smooth surface. However, the adhesion force for the three-level is the largest when in contact with a rough surface. Thus, multilevel hierarchy facilitates adaptability to various rough surfaces.

Adhesion energy stored during contact can be obtained by calculating the area of the triangle during the unloading part of the curves (11.25). Using the spring force-distance curves, Kim and Bhushan (2007a) calculated the adhesion coefficient, the number of contacts per unit length, and the adhesion energy per unit length of the one-, two-, and three-level models for an applied load of 1.6 μN and a wide range of RMS roughness (σ), as seen in the left graphs of Fig. 11.18b. The adhesion coefficient, defined as the ratio of pull-off force to applied preload, represents the strength of adhesion with respect to the preload. For the applied load of 1.6 μN , which corresponds to the weight of a gecko, the maximum adhesion coefficient is about 36 when σ is smaller than 0.01 μm . This means that a gecko can generate enough adhesion force to support 36 times its body weight. However, if σ is increased to 1 μm , the adhesion coefficient for the three-level model is reduced to 4.7. It is noteworthy that the adhesion coefficient falls below 1 when the contacting surface has an RMS roughness σ greater than 10 μm . This implies that the attachment system is no longer capable of supporting the gecko's weight. Autumn et al. (2000, 2002) showed that in isolated gecko setae contacting with the surface of a single crystalline silicon wafer, a 2.5 μN preload yielded adhesion of 20–40 μN and thus, a value of adhesion coefficient of 8–16, which supports the simulation results of Kim and Bhushan (2007a).

Figure 11.18b (top left) shows that the adhesion coefficient for the one-level model is lower than that for the three-level model, but there is only a small difference between the values of the two- and three-level models. In order to show the effect of stiffness, the results for the three-level model with springs in level III of which the stiffness is 10 times smaller than that of original level III springs are plotted. It can be seen that the three-level model with a third-level stiffness of 0.1 k_{III} has a 20–30% higher adhesion coefficient than the three-level model. The results also show that the trends in the number of contacts are similar to that of the adhesive force. The

The effect of multi-level hierarchical structure

**Fig. 11.18** (continued)

b

The effect of multi-level hierarchical structure

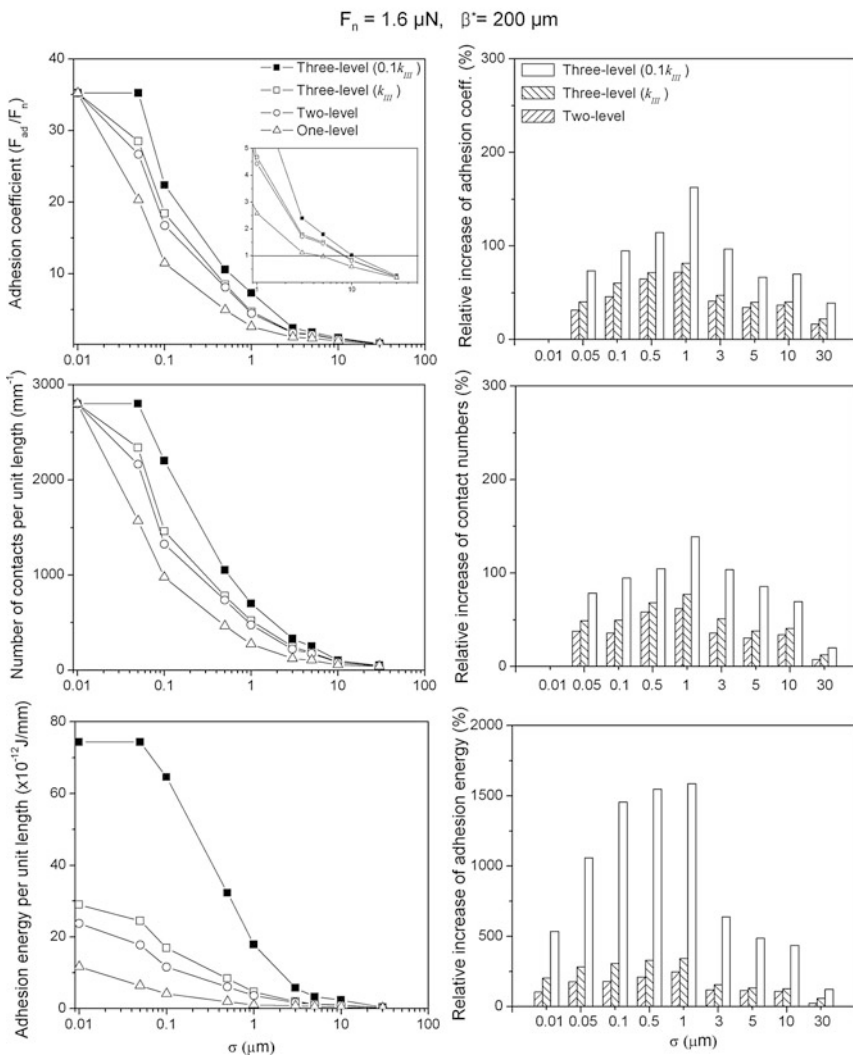


Fig. 11.18 (a) Force–distance curves of one-, two-, and three-level models in contact with rough surfaces with different σ values for an applied load of $1.6 \mu\text{N}$. (b) The adhesion coefficient, the number of contacts and the adhesion energy per unit length of profile for one- and multilevel models with an increase of σ value (left figures), and relative increases between multi- and one-level models (right side) for an applied load of $1.6 \mu\text{N}$. The value of k_{III} in the analysis is 2.908 N/m (Kim and Bhushan, 2007a)

study also investigated the effect of σ on adhesion energy. It was determined that the adhesion energy decreased with an increase of σ . For the smooth surface with $\sigma = 0.01 \mu\text{m}$, the adhesion energies for the two- and three-level hierarchical models are 2 times and 2.4 times larger than that for the one-level model, respectively, but

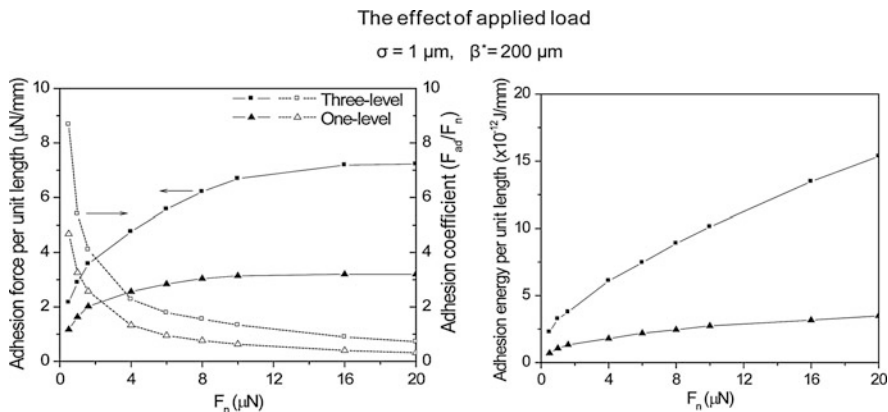


Fig. 11.19 The adhesion force, adhesion coefficient, and adhesion energy as a function of applied loads for both one- and three-level models contacting with the rough surface (Kim and Bhushan, 2007a)

adhesion energy decreases rapidly at surfaces with σ greater than $0.05 \mu\text{m}$, and in every model, it finally decreases to zero at surfaces with σ greater than $10 \mu\text{m}$. The adhesion energy for the three-level model with $0.1 k_{III}$ is 2–3 times higher than that for three-level model.

In order to demonstrate the effect of the hierarchical structure on adhesion enhancement, Kim and Bhushan (2007a) calculated the increases in the adhesion coefficient, the number of contacts, and the adhesion energy of the two- and three-level (with $0.1 k_{III}$) models relative to the one-level model. These results are shown in the right side of Fig. 11.18b. It was found that for the two- and three-level models, the adhesion coefficient increases slowly with an increase of σ and has maximum values of about 70% and 80% at $\sigma = 1 \mu\text{m}$, respectively, and then decreases for surfaces with σ greater than $3 \mu\text{m}$. The condition at which a significant enhancement occurs is related to the maximum spring deformation which is the applied load divided by the spring stiffness. If the maximum spring deformation is greater than 2–3 times larger than the σ value of the surface roughness, a significant adhesion enhancement occurs. The three-level model with $0.1 k_{III}$ shows significant adhesion enhancement. The relative increase of the adhesion coefficient and adhesion energy for the three-level model with $0.1 k_{III}$ has the maximum values at $\sigma = 1 \mu\text{m}$.

Figure 11.19 shows the variation of adhesion force and adhesion energy as a function of applied load for both one- and three-level models contacting a surface with $\sigma = 1 \mu\text{m}$. It is shown that as the applied load increases, the adhesion force increases up to a certain applied load and then has a constant value, whereas adhesion energy continues to increase with an increase in the applied load. The one-level model has a maximum value of adhesion force per unit length of about $3 \mu\text{N}/\text{mm}$ at the applied load of $10 \mu\text{N}$, and the three-level model has a maximum value of about $7 \mu\text{N}/\text{mm}$ at the applied load of $16 \mu\text{N}$. However, the adhesion

coefficient continues to decrease at higher applied loads because adhesion force is constant even if the applied load increases.

The simulation results for the three-level model, which is close to gecko setae, presented in Fig. 11.18 show that roughness reduces the adhesion force. At the surface with σ greater than $10 \mu\text{m}$, the ratio of the adhesion force to the gecko weight indicates that it cannot support itself. However, in practice, a gecko can cling or crawl on the surface of ceiling with higher roughness. Kim and Bhushan (2007a) did not consider the effect of lamellae in their study. The authors state that the lamellae can adapt to the waviness of a surface, while the setae allow for the adaptation to micro- or nanoroughness, and expect that adding the lamellae of gecko skin to the model would lead to higher adhesion over a wider range of roughness. In addition, their hierarchical model considers deformation normal to surface and the motion of seta. It should be noted that the measurements of adhesion force of a single gecko seta made by Autumn et al. (2000) demonstrated that a load applied normal to the surface was insufficient for an effective attachment of seta.

Finally, the effects of spring stiffness and number of springs on the adhesion enhancement of multilevel hierarchical model, one- and three-level models with four different spring stiffnesses and three different numbers of springs, were analyzed by Kim and Bhushan (2007b). The stiffness k_1 was taken equal to 0.0126 N/m , as before. Other stiffnesses, k_{II} and k_{III} , were normalized with respect to k_1 . The three-level model with $k_{\text{III}}/k_1 = 100$ and $k_{\text{II}}/k_1 = 10$ has similar stiffness values to gecko's seta presented in Table 11.3 and used in the previous example (Figs. 11.18 and 11.19). The left part in Fig. 11.20 shows the adhesion coefficient, the number of contacts, and adhesion energy per unit length for the one- and three-level models with four different spring stiffnesses as a function of σ value for an applied load of $1.6 \mu\text{N}$. Trends as a function of σ are the same as observed previously in Fig. 11.18b. For the case of $k_{\text{III}} = k_{\text{II}} = k_1$, one gets the highest value of adhesion coefficient of 36 on a rough surface, and it remains high up to σ value of about $1 \mu\text{m}$, and then it starts to decrease. As the stiffness values of k_{II} and k_{III} increase, the adhesion coefficient starts to decrease at lower values of σ , and it decreases rapidly with an increase in σ . The number of contacts and adhesion energy per unit length as a function of σ have trends similar to that of adhesion coefficient. The right part in Fig. 11.20 shows relative increases between one- and three-level models. The trends are the same as discussed earlier.

For the effect of the number of springs study, three different cases of the number of springs in the upper level to that in the lower level were considered. The three-level model with $N_1/N_{\text{II}} = 10$ and $N_{\text{II}}/N_{\text{III}} = 10$ is most close to the gecko's setae (discussed earlier). Figure 11.21 shows the adhesion force, adhesion coefficient, and adhesion energy as a function of applied loads for one- and three-level models with different number of springs contacting with the rough surface. The variation of number of springs on each level affects the equivalent stiffness of the model. As the number of springs on the lower level increases, the equivalent stiffness decreases. The figure shows that the three-level model with $N_1/N_{\text{II}} = 100$ and $N_{\text{II}}/N_{\text{III}} = 10$ gives the largest adhesion force and adhesion energy among every model because the equivalent stiffness is lowest.

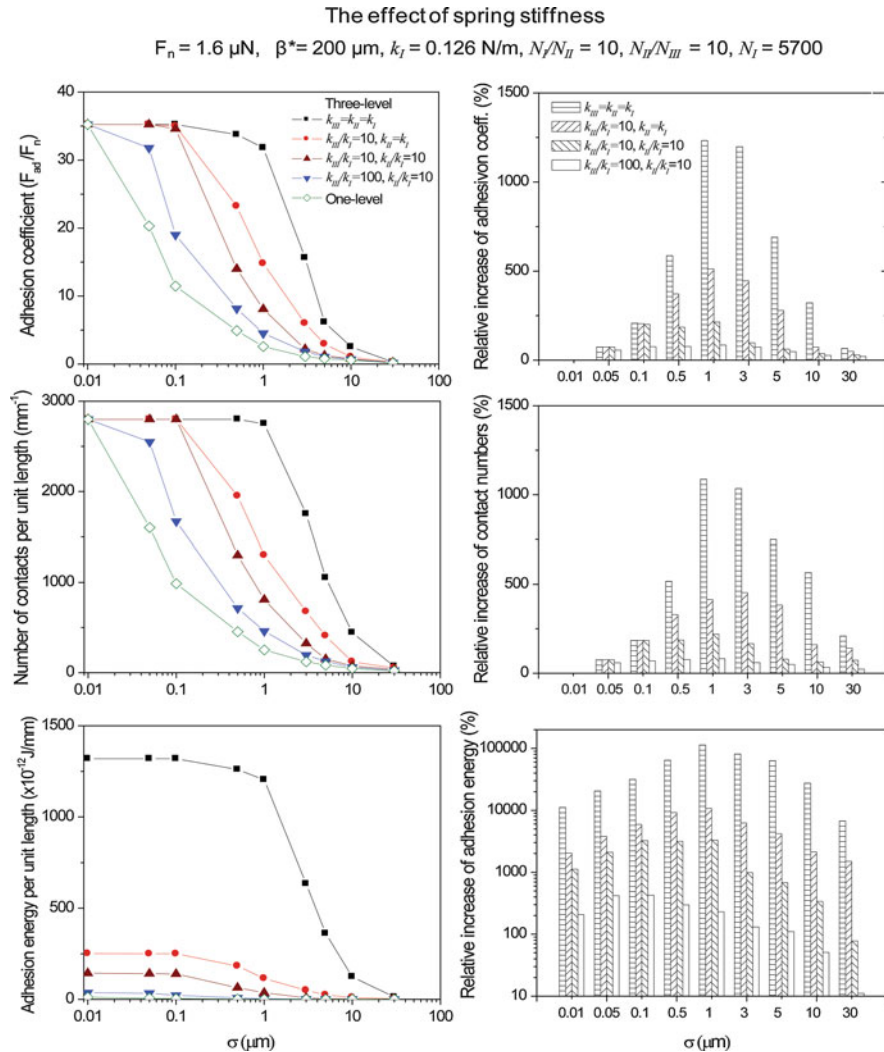
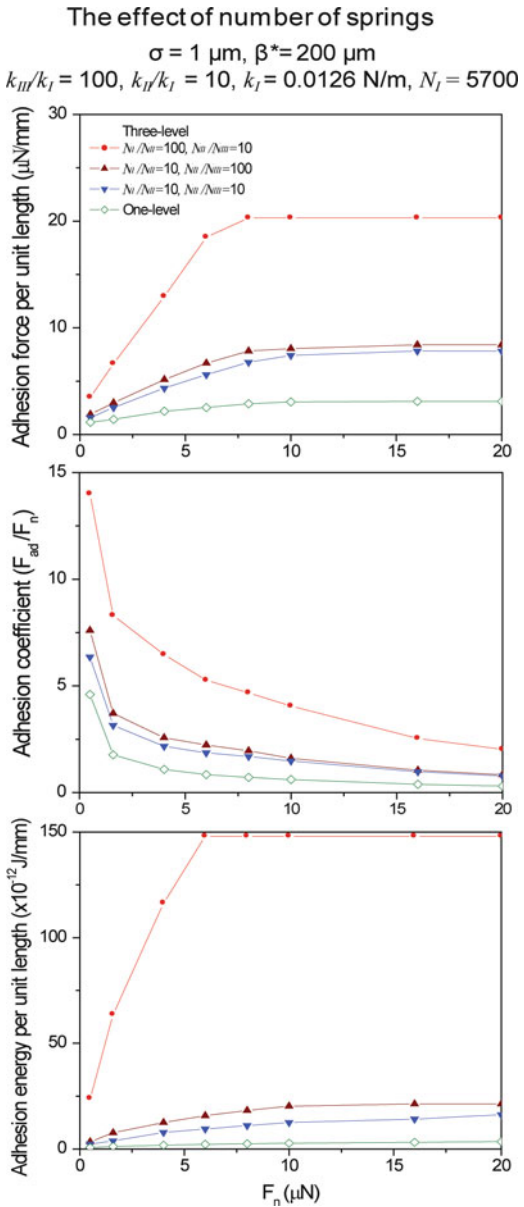


Fig. 11.20 The adhesion coefficient, the number of contacts and the adhesion energy per unit length of profile for one- and three-level models with different spring stiffnesses as a function of σ value (left figures), and relative increases between one- and three-level models (right figures) for an applied load of $1.6 \mu\text{N}$ (Kim and Bhushan, 2007b)

11.6.4 Capillary Effects

Kim and Bhushan (2008) investigated the effects of capillarity on gecko adhesion by considering capillary force as well as the solid-to-solid interaction. The Laplace and surface tension components of the capillary force are treated according to

Fig. 11.21 The adhesive force, adhesion coefficient, and adhesion energy as a function of applied loads for one- and three-level models with different number of springs contacting with the rough surface (Kim and Bhushan, 2007b)



Sect. 11.4.2. The solid-to-solid adhesive force was calculated by DMT theory according to (11.19) and will be denoted as F_{DMT} .

The work of adhesion was then calculated by (11.20). Kim and Bhushan (2008) assumed typical values of the Hamaker constant to be $H_{\text{air}} = 10^{-19} \text{ J}$ in the air and $H_{\text{water}} = 6.7 \times 10^{-19} \text{ J}$ in the water (Israelachvili, 1992). The works of

adhesion of two surfaces in contact separated by an atomic distance $D \approx 0.2\text{ nm}$ ([Israelachvili, 1992](#)) are approximately equal to 66 mJ/m^2 in air and 44 mJ/m^2 in water. Assuming tip radius R is 50 nm , the DMT adhesion forces F_{DMT} of a single contact in air and in water are $F_{\text{DMT}}^{\text{air}} = 11\text{ nN}$ and $F_{\text{DMT}}^{\text{water}} = 7.3\text{ nN}$, respectively. As the humidity increases from zero to 100%, the DMT adhesion force will take a value between $F_{\text{DMT}}^{\text{air}}$ and $F_{\text{DMT}}^{\text{water}}$. To calculate the DMT adhesion force for the intermediate humidity, an approximation method by [Wan et al. \(1992\)](#) was used. The work of adhesion W_{ad} for the intermediate humidity can be expressed as

$$W_{\text{ad}} = \int_D^\infty \frac{H}{6\pi h^3} dh = \int_D^{h_f} \frac{H_{\text{water}}}{6\pi h^3} dh + \int_{h_f}^\infty \frac{H_{\text{air}}}{6\pi h^3} dh, \quad (11.26)$$

where h is the separation along the plane. h_f is the water film thickness at a filling angle ϕ , which can be calculated as

$$h_f = D + R(1 - \cos \phi). \quad (11.27)$$

Therefore, using (11.19), (11.26), and (11.27), the DMT adhesion force for the intermediate humidity is given as

$$F_{\text{DMT}} = F_{\text{DMT}}^{\text{air}} \left\{ 1 - \frac{1}{(1 + R(1 - \cos \phi)/D)^2} \right\} + F_{\text{DMT}}^{\text{water}} \left\{ \frac{1}{(1 + R(1 - \cos \phi)/D)^2} \right\}. \quad (11.28)$$

Finally, [Kim and Bhushan \(2008\)](#) calculated the total adhesion force F_{ad} as the sum of (11.15) and (11.28):

$$F_{\text{ad}} = F_{\text{c}} + F_{\text{DMT}}. \quad (11.29)$$

[Kim and Bhushan \(2008\)](#) then used the total adhesion force as a critical force in the three-level hierarchical spring model discussed previously. In the spring model for gecko seta, if the force applied upon spring deformation is greater than the adhesion force, the spring is regarded as having been detached.

To simulate the capillary contribution to adhesion force for a gecko spatula, [Kim and Bhushan \(2008\)](#) set the contact angle on a gecko spatula tip θ_1 equal to 128° ([Huber et al., 2005b](#)). It was assumed that the spatula tip radius $R = 50\text{ nm}$, the ambient temperature $T = 25^\circ\text{C}$, the surface tension of water $\gamma = 73\text{ mJ/m}^2$, and molecular volume of water $V = 0.03\text{ nm}^3$ ([Israelachvili, 1992](#)).

Figure 11.22a shows the total adhesion force as a function of relative humidity for a single spatula in contact with surfaces with different contact angles. Total adhesion force decreases with an increase in the contact angle on the substrate, and the difference of total adhesion force among different contact angles is larger in the intermediate humidity regime. As the relative humidity increases, total adhesion force for the surfaces with contact angles less than 60° has a higher value than the DMT adhesion force not considering wet contact, whereas with the value above 60° , total adhesion force has lower values at most relative humidities.

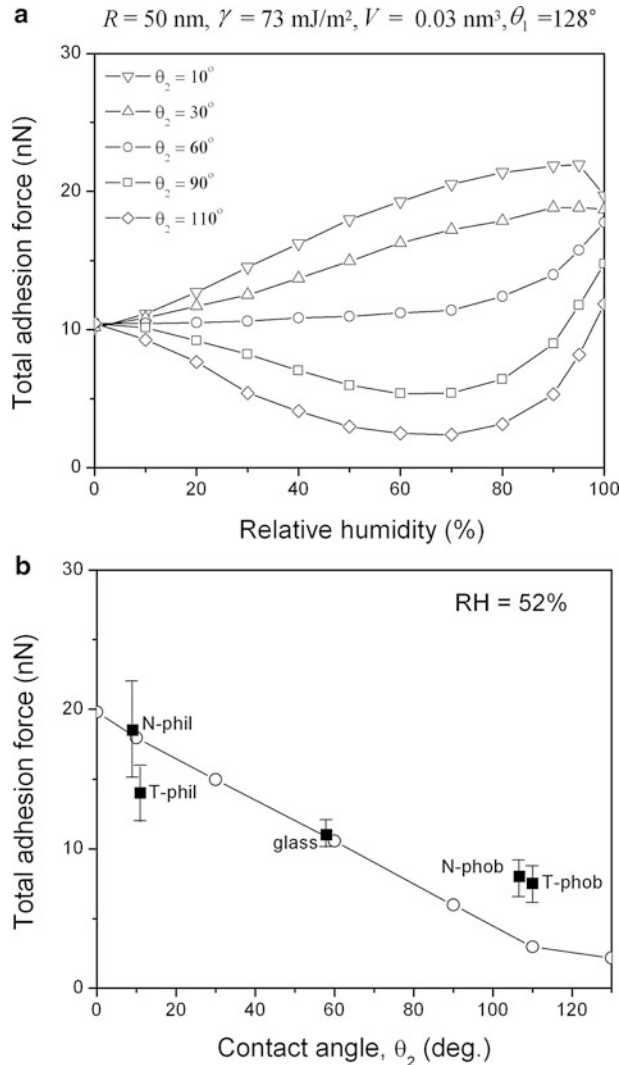


Fig. 11.22 (a) Total adhesion force as a function of relative humidity for a single spatula in contact with surfaces with different contact angles. (b) Comparison of the simulation results of Kim and Bhushan (2008) with the measured data obtained by Huber et al. (2005b) for a single spatula in contact with the hydrophilic and the hydrophobic surfaces (Kim and Bhushan, 2008)

The simulation results of Kim and Bhushan (2008) are compared with the experimental data by Huber et al. (2005b) in Fig. 11.22b. Huber et al. (2005b) measured the pull-off force of a single spatula in contact with four different types of Si wafer and glass at the ambient temperature 25°C and the relative humidity 52%. According to their description, wafer families “N” and “T” in Fig. 11.22b differ by the thickness of the top amorphous Si oxide layer. The “Phil” type is the

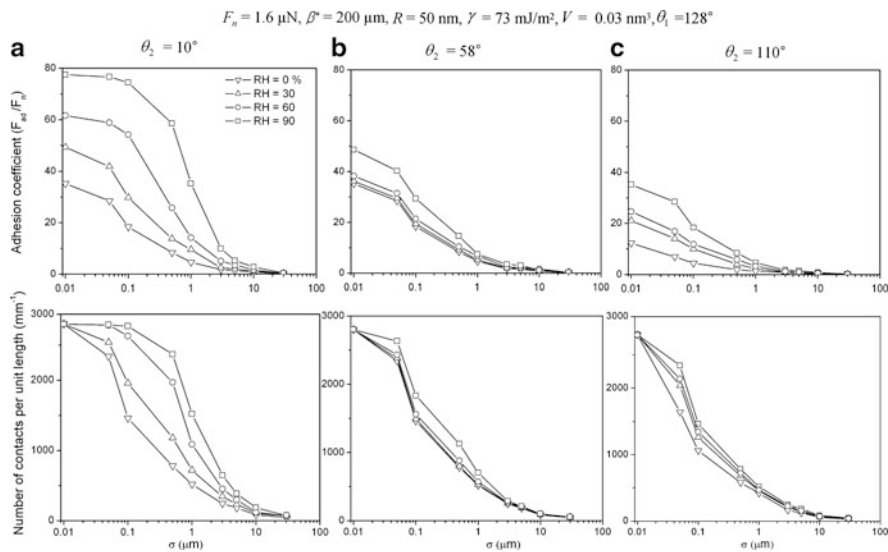


Fig. 11.23 The adhesion coefficient and number of contacts per unit length for three-level hierarchical model in contact with rough surfaces with different values of root mean square amplitudes σ and contact angles for different relative humidities (Kim and Bhushan, 2008)

cleaned Si oxide surface which is hydrophilic with a water contact angle $\approx 10^\circ$, whereas the “Phob” type is a Si wafer covered hydrophobic monolayer causing water contact angle $>100^\circ$. The glass has a water contact angle of 58° . Huber et al. (2005b) showed that the adhesion force of a gecko spatula rises significantly for substrates with increasing hydrophilicity (adhesive force increases by a factor of two as mating surfaces go from hydrophobic to hydrophilic). As shown in Fig. 11.22b, the simulation results of Kim and Bhushan (2008) closely match the experimental data of Huber et al. (2005b).

Kim and Bhushan (2008) carried out adhesion analysis for a three-level hierarchical model for gecko seta. Figure 11.23 shows the adhesion coefficient and number of contacts per unit length for the three-level hierarchical model in contact with rough surfaces with different values of the root mean square (RMS) amplitude σ ranging from $\sigma = 0.01 \mu\text{m}$ to $\sigma = 30 \mu\text{m}$ for different relative humidities and contact angles of the surface. It can be seen that for the surface with contact angle $\theta_2 = 10^\circ$, the adhesion coefficient is greatly influenced by relative humidity. At 0% relative humidity, the maximum adhesion coefficient is about 36 at a value of σ smaller than $0.01 \mu\text{m}$ compared to 78 for 90% relative humidity with the same surface roughness. As expected, the effect of relative humidity on increasing the adhesion coefficient decreases as the contact angle becomes larger. For hydrophobic surfaces, relative humidity decreases the adhesion coefficient. Similar trends can be noticed in the number of contacts. Thus, the conclusion can be drawn that hydrophilic surfaces are beneficial to gecko adhesion enhancement.

11.7 Adhesion Database of Fibrillar Structures

The mechanics of adhesion between a fibrillar structure and a rough surface as it relates to the design of biomimetic structures has been a topic of investigation by many researchers (Jagota and Bennison, 2002; Persson, 2003; Sitti and Fearing, 2003; Glassmaker et al., 2004, 2005; Gao et al., 2005; Yao and Gao, 2006; Kim and Bhushan, 2007b, c). Kim and Bhushan (2007c) developed a convenient, general, and useful guideline for understanding biological systems and for improving the attachment of fibrillar structures. This adhesion database was constructed by modeling the fibers as oriented cylindrical cantilever beams with spherical tips. The authors then carried out numerical simulation of the attachment system in contact with random rough surfaces considering three constraint conditions—buckling, fracture, and sticking of the fiber structure. For a given applied load and roughnesses of contacting surface and fiber material, a procedure to find an optimal fiber radius and aspect ratio for the desired adhesion coefficient was developed.

The model of Kim and Bhushan (2007c) is used to find the design parameters for fibers of a single-level attachment system capable of achieving desired properties—high adhesion coefficient and durability. The design variables for an attachment system are as follows: fiber geometry (radius and aspect ratio of fibers, tip radius), fiber material, fiber density, and fiber orientation. The optimal values for the design variables to achieve the desired properties should be selected for fabrication of a biomimetic attachment system.

11.7.1 Fiber Model

The fiber model of Kim and Bhushan (2007c) consists of a simple idealized fibrillar structure consisting of a single-level array of micro-/nanobeams protruding from a backing as shown in Fig. 11.24. The fibers are modeled as oriented cylindrical cantilever beams with spherical tips. In Fig. 11.24, l is the length of fibers, θ is the fiber orientation, R is the fiber radius, R_t is the tip radius, S is the spacing between fibers, and h is the distance between the upper spring base of each model and mean line of the rough profile. The end terminal of the fibers is assumed to be a spherical tip with a constant radius and a constant adhesion force.

11.7.2 Single Fiber Contact Analysis

Kim and Bhushan (2007c) modeled an individual fiber as a beam oriented at an angle, θ , to the substrate, and the contact load F is aligned normal to the substrate. The net displacement normal to the substrate can be calculated according to (11.16) and (11.17). The fiber stiffness ($k = F/\delta_{\perp}$) is given by (Glassmaker et al., 2004))

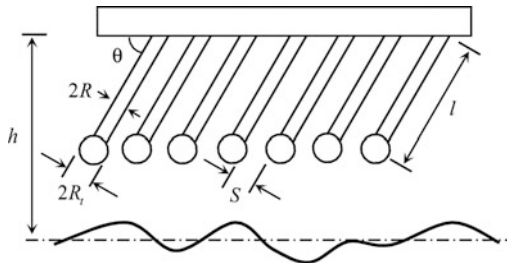


Fig. 11.24 Single-level attachment system with oriented cylindrical cantilever beams with spherical tip. In this figure, l is the length of fibers, θ is the fiber orientation, R is the fiber radius, R_t is the tip radius, S is the spacing between fibers, and h is distance between base of model and mean line of the rough profile (Kim and Bhushan, 2007c)

$$k = \frac{\pi R^2 E}{l \sin^2 \theta \left(1 + \frac{4l^2 \cot^2 \theta}{3R^2} \right)} = \frac{\pi R E}{2\lambda \sin^2 \theta \left(1 + \frac{16\lambda^2 \cot^2 \theta}{3} \right)}, \quad (11.30)$$

where $\lambda = l/2R$ is the aspect ratio of the fiber and θ is fixed at 30°

Two alternative models dominate the world of contact mechanics—the Johnson–Kendall–Roberts (JKR) theory (Johnson et al., 1971) for compliant solids and the Derjaguin–Muller–Toporov (DMT) theory (Derjaguin et al., 1975) for stiff solids. Although gecko setae are composed of β -keratin with a high elastic modulus (Russell, 1986; Bertram and Gosline, 1987) which is close to the DMT model, in general the JKR theory prevails for biological or artificial attachment systems. Therefore, the JKR theory was applied in the subsequent analysis of Kim and Bhushan (2007c) to compare the materials with wide ranges of elastic modulus. The adhesion force between a spherical tip and a rigid flat surface is thus calculated using the JKR theory as (Johnson et al., 1971)

$$F_{ad} = \frac{3}{2} \pi R_t W_{ad}, \quad (11.31)$$

where R_t is the radius of spherical tip and W_{ad} is the work of adhesion [calculated according to (11.24)]. Kim and Bhushan (2007c) used this adhesion force as a critical force. If the elastic force of a single spring is less than the adhesion force, they regarded the spring as having been detached.

11.7.3 Constraints

In the design of fibrillar structures, a trade-off exists between the aspect ratio of the fibers and their adaptability to a rough surface. If the aspect ratio of the fibers is too large, they can adhere to each other or even collapse under their own weight

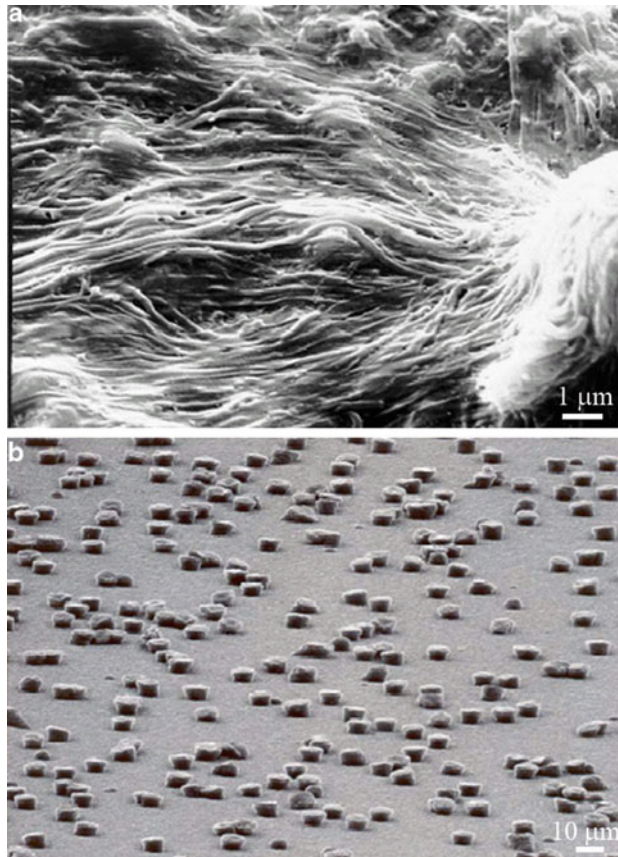


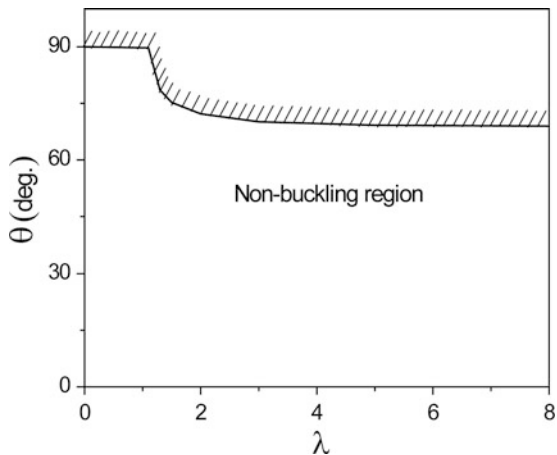
Fig. 11.25 SEM micrographs of (a) high-aspect-ratio polymer fibrils that have collapsed under their own weight and (b) low-aspect-ratio polymer fibrils that are incapable of adapting to rough surfaces (Sitti and Fearing, 2003)

as shown in Fig. 11.25a. If the aspect ratio is too small (Fig. 11.25b), the structures will lack the necessary compliance to conform to a rough surface. Spacing between the individual fibers is also important. If the spacing is too small, adjacent fibers can attract each other through intermolecular forces, which will lead to bunching. Therefore, [Kim and Bhushan \(2007c\)](#) considered three necessary conditions in their analysis: buckling, fracture, and sticking of fiber structure, which constrain the allowed geometry.

11.7.3.1 Non-buckling Condition

A fibrillar interface can deliver a compliant response while still employing stiff materials because of bending and micro-buckling of fibers. Based on classical Euler

Fig. 11.26 Critical fiber orientation as a function of aspect ratio λ for non-buckling condition for pinned-clamped microbeams ($b_c = 2$) (Kim and Bhushan, 2007c)



buckling, Glassmaker et al. (2004) established a stress-strain relationship and a critical compressive strain for buckling, ε_{cr} , for the fiber oriented at an angle, θ , to the substrate,

$$\varepsilon_{cr} = -\frac{b_c \pi^2}{3(Al^2/3I)} \left(1 + \frac{A_c l^2}{3I} \cot^2 \theta \right), \quad (11.32)$$

where A_c is the cross-sectional area of the fibril and b_c is a factor that depends on boundary conditions. The factor b_c has a value of 2 for pinned-clamped microbeams. For fibers having a circular cross section, ε_{cr} is calculated as

$$\varepsilon_{cr} = -\frac{b_c \pi^2}{3(4l^2/3R^2)} \left(1 + \frac{4l^2}{3R^2} \cot^2 \theta \right) = -b_c \pi^2 \left(\frac{1}{16\lambda^2} + \frac{\cot^2 \theta}{3} \right). \quad (11.33)$$

In (11.33), ε_{cr} depends on both the aspect ratio, λ , and the orientation, θ , of fibers. If $\varepsilon_{cr} = 1$, which means the fiber deforms up to the backing, buckling does not occur. Figure 11.26 plots the critical orientation, θ , as a function of aspect ratio for the case of $\varepsilon_{cr} = 1$. The critical fiber orientation for buckling is 90° at λ less than 1.1. This means that buckling does not occur regardless of the orientation of the fiber at λ less than 1.1. For λ greater than 1.1, the critical fiber orientation for buckling decreases with an increase in λ and has a constant value of 69° at λ greater than 3. Kim and Bhushan (2007c) used a fixed value at 30° for θ because as stated earlier, the maximum adhesive force is achieved at this orientation, and buckling is not expected to occur.

11.7.3.2 Non-fiber Fracture Condition

For small contacts, the strength of the system will eventually be determined by fracture of the fibers. Spolenak et al. (2005) suggested the limit of fiber fracture

as a function of the adhesion force. The axial stress σ_f in a fiber is limited by its theoretical fracture strength σ_{th}^f as

$$\sigma_f = \frac{F_{ad}}{R^2\pi} \leq \sigma_{th}^f. \quad (11.34)$$

Using (11.31), a lower limit for the useful fiber radius R is calculated as

$$R \geq \sqrt{\frac{3R_t W_{ad}}{2\sigma_{th}^f}} \approx \sqrt{\frac{15R_t W_{ad}}{E}}, \quad (11.35)$$

where the theoretical fracture strength is approximated by $E/10$ (Dieter, 1988). The lower limit of fiber radius for fiber fracture by the adhesion force depends on elastic modulus. By assuming $W_{ad} = 66 \text{ mJ/m}^2$ as stated earlier, Kim and Bhushan (2007c) calculated the lower limits of fiber radius for $E = 1 \text{ MPa}$, 0.1 GPa and 10 GPa to be $0.32 \mu\text{m}$, $0.032 \mu\text{m}$, and $0.0032 \mu\text{m}$, respectively.

The contact stress cannot exceed the ideal contact strength transmitted through the actual contact area at the instant of tensile instability (Spolenak et al., 2005). Kim and Bhushan (2007c) used this condition (11.34) to extract the limit of tip radius, R_t ,

$$\sigma_c = \frac{F_{ad}}{a_c^2\pi} \leq \sigma_{th}, \quad (11.36)$$

where σ_c is the contact stress, and σ_{th} is the ideal strength of van der Waals bonds which equals approximately W_{ad}/b , b is the characteristic length of surface interaction, and a_c is the contact radius. Based on the JKR theory, for the rigid contacting surface, a_c at the instant of pull-off is calculated as

$$a_c = \left(\frac{9\pi W_{ad} R_t^2 (1 - \nu^2)}{8E} \right)^{1/3}, \quad (11.37)$$

where ν is Poisson ratio. The tip radius can then be calculated by combining (11.36) and (11.37) as

$$R_t \geq \frac{8b^3 E^2}{3\pi^2 (1 - \nu^2)^2 W_{ad}^2}. \quad (11.38)$$

The lower limit of tip radius also depends on elastic modulus. Assuming $W_{ad} = 66 \text{ mJ/m}^2$ and $b = 2 \times 10^{-10} \text{ m}$ (Dieter, 1988), the lower limits of tip radius for $E = 1 \text{ MPa}$, 0.1 GPa , and 10 GPa are calculated as $6 \times 10^{-7} \text{ nm}$, $6 \times 10^{-3} \text{ nm}$, and 60 nm , respectively. In this study, Kim and Bhushan (2007c) fixed the tip radius at 100 nm , which satisfies the tip radius condition throughout a wide range of elastic modulus up to 10 GPa .

11.7.3.3 Non-sticking Condition

A high density of fibers is also important for high adhesion. However, if the space S between neighboring fibers is too small, the adhesion forces between them become stronger than the forces required to bend the fibers. Then, fibers might stick to each other and get entangled. Therefore, to prevent fibers from sticking to each other, they must be spaced apart and be stiff enough to prevent sticking or bunching. Several authors (e.g., [Sitti and Fearing, 2003](#)) have formulated a non-sticking criterion. [Kim and Bhushan \(2007c\)](#) adopted the approach of [Sitti and Fearing \(2003\)](#). Both adhesion and elastic forces will act on bent structures. The adhesion force between two neighboring round tips is calculated as

$$F_{\text{ad}} = \frac{3}{2} \pi R'_t W_{\text{ad}}, \quad (11.39)$$

where R'_t is the reduced radius of contact, which is calculated as $R'_t = (1/R_{t1} + 1/R_{t2})^{-1}$; R_{t1}, R_{t2} —radii of contacting tips; for the case of similar tips, $R_{t1} = R_{t2}$, $R'_t = 2/R_t$.

The elastic force of a bent structure can be calculated by multiplying the bending stiffness ($k_b = 3 \pi R^4 E / 4l^3$) by a given bending displacement δ as

$$F_{\text{el}} = \frac{3}{4} \frac{\pi R^4 E \delta}{l^3}. \quad (11.40)$$

The condition for the prevention of sticking is $F_{\text{el}} > F_{\text{ad}}$. By combining (11.39) and (11.40), a requirement for the minimum distance S between structures which will prevent sticking of the structures is given as ([Kim and Bhushan, 2007c](#))

$$S > 2\delta = 2 \left(\frac{4}{3} \frac{W_{\text{ad}} l^3}{E R^3} \right) = 2 \left(\frac{32}{3} \frac{W_{\text{ad}} \lambda^3}{E} \right). \quad (11.41)$$

The constant 2 takes into account the two nearest structures. Using distance S , the fiber density, ρ , is calculated as

$$\rho = \frac{1}{(S + 2R)^2}. \quad (11.42)$$

Equation (11.42) was then used to calculate the allowed minimum density of fibers without sticking or bunching. In (11.41), it is shown that the minimum distance, S , depends on both the aspect ratio λ and the elastic modulus E . A smaller aspect ratio and higher elastic modulus allow for greater packing density. However, fibers with a low aspect ratio and high modulus are not desirable for adhering to rough surfaces due to lack of compliance.

11.7.4 Numerical Simulation

The simulation of adhesion of an attachment system in contact with random rough surfaces was carried out numerically. In order to conduct 2D simulations, it is necessary to calculate applied load F_n as a function of applied pressure P_n as an input condition. Using ρ calculated by non-sticking condition, [Kim and Bhushan \(2007c\)](#) calculated F_n as

$$F_n = \frac{P_n p}{\rho}, \quad (11.43)$$

where p is the number of springs in the scan length L , which equals $L/(S + 2R)$.

Fibers of the attachment system are modeled as one-level hierarchy elastic springs (Fig. 11.16) ([Kim and Bhushan, 2007c](#)). The deflection of each spring and the elastic force arisen in the springs are calculated according to (11.21) and (11.22), respectively. The adhesion force is the lowest value of elastic force F_{el} when the fiber has detached from the contacting surface. [Kim and Bhushan \(2007c\)](#) used an iterative process to obtain optimal fiber geometry—fiber radius and aspect ratio. If the applied load, the roughness of contacting surface, and the fiber material are given, the procedure for calculating the adhesion force is repeated iteratively until the desired adhesion force is satisfied. In order to simplify the design problem, fiber material is regarded as a known variable. The next step is constructing the design database. Figure 11.27a shows the flowchart for the construction of adhesion design database, and Fig. 11.27b shows the calculation of the adhesion force that is a part of the procedure to construct an adhesion design database.

11.7.5 Results and Discussion

Figure 11.28 shows an example of the adhesion design database for biomimetic attachment systems consisting of single-level cylindrical fibers with an orientation angle of 30° and spherical tips of $R_t = 100$ nm constructed by [Kim and Bhushan \(2007c\)](#). The minimum fiber radius calculated by using non-fiber fracture condition, which plays a role of lower limit of optimized fiber radius, is also added on the plot. The plots in Fig. 11.28 cover all applicable fiber materials a from soft elastomer material such as poly(dimethylsiloxane) (PDMS) to stiffer polymers such as polyimide and β -keratin. The dashed lines in each plot represent the limits of fiber fracture due to the adhesion force. For a soft material with $E = 1$ MPa in Fig. 11.28a, the range of the desirable fiber radius is more than 0.3 μm and that of the aspect ratio is approximately less than 1. As elastic modulus increases, the feasible range of both fiber radius and aspect ratio also increases as shown in Fig. 11.28b, c. In Fig. 11.28, the fiber radius has a linear relation with the surface roughness on a logarithm scale.

If the applied load, the roughness of contacting surface, and the elastic modulus of a fiber material are specified, the optimal fiber radius and aspect ratio for

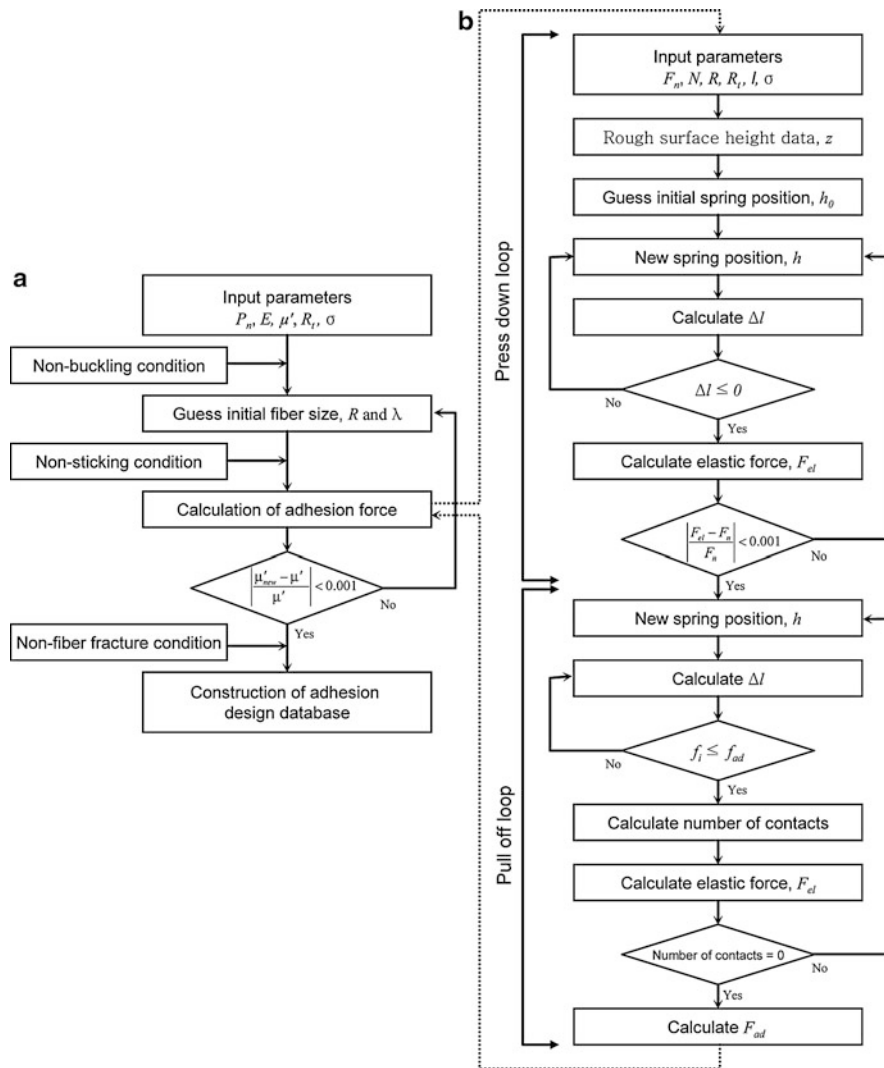


Fig. 11.27 Flowchart for (a) the construction of adhesion design database and (b) the calculation of the adhesion force. In this figure, P_n is the applied pressure, E is the elastic modulus, μ' is the adhesion coefficient, R_t is the tip radius, σ is root mean square (RMS) amplitude, R is the fiber radius, λ is the aspect ratio of fiber, F_n is the applied load, N is the number of springs, k and l are stiffness and length of structures, Δl is the spring deformation, f_i is the elastic force of a single spring, and f_{ad} is the adhesion force of a single contact (Kim and Bhushan, 2007c)

the desired adhesion coefficient can be selected from this design database. The adhesion databases are useful for understanding biological systems and for guiding the fabrication of biomimetic attachment systems. Two case studies (Kim and Bhushan, 2007c) are discussed below.

Case study I: Select the optimal size of fibrillar adhesive for a wall-climbing robot with the following requirements:

- Material: polymer with $E \approx 100 \text{ MPa}$
- Applied pressure by weight $< 10 \text{ kPa}$
- Adhesion coefficient ≈ 5
- Surface roughness $\sigma < 1 \mu\text{m}$

The subplot of adhesion database that satisfies the requirement is at the second column and second row in Fig. 11.28b. From this subplot, any values on the marked line can be selected to meet the requirements. For example, fiber radius of $0.4 \mu\text{m}$

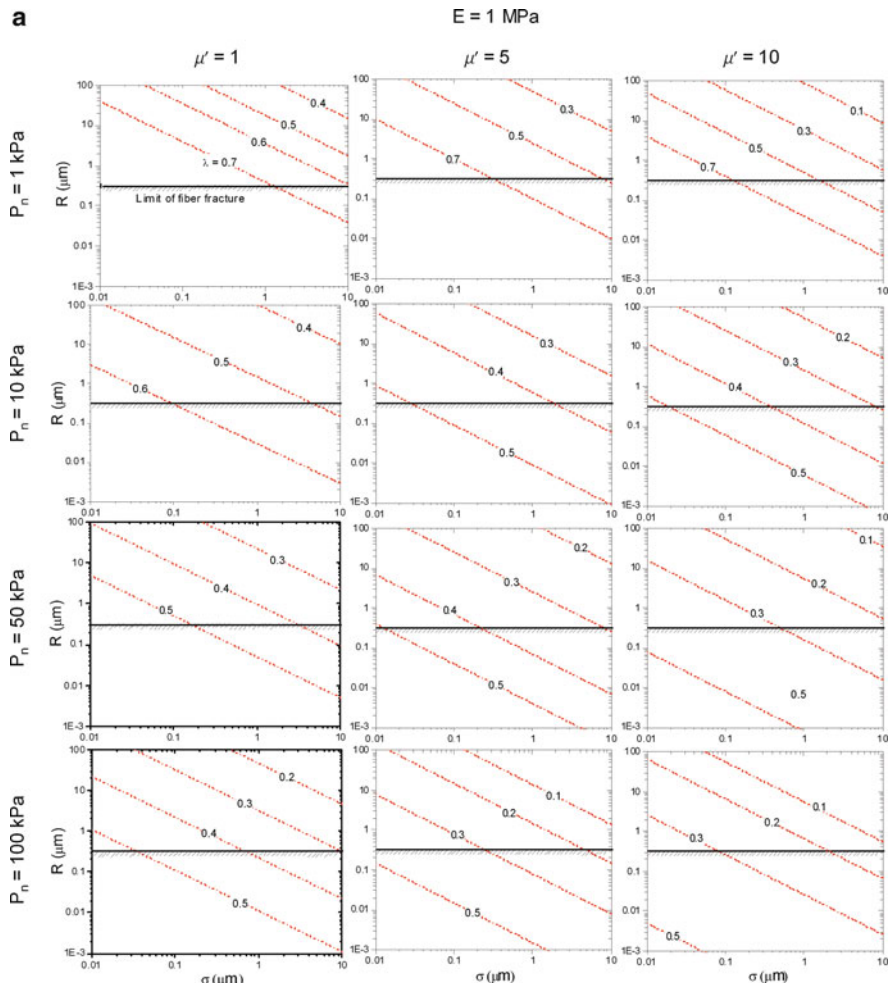
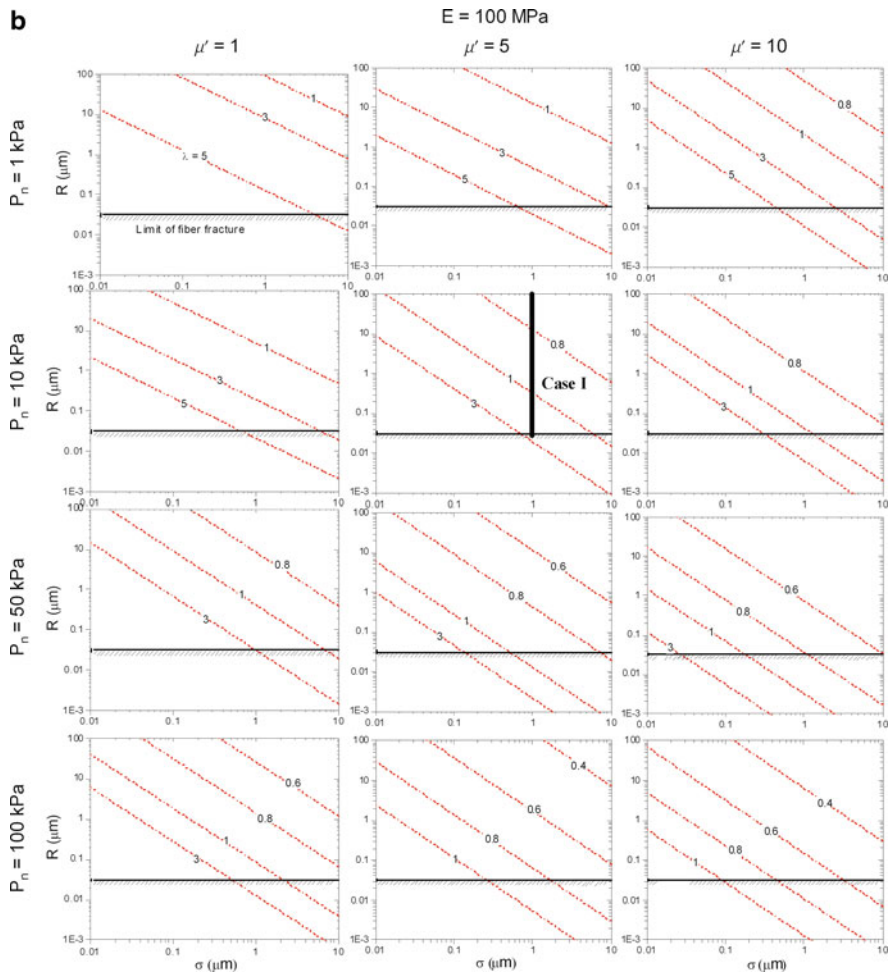


Fig. 11.28 (continued)

**Fig. 11.28** (continued)

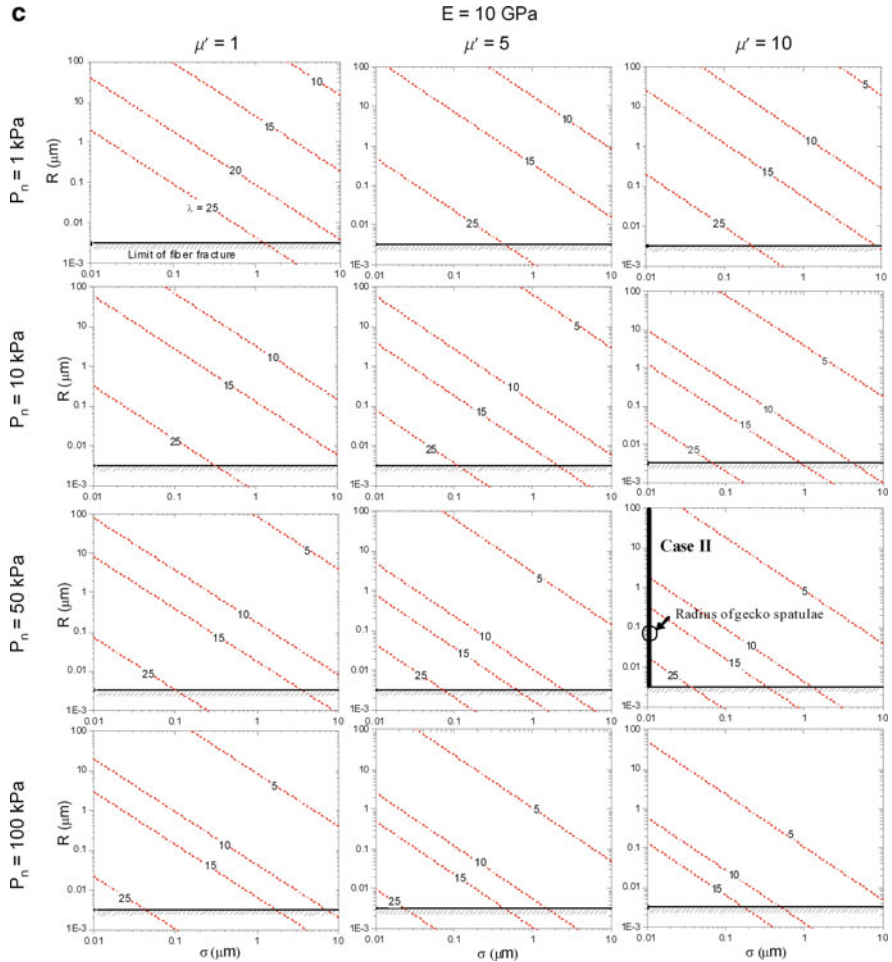


Fig. 11.28 Adhesion design database for biomimetic attachment system consisting of single-level cylindrical fibers with orientation angle of 30° and spherical tips of 100 nm for elastic modulus of (a) 1 MPa, (b) 100 MPa, and (c) 10 GPa (Kim and Bhushan, 2007c). The solid lines shown in Figs. (b) and (c) correspond to the cases I and II, respectively, which satisfy the specified requirements (Kim and Bhushan, 2007c)

with an aspect ratio of 1 or fiber radius of $10 \mu\text{m}$ with an aspect ratio of 0.8 satisfies the specified requirements.

Case study II: Compare with adhesion test for a single gecko seta (Autumn et al., 2000, 2002):

- Material: β -keratin with $E \approx 10 \text{ GPa}$
- Applied pressure = 57 kPa ($2.5 \mu\text{N}$ on an area of $43.6 \mu\text{m}^2$)
- Adhesion coefficient = 8 to 16
- Surface roughness $\sigma < 0.01 \mu\text{m}$

[Autumn et al. \(2000, 2002\)](#) showed that in isolated gecko setae contacting the surface of a single crystalline silicon wafer, a $2.5 \mu\text{N}$ preload yielded adhesion of $20\text{--}40 \mu\text{N}$ and thus a value of adhesion coefficient of 8–16. The region that satisfies the above requirements is marked in Fig. 11.28c. The spatulae of gecko setae have an approximate radius of $0.05 \mu\text{m}$ with an aspect ratio of 25. However, the radius corresponding to $\lambda = 25$ for the marked line is about $0.015 \mu\text{m}$. This discrepancy is due to the difference between a simulated fiber model and a real gecko setae model. Gecko setae are composed of a three-level hierarchical structure in practice, so higher adhesion can be generated than in a single-level model ([Bhushan et al., 2006](#); [Kim and Bhushan, 2007a, b](#)). Given the simplification in the fiber model, this simulation result is very close to the experimental result.

11.8 Fabrication of Gecko Skin-Inspired Structures

Based on the studies reported in the literature, the dominant adhesion mechanism utilized by gecko and spider attachment systems appears to be van der Waals forces. The hierarchical structure involving complex divisions of the gecko skin (lamellae–setae–branches–spatulae) enables a large number of contacts between the gecko skin and mating surface. As shown in previous calculations, the van der Waals adhesive force for two parallel surfaces is inversely proportional to the cube of the distance between two surfaces. These hierarchical fibrillar microstructured surfaces would be capable of reusable dry adhesion and would have uses in a wide range of applications from everyday objects such as adhesive tapes, fasteners, toys, microelectronic and space applications, and treads of wall-climbing robots. The development of nanofabricated surfaces capable of replicating this adhesion force developed in nature is limited by current fabrication methods. Many different techniques have been used in an attempt to create and characterize bio-inspired adhesive tapes. Attempts are being made to develop climbing robots using gecko-inspired structures ([Autumn et al., 2006b](#); [Daltorio et al., 2007](#); [Aksak et al., 2008](#); [Cutkosky and Kim, 2009](#)).

11.8.1 Single-Level Roughness Structures

A soft, compliant fibrillar structure is desirable in order to enable more fibrils to be in close proximity to a mating surface to increase van der Waals forces. [Sitti and Fearing \(2003\)](#) and [Cho and Choi \(2007\)](#) used nanoporous anodic alumina and polycarbonate membranes as a template to create polymeric nanofibers. [Geim et al. \(2003\)](#) created arrays of polyimide nanofibers using electron-beam lithography and dry etching in oxygen plasma (Fig. 11.29a left). By using electron-beam lithography, thermal evaporation of an aluminum film, and lift-off, an array of nanoscale aluminum disks were prepared. These patterns were then transferred in the polyimide film by dry etching in oxygen plasma. A 1-cm^2 sample was able

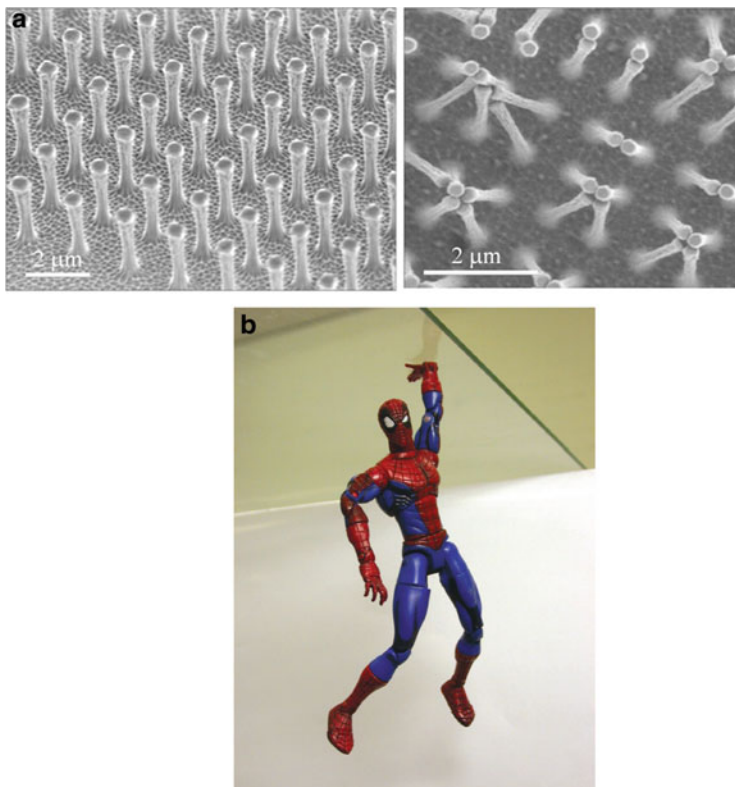
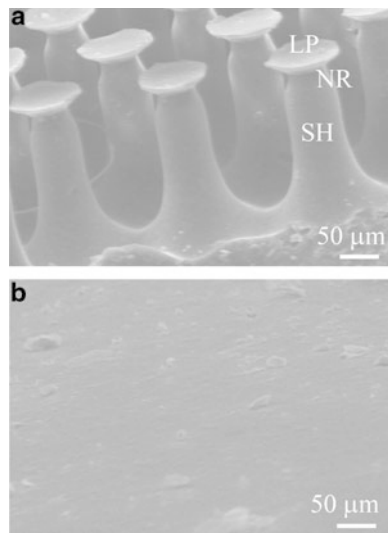


Fig. 11.29 (a) (left) An array of polyimide nanohairs and (right) bunching of the nanohairs, which leads to a reduction in adhesive force. (b) A Spiderman toy (about 0.4 N) with a hand covered with the molded polymer nanohairs, clinging to a glass plate ([Geim et al., 2003](#))

to create 3 N of adhesive force under the new arrangement. This is approximately one-third the adhesive strength of a gecko. They fabricated a Spiderman toy (about 0.4 N) with a hand covered with molded polymer nanohairs (Fig. 11.29b). They demonstrated that it could cling to a glass plate. Bunching of the nanohairs (as described earlier) if they are closely spaced was determined to greatly reduce the both the adhesive strength and durability of the polymer tape. The bunching can be clearly seen in Fig. 11.29a (right). Therefore, an optimal geometry is required.

[Gorb et al. \(2007\)](#) and [Bhushan and Sayer \(2007\)](#) characterized two polyvinyl-siloxane (PVS) samples from Gottlieb Binder Inc., Holzgerlingen, Germany: one consisting of mushroom-shaped pillars (Fig. 11.30a) and the other an unstructured control surface (Fig. 11.30b). The structured sample is inspired by the micropatterns found in the attachment systems of male beetles from the family Chrysomelidae and is easier to fabricate. Both sexes possess adhesive hairs on their tarsi; however, males bear hair extremely specialized for adhesion on the smooth surface of the female's covering wings during mating. The hairs have broad flattened tips with

Fig. 11.30 SEM micrographs of the (a) structured and (b) unstructured PVS samples. *SH* shaft, *NR* neck region, *LP* lip (Bhushan and Sayer, 2007)



grooves under the tip to provide flexibility. The mushroom shape provides a larger contact area. The structured samples were produced at room temperature by pouring two-compound polymerizing PVS into the holed template lying on a smooth glass support. The fabricated sample was comprised of pillars that are arranged in a hexagonal order to allow maximum packing density. They were approximately 100 μm in height, 60 μm in base diameter, 35 μm in middle diameter, and 25 μm in diameter at the narrowed region just below the terminal contact plates. These plates were about 40 μm in diameter and 2 μm in thickness at the lip edges. The adhesion force of the two samples in contact with a smooth flat glass substrate was measured by Gorb et al. (2007) using a microtribometer. Results revealed that the structured specimens featured an adhesion force more than twice that of the unstructured specimens. The adhesion force was also found to be independent of the preload. Moreover, it was found that the adhesive force of the structured sample was more tolerant to contamination compared to the control, and it could be easily cleaned with a soap solution.

Bhushan and Sayer (2007) characterized the surface roughness, friction force, and contact angle of the structured sample and compared the results to an unstructured control. As shown in Fig. 11.31a, the macroscale coefficient of kinetic friction of the structured sample was found to be almost four times greater than the unstructured sample. This increase was determined to be a result of the structured roughness of the sample and not the random nanoroughness. It is also noteworthy that the static and kinetic coefficients of friction are approximately equal for the structured sample. It is believed that the divided contacts allow the broken contacts of the structured sample to constantly recreate contact. As seen in Fig. 11.31b, the pillars also increased the hydrophobicity of the structured sample in comparison to the unstructured sample as expected due to increased surface roughness (Wenzel, 1936;

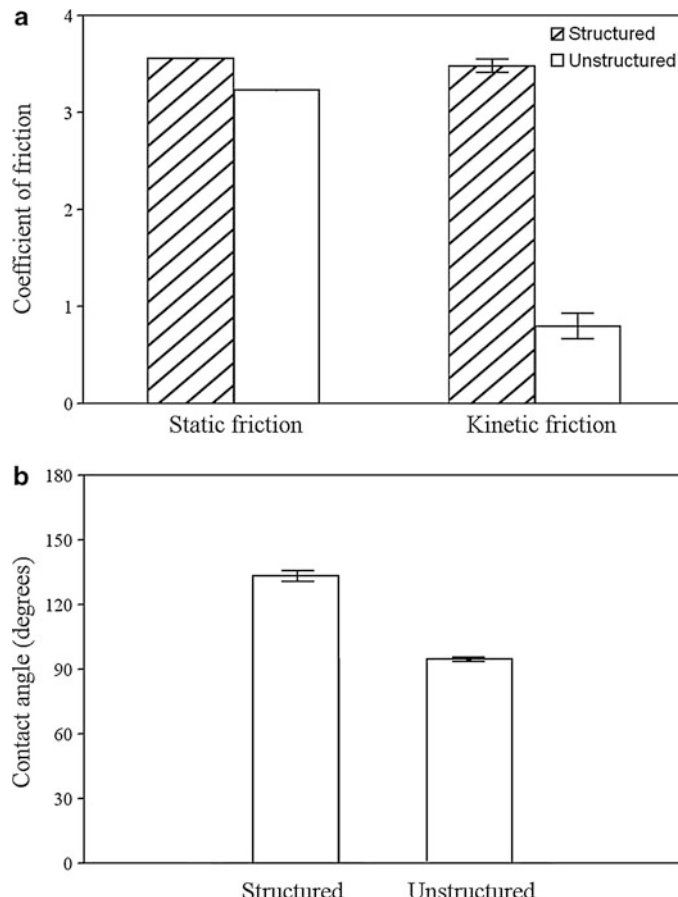


Fig. 11.31 (a) Coefficients of static and kinetic friction for the structured and unstructured samples slid against magnetic tape with a normal load of 130 mN. (b) Water contact angle for the structured and unstructured samples ([Bhushan and Sayer, 2007](#))

[Burton and Bhushan, 2005; Bhushan and Jung, 2011](#)). A large contact angle is important for self-cleaning ([Nosonovsky and Bhushan, 2008](#)), which agrees with the findings of [Gorb et al. \(2007\)](#) that the structured sample is more tolerant of contamination than the unstructured sample.

Directed self-assembly has been proposed as a method to produce regularly spaced fibers ([Schäffer et al. 2000; Sitti, 2003](#)). In this technique, a thin liquid polymer film is coated on a flat conductive substrate. As demonstrated in Fig. 11.32, a closely spaced metal plate is used to apply a DC electric field to the polymer film. Due to instabilities on the film, pillars will begin to grow until they are touching the upper metal plate. Self-assembly is desirable because the components spontaneously assemble, typically by bouncing around in a solution or gas phase until a stable structure of minimum energy is reached.

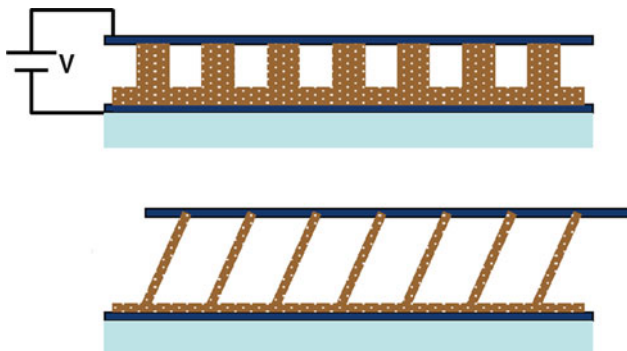


Fig. 11.32 Directed self-assembly-based method of producing high-aspect-ratio micro-/nanofibers (Sitti, 2003)

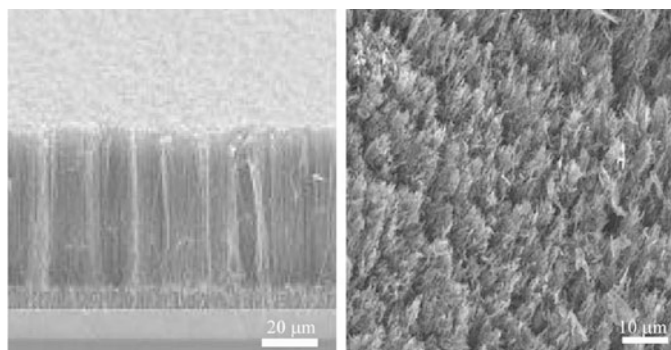


Fig. 11.33 Multiwalled carbon nanotube structures: (*left*) grown on silicon by chemical vapor deposition, (*right*) transferred into a PMMA matrix, and then exposed on the surface after solvent etching (Yurdumakan et al., 2005)

Vertically aligned multiwalled carbon nanotubes (MWCNT) have been used to create nanostructures on polymer surfaces. Yurdumakan et al. (2005) used chemical vapor deposition (CVD) to grow vertically aligned MWCNT that are 50–100 μm in length on quartz or silicon substrates. The sample with MWCNT site facing up was then dipped in poly(methyl methacrylate) (PMMA) solution. After the polymerization, PMMA–MWCNT sheets were peeled off from the silicon substrate. The MWCNTs were exposed from the silicon-facing side of the PMMA matrix by etching the top 25 μm with a solvent. SEM images of the MWCNT grown on a silicon substrate as well as transferred into a PMMA matrix and then exposed on the surface can be seen in Fig. 11.33. On a nanoscale, the MWCNT surface was able to achieve adhesive forces two orders of magnitude greater than those of gecko foot hairs. These structures provided high adhesion on the nanometer level and were not capable of producing high adhesion forces on the macroscale, because they are not compliant. Ge et al. (2007) and others have fabricated nanostructures by transferring

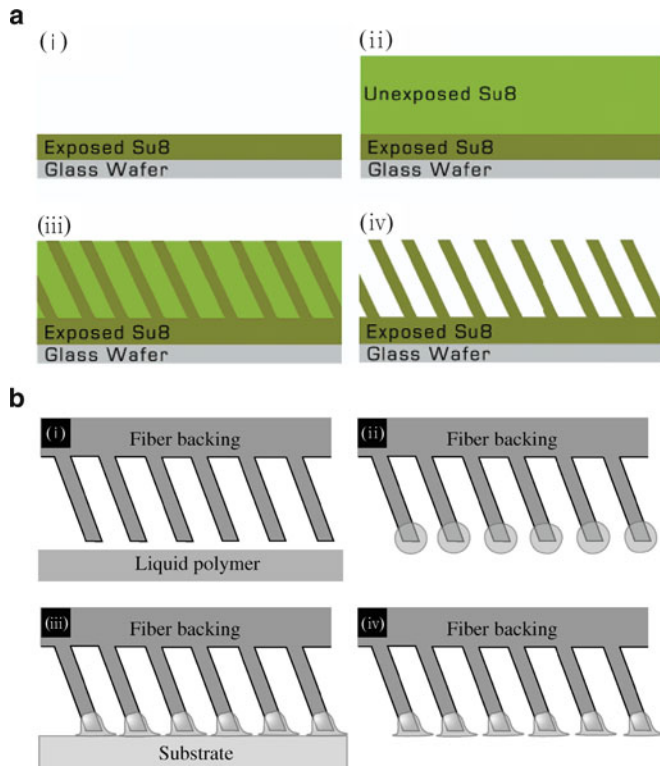


Fig. 11.34 (a) The process steps of the polymer fiber orientation (1) a thin layer of SU-8 is spun on a glass substrate then exposed and cured, (2) a thicker layer of SU-8 is spun which will become the fibers, (3) the thick layer is patterned with UV exposure by tilting the wafer, and (4) the SU-8 photoresist is developed, leaving the desired angled fiber array (Aksak et al., 2007). (b) Fiber tip fabrication process (1) bare fibers are aligned with a layer of liquid polymer, (2) the fibers are tipped into the liquid and retracted, (3) the fibers are brought into contact with a substrate, and (4) the fibers are peeled away from the substrate after curing (Murphy et al., 2007)

micropatterned, vertically aligned MWCNT arrays onto flexible polymer tape. They reported high adhesion on the macroscale. They also performed peeling experiments. Durability of the adhesive tape is an issue as some of the nanotubes can detach from the substrate with repeated use. Qu et al. (2008) measured adhesion on vertically aligned MWCNT arrays on Si substrate and reported high adhesion on the nanoscale.

Davies et al. (2008) fabricated mushroom-headed microfibers made of PDMS. In one of the fabrication strategies, a silicon wafer with a thickness which defined the stalk length was obtained, and the masks with mushroom head features were first used to pattern one side of the silicon wafer with resist. Features were etched to a depth equal to that of the thickness of the mushroom head. Next, the smaller diameter mask was used to pattern the other side of the wafer, which was then etched to produce holes through the entire thickness of the wafer, meeting mushroom-headed cavities. This mold was first coated in a fluorocarbon release agent. A PDMS

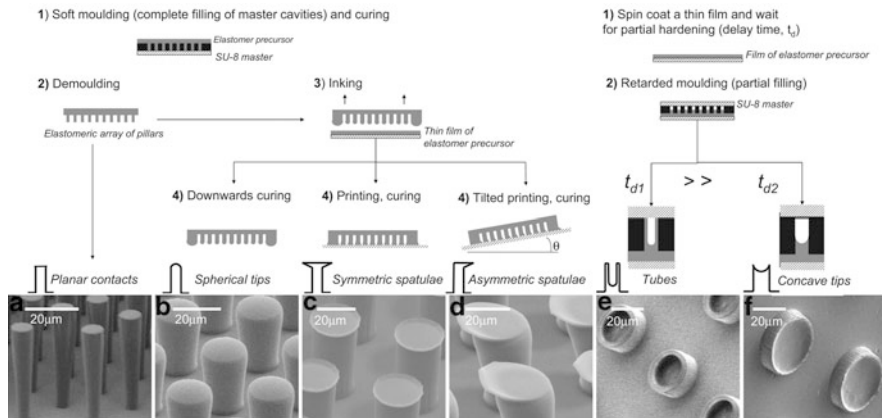


Fig. 11.35 The fabrication strategies and SEM images showing examples of the pillar arrays obtained with controlled 3D tip geometries (del Campo et al., 2007a)

solution was then spun onto this mold and cured to produce mushroom-headed microfibers. The resulting casting comprising of stalks and mushroom heads was then pulled through the mold in a single peeling process. To create angled microfiber arrays found in biological attachments using photolithography, Aksak et al. (2007) simply varied the ultraviolet (UV) exposure angle by tilting the wafer during exposure. The fibers were formed at a nonperpendicular angle to the substrate surface (Fig. 11.34a). This master template of angled SU-8 fibers was then used to form many copies of the fiber arrays from curable polyurethanes by molding. They reported that angled fibers exhibited reduced adhesion compared to similar vertical fibers due to a peeling moment. However, angled fibers are favored in biological attachment systems. Murphy et al. (2007) modified angled fiber arrays by adding soft spherical and spatula-shaped tips via dipping in a liquid polymer of interest (Fig. 11.34b). To add tips to the fibers, the fiber array sample attached to a micropositioning stage was dipped into a liquid polyurethane layer and retracted, retaining some of the liquid polymer on the tips of the fibers. To form spherical tips, the sample was placed with the fibers facing up and allowed to cure. To form spatula tips, the fiber sample was placed onto a smooth low-energy surface and then peeled away after curing. They reported very high adhesion of these fibers with soft tips because of increased contact area.

del Campo et al. (2007a, b) fabricated pillar arrays with controlled 3D tip geometries resembling those found in biological attachments. The fabrication strategy was based on complete or partial soft molding on 2D masters made by lithography with elastomeric precursors followed in some cases by inking and microprinting steps. The patterned master with high-aspect-ratio cylindrical holes was produced by photolithography using SU-8 photoresist films. The SU-8 masters were filled with elastomeric precursors (PDMS supplied as Sylgard 184 by Dow Corning) to produce arrays of cylindrical pillars (Fig. 11.35a). Arrays of pillars

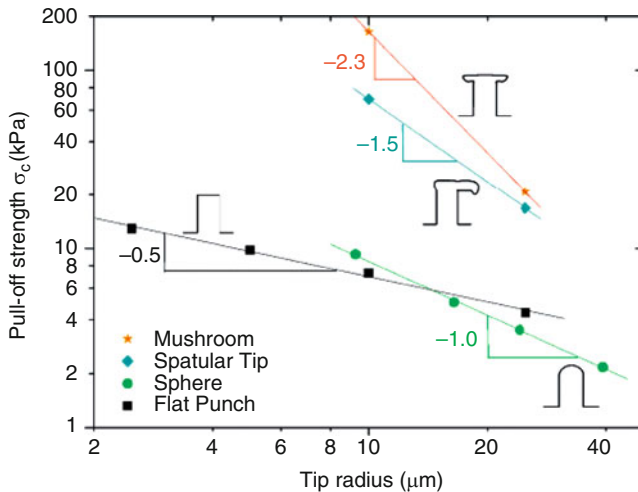


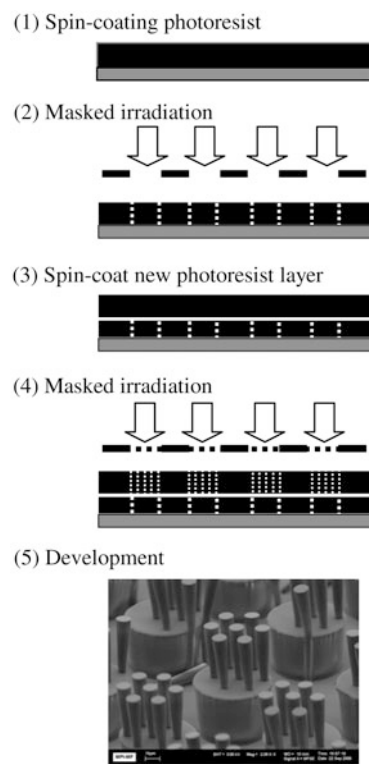
Fig. 11.36 Tip radius dependence of the pull-off force for flat, spherical, spatular, and mushroom-like contacts at a preload of 1 mN. In the case of spherical tips, the radius corresponds to the tip radius. For all other geometries, the pillar radius is used (del Campo et al., 2007b)

with spherical and spatular tips were obtained by inking the Sylgard 184-structured substrates in a thin film of Sylgard 184 precursor. Curing of arrays in upside-down orientation yielded hemispherical tips as a consequence of gravity and surface tension acting on the fluid drop (Fig. 11.35b). Alternatively, the inked stamp can be pressed against a flat substrate and then cured. This leads to pillars with a flat roof (Fig. 11.35c). The roof can be symmetric or asymmetric depending on the tilt of the substrate during curing (Fig. 11.35c, d). They also used silicones used for dental impressions. These materials possess higher initial viscosities and faster cross-linking kinetics than Sylgard 184, which results in incomplete cavity filling. By soft molding these materials after selected delay times after mixing, arrays of tubes and pillars with concave tips (Fig. 11.35e, f) were obtained. They performed adhesion tests on various geometries against a sapphire sphere. They reported that shape of pillar tip affects the contact area and adhesion behavior. Figure 11.36 shows the pull-off strength data as a function of tip radius for various tip geometries. For a given tip radius, pillars with flat punch geometry have significantly higher adhesion than spherical contacts. Pillars with mushroom tips have the highest adhesion.

11.8.2 Multilevel Hierarchical Structures

The aforementioned fabricated surfaces only have one level of roughness. Although these surfaces are capable of producing high adhesion on the micro-/nanoscale, they are not expected to produce large-scale adhesion due to a lack of compliance and bunching.

Fig. 11.37 Layer-by-layer structuring method and example of fabricated hierarchical structure with SU-8. Base pillars have $50\text{ }\mu\text{m}$ diameter and $40\text{ }\mu\text{m}$ height, and the top pillars have $9\text{ }\mu\text{m}$ diameter and $35\text{ }\mu\text{m}$ height (del Campo and Greiner, 2007)



del Campo and Greiner (2007) fabricated a hierarchical structure by two-level photolithography. Figure 11.37 shows a schematic of the process and an example of two-level SU-8 patterns obtained. Lee and Bhushan (2012) fabricated one-level and two-level hierarchical-structured superhydrophobic surfaces using either one or two stacked porous membranes as a template, respectively. By changing the density and diameter of the nanofibers, surfaces with either the *Lotus* effect or gecko effect could be fabricated. Figure 11.38 shows the SEM micrographs of selected micro-, nano-, and hierarchical structures made from polypropylene. The figure also shows the contact angle, contact angle hysteresis, and adhesive force data. It can be seen that all structures' surfaces are superhydrophobic, governed by air pocket formation on the surfaces. The oriented fibers of 100 and 600 nm diameter exhibited the gecko effect (high adhesion) due to their high fiber densities and large contact areas. Whereas, the oriented fibers of $5\text{ }\mu\text{m}$ and $14\text{ }\mu\text{m}$ diameter exhibited the *Lotus* effect due to their smaller fiber density. They used a soft adhesive to coat fiber ends to provide added adhesion by conventional adhesives.

Northen and Turner (2005) created a two-level compliant structure by employing a microelectromechanical-based approach. The multiscale structures consisted of arrays of organic-looking photoresist nanorods (organorods), $\sim 2\text{ }\mu\text{m}$ tall and $50\text{--}200\text{ nm}$ in diameter (comparable in size to gecko spatulae) (Fig. 11.39a), atop

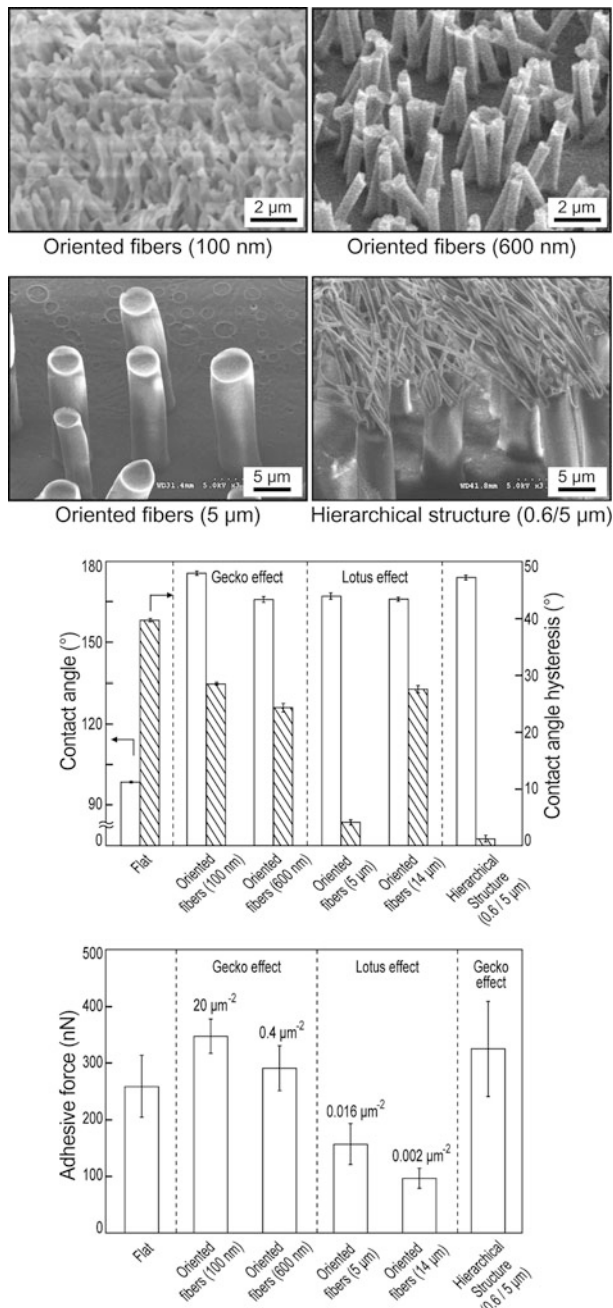


Fig. 11.38 SEM micrographs and measured contact angles, contact angle hysteresis, and adhesion forces of various samples with micro-, nano-, and hierarchical structures made of polypropylene (adapted from Lee and Bhushan, 2012)

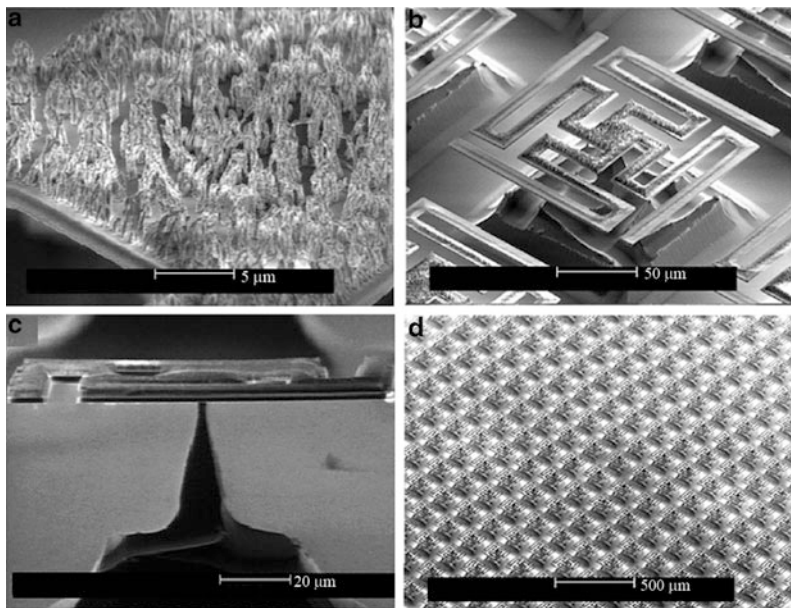


Fig. 11.39 Two-level fabricated adhesive structure composed of (a) organorods atop, (b) silicon dioxide platforms. The platforms are supported by (c) support pillars. (d) This structure was repeated multiple times over a silicon wafer (Northen and Turner, 2005)

photolithographically defined 2 μm -thick SiO_2 platforms 100–150 μm on a side (Fig. 11.39b). The platforms of various geometries are supported by single high-aspect-ratio pillars down to 1 μm in diameter and with heights up to $\sim 50 \mu\text{m}$ (Fig. 11.39c). The structures were fabricated out of 100-mm single-crystal wafers using standard bulk micromachining techniques. An array of four-fingered platform structures is shown in Fig. 11.39d. Adhesion testing was performed using a nanorod surface on a solid substrate and on the two-level structures. They reported that adhesive pressure of the two-level structures was about four times higher than that of the surfaces with only one level of hierarchy.

11.9 Summary

The adhesive properties of geckos and other creatures such as flies, beetles, and spiders are due to the hierarchical structures present on each creature's hairy attachment pads. Geckos have developed the most intricate adhesive structures of any of the aforementioned creatures. The attachment system consists of ridges called lamellae that are covered in microscale setae that branch off into nanoscale spatulae, about three billion spatulae on two feet. The so-called division of contacts provides high dry adhesion. Multiple level hierarchically structured surface construction

plays an important role in adapting to various rough surfaces, bringing the spatulae in close proximity with the mating surface. These structures, as well as material properties, allow the gecko to obtain a much larger real area of contact between its feet and a mating surface than is possible with a non-fibrillar material. Two feet of a Tokay gecko have about 220 mm^2 of attachment pad area on which the gecko is able to generate approximately 20 N of adhesion force. Although capable of generating high adhesion forces, a gecko is able to detach from a surface at will—an ability known as smart adhesion. Detachment is achieved by a peeling motion of the gecko's feet from a surface.

Experimental results have supported the adhesion theories of intermolecular forces (van der Waals) as a primary adhesion mechanism and capillary forces as a secondary mechanism, and have been used to rule out several other mechanisms of adhesion including the secretion of sticky fluids, suction, and increased frictional forces. Atomic force microscopy has been employed by several investigators to determine the adhesion strength of gecko foot hairs. The measured values of the lateral force required to pull parallel to the surface for a single seta ($194\text{ }\mu\text{N}$) and adhesive force (normal to the surface) of a single spatula (11 nN) are comparable to the van der Waals prediction of $270\text{ }\mu\text{N}$ and 11 nN for a seta and spatula, respectively. The adhesion force generated by seta increases with preload and reaches a maximum when both perpendicular and parallel preloads are applied. Although gecko feet are strong adhesives, they remain free of contaminant particles through self-cleaning. Spatular size along with material properties enables geckos to easily expel any dust particles that come into contact with their feet.

A three-level hierarchical model for a gecko lamella consisting of setae, branches, and spatulae has brought more insight into adhesion of biological attachment systems. One-, two-, and three-level hierarchically structured spring models for simulation of a seta contacting with random rough surfaces were considered. The simulation results show that the multilevel hierarchical structure has a higher adhesion force as well as higher adhesion energy than the one-level structure for a given applied load, due to better adaptation and attachment ability. It is concluded that the multilevel hierarchical structure produces adhesion enhancement, and this enhancement increases with an increase in the applied load and a decrease in the stiffness of springs. The condition at which a significant adhesion enhancement occurs appears to be related to the maximum spring deformation. The result shows that significant adhesion enhancement occurs when the maximum spring deformation is greater than two to three times larger than σ value of surface roughness. For the effect of applied load, as the applied load increases, adhesion force increases up to a certain applied load and then has a constant value, whereas adhesion energy continues to increase with an increase in the applied load. For the effect of spring stiffness, the adhesion coefficient increases with a decrease in the stiffness of springs. The hierarchical model with softer springs can generate higher adhesion enhancement in the lower applied load. For the effect of the number of springs, as the number of springs on the lower level increases, the equivalent stiffness decreases. Therefore, the three-level model with larger number of springs on the lowest level gives larger adhesion force and energy. Inclusion of

capillary forces in the spring model shows that the total adhesion force decreases with an increase in the contact angle of water on the substrate, and the difference of total adhesion force among different contact angles is larger in the intermediate humidity regime. In addition, the simulation results match the measured data for a single spatula in contact with both the hydrophilic and the hydrophobic surfaces which further supports van der Waals forces as the dominant mechanism of adhesion and capillary forces as a secondary mechanism.

There is a great interest among the scientific community to create surfaces that replicate the adhesion strength of gecko feet. These hierarchical fibrillar microstructured surfaces would be capable of reusable dry adhesion and would have uses in a wide range of applications from everyday objects such as adhesive tapes, fasteners, toys, microelectronic and space applications, and treads of wall-climbing robots. In the design of fibrillar structures, it is necessary to ensure that the fibrils are compliant enough to easily deform to the mating surface's roughness profile yet rigid enough to not collapse under their own weight. Spacing between the individual fibrils is also important. If the spacing is too small, adjacent fibrils can attract each other through intermolecular forces which will lead to bunching. The adhesion design database developed by [Kim and Bhushan \(2007c\)](#) serves as a reference for choosing design parameters.

Nanoindentation, molding, self-assembly, carbon nanotube arrays, and lithography are some of the methods that have been used to create fibrillar structures. The limitations of current machining methods on the micro-/nanoscale have resulted in the majority of fabricated surfaces consisting of only one level of hierarchy. Bunching, lack of compliance, and lack of durability are some of the problems that may arise with the aforementioned structures. Multilevel compliant systems have been created using molding, photolithography, and a microelectromechanical-based approach. Inspired by work on adding tips to the fibrillar structures, the end of the fibers could be modified to enhance adhesion. For example, a soft adhesive could be used to coat fiber ends to provide added adhesion by conventional adhesives.

Fibrillar structures show great promise in the creation of adhesive structures. Some of the structures have been incorporated into the design of treads of climbing robots.

References

- Aksak B, Murphy MP, Sitti M (2007) Adhesion of biologically inspired vertical and angled polymer microfiber arrays. *Langmuir* 23:3322–3332
- Aksak B, Murphy MP, Sitti M (2008) Gecko inspired micro-fibrillar adhesives for wall climbing robots on micro/nanoscale rough surfaces. In: Proceedings of 2008 IEEE conference on robotics and automation, Pasadena, CA, pp 3058–3063
- Aristotle (1918) *Historia Animalium*, transl. Thompson DAW, <http://classics.mit.edu/Aristotle/history_anim.html>
- Arzt E, Gorb S, Spolenak R (2003) From micro to nano contacts in biological attachment devices. *Proc Natl Acad Sci USA* 100:10603–10606
- Autumn K (2006) How gecko toes stick. *Am Sci* 94:124–132

- Autumn K, Peattie AM (2002) Mechanisms of adhesion in geckos. *Integr Comp Biol* 42:1081–1090
- Autumn K, Liang YA, Hsieh ST, Zesch W, Chan WP, Kenny TW, Fearing R, Full RJ (2000) Adhesive force of a single gecko foot-hair. *Nature* 405:681–685
- Autumn K, Sitti M, Liang YA, Peattie AM, Hansen WR, Sponberg S, Kenny TW, Fearing R, Israelachvili JN, Full RJ (2002) Evidence for van der waals adhesion in gecko setae. *Proc Natl Acad Sci USA* 99:12252–12256
- Autumn K, Majidi C, Groff RE, Dittmore A, Fearing R (2006a) Effective elastic modulus of isolated gecko setal arrays. *J Exp Biol* 209:3558–3568
- Autumn K, Dittmore A, Santos D, Spenko M, Cutkosky M (2006b) Frictional adhesion, a new angle on gecko attachment. *J Exp Biol* 209:3569–3579
- Barnes WJP, Smith J, Oines C, Mundl R (2002) Bionics and wet grip. *Tire Technol Int* 2002:56–60
- Bergmann PJ, Irschick DJ (2005) Effects of temperature on maximum clinging ability in a diurnal gecko: evidence for a passive clinging mechanism? *J Exp Zool* 303A:785–791
- Bertram JEA, Gosline JM (1987) Functional design of horse hoof keratin: the modulation of mechanical properties through hydration effects. *J Exp Biol* 130:121–136
- Bhushan B (1996) Tribology and mechanics of magnetic storage devices, 2nd edn. Springer, New York
- Bhushan B (1999) Principles and applications of tribology. Wiley, New York
- Bhushan B (2002) Introduction to tribology. Wiley, New York
- Bhushan B (2007) Adhesion of multi-level hierarchical attachment systems in gecko feet. *J Adhes Sci Technol* 21:1213–1258
- Bhushan B (2010) Springer handbook of nanotechnology, 3rd edn. Springer, Heidelberg
- Bhushan B (2011) Nanotribology and nanomechanics I – Measurement techniques, II – Nanotribology, biomimetics, and industrial applications, 3rd edn Springer, Heidelberg
- Bhushan B, Jung YC (2011) Natural and biomimetic artificial surfaces for superhydrophobicity, self-cleaning, low adhesion, and drag reduction. *Prog Mater Sci* 56:1–108
- Bhushan B, Sayer RA (2007) Surface characterization and friction of a bio-inspired reversible adhesive tape. *Microsyst Technol* 13:71–78
- Bhushan B, Peressadko AG, Kim TW (2006) Adhesion analysis of two-level hierarchical morphology in natural attachment systems for ‘smart adhesion’. *J Adhes Sci Technol* 20:1475–1491
- Bikerman JJ (1961) The science of adhesive joints. Academic, New York
- Burton Z, Bhushan B (2005) Hydrophobicity, adhesion, and friction properties of nanopatterned polymers and scale dependence for micro- and nanoelectromechanical systems. *Nano Lett* 5:1607–1613
- Cai S, Bhushan B (2007) Effects of symmetric and asymmetric contact angles and division of menisci on meniscus and viscous forces during separation. *Philos Mag* 87:5505–5522
- Cai S, Bhushan B (2008) Meniscus and viscous forces during separation of hydrophilic and hydrophobic surfaces with liquid mediated contacts, (invited). *Mater Sci Eng R* 61:78–106
- Cho WK, Choi IS (2007) Fabrication of hairy polymeric films inspired by geckos: wetting and high adhesion properties. *Adv Funct Mater* 18:1089–1096
- Chui BW, Kenny TW, Mamin HJ, Terris BD, Rugar D (1998) Independent detection of vertical and lateral forces with a sidewall-implanted dual-axis piezoresistive cantilever. *Appl Phys Lett* 72:1388–1390
- Cutkosky MR, Kim S (2009) Design and fabrication of multi-materials structures for bio-inspired robots. *Philos Trans R Soc A* 367:1799–1813
- Dalton KA, Gorb S, Peressadko A, Horchler AD, Ritzmann RE, Quinn RD (2007) A robot that climbs walls using micro-structured polymer adhesive. In: Proceedings of 30th annual meeting of the adhesion society, pp 329–331
- Davies J, Haq S, Hawke T, Sargent JP (2008) A practical approach to the development of a synthetic gecko tape. *Int J Adhesion Adhesives* 29:380–390
- del Campo A, Greiner C (2007) SU-8: a photoresist for high-aspect-ratio and 3D submicron lithography. *J Micromech Microeng* 17:R81–R95

- del Campo A, Greiner C, Alvares I, Arzt E (2007a) Patterned surfaces with pillars with controlled 3D tip geometry mimicking bioattachment devices. *Adv Mater* 19:1973–1977
- del Campo A, Greiner C, Arzt E (2007b) Contact shape controls adhesion of bioinspired fibrillar surfaces. *Langmuir* 23:10235–10243
- Dellit WD (1934) Zur Anatomie und Physiologie der Geckozehe. *Jena Z Naturwissen* 68:613–658
- Derjaguin BV, Muller VM, Toporov YuP (1975) Effect of contact deformation on the adhesion of particles. *J Colloid Interface Sci* 53:314–326
- Dieter GE (1988) Mechanical metallurgy. McGraw Hill, London
- Fan PL, O'Brien MJ (1975) Adhesion in deformable isolated capillaries. In: Lee LH (ed) *Adhesion science and technology*, vol 9A. Plenum, New York, p 635
- Federle W (2006) Why are so many adhesive pads hairy? *J Exp Biol* 209:2611–2621
- Federle W, Riehle M, Curtis ASG, Full RJ (2002) An integrative study of insect adhesion: mechanics of wet adhesion of pretarsal pads in ants. *Integr Comp Biol* 42:1100–1106
- Federle W, Barnes WJP, Baumgartner W, Drechsler P, Smith JM (2006) Wet but not slippery: boundary friction in tree frog adhesive toe pads. *J R Soc Interface* 3:689–697
- Gao H, Wang X, Yao H, Gorb S, Arzt E (2005) Mechanics of hierarchical adhesion structures of geckos. *Mech Mater* 37:275–285
- Ge L, Sethi S, Ci L, Ajayan M, Dhinojwale A (2007) Carbon nanotube-based synthetic gecko tape. *PNAS* 104:10792–10795
- Geim AK, Dubonos SV, Grigorieva IV, Novoselov KS, Zhukov AA, Shapoval SY (2003) Microfabricated adhesive mimicking gecko foot-hair. *Nat Mater* 2:461–463
- Gennaro JGJ (1969) The gecko grip. *Nat Hist* 78:36–43
- Glassmaker NJ, Jagota A, Hui CY, Kim J (2004) Design of biomimetic fibrillar interfaces: 1. Making contact. *J R Soc Interface* 1:23–33
- Glassmaker NJ, Jagota A, Hui CY (2005) Adhesion enhancement in a biomimetic fibrillar interface. *Acta Biomater* 1:367–375
- Gorb S (2001) Attachment devices of insect cuticles. Kluwer, Dordrecht
- Gorb S, Varenberg M, Peressadko A, Tuma J (2007) Biomimetic mushroom-shaped fibrillar adhesive microstructures. *J R Soc Interface* 4:271–275
- Hamaker HC (1937) London van der Waals attraction between spherical bodies. *Physica* 4:1058
- Han D, Zhou K, Bauer AM (2004) Phylogenetic relationships among gekkotan lizards inferred from C-mos nuclear DNA sequences and a new classification of the gekkota. *Biol J Linn Soc* 83:353–368
- Hanna G, Barnes WJP (1991) Adhesion and detachment of the toe pads of tree frogs. *J Exp Biol* 155:103–125
- Hansen WR, Autumn K (2005) Evidence for self-cleaning in gecko setae. *Proc Natl Acad Sci USA* 102:385–389
- Hiller U (1968) Untersuchungen zum Feinbau und zur Funktion der Haftborsten von Reptilien. *Z Morphol Tiere* 62:307–362
- Hinds WC (1982) Aerosol technology: properties, behavior, and measurement of airborne particles. Wiley, New York
- Hora SL (1923) The adhesive apparatus on the toes of certain geckos and tree frogs. *J Asiat Soc Beng* 9:137–145
- Houwink R, Salomon G (1967) Effect of contamination on the adhesion of metallic couples in ultra high vacuum. *J Appl Phys* 38:1896–1904
- Huber G, Gorb SN, Spolenak R, Arzt E (2005a) Resolving the nanoscale adhesion of individual gecko spatulae by atomic force microscopy. *Biol Lett* 1:2–4
- Huber G, Mantz H, Spolenak R, Mecke K, Jacobs K, Gorb SN, Arzt E (2005b) Evidence for capillarity contributions to gecko adhesion from single spatula and nanomechanical measurements. *Proc Natl Acad Sci USA* 102:16293–16296
- Irschick DJ, Austin CC, Petren K, Fisher RN, Losos JB, Ellers O (1996) A comparative analysis of clinging ability among pad-bearing lizards. *Biol J Linn Soc* 59:21–35
- Israelachvili JN (1992) *Intermolecular and surface forces*, 2nd edn. Academic, San Diego

- Israelachvili JN, Tabor D (1972) The measurement of van der Waals dispersion forces in the range of 1.5 to 130 nm. *Proc R Soc Lond A* 331:19–38
- Jaenicke R (1998), Atmospheric aerosol size distribution. In: Harrison RM, van Grieken R (eds) *Atmospheric particles*. Wiley, New York, pp. 1–29
- Jagota A, Bennison SJ (2002) Mechanics of adhesion through a fibrillar microstructure. *Integr Comp Biol* 42:1140–1145
- Johnson KL, Kendall K, Roberts AD (1971) Surface energy and the contact of elastic solids. *Proc R Soc Lond A* 324:301–313
- Kesel AB, Martin A, Seidl T (2003) Adhesion measurements on the attachment devices of the jumping spider *Evarcha arcuata*. *J Exp Biol* 206:2733–2738
- Kim TW, Bhushan B (2007a) The adhesion analysis of multi-level hierarchical attachment system contacting with a rough surface. *J Adhes Sci Technol* 21:1–20
- Kim TW, Bhushan B (2007b) Effect of stiffness of multi-level hierarchical attachment system on adhesion enhancement. *Ultramicroscopy* 107:902–912
- Kim TW, Bhushan B (2007c) Optimization of biomimetic attachment system contacting with a rough surface. *J Vac Sci Technol A* 25:1003–1012
- Kim TW, Bhushan B (2008) The adhesion model considering capillarity for gecko attachment system. *J R Soc Interface* 5:319–327
- Kluge AG (2001) Gekkotan lizard taxonomy. *Hamadryad* 26:1–209
- Lee H, Bhushan B (2012) Fabrication and characterization of hierarchical nanostructured smart adhesion surfaces. (unpublished)
- Losos JB (1990) Thermal sensitivity of sprinting and clinging performance in the tokay gecko (*Gekko gecko*). *Asiat Herp Res* 3:54–59
- Maderson PFA (1964) Keratinized epidermal derivatives as an aid to climbing in gekkonid lizards. *Nature* 2003:780–781
- Murphy MP, Aksak B, Sitti M (2007) Adhesion and anisotropic friction enhancement of angled heterogeneous micro-fiber arrays with spherical and spatula tips. *J Adhes Sci Technol* 21:1281–1296
- Northen MT, Turner KL (2005) A batch fabricated biomimetic dry adhesive. *Nanotechnology* 16:1159–1166
- Nosonovsky M, Bhushan B (2008) Multiscale dissipative mechanisms and hierarchical surfaces: friction, superhydrophobicity, and biomimetics. Springer, Heidelberg
- Ohler A (1995) Digital pad morphology in torrent-living ranid frogs. *Asiat Herpetol Res* 6:85–96
- Orr FM, Scriven LE, Rivas AP (1975) Pendular rings between solids: meniscus properties and capillary forces. *J Fluid Mech* 67:723–742
- Peattie AM, Full RJ (2007) Phylogenetic analysis of the scaling of wet and dry biological fibrillar adhesives. *Proc Natl Acad Sci USA* 104:18595–18600
- Persson BNJ (2003) On the mechanism of adhesion in biological systems. *J Chem Phys* 118:7614–7621
- Persson BNJ, Gorb S (2003) The effect of surface roughness on the adhesion of elastic plates with application to biological systems. *J Chem Phys* 119:11437–11444
- Pesica NS, Tian Y, Zhao B, Rosenberg K, Zeng H, McGuiggen P, Autumn K, Israelachvili JN (2007) Peel-zone model of tape peeling based on the gecko adhesive system. *J Adhes* 83: 383–401
- Phipps PBP, Rice DW (1979) Role of water in atmospheric corrosion. In: Brubaker GR, Phipps PBP (eds) *Corrosion chemistry*, ACS symposium series, vol 89. American Chemical Society, Washington, D.C, pp. 235–261
- Qu L, Dai L, Stone M, Xia Z, Wang ZL (2008) Carbon nanotube arrays with strong shear binding-on and easy normal lifting-off. *Science* 322:238–242
- Rizzo N, Gardner K, Walls D, Keiper-Hrynkko N, Hallahan D (2006) Characterization of the structure and composition of gecko adhesive setae. *J R Soc Interface* 3:441–451
- Ruibal R, Ernst V (1965) The structure of the digital setae of lizards. *J Morphol* 117:271–294
- Russell AP (1975) A contribution to the functional morphology of the foot of the tokay, *Gekko gecko*. *J Zool Lond* 176:437–476

- Russell AP (1986) The morphological basis of weight-bearing in the scanners of the tokay gecko. *Can J Zool* 64:948–955
- Schäffer E, Thurn-Albrecht T, Russell TP, Steiner U (2000) Electrically induced structure formation and pattern transfer. *Nature* 403:874–877
- Schleich HH, Kästle W (1986) Ultrastrukturen an Gecko-Zehen. *Amphibia Reptilia* 7:141–166
- Schmidt HR (1904) Zur Anatomie und Physiologie der Geckopfote. *Jena Z Naturwissen* 39:551
- Shah GJ, Sitti M (2004) Modeling and design of biomimetic adhesives inspired by gecko foot-hairs. In: IEEE international conference on robotics and biomimetics, pp 873–878
- Simmermacher G (1884) Untersuchungen über Haftapparate an Tarsalgliedern von Insekten. *Zeitschr Wissen Zool* 40:481–556
- Sitti M (2003) High aspect ratio polymer micro/nano-structure manufacturing using nanoembossing, nanomolding and directed self-assembly. *Proc IEEE/ASME Adv Mechatronics Conf* 2:886–890
- Sitti M, Fearing RS (2003) Synthetic gecko foot-hair for micro/nano structures as dry adhesives. *J Adhes Sci Technol* 17:1055–1073
- Spolenak R, Gorb S, Arzt E (2005) Adhesion design maps for bio-inspired attachment systems. *Acta Biomater* 1:5–13
- Stork NE (1980) Experimental analysis of adhesion of *Chrysolina polita* on a variety of surfaces. *J Exp Biol* 88:91–107
- Stork NE (1983) A comparison of the adhesive setae on the feet of lizards and arthropods. *J Nat Hist* 17:829–835
- Tian Y, Pesika N, Zeng H, Rosenberg K, Zhao B, McGuigan P, Autumn K, Israelachvili J (2006) Adhesion and friction in gecko toe attachment and detachment. *Proc Nat Acad Sci USA* 103:19320–19325
- Tinkle DW (1992) Gecko. In: Cummings M (ed) *Encyclopedia Americana*, vol 12. Grolier, London, p 359
- Van der Kloot WG (1992) Molting. In: Cummings M (ed) *Encyclopedia Americana*, vol 19. Grolier, London, pp 336–337
- Wagler J (1830) *Naturliches System der Amphibien*. J. G. Cotta'schen Buchhandlung, Munich
- Wan KT, Smith DT, Lawn BR (1992) Fracture and contact adhesion energies of mica-mica, silica-silica, and mica-silica interfaces in dry and moist atmospheres. *J Am Ceram Soc* 75:667–676
- Wenzel RN (1936) Resistance of solid surfaces to wetting by water. *Ind Eng Chem* 28:988–994
- Williams EE, Peterson JA (1982) Convergent and alternative designs in the digital adhesive pads of scincid lizards. *Science* 215:1509–1511
- Yao H, Gao H (2006) Mechanics of robust and releasable adhesion in biology: bottom-up designed hierarchical structures of gecko. *J Mech Phys Solids* 54:1120–1146
- Young WC, Budynas R (2001) *Roark's formulas for stress and strain*, 7th edn. McGraw Hill, New York
- Yurdumakan B, Raravikar NR, Ajayan PM, Dhinojwala A (2005) Synthetic gecko foot-hairs from multiwalled carbon nanotubes. *Chem Commun* 3799–3801
- Zimon AD (1969) Adhesion of dust and powder, transl by M. Corn. Plenum, New York
- Zisman WA (1963) Influence of constitution on adhesion. *Ind Eng Chem* 55(10):18–38

Chapter 12

Outlook

Biomimetics allows engineers and scientists to mimic biology or nature to develop materials and devices of commercial interest. Properties of biological materials and surfaces result from a complex interplay between surface morphology and physical and chemical properties. Hierarchical structures with dimensions of features ranging from the macroscale to the nanoscale are extremely common in nature to provide properties of interest.

There is significant interest in eco-friendly materials and surfaces. Nature uses surface morphology including hierarchical structured surfaces to provide functionality of interest. The materials used are commonly found materials. These materials and surfaces are eco-friendly or green and are now being exploited for various commercial applications. This recognition has led to “Green Science and Technology,” the term used for the first time in this book. As an example, this author has made efforts to popularize the term “Green Tribology.” Biologically inspired green surfaces can be used for various applications.

This emerging field of biomimetics is highly interdisciplinary and has attracted biologists, physicists, chemists, materials scientists, and engineers. The cross-fertilization of ideas is providing progress at a fast pace if the number of research papers and symposia on this topic is any guide. The major emphasis on nanoscience and nanotechnology science in the early 1990s has provided impetus in mimicking nature using nanofabrication techniques for commercial applications.

There are a large number of objects including bacteria, plants, land and aquatic animals, and seashells, with properties of commercial interest. This book has focused on surfaces with superomniphobicity, self-cleaning, antifouling, low/high/reversible adhesion, and drag reduction, which include *Lotus* leaf, *Salvinia*, rose petal, oleophobic/oleophilic surfaces, sharkskin, and gecko feet. The development of these types of surfaces is important for basic research as well as various applications, including self-cleaning windows; exterior paints for buildings, navigation ships, textiles, and solar panels; antifouling membranes for desalination and water purification, for reduction in fluid flow, e.g., in micro-/nanochannels; and climbing robots. Oleophobic surfaces have the potential for self-cleaning and antifouling from biological and organic contaminants both in air and underwater applications.

This book provides a useful guide for the development of biomimetic artificial surfaces. Some flexible and low-cost techniques are described for the fabrication of hierarchical structured surfaces. A proper control of roughness constitutes the main challenge in producing a reliable hierarchical surface. The fabrication of complex structures with compatible materials remains a challenge in order to be viable for commercial exploitation.

Index

- Adhesion
 rose petals, 192
 Salvinia molesta, 184
- Tokay Gecko
 capillarity effects, 305–309
 capillary forces, 286, 287
 design database, for biomimetic attachment system, 316–321
 fiber model, 310
 hierarchical spring model, 292
 humidity effects, 291
 hydrophobicity effects, 292, 293
 Laplace pressure, 276
 mechanics, 292
 multilevel hierarchical spring analysis, 295–298
 non-buckling condition, 312–313
 non-fiber fracture condition, 313–314
 non-sticking condition, 315
 numerical simulation, 316, 317
 single fiber contact analysis, 310–311
 single seta, 288, 289
 single spatula, 288–289
 single spring contact analysis, 294–295
 size, stiffness and densities, seta, 294
 surface energy approach, 276
 temperature effects, 290–291
 van der Waals forces, 285
 viscous force, 276
 Young's modulus, 277
- Adhesive force
 Lotus effect, 61–62
 structured surfaces, 81
- Atmospheric icing, 13
- Bioinspired antique jewelry, 5
- Biomimetics, definition, 1
- Blade riblets, 238–240
- Bouncing droplet, 82
- Capillary forces, Tokay Gecko
 Laplace force, 286–287
 surface tension, 287
- Carcharhinus galapagensis*, 4
- Cassie–Baxter and Wenzel transition
 micropatterned Si surfaces
 bouncing water droplet, 96–97
 destabilizing factors, 96
 droplet evaporation, 100–104
 energy barrier approach, 98
 linear 1-D phenomenon, 105–106
 1 mm radius droplets, 113–118
 nondimensional spacing factor, 104
 pitch value effect, 98–100
 wetting regime
 adhesion hysteresis, 39
 energy barrier, 38
 free energy profiles, 40–41
 surface roughness, 39
 waves and vibration, 40
- Cassie-impregnating wetting regime, 15
- Cassie interface, 22
- CNT composites
 contact angle, 156–157
 surface durability
 AFM and ball-on-flat tribometer tests, 158–162
 waterfall/jet tests, 157–158
- Composite-homogeneous interface
 bouncing droplet, 142–146
 vibrating droplet

- adhesive and inertia forces, 150, 152
- microstructured surface, 148, 151
- model, adhesion and inertia forces, 146–148
- resonance frequency, 148–149
- Composite interface stability
 - destabilizing factors, 35
 - Lotus leaf, 37–38
 - multiscale phenomenon, 34
 - transition, 37
 - two-dimensional pillars, semicircular bumps/grooves, 36
- Contact angle
 - composite interface stability
 - destabilizing factors, 35
 - Lotus leaf, 37–38
 - multiscale phenomenon, 34
 - transition, 37
 - two-dimensional pillars, semicircular bumps/grooves, 36
 - definition, 19–20
 - DI water, 81
 - homogenous and heterogeneous interfaces
 - apparent contact angle definition, 31
 - component, 29
 - limitations, 26–28
 - liquid front propagation, 28–29
 - rough and chemically heterogeneous surfaces, 30
 - roughness/heterogeneity, 31
 - surface roughness, 29
 - hysteresis, 32–34
 - wetting regime transition
 - adhesion hysteresis, 39
 - energy barrier, 38
 - free energy profiles, 40–41
 - surface roughness, 39
 - waves and vibration, 40
- Contact angle hysteresis (CAH), 11
- Dahlia* petal, 190, 191
- Dermal denticles, 227
- Directed self-assembly method, 324, 325
- 2D riblets
 - blade riblets, 238–240
 - sawtooth riblets
 - characteristic dimensions, 236, 239
 - definition, 239
 - drag reduction geometries, 240–241
 - effective streamwise protrusion height, 240–241
 - yaw angle, 242
 - scalloped riblets
- definition, 240
- drag reduction geometries, 240–241
- effective streamwise protrusion height, 240–241
- optimization data, 239, 240
- 3D riblets
 - molded epoxy scale, 244–245
 - scale bristling, 246
 - sharkskin replica, 244
 - staggered segmented-blade riblets, 243
 - types, 242
- Droplet evaporation, 82
- Drosera*, 2, 4
- Fern hair, *Salvinia molesta*, 181
- Fluid drag mechanisms
 - fish mucus and polymers, 256–257
 - fluid slip effects, 253–256
 - friction/viscous drag, 229
 - fully developed turbulent flow, 229
 - laminar-turbulent flow transition, 229–230
 - pressure/form drag, 229
 - role of riblets
 - flow through duct, 234, 235
 - streamwise and cross-stream flow velocity profiles, 233
 - vortex translation, 232
 - streamwise vortex formations, 230
 - surface material-fluid pairs, 252–253
 - turbulent flow visualization, 231–232
- Freezing rain, 13
- Friction coefficient, Lotus effect, 61–62
- Fruit fly, 271, 273
- Gecko, 3, 4
- Gerris remigis*, 2, 4
- Giant Salvinia. *See* *Salvinia molesta*
- Green Science and Technology, 339
- Hierarchical roughness, Lotus effect, 62–64
- Hierarchical structured surfaces
 - chemical structure of components, 122
 - composite-homogeneous interface
 - bouncing droplet, 142–146
 - vibrating droplet, 146–152
 - fluid drag reduction, 152
 - glass recrystallization chamber, 123–124
- Lotus tubules
 - adhesive force, 139–140
 - microstructures, 137–138

- static contact angle, contact angle hysteresis, and tilt angle, 137, 139
- Lotus wax morphology, 123–124
- mechanical durability (*see* Mechanically durable hierarchical structured surfaces)
- nanogrooves, 121
- n-hexatriacontane
- nanostucture formation, 125–126
 - roughness statistics, 125, 127
 - static contact angle, contact angle hysteresis, and tilt angle, 125, 128
 - wax platelets, 129–132
- self-cleaning efficiency, 140–142
- thermal evaporation system, 122–123
- T. majus* tubules
- droplet evaporation, 136
 - morphology, 133–134
 - nanostucture formation, 133–134
 - static contact angle, contact angle hysteresis, and tilt angle, 133, 135
- two-step molding process, 120–121
- Icephobicity, 13
- Ideal hierarchical surface structure, 119
- Isurus oxyrinchus*, 227
- Johnson–Kendall–Roberts (JKR) theory, 276
- Layer-by-layer structuring method, 329
- Lotus effect
- leaf surfaces
 - adhesive force and coefficient of friction, 62–63
 - atomic force microscope (AFM), 51–52
 - contact angles, 53–54
 - dried lotus, 57, 58
 - epicuticular waxes, 49
 - Fagus and Magnolia, 57, 60
 - fresh and dried Lotus, 57, 59
 - optical profiler, 54–56
 - role of hierarchical roughness, 62–64
 - roughness factor and contact angle, 60, 62
 - self-cleaning, 50
 - SEM micrographs, 52
 - multilevel hierarchical structures, 329
- Lotus tubules, hierarchical structured surfaces
- adhesive force, 139–140
 - microstructures, 137–138
- static contact angle, contact angle hysteresis, and tilt angle, 137, 139
- Lotus wax morphology, 123–124
- Mechanically durable hierarchical structured surfaces
- CNT composites
- AFM and ball-on-flat tribometer tests, 158–162
 - contact angle, 156–157
 - waterfall/jet tests, 157–158
- nanoparticle composites
- durability, AFM and ball-on-flat tribometer tests, 168–169
 - microparticles, contact angle, 166–168
 - micropattern, contact angle, 165–166
 - silica, 163, 164
 - structures, 163–164
- Micro- and nanopatterned polymers
- adhesive force, 91–92
 - contact angle, 89–91
 - submicron droplet effect, 91, 92
 - surface patterns, 88–89
- Microdroplet condensation and evaporation, 83
- Microelectromechanical (MEMS) force sensor, 288
- Micropatterned Si surfaces
- Cassie–Baxter and Wenzel transition criteria
 - bouncing water droplet, 96–97
 - destabilizing factors, 96
 - droplet evaporation, 100–104
 - energy barrier approach, 98
 - linear 1-D phenomenon, 105–106
 - 1 mm radius droplets, 113–118
 - nondimensional spacing factor, 104
 - pitch value effect, 98–100
 - contact angle hysteresis and wetting–dewetting asymmetry, 106–110
 - microdroplets
 - growing and merging process, ESEM, 110
 - vs. 1 mm radius droplet, 113
 - pitch value, 112
 - static contact angle and contact angle hysteresis, 111
 - static contact angle, geometric parameters, 94–95
 - surface height maps and 2-D profiles, 94
 - surface topography, 93
 - 1,1,-2,2,-tetrahydroperfluorodecyltrichlorosilane, 93

- Micropatterned structures, *Salvinia molesta*.
See *Salvinia molesta*
- Multilevel hierarchical spring analysis, Tokay Gecko
- adhesion coefficient, 300
 - adhesion energy, 298, 299
 - adhesion force and adhesion energy *vs.* applied load, 303–306
 - elastic force, 297
 - force–distance curves, 298, 301–302
 - length and stiffness, 295–296
 - spring deflection, 297
 - spring force, 297
 - surface parameters, 298, 300
- Mushroom-headed microfibers, 326–327
- Nano- and micropatterned polymers
- adhesive force, 91–92
 - contact angle, 89–91
 - submicron droplet effect, 91, 92
 - surface patterns, 88–89
- Nanoparticle composites
- contact angle
 - microparticles, 166–168
 - micropattern, 165–166
 - durability, AFM and ball-on-flat tribometer tests, 168–169
 - microstructures and hierarchical structures, 163–164
 - silica, 164–165
- Natural superhydrophobicity
- and high-adhesion surfaces, 15
 - low adhesion/drag reduction surfaces, 13–14
- Natural superoleophobicity, 15
- Nature
- montage, 2, 4
 - objects and function, 2–3
- Nelumbo nucifera*, 2, 4
- hierarchical structure, 13
 - papillose epidermal cells, 13
 - schematic representation, wetting, 14
- n*-Perfluoroeicosane, 213–214
- Oleophobic/oleophilic surfaces
- contact angle
 - solid–air–oil interface, 211
 - solid–air–water interface, 210
 - solid–water–oil interface, 210–211
 - experimental techniques, 211–213
 - wetting behavior
- on flat and micropatterned surfaces, 214–219
- on nano- and hierarchical structures, 220–221
- sharkskin replica, 221, 222
- One-level hydrophobic structures
- coating, 72–73
 - roughening, 67–72
- Peeling, Tokay Gecko
- attachment and detachment process, 278, 280
 - contact mechanics, 278, 279
 - finite element model, 278
 - spatulae orientation, 277–278
 - tape-peeling model, 279–281
- Pinguicula*, 2, 4
- Pinning effect, *Salvinia molesta*, 179, 180
- Reversible adhesion, 269
- Riblet fabrication
- antifouling, 251
 - dimension selection, 248
 - drag reduction in pipe flow, 249
 - environmental factors, 249
 - FastSkin swimsuits, 249
 - form factor, 248
 - grinding method, 252
 - hierarchical riblet structure, 250
 - micromolding and microembossing, 251
 - rolling techniques, 251
- Riblet geometries
- characteristic dimensions, 239
 - 2D (*see* 2D riblets)
 - 3D
 - molded epoxy scale, 244–255
 - scale bristling, 246
 - sharkskin replica, 244
 - staggered segmented-blade riblets, 243
 - types, 242
 - dimensions and drag reduction dependence, 234, 236–239
 - pipe flow, 246
 - types, 235–236
- Rosa Hybrid Tea cv. Bairage, 190
- adhesive force, 192
 - contact angle hysteresis, 192
 - surface height maps and 2D profiles, 194
 - water droplets on, 191, 192
- Rosa Hybrid Tea cv. Showtime, 190

- Rose petals
adhesive force, 192, 193
bump density, 195
coefficient of friction, 192
microbump map statistics, 191
microstructures, 195–196
optical micrographs, 190
peak radius, 195
SEM, 190
static contact angle and contact angle hysteresis, 191–193
superhydrophobic surface fabrication, high and low adhesion
air pocket formation, 202
droplets on hierarchical structure, 202–205
fractional liquid–air interface, 201
nanostructure formation, 196–197
platelets, 197
roughness factor, 200–201
static contact angle and contact angle hysteresis, 197–200
surface height maps and 2D profiles, 192, 194–195
- Roughness-induced superomniphobic surfaces
contact angle hysteresis (CAH), 11
natural superhydrophobicity
and high-adhesion surfaces, 15
low adhesion/drag reduction surfaces, 13–14
natural superoleophobicity, 15
static contact angle, 11
superhydrophilicity, 11
superhydrophobicity, 11
- Salvinia effect, 179
Salvinia molesta
adhesion, 184
air-trapping ability, 181
composition, 179, 180
contact angle, 182–184
force-distance curves, 185
giant liquid slip, 179
leaf characterization, 181–182
pinning effect, 179, 180
structural surface fabrication, 181–182
- Sawtooth riblets
characteristic dimensions, 236, 239
definition, 239
drag reduction geometries, 240–241
effective streamwise protrusion height, 240–241
yaw angle, 242
- Scalloped riblets
definition, 240
drag reduction geometries, 240–241
effective streamwise protrusion height, 240–241
optimization data, 237, 239–240
- Self-cleaning, 13–15
- Sharkskin, 209
dermal denticles, 227
fluid drag mechanisms
fish mucus and polymers, 256–257
fluid slip effects, 253–256
friction/viscous drag, 229
fully developed turbulent flow, 229
laminar-turbulent flow transition, 229–230
pressure/form drag, 229
role of riblets, 233–235
streamwise vortex formations, 230
surface material–fluid pairs, 252–253
turbulent flow visualization, 231–232
- Riblet fabrication
antifouling, 251
dimension selection, 248
drag reduction in pipe flow, 249
environmental factors, 249
FastSkin swimsuits, 249
form factor, 248
grinding method, 252
hierarchical riblet structure, 250
micromolding and microembossing, 251
rolling techniques, 251
- Riblet geometries
characteristic dimensions, 239
2D (see 2D riblets)
3D (see 3D riblets)
dimensions and drag reduction dependence, 234, 236–239
pipe flow, 246
types, 235–236
scale patterns, 227–228
wetting behavior, 221, 222
- Solid-air–oil interface
contact angle, 211
wetting
on flat and micropatterned surfaces, 214–215, 218, 219
on nano- and hierarchical structures, 220, 221
on sharkskin replica, 221, 222
- Solid-air–water interface
contact angle, 210
wetting

- on flat and micropatterned surfaces, 214–215, 218, 219
- on nano- and hierarchical structures, 220, 221
- on sharkskin replica, 221, 222
- Solid–water–oil interface
 - contact angle, 210–211
 - schematics of, 213
 - wetting
 - on flat and micropatterned surfaces, 214, 218, 219
 - on nano- and hierarchical structures, 221
 - on sharkskin replica, 221, 222
- Spiderweb, 4–5
- Static contact angle, 11
- Submicron droplets generation, 83–86
- Superhydrophilicity, 11
- Superhydrophobic and hydrophilic leaf
 - adhesive force and coefficient of friction, 61–62
 - atomic force microscope (AFM), 51–52
 - contact angles, 53–54
 - dried lotus, 57, 58
 - Fagus and Magnolia, 57, 60
 - fresh and dried Lotus, 57, 59
 - optical profiler, 54–56
 - roughness factor and contact angle, 60, 62
 - SEM micrographs, 52
- Superhydrophobicity, 11
- Superhydrophobic surface
 - micro- and nanostructure fabrication, 67, 68
 - micro-/nanoroughness, 67–69
 - one-level structure creation
 - casting and nanoimprint methods, 72
 - coatings, 72–73
 - etching method, 71
 - stretching method, 71
 - pros and cons of fabrication techniques, 67, 70
 - two-level structure creation
 - carbon nanotube composite, 75
 - double-roughened surface, 73
 - micropatterned silicon surface, 74
 - silica nanoparticles, 75
 - sticking phenomenon, 74
- Surface roughness, 81
- Syrphid fly, 271, 273

- T. majus* tubules
 - droplet evaporation, 136
 - morphology, 133–134
- nanostructure formation, 133–134
- static contact angle, contact angle hysteresis, and tilt angle, 133, 135
- Tokay Gecko
 - adhesion
 - capillarity effects, 305–309
 - design database, for biomimetic attachment system, 316–321
 - fiber model, 310
 - hierarchical spring model, 292
 - humidity effects, 291
 - hydrophobicity effects, 292, 293
 - Laplace pressure, 276
 - mechanics, 292
 - multilevel hierarchical spring analysis, 295–298
 - non-buckling condition, 312–313
 - non-fiber fracture condition, 313–314
 - non-sticking condition, 315
 - numerical simulation, 316, 317
 - single fiber contact analysis, 310–311
 - single seta, 288, 291
 - single spatula, 288–289
 - single spring contact analysis, 294–295
 - size, stiffness and densities, seta, 294
 - surface energy approach, 276
 - temperature effects, 290–291
 - viscous force, 276
 - Young's modulus, 277
- attachment mechanisms
 - adhesive forces, 284
 - capillary forces, 286–287
 - van der Waals forces, 285
- construction
 - hierarchical structures, foot, 272, 274
 - schematic drawings, 275
 - surface characteristics, 272, 275
- hairy attachment systems
 - arolia and euplantulae, 270–271
 - setae, 271, 272
- length, 269
- multilevel hierarchical structure, 277
- peeling
 - attachment and detachment process, 278, 280
 - contact mechanics, 278, 279
 - finite element model, 278
 - spatulae orientation, 277–278
 - tape-peeling model, 279–281
- self-cleaning
 - molting, 282
 - spatulae, SEM of, 282, 283
 - substrate–particle interactions, 282

- skin-inspired structure fabrication
 multilevel hierarchical structures,
 328–331
 single-level roughness structures,
 321–328
- Two-level hierarchical structures
 carbon nanotube composite, 75
 double-roughened surface, 73
 micropatterned silicon surface, 74
 silica nanoparticles, 75
 sticking phenomenon, 74
- Vibrating droplet, 82–83
- Waterfall/jet tests, 86–87
- Wear and friction tests, structured surfaces,
 87–88
- Wenzel and Cassie–Baxter Equations
 apparent contact angle definition, 31
- component, 29
- limitations
 apparent contact angle, 27
 disjoining pressure, 27
 multiscale process, 28
 receding and advancing contact angle,
 26, 27
 Tolman's length, 28
- liquid front propagation, 28–29
- rough and chemically heterogeneous
 surfaces, 30
- roughness/heterogeneity, 31
- surface roughness, 29
- Wetting regime transition
 adhesion hysteresis, 39
 energy barrier, 38
 free energy profiles, 40–41
 surface roughness, 39
 waves and vibration, 40
- Wire force gauge, 288
- Work of adhesion, Tokay Gecko, 295

Biography



Dr. Bharat Bhushan received an M.S. in mechanical engineering from the Massachusetts Institute of Technology in 1971, an M.S. in mechanics and a Ph.D. in mechanical engineering from the University of Colorado at Boulder in 1973 and 1976, respectively, an MBA from the Rensselaer Polytechnic Institute at Troy, NY, in 1980, Doctor Technicae from the University of Trondheim at Trondheim, Norway, in 1990, a Doctor of Technical Sciences from the Warsaw University of Technology at Warsaw, Poland, in 1996, and Doctor Honouris Causa from the National Academy of Sciences at Gomel, Belarus, in 2000 and University of Kragujevac, Serbia, in 2011. He is a registered professional engineer. He is presently an Ohio Eminent Scholar and The Howard D. Winbigler Professor in

the College of Engineering, and the Director of the Nanoprobe Laboratory for Bio- & Nanotechnology and Biomimetics (NLB²) at the Ohio State University, Columbus, Ohio. His research interests include fundamental studies with a focus on scanning probe techniques in the interdisciplinary areas of bio/nanotribology, bio/nanomechanics and bio/nanomaterials characterization, and applications to bio/nanotechnology and biomimetics. He is an internationally recognized expert of bio/nanotribology and bio/nanomechanics using scanning probe microscopy and is one of the most prolific authors. He is considered by some a pioneer of the tribology and mechanics of magnetic storage devices. He has authored 8 scientific books, 90+ handbook chapters, 700+ scientific papers (h-index—52+; ISI Highly Cited in Materials Science, since 2007; ISI Top 5% Cited Authors for Journals in Chemistry since 2011), and 60+ technical reports, edited 50+ books, and holds 17 US and foreign patents. He is a co-editor of Springer NanoScience and Technology Series and a co-editor of Microsystem Technologies. He has given more than 400 invited presentations in six continents and more than 160 keynote/plenary addresses at major international conferences.

Dr. Bhushan is an accomplished organizer. He organized the first symposium on Tribology and Mechanics of Magnetic Storage Systems in 1984 and the first international symposium on Advances in Information Storage Systems in 1990, both of which are now held annually. He is the founder of an ASME Information Storage and Processing Systems Division founded in 1993 and served as the founding chair during 1993–1998. His biography has been listed in over two dozen Who's Who books including Who's Who in the World and has received more than two dozen awards for his contributions to science and technology from professional societies, industry, and US government agencies. He is also the recipient of various international fellowships including the Alexander von Humboldt Research Prize for Senior Scientists, Max Planck Foundation Research Award for Outstanding Foreign Scientists, and the Fulbright Senior Scholar Award. He is a foreign member of the International Academy of Engineering (Russia), Byelorussian Academy of Engineering and Technology, and the Academy of Tribotronics of Ukraine, an honorary member of the Society of Tribologists of Belarus, a fellow of ASME, IEEE, STLE, and the New York Academy of Sciences, and a member of ASEE, Sigma Xi, and Tau Beta Pi.

Dr. Bhushan has previously worked for the R&D Division of Mechanical Technology, Inc., Latham, NY; the Technology Services Division of SKF Industries, Inc., King of Prussia, PA; the General Products Division Laboratory of IBM Corporation, Tucson, AZ; and the Almaden Research Center of IBM Corporation, San Jose, CA. He has held visiting professor appointments at University of California at Berkeley; University of Cambridge, UK; Technical University Vienna, Austria; University of Paris, Orsay; ETH Zurich; and EPFL Lausanne.